AD-A268 721

AFOSR-TR- 93 0630

LBL-32305

INTERNATIONAL SYMPOSIUM ON MOLECULAR BEAMS

DTIC
ELECTE
AUG 2 5 1993
S C D

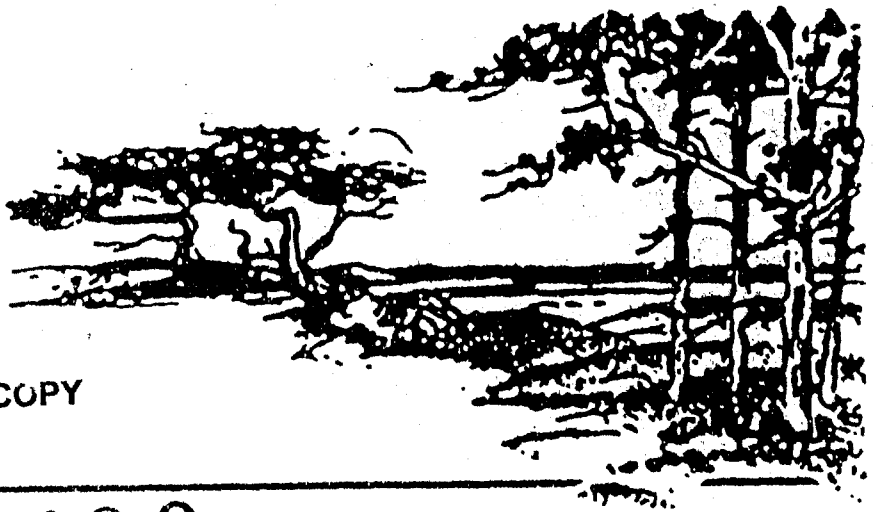

BEST AVAILABLE COPY

93 8 23 068

DISCLAIMER

This document was prepared as an account of work sponsored by the United States Government. Neither the United States Government nor any agency thereof, nor The Regents of the University of California, nor any of their employees, makes any warranty, express or implied, or assumes any legal liability or responsibility for the accuracy, completeness, or usefulness of any information, apparatus, product, or process disclosed, or represents that its use would not infringe privately owned rights. Reference herein to any specific commercial product, process, or service by its trade name, trademark, manufacturer, or otherwise, does not necessarily constitute or imply its endorsement, recommendation, or favoring by the United States Government or any agency thereof, or The Regents of the University of California. The views and opinions of authors expressed herein do not necessarily state or reflect those of the United States Government or any agency thereof or The Regents of the University of California and shall not be used for advertising or product endorsement purposes.

Lawrence Berkeley Laboratory is an equal opportunity employer

This work was prepared for the U.S. Department of Energy under Contract No. DE-AC03-76SF00098.

BEST AVAILABLE COPY

DISCLAIMER NOTICE

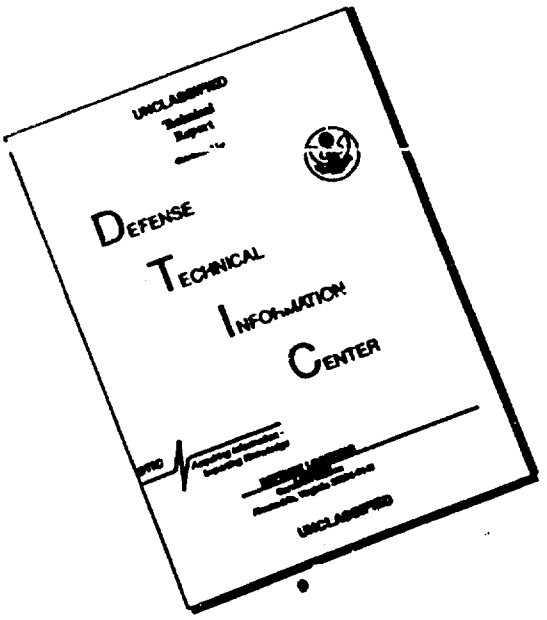

THIS DOCUMENT IS BEST QUALITY AVAILABLE. THE COPY FURNISHED TO DTIC CONTAINED A SIGNIFICANT NUMBER OF PAGES WHICH DO NOT REPRODUCE LEGIBLY.

REPORT DOCUMENTATION PAGE

Form Approved
OMB No. 0704-0188

Public reporting burden for this collection of information is estimated to average 1 hour per response, including the time for reviewing instructions, searching existing data sources, gathering and maintaining the data needed, and completing and reviewing the collection of information. Send comments regarding this burden estimate or any other aspect of this collection of information, including suggestions for reducing this burden, to Washington Headquarters Services, Directorate for Information Operations and Reports, 1215 Jefferson Davis Highway, Suite 1204, Arlington, VA 22202-4302, and to the Office of Management and Budget, Paperwork Reduction Project (0704-0188), Washington, DC 70503.

1. AGENCY USE ONLY (Leave blank)	2. REPORT DATE	3. REPORT TYPE AND DATES COVERED
	August 9, 1993	Final 04/01/92 - 03/31/93

4. TITLE AND SUBTITLE

XIV INTERNATIONAL SYMPOSIUM ON MOLECULAR BEAMS

5. FUNDING NUMBERS

F49620-92-J-0170

FQ8671-9200875

6. AUTHOR(S)

Professor Yuan T. Lee
Department of Chemistry

7. PERFORMING ORGANIZATION NAME(S) AND ADDRESS(ES)

University of California
Berkeley, CA 94720

8. PERFORMING ORGANIZATION REPORT NUMBER

LBL-32305

AFOSR-TR- 93 0630

9. SPONSORING/MONITORING AGENCY NAME(S) AND ADDRESS(ES)

AFOSR/NC
Building 410
Bolling AFB, DC 20332-6448

10. SPONSORING/MONITORING AGENCY REPORT NUMBER

11. SUPPLEMENTARY NOTES

12a. DISTRIBUTION AVAILABILITY STATEMENT

Unrestricted

12b. DISTRIBUTION CODE

13. ABSTRACT (Maximum 200 words)

The symposium was held on June 7-12, 1992 in Pacific Grove, California. It brought together scientists who work with isolated molecules to share conceptual and practical advances involved with the study of matter in a rarefied, collimated and isolated state represented by the beam. There were 26 invited talks, 25 submitted oral presentations and 78 poster papers in nine sessions on a broad range of topics. The invited talks gave general reviews and reported on recent advances on: the dissociation and predissociation dynamics of large molecular cluster ions and open shell clusters, low energy crossed beam ion-molecule reactions, the hydrogen exchange reaction, new method for manipulating laser cooled atoms, application of laser cooling to the time and frequency domain, molecular probes of quantum clusters, size dependence of elemental clusters, bouncing gases off liquid surfaces, high resolution UV and IR spectroscopy of molecular complexes, reaction dynamics beyond the Born-Oppenheimer approximation, the chemistry of hydrogen in bulk metal, and molecular dissociation on surfaces. The symposium successfully brought together chemists and physicists for a fruitful cross-fertilization of ideas and dissemination of results. The goal of facilitating students and young scientists to attend was fulfilled. There were 64 students and postdoctoral fellows among the 164 attendees.

14. SUBJECT TERMS	15. NUMBER OF PAGES
Molecular beams, clusters, reaction dynamics, spectroscopy	478
	16. PRICE CODE

17. SECURITY CLASSIFICATION OF REPORT	18. SECURITY CLASSIFICATION OF THIS PAGE	19. SECURITY CLASSIFICATION OF ABSTRACT	20. LIMITATION OF ABSTRACT
Unclassified	Unclassified	Unclassified	UL

XIVTH INTERNATIONAL SYMPOSIUM ON MOLECULAR BEAMS
JUNE 7-12, 1992

Ashraf Ali
Goddard Space Flight Center
NASA/Astro Chemistry Branch
Code 691
Greenbelt, MD
20771
(301) 286-2133
FAX: (301) 286-3271

Roger W. Anderson
Department of Chemistry
University of California, Santa Cruz
NS2 UCSC, Thimann Laboratories
Santa Cruz, CA
95065
(408) 459-2854
FAX: (408) 459-2935

Deon S. Anex
Department of Chemistry
University of California, Berkeley
Berkeley, CA
94720
(510) 486-5741
FAX:

Francisco J. Aoiz
University Complutense Madrid
Dpt. Quimica Fisica
F. Quimica Ciudad Universitaria
Madrid, 28040
Spain
34-1-394-4126
FAX: 34-1-394-4135

Don W. Arnold
Department of Chemistry
Univ. of California, Berkeley
Berkeley, CA
94720
(510) 643-9301
FAX:

Dean B. Atkinson
Chemistry Department
University of Arizona
Tucson, AZ
85721
(602) 621-4220
FAX: (602) 621-8407

Daniel J. Auerbach
IBM Research Division
Almaden Research Center
650 Harry Road, K31-802
San Jose, CA
95120-609
(408) 927-2432
FAX: (408) 927-2100

Young K. Bae
Brookhaven Laboratory
Upton, NY
11973
FAX: (516) 282-5815

Barbara A. Balko
Chemistry Department
University of Oregon
Eugene, OR
97403
(503) 346-4648
FAX: (503) 346-3422

Davide Bassi
Dipartimento di Fisica
Universitá degli Studi di Trento
I-38050 Povo, Trento
Italy
461-88-1557
FAX: 461-88-1696

Steven M. Beck
The Aerospace Corporation
P. O. Box 92957
Mail Stop M2/253
Los Angeles, CA
90009-295
(310) 336-6069
FAX: (310) 336-1636

Holly M. Bevsek
Department of Chemistry
University of Pittsburgh
Pittsburgh, PA
15260
(412) 624-8645
FAX:

Hannelore I. Bloemink
Huygens Laboratory
Leiden University
P. O. Box 9504
2300 RA Leiden
The Netherlands
31-71-275920
FAX: 31-71-275819

Ellen Boehmer
Department of Chemistry
University of Southern California
SSC-405
Los Angeles, CA
90089-048
(213) 740-7364
FAX: (213) 746-4945

Allan S. Bracker
Department of Chemistry
Univ. of California, Berkeley
Berkeley, CA
94720
(510) 486-5741
FAX: (486-5311

Philippe Brechignac
Université Paris-Sud
Laboratoire de Photophysique
CNRS
F-91405, Orsay, Cedex
France
33-1-69-41-6779
FAX: 33-1-69-41-6777

Darin R. Bristow
Chemistry Department
University of Arizona
Tucson, AZ
85721
(602) 621-4220
FAX: (602) 621-8407

Philip R. Brooks
Department of Chemistry
Rice University
P.O. Box 1892
Houston, TX
77251
(713) 527-8101, x3266
FAX: (713) 285-5155

Michel Broquier
Laboatoire de Photophysique
du CNRS, Batiment 213
Université de Paris-Sud
Orsay, 91405, Cedex
France
(1) 69416313
FAX: (1) 69416777

Bernhard Brutschy
Freie Universitat Berlin
Inst. fur Physikalische
and Theoretische Chemie
TakustraBe 3,
D-1000 Berlin 33
Germany
FAX: 030-8386612

Udo Buck
Max Planck Institut
fur Stromungsforschung
Bunsenstr. 10
D-3400 Gottingen
Germany
49-551-7092572
FAX: 49-551-7092607

Laurie J. Butler
University of Chicago
James Franck Institute
5640 S. Ellis Avenue
Chicago, IL
60637
(312) 702-7206
FAX: (312) 702-5863

Roberto Cambi
Dipartimento di Chimica dell
Via Elce di Sotto, 8
Perugia, 06100
Italy
(075) 5855520
FAX: (075) 5855606

Sylvia T. Ceyer
Department of Chemistry
Massachusetts Inst. of Technology
77 Massachusetts Avenue
Cambridge, MA
02139-430
(617) 253-4537
FAX: (617) 253-7030

Pavel L. Chapovsky
Huygens Laboratory
Leiden University
P. O. Box 9504
2300 RA Leiden
The Netherlands
31-71-275932
FAX: 31-71-275819

Ori Cheshnovsky
Chemistry Department
Tel-Aviv University
69978 Tel-Aviv
Israel
972-3-6408628
FAX:

James D. Chesko
Department of Chemistry
University of California, Berkeley
Berkeley, CA
94720
(510) 486-5741
FAX: (510) 486-5311

Su-Yu Chiang
Department of Chemistry
University of California, Berkeley
Berkeley, CA
94720
(510) 486-6447
FAX: (510) 486-5311

Steven Chu
Physics Department
Stanford University
Stanford, CA
94305-406
(415) 723-3571
FAX: (415) 723-9173

Pedro Cid-Aguero
Department of Chemistry
University of New Mexico
103 Clark Hall
Albuquerque, NM
87131-109
(505) 277-3213
FAX: (505) 277-2609

Joseph I. Cline
Dept. of Chemistry,MS 216
University of Nevada
Reno, NV
89557-002
(702) 784-6041
FAX: (702) 784-6804

Jennifer I. Colonell
University of Chicago
JFI
5640 S. Ellis Avenue
Chicago, IL
60637
(312) 702-7205
FAX: (312) 702-5863

Daniela P. Consalvo
Molecular and Laser Physics
University of Nijmegen
Toernooiveld
6525 ED Nijmegen
The Netherlands
0031/80/653029
FAX: 0031/80/553450

Robert E. Continetti
Department of Chemistry
Univ. of California, Berkeley
Berkeley, CA
94720
(510) 643-9301
FAX:

R. James Cross, Jr.
Department of Chemistry
Yale University
P.O. Box 6666
New Haven, CT
06511
(203) 432-5203
FAX: (203) 432-6144

Donna M. Cyr
Chemistry Department
Yale University
225 Prospect Street
New Haven, CT
06511
(203) 432-3988
FAX: (203) 432-6144

Douglas R. Cyr
Univ. of California, Berkeley
Berkeley, CA
94720
(510) 643-9301
FAX:

H. Floyd Davis
Department of Chemistry
University of California, Berkeley
21-DG26, Giauque Hall
Hildebrand
Berkeley, CA 94720
(510) 486-5741
FAX: (510) 486-5311

Maarten F.M. DeKieviet
Department of Chemistry
Princeton University
Frick Chem. Labs. Room 106
Princeton, NJ
08544
(609) 258-3357
FAX: (609) 258-6746

Adalbert M.G. Ding
Optical Institute
Technical Universite Berlin
Sekr. P11.
StraBe d. Juni 135
D-100 Berlin 12
Germany
(30) 314-25988
FAX: (30) 315-82-100

R. Bruce Doak
Dept. of Physics & Astronomy
Arizona State University
Tempe, AZ
85287-150
(602) 965-0640
FAX: (602) 965-7954

Jan P.J Driessen
Joint Inst. for Laboratory
University of Colorado
P.O. Box 440
Boulder, CO
80309-044
(303) 492-2942
FAX: (303) 492-5235

Michael A. Duncan
Department of Chemistry
University of Georgia
Athens, GA
30602
(404) 542-1998
FAX: (404) 542-9454

Roberta Fantoni
ENEA INN/SVIL
C.P. 65
I-00044 Frascati
Italy
39-6-9400-5568
FAX: 39-6-9400-5400

John B. Fenn
Dept. of Chemical Engineering
Yale University
P. O. Box 2159 Yale Station
New Haven, CT
06520-215
(203) 432-4379
FAX: (203) 432-7232

Troy W. Francisco
Department of Chemistry
Univ. of North Carolina, Chapel Hill
3290 Venable Hall
Chapel Hill, NC
27599-329
(919) 962-1579
FAX: (919) 962-2388

Ethan B. Gallogly
Department of Chemistry
University of California, Davis
Davis, CA
95616
(916) 752-8475
FAX: (916) 752-8995

W. Ronald Gentry
Department of Chemistry
University of Minnesota
207 Pleasant Street, S.E.
Minneapolis, MN
55455
(612) 625-2894
FAX: (612) 626-8659

Brian D. Gilbert
Department of Chemistry
Indiana University
Bloomington, IN
47405
(812) 855-6700
FAX:

Christopher M. Gittins
Department of Chemistry, Bldg.
Massachusetts Institute of
Cambridge, MA
02139
(617) 253-6295
FAX: (617) 253-7030

Thomas Glenewinkel-Meyer
Department of Chemistry
University of Wisconsin
1101 University Avenue
Madison, WI
53706
(608) 262-6101
FAX: (608) 262-0381

David S. Green
Department of Chemistry
Stanford University
Stanford, CA
94305-508
(415) 723-4332
FAX: (415) 725-0259

Richard J. Green
Department of Chemistry
Stanford University
Stanford, CA
94305-508
(415) 723-4332
FAX: (415) 725-0259

Nadine Halberstadt
University Paris-sud
CNRS
Laboratoire de Photophysique
Moleculaire, Bat. 213
91405 Orsay Cedex
France
FAX: 33-1-6941-6777

Tom F. Hanisco
Dept. of Chemistry, 0314
University of California, San Diego
La Jolla, CA
92093
(619) 534-3498
FAX: (619) 534-7042

Yoshihiko Hatano
Tokyo Institute of Technology
Ohkayama 2-12-1, Meguro-ku
Tokyo 152,
Japan
03-3726-111,ext. 2235
FAX: 81-3-3729-0099

Michael Hawley
Chemical Dynamics & Diagnostics Br.
Department of the Navy
Naval Research Laboratory
Code 6111
Washington, D.C. 20375
(202) 767-6816
FAX:

Brian Elliott Hayden
Department of Chemistry
University of Southampton
Highfield, Southampton, S09 5NH
United Kingdom
(0703) 592776
FAX: (070) 593781

Michael C. Heaven
Department of Chemistry
Emory University
1515 Pierce Drive
Atlanta, Georgia
30322
(404) 727-6617
FAX: (404) 727-6586

Victor J. Herrero
Instituto de Estructura
de la Materia (CSIC)
Serrano 119-123
28006, Madrid, Espana
Spain
FAX: 34-1-5642431

Dudley R. Herschbach
Department of Chemistry
Harvard University
Cambridge, MA
02138
(617) 495-3218
FAX: (617) 495-1792

B. Jane Hinch
Dept. of Chemistry, Busch Campus
Laboratory for Surface Modification
Rutgers University
Piscataway, NJ
08855
(908) 932-0663
FAX: (908) 932-5312

Hongtao Hou
Department of Chemistry
University of California, Berkeley
Berkeley, CA
94720
(510) 486-6447
FAX: (510) 486-5311

Paul L. Houston
Baker Lab. of Chemistry
Cornell University
Ithaca, NY
14853-130
(607) 255-4303
FAX: (607) 255-8549

Stanislav Ionov
Department of Chemistry
University of Southern California
405 Hilgard Avenue
Los Angeles, CA
90089-048
(213) 740-7364
FAX: (213) 746-4945

William M. Jackson
Department of Chemistry
University of California, Davis
Davis, CA
95616
(916) 752-7082
FAX: (916) 752-8995

Dennis C. Jacobs
Dept. of Chemistry & Biochemistry
University of Notre Dame
Notre Dame, IN
46556
(219) 239-8023
FAX: (219) 239-6652

Kenneth C. Janda
Department of Chemistry
University of California, Irvine
Irvine, CA
92717
(714) 856-6015
FAX: (714) 856-8571

Maurice H.M. Janssen
Chemistry Department
Free University, Amsterdam
De Boelelaan 1083
Amsterdam 1081 HV
The Netherlands
+31 (20) 5485362
FAX:

Konstantinos Kalogerakis
Department of Chemistry
Stanford University
Stanford, CA
94305-508
(415) 723-4332
FAX: (415) 725-0259

Toshio Kasai
Department of Chemistry
Osaka University
Faculty of Science
Toyonaka, Osaka 560
Japan
06-844-1151, ext. 4206
FAX: 06-855-8139

Mark Keil
Department of Chemistry
University of Alberta
Edmonton, Alberta
Canada
T6G 2G2
(403) 492-2853
FAX: (403) 492-8231

Theofanis N. Kitsopoulos
Sandia National Laboratory
Organization 8353
Livermore, CA
94551
(510) 294-1495
FAX: (510) 294-2276

William Klemperer
Department of Chemistry
Harvard University
12 Oxford Street
Cambridge, MA
02138
(617) 495-4094
FAX: (617) 495-1792

Mark B. Knickelbein
Chemistry Division
Argonne National Laboratory
A-Wing, Building 200
9700 S. Cass Avenue
Argonne, IL 60439
(708) 252-3462
FAX: (708) 252-4993

Wei Kong
Department of Chemistry
University of Waterloo
Waterloo Ontario
N2L 3G1,
FAX:

Vitaly V. Kresin
Mail Stop L-268
Lawrence Livermore Laboratory
P. O. Box 808
Livermore, CA
94550
(510) 422-7248
FAX: (510) 422-7300

Andrew H. Kung
Lawrence Berkeley Laboratory
1 Cyclotron Road
Berkeley, CC
94720
(510) 643-6413
FAX:

Christoph P. Lahmann
Freie Universität Berlin
Institut füu Physikalische Chemie
Takustr. 3
D-1000, Berline 33
Germany
49-30-8385361
FAX: 49-30-838-6612

Derek C. Lainé
Physics Department
University of Keele
Keele Staffordshire, ST5 5BG
United Kingdom
44-782-5833338
FAX: 44-782-711093

Darin R. Latimer
Chemistry Department
University of Arizona
Tucson, AZ
85721
(602) 621-4220
FAX: (602) 621-8407

Yuan T. Lee
Chemical Sciences Division
Department of Chemistry
University of California, Berkeley
Berkeley, CA
94720
(510) 486-6154
FAX: (510) 486-5311

Florence J. Lin
Department of Mathematics
University of California, Berkeley
Berkeley, CA
94720
FAX: (510) 642-8204

W. Carl Lineberger
University of Colorado, JILA
Boulder, CO
80309
(303) 492-7834
FAX: (303) 492-8994

Cheryl A. Longfellow
Department of Chemistry
University of California, Berkeley
Berkeley, CA
94720
(510) 486-5741
FAX: (510) 486-5311

Elizabeth J. Longley
University of Pittsburgh
Chevron Science Center
Pittsburgh, PA
15260
FAX:

Nan-Quan Lou
Dalian Inst. of Chemical Physics
Chinese Academy of Sciences
Dalian, Liaoning, 116012
People's Republic of China
86-411-331841
FAX: 86-411-332426

Ruth I. McKay
Department of Chemistry
Stanford University
Stanford, CA
94305-508
(415) 723-4340
FAX: (415) 725-0259

W. Leo Meerts
University of Nijmegen
Toernooiveld
6525 xx Nijmegen
The Netherlands
80-653023
FAX: 80-553450

Gerard Meijer
Dept. of Molecular and Laser Physics
University of Nijmegen
Toernooiveld
6525 ED Nijmegen
The Netherlands
31-80-652277
FAX: 31-80-553450

Tzong-Tsong Miau
Department of Chemistry
University of California, Berkeley
Berkeley, CA
94720
(510) 486-5741
FAX: (510) 486-5311

David R. Miller
Dept. A.M.E.S. - 0310
University of California, San Diego
La Jolla, CA
92093-031
(619) 534-3182
FAX: (619) 534-5354

Roger E. Miller
Department of Chemistry
Univ. of North Carolina
Chapel Hill, NC
27599
(919) 962-0528
FAX: (919) 962-2388

Timothy K. Minton
Mail Stop 67-201
Jet Propulsion Laboratory
4800 Oak Grove Drive
Pasadena, CA
91109
(818) 354-8580
FAX: (818) 393-6869

James D. Myers
Department of Chemistry
University of California, Berkeley
Berkeley, CA
94720
(510) 486-6447
FAX: (510) 486-5311

Ron Naaman
Dept. of Chemical Physics
Weizmann Institute of Science
Rehovot 76100,
P. O. B. 26
Israel
972-8-342367
FAX: 972-8-344123

Masato Nakamura
Aono Atomcraft Project
ERATO, JRDC
1-7-13, Kaga, Itabashi-ku
Tokyo, 173
Japan
FAX: +81-3-3961-1408

Gilbert M. Nathanson
Department of Chemistry
University of Wisconsin
1101 University Avenue
Madison, WI
53706
(608) 262-8098
FAX: (608) 262-0381

Daniel M. Neumark
Department of Chemistry
University of California, Berkeley
Berkeley, CA
94720
(510) 642-3502
FAX: (510) 642-6262

Hans Neusser
Institut fur Physikalische
und Theoretische Chemie
Technische Universitat Munchen
LichtenbergstraBe 4
8046 Garching
Germany
89/32093388
FAX: 89/32093389

Simon W. North
Department of Chemistry
University of California, Berkeley
Berkeley, CA
94720
(510) 486-6447
FAX: (510) 486-5311

Simone M. O'Shaughnessy
Physics Department
Keele University
Keele, Staffordshire, ST5 5BG
United Kingdom
0782-583308
FAX: 0782-711093

Ann E. Orel
Dept. of Applied Science
Univ. of California, Davis
c/o Lawrence Livermore Natl. Lab.
P. O. Box 808, L-794
Livermore, CA 94550
(510) 422-3363
FAX: (510) 422-9180

Andrew J. Orr-Ewing
Department of Chemistry
Stanford University
Stanford, CA
94305
(415) 723-4334
FAX: (415) 725-0259

David L. Osborn
Department of Chemistry
Univ. of California, Berkeley
Berkeley, CA
94720
(510) 643-9301
FAX: (510) 642-8369

Charles S. Parmenter
Indiana University
c/o University of Colorado
JILA, Campus Box 440
Boulder, CO
80309
(303) 492-8498
FAX: (303) 492-5235

Brooks H. Pate
Natl Inst. of Science & Technology
Molecular Physics, Bldg. 221
Gathersburg, MD
20899
(301) 975-2380
FAX: (301) 975-3038

Anthony W. Pearson
Department of Chemistry
University of California, Santa Cruz
NS2 UCSC
Santa Cruz, CA
95065
FAX:

John M. Price
Department of Chemistry
University of California, Santa
Santa Barbara, CA
93106
(805) 893-8552
FAX:

Edwin Quiñones-Gonzales
Department of Chemistry
University of Puerto Rico
Rio Piedras Campus
P. O. Box 23346-UPR Station
Rio Piedras, Puerto Rico 00931-334
FAX:

Klaus Rademann
Philipps University
FB14 Hans-Meerwein-Strasse
Marburg, W-3550, Germany
06421-28-2402
FAX: 06421-28-5551

Age Raukema
FOM-Institute for Atomic
and Molecular Physics
Kruislaan 407
1098 SJ Amsterdam
The Netherlands
(31) 20-6081234
FAX: (31) 20-6684106

Katharine L. Reid
Department of Chemistry
Stanford University
Stanford, CA
94305
(415) 723-4340
FAX: (415) 725-0259

Scott A. Reid
Department of Chemistry
University of Southern California
SSC-612
Los Angeles, CA
90089-048
(213) 740-4105
FAX: (213) 746-4945

Jörg Reuss
Molecular & Laser Physics
University of Nijmegen
Facility of Science
Drihuizvwed 200
Nijmegen
The Netherlands
31-80-652101
FAX: 31-80-553450

Mark August Roehrig
Chemistry Department
University of Arizona
Tucson, AZ
85721
(602) 621-6618
FAX: (602) 621-8407

Christopher Rogaski
Department of Chemistry
University of California, Santa
Santa Barbara, CA
93106
(805) 893-8552
FAX:

Sanford A. Safron
Department of Chemistry
Florida State University
Tallahassee, FL
32306-300
(904) 644-5239
FAX: (904) 644-8281

Adi A. Scheidemann
Department of Chemistry
University of Washington
Mail Stop BG 10
Seattle, WA
98195
(206) 543-7961
FAX: (206) 685-8665

Stephan Schlemmer
Department of Chemistry
Univ. of California, Berkeley
Berkeley, CA
94720
(510) 642-5891
FAX: (510) 642-8369

Claus P. Schulz
Fakultät fr Physik
University Freiburg
Hermann-Herderstr.3
D-7800 Freiburg/Br
Germany
++49-761-203-4097
FAX: ++49-761-203-4527

Giacinto Scoles
Chemistry Department
Princeton University
Princeton, NJ
08544
(609) 258-5570
FAX: (609) 258-6746

Mario Scotoni
Dipartimento di Fisica
Universitá degli Studi di Trento
I-38050 Povo, Trento
Italy
461-88-1557
FAX: 461-88-1696

David C. Scott
Department of Chemistry
University of Southern California
SSC 601
Los Angeles, CA
90089-048
(213) 740-7015
FAX: (213) 746-4945

Jeffrey Segall
Department of Chemistry
University of Southern California
Mail Code 0482
Los Angeles, CA
90089-048
(213) 740-7364
FAX: (213) 746-4945

Neil E. Shafer
Department of Chemistry
Stanford University
Stanford, CA
94305-508
(415) 725-2983
FAX: (415) 725-0259

Ramesh D. Sharma
Optical Environment Division
Phillips Laboratory (AFSC)
Hanscom Air Force Base
Hanscom, MA
01731-500
(617) 377-4198
FAX: (617) 377-8780

William R. Simpson
Department of Chemistry
Stanford University
Stanford, CA
94305
(415) 723-4398
FAX: (415) 725-0259

Richard E. Smalley
Rice Quantum Inst. & William Marsh
Department of Chemistry & Physics
Rice University
Houston, TX
77251
(713) 527-4845
FAX: (713) 285-5320

Laura A. Smoliar
Department of Chemistry
Univ. of California, Berkeley
Berkeley, CA
94720
(510) 486-5741
FAX: (510) 486-5311

Marcel Snels
CNR Tito (PZ)
Via S. Loja - Zoma
Industriale Di Tito Scalo
Potenza, 85050
Italy
39-6-49913312
FAX: 39-971-427222

Daniel Solgadi, Jr.
Laboatoire de Photophysique
du CNRS, Batiment 213
Université de Paris-Sud
Orsay, 91405, Cedex
France
(1) 69416313
FAX: (1) 69416777

Stephanie Soulen
Stanford University
Chemical Engineering
Stauffer III, Room 113
Stanford, CA
94305-502
(415) 723-3750
FAX: (415) 723-9780

Caroline P. Starrs
Department of Chemistry
University of Waterloo
Waterloo, Ontario
N2L 3G1
(519) 885-1211, ext. 3845
FAX: (519) 746-0435

Wolfgang Stiller
Theoretical Kinetics Group
Ferdinand-Lassalle Str. 6
D-0-7050, Leipzig
Germany
FAX:

James A. Stinnett
Stanford University
Chemical Engineering
Stauffer III, Room 113
Stanford, CA
94305-502
(415) 723-3750
FAX: (415) 723-9780

Franco Strumia
University of Pisa
Dept. Fisica
Torricelli 2
Pisa, 56126
Italy
011-39-50-45222
FAX: 011-39-50-48277

Arthur Suits
Baker Laboratory
Cornell University
Box 199
Ithaca, NY
14853
(607) 255-6419
FAX: (607) 255-8549

Toshinori Suzuki
Department of Chemistry
University of California, Berkeley
Berkeley, CA
94720
(510) 486-6447
FAX: (510) 486-5311

Yusheng Tao
Dalian Institute of Chemical Physics
Chinese Academy of Sciences
P. O. Box 110, Dalian
China
471991 ext. 621
FAX: 86-411-332426

Jeffrey L. Tomer
Department of Chemistry/216
University of Nevada
Reno, NV
89557
(702) 784-6041
FAX: (702) 784-6804

Paolo Tosi
Dipartimento di Fisica
Universitá degli Studi di Trento
I-38050 Povo, Trento
Italy
461-88-1557
FAX: 461-88-1696

Athanassios Tsekouras
Department of Chemistry
Stanford University
Stanford, CA
94305
(415) 723-4333
FAX: (415) 725-0259

Shao-Hui Tseng
Department of Chemistry,BG-10
University of Washington
Seattle, WA
98195
(206) 543-4108
FAX: (206) 685-8665

A. Ureña
Departamento de Quimica Fisica
Facultad de Ciencias Quimicas
Universidad Complutense
28040 Madrid
Spain
FAX:

Franco Vecchiocattivi
Dipartimento di Chimica
Universitàt Di Perugia
Via Elce di Sotto, 8
06100 Perugia
Italy
39-75-585-5509
FAX: 39-75-585-5606

Gert von Helden
Department of Chemistry
Univ. of California, Santa Barbara
Santa Barbara, CA
93106
(805) 893-2673
FAX: (805) 893-8703

Marc J.J. Vrakking
Department of Chemistry
University of California, Berkeley
Berkeley, CA
94720
(510) 486-5741
FAX: (510) 486-5311

Helmut Weiss
Instut für Physikalische Chemie
Callinstr. 3-3a
3000 Hanover 1,
Germany
(0511) 762-4270
FAX: (0511) 762-4009

Karl H. Welge
Department of Physics
University of Bielefeld
D-4800 Bielefeld 1
Germany
0049-521-106-5441
FAX: 49-521-106-5244

K. Birgitta Whaley
Department of Chemistry
University of California, Berkeley
Berkeley, CA
94720
(510) 643-6820
FAX: (510) 642-8369

Fiona Winterbottom
Chemistry Department
University of Southern California
Los Angeles, CA
90089-048
(213) 740-7015,4105
FAX: (213) 746-4945

Alec M. Wodtke
Department of Chemistry
Univ. of California, Santa Barbara
Santa Barbara, CA
93106
(805) 893-8552
FAX: (805) 893-4120

Ludger Wöste
Freie Universitat Berlin
Fachbreich Physik
Inst. fur Experimentalphysik
Armilmallee 14
D-1000 Berlin 33
Germany
49-30-838-5566
FAX: 49-30-838-5567

Jinchun Xie
Department of Chemistry
Stanford University
Stanford, CA
94305
FAX:

Xueming Yang
Department of Chemistry
Princeton University
Princeton, NJ
08544
(609) 258-3357
FAX: (609) 258-6746

Jingsong Zhang
Department of Chemistry
University of California, Berkeley
Berkeley, CA
94720
(510) 486-5741
FAX: (510) 486-5311

Qi-He Zhu
Institute of Chemistry
Chinese Academy of Sciences
Zhong-Guan-Cun
Beijing 100080
People's Republic of China
86-01-2554245
FAX: 86-01-2569564

XIVth INTERNATIONAL SYMPOSIUM ON MOLECULAR BEAMS

Accesion For	
NTIS CRA&I	☒
DTIC TAB	☐
Unannounced	☐
Justification	
By	
Distribution /	
Availability Codes	
Dist	Avail and / or Special
A-1	

JUNE 7–12, 1992

Asilomar Conference Center
Pacific Grove, California USA

DTIC QUALITY INSPECTED 3

It is a pleasure to acknowledge the following organizations for their support of this conference:

The National Science Foundation, the Air Force Office of Scientific Research, and the Department of Energy.

Table of Contents

Dedication - Professor William Klemperer iv

List of Committees vi

Program vii

Listing of Posters xi

Session I: Clusters I 1

Session II: Reaction Dynamics 21

Session III: Atomic and Molecular Spectroscopy 39

Session IV: Poster Session (abstracts begin on page 193) 65

Session V: Clusters II 67

Session VI: New Techniques 89

Session VII: Molecular Spectroscopy 109

Session VIII: Photodissociation & Dynamics 135

Session IX: Surfaces 165

Poster Session Abstracts 193

Author Index 469

Professor B.F. Klemperer

This year's "extra" North-American edition of the International Symposium on Molecular Beams, as two of the previous European editions, is dedicated to a scientist who has given an exceptional contribution to the development of the field.

Indeed very few molecular beam scientists have, through their experiments and through the work of their students, had an impact on the rest of the community comparable to that of Bill Klemperer.

Professor Klemperer was born in New York City in 1927. After service in the United States Navy, he entered Harvard College and received a B.A. degree in 1950. His Ph.D. degree was obtained at the University of California, Berkeley (1954), where he studied with Professor George Pimentel. He joined the faculty at Harvard University as an Instructor in Analytical Chemistry in 1954. He has remained there except for brief absences in 1968-69 when he spent a sabbatical year at Cambridge, England, and in 1979-81 when he was at The National Science Foundation as Assistant Director for Mathematical and Physical Sciences. Professor Klemperer is a member of The National Academy of Sciences, The American Academy of Arts and Sciences, The American Chemical Society and The American Physical Society. He has received the Wetherill Medal from the Franklin Institute, the Irving Langmuir Award in Chemical Physics from The American Chemical Society, the Earle K. Plyler Award from The American Physical Society and the Bomen Michelson Award from The Coblentz Society. He has also received the Distinguished Service Medal from The National Science Foundation.

Professor Klemperer's research interests lie in the area of molecular structure, energy transfer and intermolecular forces. Most of the research done in this area by him and his collaborators have involved experimental spectroscopic methods and molecular beams. In the latter area he was responsible for initiating and developing the high resolution methods to determine the structure and electrostatic properties of van der Waals molecules. He has also worked on modelling molecule formation and detection in the interstellar medium. The scientific message contained in his papers is always crystal clear and the logic of presentations cogent and direct. Because of this and because of his exceptional human qualities he has had a lasting influence on the students and postdoctoral fellows who were fortunate enough to work in his laboratory.

Therefore, we are extremely happy to have the opportunity to dedicate this book of abstracts to Bill Klemperer wishing him and his family all the best for his 65th Birthday and beyond.

Fellows of the Symposium:

F.M. Devienne, J.B. Fenn

Symposium Secretary:

J. Reuss

International Advisory Committee:

D. Bassi (Italy), J. Baudon (France), C. Bréchignac (France), M. Broyer (France), R. Campargue (France, O. Cheshnovsky (Israel), A. Ding (Germany), W.R. Gentry (USA), A. Giardini-Guidoni (Italy), A. Gonzalez-Ureña (Spain), H. Haberland (Germany), K. Janda (USA), A. Kleyn (NL), T. Kondow (Japan), J. Korving (NL), D.C. Lainé (UK), V.B. Leonas (USSR), K.H. Meiwes-Broer (Germany), A. Moutinho (Portugal), Lou Nan Quan (China), D. Pratt (USA), J. Reuss (NL), L. Rusin (USSR), E. Schumacher (Switzerland), G. Scoles (USA), F. Vecchiocattivi (Italy), J.C. Whitehead (UK), L. Wöste (Germany), I. Yamada (Japan).

Local Organizing Committee

D. Auerbach, J. Bowman, S. Ceyer, Y.Q. Chen, W.R. Gentry, K. Janda, Y.T. Lee (co-chair), W. Knight, T. Kondow, A.H. Kung, D. Miller, D.M. Neumark, D. Pratt, G. Scoles (co-chair)

Monday — June 8, 1992

7:30 a.m. BREAKFAST

8:30 a.m. **G. Scoles,** *Opening Remarks*

Session I: Clusters I

8:35 **D.M. Neumark,** *Chair*

8:45 **W.C. Lineberger,** *Time-Resolved Dissociation/Recombination Dynamics in Large Molecular Cluster Ions*

9:30 **M.C. Heaven,** *Predissociation Dynamics of Open-Shell Clusters*

10:00 BREAK

10:30 **U. Buck,** *Size Effects and Vibrational Dynamics of Large Clusters from He Atom Scattering*

11:15 **N. Halberstadt,** *IVR. in a Triatomic van der Waals Molecule: Ar . . . Cl_2*

11:45 **E.Th. Kerstel, G. Scoles, X. Yang,** *Predissociation Dynamics and Structure of Hydrogen Bonded Cyanoacetylene Complexes*

12:00 **R.I. McKay, E.J. Bieske, F.R. Bennett, A.E.W. Knight,** *Low Frequency Vibrational Motion of Aromatic – Rare Gas Cationic Clusters Observed via Resonance-Enhanced Photofragment Spectroscopy*

12:15 p.m. LUNCH

1:00 INFORMAL DISCUSSION

6:00 DINNER

Session II: Reaction Dynamics

7:30 p.m. **A.G. Ureña,** Chair

7:45 **P. Tosi, O. Dmitrijev, Y. Soldo and D. Bassi,** *Low Energy Crossed Beam Experiments on Ion-Molecule Reactions*

8:15 **L. Schnieder, K. Welge**, *The Hydrogen Exchange Reaction in Crossed Beams*

8:45 **J. Zhang, T.T. Miau,Y.T. Lee,** *Crossed Molecular Beam Studies of the Reactions Cl + O_3 and Br + O_3*

9:00 **F. Vecchiocattivi,** *Autoionization Dynamics of Collisional Complexes*

9:30 **D.R. Herschbach,** *Pendular Molecules and Perverse Reaction Paths*

10:00 INFORMAL DISCUSSION

Tuesday — June 9, 1992

7:30 a.m. BREAKFAST

Session III: Atomic & Molecular Spectroscopy

8:30 a.m. **A.M. Wodtke**, *Chair*

8:45 **S. Chu**, *New Method for Manipulating Laser Cooled Atoms*

9:30 **F. Strumia**, *Application of Laser Cooling to the Time and Frequency Metrology*

10:00 BREAK

10:30 **Y. Hatano**, *Dissociation Dynamics of Superexcited Molecules*

11:00 **T.J. Slotterback, K.C.Janda, J.R. Johnson, D.W. Pratt, C.M. Western**, *High Resolution Spectroscopy of ICl: Rehybridization as a Function of Bond Length*

11:15 **W. Kong, D. Rodgers, J.W. Hepburn,** *Ultrahigh Resolution Threshold Photoelectron Spectroscopy of Small Molecules Using Extreme Ultraviolet Lasers*

11:30 **C. Gittins, N. Harris, R. Field,** *Rydberg States of CaF: Healing a Scar in the 's' Σ Series*

11:45 **B.D. Gilbert, C.S. Parmenter, C.J. Pursell,** *Rovibrational Energy Transfer in S_1 D_2CO Using Crossed Molecular Beams*

12:00 p.m. LUNCH

1:00 INFORMAL DISCUSSION

6:00 DINNER

Session IV: Poster Session

7:30 p.m. SESSION IV POSTERS *(posters are listed beginning on page 194)*

10:00 INFORMAL DISCUSSION

Wednesday — June 10,1992

7:30 a.m. BREAKFAST

Session V: Clusters II

8:30 a.m. **L. Wöste,** *Chair*

8:45 **R.E. Smalley**, *Doping the Fullerenes*

9:30 **K.B. Whaley, R.N. Barnett, M. McMahon**, *Molecular Probes of Quantum Clusters: Impurity Species in He_N and $(H_2)_N$*

10:00 BREAK

10:30 **K. Rademann**, *Elemental Clusters in Molecular Beams: Size Dependent Effects*

11:15 **S. Goyal, D.L. Schutt, G. Scoles,** *On the Spectroscopy of Seeded Hydrogen and Helium Clusters*

11:30 **C.P. Schulz, A. Goerke, I.V. Hertel,** *Scattering Experiments with Small Sodium Clusters: Elastic, Inelastic and Reactive Processes*

11:45 **V.V. Kresin, W.D. Knight,** *Collective Resonances of Valence Electrons in Free Metal Clusters*

12:00 **M.A. Duncan,** *Spectroscopy of Metal Atom and Metal Cluster Complexes*

12:15 p.m. LUNCH

1:00 INFORMAL DISCUSSION

6:00 BANQUET – CROCKER DINING HALL

Session VI: New Techniques

8:00 p.m. **J.B. Fenn**, *Chair*

8:15 **M.E. King, S.T. Govoni, M.E. Saecker, D.V. Kowalski, M. Hanning-Lee, T.K. Minton and G.M. Nathanson**, *Bouncing Gases off Liquid Surfaces*

8:45 **Y.K. Bae, R.J. Beuhler, Y.Y. Chu, G. Friedlander, L. Friedman**, *Cluster Impacts: A Chemical Approach to Fusion*

9:15 **G. Tepper, D. Miller**, *Diffractive Scattering of Hydrogen Clusters from LiF(001)*

9:30 **J.P.J. Driessen, C.J. Smith, L. Eno, R. de Vivie, S.R. Leone,** *Three Vector Correlation Study of Ca(4s5p, $^1P_1$)+ He→Ca(4s5p,$^3P_2$)+He*

9:45 **J.M. Price, A. Ludviksson, M. Nooney, M. Xu, R.M. Martin, A.M. Wodtke**, *Time of Flight Measurements of Single Rovibrational States of Carbon Monoxide*

10:00 **R.E. Continetti, D.R. Cyr, D. Osborne, D.M. Neumark**, *Fast Beam Photodissociation of Free Radicals*

10:15 INFORMAL DISCUSSION

Thursday — June 11, 1992

7:30 a.m. BREAKFAST

Session VII: Molecular Spectroscopy

8:30 a.m. **W. Klemperer**, *Chair*

8:45 **H.J. Neusser**, *High Resolution UV Spectroscopy of Molecular van der Waals Complexes*

9:30 **K.K. Lehmann, G. Scoles, G.T. Fraser, B.H. Pate**, *Vibrational Dynamics and Molecular Structure: High Resolution Infrared Spectroscopy of the Fundamental and First Overtone of the Hydride Streches in Large Molecules*

10:00 BREAK

10:30 **W.L. Meerts**, *High Resolution Laser Spectroscopy from the XUV to the Visible*

11:00 **G. Meijer, G. Berden, W.L. Meerts, H.E. Hunziker, M.S. De Vries, H.R. Wendt,** *Spectroscopy on Triphenylamine and Its van der Waals Complexes*

11:30 **S. te Lintel Hekkert, A. Linskens, J. Reuss,** *Molecular Beam Study of IR Multiphoton Excitation with High Resolution*

11:45 **J.M. Price, C.A. Rogaski, J. Mack, G.V. Helden, X. Yang, A.M. Wodtke,** *Stimulated Emission Pumping of Acetaldehyde and Propynal: Influence of Molecular Structure on the High Resolution Vibrational Spectrum*

12:00 p.m. LUNCH

1:00 INFORMAL DISCUSSION

6:00 DINNER

Session VIII: Photodissociation & Dynamics

7:30 p.m. **W.R. Gentry,** *Chair*

7:45 **L.J. Butler**, *Chemical Reaction Dynamics Beyond the Born-Oppenheimer Approximation*

8:15 **A. Suits, L.S. Bontuyan,P.L. Houston**, *Differential Cross Sections for State-Selected Products by Direct Imaging: Ar + NO*

8:45 **E.R. Lovejoy, S.K. Kim, and C.B. Moore,** *Observation of Transition State Vibrational Thresholds in the Rate of Dissociation of Ketene*

9:00 **S.I. Ionov, G.A. Brucker, Y. Chen, C. Jaques, C. Wittig,** *Real-Time Observation of a Step-Like k_{uni} vs. E Dependence for the Near Threshold Decomposition of NO_2*

9:15 **H.F. Davis, Y.T. Lee,** *Mode Specific Photodissociation Dynamics of OCIO*

9:30 **Th. Glenewinkel-Meyer, J.A. Bartz, F.F. Crim,** *Photodissociation of Silane in a Supersonic Expansion*

9:45 **M. Fieber-Erdmann, T. Drewello, W. Krätschmer and A. Ding**, *Double Photoionization Dynamics of Free Fullerenes*

10:00 INFORMAL DISCUSSION

Friday — June 12, 1992

7:30 a.m. BREAKFAST

Session IX: Surfaces

8:30 a.m. **R. Naaman**, *Chair*

8:45 **A.D. Johnson, S.P. Daley, A.L. Utz, S.T. Ceyer**, *The Chemistry of Hydrogen in Bulk NI*

9:30 **B.E. Hayden**, *Molecular Beam Studies of Dissociation at Surfaces*

10:00 BREAK

10:30 **S.A. Safron, J. Duan, G.G. Bishop, E.S. Gillman, G. Chern and J.G. Skofronick**, *Investigation of Homo- and Heteroepitaxial Growth on Ionic Insula. ors via He Atom Scattering*

11:00 **H. Weiss**, *Adsorption on Insulator Surfaces Studied by Helium Atom Scattering: Structure and Dynamics*

11:30 **J.I. Colonell, T.J. Curtiss, K.A. Peterlinz, S.J. Sibener,** *Coverage Dependent Desorption Kinetics of CO and H_2 from Rh(111) Using Time-Resolved Specular Helium Scattering*

11:45 **B.J. Hinch, R.B. Doak, L.H. Dubois,** *Aluminum Chemical Vapor Deposition and Surface Topographical Changes as Monitored by Helium Atom Diffraction*

12:00 **D.J. Auerbach, C.T. Rettner, H.A. Michelsen,** *Interaction Dynamics of Hydrogen at a Cu(111) Surface*

12:15 p.m. **Y.T. Lee,** *Closing Remarks*

No.

Listing of Poster Papers

1. Anex, D.S., Stolow, A., Lee, Y.T., Molecular Beam Studies of the Photodissociation of Silane 157 nm
2. Aoiz, F. J., Herrero, V.J., Rabanos, V. Saez, Quasiclassical State Resolved Cross Sections for the Reaction $D + H_2(\upsilon=0, j=0) \rightarrow HD(\upsilon',j') + H$. Evidence for Classical Collision Complexes
3. Aquilanti, V., Candori, R., Cappelletti, D., Luzzatti, E., Pirani, F., Magnetic Analysis of Molecular Beams in the Transmission Mode: Zeeman Effect for Diatomic Molecules
4. Aquilanti, V., Cappelletti, D., Liuti, G., Lorent, V., Pirani, F., Interatomic Forces of Chlorine Atoms with Rare Gases, Hydrogen and Methane
5. Arnold, D.W., Bradforth, S.E., Him, E.H., Neumark, D.M.., Halide Anion-Carbon Dioxide Clusters: From Electrostatic to Covalent Bonding
6. Atkinson, D., Cavanaugh, K., Smith, M., Characterization of a Pulsed Uniform Supersonic Flow Reactor for Low Temperature Studies of Radical-Molecule Reactions
7. Balko, B.A., Zhang, J., Lee, Y.T., 193 nm Photodissociation of 1,1 and 1,2 Difluorethylene
8. Barker, J.A., Rettner, C.T., A Benchmark Gas/Surface PES:XE/Pt(111)
9. Barnes, M.D., Brooks, P.R., Curl, R.F., Harland, P.W., Exploring the Transition Region in Chemical Reactions
10. Beck, R.D., Blake, T.A., Eggers, D., Lewerentz, M., Tseng, S-H., Watts, R.O., Lovas, F.J., High Resolution Spectroscopy of Methylacetylene Clusters
11. Beck, S.M., Hecht, J.H., Photofragmentation of Mass-Selected $(C_6H_6)_n^+$ and $(C_6H_{12})_n^+$ Clusters: Spectra and Measurement of Monomer-Cluster Binding Energy for n=7-15
12. Bewig, L., Buck, U., Mehlmann, Ch., Winter, M., Fragmentation Analysis of Size Selected Neutral Sodium Clusters
13. Bristow, G.H., Mazely, T.L., Smith, M.A., An Investigation of Non-Equilibrium Relaxation in Free Expansions. A Boltzmann Solution for Mixed Atomic Flow
14. Brutschy, B., Riehn, Ch., Lahmann, Ch., Wassermann, B., IR -Depletion of Mixed Molecular Clusters, Probed with Rosonant Two Photon Ionization Spectroscopy
15. Burose, A.W., Dresch, T., Ding, A.M.G., EEELS Studies on Free Fullerenes Using Electron Energies Between 10 eV and 1100 eV
16. Cid-Aguero, P., Walters, E.A., Grover, J.R., Photoionization Studies of Thiophene and Thiophene Clusters in a Molecular Beam
17. Consalvo, D., Bergen, G., Drabbels, M., Meerts, W.L., Parker, D.H., Reuss, J., High Resolution Lif Study of a Cage Molecule, DABCO
18. Coreno, Marcello, Giardini-Guidoni, A., Mele, A., Piccirillo, S., Resonant Two Photon Ionization of Aromatic Molecules in a Supersonic Molecular Beam
19. Cyr, D.M., Bishea, G.A., Scarton, M.G., Lavrich, D.J., Johnson, M.A., Photo-Initiated Intra-Cluster Dissociative Electron Transfer Reactions
20. DeKieviet, M.F.M., Scoles, G., A New Bolometer-Based Surface Scattering Apparatus of Improved Sensitivity and Resolution
21. Ding, C., Yang, D., Zhou, Y., Zhu, Q., Multiphoton Ionization Photoelectron Spectroscopy of OCS
22. Douin, S., Hermine, P., Parneix, P., Brechignac, P., Amar, F.G., Site Specificity of Solvent Shifts in Aniline-$(Argon)_n$ Clusters: A Two-Photon Two-Color Resonant Ionization Study
23. Fantoni, R., Giorgi, M. Lipinska-Kalita, K., Snels, M., C.A.R.S. Monitor of Laser Induced Dissociation of Molecules and Clusters in a Supersonic Jet
24. Fischer, I., Strobel, A., Niedner-Schatteburg, G., Muller-Dethlefs, K., Bondybey, V.E., High Resolution Photoelectron Spectroscopy of NO and of the NO Dimer
25. Gallogly, E., Jackson, W.M., Crossed Molecular Beam Studies of Buckminsterfullerene

26. Gambogi, J., Lehmann, K.K., Pate, B.H., Scoles, G., Yang, X., The Influence of Methyl Groups on the Rate of Intramolecular Vibrational Energy Relaxation
27. Green, D.S., Wallace, S.C., Complex Resonances in the Two-Photon Vibronic Spectra of Xenon Dimers
28. Hanisco, T.F., Yan, C., Kummel, A.C., Energy and Momentum Distributions and Projections in the Scattering of CO off Ag(111)
29. Hawley, M., Nelson, H.H., Detection of Methyl Fragment Internal State Distribution from the 193 nm Photodissociation of Dimethyl Sulfoxide in a Free Jet
30. He, G., Lou, N., Molecular Beam Studies of the Reactions of Alkaline Earth Metal Atoms with Halogenated Hydrocarbons
31. He, G., Lou, N., Molecular Beam Studies of the Reactions of Alkaline Earth Metal Atoms with Halogenated Hydrocarbons
32. Janssen, M.H.M., Parker, D.H., van der Avoird, A., Stolte, S., Steric Effects in Gas-Phase Reactions of Ca(1D2) + CH3X(JKM) (X = F, Cl)
33. Kasai, T., Matsunami, T., Fukawa, T., Ohoyama, H., Kuwata, K., Effect of Molecular Orientation in Electron Ionization of Oriented Chlorometane in the (111) Eigensate
34. Knickelbein, M.B., Menezes, W.J.C., The Optical Response of Small Niobium Clusters
35. Latimer, D.R., Hawley, M., Melosh, N., Smith, M.A., Inelastic and Relaxation Processes in Ion-Molecule Collisions at Very Low Temperatures
36. Lin, F.J., Marsden, J.E., Geometric Mechanics and Molecular Reaction Dynamics
37. Markovich, G., Pollack, S., Giniger, R., Cheshnovsky, O., The Solvation of Iodine Anions in Water Clusters: PES Studies
38. Martin, J.S., Greeley, J.N., Jacobs, D.C., Effect of Incident Vibrational and Translational Energies on the Reaction of NO+(v) with GaAs(110)
39. Martrenchard-Barra, S., Lardeux-Dedonder, C., Jouvet, C., Solgadi, D., Brenner, V., Millié, P., Stability of Very Small Doubly Charged Clusters: Experiment and Theory
40. Martrenchard-Barra, S., Lardeux-Dedonder, C., Jouvet, C., Solgadi, D., Tramer, A., Solvation of Hg_{1and2} by Clusters of Argon, Dimethylether, Ammonia and Water
41. McMaster, M.C., Stinnett, J.A., Soulen, S.A., Madix, R.J., Molecular Beam Studies of Alkane Adsorption Dynamics on Clean and Adsorbate-Modified Pt(111)
42. Menédez, M., Garay, M., Verdasco, E., Castaño, J., González Ureña, A., Searching for Resonances in the Total Reaction Cross-Section: A Crossed Beam Study of the Ca (^{1}D) + HC1 Æ CaC1 (A) + H Reaction
43. Meng, C.K., Nohmi, T., Fuerstenau, S.D., Fenn, J.B., Shen, S., Banks, Jr., J.F., Electrospray Ionization - A New Window on the Solution Scene
44. Minton, T.K., Nelson, C.M., Moore, T.A., Okumana, M., Direct Observation of CIO from Chlorine Nitrate Photolysis
45. Mons, M., Schmidt, M., Le Calve, J., Structure-Dependent Intramolecular Vibrational Redistribution in the Benzene-Ar_n Complexes
46. Myers, J.D., Lee, Y.T., Photodissociation of Cyclopentadiene at 193 nm
47. Nakamura, M.., A Simple Method for Product Rotational Distribution in Atom-Diatom Chemical Reactions
48. Nakamura, M., Tsukada, M., Aono, M., Computer Simulations on Interaction of Low Velocity Rare Gas Beams with Solid Surfaces
49. North, S.W., Chu, P., Lee, Y.T., Photodissociation of Methyl Radicals at 193 nm
50. O'Shaughnessy, S.M., Laine, D.C., Line-Tunable Supersonic Beam Iodine Laser in the Visible and Near-Infrared
51. Orel, A.E., Krause, J.L., Lengsfield, B.H., Accurate Non-Adiabatic Couplings: Predissociation of H_3
52. Paz, Y., de Vries, M.S., Naaman, R., Vibrational Population Inversion in Aniline Scattered from Various Organic Surfaces

53. Pearson, A., Anderson, R.W., Fractal Structure in Cluster Growth

54. Price, J.M., Mack, J.A., Helden, G.V., Yang, X., Wodtke, A.M., The Structure of Acetaldehyde in its First Excited Singlet State: Experiment and Theory

55. Raukema, A., Box, F.M.A., Kleyn, A.W., A Molecular Beam Study of the O_2/Ag(111) Interaction

56. Rawluk, L.J., Keil, M., Alexander, M., Mayne, H.R., Barrett, J.J., Inelastic Scattering of Hydrogen Fluoride by Argon: Comparison of Experiment to Theory

57. Reid, K.L., Leahy, D.J., Park, H., Zare, R.N., Rotationally Resolved Circular Dichroism in Photoelectron Angular Distributions from NO(A2ÆÂ+)

58. Riehn, Ch., Lahmann, Ch., Brutschy, B., Baumgärtel, H., Proton Transfer in Mixed Molecular Clusters

59. Roehrig, M.A., Kukolich, S.G., Pulsed Molecular Beam Microwave Measurements On The HCCH-CO van der Waals Complex

60. Rogaski, C.A., Wodtke, A.M.., High Resolution Molecular Beam Spectroscopy of Highly Vibrationally Excited Propynal (C_3H_20): Structural Immunity to IVR

61. Rudich, Y., Naaman, R., Energy Distribution In HCl(v=1) Following the Vibrational Predissociation of C_2H_2-HCl Complex

62. Scheidemann, A., Kresin, V., Knight, W.D., Inelastic Electron Scattering by Alkali Clusters

63. Schulz, C.P., Nitsch, C., Hüglin, C., Unger, G., Hertel, I.V., Spectroscopic Study of Solvated Sodium Atoms

64. Scotoni, M., Leonardi, C., Menegotti, L., Bassi, D., Opto-Thermal Spectroscopy of Benzene C-H Stretch Overtones

65. Shao, J., Yuan, L., Yang, H., Gu, Y., Li, K., Wang, K., Tao, Y., A Preliminary Investigation of the $O(^1D)+H_2,D_2$,HD Reactions: Chemical Laser Determination of the Nascent Product Vibrational Distributions and the $O(^1D)$ +HD Macroscopic Branching Ratio

66. Sindoni, J.M., Sharma, R.D., A Proposal to Produce Velocity-Selected and State-Selected Molecular Beams Using the Ballistic Effect

67. Smoliar, L., Anex, D., Lee, Y.T., Molecular Beam-Surface Scattering: Investigation of Energy Transfer in Impulsive Collisions

68. Stalder, K.R., Mass Spectroscopic Measurements of Molecular Beams Formed From Hydrocarbon Arcjet Plasmas That Deposit Diamond Thin Films

69. Starrs, C., Jego, M.N., Mank, A., Hepburn, J.W., Mode Specific Photodissociation of the $^1B_2$ State of CS_2

70. Stiller, W., Molecular-Statistical Derivation of the Arrhenius Law for Homogeneous Bimolecular Diluted Gas-Phase Reactions

71. Tomer, J.L., Wall, M.C., Tonner, D. S., Cline, J.I., Structure and Conformation in the Photofragmentation Dynamics of Large Molecules

72. Tsekouras, A.A., Leach, C.A., Kalogerakis, K.S., Zare, R.N., Dynamics of the Ba + HI Reaction: BaI(v) Rotational Distributions and Specific Opacity Functions

73. van der Meer, G.J., Bloemink, H.I., Chapovsky, .L. Hermans, L.J.F., Molecular Collisions Studied by Light-Induced Drift

74. von Helden, G., Hsu, M-T., Kemper, P.R., Bowers, M.T., Structures of Carbon Cluster Ions From 3 to 60 Atoms: Linears to Rings to Fullerenes

75. Wang, X.H., Yen, Y.F., Cross, R.J., Saunders, M., Exciting Chemical Reactions

76. Weckwerth, R., Knoesel, E., Ding, A., Reactivity of Carbon Cluster Ions with AR, O_2, and D_2

77. Winterbottom, F., Reid, S.A., Scott, D.C., de Juan, J., Reisler, H., A Crossed Beam Study of the Reaction $C(^3P)$ + N_2O: Energy Partitioning Between the NO ($X^2\Pi$) and CN ($X^2\Sigma^+$) Products

78. Zajfman, D., Feldman, H., Heber, O., Kella, D., Majer, D., Vager, Z., Naaman, R., Electron Photo Detachment Cross Sections of Small Carbon Clusters, Evidences for Non Linear Isomers

Session I:

Clusters I

TIME RESOLVED DISSOCIATION/RECOMBINATION DYNAMICS IN LARGE MOLECULAR CLUSTER IONS

W. Carl Lineberger

Department of Chemistry and Biochemistry, University of Colorado
Joint Institute for Laboratory Astrophysics

Boulder, Colorado 80309-0440

Photoabsorption by a chromophore in a large, mass-selected, partially solvated ion is detected via evaporation of solvent molecules from the cluster. The shape and size evolution of the absorption spectrum as a function of cluster size provides the mechanism to identify the chromophore ion, and to determine the extent of charge delocalization within the cluster ion. Picosecond pump-probe techniques are utilized to investigate the cage effect for photodissociated I_2^- ions surrounded by a known number of CO_2 solvent molecules. The time-resolved studies show clearly the increasing effectiveness of the solvent cage as the degree of solvation is increased. The complex time dependence observed for the absorption recovery spectrum gives detailed information about coherent molecular motion within the complex, and provides direct observation of the breakup of the solvent cage. Simple models for the intracluster dynamics will be presented.

Predissociation Dynamics of Open-Shell Clusters.

Michael C. Heaven, Department of Chemistry, Emory University, Atlanta, GA 30322.

The open-shell van der Waals complexes OH-Ar and OD-Ar have attracted much experimental[1-13] and theoretical[14-23] attention during the past few years. Interest in OH/D-Ar stems from several sources. The complexes are easily detected and small enough for rigorous theoretical treatment. Novel couplings of the electronic and rotational (overall and internal) angular momenta are exhibited by the ground state[10,13,14,19,20]. There is a large difference in the intermolecular potential energy surfaces for the ground ($X^2\Pi$) and electronically excited ($A^2\Sigma^+$) states. This circumstance permits access to many levels of the *A* state, and thereby characterization of a significant fraction of the potential surface[17,21,23]. Vibrational predissociation of the *A* state is readily observed, and the internal energy distribution of the OH/D fragments can be deduced from emission spectra[9,24]. The predissociation dynamics may be interpreted using potential energy surfaces derived from the spectroscopic data.

Other OH/D- rare gas atom complexes are of interest for the same reasons. In recent studies of OH/D-Ne[24-26], we noted a number of similarities and contrasts with the properties of OH/D-Ar. Compared with OH/D(*A*)-Ar, the binding energy of OH/D(*A*)-Ne is about seven times weaker and internal rotation is more facile. As one would expect, these differences have dramatic effects on the vibrational predissociation dynamics. Having explored the dynamics of weak and moderately bound OH/D-Rg complexes, we were interested in extending these studies to the more strongly bound OH/D(*A*)-Kr complex.

Prior to the work presented here, gas phase spectra for OH/D-Kr had not been reported. Matrix data for this complex were obtained by Goodman and Brus[27], who examined the *A*-*X* transition of OH in solid Kr. The vibronic structure observed in excitation was that of the binary OH-Kr complex. A progression of eight -Kr stretch levels was seen in conjunction with the OH *A*-*X* 2-0 transition. The intensity maximum of the emission spectrum was red-shifted from that of OH-Ar by approximately 1900 cm^{-1}. These results implied that OH-Kr was more deeply bound than OH-Ar, and that the OH-Kr equilibrium bond length experienced a greater contraction on electronic excitation. Since gas-phase OH(*A*)-Ar is bound by more

than 1000 cm^{-1} [17,21,23], the matrix data for OH(*A*)-Kr suggest an unusually strong interaction.

We have recently obtained excitation and wavelength-resolved fluorescence spectra for OH/D-Kr in the gas phase. The complexes were generated in a free-jet expansion driven by a Ne/Kr mixture. Bands belonging to OH/D-Kr were seen in the vicinity of the OH/D *A*-*X* 0-0 and 1-0 transitions. Despite the congestion caused by presence of several Kr isotopes, seventeen bands were rotationally resolved and analyzed. For the ground state, the zero-point rotational constant defined a Kr to OH center of mass distance of 3.78±0.01 Å. The relatively small effect of H/D isotopic substitution on the ground state rotational constant was consistent with a linear hydrogen-bonded equilibrium geometry. Assignment of the *A* state vibrational levels was accomplished by means of the Kr isotope effect. A lower limit for the dissociation energy for OH(*A*,v=0)-Kr of D_e>1840 cm^{-1} was derived from the vibrational constants. Extrapolation of the rotational constants yielded an equilibrium intermolecular separation of 2.67±0.12 Å. The properties defined by the spectroscopic analysis indicated weak, van der Waals bonding in the ground state, and incipient chemical bonding in the excited state.

Vibrational predissociation of OH/D-Kr was observed through homogeneous broadening of the rotational lines. The predissociation rates ranged from less than1 $x10^{10}$ to 4 $x10^{11}$ s^{-1}, with a general trend of decreasing decay rate with increasing excitation of the intermolecular stretch. Wavelength resolved fluorescence spectra showed that predissociation of OH-Kr partitioned approximately 40% of the available energy into OH(*A*, v=0) rotation. Predissociation of OD-Kr released ≈25% of the energy to OD(*A*, v=0) rotation.

When levels which release similar amounts of excess energy are compared, the OH/D(*A*,v=1)-Rg vibrational predissociation rates increase with the interaction strength. There is, however, a distinct difference between the predissociation dynamics of OH/D-Ne[24,26] and those of OH/D-Ar[9,24] and OH/D-Kr. While OH/D-Ne predissociates roughly 10^5 times slower than OH/D-Ar, the difference in the rates for OH/D-Ar and OH/D-Kr is less extreme; a factor of 10 at most. A corresponding trend is seen in the amount of energy released to OH/D rotation. OH/D-Ne channels the maximum amount of energy into product rotation[24,26]. The rotational distributions resulting from OH/D-Ar[9,24] and OH/D-Kr predissociations are much cooler, and fairly similar. It appears that the stiffer bending potentials of the heavier complexes limit the amount of angular momentum which can be imparted. Analytical

models of colinear vibrational predissociation[28,29] are successful in predicting the qualitative trends of the OH/D-Rg predissociation dynamics, but they are simplified to the point where they cannot be used to rationalize the quantitative differences.

References

1. W. F. Fawzy and M. C. Heaven, J. Chem. Phys. **89**, 7030 (1988).
2. M. T. Berry, M. R. Brustein, J. R. Adamo, and M. I. Lester, J. Phys. Chem. **92**, 5551 (1988).
3. M. T. Berry, M. R. Brustein, and M. I. Lester, Chem. Phys. Lett. **153** 17 (1988).
4. K. M. Beck, M. T. Berry, M. R. Brustein, and M. I. Lester, Chem. Phys. Lett. **162**, 203 (1989).
5. M. T. Berry, M. R. Brustein, and M. I. Lester, J. Chem. Phys. **90**, 5878 (1989).
6. W. M. Fawzy, and M. C. Heaven, J. Chem. Phys. **92**, 909 (1990)
7. S. K. Kulkarni, Y. Lin, and M. C. Heaven, Chem. Phys. Lett. **167**, 597 (1990).
8. S. K. Bramble, and P. A. Hamilton, Chem. Phys. Lett. **170**,107 (1990).
9. M. T. Berry, M. R. Brustein, and M. I. Lester, J. Chem. Phys. **92**, 6469 (1990).
10. M. T. Berry, M. R. Brustein, M. I. Lester, C. Chakravarty and D. C. Clary, Chem. Phys. Lett. **178**, 301 (1991).
11. B.-C. Chang, L. Yu, D. Cullin, B. Rehfuss, J. Williamson, T. A. Miller, W. M. Fawzy, X. Zheng, S. Fei, and M. C. Heaven, J. Chem. Phys. **95**, 7086 (1991).
12. J. Schleipen, L. Nemes, J. Heinze, J. J. ter Meulen, Chem. Phys. Lett. **175**, 561 (1990).
13. Y. Ohshima, M. Iida, and Y. Endo, J. Chem. Phys. **95**, 7001 (1991).
14. W. M. Fawzy and J. T. Hougen, J. Mol. Spec. **137**, 154 (1989).
15. A. Degli Esposti and H.-J. Werner, J. Chem. Phys. **93**, 3351 (1990).
16. C. Chakravarty, and D. C. Clary, Chem. Phys. Lett. **173**, 541 (1990).
17. J. M. Bowman, B. Gazdy, P. Schafer, and M. C. Heaven, J. Phys. Chem. **94**, 2226 (1990); **94**, 8858 (1990).
18. C. Chakravarty, D. C. Clary, A. Degli Esposti, and H.-J. Werner, J. Chem. Phys. **93**, 3367 (1990).
19. C. Chakravarty and D. C. Clary, J. Chem. Phys. **94**, 4149 (1991).
20. M.-L. Dubernet, D. Flower, and J. M. Hutson, J. Chem. Phys. **94**, 7602 (1991).
21. Y. Guan and J. T. Muckerman, J. Phys. Chem. **95**, 8293 (1991).

22. C. Chakravarty, D. C. Clary, A. Degli Esposti, and H.-J. Werner, J. Chem. Phys. **95**, 8149 (1991).
23. U. Schnupf, J. M. Bowman, and M. C. Heaven, Chem. Phys. Lett. **189**, 487 (1992).
24. Y. Lin, Ph.D. thesis, Emory University, 1991.
25. Y. Lin, S. K. Kulkarni, and M. C. Heaven, J. Phys. Chem. **94**, 1720 (1990).
26. Y. Lin, S. Fei, X. Zheng, and M. C. Heaven, J. Chem. Phys. In press.
27. J. Goodman and L. E. Brus, J. Chem. Phys. **67**, 4858 (1977).
28. J. A. Beswick and J. Jortner, J. Chem. Phys. **68**, 2277 (1978).
29. G. E. Ewing, J. Chem. Phys. **72**, 2096 (1980).

Size effects and vibrational dynamics of large clusters from He atom scattering

U. Buck
Max-Planck-Institut für Strömungsforschung,
D-W-3400 Göttingen, Germany

The knowledge of the frequency spectrum of a cluster plays an important role both for the interpretation of static and structural properties as well as for the dynamical behaviour of the vibrational modes. The latter process is very sensitive to the transition of the cluster from the discrete spectrum of vibrational modes of the molecular system to the lattice vibrations and the continuous phonon dispersion curves of the solid. He atom scattering appears to be the ideal method to study experimentally these spectra, since this method is mainly sensitive to surface properties and obeys nearly no selection rules. In the last 10 years this technique has been developed into a very successful and reliable method for measuring surface phonons of the solid [1]. Here, we report first measurements of He atom scattering from large Ar_n clusters in the range form $\bar{n} = 30$ to $\bar{n} = 4500$ [2]. There are two different types of observables: (1) The angular distributions which contain among other things information on the geometry and the size of the investigated clusters through the diffraction oscillations. (2) The inelastic energy transfer which is related to the excitation of the vibrational modes.

The experiments have been carried out in a crossed molecular beam machine with time-of-flight analysis of the scattered He atoms using the pseudorandom chopping technique with a flight path of 450 mm. The helium atom beam is produced by expansion of the gas under high stagnation pressure (typically 30 bar) through a small orifice (diameter 30 μm) into the vacuum. Most of the measurements were carried out at a temperature of $T_0 = 77$ K. With a speed ratio of $S = 90$, an internal temperature of lower than 0.1 K and a corresponding relative width of the velocity distribution of $\Delta v/v = 0.018$ is obtained. This leads at collision energies of about 25 meV to a resolution of better than 1 meV. The cluster beam is generated by expansion from stagnation pressures of 1.2 to 5.0 bar through different nozzles of conical shape [3] which vary in diameter (60 μm to 130 μm), length (1 mm, 10 mm) and opening angle (20^0 to 30^0). The

beam contains only a distribution of cluster sizes. The maximum can be shifted to nearly any desired position by varying the different shape parameters of the nozzle and the stagnation pressure. The corresponding average cluster sizes $\bar{n}$ are taken from measurements by mass spectrometer [4] and electron diffraction [5] making use of special scaling laws [6].

The angular distributions have been measured for the collision energy of E = 70 meV and cluster sizes ranging from $\bar{n}$ = 55 to $\bar{n}$ = 4500 for deflection angles between 3^0 and 80^0. They can be characterized by three different regions. (1) At small angles up 30^0 they are dominated by oscillations with large angular separation which are caused by monomers. (2) Then an angular range (30^0 - 60^0) follows with oscillations of smaller angular separation which varies with cluster size. Calculations demonstrate that they can be attributed to diffraction oscillations of the different clusters. The resulting sizes which are derived from the model of a sphere of homogeneously distributed Lennard-Jones (12-6) potentials [7] or the realistic structure of the corresponding cluster (icosaeder for n = 55) are smaller than the values derived from the scaling laws [2]. At larger angles (50^0 to 80^0) irregular peaks and a general intensity drop is observed which is probably an indication of absorption features and remaining diffraction peaks. We conclude that the preliminary determination of cluster sizes based on diffraction oscillations is not in agreement with the commonly accepted scaling based on the source parameters.

The excitation of the vibrational modes is obtained from the time-of-flight spectra taken at different laboratory deflection angles. Measurements were carried out at a collision energy of 25.0 meV for the same deflection angle (30^0) and different $\bar{n}$ (55, 80, 115, 3000) as well as for the similar $\bar{n}$ (30, 115) and different deflection angles (10^0, 30^0, 36^0, 50^0). The results for $\Theta = 10^0$ indicate that the energy transfer is small with a most probable value of 1 meV. The results for $\Theta = 30^0$ are quite different. Here, the most probable energy transfer is found between 2 meV and 4 meV with the largest detectable energy transfer at about ΔE = 8 meV. The results for the maximum depend on the cluster size, while the cut off value is nearly the same.

These data can be compared with what is known on the density of vibrational states. The measured bulk phonon density of solid Ar at 10 K shows a large peak

at 8 meV and a second peak around 5 meV. For clusters and particles of finite size only calculations are available [8-12]. They all demonstrate that two further peaks appear around 1-3 meV which are attributed to surface modes [13]. The overall size of the particles is reflected only in the relative amount of the intensities of the different peaks to each other. A first comparison with the simulated frequency spectra of Ar_{55} gives information about the cluster size and the temperature. It is, however, noted that in the final comparison the collisional excitation of the different modes has to be taken into account.

These first results of the measurement of diffraction oscillations in the angular distribution and of the vibrational energy transfer of free clusters by helium atom scattering look very promising and open a range of new experimental possibilities. The great advantage of this technique is the general applicability to any kind of system and vibrational mode including the acoustical and optical phonons.

[1] J.P. Toennies, Physical Scripta T19, 39 (1987)
[2] U. Buck, R. Krohne, and J. Siebers, in Nuclear Physics Concepts in Atomic Cluster Physics, eds. H.O. Lutz, R. Schmidt and R. Dreizler, Springer, Berlin, 1992
[3] W. Obert, Rarefied Gas Dynamics, ed. R. Campargue, CEA, Paris, 11, 1181 (1979)
[4] O.F. Hagena and W. Obert, J.Chem.Phys. 56, 1793 (1972)
[5] J. Farges, M.F. de Feraudy, B. Raoult and G. Torchet, J.Chem.Phys. 84, 3491 (1986)
[6] O.F. Hagena, Z.Phys.D 4 291 (1987)
[7] J. Gspann and H. Vollmer, in Rarefied Gas Dynamics, ed. R. Campargue, CEA, Paris 11, 1193 (1979)
[8] J.M. Dickey and A. Paskin, Phys.Rev.B 1, 851 (1970)
[9] W.D. Kristensen, E.J. Jensen and R.M.J. Cotterill, J.Chem.Phys. 60, 4161 (1974)
[10] T.L. Beck and T.L. Marchioro II., J.Chem.Phys. 93, 1347 (1990)
[11] J.A. Adams and R.M. Stratt, J.Chem.Phys. 93, 1358 (1990)
[12] A. Tamura and T. Ichinokawa, J.Phys.C 16, 4779 (1983)
[13] Y. Ozaki, M. Ichihashi and T. Kondow, Chem.Phys.Lett, 182, 57 (1991)

IVR IN A TRIATOMIC VAN DER WAALS MOLECULE: Ar···Cl_2

Nadine Halberstadt

Laboratoire de Photophysique Moléculaire [a], Université de Paris Sud, 91405 Orsay, France

Octavio Roncero [b] and **Kenneth C. Janda**

Department of Chemistry, University of Pittsburgh, Pittsburgh, PA 15260, USA

We have performed time-independent quantum mechanical calculations for the vibrational predissociation of Ar···Cl_2 excited in the B electronic state[1,2]. It is particularly interesting to study this energy transfer process in Ar···Cl_2, because it is in the middle of the Rg···Cl_2 series (Rg denoting a rare gas atom): on the one side, the He and Ne complexes[3-6] exhibit a very selective behaviour, characteristic of the direct coupling of a quasibound state Rg···$Cl_2(v')$ to the dissociative continua Rg + $Cl_2(v < v', j)$; on the other side, vibrational predissociation of the heavier Xe and Kr complexes[7] represents the statistical limit, owing to multiple collisions as the fragments separate. For Ar···Cl_2, the Van der Waals well depth is of the same order of magnitude as the Cl_2 stretching level spacing. The experiments on the vibrational predissociation of this complex[8] show that when the $\Delta v = -1$ channel is closed, the observed rotational distribution of the $\Delta v = -2$ channel is highly structured, the position of the extrema being a strong function of the initially excited vibrational level. It was argued that this could be understood in terms of a sequential relaxation mechanism (IVR) presented in Fig. 1, in which the nature of the intermediate resonance state(s) plays a key role in determining the final product energy distribution.

We have performed a fully converged time-independent quantum mechanical calculation in the region of $v' = 6$ where the $\Delta v = -1$ channel is still open, and in the region of $v' = 11$ where the first open channel is $\Delta v = -2$ ($v = 9$). We used a model potential built as a sum of atom-atom pairwise interactions. The results are in agreement with the main experimental finding that the final rotational distribution is highly structured, and strongly dependent on the initial vibrational level excited. In addition, the product rotational distribution is predicted to be very different for the different vibrational channels.

In collisional vibrational relaxation, transitions corresponding to $|\Delta v| > 1$ are known to proceed *via* $\Delta v = \pm 1$ coupling. By repeating the $v' = 6$ calculation without the potential coupling terms corresponding to $|\Delta v| > 1$, we were able to show that this is also the case in the vibrational predissociation of this Van der Waals complex. In a time-dependent picture, the mechanism for losing more than one vibrational quantum of Cl_2 is sequential, proceeding through several $\Delta v = -1$ steps.

Smaller basis set calculations, tested for accuracy against the fully converged results, were performed for $v' = 10$ and 11 in order to more completely characterize the IVR

[a] Laboratoire du CNRS.

[b] Permanent address: Instituto de Física Fundamental, CSIC-UCM, Serrano 123, 28006 Madrid, Spain

dynamics. In the region of the principal transition for $v' = 11$, a weak transition is observed $1.03\,cm^{-1}$ to lower energy of the principal resonance. Although the peak intensity of this "dark" state transition is 1/50 times that of the "bright" state transition, its width is 9 times greater so that the integrated intensity is 15% of the principal transition. The product rotational distributions for decay of the bright and dark states are very similar. These phenomena are consistent with the sparse limit for the IVR process illustrated in Fig. 1.

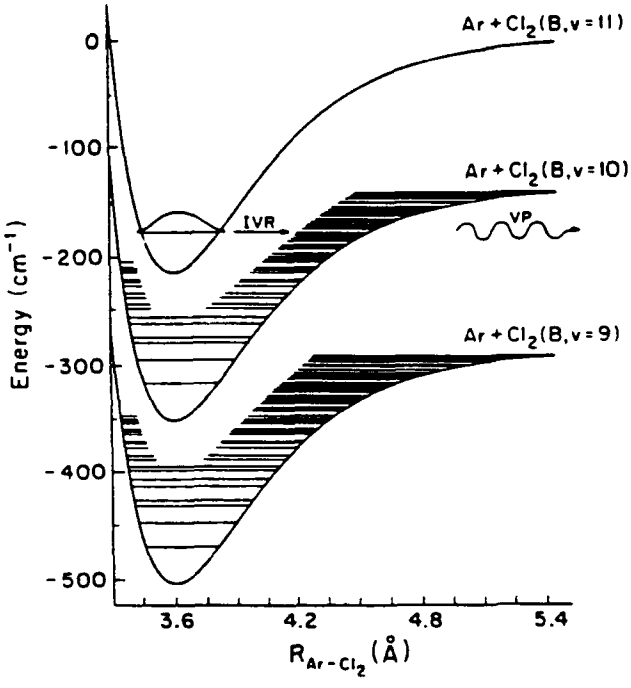

Fig. 1 Energy level scheme for IVR. This figure provides a one-dimensional representation of the IVR path for Ar···Cl_2. The zero-order bright state $(B, v' = 11, g)$ carries the oscillator strength from the ground state $(X, v'' = 0, g)$. Here B and X refer to the Cl_2 electronic state; v' and v'' refer to the Cl_2 stretch quantum number and g indicates the ground state of the van der Waals manifold. The dark state, or doorway state, $(B, v' = 10, \lambda)$ is a highly excited level, λ, of the van der Waals manifold with a zero-order Cl_2 stretch quantum number equal to 10, that has about the same energy as the $v' = 11$ bright state. It does not get oscillator strength from the ground state $(X, v'' = 0, g)$ because the Van der Waals interaction potentials are very similar in the bound and B electronic states. The zero-order description of the $\Delta v = -2$ continuum states $(B, v' = 9, \epsilon)$ is given by $v' = 9$ for the Cl_2 stretch, j for the Cl_2 rotation and ϵ for the translational energy.

The coupling V responsible for IVR was found to be 0.37 cm^{-1}. By independent bound state calculations on Ar···Cl_2[1], we have estimated the density of levels ρ in the energy region of the $v' = 11$ resonance to be of the order of 0.5 level/cm^{-1}. Hence the characteristic constant of IVR is $\rho V \simeq 0.2$, indicating that this is the sparse limit for IVR. It would be quite interesting to look for the different regimes of IVR in Ar···Cl_2 or other similar complexes ($\rho V << 1$ would be the Fermi resonance limit, *i.e.* accidental resonance between a bright and a dark state, and $\rho V >> 1$ the dense limit for IVR, where the dark levels build a quasi-continuum and give the bright state an IVR width). Going to higher values for v', the density of levels will be decreasing but the coupling should be increasing since the vibrational levels of Cl_2 are closer together.

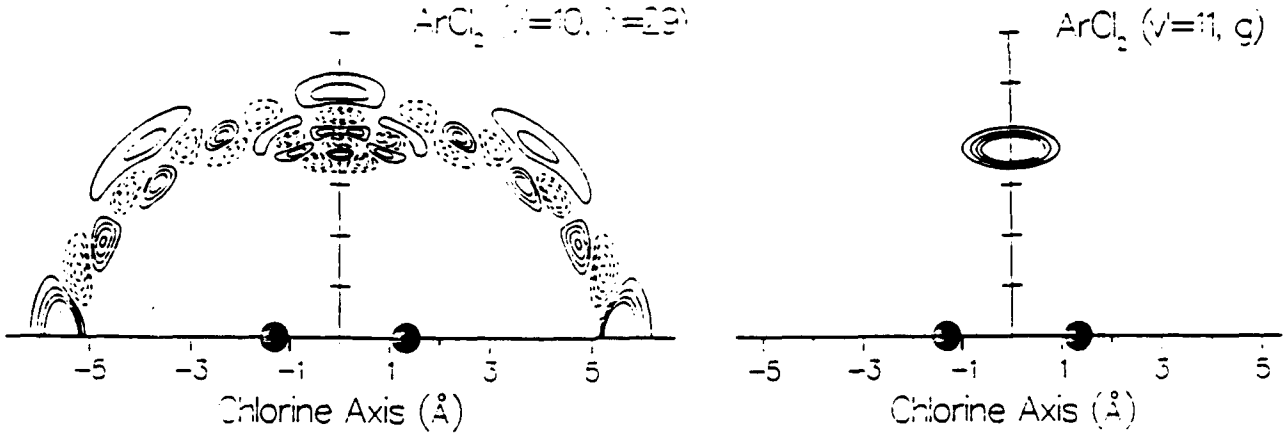

Figure 2: contours of the zero-order bright (left) and dark (right) wave functions for $v' = 11$

The bound state calculation also allowed us to assign the zero-order bright state to $(B, v' = 11, g)$ (ground Van der Waals level of the $v' = 11$ manifold) as expected, and the zero-order dark state to $(B, v' = 10, \lambda = 29)$, the 28^{th} excited even Van der Waals level of the $v' = 10$ manifold (since Cl_2 is homonuclear, the $J = 0$ Van der Waals levels are even or odd with respect to reflection in a plane perpendicular to the Cl_2 axis). A natural expansion analysis of this wave function has shown that it is not assignable to a simple stretch-bend combination in the Jacobi coordinates used here, as could be expected from the complicated shape of the wave function.

Finally, a Golden Rule calculation of the dissociation from the dark state gave a rotational distribution which compares surprisingly well with the result of the exact calculation. This, together with the fact that both resonances lead to the same final rotational distribution, gives a direct confirmation of the hypothesis of Evard *et al.* [8] that the product rotational distribution for $\Delta v = -2$ dissociation of Ar···Cl_2 is determined by the dynamics of the doorway state. As was the case for Ne and He···Cl_2, this rotational distribution is quite different from the decomposition of the quasibound state in terms of free rotor wave functions.

The calculated lifetimes for vibrational predissociation from $v' = 6$ and $v' = 11$ are 2.6 nsecs and 251 psecs, respectively. Although for $v' = 11$ dissociation has to proceed *via* $\Delta v = -2$ and releases 117.6 cm^{-1} excess energy, it is still 10 times faster than for $v' = 6$ for which $\Delta v = -1$ is open with only 17.8 cm^{-1} excess energy. From $v' = 10$, dissociation is 3 times faster than from $v' = 11$ although it corresponds to about 11 cm^{-1} additional excess energy. The failure of the calculated VP rates to obey the energy gap law is due to IVR: since the energy mismatch and the coupling between the bright and dark states as well as the nature of the dark states involved will be different for every initial level, it is not possible tc predict how the dynamics will vary as a function of the initial state quantum numbers without performing the full calculation with an accurate potential.

COPY AVAILABLE TO DTIC DOES NOT PERMIT FULLY LEGIBLE REPRODUCTION

References

[1]N. Halberstadt, S. Serna, O. Roncero and K.C. Janda, J. Chem. Phys., to be published.

[2]N. Halberstadt, J.A. Beswick, O. Roncero and K.C. Janda, J. Chem. Phys. **96**, 2404 (1992).

[3]J.I. Cline, D.D. Evard, B.P. Reid, N. Sivakumar, K.C. Janda and N. Halberstadt, J. Chem. Phys. **89**, 3535 (1988).

[4]J.I. Cline, N. Sivakumar, D.D. Evard, C.R. Bieler, B.P. Reid, N. Halberstadt and K.C. Janda, J. Chem. Phys. **90**, 2606 (1989).

[5]K.C. Janda and C.R. Bieler, Chapter 6 of *Atomic and Molecular Clusters*, E. Bernstein, Ed., Elsevier, 1990.

[6]N. Halberstadt, J.A. Beswick and K.C. Janda, J. Chem. Phys. **87**, 3966 (1987).

[7]C.R. Bieler, K.E. Spence and K.C. Janda, J. Phys. Chem. **95**, 5058 (1991).

[8]D.D. Evard, C.R. Bieler, J.I. Cline, N. Sivakumar and K.C. Janda, J. Chem. Phys. **89**, 2829 (1988).

Predissociation Dynamics and Structure of Hydrogen Bonded Cyanoacetylene Complexes

Erik Th. Kerstel, Giacinto Scoles and Xueming Yang

Deparment of Chemistry, Princeton University, Princeton, N.J 08544

Hydrogen bonded complexes have been the subject of extensive experimental and theoretical studies in recent years because of the fundamental importance of this type of bonding. These complexes are also of interest because of their unique dynamical properties such as mode specific and non-statistical vibrational predissociation. The HCN dimer has been an excellent example of the nonstatistical behaviour in predissociation[1]. The $v_1 = 1$ state of the inner C-H stretching of the HCN dimer has a much shorter lifetime (6 ns) than the outside C-H stretching $v_2 = 1$ state (>1060 ns).

In this report, we will present our recent studies on the following systems: $(HCCCN)_2$ and HCCCN-HCN. These dimers were prepared in a continous molecular beam. High resolution infrared spectroscopic investigation of both the inner and outside C-H stretches were carried out using optothermal detection. The structure of both dimers are found to be linear. The van der Waals bond length was determined for both molecules. Predissociation at the $v = 1$ state of both the inner and outside C-H stretching modes was also studied in both cases.

For the outside C-H stretching band (the v_1 band) of $(HCCCN)_2$ and HCCCN- HCN, the linewidths of the transitions are intrument limited to about 10 MHz. This corresponds to a lower limit for the predissociation lifetime of 16 ns. The center of the v_1 dimer band of $(HCCCN)_2$ is 2.95 cm^{-1} red shifted from that of the monomer band. The rotational

constant B's of both the ground and the $v_1 = 1$ states of $(HCCCN)_2$ were determined to be 337.794 MHz, 337.737 MHz respectively.

In the region of the inside C-H stretching band (the v_2 band) of the HCCCN dimer, two bands were observed displaced by 0.8 cm^{-1} from each other (see the experimental and simulated spectrum in Fig. 1). The center of the stronger band is about 67 cm^{-1} red

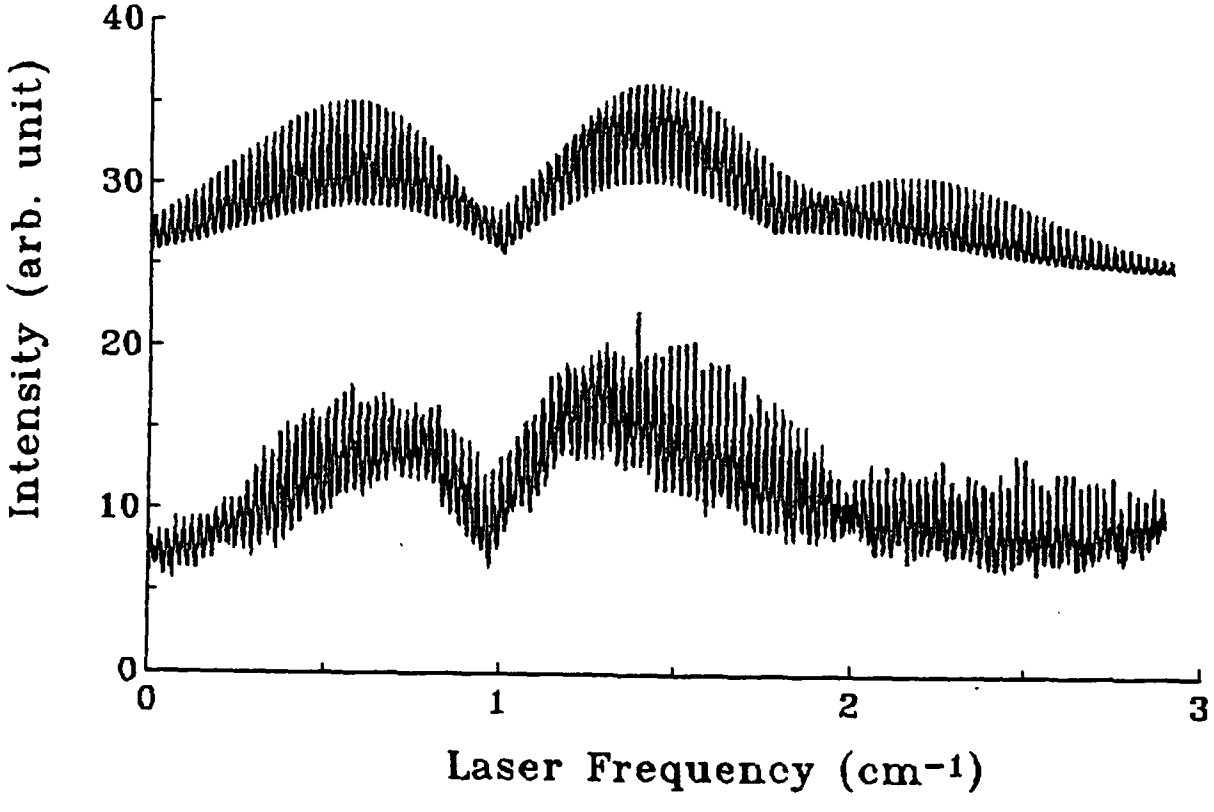

Fig. 1 The observed and simulated spectrum of the two bands in the inner C-H stretching fundamental region of the cyanoacetylene dimer.

shifted from that of the monomer band. The source of the second band is not clear at this time. One possibility is that it be a hot band. This is interesting because for all rotational transitions observed the linewidths for the weaker band transitions are narrower than that of the strong band, while normally, one would expect the linewidths of the hot band

transitions to be at least as broad as those of the cold band.[1] The stronger band transitions have a linewidth of 295 MHz, which corresponds to a predissociation lifetime of 530 ps, while the linewith of the waeker band features is about 190 MHz, which corresponds to a predissociation lifetime of 825 ps. It is also possible that the weaker band transtions be caused by a perturbation. Further investigations are in progress to resolve this issue.

Finally, non-statistical behavior of predissociation will also be discussed for both dimers using a collisional energy transfer theory developed by Schwartz, Slawsky, and Herzfeld.[2]

Acknowledgements: We would like thank Professor Kevin Lehmann for many helpful discussions and Joan Gambogi for help during the experiment. This work was supported by the NSF grant CHE-9016491.

References

[1] K. W. Jucks and R. E. Miller, J. Chem. Phys. 88, 6059(1988).

[2] R. N. Schwartz, Z. I. Slawsky, and K. F. Herzfeld, J. Chem. Phys. 20, 1951(1952).

Low Frequency Vibrational Motion of Aromatic – Rare Gas Cationic Clusters observed via Resonance-Enhanced Photofragment Spectroscopy

Ruth J. McKay†, Evan J. Bieske*, Fred R. Bennett* and Alan E.W. Knight,
Molecular Dynamics Laboratory, Griffith University, Nathan, Q 4111
AUSTRALIA.

† Currently at Department of Chemistry, Stanford University, Stanford CA 94305-5080 USA
* Currently at Institut für Physikalische Chemie, Universität Basel, Klingelbergstrasse 80, Basel CH-4056 Switzerland

Ionic clusters consisting of a polyatomic ion surrounded by a few "solvent" atoms provide a connecting link between the isolated gas phase ion and the ion solvated in a condensed medium. Analysis of the low frequency vibrational structure associated with the motion of these cluster atoms can reveal details concerning the intermolecular potential associated with the cluster bonds. Bonds within an ionic cluster will involve contributions from charge-induced dipole attractive forces. Information concerning the vibrational motion of polyatomic cluster ions has been difficult to obtain using conventional spectroscopic methods.

We have developed a new combination of the standard experimental techniques of supersonic cooling, resonance-enhanced multiphoton ionization, time-of-flight mass spectroscopy and photodissociation spectroscopy. This new spectroscopic technique, which we have termed *Resonance-enhanced Photofragment* spectroscopy, takes advantage of the facile predissociation of an electronically excited cluster and affords us a method for studying the vibrational structure associated with an electronically excited cationic polyatomic cluster. This technique will also allow investigation of the electronic ground state of the ionic cluster.

Using our technique we have obtained vibrationally resolved, species-specific, resonance-enhanced photofragment spectra of the aromatic cation *p*-difluorobenzene$^+$ clustered with $(Ar)_1$, $(Ar)_2$ and $(Kr)_1$. The resonance-enhanced photofragment spectrum of the pDFB$^+$•$(Ar)_1$ cluster ion is shown, along with the excitation spectrum of its neutral counterpart pDFB-$(Ar)_1$, in the accompanying figure. Long progressions associated with low frequency vibrational motions of the cluster bonds can be observed built on vibronic structure associated with vibrational

motion localized in the parent $pDFB^+$ cation, sampling a large portion of the potential well associated with the cluster bond. Observed changes in the spectroscopy of the cluster bond upon ionization follow intuitive directions.

A model which allows anharmonic coupling within the extensive manifold of stretching and bending vibrational motions of the cluster bond has been developed in an attempt to fit the observed spectra. Eigenvalues and vectors of the anharmonically mixed manifold of vibrational states, combined with calculated Franck-Condon overlap integrals can be used to predict individual transition strengths and hence spectral intensities, along with transition energies. The model can be used to reproduce the anomalous intensity distributions observed in a number of laboratories for the low frequency vibrational transitions in the aromatic – gas cluster ions.

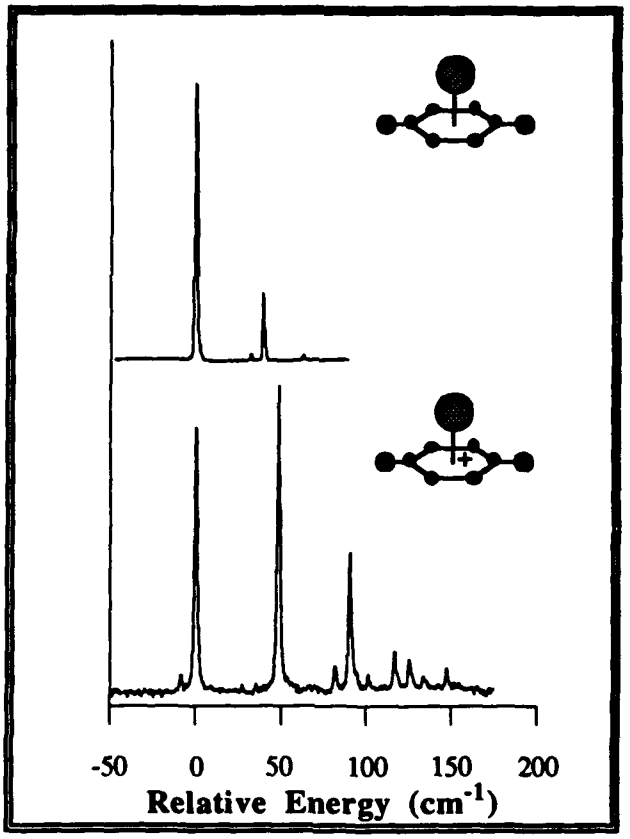

The electronic origin regions of the spectrum of the neutral and cationic pDFB-$(Ar)_1$ clusters, showing low frequency vibrational motions associated with the cluster bond in the electronic excited clusters. Band displacements (cm^{-1}) are shown relative to the respective 0_0^0 transition.
TOP: REMPI - TOFMS excitation spectrum of the pDFB-$(Ar)_1$ van der Waals cluster measured near the $S_1 \leftarrow S_0$ electronic origin. **BOTTOM:** Resonance-enhanced photofragment spectrum of the $pDFB^+ \bullet (Ar)_1$ cluster ion near the $D_3 \leftarrow D_0$ electronic origin.

Session II:

Reaction Dynamics

Low Energy Crossed-Beam Experiments on Ion-Molecule Reactions

Paolo Tosi, Oleg Dmitrijev, Yvonne Soldo and Davide Bassi
Dipartimento di Fisica and Unitá I.N.F.M.
Università degli Studi di Trento
I 38050 Povo (TN), Italy

Supersonic beams are a powerful tool to investigate ion-molecule reactions. In particular crossed-beam configurations have been extensively used to measure differential cross-sections at high and moderate energies.
In the low energy range ion-beam experiments suffer of a major drawback, consisting of the difficulty to handle an ion beam with an energy below a few eV. An alternative approach is based on the possibility to confine the ion beam in the transverse direction by means of appropriate time-dependent electric fields. In particular the introduction in the early seventies of the radio-frequency (r.f.) octopole guides by Teloy and Gerlich [1] has revolutionized techniques used to measure integral cross-sections at very low collision energies. In fact this device [2,3] has made the handling of low energy ion beams possible thus giving way to a great number of new experiments. These furnished a large number of data allowing to make a great step forward in the field.
Unfortunately most of these experiments use an ion beam-scattering cell configuration and therefore they have a limited energy resolution due to the distribution of relative velocities created by the thermal motion of the target neutral gas in the scattering cell. Actually this so-called Doppler broadening is important only in the low energy range (< 1 eV) but, especially at the lowest energies, its effects are quite severe. As a result the measured cross-section differs significantly from the true cross-section and any sharp feature is lost. Thus an effort to reach high resolution conditions at low collision energies might allow the discovery of new effects and stim-

ulate theoretical interpretation.
With this goal in mind a natural development of the r.f.-guided ion beam instruments was the replacement of the scattering cell with a supersonic neutral beam. In our group we have developed a new apparatus where a liquid nitrogen cooled, continuous supersonic molecular beam is crossed at the center of an octopole guide with an ion beam [2,4,5]. This crossed-beam configuration enables to reach an energy resolution about one order of magnitude higher than experiments using a room-temperature scattering cell and to investigate the detailed structure of the integral reactive cross-section at low energies.
In this talk recent work of the Trento group is reviewed, with particular emphasis on our effort to reach high resolution conditions at low collision energies. Hopefully these measurements provide some contributions on our understanding of the reaction mechanisms in these systems and in particular of non-adiabatic effects in ion-molecule reactions.

$Ar^+ + X_2 \rightarrow ArX^+ + X$, X=H,D

$Ar^+ + X_2$ correlate with the products $ArX^+ + X$ only adiabatically, via the charge transfer intermediate $X_2^+ + Ar$. In our experiment X_2 is only in the $v = 0$ vibrational state while in the charge transfer process several vibrational levels of X_2^+ can be populated. As a consequence the vibronic curves related to the different vibrational states of X_2^+ can give effective adiabatic paths to the reaction and it is expected that by varying the collision energy the progressive openings of these paths should be observed. We have reported measurements of the energy dependence of the integral cross-section [5]. The measured cross-section shows a nonmonotonic velocity dependence that is attributed to the successive opening, as the collision energy increases, of the vibrational levels of the intermediate complex.
In a continuous collaboration between Aquilanti's group at the University of Perugia and ours [5,6], a full treatment of the dynamics of these reactions has been developed. The main contribution to the entrance channel $Ar^+ + X_2$, which is of the charge-induced dipole type for the long range attraction, has been estimated by making use of recently developed empirical correla-

tions [7]. A further contribution is given by the electronic anisotropy term, arising from the open shell nature and spin-orbit splitting in $Ar^+(^2P_{3/2,1/2})$ [8]. Therefore we obtain three surfaces, 1 $^2A'$, 1 $^2A''$, 2 $^2A'$ which, in the two-body asymptotic limit, can be given the collinear designation $^2\Sigma_{1/2}$, $^2\Pi_{3/2}$ and $^2\Pi_{1/2}$ respectively [8]. The conservation of the quantum number Ω, that at large distances tends to $|m_J|$, allows to correlate the asymptotic $Ar^+(^2P_{3/2})$ + H_2 state with the short distance $^2\Sigma_{1/2}$ and $^2\Pi_{3/2}$ states resulting in the $V_{\frac{3}{2}\frac{1}{2}}$ and $V_{\frac{3}{2}\frac{3}{2}}$ surfaces and $Ar^+(^2P_{1/2})$ + H_2 with the $^2\Pi_{1/2}$ state yielding the $V_{\frac{1}{2}\frac{1}{2}}$ surface. Thus an important effect due to the spin-orbit interaction is the partial mixing of Σ and Π character in the adiabatic surfaces at large and intermediate distances. In particular it is possible to show that while $V_{\frac{3}{2}\frac{3}{2}}$ has a pure Π character, the $V_{\frac{3}{2}\frac{1}{2}}$ and $V_{\frac{1}{2}\frac{1}{2}}$ potentials acquire pure Σ and pure Π character respectively only at short distances [6]. For the intermediate charge-transfer complex in the collinear configuration (assumed to provide the lowest reaction paths with no activation energy). we have considered both charge-induced dipole and dispersion attractions, as well as a repulsive term due to the configuration interaction. However several surfaces for this intermediate complex have to be considered, corresponding to the possible vibrational quanta v of H_2^+. By simmetry considerations, that is taking into account that the charge-transfer intermediate has essentially a Σ character in the collinear configuration, it is possible to identify the crossings which are avoided and therefore may lead to efficient adiabatic behavior. In our model [6] we assume that the reactivity of the system depends on its ability to reach one of the surfaces describing $X_2^+(v)$ + Ar. The transition probabilities have been calculated using an extended Landau-Zener type theory including quantum mechanical tunneling [6].

$N_2^+ + X_2 \rightarrow N_2X^+ + X$, X=H,D

A strong analogy exists between the present system and the $(Ar\text{-}X_2)^+$ previously discussed. From the point of view of the electronic states the nitrogen system is simpler since only one potential energy surface is associated with the reactants as compared to the three surfaces which have to be considered in the case of Ar^+. However the nitrogen's molecular nature results in a

much larger number of reactants' relative orientations. A further complication is given by the fact that the vibronic states should in principle include the vibrational levels of both the molecules.
Our experimental data support the idea that the reaction proceeds *via* transitions from the $N_2^+ + X_2$ to the $X_2^+ + N_2$ diabatic surfaces. The broad features observed in the energy dependence of the cross-section are attributed to the opening as the collision energy is increased of new reactive channels *via* excited vibronic curves of the intermediate charge-transfer complex. The estimate of the interaction potentials and the proposed model for the reaction dynamics yield a consistent explanation of the fact that product ions are internally excited.

References

[1] Teloy, E.; Gerlich, D. *Chem.Phys.* **1974**, 4, 417.

[2] Tosi, P.; Fontana, G.; Longano S.; Bassi, D. *In.J.Mass Spectrom.Ion Processes* **1989**, 93, 95.

[3] Gerlich, D. *Adv. in Chem.Phys.* **1992**, 82; State-Selected and State-to-State Ion-Molecule Reaction Dynamics: Experiment, part I; edited by Ng, C.Y. and Baer, M.

[4] Tosi, P.; Boldo, F.; Eccher, F.; Filippi, M.; Bassi, D. *Chem.Phys.Letters* **1989**, 164, 471.

[5] Tosi, P.; Eccher, F.; Bassi, D.; Pirani, F.; Cappelletti, D.; Aquilanti, V. *Phys.Rev.Letters* **1991**, 67, 1254.

[6] Aquilanti, V.; Cappelletti, D.; Pirani, F.; Tosi, P.; Soldo, Y.; Bassi, D. *to be published.*

[7] Cappelletti, D.; Liuti, G.; Pirani, F. *Chem.Phys.Letters* **1991**, 183, 297.

[8] Aquilanti, V.; Liuti, G.; Pirani, F.; Vecchiocattivi, F. *J. Chem. Soc. Faraday Trans.* II **1989**, 85, 955.

The Hydrogen Exchange Reaction in Crossed Beams

L. Schnieder, K. Welge

Fakulaet fuer Physik, Universitaet Bielefeld, 4800 Bielefeld 1, Germany

We report on advances made in our laboratory in the experimental investigation of the hydrogen exchange reaction under crossed beam conditions.

While substantial progress has been made in recent years in the theoretical treatment, by exact quantum mechanical calculations [1], and in the measurements of quantum state specific total reaction cross sections under bulk conditions [2], the measurement of state-resolved differential cross sections is still a challenging, largely unsolved problem. Conventional techniques, based on time-of-flight (TOF) measurement of the reaction products, though highly developed, have not yet reached the point where vibrational product states are clearly resolved [3].

We have developed a new TOF technique [4], specifically for hydrogen atoms, based on the selective excitation of the hydrogen atom reaction product to long-living Rydberg states. The technique was first applied in the study of photodissociation processes. More recently, in experiments on the $H + D_2 \rightarrow HD + D$ exchange reaction, it has successfully resolved vibrational product channels (figure 1) [5].

Further improvements in the experiment now allow the resolution of rotational states of the HD product (figure 2). The measurements have been made for scattering angles between 0 and 60 degrees in the lab frame, for collision energies of 0.54 and 1.29 eV. The results agree very well with the quasi-classical trajectory calculations recently obtained by Aoiz [6]. Exact quantum-mechanical calculations are not yet available for this type of reaction.

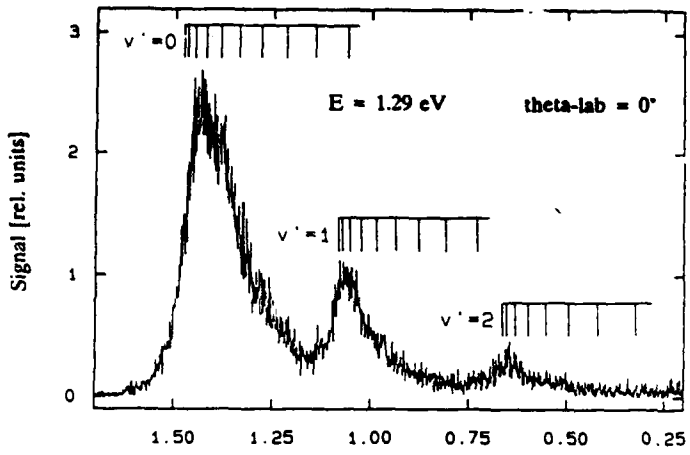

Fig. 1 Energy distribution of D-atoms from the reaction H + D_2 → HD + D for a collision energy of 1.29 eV and a laboratory scattering angle of O°.

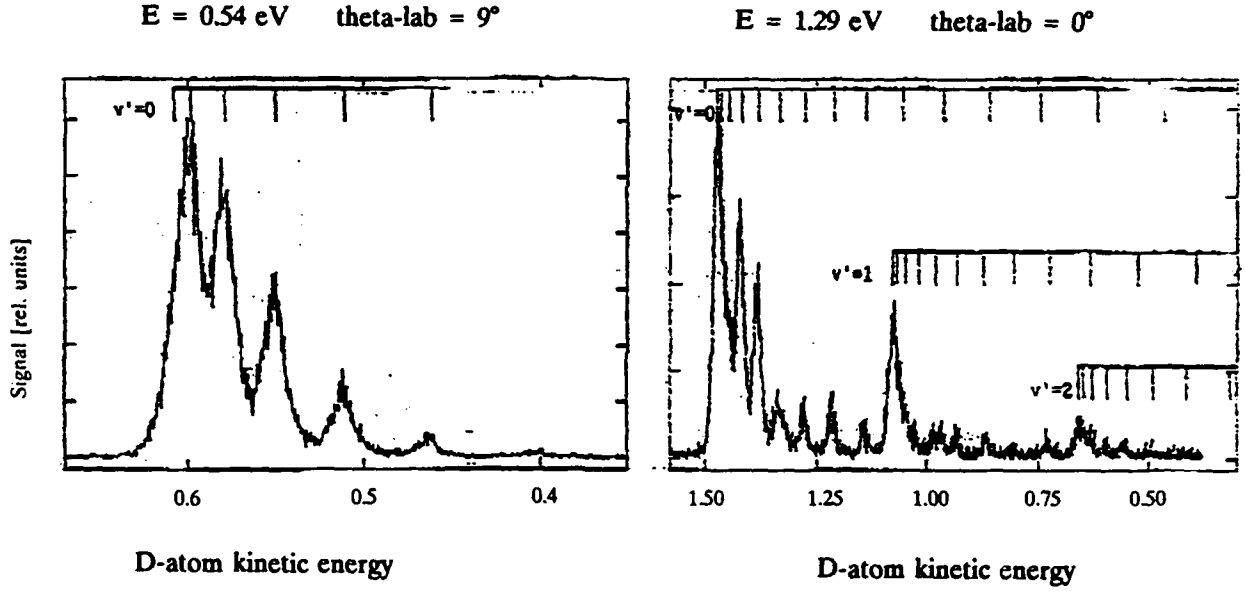

Fig. 2 Energy distribution of D-atoms from the reaction H + D_2 → HD + D at collision energies of 1.29 eV and 0.54 eV at laboratory scattering angles of O° and 9° respectively.

REFERENCES

[1] M. Mladenovic, M. Zhao, D. Truhlar, D. Schwenke, Y. Sun, and D. Kouri, J. Phys. Chem. **92**, 7035 (1988); J.Z.H. Zhang and W.H. Miller, J. Chem. Phys. **91**, 1528 (1989).

[2] D.P. Gerrity and J.J. Valentini, J. Chem. Phys. **81**, 1298 (1984); E.E. Marinero, C.T. Rettner, and R.N. Zare, J. Chem. Phys. **80**, 41 (1984).

[3] R. Goetting, H.R. Mayne, and J.P.Toennies, J. Chem. Phys. **85**, 6396 (1986); S.A. Buntin, C.F. Giese, and W.R. Gentry, Chem. Phys. Lett. **168**, 517 (1990); R.E. Continetti, B.A. Balko, and Y.T. Lee, J. Chem. Phys. **93**, 5719 (1990).

[4] L. Schnieder, W. Meier, K.H. Welge, M.N.R. Ashfold, and C.M. Western, J. Chem. Phys. **92**, 7027 (1990).

[5] L. Schnieder, K. Seekamp-Rahn, F. Liedeker, H. Steuwe, and K.H. Welge, Faraday Discuss. Chem. Soc. **91**, 259 (1991).

[6] private communication.

CROSSED MOLECULAR BEAM STUDIES OF THE REACTIONS

$Cl + O_3$ AND $Br + O_3$

Jingsong Zhang, T.T.Miau and Yuan T. Lee

Chemical Sciences Division, Lawrence Berkeley Laboratory
Department of Chemistry, University of California, Berkeley, CA 94720

ClO and BrO radicals play the key roles in chemically catalyzed ozone depletion in Stratosphere. It is now believed that about 75% of the Antarctic ozone loss results from reactions involving ClO dimer, while another 20% from reactions involving BrO and ClO.[1,2] The first step of the catalytic cycle of ozone destruction is the production of ClO and BrO radicals from $Cl + O_3$ and $Br + O_3$ reactions.

1. $Cl + O_3$

We have studied $Cl + O_3$ reaction by crossed molecular beam method. Cl atomic beam is generated by thermal dissociation of Cl_2 in a high temperature graphite nozzle source.[3] Product ClO time-of-flight (TOF) spectra and angular distribution measurements have been taken at four different collision energies from 6 kcal/mole to 30 kcal/mole.

The following reaction channels are thermodynamically accessible at all collision energies.

$$Cl(^2P) + O_3(^1A_1) \text{ ------> } ClO(^2\Pi) + O_2(^3\Sigma^-_g) \quad (1)$$

$$\text{------> } ClO(^2\Pi) + O_2(^1\Delta_g) \quad (2)$$

$$\text{------> } ClO(^2\Pi) + O_2(^1\Sigma^+_g) \quad (3)$$

Above 18 kcal/mole collision energies, two extra processes are thermodymanically accessible.

$$Cl(^2P) + O_3(^1A_1) \text{ ------> } ClOO + O(^3P) \quad (4)$$

$$\text{------> } OClO + O(^3P) \quad (5)$$

We can not observe any evidence for channels (4) and (5). As for channels (2) and (3), two groups have given branching ratios of 5×10^{-3} or less,[4] the product energy distribution in our results also suggest that these two channels are unlikely to be important. So the $Cl + O_3$ reaction occurs almost exclusively through process (1).

Previous experimental work has mainly concentrated on measuring the rate

constants of this reaction.[5] The insensitivity of the rate constants to the reaction enthalpy for the X + O_3 (X = Cl, Br, F, O, N) reactions suggests that they proceed through early transition states which resemble reactants most. A matrix isolation study of the reaction Cl + O_3 failed to observe evidence for any ClO_3 isomers.[6]

A semi-empirical ClO_3 potential energy surface (PES) has been constructed by Murrell[7] which suggests an early transition state for the collinear collision pathway. The classic trajectory calculations on this PES show that ClO product is predominantly forward scattered with respect to Cl atom and there is no evidence of long-lived complex formation along the collinear pathway. The key features of the H + O_3 PES has been determined using *ab initio* quantum mechanical methods by Schaefer.[8] The authors expect the key features of the H + O_3 PES to be transferable to X + O_3 (X = Cl, OH, NO, and NH_2) systems. However, they can not locate the planar transition state, instead they suggest a nonplanar pathway in which H atom attacks vertically to the ozone molecule plane.

In general , our results show that there is a large translational energy release in products and product ClO is scattered in a wide range of angle. With collision energy increased, ClO lab angular distributions peak more in the forward direction.

Preliminary analysis for reaction at 13 kcal/mole collision energy suggests that there are two types of product energy release modes. One has about 35% total available energy into translational energy, while the second has about 50% (with about 8 kcal/mole more into translational energy). The ClO center of mass (CM) angular distribution in the first mode covers a large range from 10° to 180°, while that of the second is constrained in forward direction peaking around 30° in CM frame. The two types of contributions suggest that there are two possible main reaction pathways which leads to the oxygen abstraction, i.e., Cl atom could attack different oxygen sites on ozone molecule. The semi-empirical calculation by Murrell has not explored other energetically favorable reaction pathways, an *ab initio* calculation on Cl + O_3 system is most helpful.

2. Br + O_3

We have also studied Br + O_3 reaction. Product BrO time-of-flight (TOF) spectra and angular distribution measurements have been taken at five different collision energies from 5 kcal/mole to 26 kcal/mole.

The following reaction channels are thermodynamically accessible at all collision energies.

$$Br(^2P) + O_3(^1A_1) \text{ ------> } BrO(^2\Pi) + O_2(^3\Sigma^-_g) \quad (1)$$

$$\text{------> } BrO(^2\Pi) + O_2(^1\Delta_g) \quad (2)$$

$$\text{------> } BrO(^2\Pi) + O_2(^1\Sigma^+_g) \quad (3)$$

We failed to detect BrOO or OBrO at the highest collision energy 26 kcal/mole. For channels (2) and (3), as in the Cl + O_3 reaction, the product energy distribution in our results also suggest that these two channels are unlikely to be important. So the Br + O_3 reaction occurs almost exclusively through process (1).

In general, results from Br + O_3 reaction are very similar to those of Cl + O_3 reaction. There is again a large translational energy release in products peaking away from zero and that product BrO is scattered in a large range of angle. With collision energy increased, BrO lab angular distributions peak more forward with respect to Br atom.

Preliminary analysis for reaction at 18 kcal/mole collision energy suggests that there are also two types of product energy release modes. One has about 35% total available energy into translational energy, while the second has about 50% (with about 8 kcal/mole more into translational energy). The BrO center of mass (CM) angular distribution in the first mode covers a large range from 10° to 180° with small peak at 65° in CM frame, while that of the second is constrained in forward direction peaking around 30° in CM frame. This behavior is almost identical to that of Cl + O_3 system. The two types of contributions suggest that there are two possible main reaction pathways which leads to the oxygen abstraction, i.e., Br atom could attack different oxygen sites on ozone molecule. An *ab initio* calculation on Br + O_3 system is also most helpful.

References:

1. J.G.Anderson, D.W.Toohey, W.H.Brune, Science **251**, 39 (1991)

2. L.T.Molina, M.J.Molina, J. Phys. Chem. **91**, 433 (1987)

3. J.J.Valentini, M.J.Coggiola, Y.T.Lee, Rev. Sci. Inst. **48**, 58 (1977)

4. (a) J.W.Vanderzanden, J.W.Birks, Chem. Phys. Letters **88**,109 (1982) (b) K.Y.Choo, M.Leu, J. Phys. Chem. **89**, 4832 (1985)

5. (a) D.W.Toohey, W.H.Brune, J.G.Anderson, Int. J. Chem. Kinet. **20**, 131 (1988) (b) J.M.Nicovich, K.D.Kreutter, P.H.Wine, Int. J. Chem. Kinet. **22**, 399 (1990)

6. R.O.Carter,III, L.Andrews, J. Phys. Chem. **85**, 2351 (1981)

7. S.C.Farantos, J.N.Murrell, Int. J. Quan. Chem. **14**, 659 (1978)

8. (a) M.M.L.Chen, R.W.Wetmore, H.F.Schaefer III, J. Chem. Phys. **74**, 2938 (1981) (b) M.Dupuis, G.Fitzgerald, B.Hammond, W.A.Lester, H.F.Schaefer III, J. Chem. Phys. **84**, 2691 (1986)

AUTOIONIZATION DYNAMICS OF COLLISIONAL COMPLEXES

Franco Vecchiocattivi
Dipartimento di Chimica, Università di Perugia
06100 Perugia, Italy

Autoionization is a process which occurs when an atom or a molecule is at an energy level degenerate with the ionization continuum. This process is very fast and in most cases occurs within a time of the order of 10^{-15} s, that is much shorter than most characteristic radiative decay times. Therefore when a given discrete autoionizing state is produced by photo-excitation, ejection of an electron is much more probable than radiative de-excitation. This is the basic principle of photoionization. However, autoionization processes are also possible in slow molecular collisions because the autoionization time is even shorter than the characteristic molecular collision time at thermal energies (~10^{-12} s). The basic requirement is that the two partners should have enough internal energy to produce an autoionizing collision complex.

It follows that collisional autoionization must present several analogies with photoionization. For example, in both cases when the electron is ejected, its energy and momentum provide a detailed spectroscopy of the ionic product which can be correlated with its subsequent dynamical evolution. However, while in photoionization the conditions of the autoionized molecules are determined by the energy and polarization of the photon, in the collisional autoionization process these conditions are determined by the collision characteristics of the system under consideration, such as relative velocity, internal states of the reactants, relative orientation, etc.

A collisional autoionization process can be schematically written as follows:

$$X + Y \rightarrow [X...Y]^*$$

where X and Y are atoms or molecules and $[X...Y]^*$ the collision

complex in an autoionizing state,

$$[X...Y]^* \rightarrow [X...Y]^+ + e^-.$$

After an $[X...Y]^+$ ionic complex is formed, the collision continues towards the final ionic products

$$[X...Y]^+ \rightarrow \text{ion products}$$

Several experimental techniques are used to study the microscopic dynamics of these collisional autoionization processes. It is well established that the most valuable information about the dynamics of a collisional process is provided by molecular beam scattering experiments. In fact, in these cases it is possible to study single collision events and also to define the translational and internal energy of the two collision partners, thus avoiding statistical averaging.

The rare gas atoms, excited to their first levels, are very suitable for these experimental studies[1] because of their high energy content and relatively long life-time which allow them to survive along beam paths in typical molecular beam apparatuses.

Collisional autoionization processes involving metastable rare gas atoms have been studied in our laboratory in the last years[2-5] by measuring the collision energy dependence of the collisional autoionization cross section for each possible final ionic product, in atom-atom[2,3] and atom-molecule[4,5] systems. The experimental apparatus consists of a metastable rare gas beam, produced by electron impact or electrical discharge in a rare gas, crossing with a target beam. The product ions are extracted from the scattering volume and analyzed by a mass filter. The collision energy dependence of the ionization efficiency is obtained by time of flight technique. Recently such apparatus has been improved by changing the experimental configuration in order to increase considerably the signal to background ratio. The new configuration allows us to obtain the ionization cross sections with a higher degree of accuracy, and to perform also integral elastic cross section measurement with a resolution large enough to resolve the glory interference structure. These results implement the information about the dynamics of such processes providing information about the intermolecular potential between the neutral

reactant collision partners.

At the symposium recent results about the Ne^*-HCl, Ne^*-Cl_2, and Ne^*-CF_4 will be presented and discussed.

ACKNOWLEDGMENTS

This research work as been performed together with B.Brunetti and in collaboration with A.Aguilar, S.Falcinelli, M.Gonzalez, and S.Paul. Financial supports by EEC Science Program, CNR bilateral agreement, and a NATO Grant for International Collaboration, are gratefully acknowledged.

REFERENCES

1. B.Brunetti and F.Vecchiocattivi, in Current Topics in Ion Chemistry and Physics, C.Y.Ng ed., Wiley & Sons (1992), vol.I.

2. A.Aguilar, B.Brunetti, M.Cardinalini, F.Vecchiocattivi, and G.G.Volpi, Gazz.Chim.Ital. 113, 711 (1983); A.Aguilar, B.Brunetti, S.Rosi, F.Vecchiocattivi, and G.G.Volpi, J.Chem.Phys. 82, 773 (1985); B.Brunetti, F.Vecchiocattivi, and G.G.Volpi, J.Chem.Phys. 84, 536 (1986).

3. L.Appolloni, B.Brunetti, J.Hermanussen, F.Vecchiocattivi, and G.G.Volpi, Chem.Phys.Lett. 129, 287 (1986); L.Appolloni, B.Brunetti, J.Hermanussen, F.Vecchiocattivi, and G.G.Volpi, J.Chem.Phys. 87, 3804 (1987); B.Brunetti, and F.Vecchiocattivi, in Electronic and Atomic Collisions, J.Geddes et al. eds, North Holland, Amsterdam (1988), p.495.

4. L.Appolloni, B.Brunetti, F.Vecchiocattivi, and G.G.Volpi, J.Phys.Chem. 92, 918 (1988); B.Brunetti, and F.Vecchiocattivi, in Collision Theory for Atoms and Molecules, F.A.Gianturco ed., Plenum, New York (1989), p.413; A.Aguilar, B.Brunetti, M.Gonzalez, and F.Vecchiocattivi, Chem.Phys. 145, 211 (1990); S.Bianco, B.Brunetti, M.Gonzalez, and F.Vecchiocattivi, in Nonequilibrium Processes in Partially Ionized Gases, M.Capitelli, and J.N.Bardsley, Plenum, New York (1990), p.393; A.Aguilar, S.Bianco, B.Brunetti, M.Gonzalez, and F.Vecchiocattivi, Molecular Phys. 71, 897 (1990).

5. A.Aguilar, B.Brunetti, S.Falcinelli, M.Gonzalez, and F.Vecchiocattivi, J.Chem.Phys. 96, 433 (1992).

Pendular Molecules and Perverse Reaction Paths

Dudley R. Herschbach

Department of Chemistry
Harvard University
Cambridge, Massachusetts 02138

Recent experiments and calculations have demonstrated the feasibility of producing beams of linear molecules or ions with internuclear axes substantially oriented or aligned. This exploits the drastic rotational cooling attainable in supersonic jets and the anisotropy of the Stark and Zeeman effects, which allows low rotational states to be tapped in *pendular states* confined to librate over a limited angular range about the field direction. To create these states there is no need to use a focusing field but rather only a short, strong uniform field. Since the pendular states comprise field-induced superpositions or hybrids of free rotor states, they exhibit characteristic spectroscopic features that provide convenient means to assess how well the molecular axis is oriented or aligned. Beyond enabling "heads-or-tails" control of target molecules in collisions, pendular states may enhance the clockwork in ultrafast laser photochemistry.

Many elementary bimolecular reactions offer two or more candidate reaction paths, involving either qualitatively distinct spatial conformations or electronic states. Examples in which the preferred path proves to be unexpected or seemingly *perverse*, as judged by opinion polls of chemist voters, emphasize that molecules know much more than chemists. This talk will consider chiefly such examples among metal oxidation reactions. Particularly instructive is a new look at the venerable Chapman mechanism, proposed over 50 years ago to account for the mesospheric sodium nightglow and the luminescence of meteor trails. This involves reaction of Na atoms with O_3 to form NaO, followed by reaction of NaO with O atoms to regenerate Na atoms, of which a large fraction ($f > 1/3$) must be electronically excited to account for the nightglow. Molecular beam magnetic deflection experiments have now shown that the first step produces NaO predominantly in an excited electronic $^2\Sigma^+$ state rather than the ground $^2\Pi$ state (so the

"hole" in the oxide anion valence shell points towards the alkali cation!). Whereas a previous experiment found that in the second step the $^2\Pi$ does not produce electronic excitation, a correlation diagram analysis predicts the $^2\Sigma^+$ state will do so very efficiently (f ~ 2/3). The specificity of these reaction paths does not stem from energetic or symmetry properties, but can be attributed to preservation of maximal bonding in the transition states.

Session III:

Atomic & Molecular Spectroscopy

New Method for Manipulating Laser Cooled Atoms

Steven Chu

Department of Physics
Stanford University
Stanford, California 94305 USA

Some recent advances in the manipulation of neutral atoms with light at Stanford will be highlighted.

Cooling and trapping techniques are now capable of producing over 4×10^{10} atoms at a temperature of 3×10^{-6} Kelvin and a density of over 10^{11} atoms/cm^3. These atoms can also be launched in a slow atomic beam of accurately determined velocity with a flux of over 10^{11} atoms/sec.[1]

Atom interferometers based on an atomic fountain of laser cooled atoms[2] have already demonstrated a resolution in the measurement of the acceleration of an atom due to gravity of $\Delta g/g = 3 \times 10^{-8}$ and the ultimate resolution may be better than $\Delta g/g = 10^{-11}$. Precise gyroscopes based on atom interferometry should also be possible.[3]

A new method of laser cooling will be described. Atoms have been cooled to a temperature more than an order of magnitude lower than the temperature corresponding to an rms velocity equal to the velocity an atom would have recoiling from the spontaneous emission of a single photon. Temperatures in the ten nano-kelvin range should be possible with this technique.[4]

Other applications of laser cooled atoms currently in progress at Stanford include the precise measurement of the recoil velocity of an atom (leading to an atomic mass standard and an improved value of the fine structure constant),[5] the scattering of nano-

kelvin atoms from surfaces as a method of measuring the Casimir force between an atom and a dielectric surface[6] will be described if time permits.

References

1. K.E. Gibble, S. Kasapi, and S. Chu, Optics Letters **17**, 526 (1992).

2. M. Kasevich, E. Riis, S. Chu and R.G. DeVoe, Phys. Rev. Lett. **63**, 612 (1989).

3. M. Kasevich and S. Chu, Appl. Phys. B **54**, (1992), in press; M. Kasevich and S. Chu, Phys. Rev. Lett. **67**, 181 (1991).

4. M. Kasevich and S. Chu, submitted to Phys. Rev. Lett., 1992.

5. S. Chu and M. Kasevich, in *Laser Spectroscopy X*, eds. M. Ducloy and E. Giacobino, in press, (1992).

6. M. Kasevich, K. Moler, E. Riis, E. Sunderman, D.S. Weiss, and S. Chu, in *Atomic Physics 12*, eds. J. Zorn, R.R. Lewis, (Am. Inst. of Phys., 1991) pp. 47-57.

APPLICATION OF LASER COOLING TO THE TIME AND FREQUENCY METROLOGY

F. Strumia

Dipartimento di Fisica dell'Università di Pisa

An AFS (Atomic Frequency Standard) is a high spectral purity electromagnetic oscillator phase locked to a suitable atomic or molecular transition to improve both the frequency stability and frequency definition. The development of very fast diodes (MIM diodes) allowed the frequency synthesis up to the visible,and the comparison of the microwave standards with the visible and near infrared lasers. Unfortunately, the precision and resolution of the frequency measurements in the microwave region is not yet fully extended to the visible region. Today devices permit a frequency multiplication and phase locking of oscillators with the stability and resolution of the Cs primary standard only up to about 10^{13} Hz. This confines the development of new kinds of Time Standards of improved performances to the microwave and FIR (Far-infrared) spectral region. New frequency standards in the visible region, with a precision equal or better than that of Cs, well be important as independent standards. An AFS referred to a transition observed in an atomic beam is of particular interest for precision and reproducibility, because the reference system is immune from environment perturbations to the maximum degree. There are yet a crucial limitation: the Q of the reference transition has an upper limit since the interrogation time depends on the beam velocity and the interrogation length: $\Delta t = L / v$ and $Q = \nu/\Delta\nu = \nu L/v$.

Improved performances can be obtained either by increasing the transition frequency and/or by reducing the velocity. The Magnesium and Calcium atoms have transitions in the far infrared and in the visible spectral regions, that can be a very useful references [1]. In fact the metastable triplet states $^3P_0$, $^3P_1$, and $^3P_2$ and the associated magnetic dipole transitions, at 0.6 and 1.2 THz for Mg, have a set of properties that are of particular interest. The radiative decay of the ^3P levels toward the ground $^1S_0$ state is strongly forbidden except the $^3P_1$ level, that has a lifetime of about 10^{-3} s. It is then possible to obtain a spontaneous time of flight state selection, and to monitor the SMM transition $^3P_0$–$^3P_1$ by the fluorescence in the visible from the $^3P_1$ - $^1S_0$ transition. Thus, we have a good S/N ratio, with a Q about two order of magnitude larger than that of the Cs AFS. In addition, the dependence of the frequency upon external magnetic field is about four orders of magnitude smaller than for the corresponding Cs transition. Also the red and blue intercombination lines of Mg and Ca, that have a natural linewidth smaller

than 1 kHz, can be used as a high quality reference for the stabilization of visible lasers. Preliminary excellent results were obtained recently, proving the future relevance of these AFS as length/time standards in the visible region.

At Istituto Elettrotecnico Nazionale "G.Ferraris", Torino, Italy a prototype of AFS based on the Mg line at 601 277 157 870(4) Hz was realized, by using the optical Ramsey interrogation scheme on a thermal effusive atomic beam. A linewidth of 1.2 kHz ($Q \approx 5 \times 10^8$) and S/N = 250 was demonstrated with a distance of 30 cm between the two oscillating fields. A limiting factor is the presence in the detection region of a consistent fraction of atoms excited in the $^3P_1$ level by the discharge, and not yet decayed to the ground state, thus producing a large background fluorescence signal, larger than the resonance useful signal. This background could be strongly reduced by pumping the atoms out of the $^3P_1$ level before entering the interrogation region. Effective optical pumping has been demonstrated recently by using 517 nm radiation produced by a single mode dye laser and by using the 383 nm radiation obtained by frequency doubling a diode laser.

A more dramatic improvement of the AFS could be obtained by reducing the velocity of the atomic beam. The benefits being crucial in many key points: 1 the Q of the transition increases; 2- a more efficient detection of the transition is possible, thus increasing the S/N ratio. This is of particular relevance for Mg AFS; 3- the RF power required for interrogating the atomic transition decreases as v^{-2}. This will strongly attenuate the technical problems for extending the synthesis of the interrogating radiation toward higher frequencies; 4)- the relevance of most of the small perturbations that are responsible for the maximum attainable accuracy and reproducibility will be reduced [1]. Laser cooling is a very effective method to produce low velocity atomic beams. For Ca beams it was realized by the method of magnetic tuning. Intense Calcium beams are easily available with a final velocity of about 10 m/s, namely 60 times smaller than the most probable velocity of the therm.. beam. The same cooling technique can be applied to Mg. Unfortunately, here the resonance optical transition falls at 285 nm, and CW radiation can be produced by frequency doubling only. Evidence of cooling was observed but a more laser power is necessary.

These results give a decelerated atomic beam of Ca and Mg in the ground state. This beam is useful for AFS in the visible region, by locking a laser to the intercombination line at 657.2 nm or 457.1 nm respectively. The microwave standard requires, on the contrary, low velocity atoms in the metastable $^1P_0$ state. This can be realized by cooling the atoms directly on the metastable states. The cooling transition must be that connecting the metastable $^3P_2$ level to a $^3D_3$ level. The m_J=+2 — m_J=+3 Zeeman component is an effective two-level system for a circularly polarized light beam, if no

other decay channel exists for the upper $^3D_3$ level. This is not the case of Calcium where other possible decay channels are allowed. In fact in a recent experiment we do not observe evidence of cooling, because of the strong decay through the $^3F^*$ level. In Mg the level system is more simple: the wavelength of the first $^3P_2$–$^3D_3$ transition is 383.83 nm, and no other decay channels are present. Recent development in the laser technology make this wavelength directly available from the new Exalite dye laser. Frequency doubling of commercially available diode laser is, yet, the most interesting option, especially when a long term operation is required.

For the Ca and Mg AFS the interest is primarily for three wavelengths, namely 654 nm, the Ca intercombination line, 422.7 nm, the $^1S_0$ – $^1P_1$ resonance transition of Ca, and 383 nm, the Mg transitions leaving from the triplet metastable levels. The first wavelength is available from the new red laser diodes, while the others can be produced by frequency doubling. In particular the efficient $KNbO_3$ crystal has the condition of 90° non-critical phase-matching at a temperature around -13°C for the 422.7 nm radiation. The less efficient $LiIO_3$ crystal must be used in condition of angle tuned phase-matching for reaching the 383 nm. We have obtained a result close to the calculated efficiency for the single-pass operation: 0.15 μW produced from 30 mW of input power with a 15 mm long crystal. A power in the 0.3 to 5 mW range is necessary for a successful laser cooling. Such a power can be reached by using more powerful diode lasers (100~200 mW) and, more important, by placing the frequency doubling crystal inside a resonant optical cavity. An increase in the duplication efficiency of three to four order of magnitude is expected. We have tested the feasibility of this method by placing the same crystal of the single pass experiment in a linear cavity. In a preliminary result, we observed an UV power of 45 μW, corresponding to an enhancement of 300. So the power level for an effective laser deceleration of metastable Mg atoms could be reached by using diode laser with an output power of about 100 mW. This will lead to significant improvement of the atomic frequency standards in the future. Two AFS are of particular interest: i- a submillimeter one at 601 GHz using a Mg beam optically pumped and/or laser decelerated; ii- a visible AFS at 657 nm using a laser cooled Ca beam, and using a red diode laser at 657 nm. Both AFS will have a short term stability better than 10^{-13} s^{-1}, and a precision of the order of 10^{-15}. The solid state sources will warrant a stable and long lifetime operation, a condition not fulfilled by other kinds of laser.

[1] F. Strumia: "Application of laser cooling to the AFS", in "Laser Science and Technology", A.N. Chester e S. Martellucci, Plenum, N.Y. 1988, pagg. 367-401.

Dissociation Dynamics of Superexcited Molecules

Yoshihiko HATANO
Department of Chemistry
Tokyo Institute of Technology
Meguro-ku, Tokyo 152, JAPAN

A molecule which receives energy exceeding its ionization threshold(Ip) does not always ionize because the molecule except monoatomic molecules has dissociation channels into neutral fragments. The ionization process competes with the neutral fragmentation. These processes are schematically represented in the following for a molecule AB which denotes not only a diatomic molecule but also more generally a polyatomic molecule.

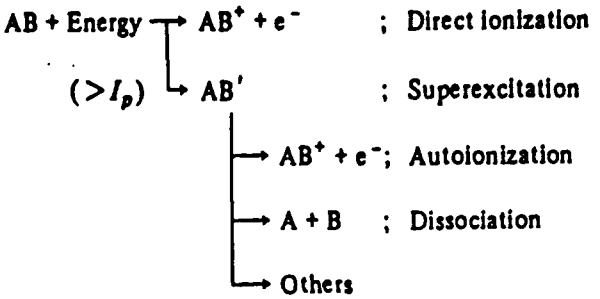

In this mechanism AB' is a superexcited molecule which decays through autoionization and dissociation(or neutral fragmentation). An ionization efficiency η is defined as σ_i/σ_t where σ_i is the sum of the cross sections for both direct ionization and autoionization processes and σ_t is the cross section for the total energy absorption, i.e., the sum of the cross sections for direct ionization and superexcitation. In the case of photoabsorption processes η is called an ionization quantum yield. The value of η for molecules not for atoms in the energy region below the ionization threshold should be zero in general, while that above the threshold increases with increasing the energy and approaches unity in the energy region enough above the threshold. In the energy region above, but close to, the threshold the dissociation process plays a very important role in the decay of a superexcited molecule.

To substantiate molecular superexcited states, both exprimental and theoretical studies have been focussed mainly on the formation of ions and electrons[1,2]. It should be noticed, however, that studies on the neutral dissociation process is also of great importance for better substantiation of molecular superexcited states[3,4]. It is indispensable to measure the kinetic energy of dissociation fragments and their angular distribution as well as to measure the threshold energy of dissociation. The former is translational spectroscopy[4], and the latter is excitation spectrum measurements[3]. Electron impact experiments as combined with these measurements have been extensively made in the past a couple of ten years. From such experiments evidence has been obtained for the electronic structures of superexcited states and their dissociation processes. The superexcited states of molecules are molecular high Rydberg states converging individually to each ionic state and classified into the following three types[4].

1) Vibrationally excited states.
2) Doubly excited states.
3) Inner-core excited states.

Recently synchrotron radiation photons and laser multi-photons as excitation sources have been used to substantiate further in detail the electronic structures of superexcited states and their dissociation processes[5,6].

The following topics are chosen in this paper with particular emphasis on the recent application of synchrotron radiation to dissociation dynamics studies of superexcited molecules.

1) Dissociation dynamics of doubly excited molecular hydrogen[7-9],
2) Angular momentum population of excited hydrogen atoms produced by photodissociation of H_2[10],
3) Dissociation dynamics of N_2, O_2, CO and CO_2 in the superexcited states[11,12], and
4) Absolute measurements of photoabsorption cross sections, photoionization cross sections, photodissociation cross sections, and photoionization quantum yields of CH_4, Si_4H_4, Si_2H_6, C_2H_2, and some other complex molecules[13-16].

References

1) H.Nakamura, Int.Rev.Phys.Chem.,10,123(1991).
2) K.Kimura, ibid.,6,195(1987).
3) F.J.de Hear, H.A.van Sprang, and G.R. Möhlmann, J. Chim. Phys.,77,773(1980).
4) Y.Hatano, Comments on At.Mol.Phys.,13,259(1983).
5) Y.Hatano,"Chemistry of Synchrotron Radiation" in Radiation Research, ed. E.M.Fielden, J.F,Fowler, J.H.Hendry, and D.Scott, Taylor & Francis(1987),p.35.
6) Y.Hatano, "Dynamics of Superexcited Molecules" in "Dynamics of Excited Molecules", ed., K.Kuchitsu, Elsevier, to be published.
7) S.Arai, T.Yoshimi, M.Morita, K.Hironaka, T.Yoshida, H.Koizumi,K.Shinsaka, Y.Hatano, A.Yagishita, and K.Ito, Z.Phys. D;Atoms, Molecules, and Clusters,4,65(1986).
8) M.Glass-Maujean, J.Chem.Phys.,85,4830(1986).
9) S.Arai, T.Kamosaki, M.Ukai, K.Shinsaka, Y.Hatano, Y.Ito, H.Koizumi, A.Yagishita, K.Ito, and K.Tanaka, ibid.,88,3016(1988).
10) N.Kouchi, K.Kameta, Y.Hatano, and K.Tanaka, Chem.Phys. Lett.,190,319(1992).
11) M.Ukai, K.Kameta, N.Kouchi, K.Nagano, Y.Hatano, and K.Tanaka, J.Chem.Phys.,in press.
12) M.Ukai, N.Kouchi, K.Kameta, N.Terazawa, Y.Chikahiro, Y.Hatano, and K.Tanaka, Chem.Phys.Lett.,in press.
13) K.Kameta, M.Ukai, R.Chiba, K.Nagano, N.Kouchi, Y.Hatano, and K.Tanaka, J.Chem.Phys.,95,1456(1991).
14) M.Ukai, K.Kameta, R.Chiba, K.Nagano, N.Kouchi, Y.Hatano, H.Umemoto, Y.Ito, and K.Tanaka, ibid., 95, 4142(1991).
15) K.Kameta, M.Ukai, N.Terazawa, K.Nagano, Y.Chikahiro, N.Kouchi, Y.Hatano, and K.Tanaka, ibid.,95,6188(1991)
16) K.Kameta, M.Ukai, T.Kamosaki, K.Shinsaka, N.Kouchi, Y.Hatano, and K.Tanaka, J.Chem.Phys.,in press.

High Resolution Spectroscopy of ICl: Rehybridization as a function of bond length

Timothy J. Slotterback and Kenneth C. Janda
Department of Chemistry, University of California, Irvine

Jeffery R. Johnson, and David W. Pratt
Department of Chemistry, University of Pittsburgh

and

Colin M. Western
Department of Chemistry, University of Bristol

Fluorescence excitation spectra for the A $^3\Pi_1 \leftarrow$ X, $^1\Sigma^+$ transition of $I^{35}Cl$ has been studied for A state vibrational levels ranging from v'=11 to v'=34. As can be seen in Fig. 1, these vibrational levels span the top half of the A state potential. The spectra were recorded with sufficient resolution to obtain hyperfine constants for both the I and the Cl atoms. The hyperfine constants, especially those of the I atom, were found to vary rather rapidly with vibrational level. This variation is analyzed in terms of electronic rehybridization as a function of the internuclear separation. In the LCAO-MO approximation, the unpaired electron for each of the atoms in the ICl A state should have an equal probability of being found in the p_z orbital (aligned along the internuclear axis) or in the p_x and p_y orbitals (perpendicular to z). This results from the common assignment of the A $\leftarrow$ X transition as involving a $\sigma^* \leftarrow \pi^*$ electron promotion. This model for the bonding approximately predicts the correct Cl atom hyperfine constants for a wide range of R values. For large R the probability that the unpaired electron is in the Cl p_z orbital increases from 55% to 65%. The hybridization of the I atom, however, is quite different than the LCAO-MO model predicts. At large R, the probability that the electron is in the p_z orbital is only 15%, and at separations down to 2.8 Å it is still only 30%.

The spectra for this study were obtained using a single frequency, Ar^+ pumped-ring jet dye laser and a triply skimmed molecular beam as illustrated in Fig. 2. A key factor in obtaining clean spectra was a liquid N_2 cooled plate positioned under the laser beam-molecular beam interaction region to cryopump I_2 molecules. Figure 3 shows a sample of the quality of the spectra. This data is for v'=32, which is the highest vibrational level for which the signal-to-noise ratio was sufficient to cleanly resolve the Cl atom hyperfine structure. The top portion of the figure shows a 0.58 cm^{-1} region of the band-head portion of the spectrum. In the absence

of hyperfine splittings, individual rotational lines would occur in the positions as indicated. At this resolution the splitting due to the I atom hyperfine interactions are readily apparent. The bottom portion of the spectrum shows an expanded view of a 0.01 cm^{-1} portion of the spectrum. At this resolution the Cl atom hyperfine splitting can be observed. An example of the quality of the fits to the spectra is shown in Fig. 4. Typically, 180 lines were well enough resolved for each vibronic band that they could be employed in the fit. The fit involves determination of a band origin, rotational constants, a Λ doubling parameter, one magnetic and two electrical hyperfine constants for each atom and a spin-rotation constant for the I atom. (All constants for the **X** state were taken from the literature[1].) In each case a sufficient variety of lines was available to lower the correlation error in the fitting process to an acceptable level.

We believe that this is the first time that hyperfine constants for two different atoms in a diatomic molecule have been measured over a wide range of vibrational energies. (Similar work for I_2 has been reported by Bacis **et al.**[2].) Therefore, the theoretical framework for interpreting the constants is not available in the literature. Usually, electrical hyperfine constants are interpreted in terms of LCAO-MO orbital population analysis.[3] In this model, the hyperfine constants of the molecule are fixed once an orbital assignment is made, because the molecular hyperfine constants can then be predicted from free atomic values. This model is widely used to obtain the degree of charge transfer in a chemical bond. For the **A** state of ICl, we find that the LCAO-MO model can not even qualitatively describe the I atom hyperfine constants for upper vibrational levels.[4] That is, not only are the predicted values incorrect, but even the signs are wrong.

We are implementing an analysis of the data based on a valence-bond model where the molecular wave function at each value of the internuclear separation is described as a sum over combinations of the separated atomic wave functions that have the proper angular momenta. This analysis is still in progress, but has so far led to the conclusions outlined in the first paragraph of this abstract.

1. E. Herbst and W. Steinmetz, J. Chem. Phys. **56**, 5342 (1972).
2. R. Bacis. M. Broyer, S. Churassy, J. Verges, and J. Vigué, J. Chem. Phys., **73**, 2641 (1980).
3. C. H. Townes and A. L. Schawlow, **Microwave Spectroscopy**, Dover Publications, New York, 1975, Chapter 9.
4. Jeffrey R. Johnson, Timothy J. Slotterback, D. W. Pratt, K. C. Janda and C. M. Western, J. Phys. Chem. **94**, 5661 (1990).

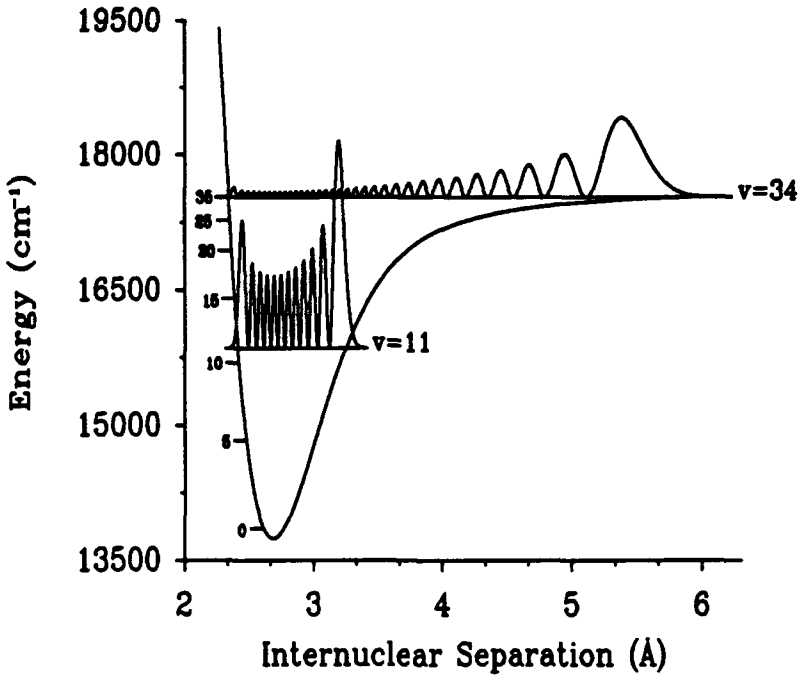

Figure 1: A state potential[2] illustrating the vibrational wavefunctions squared for the v' = 11 and 34 levels of $I^{35}Cl$.

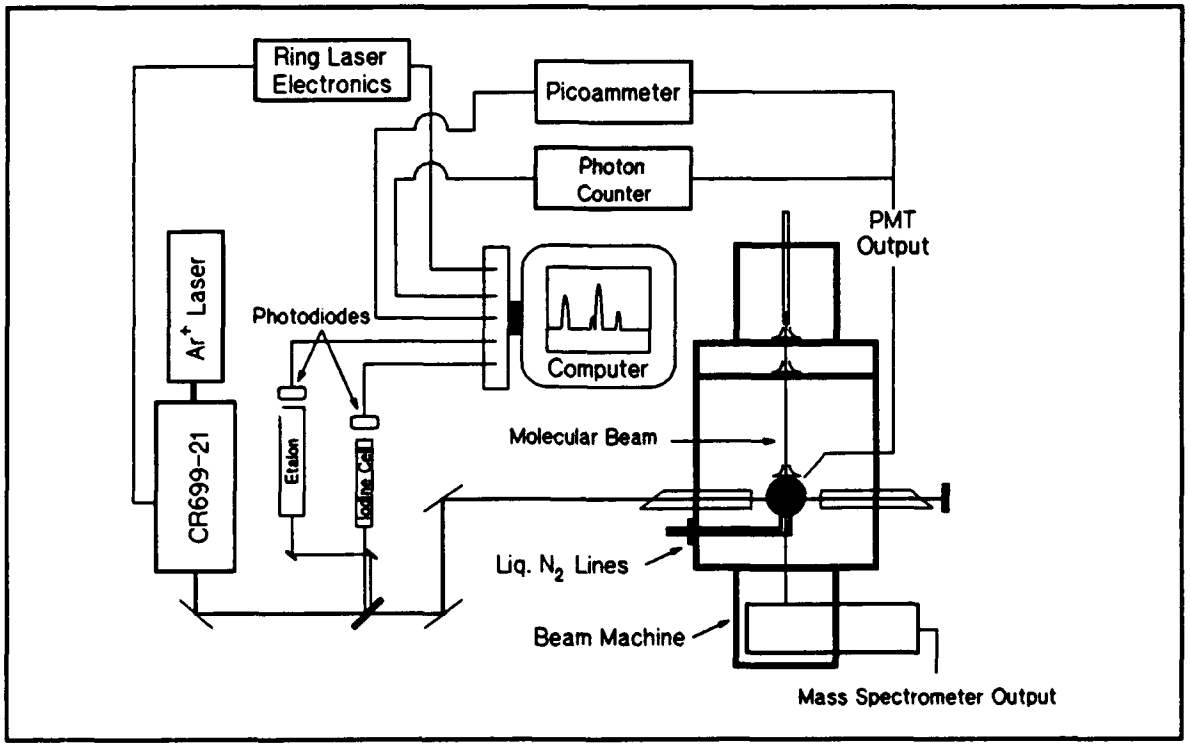

Figure (2): Schematic representation of High Resolution Spectrometer.

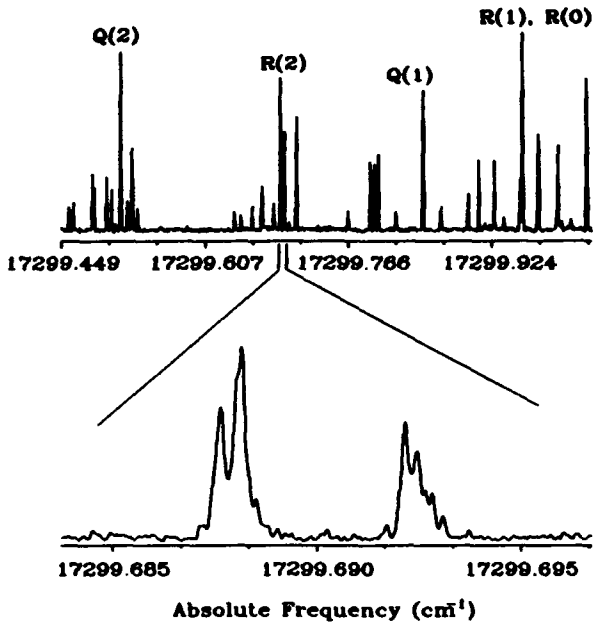

Figure 3: (Top) 0.58 cm^{-1} portion of the bandhead data collected for the **A** ← **X**, **32** ← **0** transition of $I^{35}Cl$. (Bottom) An expanded view of the the hyperfine structure of the R(2) rotational transition.

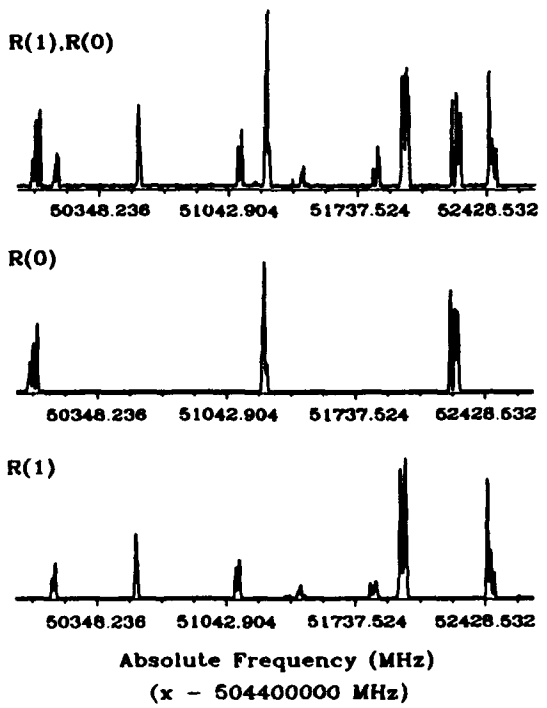

Figure 4: (Top) 0.092 cm^{-1} portion of $I^{35}Cl$ **A** ← **X**, **21** ← **0** transition. (Center) Simulation of R(0) transition. (Bottom) Simulation of R(1) transition.

Asilomar abstract II

Ultrahigh Resolution Threshold Photoelectron Spectroscopy of Small Molecules Using Extreme Ultraviolet Lasers.

W. Kong, D. Rodgers, and J.W. Hepburn
Department of Chemistry
University of Waterloo
Waterloo, Ont. N2L 3G1
CANADA

We have recently finished building a new apparatus for extreme ultraviolet photoionization spectroscopy in supersonic molecular beams. One of the experiments that can be carried out on this apparatus is ultrahigh resolution threshold photoelectron spectroscopy on jet cooled molecules, radicals, and clusters. In this paper, we discuss the application of the pulsed field ionization technique at photon energies between 14 eV and 17 eV, corresponding to wavelengths between 88nm and 73nm.

The exact mechanism for "ZEKE" spectroscopy has been the subject of recent debate, but our results, and recent work by other groups[1,2], show conclusively that the process is dominated by field ionization of very high Rydberg states. It is still possible to model this process, and in figure 1, a pulsed field ionization spectrum of the CO^+ ($X^2\Sigma^+$)v=0 state is shown, along with a calculated spectrum, based on the model proposed by Buckingham[3]. The spectrum shown in figure 1 was recorded by single photon excitation of a skimmed supersonic beam of CO, followed by ionization with a weak pulsed field (about 0.4V/cm). We will discuss our results on both the *X* state and $A^2\Pi$ state of CO^+, along with the results of model calculations on this system.

We have also studied the application of this technique to excited states of polyatomics, focussing initially on N_2O. In figure 2, the TPES spectrum of the zero point level of the $A^2\Sigma^+$

state of N_2O^+ is shown, along with a preliminary simulation, based on the Buckingham model. Work on other states of N_2O^+ will be discussed, including work done in the Franck-Condon gap region, corresponding to highly excited vibrational levels of the ground state of N_2O^+.

Our results have a significant impact on the understanding of the behaviour of highly excited Rydberg states of small molecules, and carry implications on the ability to use pulsed field ionization to rotationally and vibrationally state select ions for reaction dynamics studies. Applications of this technique to other systems will be discussed, along with a brief discussion of some of the other capabilities of this new apparatus.

1. R.G. Tonkyn, J.W. Winniczek, and M.G. White, *Chem. Phys. Lett.* **164**, 137 (1989)

2. S. Hillenbrand, L. Zhu, and P.M. Johnson, *J. Chem. Phys.* **95** 2237 (1991)

3. A.D. Buckingham, B.J. Orr, and J.M. Sichel, *Phil. Trans. Roy. Soc. Lond. A* **268** 147 (1970)

Acknowledgements

This work was supported by NSERC(Canada), and the Canadian networks of centres of excellence programme, administered by NSERC.

Figure 1: Threshold photoelectron spectrum of CO

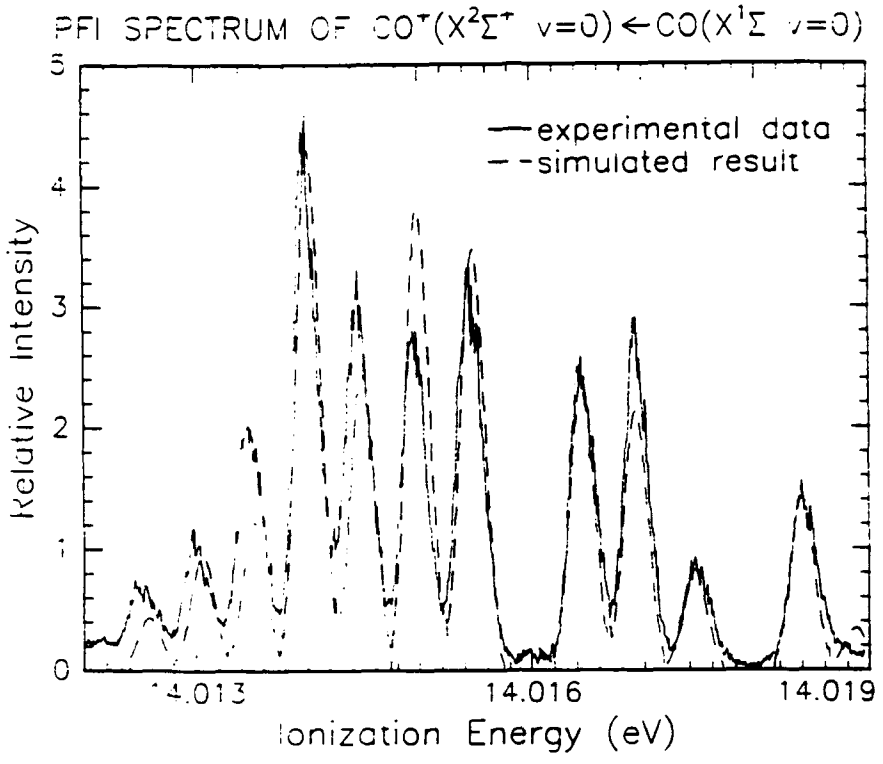

Figure 2: Threshold photoelectron spectrum of N_2O

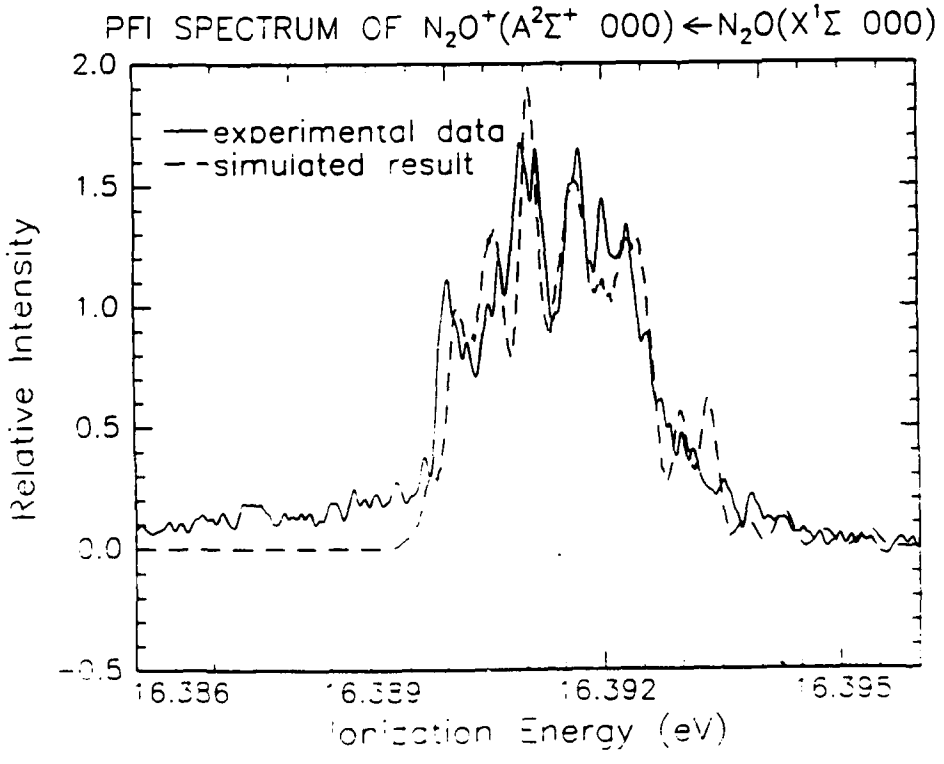

COPY AVAILABLE TO DTIC DOES NOT PERMIT FULLY LEGIBLE REPRODUCTION

Rydberg States of CaF: Healing a Scar in the 's'Σ Series

Chris Gittins, Nicole Harris, and Robert Field
Dept. of Chemistry, Massachusetts Institute of Technology, Cambridge MA

CaF Rydberg states are well described by the zero-order model of an electron interacting with a molecular ion core consisting of two relatively compact, closed-shell atomic ions. The large permanent electric dipole moment of the $(CaF)^+$ ion is an ion-core/outer electron long-range coupling mechanism unique to molecular (as opposed to atomic) systems. Typically, Rydberg series are characterized by quantum numbers n, ℓ, and λ. The $(CaF)^+$ permanent dipole couples states of $\Delta\ell = \pm 1$, completely mixing ℓ for all core-penetrating Rydberg series. This is in contrast to molecules such as NO, H_2, and Na_2, whose Rydberg series are more extensively studied, where ℓ is not completely destroyed.

Given that a Rydberg series consists of an infinite number of electronic states, deperturbation of Rydberg rovibronic energies back to a set of zero-order $n\ell\lambda$ Rydberg potential curves, $V_{n\ell\lambda}(R)$, is not feasible. Multichannel quantum defect theory (MQDT) replaces the $V_{n\ell\lambda}(R)$ curves with a single potential energy curve for the ion-core, and a set of quantum defect functions, $\delta_{\ell'\lambda}(R)$. The quantum defect function is a direct measure of the Rydberg orbital's sampling of the molecular ion core. The intra-core nodal structure of the wavefunction of each member of every core-penetrating Rydberg series is effectively n-invariant, and replicates that of the valence state on which the series terminates, hence an understanding of the CaF valence structure is crucial to understanding the core-penetrating Rydberg series.

Recent optical-optical double resonance (OODR) experiments have revealed that the previously identified $D^2\Sigma^+$ state [1] of CaF is actually v=1 of the C' $^2\Sigma^+$ valence state [2,3]. This observation is consistent with the prediction of Bundgen, Engels, and Peyerimhoff [4], whose ab initio calculations placed only one $^2\Sigma^+$ state in the vicinity of 30000 cm^{-1}. We have observed the three lowest vibrational levels of the C' state and made the reassignment on the basis of the rotational constant, B_e=0.366 cm^{-1}, and vibrational energy level spacing, 650 cm^{-1}.

Reassignment of the "D" state is also in accord with the analysis of Murphy, et al.[5]. Murphy and co-workers have been able to identify six distinct Rydberg series in CaF: three $^2\Sigma^+$, two $^2\Pi$, and one $^2\Delta$, consistent with 's', 'p', and 'd' core penetrating orbitals. Reclassification of the "D" state removes the anomalies in the 's'Σ(n=5) and 'p'Σ(n=4) series because the C' state replaces it in the 's'Σ series, and the entire 'p'Σ series is now shifted to n-values lower by 1.

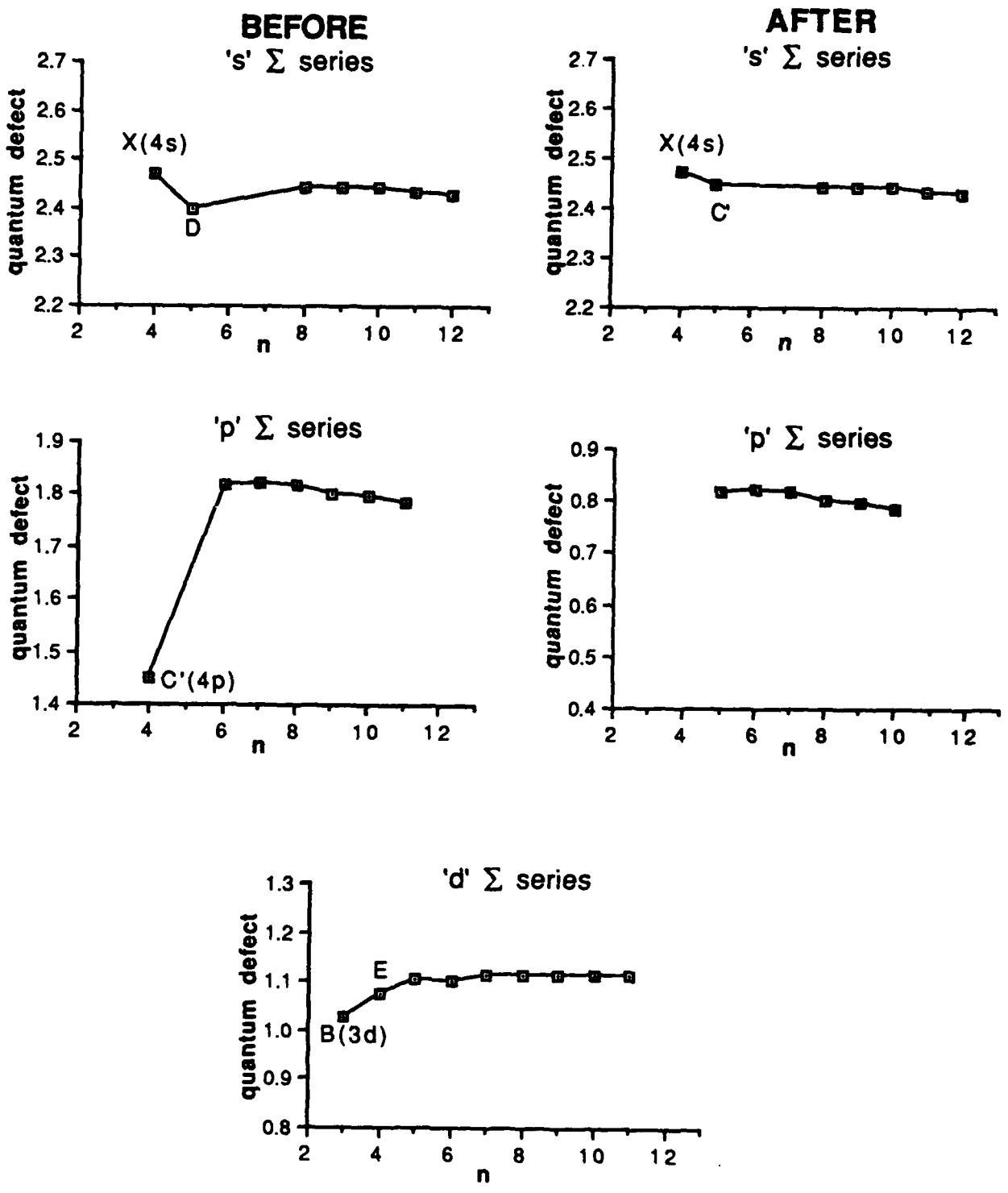

Fig.1 Quantum defect plots before and after the reassignment of the "D" state

CaF was produced in a Smalley-type laser ablation-free jet expansion source [6]. A Ca metal target was ablated with a ~9 mJ pulse from a frequency doubled, Q-switched Nd:YAG laser focussed to a spot several mm in diameter. The resulting Ca plasma was entrained in a flow of Ar(3 atm) + SF_6(trace) provided by a pulsed nozzle. Shot-to-shot fluctuations in CaF number density, as monitored by fluctuations in $A^2\Pi_{3/2}$-$X^2\Sigma^+$ (0,0) fluorescence excitation signal, were on the order of 50%. Rotational cooling of the molecules was substantial, T_{rot}≈30 K, and no vibrational hot bands were observed in the A-X system.

The OODR experiment involved two pulsed dye lasers. The PUMP laser ($\Delta\nu$≈0.05 cm^{-1}) is tuned to a transition in the $A^2\Pi_{3/2}$-$X^2\Sigma^+$(0,0) system, and the PROBE laser ($\Delta\nu$≈0.10 cm^{-1}), delayed ~5 ns relative to the PUMP, is scanned through the C'-A transitions. The C' state was detected by monitoring UV fluorescence to the ground state. This method precluded the detection of $^2\Delta$ states. By populating a single rotational, parity level in the intermediate state, the OODR spectrum is reduced to a two line pattern (for a $^2\Sigma^+$ final state), allowing for rapid calculation of the rotational constant and other fine structure parameters.

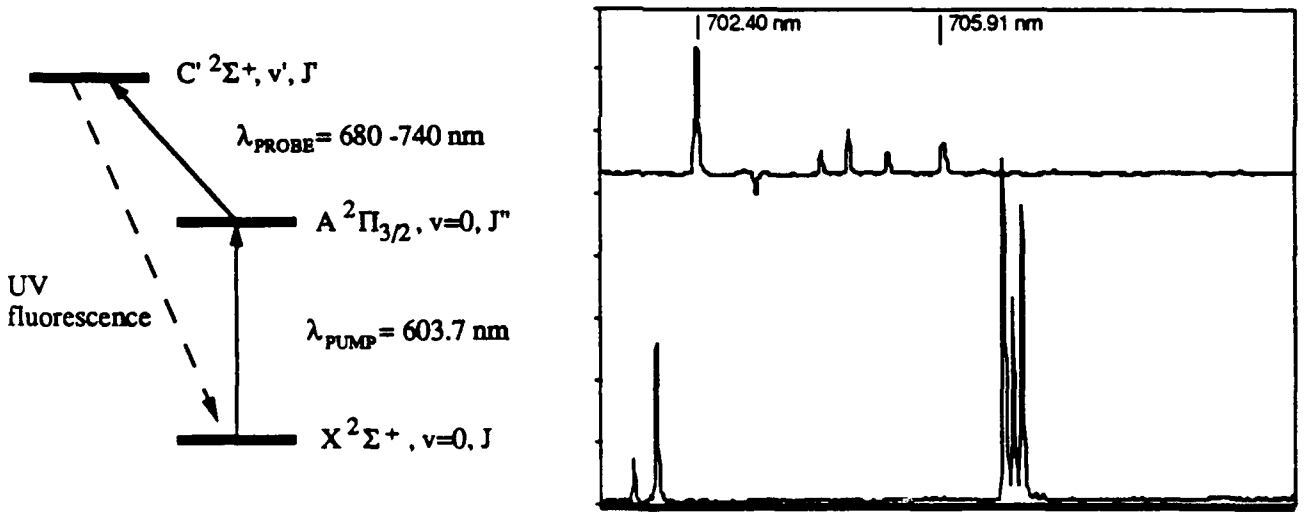

a) b)

Fig. 2a. Energy level scheme in OODR experiment
2b. Typical OODR spectrum pumping $R_2(2.5)$ + $Q_{21}(3.5)$ lines in the $A^2\Pi_{3/2}$-$X^2\Sigma$ (0,0) band. Doublet on the left side of the bottom trace is C' $^2\Sigma^+$, v=1, triplet is C $^2\Pi_{3/2}$, v=1. Top trace is Ne optogalvanic signal used for wavelength calibration.

References

1. C.Fowler, *Phys.Rev.* 59, 645 (1941).
2. P.Bernath, Ph.D. Thesis, M.I.T.(1981).
3. B.Pouilly and J.Schamps, U. of Lille, private communication.
4. P.Bundgen, B.Engels, and S.D.Peyerimhoff, *Chem.Phys.Lett.* 176, 407 (1991).
5. J.E.Murphy, J.M.Berg, A.J.Merer, N.Harris, and R.W.Field, *Phys.Rev.Lett.* 65, 1861 (1990).
6. J.B.Hopkins, P.R.R.Langridge-Smith, M.D.Morse, and R.E.Smalley, *J.Chem.Phys.* 78, 1627(1983).

ROVIBRATIONAL ENERGY TRANSFER IN S_1 D_2CO USING CROSSED MOLECULAR BEAMS.

B.D. Gilbert, C.S. Parmenter, and C.J. Pursell, Department of Chemistry, Indiana University, Bloomington, IN 47405

State-to-state energy transfer from selected rovibronic levels in S_1 D_2CO has been studied with crossed molecular beams. A UV laser is used to prepare an initial S_1 state in D_2CO. After inelastic scattering from He, Ar or H_2 in the secondary beam, the newly populated S_1 states are monitored with dispersed $S_1 \rightarrow S_0$ fluorescence. The detection of new states produced by the inelastic scattering is limited only by the fluorescence resolution and sensitivity. In the case of D_2CO, we have been able to obtain relative inelastic cross sections for both rotationally and rovibrationally inelastic scattering. These data reveal distinctive propensity rules. They also provide instructive comparisons with analogous inelastic scattering from the 12-atom molecule glyoxal. Perhaps most importantly, they establish benchmarks for 3-dimensional quantal scattering calculations recently provided by Kroes, Echave and Clary.

Inelastic Scattering from S_1 D_2CO

The energy levels of interest for D_2CO in the S_1 state ($^1A_2$) are shown in Figure 1. In the S_1 state the molecule is non-planar by 33°, which results in a double minimum potential. The ν_4 mode, which is the out-of-plane bending vibration, is therefore extremely anharmonic (i.e. ν_4 = 67 cm^{-1}, $2\nu_4$ = 386 cm^{-1}, $3\nu_4$ = 667 cm^{-1}), as is evident in Figure 1. Though excitation of the S_1 state is electronic dipole forbidden, strong vibronically allowed transitions involving ν_4 exist.

Figure 1. Energy Levels of Formaldehyde

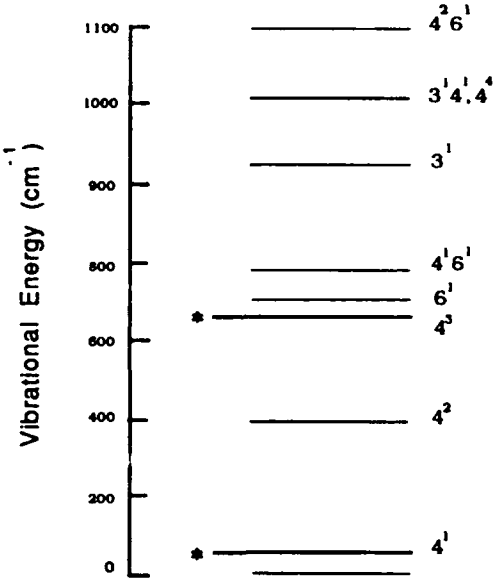

Presently, we have been studying rovibrational energy transfer from the ν_4 fundamental, 4^1. Because D_2CO is a near prolate symmetric top with large rotational constants, optical selection prepares a unique J′, K′ level in the 4^1 state, where K′ represents rotation around the a-axis (i.e. the C-O bond). Therefore, unlike our previous study of glyoxal in which a unique K′ level was prepared with a distribution of J′ states, J′ and K′ are uniquely defined for D_2CO in the 4^1 state as J′ = 3, K′ = 0.

The emerging results for inelastic scattering from He, Ar and H_2 indicate that the three collisional partners exhibit similar general trends. First, rotationally inelastic scattering (i.e. final states 4^1, $K' > 0$) occurs with a $\Delta K = 0, \pm 2, \pm 4, \ldots$ selection rule due to nuclear spin conservation. Second, the rotationally inelastic cross sections scale approximately exponentially with ΔE, the total energy being exchanged, and with similar scaling constants for the three collisional partners. Third, vibrationally inelastic scattering occurs to only the zero-point vibrational level (i.e. final state 0^0, $K' > 0$), and with a $\Delta K = \pm 1, \pm 3, \ldots$ selection rule. The latter is again due to spin conservation. The $\Delta v = -1$ "propensity" in the ν_4 mode is probably due to the large difference in ΔE for going up versus down in ν_4 (i.e. $\Delta v = +1$ has $\Delta E = 319$ cm^{-1}, whereas $\Delta v = -1$ has $\Delta E = 67$ cm^{-1}). Finally, the rovibrationally inelastic cross sections scale approximately exponentially with ΔE. In fact, when the log of the rotationally (4^1, $K' > 0$) and rovibrationally (0^0, $K' > 0$) inelastic cross sections are plotted together, they nearly fall on the same straight line. In other words, where similar ΔE occurs, the rovibrational cross sections are very similar to the rotational cross sections.

Comparison with Quantal Theory

These experimental results can be compared to recent theoretical work. Kroes, Echave and Clary (1) have carried out full quantum mechanical calculations of inelastic cross sections for S_1 D_2CO scattering by He and Ar using their azimuthal and vibrationally close-coupled, infinite-order sudden (AVCC-IOS) method (2). They predict large cross sections for collision-induced relaxation of the ν_4 mode, in agreement with experiment. The cross sections for pure rotational excitation (i.e. 4^1, $K' > 0$) fit well an exponential energy gap law for both partners, also in agreement with experiment. The rovibrational cross sections (i.e. 0^0, $K' > 0$), however, are predicted to have considerable structure. For example, the rovibrational cross sections for collisions with Ar are predicted to have two maxima (i.e. at 0^0, $K' = 1$ and 0^0, $K' = 7$). Thus far, we have been unable to observe this structure. It is extremely encouraging, however, to see such good agreement between theory and experiment for such an anharmonic species.

Comparison with Scattering from S_1 Glyoxal

An additional comparison can be made with the scattering results of S_1 glyoxal (3). Briefly, rotational and rovibrational scattering from the (7^2, $K' = 0$) and the (0^0, $K' = 0$) levels were studied. Only those vibrational levels reached by $\Delta v = \pm 1$ in the lowest frequency mode ν_7, the OHC-CHO torsion, are seen. All the cross sections scale exponentially with the amount of energy transferred. Additionally, for scattering

from the (0^0, K′ = 0) level, the rotational and rovibrational cross sections are approximately equal when similar ΔE occurs. The theoretical work of Kroes, et al. (4,5) is in good agreement with these results. The results of our present study of D_2CO are also consistent with these results. In fact, it is interesting to note the similarity of the ν_4 mode in D_2CO and the ν_7 mode in glyoxal, and rotation around the a-axis (i.e. K-rotation). Figures 2 and 3 illustrate these motions in D_2CO and glyoxal, respectively. Rotation about the a-axis can be viewed as "in-phase" motion for both molecules, whereas the ν_4 vibration in D_2CO and the ν_7 mode in glyoxal can be viewed as "out-of-phase" motion. From this simple picture, it is clear that rotation about the a-axis and the ν_4 vibration in D_2CO and the ν_7 vibration in glyoxal are very similar motions. It is therefore not surprising that both D_2CO and glyoxal have similar rotationally and rovibrationally inelastic cross sections when similar ΔE occurs.

Figure 2. Motion in Formaldehyde

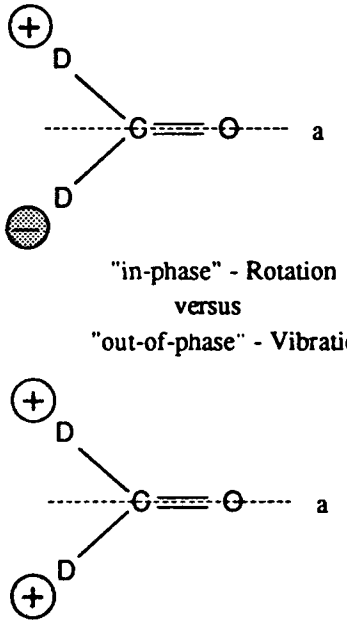

Figure 3. Motion in Glyoxal

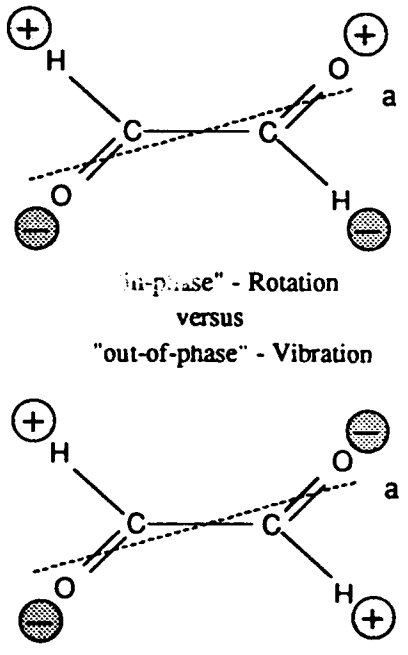

REFERENCES

1. G.J. Kroes, J. Echave, and D.C. Clary, Chem. Phys. (in press 1992).
2. D.C. Clary, J. Chem. Phys. 81, 4466 (1984); J. Phys. Chem. 91, 1718 (1987).
3. K.W. Butz, H. Du, D.J. Krajnovich, and C.S. Parmenter, J. Chem. Phys. 89, 4680 (1988).
4. G.J. Kroes, R.P.H. Rettschnick, C.E. Dateo, and D.C. Clary, J. Chem. Phys. 93, 287 (1990).
5. G.J. Kroes, and R.P.H. Rettschnick, J. Chem. Phys. 94, 360 (1991).

Session IV:

Poster Session

Poster Session Abstracts
BEGIN ON PAGE 195

Session V:

Clusters II

Doping the Fullerenes

R. E. Smalley

Rice Quantum Institute and
Departments of Chemistry and Physics
Rice University
Houston, Texas 77251

Abstract

Fullerenes are a new class of carbon molecules, the first truly molecular form of pure carbon yet isolated. Consisting of hollow cages composed of three-connected networks of carbon atoms arranged to form 12 pentagons and a varying number of hexagons, these spheroidal molecules may be most useful when they are mixed with small numbers of other atoms. These "dopant" atoms may be located either (1) outside the cage, producing fulleride salts, or (2) inside the cage, producing a sort of superatom, or (3) as part of the cage itself, replacing one or more of the carbon atoms in the cage network. Examples of all three types of doping have already been demonstrated.

Molecular Probes of Quantum Clusters: Impurity Species in He_N and $(H_2)_N$

K. B. Whaley, R. N. Barnett and M. McMahon

Department of Chemistry
University of California, Berkeley
CA 94720

Like their bulk counterparts, clusters of helium and hydrogen are dominated by quantum effects. The size dependent scaling of their properties therefore requires a full quantum mechanical treatment. Monte Carlo techniques allow the cluster ground states to be studied explicitly, and in some cases can also be extended to the study of excited states.[1] Such theoretical studies of the Bose species ^4He_N allow the density distributions and compressional excitation spectra, the finite size analogue of the phonon spectra, to be characterized, with consequent implications for the scaling of superfluid behavior.[2] For $(H_2(J=0))_N$, also a Bose cluster, ground state studies are also important to establish the liquid/solid nature of the clusters. The possibility of superfluid states of these clusters and understanding the manifestation and dynamical consequences of these represents a unique question in the quantum mechanics of small particles.

Following earlier studies of the pure Bose clusters[1-2], we extend the Monte Carlo approach to the study of quantum clusters containing an impurity or "probe" species. The systems discussed here are H_2 *in* He_N and SF_6 *in* He_N. Ground state (non-rotating and non-vibrating) variational and exact calculations for these heterogeneous species yield information on the location of the impurity and the helium density distribution around it. They also allow subtle structural information not apparent in the pure helium clusters to be inferred. The H_2 is extensively delocalized throughout the clusters (Figure 1) with some degree of localization between the cluster center and its exterior.[3] In contrast, SF_6 behaves

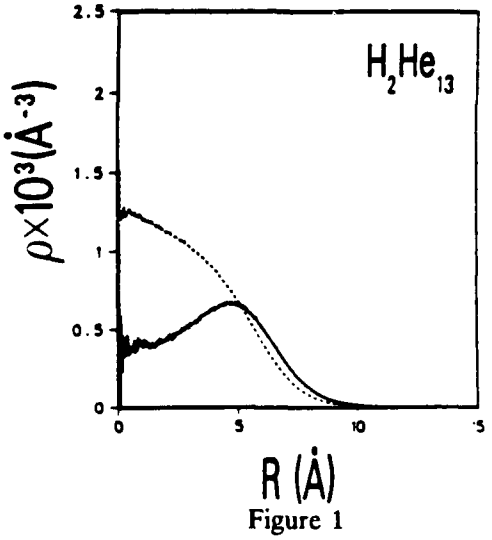

Figure 1

He (dashed) and H_2 (dotted) density profiles for the mixed cluster H_2He_{13}.

much more classically and is very strongly localized at the cluster center (Figure 2). Furthermore this species induces a large degree of ordering in the surrounding helium, consistent with the formation of a solid-like and a series of liquid-like shells.

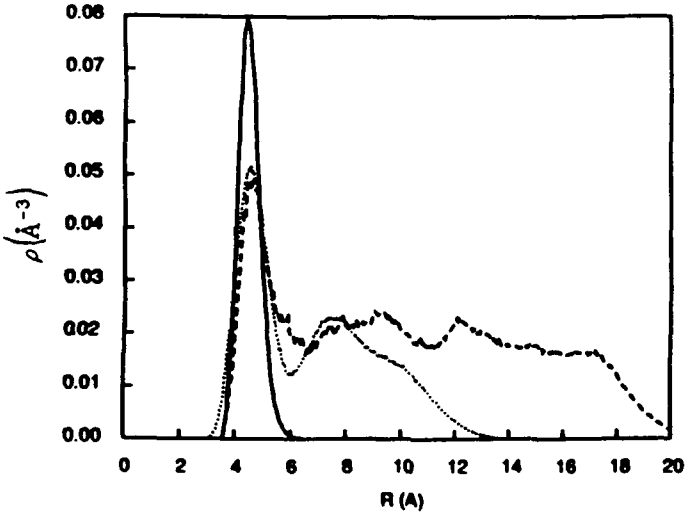

Figure 2

He density profiles for the mixed clusters SF_6He_N, N=20 (solid), 111 (dotted) and 499 (dashed).

The study of impurity molecules is important because of their potential role as non-dissociative probes of the cluster dynamics. This requires two aspects: (i) the incorporation of the impurity-solvent interaction and wavefunction, and (ii) analysis of the coupling between the molecular excitations and the cluster excited and evaporative states. We shall discuss both of these issues here, and present results for the cluster ground state structures containing an impurity as well as for the excited states of pure He_N and $(H_2)_N$.

The general variational approach to excited states will be summarized, and the distinction and different analysis required for vibrational (compressional) and rotational states emphasized. Monte Carlo study of the latter allows information on the centrifugal distortions in the rotationally excited states to be extracted. Results for rotationally excited helium and hydrogen clusters will be presented, and compared with earlier predictions made for compressionally excited clusters. Extension to the study of energy transfer from excited probe molecules and the implications for making direct contact with experimental spectroscopic measurements will be briefly discussed.

References

1. M.V. Rama Krishna and K.B. Whaley, J. Chem. Phys. **93**, 6738 (1990); R.N. Barnett and K.B. Whaley, Phys. Rev. A (submitted).

2. M.V. Rama Krishna and K. B. Whaley, J. Chem. Phys. **93**, 746 (1990); M.V. Rama Krishna and K.B. Whaley, Phys. Rev. Lett. **64** , 1126 (1990).

3. R.N. Barnett and K.B. Whaley, J. Chem. Phys. **96**, 2953 (1992).

Elemental Clusters in Molecular Beams: Size Dependent Effects

K. Rademann
Philipps-University Marburg, Physical Chemistry and Center of Materials Research
Fachbereich 14, Hans-Meerwein-Strasse, W-3550 MARBURG/Lahn, Germany

Abstract: (XIVth International Symposium on Molecular Beams, June 7-12, 1992)

We present recent results on the formation and spectroscopy of elemental clusters (of group IIa, IIb and group VI elements) in seeded supersonic beams. The cluster distributions (with typically 2 to 100 atoms) are characterized by time-of-flight photoionization mass spectrometry performed at various discrete photon energies in the vacuum ultraviolet. The mass analyzer is an integrated part of a photoelectron-photoion coincidence spectrometer. Photoelectron spectroscopy is performed by means of a magnetic mirror type time-of-flight kinetic energy analyzer, which accepts almost all electrons emitted into 4π steradians. Therefore it is possible to record photoelectron spectra as fast as mass spectra. As single electrons are detected in coincidence with single ions, we finally obtain spectroscopic information about *mass specified neutral clusters*. The basic physical quantities that can be extracted out of mass selected photoelectron spectra are ionization potentials, vibrational energies, energetics of ionic states, relative photoionization cross sections, partial photoionization cross sections, and the photon energy dependence of these cross sections. Together with quantum chemical calculations reliable geometries of selenium aggregates (Se_x, $4<x<9$) have been obtained. For instance, the symmetry (C_{1h}), the exact bond lengths and bonding angles in the ring-like Se_7 molecule have been determined precisely.

Particularly interesting are clusters composed of divalent atoms. While the dimers (Be_2, Mg_2, ..,Ba_2, Zn_2, Cd_2, and Hg_2) are generally weakly bound, metallic cohesion must (and does) prevail in larger aggregates. As will be shown, mercury clusters have been studied extensively in this respect. As far as clusters comprised of other divalent elements are concerned, there is almost no spectroscopic information available about electronic structures and geometries. It is very interesting to note that theoretical

calculations predict non-crystalline structures to be the most stable ones (see e.g. Ref. [1] for Be_{13}). Experimentally, Rayane et al. [2] have recently shown, that abundance distributions of Ba_x-clusters (x<34) indicate a rather pronounced stability of aggregates with icosahedral structures. Also magnesium and calcium clusters appear to form (after laser heating) geometrical shells of atoms as deduced from mass spectrometric intensity variations [3]. On the other hand, Knight et al. [4,5] have suggested that electronic shell structure should be observable in clusters of IIa and IIb metals. Generally speaking, electronic shell structure can be observed *indirectly* in mass spectrometric abundance distributions [6], in the size dependence of ionization potentials[2] and for instance in polarizability measurements[7]. Clearly, a most *direct* experimental way to unravel cluster size dependent electronic effects is photoelectron spectroscopy[8-11].

Recently we have succeeded in detecting neutral cadmium clusters Cd_x (x<80) in seeded supersonic expansions of cadmium vapour. Remarkable intensity variations are detected in mass abundance spectra. There are large intensity ratios for Cd_{10}/Cd_{11} as well as Cd_{20}/Cd_{21} indicating the closing of electronic shells with 20 and 40 electrons. The photoelectron spectra of neutral cadmium clusters show indeed the formation and filling of shells. Discrete electronic states (2s, 1f, 2p) have been observed directly. Pronounced shell closings are also clearly detected for clusters with 70 electrons (Cd_{35}), 92 electrons (Cd_{46}), and 138 electrons (Cd_{69}). Furthermore, we have obtained quantitative information on the size dependence of ionization potentials and photoionization cross sections. The cadmium cluster ionization potentials (7.8 eV for the dimer Cd_2 down to 5.3 eV for Cd_{30}) decrease rather smoothly with increasing cluster size.

[1] E. Blaisten-Barojas and S.N. Khanna, Phys. Rev. Lett. 61 (1988) 1477
[2] D. Rayane, P. Melinon, B. Cabaud, A. Hoareau, B. Tribollet, M. Broyer, Phys. Rev. A39(1989)6065
[3] T. P. Martin et al. Chem. Phys. Lett. 176(1991)343; Chem. Phys. Lett. 183(1991)119
[4]W.D.Knight,K.Clemenger,W.A. de Heer, W. A. Saunders, M. Y. Chou, M.L.Cohen:Phys. Rev. Lett. 52(1984)2141
[5] W.A. de Heer, W.D.Knight, M.Y. Chou, M.L. Cohen, Solid State Physics 40(1987)93
[6] I. Katakuse and T. Ichihara, et al. Int. J. Mass Sepctrom. Ion Processes 91(1989)85
[7] W. A. de Heer, P. Milani, A. Chatelain, Phys. Rev. Lett. 63 (1989)2834
[8] O. Cheshnovsky, K. J. Taylor, J. Conceicao, R. E. Smalley, Phys. Rev. Lett. 64 (1990)1785
[9] D.G. Leopold, J. H: Ho, W.C. Lineberger, J. Chem. Phys. 86(1987)1715
[10] G. Ganteför, M. Gausa, K.H. Meiwes-Broer, H. O: Lutz, Z. Phys. D9(1988)253
[11] K. Rademann, T. Rech, B. Kaiser,U. Even, F. Hensel, Rev. Sci. Instrum. 62(1991)1932

On the Spectroscopy of Seeded Hydrogen and Helium Clusters

S. Goyal, D.L. Schutt and G. Scoles
Department of Chemistry
Princeton University
Princeton, NJ 08544 USA.

The study of highly quantum clusters is a subject of great fundamental and applied interest. These systems offer the possibility of investigating the influence of finite size effects on superfluidity, without the perturbing action of containment walls. Clusters of para-hydrogen also offer the possibility of examining whether or not para-hydrogen can exhibit superfluid behavior, which may arise as a result of the increased molecular mobility in clusters of a few hundred monomers over that of the corresponding bulk solid at the same temperature. The applied interest stems instead from the need to investigate the properties of all possible phases of hydrogen mixtures with light metals (including those prepared by cluster co-deposition) which, in turn, derives from their possible use as thrust maximizing fuel in rocket engines.

To achieve these goals we have recently built a photo-evaporation detection molecular beam spectrometer with a cluster source that can be cooled down to 14K while maintaining a gas throughput of a few cm^3 STP per second. Following cluster formation and collimation, the clusters pick-up an IR active molecule in a scattering cell (where a pressure is maintained of the order of 10^{-4} torr) and proceed to a point downstream where they are interrogated by the line tunable output of three isotopically substituted CO_2 lasers and one N_2O laser. The spectrometer can be operated with either one of two bolometer detectors. The first bolometer, used for helium clusters, operates at 1.4K, where as the second bolometer operates at 5K in order to avoid condensing hydrogen on its surface. The increase in bolometer temperature decreases the sensitivity by only a factor of 5 over the traditional low temperature bolometer.

We report here the first results obtained using SF_6 as the IR chromophore. For helium clusters, two absorptions located at 945.8 cm^{-1} and 946.1 cm^{-1} are assigned to an SF_6 molecule residing at the surface of the cluster. Two other absorptions located at 932.9 cm^{-1} and 954.7 cm^{-1} are attributed to a dimer of SF_6 which forms on the surface of the helium cluster when two SF_6 molecules are collected by the same cluster in the pick-up cell. The guest species are found at the surface of the cluster, in spite of the favorable solvation energy gain, as a result of a centrifugal force field introduced by the angular momentum acquired by the system during the pick-up process. If this process is confirmed by further experimental and theoretical investigations, it will provide the first experimental evidence of superfluidty in free helium clusters. In contrast to its behavior in ^4He clusters, SF_6 is solvated by molecular hydrogen clusters. The spectrum, which exhibits three absorptions, one for the monomer at 942.25 cm^{-1} at two for the dimer at 928.6 cm^{-1} and 949.6 cm^{-1}, shows solvation for both the monomer and the dimer. The fact that there is a single absorption for the monomer indicates the absence of the symmetry breaking proximity of the surface and, therefore, a homogeneous environment for the chromophore. Solvation is also corroborated by the magnitude of the shift (approximately 6 cm^{-1}) from the gas phase absorption which, given the polarizability and density of hydrogen, is too large for a surface species. Finally, in contrast with the corresponding dimer lines in the He clusters, both absorptions of the dimer are shifted (in hydrogen) by the same amount indicating the presence of a homogeneous environment, as in the case of the monomer.

FIGURE CAPTION

The spectrum of SF_6 attached to a helium cluster produced in a 100 bar expansion from a 16 K nozzle. The darkened circles are the measured intensities and the solid line is a trace of gaussians fitted to the data.

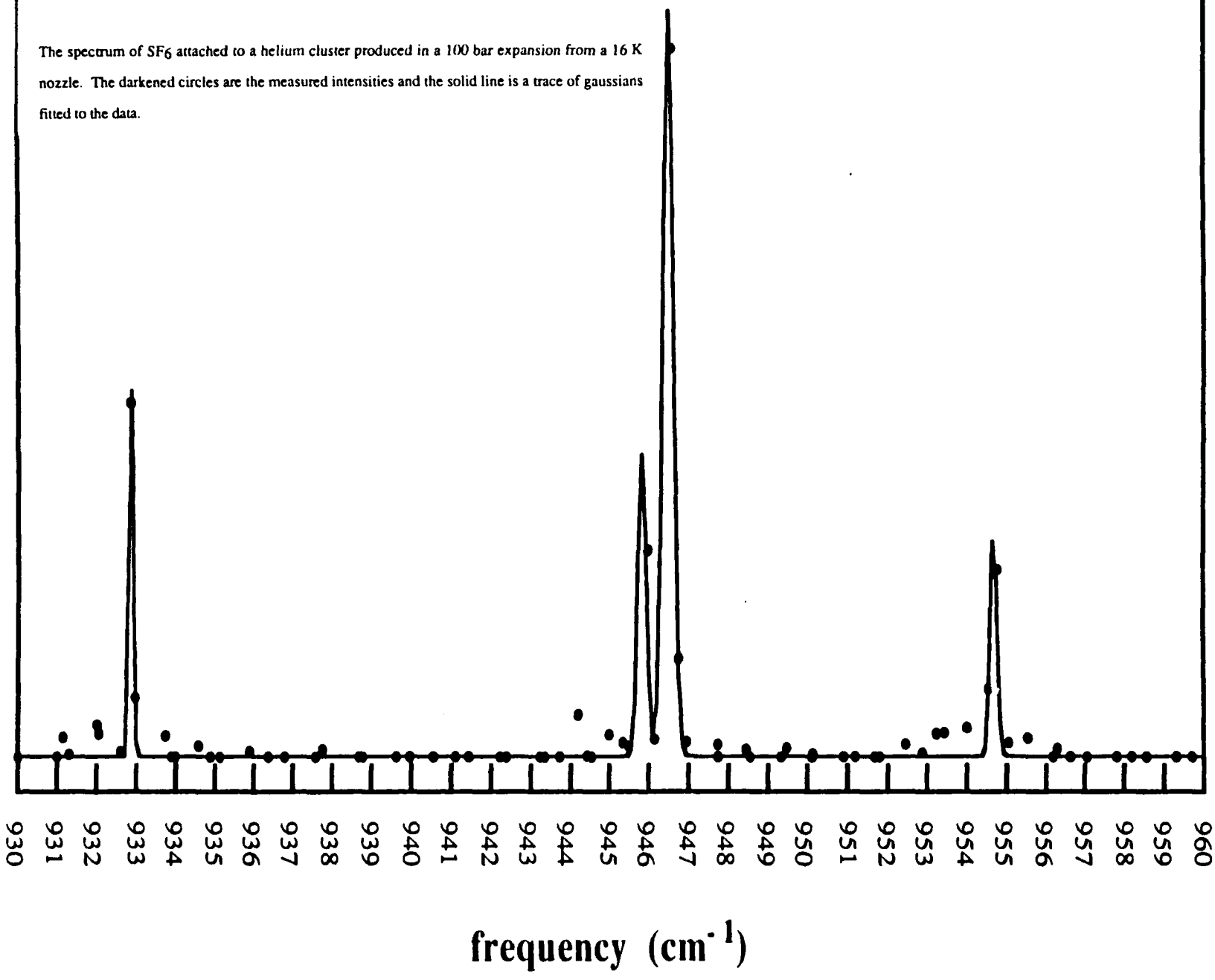

Scattering Experiments with small Sodium Clusters: Elastic, inelastic and reactive Processes

C.P. Schulz, A. Goerke, and I.V. Hertel

Fakultät für Physik, Albert–Ludwigs–Universität
D–7800 Freiburg, Germany F.R.

The physical and chemical properties of alkali metal clusters are of continuous interest for many researchers. Optical response functions have been studied for a number of neutral clusters [1]. Recently different types of shell formation have been observed for very large Na_n clusters ($n \leq 23000$) [2]. To our knowledge up to now no experimental data on the interaction of Na clusters with particles, i.e. scattering experiments are available. Three different processes are of interest. First, elastic scattering with unstructured particles such as rare gas atoms can be used to size select small Na clusters. Subsequent photoexcitation and photoionization of the scattered clusters can lead to unambiguous information on the photoabsorption and fragmentation compared to experiments using unselected clusters beams. This method has been introduced by Buck and co–workers [3] to size select rare gas and other molecular clusters before electron impact ionization. Second, inelastic processes can give new insight into basic excitation (vibrations and rotations). Particularly for small alkali clusters ($n < 8$) a rotational excitation is expected because of the non–spherical shape of these clusters. The third process of interest is the reactive scattering of Na_n clusters under single collision conditions which enables us to gain information on the reactivity of the different cluster sizes.

We have set up a crossed beam experiment which enables us to investigate collisions of small sodium clusters ($n \leq 8$) with atoms and molecules. The sodium clusters are produced by an oven and supersonic expansion of neat sodium vapour through a 0.1 mm orifice. Sufficient cluster intensities have been achieved with sodium vapour pressures of about 200 mbar. The sodium cluster beam is crossed at 90^0 with a pulsed gas beam. The scattered clusters enter the fixed detector system where they are excited and ionized by pulsed lasers. Subsequently, the photoions are mass analysed in a time–of–flight arrangement. The intensity of the scattered clusters as a function of the scattering angle can be measured by rotating the two beams around the scattering center. Angular resolved scattering data have been taken for variety of combinations of scattering targets and ionizing laser wavelengths. Here we want to mention some results for each of the three processes as discussed before.

For elastic scattering each cluster size has a maximum scattering angle which is defined simply by the kinematics of the experiment. Thus intensity steps at this maximum angle observed in the angular dependence of the ion signal of a smaller cluster indicate a fragmentation process during the photoionization. We have observed a number of fragmentation process after single photon ionization and have studied these as a function of laser wavelength. Beside the expected loss of neutral monomers and dimers we have also found some indication for a neutral trimer loss in the process:

$$Na_8 + h\nu \rightarrow (Na_8^+)^* \rightarrow Na_5^+ + Na_3.$$

From the measured intensity as a function of laser wavelength, the rate constant for this process can be estimated.

Through the course of our study we have found that for alkali clusters also inelastic processes play an important role. This can be explained by the non–spherical shape of the small sodium clusters ($n < 8$) which leads to significant rotational excitation during the collision process. An example of the inelastic scattering of Na_4 by Neon is shown in fig.1. The intensity of the scattered Na_4 clusters as a function of the scattering angle is plotted. The scattered clusters are ionized with three different wavelength near the ionization threshold. By using a laser wavelength of 233 cm^{-1}

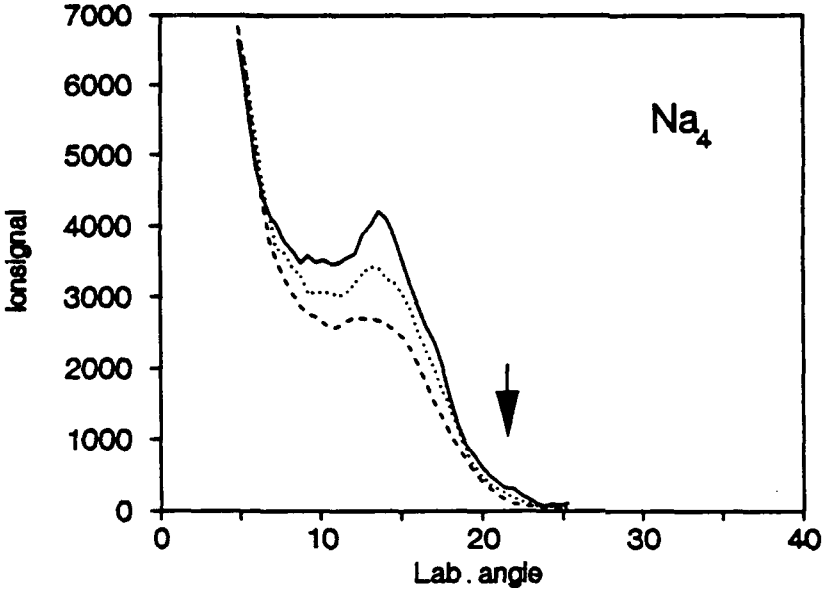

Fig. 1: Intensity of scattered Na_4 clusters as a function of the scattering angle. Three different laser wavelength have been used for ionization: 290 nm (dashed line) above the ionization threshold; 292 nm (dotted line) at the threshold; 294 nm (solid line) below the threshold showing rotational excitation during the collision process (rotational rainbow)

below the ionization threshold (294 nm; solid line) only those Na_4 clusters can be ionized which have gained an additional internal energy. The local intensity maximum near 15^0 observed for 294 nm compared to measurements with higher photon energies (dotted line: 292 nm; dashed line: 290 nm) can be attributed to rotational excitation of Na_4 during the scattering process. The experimental results will be compared with classical trajectory calculations based on a calculated potential for Na_x + Rg using an extended Hückel method.

Another aspect of the scattering experiment presented here is the reactive scattering. We have chosen molecular oxygen as a reagent molecule, because it is known from thermochemical data that the reaction will only proceed via clusters ($Na_n \geq 3$). The products and elastically or inelastically scattered clusters are detected in a mass spectrometer after ionisation with a pulsed lasers near 250 nm (~ 5 eV) as previously described. Fig.2 shows a mass spectrum at a scattering angle of 10^0. Two

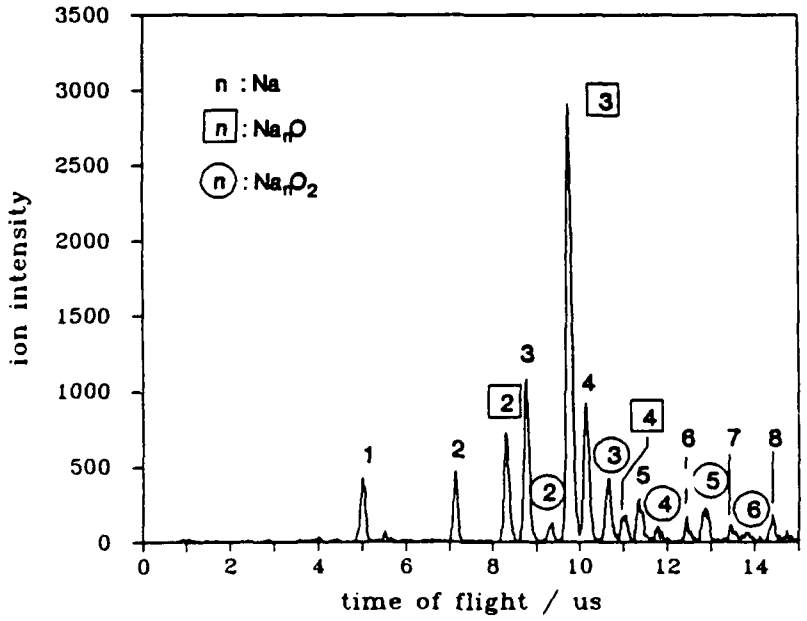

Fig.2: Time–of flight mass spectrum at 10^0 scattering angle for the reaction of Na_n clusters with molecular oxygen in a crossed beam experiment. The products are photo-ionized with 250 nm. The products Na_xO and Na_xO_2 are observed.

series of products are observed: Na_xO (x: 2, 3, 4) and Na_xO_2 (x: 2 to 6). The intensity of reaction products show an odd–even alternation whereby the products with an odd number of sodium atoms are more abundant. From the observed angular distribution, it can be concluded that the major part of excess energy remains in the products. The experimental findings will be discussed in the light of the harpooning mechanism with subsequent complex formation.

References:

1. C.R.C.Wang, S.Pollack, M.M.Kappes: Chem.Phys.Lett. 166, 26 (1990)
2. T.P.Martin, T.Bergmann, H.Göhlich, T.Lange: Z.Phys.D 19, 25 (1991)
3. U.Buck: J.Phys.Chem. 92, 1023 (1988)

COLLECTIVE RESONANCES OF VALENCE ELECTRONS IN FREE METAL CLUSTERS

Vitaly V. Kresin* and Walter D. Knight**

*Lawrence Livermore National Laboratory
University of California
Livermore, CA 94550

**Department of Physics
University of California
Berkeley, CA 94720

Photodissociation experiments on simple metal clusters in molecular beams have established that they exhibit strong dipole resonances [1]. These giant resonances are due to collective oscillations of the delocalized valence electron cloud.

With modern cluster-beam and spectroscopic techniques, the evolution of the resonance spectra can be studied as a function of cluster size, ionization state, composition, etc. In the course of these studies, interesting regularities emerge, and deviations from behavior expected for classical metallic particles are observed. We will review the experimental picture of collective-resonance spectroscopy and describe some aspects of the theoretical understanding of the data.

Collective resonances have been observed in neutral and positively charged clusters of sodium, potassium, cesium, lithium, etc., as well as in mixed clusters [2-6]. These spectra share a number of conspicuous features, including the following:

- The resonances are found to be shifted to lower frequencies, as compared with the prediction of classical theory.
- The resonance peaks contain a large fraction, but not all, of the valence electrons' dipole oscillator strength.
- Open-shell (ellipsoidally distorted) clusters exhibit several resonance peaks.
- In some closed-shell (spherical) clusters, the photoabsorption resonance is also shared among several peaks.
- The widths of the resonances do not vary strongly with cluster size, but appear to depend on the degree of its internal thermal excitation.
- In addition to the main prominent resonances, there are indications of fixed wavelength regions where absorption occurs for all cluster sizes.

The size-dependent response properties of small clusters are defined by the interplay between size quantization, electron screening, and diffuseness of the electron cloud (spill-out).

Many observed features can be successfully and quantitatively understood in a unified way by means of an analytical theoretical approach based on the techniques of many-body physics [7]. Among the conclusions of this analysis are:

- The response properties of cluster valence electrons are defined by the degree of electron spill-out beyond the ionic background core. The greater the relative magnitude of the spill-out (i.e., the more reduced the average valence electron density), the stronger the frequency shift of the collective resonances. In positively ionized clusters the spill-out is weaker than in neutral ones; this results in a smaller frequency shift, in agreement with experiment.
- It is predicted that small clusters should exhibit an additional collective resonance mode located at higher frequencies. This mode, unique to the small size range, is responsible for the fact that some dipole oscillator strength is observed to be missing from the lower-frequency resonances. The position and spectral weight of the predicted mode are also determined by the degree of valence electron spill-out.
- In cases when a collective resonance peak happens to lie near a single-electron energy level, the former will break up into two. This effect of degeneracy lifting can be analyzed quantitatively, and is responsible for the splitting of resonance peaks in spherical clusters.
- In a spheroidal or ellipsoidal open-shell cluster the magnitude of the depolarization field is different along its deformation axes. As a result, the photoabsorption spectrum will display two or three peaks corresponding to oscillations along the principal axes of the cluster. In order to analyze this process, it is necessary to take into account the effect of shape distortion both on the depolarization field and on the density distribution of the valence electron cloud; this can be accomplished by means of a special coordinate transformation. Conversely, if the resonance frequencies are known, the cluster deformation parameters can be deduced from the data.

In cases when interaction with single-electron levels is superimposed on the shape-related splitting, the resulting absorption profiles may become quite complicated.

Further experiments are needed in order to improve our understanding of electron dynamics in small clusters. Additional data are required to test the theoretical predictions and to establish the limits of the models. We will address some of the following areas:

- Measurement of photoabsorption spectra for a wider range of spherical clusters in order to trace the dependence of resonance frequencies upon cluster size.
- Accurate determination of oscillator strength distribution in cluster photoabsorption profiles.
- Search for the predicted new higher-frequency resonance mode described above.
- Measurements of resonance frequencies for a variety of open-shell clusters in order to study the correlation between cluster shapes and resonance positions.

• Study of the influence of cluster temperature on the width of absorption peaks; interaction between electronic and vibrational levels.

Work carried out at Berkeley under U.S. National Science Foundation Grant No. DMR-89-13414 and at the Lawrence Livermore National Laboratory under the auspices of the U.S. Department of Energy under contract No. W-7405-ENG-48.

REFERENCES

[1] W.A. de Heer *et al.*, Phys. Rev. Lett. **59**, 1805 (1987).
[2] K.Selby *et al.*, Phys. Rev. B **43**, 4565 (1991).
[3] C.Bréchignac *et al.*, Chem. Phys. Lett. **164**, 433 (1989); Chem. Phys. Lett. to be published.
[4] C.R.C.Wang *et al.*, Z. Phys. D **19**, 13 (1991).
[5] H.Fallgren *et al.*, Z. Phys. D **19**, 81 (1991).
[6] J.Blanc, *et al.*, Z. Phys. D **19**, 7 (1991).
[7] V.V.Kresin, Phys. Rev. B **42**, 3247 (1990); Z. Phys. D **19**, 105 (1991).

SPECTROSCOPY OF METAL ATOM AND METAL CLUSTER COMPLEXES

Michael A. Duncan
Department of Chemistry
University of Georgia
Athens, Georgia 30602

Metal cluster species have attracted considerable attention over the last several years. Various studies have focused on the reactivity of these systems and their dissociation dynamics. A central goal in these studies is to understand the unique bonding properties of clusters and the corresponding molecular structure. Unfortunately, with few exceptions, spectroscopy has not been successful for metal or metal-containing clusters. However, new experiments in our laboratory have made it possible to produce and study a variety of complexes containing metal atoms or metal dimers. Vibrationally resolved electronic spectra for these species now probe directly the nature of the bonding interactions at metal centers. We describe here two general classes of complexes. Complexes containing *neutral* metal dimers and rare gas atoms (e.g., Ag_2-Ar, Ag_2-Xe) are studied with resonant two-photon photoionization spectroscopy (R2PI). Complexes containing a metal *ion* with electrostatically-bound molecules (e.g.,Ag^+-benzene, Mg^+-CO_2) are studied with resonance enhanced photodissociation spectroscopy. Several examples of successful spectroscopic studies now exist for both kinds of complexes.

The prototype system for our studies of neutral metal complexes is the silver dimer, Ag_2. Ag_2 is a closed-shell molecule ($^1\Sigma_g^+$ ground state) with well-characterized spectroscopy in its ground and excited electronic states. Complexes with silver dimer and rare gas atoms or small molecules, therefore, may be regarded as van der Waals complexes, and spectra are expected to be slightly shifted from those of the bare dimer. These systems may be useful models for adsorption on larger metal surfaces. We have studied spectroscopy for complexes of Ag_2 with the series of rare gas atoms, Ar, Kr, and Xe. Vibrationally resolved spectra and dissociation energies have been obtained for the triatomic complexes Ag_2-Ar, Ag_2-Kr and Ag_2-Xe.

Figure 1 provides the spectrum of Ag_2-Xe, which is typical of the vibronic level patterns found for these complexes. A fortuitous geometry change in the system makes it possible to observe progressions in each of the three vibrational modes. There are also numerous combination bands. In all, neary 200 vibronic bands are observed, all of which can be assigned to progressions and combinations of just three vibrational modes. The resulting vibrational constants for the three complexes are given in Table 1. Dissociation energies are obtained for these complexes via a Birge-Sponer extrapolation of the metal dimer-rare gas stretching progression. Dissociation energies are also presented in Table 1. The binding energies in these systems are expected to be proportional to the ratio of the rare gas polarizabilities. We have found some justification for this premise, but the xenon complex is bound far greater than would be predicted.

Metal ion systems observed in our laboratory are subdivided into those with or without structured spectra. A variety of metal benzene ions have been studied with photodissociation, and none yet studied exhibit any vibrational structure. These complexes dissociate via intramolecular charge transfer on a repulsive upper state. Although the metal atom has a lower ionization potential than benzene, the benzene cation is the primary dissociation product in these systems. While no vibrational frequencies are observed, metal ion-benzene bond energies may be derived.

Stuctured spectra are obtained for magnesium ion complexes with small molecules (e.g., Mg^+-CO_2, Mg^+-H_2O). In both of these systems, the metal-molecular stretching vibration exhibits a progression with several members. Figure 2 shows the photodissociation spectrum for the Mg^+-CO_2 complex (origin = 29,625 cm^{-1}). In the water complex, the H_2O bending mode is also active. Extrapolation of the metal-molecular stretch progression yields dissociation energies for these complexes. Spectral analysis, in coordination with *ab initio* calculations (a la Bauschlicher and coworkers), allows determination of the complex structures. The Mg^+-CO_2 complex is linear, while the Mg^+-H_2O complex has C_{2v} symmetry; both have Mg^+-oxygen bonds. The spectroscopic constants for these complexes are given in Table 2. At certain wavelengths, the magnesium ion complexes undergo photoinitiated reactions, yielding metal oxide ions as products. There are indications for an orbital selectivity effect in this photochemistry. Similar experiments are ongoing for magnesium ion complexes with multiple ligands.

Table 1. Spectroscopic constants for Ag_2-Ar, Ag_2-Kr and Ag_2-Xe complexes. All entries are given in cm^{-1} units. The $^{107}Ag_2{}^{129}Xe$ isotope is compared to data obtained earlier for a composite of silver (in Ag_2Ar) and silver-krypton (in Ag_2Kr) isotopes.

	Ag_2-Ar	Ag_2-Kr	Ag_2-Xe	$^{107,109}Ag_2$
ν_{00}	35,329	34,998	34,281	35,808.7
ω_1'	156.3	157.7	165.3	151.3
x_1'	0.71	0.64	0.68	0.70
ω_2'	28.3	27.9	25.7	-
x_2'	2.73	1.76	-0.68	-
ω_3'	73.9	72.6	79.9	-
x_3'	1.72	1.06	0.57	-
D_0'	755	1205	2761	-
D_0''	275	394	1233	-

Figure 1. The resonant two-photon ionization spectrum of the Ag_2-Xe complex. The spectrum was obtained by measuring the intensity of the $^{107}Ag^{129}Xe$ ion in the mass spectrometer while the photoionization laser was tuned through intermediate state resonances.

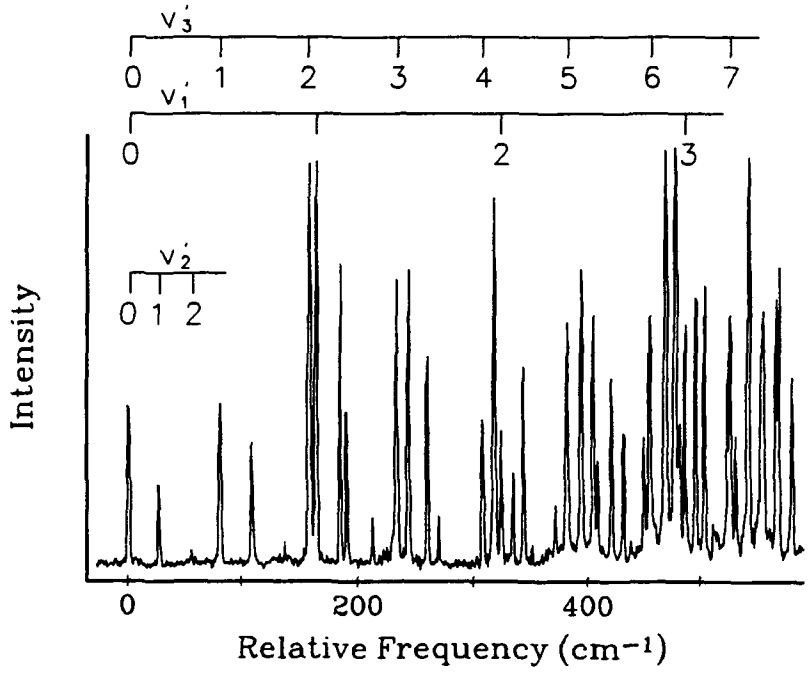

Figure 2. The photodissociation spectrum of Mg^+-CO_2. To record this spectrum, the parent ion was mass selected and photodissociated with a tunable dye laser. The Mg^+ fragment ion intensity was measured as a function of energy.

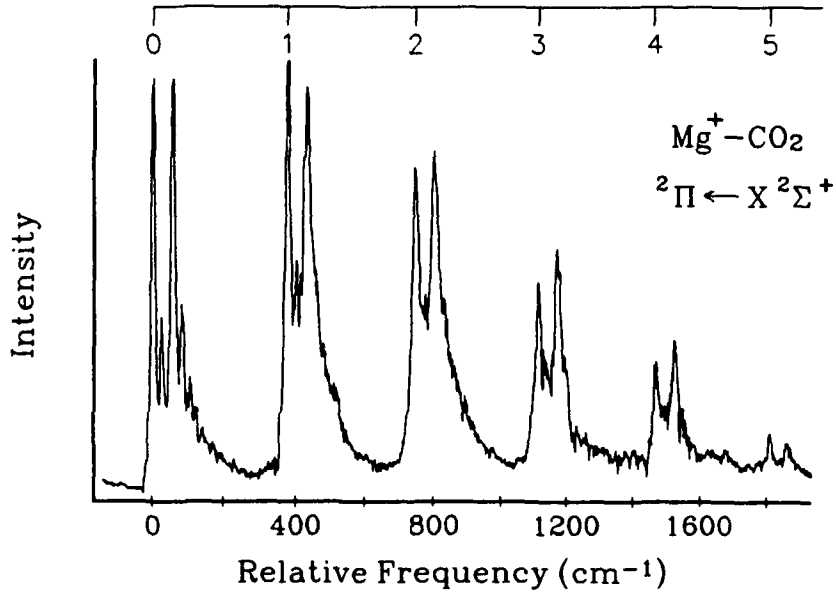

Table 2. Vibrational constants and dissociation energies for metal-molecular complexes and their comparison to theory. Theoretical data are from Bauschlicher and coworkers.

	Experiment		Theory	
	Mg^+-CO_2	Mg^+-H_2O	Mg^+-CO_2	Mg^+-H_2O
Mg^+-R stretch	381.8 cm^{-1}	530.8	359	505
D_0'' (kcal/mole)	14.7		16.4	32.2

Acknowledgements. This research is supported by the National Science Foundation, the U.S. Department of Energy, and the Air Force Office of Scientific Research.

Session VI:

New Techniques

Bouncing Gases off Liquid Surfaces

Mackenzie E. King[a], Steven T. Govoni[a], Mary E. Saecker[a], Daniel V. Kowalski[a],

Mark Hanning-Lee[b], Timothy K. Minton[b], and Gilbert M. Nathanson[a]

[a]Department of Chemistry, University of Wisconsin, Madison, WI 53706

[b]Jet Propulsion Laboratory, Pasadena, CA 91109

When an atom or molecule from the gas phase strikes a low vapor pressure liquid, it can bounce off the surface or momentarily stick to the liquid phase molecules. These collisions are the first step in solvation, reaction, and film formation and they control the approach to gas-liquid equilibrium. We have been studying these processes by directing a collimated and monoenergetic beam of molecules at continuously renewed liquid surfaces in vacuum. By monitoring the identity, velocity, and direction of the recoiling products, we are learning how liquid phase molecules respond to collisions from the gas phase.

The questions we are trying to answer are: what do the surfaces of liquids look like on the atomic scale? Are polyatomic liquid surfaces highly corrugated or are they smoother than expected because surface tension pulls them taut? Do liquids respond like solids on the subpicosecond timescale of a gas-liquid collision, simply reflecting the incoming molecule back into the gas phase and inhibiting solvation? Or do they efficiently absorb the energy of the collision and momentarily trap the gas molecule, allowing it to dissolve? Can we follow the course of a chemical reaction, like the hydrogen bonding and dissolution of water in glycerol or the protonation of D_2O by concentrated sulfuric acid?

Our experiments show that gas-liquid energy transfer depends critically on liquid composition.[1] We observe that collisions between nonpolar gases and hydrocarbon, fluorocarbon, and polyalcohol liquids lead both to direct inelastic scattering and trapping desorption. Due to their light mass, hydrocarbons are more effective than perfluorinated

polyethers or polyalcohols at momentarily trapping nonpolar gases ranging from the inert gases to methane and sulfur hexafluoride. Hydrocarbon liquids also efficiently steal energy away from those molecules which do rebound inelastically, while perfluorinated liquids absorb much less of the impact energy. We also find that the roughness of liquid surfaces depends sensitively on collision energy. To incoming gases at low energies, the liquids appear quite corrugated and reflect incoming inert atoms in a broad, cosine-like angular distribution. The recoil patterns become much sharper and more specular at high energies, however, possibly because the collision itself deforms the liquid upon impact.

Protic species like water and ammonia interact strongly with hydrogen bonding liquids and with concentrated acids. We observe that D_2O solvates extensively upon collision with sulfuric acid but sticks only momentarily to glycerol. No HOD products are observed when D_2O strikes glycerol and no water molecules permanently solvate, but incoming D_2O do transfer more energy to glycerol than to the soft hydrocarbons or the stiff perfluorinated liquids. In direct contrast, D_2O molecules that collide into H_2SO_4 either scatter impulsively from the acid or disappear completely, presumably undergoing irreversible solvation and protonation after sticking to the surface.

[1]M.E. Saecker, S.T. Govoni, D.V. Kowalski, M. E. King, G. M. Nathanson, Science 252, 1421 (1991).

Cluster Impacts: A Chemical Approach to Fusion*

Y. K. Bae, R. J. Beuhler, Y. Y. Chu, G. Friedlander and L. Friedman

Chemistry Department, Brookhaven National Laboratory
Upton, New York 19973

Impacts of accelerated cluster ions on solid surfaces can generate extremely high energy and particle density atomic assemblies in small-scale experiments. Cluster impact fusion studies were undertaken to explore energy transfer in assemblies produced by impact of heavy water clusters on deuterated surfaces using D-D fusion reactions as a diagnostic tool. Fusion events were observed as evidenced by the detection of characteristic protons, tritons and ^{3}He. The observed fusion rates were many orders of magnitude larger than could be accounted for by conventional theory. Therefore, the possibility of contamination of the cluster beams with high velocity ions of low molecular weight was carefully investigated. A variety of tests including time-of-flight experiments led to the conclusion that clusters rather than artifacts were responsible for the observed fusion events.

Recent tests with magnetic and electrostatic filtration of fully accelerated cluster ion beams have, however, shown that most of the fusion events observed earlier resulted from low molecular weight artifacts. The earlier cluster fusion rates were overestimated by at least two orders of magnitude. The search for cluster fusion involving cooperative many-body effects that cannot be accounted for by isolated atomic collisions is continuing with more sensitive and selective techniques. Results of these studies will be presented.

*Research carried out under contract DE-AC02-76CH00016 with the U.S. Department of Energy and supported by its Office of Basic Energy Sciences.

Diffractive Scattering of Hydrogen Clusters From LiF(001)

Gary Tepper and David Miller
Dept. AMES - 0310
University of California, San Diego
La Jolla, Ca. 92093-0310

The interaction of a cluster with a solid surface is an interesting dynamics problem in inelastic energy transfer and a useful technology in thin film growth. While some molecular beam scattering experiments and analysis (1-3) have been reported in the classical regime, the details are convoluted by the large number of inelastic channels and energies involved, which give rise to broad scattering distributions and insensitivity to the potential parameters. We wish to report on our initial experiments using light hydrogen clusters which scatter coherently from crystalline surfaces; here we report data on the dimer $(H_2)_2$. Because of the small binding energy of order 0.31 meV (4), small compared with the incident energies and the surface phonon energies, one would not expect the complex to survive the interaction classically. However, the quantum coherent scattering channel provides elastic channels, and we are able to detect the scattering process. By analyzing the elastic scattering probabilities we are able to assess the fragmentation probability, and to qualitatively obtain information on the interaction between the dimer and the surface.

Figure 1 is a schematic of the UHV apparatus. The clusters are formed by a free-jet expansion into the source chamber pumped by a 20" diffusion pump.

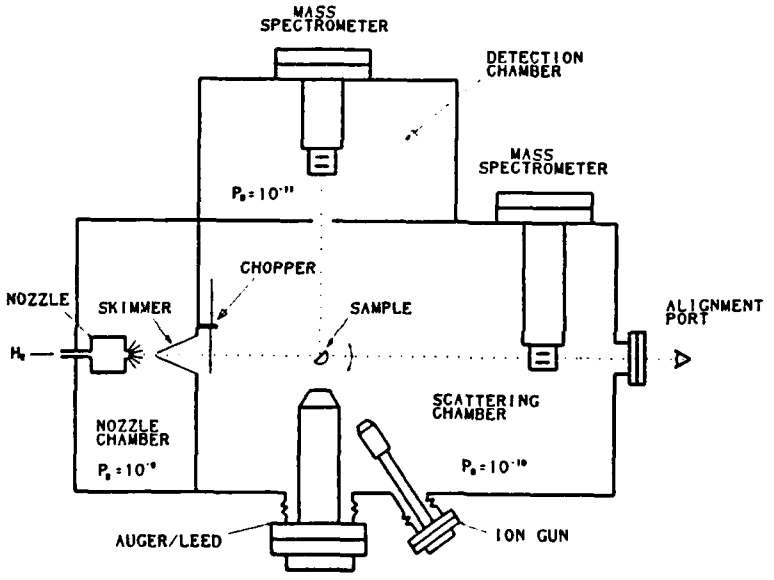

Figure 1. Schematic of surface scattering apparatus

The beam is collimated and scattered from the LiF (001) crystal along the <100> direction. As indicated the crystal is rotated and the detector, a quadrupole mass spectrometer, is held fixed such that the sum of the incident and scattering angle is fixed at 96.0 degrees. The LiF surface was chosen for these initial studies because it has been calibrated and characterized with helium scattering by many investigators and it is reasonably straightforward to clean and characterize. The incident beam is characterized in-line with a second mass spectrometer and the two mass spectrometers were cross calibrated by moving the detector to the incident beam station. Helium and hydrogen scattering were both used to calibrate the scattering experiments, not only for correct geometries but in comparison to earlier scattering amplitudes and theory (5,6). Since the dimer ionizes to H_3+ (7) the primary noise is due to the naturally occurring mass three isotope, which provides a background level noise. However, since the diffraction process scatters the isotope and the mass four dimer into different angular directions their scattering signals are easily resolved. Figure 2 shows results for the dimer at an incident energy of 77.7 meV.

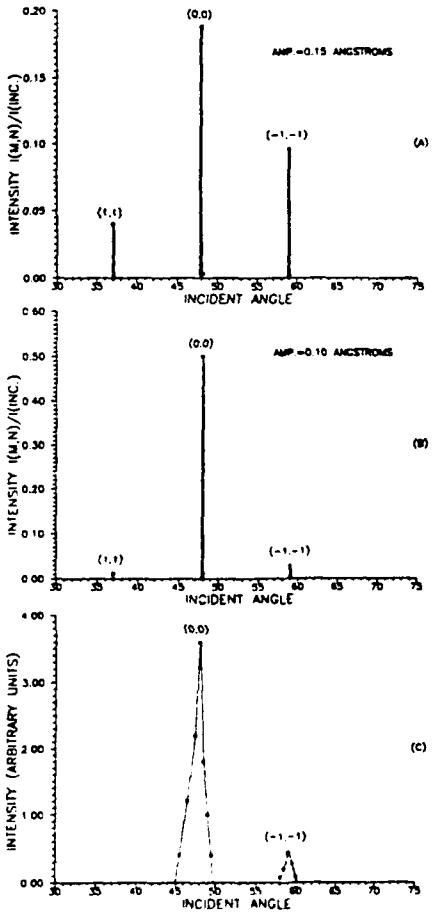

Figure 2. (a,b) Elastic Eikonal Intensity Calculations for Different Potential Corrugations. (c) Diffraction of 77.7 mev $(H_2)_2$ From LiF(001) Along <100>

For this geometry both first and second order diffraction peaks are allowed kinematically, however, to date we have only resolved the (-1,-1) peak. The upper two panels show the results for the most simple elastic scattering calculation, the Eikonal hard wall (8), which is very reasonable for the hydrogen monomer.Two calculations are indicated with two different hard-wall corrugation amplitudes. The corrugation is a measure of how a surface of constant electron charge density, or repulsive turning potential varies across the surface. Figure 2(a) uses a corrugation amplitude of 0.15 Å which is 75 percent of the monomer corrugation amplitude, while the second (b) is adjusted to AMP.= 0.1 Å to fit the data. The latter fit confirms the expected result, that the dimer is larger so that the surface appears smoother. Using such qualitative fits, together with our calibrations we have estimated that about 5% of the dimers survive the collision. These calculations and the possible uses of this dimer probe will be discussed. We note that the diffraction does provide a rather monodispersed beam of collimated dimers for further investigation.

References

1. Guo-Quin Xu, S.L. Bernasek, and J.C.Tully, J.Chem.Phys. Vol.88, 3376 (1988)

2. R.D. Beck, P. St.John, M.l. Homer, and R.L. Whetten, Materials Research Society Symposium Proceedings, Vol.206, 341 (1990)

3. J. Gspann and G. Krieg, J.Chem.Phys. Vol.61, 4037 (1974)

4. A. Watanabe and H.L. Welsh, Phys.Rev.Lett. Vol.13, 810 (1964)

5. G. Boato, P. Cantini, and L. Mettera, J.Chem.Phys. Vol.65, 544 (1976)

6. G. Wolken Jr., J.Chem.Phys. Vol.58, 3047 (1973)

7. S.L. Anderson, T. Hirooka, P.W. Tiedemann, B.H. Mahan, and Y.T. Lee, J.Chem.Phys. Vol.73, 4779 (1980)

8. U. Garibaldi, A.C. Levi, R. Spadacini, and G.E. Tommei, Surface Science Vol.48, 649 (1975)

Three vector correlation study of $Ca(4s5p,^1P_1)+He \rightarrow Ca(4s5p,^3P_2)+He$

Jan P. J. Driessen, Christopher J. Smith, Larry Eno,
Regina de Vivie, Stephen R. Leone,
Joint Institute for Laboratory Astrophysics,
University of Colorado, Boulder, Colorado, 80309-0440

In a crossed beam atomic energy transfer experiment, we study the relationship between initial state alignment and final state alignment of atomic orbitals with respect to the initial relative velocity vector.[1] Fully state-to-state resolved cross sections are obtained for the collisional energy transfer process:

$$Ca(4s5p\ ^1P_1) + He \rightarrow Ca(4s5p\ ^3P_2) + He + \Delta E = 156\ cm^{-1}. \quad (1)$$

A laser pump and probe method is used to prepare and detect the alignment of the Ca atoms. In this three vector correlation experiment, one structured species is studied in both the initial state (laser preparation) and in the final state (laser probing). The crossed beam setup defines the initial relative velocity vector. A pulsed laser beam prepares $Ca(4s5p\ ^1P_1)$ in a single magnetic sublevel $|j_1(=1)\mu_1\rangle$ with respect to the laser polarization vector. Subsequent collision with He at a well-defined relative velocity yields $Ca(4s5p\ ^3P_2)$. The near resonant $Ca(4s5p\ ^3P_2)$ is probed by a second polarized pulsed laser, revealing its magnetic sublevel $|j_2(=2)\mu_2\rangle$ distribution with respect to the probe laser polarization vector.

An important distinction between two- and three-vector correlation experiments is the number of angles needed to specify the geometry of any arbitrary arrangement of the vectors.[1,2] In a two-vector correlation (*e.g.* E_1 and v_i) only one polar angle β is required (Fig. 1a). For a three-vector correlation, Fig. 1b shows the pertinent angles. Two polar angles, β_1 and β_2, and one azimuthal difference angle, $\Delta\alpha=\alpha_1-\alpha_2$, are necessary. Because of this angle $\Delta\alpha$, the azimuthal symmetry of this three-vector correlation experiment about v_i is broken. Theoretically this means that the coherence of the laser excited states (E_1 and E_2) play an essential role in the outcome to the collision process.

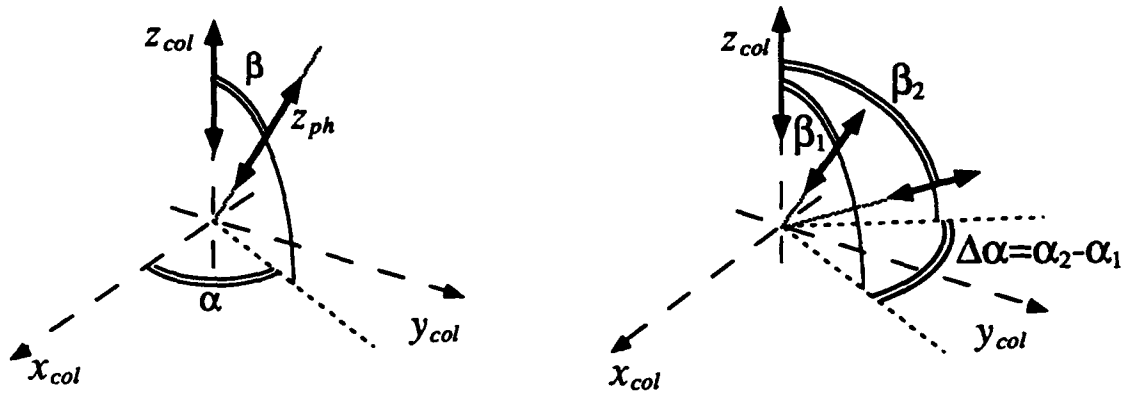

a) two-vector correlation *b) three-vector correlation*

Figure 1. Relevant angles in a two- and three-vector correlation experiment.

The laboratory cross section $\sigma_{j_2\mu_2-j_1\mu_1}(\beta_1,\beta_2,\Delta\alpha)$ is itself expanded in terms of a more fundamental (angle independent) set of cross sections as determined in the so-called collision frame, where projections of the structured species $|jm\rangle$ are taken with respect to the direction of the initial relative velocity vector.[3,4]

$$\sigma_{j_2\mu_2-j_1\mu_1}(\beta_1,\beta_2,\Delta\alpha) = \sum_{\substack{m_1m_1' \\ m_2m_2'}} \rho_{m_1m_1'}\ \rho^*_{m_2m_2'}\ \sigma_{j_2m_2m_2'-j_1m_1m_1'}$$

$$\text{with } \rho_{m_1m_1'} = D^{j_1}_{m_1\mu_1}(\alpha_1,\beta_1,0°)\ D^{j_1\,*}_{m_1'\mu_1}(\alpha_1,\beta_1,0°) \tag{2}$$

$$\rho^*_{m_2m_2'} = D^{j_2\,*}_{m_2\mu_2}(\alpha_2,\beta_2,0°)\ D^{j_2}_{m_2'\mu_2}(\alpha_2,\beta_2,0°)$$

where the $D^j_{m\mu}(\alpha,\beta,\gamma=0°)$ are rotation matrix elements which describe how a single laser excited magnetic sublevel $|j\mu\rangle$ in the laser frame transforms to a linear combination of $|jm\rangle$ sublevels in the collision frame. The angle dependent coefficients in this expansion can be interpreted as density matrix elements which describe the structured initial and final state in the collision frame. The fundamental cross sections in the expansion involve pairs of collision frame scattering amplitudes integrated over all scattering angles.

$$\sigma_{j_2m_2m_2'-j_1m_1m_1'} = \frac{k_{j_2}}{k_{j_1}} \int_{4\pi} f_{j_2m_2-j_1m_1}(\theta,\phi)\ f^*_{j_2m_2'-j_1m_1'}(\theta,\phi)\ d\Omega \tag{3}$$

Two types of fundamental cross sections can be recognized. First, the (real-positive) *conventional cross sections* involve integrating the absolute value squared of a (single) scattering amplitude. In Eq. (2) they are multiplied by (real-positive) diagonal elements of the density matrices, and thus they indicate how the population distributions of the initial and final state are connected. By contrast, the complex-valued *coherence cross sections* contain two different scattering amplitudes. In Eq. (2) they are multiplied by (complex-valued) off-diagonal elements of the density matrices, and describe how the coherences in the initial state affect the coherences in the final state. As discussed in a recent article by Driessen and Leone, one can also interpret the coherence cross sections as describing how atomic structure in directions other than the collision frame z-axis (relative velocity vector v_i) is preserved.[2]

The three vector correlation process is studied in a crossed beam setup. The important aspects of the collision experiment are depicted in Figure 2. The relevant transitions are shown in the Ca level diagram of Fig. 2a. The two (linearly polarized) laser beams are counterpropagating in the apparatus, resulting in $\Delta\alpha=0$. Because both beams intersect perpendicular to the collision plane, the angles β_1 and β_2 can be varied through a full 360° range, as is shown in Fig. 2b. The probe laser is tuned to two transitions, $4s5p\ ^3P_2 \rightarrow 3d^2\ ^3P_1$ and $4s5p\ ^3P_2 \rightarrow 3d^2\ ^3P_2$, which essentially investigate different subsets of magnetic sublevels $|j_2\mu_2\rangle$. By deconvolution from the angular dependence of the laboratory cross section(s) according to Eq. (2), we are able to determine the fundamental cross sections.

Fourteen fundamental cross sections, given by Eq. (3), are needed to describe the energy transfer process of Eq. (1) completely. Eight of these cross sections are real and positive (conventional type - describing population transfer), and six are complex (coherence type - containing phase information). By symmetry, only fifteen unique parameters for the real and imaginary parts of the cross sections are required, nine of which we are able to obtain using linear polarizations and collinear laser beams.[1] Measurements with circularly polarized laser light will provide several more parameters.

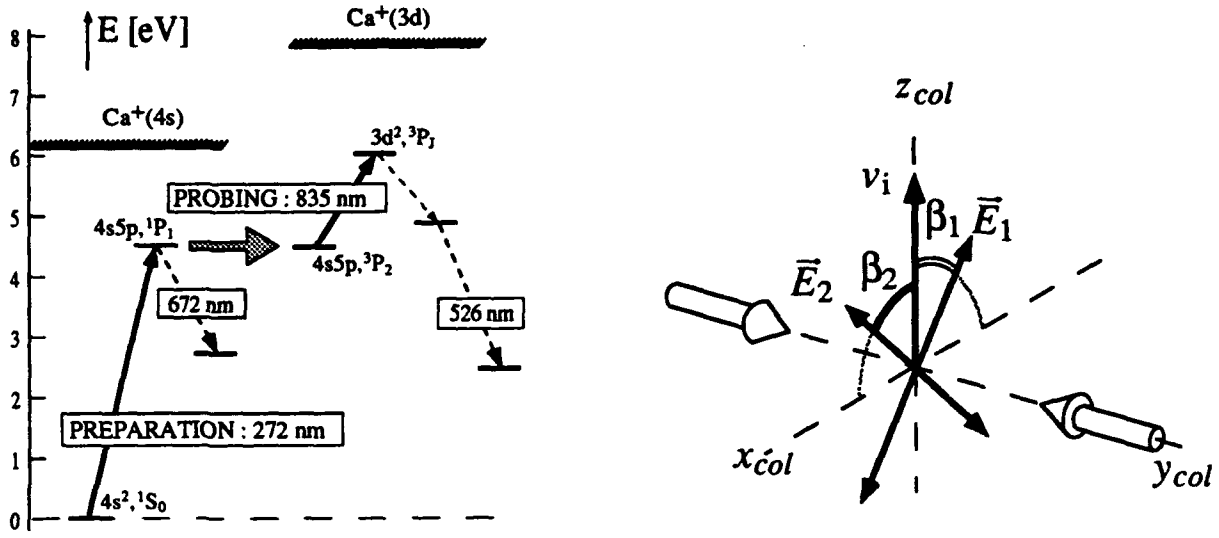

a) Ca level-diagram *b) angular arrangement*

Figure 2. Relevant aspects of experimental setup.

Because linear laser polarizations are used, we essentially study alignment distributions (symmetric *m*-distributions). However, using coherence information and symmetry principles, we are able to obtain orientation information (asymmetric *m*-distributions) for the $m_1 = \pm 1 \rightarrow m_2 = \pm 1$ transitions, *i.e.* resolve the *m*-preserving (1→1) and the *m*-changing (1→-1) transitions. The experimental results of this three vector correlation study will be presented in more detail at the conference.

References.

1) C.J. Smith, J.P.J. Driessen, L. Eno, and S.R. Leone, *J. Chem. Phys.* submitted for publication.

2) J.P.J. Driessen, and S.R. Leone, *J. Phys. Chem.* (feature article) submitted.

3) M.H. Alexander, P.J. Dagdigian, and A.E. DePristo, *J. Chem. Phys.* **66**, 59 (1977).

4) J.P.J. Driessen, and L. Eno, *J. Chem. Phys.* submitted for publication.

Time of Flight Measurements of Single Rovibrational States of Carbon Monoxide

J.M. Price, A. Ludviksson, M. Nooney, M. Xu, R.M. Martin, and A.M. Wodtke

Department of Chemistry, University of California, Santa Barbara, CA 93106.

Although there are many examples of chemical dynamics experiments designed to measure just molecular quantum state, angular, or kinetic energy release distributions[1], there are relatively few examples of kinetic or angular distribution measurements on selected molecular quantum states. We wish to report a new technique for making quantum state resolved kinetic energy measurements which combines the high kinetic energy resolution of the time-of-flight method with the rotational and vibrational state resolution of laser spectroscopy[2].

Experimentally, a pulsed molecular beam consisting of either 10% CO in He or neat CO is collimated with an electro-formed skimmer and passes into a differential pumping chamber where it is crossed with 0.3 mJ/pulse of tunable ultraviolet light (199 nm) with a repetition rate of 10 Hz. When tuned to transitions in the CO Cameron system ($G_v(v'=1)$ = 50189.38 cm^{-1}, or about 6.22 eV) the laser beam is of sufficient intensity to transfer molecules to the lowest excited electronic state of CO, the $a^3\Pi$. The radiative lifetime of this state is strongly J-dependent, ranging from about 1 to 500 milliseconds.

Some 300 μsec after excitation, and after passing from the differential pumping chamber into an ultrahigh vacuum surface science chamber, the metastables encounter an atomically clean Ag surface located 0.4 m from the laser crossing region, possessing a work function of 4.5 eV. The metastable electronic energy significantly exceeds the work function of the surface and collisions with the surface eject electrons with high efficiency. The ejected electrons are collected by a set of biased grids and multichannel electron multiplier plates amplify the signal by about 10^6. This transient signal is capacitively coupled to a fast preamplifier (20x amplification) and the amplifier output is passed to either a transient digitizer, boxcar integrator or, for the case of very weak transitions, a discriminator and multichannel scaler for pulse counting.

The laser system used is a ND:Yag (Lumonics HY600) pumped dye laser (Lambda Physik FL3002e). Near 600 nm, 20 mJ pulses of light can easily be obtained from this laser using Rhodamine B dye. This visible light undergoes frequency doubling in a KDP crystal, yielding 6 mJ/pulse of UV light near 300 nm with a polarization 90° out of phase with the visible. The UV light and the remaining visible light are brought back into phase by passing them through a 266 nm half-wave plate. These beams are then directed through a frequency mixing crystal (BBO, 80° cut angle) yielding 0.5 mJ/Pulse of tunable UV between 197.5 and 210 nm, which is separated from the remaining visible and ultraviolet with a Pellin-Broca prism. The entire system can be scanned over a wide range employing the Lambda Physik microprocessor for tuning the grating and the doubling crystal and a home-made active feedback tracker for tuning the sum-frequency generation crystal[3].

Figure 1 shows the results of tuning the wavelength of the laser which interacts with a pulsed molecular beam of CO some 40 cm away from where the molecules eventually impinge on the surface. The signal observed is proportional to the number of electrons emitted from the surface some 300 μsec after the laser fires. Resolved rovibronic transitions

belonging to the well known CO Cameron band $a^3\Pi_1$ ($v'=1$) - $X^1\Sigma^+$ ($v''=0$) (a transition to a metastable triplet state) could be immediately assigned[4]. Based on the relative intensities of the three strongest features in the spectrum, the rotational temperature of the molecular beam was determined to be less than 3 K.

Figure 2 shows two quantum state resolved time-of-flight spectra. Here, the electron current from the surface is plotted as a function of time after the laser pulse. As the electron current is proportional to the number of metastables hitting the surface, the y-axis is proportional to the instantaneous metastable flux as a function of arrival time. The excitation frequency of the laser corresponds to the $R_2(0)$ band of CO[5] (See Fig. 1).

Figure 2a shows the time-of-flight spectrum for a pulsed molecular beam consisting of pure CO. Figure 2b is the analogous spectrum of a molecular beam of 10% CO in He carrier gas which is expected to have a narrower velocity distribution and a faster average velocity in the pulsed molecular beam. The predicted arrival times for these features have been calculated from the approximate expressions for the terminal velocity of a seeded molecular beam[6] and the geometry of the experimental apparatus. The calculated arrival times of 505μsec and 282μsec are in good agreement with the observed values of 506μsec and 281μsec respectively, for the neat and seeded CO beams.

These observations are unambiguous and convincing proof that quantum state selected time-of-flight spectra can be obtained with this technique. Possible applications are numerous and span the fields of spectroscopy and reaction dynamics. We have already made use method to measure extremely weak forbidden electronic transitions yielding the relative absorption probabilities of several low J lines in the forbidden Cameron system of CO, which have been used to confirm the theoretical picture of intensity borrowing from the $A^1\Pi_1$ level via spin-orbit coupling[2]. The sensitivity of the method is sufficient to observe rovibronic transitions which have emission lifetimes of several tenths of a second making a potentially valuable tool for the spectroscopic study of metastables. The detection efficiency of this technique is estimated to be 2.0×10^{-4}, comparable with electron impact ionization and mass selected detection which suggests it may also prove useful in reaction dynamic experiments where the product state and kinetic energy distributions of species possessing a metastable electronic state may be determined with high accuracy. Yet another application lies in the study of molecular desorption from surfaces. Thermal, electron stimulated, or laser induced desorption of CO from a surface in a UHV chamber followed by quantum state specific time-of-flight could give very detailed information regarding the product internal and kinetic energy distributions of the desorbing molecules. According to the principle of microscopic reversibility, this could be related to the internal state and collision energy dependence of the time-reversed sticking coefficients.

Finally, although this paper focuses on the carbon monoxide molecule, this technique should be applicable to a number of molecules with low lying spin forbidden transitions. We have already demonstrated that the sensitivity of the technique allows for the measurement of very weak transition probabilities, some with lifetimes approaching 0.5 seconds. A wide range of metastable energies down to ~2 eV may be probed as well by the proper selection of a low work function surface. Some candidates for small molecules that could be observed with this technique include CS, N_2, and Cl_2. Each of these has at least one metastable state with a lifetime greater than 100 μsec.

In conclusion, a new technique for performing quantum state resolved time-of-flight measurements has been demonstrated. The technique relies on state selective laser production

of electronic metastable states using forbidden transitions and metastable detection through metastable quenching and secondary electron emission on a surface. The technique allows the high kinetic energy resolution of time-of-flight measurements to be combined with the quantum state resolution of laser spectroscopy.

REFERENCES:

1. Y.T. Lee, Laser Chem., **2**, 219 (1983); Y.T. Lee, Y.R. Shen, Physics Today, 1 Nov. (1988); J.H. Ling, K.R. Wilson, J.Chem. Phys., **65**, 881 (1976); R.N. Zare, Molec. Photochem., **4**, 1 (1972); S.R. Leone, Ann. Rev. Phys. Chem. **35**, 109 (1984); K.H. Welge, R. Schmiedl, Adv. Chem. Phys., **47**, 133 (1981).

2. J. M. Price, A. Ludviksson, M. Nooney, M. Xu, R. M. Martin, A. M. Wodtke, J. Chem. Phys., **96**, 1854 (1992)

3. C.T. Rettner and D.S. Bethune, Rev. Sci. Instr. **60**, 12, 3824 (1989).

4. R.W. Field, S.G. Tilford, R.A. Howard, J.D. Simmons, J.Mol. Spectrosc., **44**, 347 (1972).

5. The notation $R_2(0)$ means that the transition terminates in the F=2 spin orbit state of the molecule, from J"=0. The R indicates that the upper state J'=1 ($\Delta J = +1$ for an R branch). This band is expected to have the maximum intensity for an ensemble of molecules with a low rotational temperature (< 10K). See also Figure 2.

6. Atomic and Molecular Beam Methods, G. Scoles, Ed., Oxford University Press, New York (1987).

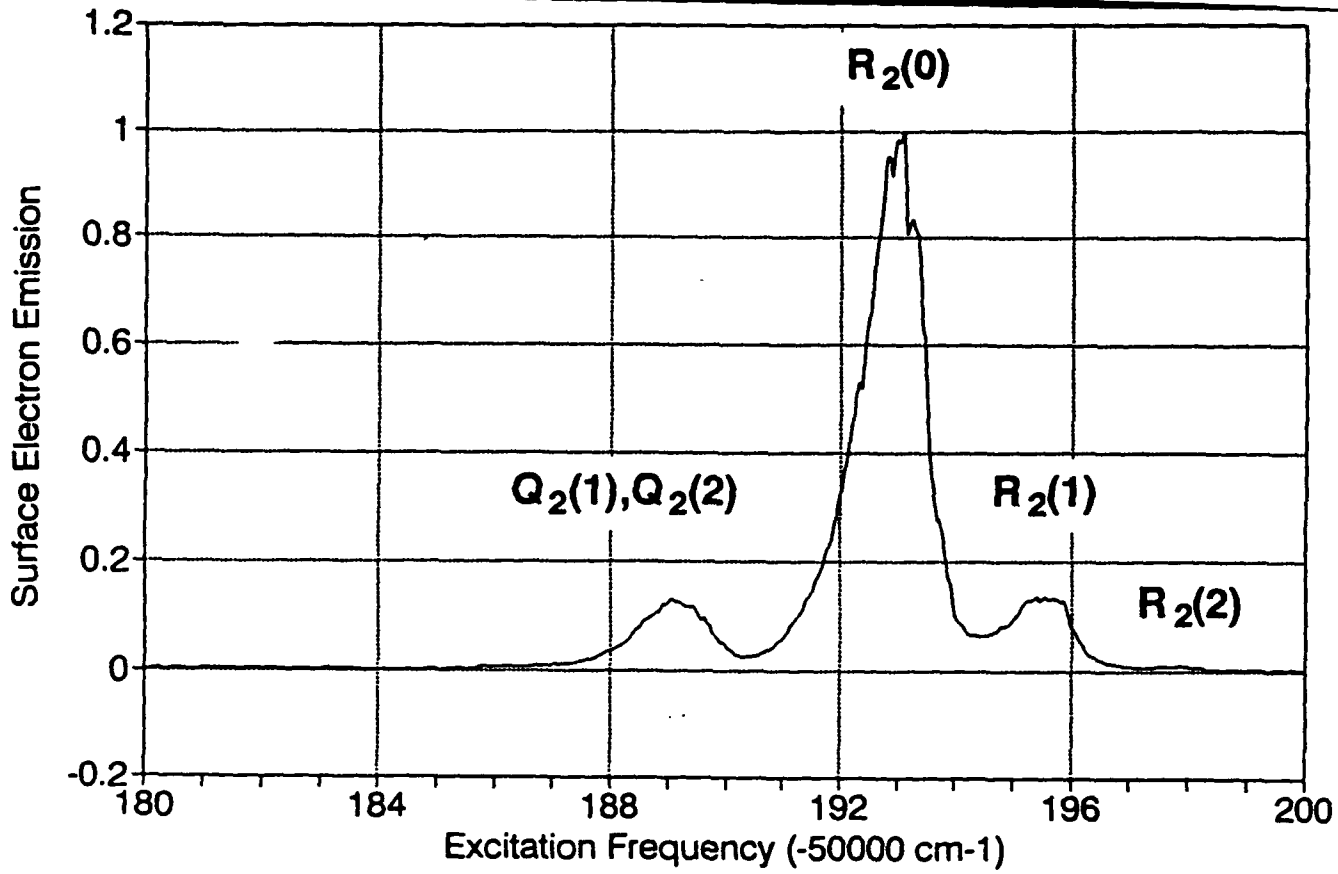

Figure 1.-- ***Laser wavelength dependence of the integrated electron current***: The observed transitions are assigned to the CO Cameron system.

Figure 2.-- ***State resolved TOF spectra for CO in v"=0, j"=0 in a pulsed molecular beam.*** (a) 100% CO beam. (b) 10% CO in 90% He beam.

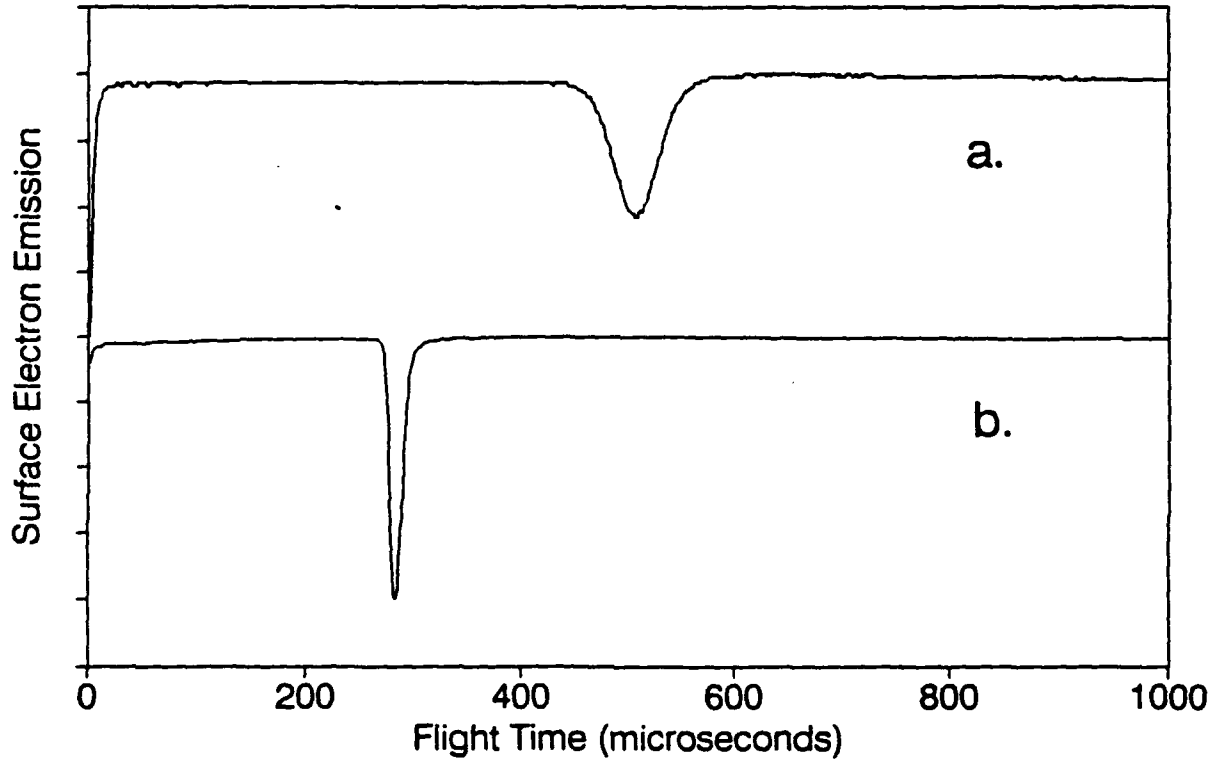

FAST BEAM PHOTODISSOCIATION OF FREE RADICALS

R. E. Continetti, D. R. Cyr, D. Osborne, and D. M. Neumark

Department of Chemistry, University of California, Berkeley, CA 94720

While many photodissociation studies of stable molecules have been performed in recent years, it has proved difficult to extend these experiments to studies of reactive free radicals. This is largely due to the difficulty of implementing a clean, well-characterized source of free radicals. We have developed a novel approach to this problem by setting up an experiment in which free radicals are generated by photodetachment of a mass-selected anion beam, rather than the more conventional strategies in which radicals are formed by photolysis of a stable precursor or by a chemical reaction. Since nearly all radicals have a positive electron affinity, this approach should be quite general.

In the experiment, an 8 keV beam of cold, mass-selected anions is photodetached with a pulsed laser. The resulting neutral radicals are photodissociated with a second pulsed laser, and the photofragments are detected with high (~50%) efficiency using a microchannel plate detector which lies about 100 cm downstream from the photodissociation laser. The center of the detector is blocked so that the undissociated radicals do not impinge on it, but the photofragments move off the beam axis and strike the detector. The experiment can be operated in several modes. We can measure the total photofragment signal as a function of dissociation laser wavelength, thereby mapping out the dissociative electronic transitions of the radical. We can measure the time-of-flight distribution of the photofragments, thereby obtaining an approximated kinetic energy distribution at a fixed photodissociation wavelength. Finally, we have recently installed a two-particle position and time sensing detector that will enable us to determine detailed photofragment energy and angular distributions.

Thus far, we have performed dissociation cross section and time-of-flight measurements on the N_3, NCO, and CH_2NO_2 radicals. We found that the $A(^2\Sigma^+) \leftarrow X\ (^2\Pi)$ transition in N_3 near 270 nm results in predissociation to the spin-allowed $N(^2D) + N_2$ channel. In contrast, in NCO, the $B(^2\Pi) \leftarrow X(^2\Pi)$ transition leads to predissociation to the spin-forbidden $N(^4S)$ + CO channel for

dissociation wavelengths above 260 nm; at lower wavelengths, the spin-allowed $N(^2D)$ + CO channel opens and is the dominant channel. From these results, we obtain $\Delta H_f(NCO)$ = 31 kcal/mol, about 5 kcal/mol lower than the literature value. Our experiments on CH_2NO_2 photodissociation at several wavelengths indicate that the primary products are CH_2 + NO_2, and that the NO_2 is most likely electronically excited.

We have recently begun testing our two-particle position and time-sensing detector by photodissociating O_2 via the Schumann-Runge band. We form vibrationally excited O_2 by photodetachment of O_2^- and excite rotational transitions of the $v'=7 \leftarrow v''=4$ band near 210 nm. This work has shown that the current energy resolution of the detector is 50 meV. We plan to study N_3 photodissociation with this detector very soon, as this resolution should be sufficient to resolve the vibrational state distribution of the N_2 fragment.

Session VII:

Molecular Spectroscopy

High Resolution UV Spectroscopy of Molecular van der Waals Complexes

H.J.Neusser

Institut für Physikalische und Theoretische Chemie
Technische Universität München
Lichtenbergstraße 4, W-8046 Garching
Germany

Interest in the spectroscopy of weakly-bound complexes has grown immensely in the last ten years. The increasing number of complex studies can be attributed to the convenient method of producing isolated gas phase atomic and molecular complexes in cooled supersonic beams. The cold molecular beam provides another important advantage for high resolution spectroscopy, i.e. the reduction of the transversal velocity distribution and consequently of Doppler-broadening by selecting the central part of the beam with a skimmer. Thus, elimination of Doppler-broadening can be obtained without using nonlinear techniques like saturation spectroscopy or Doppler-free two-photon absorption. With this technique we were able to resolve the rotational structure in the vibronic bands of benzene-noble gas dimers and trimers and dimers of benzene with small molecules.

The general goal of our high resolution studies is the quantitative microscopic understanding of van der Waals bonding intrinsic to solvation processes. This goal necessitates investigation of the structure of the complex, its binding energy, the shape of the van der Waals potential, and its dynamic behaviour, i.e. the examination of its energy redistribution and its dissociation.

In a supersonic jet expansion it is not possible to produce a single complex species, but rather, in addition to the monomer constituents of the gas mixture, complexes of various composition and size are produced. The spectra of the different species may overlap and it is often difficult to disentangle them in the fluorescence excitation spectra. For this reason we combined high resolution Doppler-free excitation with resonance-enhanced two-photon ionization /1/. The produced ions can be mass-analyzed and integrated for a selected mass. This leads to highly resolved ($\Delta\nu$ = 130 MHz) mass-selected two-photon ionization spectra reflecting the UV intermediate state spectrum of the selected complex. Pulsed excitation with high spectral resolution is necessary for an efficient two-photon ionization. Light having these properties is provided by amplification of a single-mode cw laser in a three-stage amplifier system pumped by an excimer laser. The light pulses are Fourier-transform-limited with a bandwidth of 80 MHz and a peak power of nearly 1 MW. Absorption of the narrow-band frequency-doubled light pulses leads to an excitation of the S_1 electronically excited state of the complexes within the molecular beam. A second broad-band laser pulse (0.2 cm^{-1}) ionizes the excited complexes. Both light beams interact perpendicularly with the molecular beam so that Doppler-broadening is reduced

to some 40 MHz and sharp intermediate state spectra can be obtained when the first laser is scanned. The ions are mass selected and detected in a linear time-of-flight mass spectrometer with a resolution of $m/\Delta m = 250$.

The high spectral resolution achievable is demonstrated in Fig.1 by the Doppler-free spectra of the strongest one-photon vibronic bands, 6^1_0 and $6^1_0 1^1_0$ of C_6D_6·Ar. The complexes are produced by expansion of 50 Torr benzene seeded in Ar under a backing pressure of 2.6 atm. Both bands display the rotational structure of a prolate symmetric top with a rotational temperature $T_{rot} \approx 3$ K. On the low and high energy side of the spectrum well resolved strong lines appear, which are assigned to the P- and R-branch, respectively. The seven strong features in the center of the band are subbranches of the Q-branch with partly overlapping rotational lines. For a precise determination of the rotational constants a computer fit to the line positions was performed, according to a rigid symmetric top energy formula. The absence of an asymmetry splitting of the lines with low K values within the experimental resolution demonstrates, that the C_6D_6·Ar complex is a prolate symmetric top, with the Ar atom located above the benzene ring on the C_6 rotational axis. From the vibrationally averaged rotational constants B''_0 and B'_v accurate values for the effective van der Waals bond distance $\langle r_{Ar} \rangle$ in the S_0- and the S_1-state are calculated. Due to a slightly larger

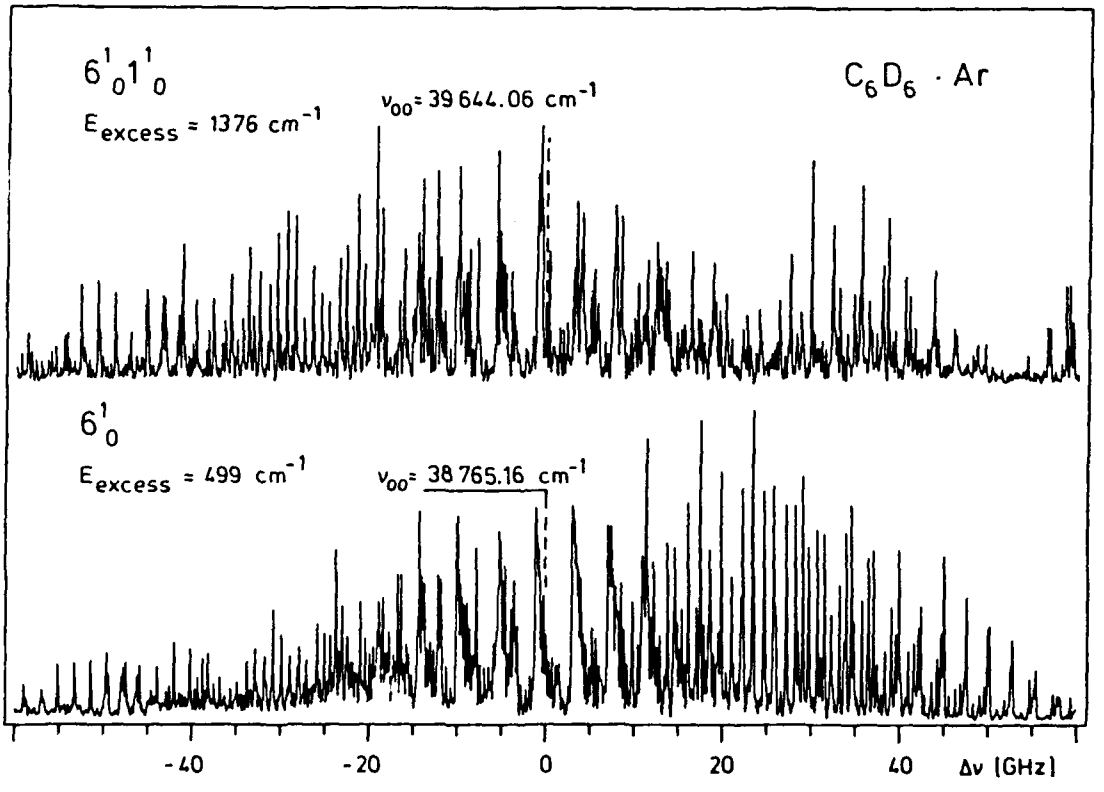

Fig.1: *Rotationally resolved spectra of two vibronic bands of the deuterated benzene-Ar dimer at different excess energies*

ring size and a higher polarizability of benzene in the S_1-state the bond distance *decreases* from 3.58 Å to 3.52 Å upon electronic excitation. Similar information was obtained for complexes of benzene with other noble gases (Ne/2/, Kr, Xe/3/) and with small molecules (N_2)/4/.

In recent experiments we were able to measure the rotationally resolved spectrum of weak van der Waals bands close to the 6^1_0 band shown at the bottom of Fig.1. Here, in addition to the skeletal ν_6 vibration of the benzene molecule, van der Waals vibrations are excited. A clear assignment of these bands was possible on the basis of the rotationally resolved spectrum. We found a strong anharmonicity for the van der Waals stretching vibration, indicating a low dissociation energy of less than 200 cm^{-1} for the van der Waals bond.

It is interesting to note that the measured linewidth in both spectra shown in Fig.1 corresponds to the experimental linewidth of 130 MHz. There is no additional broadening of the lines due to dissociation even in the case of the $6^1_0 1^1_0$ band of both the $C_6H_6 \cdot Ar$ and $C_6D_6 \cdot Ar$ complex when a vibrational excess energy of 1376 cm^{-1} ($C_6D_6 \cdot Ar$) is deposited in the benzene molecule which is several times the binding energy of the complex. This clearly demonstrates that there is a slow energy transfer between the molecular modes and the van der Waals modes resulting in a stable complex on the nanosecond time scale.

With the technique of mass-selective two-photon ionization it is also possible to mass-selectively measure spectra of larger complexes with more Ar atoms attached to the benzene ring. The first experiments yielded a rotationally resolved spectrum of the benzene-Ar_2 ($C_6H_6 \cdot Ar_2$) complex /5/.From the sharpness of the rotational lines it is clear that there are no fast isomerization nor existing migration processes of the Ar atoms about the benzene ring and the complex displays a rigid structure. The structure deduced from the spectrum is shown in Fig.2: both Ar atoms lie on the C_6 axis on either side of the benzene plane each at

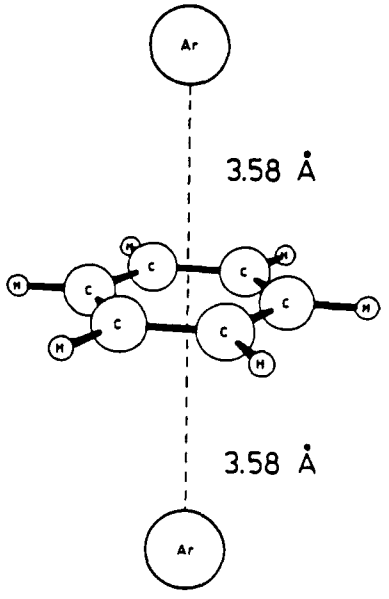

Fig.2: *Experimentally determined structure of the benzene-Ar_2 complex*

a distance of 3.58 Å. This bond distance agrees exactly with that in benzene-Ar (with one Ar atom). From this we conclude that the interaction between the two noble gas atoms is effectively shielded by the aromatic ring and three-body interaction is not of importance in this configuration. The goal of our present experiments is to prove whether other isomers of the benzene-Ar_2 exist and whether even larger complexes exhibit a rigid structure.

In conclusion it is shown that Doppler-free UV spectroscopy provides hitherto unattainable information on the structure, the bond length and rigidity of van der Waals complexes. Such data represents basic information necessary for a microscopic understanding of the van der Waals interaction in organic molecules.

References:

/1/ Th.Weber, A.von Bargen, E.Riedle, H.J.Neusser, J.Chem.Phys. 92, 90 (1990)
/2/ Th.Weber, E.Riedle, H.J.Neusser, E.W.Schlag, J.Mol.Structure 249, 69 (1991)
/3/ Th.Weber, E.Riedle, H.J.Neusser, E.W.Schlag, Chem.Phys.Lett. 183, 77 (1991)
/4/ Th.Weber, E.Riedle, H.J.Neusser, E.W.Schlag, Chem.Phys.Lett. 175, 79 (1990)
/5/ Th.Weber, H.J.Neusser, J.Chem.Phys. 94, 7689 (1991)

Vibrational Dynamics and Molecular Structure: High Resolution Infrared Spectroscopy of the Fundamental and First Overtone of the Hydride Stretches in Large Molecules

Kevin K. Lehmann and G. Scoles, *Department of Chemistry, Princeton University, Princeton, NJ 08544.*
Gerald T. Fraser and Brooks H. Pate, *National Institute of Standards and Technology, Molecular Physics Division, Gaithersburg, MD 20899.*

Recently an increasing number of high resolution studies of the infrared spectra of large polyatomics have been undertaken.[1-4] In the region of the hydride stretch fundamentals of these molecules (> 3000 cm^{-1}) intramolecular vibrational energy redistribution (IVR) dominates the molecular dynamics when the density of background vibrational states is greater than about 10 states/cm^{-1}. The spectroscopic consequence of the IVR dynamics is the presence of extensive local perturbations. Fully resolved spectra in this regime provide quantitative information about the IVR process. Since the total excitation energy is quite low on chemical scales, the IVR dynamics can be studied explicitly without having to disentangle the effects of other dynamic processes (such as dissociation, or internal conversion and intersystem crossing in excited electronic states). The understanding gained from these studies can then be used to aid interpretation of spectra obtained in higher energy regions.

The information available from highly perturbed spectra provide insight on the general features of the vibrational dynamics as well as quantitative information on the IVR process. Questions of the extent of vibrational coupling and the mechanisms responsible (i.e. anharmonic interactions or rotationally mediated couplings) are typically addressed by high resolution studies. However, for chemical applications, perhaps the most important information available from these spectra is the homogeneous IVR rate. The IVR lifetime obtained from the high resolution spectrum is a measure of the time scale of energy localization in the hydride stretch following coherent (short pulse) excitation. This quantity has obvious implications for the prospects of laser induced, bond-specific chemistry induced by overtone excitation.[5] Results of lifetime measurements in acetylenic compounds, with various structural modifications are discussed below.

As mentioned above, the dominant feature of the high resolution spectrum of molecules undergoing IVR is the presence of extensive local perturbations. The fractionation of the spectral intensity over the weakly coupled, near-resonant bath states makes great demands on the sensitivity of the spectrometer used for these studies. Optothermal detection using very sensitive semiconductor bolometers is ideally suited for these studies.[6] Optothermal spectrometers detect changes in the thermal content of the molecular beam following laser excitation. Typically, the detected quantity is the laser deposited energy, which is proportional to the laser power (in the linear regime). As a result very weak absorptions can be measured provided a powerful laser is available in the spectral region of interest.

This detection principle has allowed the measurement of the overtone transitions of the hydride stretches up to v=4.[7,8] We have used a high power color center laser operating near 1.5 μm to measure the first overtone region of a number of large molecules. The 1.5 μm laser provides about 200 mW of power, compared to about 20 mW of power available

in the 3.0 μm hydride fundamental region obtained from another color center laser. The additional laser power available in the 1.5 μm region permits us to obtain spectra of the first overtone of the hydride stretches with comparable sensitivity to the spectra in the fundamental. The additional information provided by overtone spectra is crucial for assessing the validity of extrapolating results based on the fundamentals to the higher overtone regions.

Using the optothermal spectrometer in Princeton we have studied a large number of acetylenic compounds in both the fundamental and first overtone of the acetylenic C-H stretch. Acetylenes are well suited for these studies. The acetylenic C-H stretch normal mode frequency and anharmonicity are quite insensitive to the structure of the rest of the molecule. Therefore, the vibrational motion of the initially excited acetylenic C-H stretch is expected to be similar in all substituted acetylenes. The IVR characteristics can then be studied as a function of the molecular structure of the remainder of the molecule. Previous studies have suggested that structural modifications can greatly affect the IVR behavior of molecules.

The synthetic versatility of acetylenes has allowed us to study three structural modifications: the presence of a heavy central atom which can potentially act to slow vibrational energy transfer,[9] the presence of hindered rotors which through their large amplitude motion can serve to increase the rate of energy transfer,[10] and the effect of deuteration of the non-acetylenic hydrogens which, in some cases, has been suggested to decrease the IVR rate.[11] In general, we have found that the different chemical structures can significantly affect the IVR rate. For the eight molecules that comprise these studies the homogeneous IVR lifetime ranges from about 10 nsec down to about 40 psec. The longer lifetimes we have measured (> 1 nsec) are the longest lifetimes to be reported for molecules undergoing IVR and are significantly longer than picosecond (and shorter) lifetimes often presumed.

We have observed that for the series of molecules $(CH_3)_3X$-C≡CH (X = C, Si, and Sn) that the IVR rate is decreased as the mass of the central atom is increased, this despite the fact that the density of states dramatically increases as the central atom is made heavier.[3b] Furthermore, we find that the IVR rate in the overtones is not dramatically faster. In fact, the X=Si molecule actually has a longer lifetime in the overtone. Although our results qualitatively support the idea of a heavy atom effect in inhibiting vibrational energy transfer, it is difficult to achieve a quantitative understanding of the data based solely on this effect.

In the hope of understanding the role of hindered torsions in the IVR rate we have studied three "mono-substituted propynes" : 1-butyne, propargyl amine, and propargyl alcohol. These molecules have very similar spectroscopic constants, but the nature of the potential of the hindered internal rotor is substantially different for the series. However, we find that the lifetimes of these three molecules are very similar (200 - 400 psec). This similarity suggests that the nature of the hindered internal rotor does not play a major role in the vibrational relaxation of the acetylenic C-H stretch.

Lastly, we have studied two deuterated species, $(CD_3)_3X$-C≡CH (X= C and Si). Compared to their normal isotope parents, the deuterated molecules show faster relaxation. Also, unlike the normal isotope silicon compound, the lifetime in the first overtone of $(CD_3)_3Si$-C≡CH is decreased. The lifetime of the carbon compound is found to decrease more dramatically upon deuteration than observed for the silicon compound.

Although we have been able to demonstrate that structural modifications can have dramatic effects on the IVR rate, we have not been able to fully understand the measurements within the theoretical framework that has been developed to handle these cases. However, we expect that more lifetime information will greatly aid the theoretical development of calculating IVR rates. The availability of a number of lifetimes, at different levels of excitation will provide stringent tests of theoretical calculations. The hopeful outcome will be the ability to predict molecules which will have very slow IVR rates at higher levels of excitation that could possibly be used to perform bond-specific chemistry.

Although we have been successful in obtaining spectra for the substituted acetylenes, the study of some other hydride stretches has been much less fruitful. In particular, spectra of large alcohols have thus far eluded high resolution searches. Even in molecules where a spectrum can be obtained in the methylene C-H stretches, the O-H stretch region has so far resisted detection.[1b,4] Presumably this indicates a much more rapid IVR process in the O-H stretch of large molecules. Using an optothermal spectrometer equipped with a quadrupole state focuser (Electric Resonance Optothermal Spectrometer[12]) we have very recently been able to measure the high resolution spectrum of the O-H stretch in ethanol and propargyl alcohol.

The EROS spectrometer provides about one order of magnitude gain in sensitivity over the conventional optothermal spectrometer configuration. The gain in sensitivity comes from two different sources. First of all, there is an increased solid angle collection efficiency for ground states with positive Stark interaction energy. These states are preferentially enhanced in the spectrum. Secondly, the measured quantity in these experiments is the change in kinetic energy reaching the bolometer, not the increase in energy due to laser excitation. For large molecules seeded in supersonic He beams the kinetic energy can be substantially greater than the photon energy. For example, a molecule of mass 100 in a seeded He beam has about 15,000 cm^{-1} of kinetic energy.

The speculation of faster IVR in the O-H stretches is apparently justified. We find that the spectrum of *trans* ethanol is essentially a continuum of lines. The a-type Q branch is identifiable due to its much increased line density. Unlike the case of the terminal acetylenes, there is no discernible rotational structure (individual R(J) or P(J) line sets). This suggests that the IVR lifetime homogeneously broadens the spectral features on the order of the rotational spacing. An estimate of the IVR lifetime in ethanol is 8 psec. The improved sensitivity of the EROS spectrometer should allow the study of other molecules undergoing rapid IVR in the low energy regions of the fundamentals and low overtones.

References

1 a) A.M. de Souza, D. Kaur, and D.S. Perry, J. Chem. Phys. **88**, 4569 (1988).
b) J. Go, G.A. Bethardy, and D.S. Perry, J. Phys. Chem. **94**, 6153 (1990).

2 A. McIlroy and D.J. Nesbitt, J. Chem. Phys. **92**, 2229 (1990).

3 a) B.H. Pate, K.K. Lehmann, and G. Scoles, J. Chem. Phys. **95**, 3891 (1991).
b) E.R. Th. Kerstel, T.F. Mentel, K.K. Lehmann, B.H. Pate, and G. Scoles, J. Phys. Chem. **95**, 8282 (1991).

4 C.L. Brummel, S.W. Mork, and L.A. Philips, J. Chem. Phys. **95**,7041 (1991).

5 A. Sinha, M. Hsiao, and F.F. Crim, J. Chem. Phys. **92**,6333 (1990).

[6] T.E. Gough, R.E. Miller, and G. Scoles, Appl. Phys. Lett. **30**, 338 (1977).
[7] C. Douketis, D. Anex, G. Ewing, and J.P. Reilly, J. Phys. Chem. **89**, 4173 (1985).
[8] M. Scotoni, A. Boschetti, N. Oberhofer, and D. Bassi, J. Chem. Phys. **94**, 971 (1991).
[9] a) P.Rogers, D.C. Montague, J.P. Frank, S.C. Tyler, and F.S. Rowland, Chem. Phys. Lett. **89**, 9 (1982).
b) V. Lopez and R.A. Marcus, Chem. Phys. Lett. **93**, 232 (1982).
[10] a) C.S. Parmenter and B.M. Stone, J. Chem. Phys. **84**, 4710 (1986).
b) D.B. Moss, C.S. Parmenter, and G.E. Ewing, J. Chem. Phys. **86**, 51 (1987).
[11] a) V.A. Walters, S.D. Colson, D.L. Snavely, K.B. Wiberg, and B.M. Jamison, J. Phys. Chem. **89**, 3857 (1985).
b) C.C. Matrens and W.P. Reinhardt, J. Chem. Phys. **93**, 5621 (1990).
[12] G.T. Fraser and A.S. Pine, J. Chem. Phys. **91**, 637 (1989).

High Resolution Laser Spectroscopy from the XUV to the visible

W.L. Meerts

Department of Molecular and Laser Physics, University of Nijmegen
Toernooiveld, 6525 ED Nijmegen, The Netherlands

The method of laser induced fluorescence (LIF) is well established as a very sensitive and versatile technique in molecular spectroscopy. Using a pulsed laser and a molecular jet a resolution of 0.1 cm^{-1} is attainable in the visible and UV region. This resolution is generally not sufficient to study rotational resolved spectra, splittings due to for example internal rotations in the molecule, and effects due to intersystem crossings. Especially rotational resolved spectra for cluster molecules need high resolution. In order to improve the resolution to the MHz level we combined a single frequency stabilized laser with a strongly collimated molecular beam.

The laser system consists of a single frequency continuous wave ring dye laser (a modified Spectra Physics 380D) pumped by a Argon-ion laser. The dye laser is usually operated with the dyes Rhodamine 6G, DCM or stibene. The fundamental frequency of the dye laser is controlled with a stabilization system. Stabilized scans of 60 GHz in the visible can be made. The band width of the dye laser is 2 MHz and determined by the frequency jitter of the laser.

For precise absolute frequency measurements the absorption spectrum of the iodine molecule is recorded. Comparison of the measured iodine absorption spectrum with the well determined reference spectrum allows the measurement of the absolute laser frequency with an accuracy better than 100 MHz. For relative frequency measurements the transmission peaks of a high finesse temperature stabilized, sealed off Fabry-Perot interferometer (Burleigh CFT-500) with a free spectral range of 149.67 MHz is used.

Most electronic transitions of molecules are in the ultraviolet part of the electromagnetic spectrum. Hence a doubling crystal is placed in the auxiliary waist in the cavity of the ring dye laser. With three different $LiIO_3$ crystals tunable continuous wave single frequency UV radiation is obtained in the range 294-330 nm with output powers up to 15 mW. UV radiation in the region of 215-230 nm was generated using a BBO crystal. In that case the typical output was 100 μ W.

The UV radiation is used to excite the molecules in a molecular beam. The molecular beam is formed by an expansion of the molecules under investigation with a seeding gas through a quartz nozzle with a typical diameter of 100 μm. A sample of the molecules is stored in a quartz vessel. Both the quartz vessel and the quartz nozzle could be heated up to 500 °C in order to increase the vapour pressure of the sample.

A mixture of the vapor pressure of the sample and the seeding gas (usually argon or helium) is expanded into the vacuum chamber. In the expansion the internal degrees of freedom of the molecules are cooled down and only the lowest vibrational and rotational states are populated. In this way the spectra are simplified to a large extend. A typical rotational temperature in our molecular beam is 3 K. A molecular beam is formed out of the expansion by two conical skimmers with diameters of 1.5 mm.

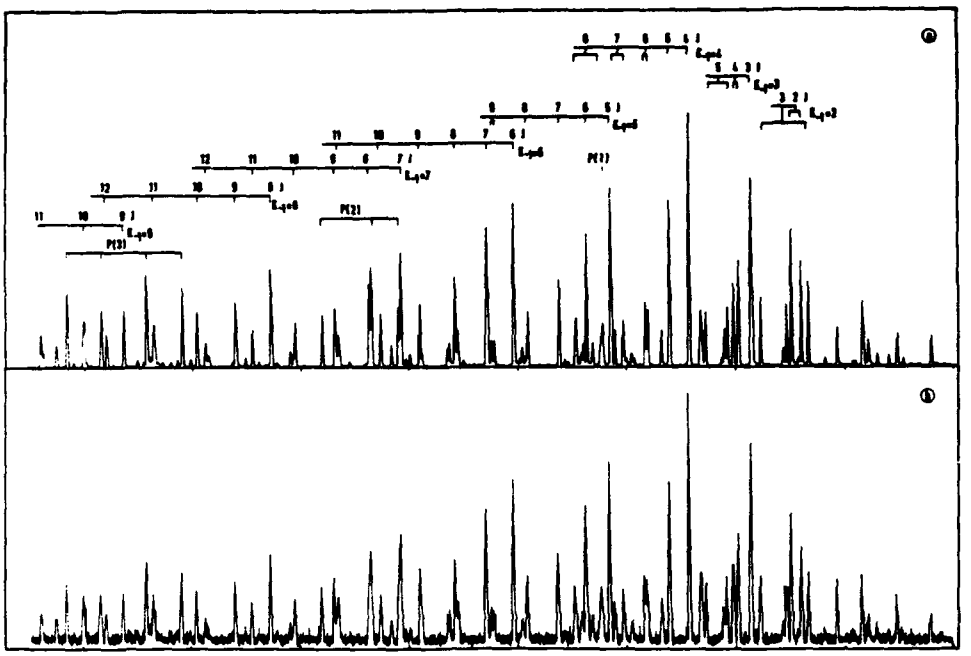

Figure 1: High resolution fluorescence (a) and phosphorescence detected (b) spectra of the Q-branch of the $(3a_g)_0^1$ vibronic transition in naphthalene. The intensity axis is in arbitrary units. The frequency increases from left to right and is marked every GHz.

At a distance of 30 cm from the nozzle orifice the molecular beam is crossed perpendicularly by the laser beam. Various detection methods are applied. Most frequently we collect the total undispersed laser induced fluorescence with two spherical mirrors and imaged on a photomultiplier tube. The total line width of the molecular transitions is mostly determined by the residual Doppler width and amounts to 12 MHz with the use of argon as seeding gas. At a distance of 60 cm from the nozzle orifice a second interaction zone is placed. At this position the molecules can interact with a second laser to perform UV-UV pump-probe experiments.

In the studies of energy redistribution in for example pyrazine we applied two alternative detection methods. In the first one we detected the total energy left in the molecule after excitation at 30 cm from the orifice with a bolometer detector placed 60 cm from the nozzle. This allows to detect the so called dark states. In the second method we detect the the phosphorescence of the molecules in triplet states by collecting the beam on a cold surface and observing the light coming of this surface with a light pipe and a photomultiplier. This latter method is very effective for the detection of states that don't fluoresce. It is quite sensitive since no background signals are present. Figure 1 compares the results of the fluorescence and phosphorescence detection in naphthalene. Results on high resolution experiments of tri-phenylamine and its van der Waals complexes are presented in another contribution to this meeting.

In order to study weak or "forbidden" transitions strong radiation fields are needed. Also

COPY AVAILABLE TO DTIC DOES NOT PERMIT FULLY LEGIBLE REPRODUCTION

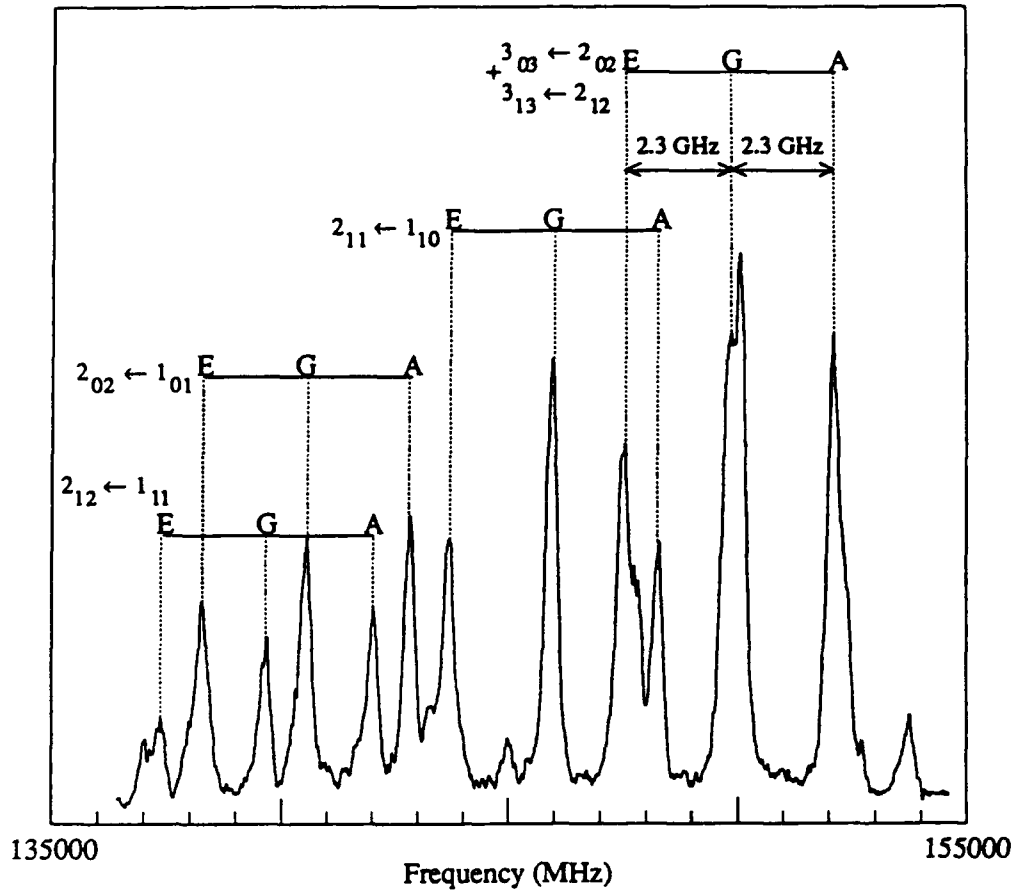

Figure 2: Part of the rotational resolved $n\pi^*$ $S_1 \leftarrow S_0$ transition in acetone detected with the PDA system. Indicated are the rotational quantum numbers. The splittings due to the internal rotation of the methyl rotors are clearly observed. This allowed the determination of the barrier to internal rotation in the excited S_1 state.

to penetrate further in the UV and XUV either through the use of four wave mixing processes or multiphoton transitions, high powers are required. This cannot longer be achieved with cw lasers. To maintain a resolution as best as possible we have chosen to use the method of pulsed dye amplification in combination with a molecular jet.

The narrow bandwidth radiation with a high peak power is obtained by pulsed amplification (PDA) of radiation from a cw ring dye laser. The ring dye laser (Spectra Physics, 380D) is pumped by an Argon ion laser (Spectra Physics, 2045-15) and operates on Rhodamine, DCM or stilbene dye. The The bandwidth of the ring dye laser is less than 0.5 MHz and the output power is typically 400 mW. This radiation is amplified by a home built four-stage pulsed dye amplifier (PDA) system similar to the system described by Cromwell *et al.* [ref 1]. A frequency doubled or tripled Q-switched Nd:YAG laser (Quantel YG 681C-10) with a pulslength of 5 ns and a pulse energy of 550 mJ (green) 200 mJ (UV) pumps the PDA system. The pulse energy of the amplified laser beam is 100 mJ. The bandwidth, which is

merely determined by the Fourier limit of the pulsed pump laser amounts to 135 MHz. This light is then frequency doubled in KDP or BBO crystals. The UV beam is separated from the fundamental beam by a Pellin Broca prism. The pulse energy of the UV light is 20 mJ and 1 mJ for doubling of the red dyes and stilbene, respectively.

A molecular beam is formed by expanding a mixture of the gas (eg. acetone or CO) in argon through a modified electromagnetic fuel injector valve (Bosch) with an orifice diameter of 1 mm into a vacuum chamber. During operation the background pressure in the vacuum chamber is $5{\cdot}10^{-5}$ torr.

The laser beam with a diameter of 3 mm crosses the molecular beam 45 mm downstream the nozzle. The laser induced fluorescence is collected by a quartz lens system and imaged onto the photomultiplier. The fluorescence signal is processed by a digital oscilloscope (LeCroy 7400) and a boxcar integrator (SRS 250) interfaced with a computer.

Figure 2 gives an example of the spectrum of the rotational resolved $n\pi^*$ $S_1 \leftarrow S_0$ transition in acetone around 330 nm. This transition in acetone has a very low oscillator strength and could only be detected with a pulsed laser system. The resolution of the PDA was needed to resolve the rotation structure and the effects due to internal rotation of the methyl rotors. We were able to assign a large number of the lowest vibrational transitions in the S_1 state and to determine the barrier to internal rotation in this state. A discussion will be presented. Results on one- and two-photon experiments on DABCO are presented in another contribution to this meeting.

The Rydberg states $L(v = o)$, $L'(v = 1)$, $K(v = 0)$, $W(v = 0)$ and $W'(v = 2)$ are studied by a double resonance technique. Jet-cooled CO is two-photon excited by a pulsed laser from the $X'\Sigma^+$ ground state to the $B'\Sigma^+$ state. The population of the B state is monitored by the fluorescence from the $B \rightarrow A$ state.

The narrow bandwidth radiation PDA system is used to excite the CO molecules from the B state to the Rydberg states. A transition to a Rydberg state is detected by a decrease in $B \rightarrow A$ fluorescence caused by a depletion of the B state.

In this way the position of the Rydberg states is determined within 300 MHz. The lifetime of these states, which are known to predissociate, is determined by measuring the width of a transition. The observed lifetimes are different for each state and show a strong J dependence.

The author like to thank all his collaborators that made contributions to the research presented above: G. Berden, D. Consalvo, M. Drabbels, J. Heinze, J.J. ter Meulen, G. Meijer, D. Parker, J. Reuss, P. Uijt de Haag and H. Zuckermann.

[ref 1] E. Cromwell, T. Trickl, Y.T. Lee and A.H. Kung, Rev. Sci. Instrum. 60 (1989) 2888

SPECTROSCOPY ON TRIPHENYLAMINE AND ITS VAN DER WAALS COMPLEXES

GERARD MEIJER, GIEL BERDEN AND W. LEO MEERTS
Dept. of Molecular and Laser Physics,
University of Nijmegen,
Toernooiveld, 6525 ED Nijmegen, The Netherlands
and
HEINRICH E. HUNZIKER, MATTANJAH S. DE VRIES AND H. RUSSELL WENDT
IBM Almaden Research Center,
650 Harry Road, San José CA 95120, USA

Both vibrationally and rotationally resolved spectra of the $S_1 \leftarrow S_0$ transition in jet-cooled triphenylamine (TPA) around 340-320 nm are measured.
Medium resolution spectra (0.5-1.0 cm^{-1} resolution) are recorded using (1+1)-Resonance Enhanced Multi Photon Ionization (REMPI) with mass selective Time-Of-Flight (TOF) detection in a pulsed molecular beam apparatus, and are shown in Figure 1. The origin of

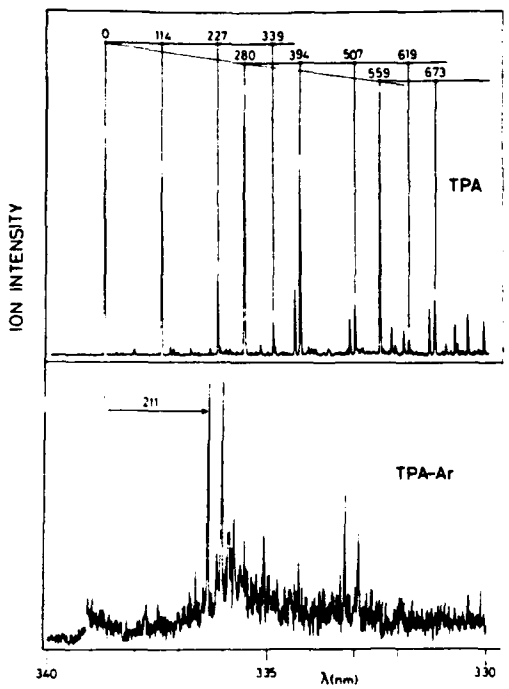

Figure 1:
Vibrationally resolved (1+1)-REMPI spectrum of jet-cooled TPA (A) and TPA-Ar (B). In both cases the parent ion is mass-selectively detected. In the spectrum of TPA, two vibrational progressions are indicated (values in cm^{-1}). In the lower panel the shift of the van der Waals complexes relative to the free TPA is indicated (in cm^{-1}).

COPY AVAILABLE TO DTIC DOES NOT PERMIT FULLY LEGIBLE REPRODUCTION

the $S_1 \leftarrow S_0$ transition is at 29520.7 cm^{-1}, higher than halfway to the ionization potential (IP) found at 6.89 eV. A vibrational progression in the symmetric torsion mode (114 cm^{-1}) as well as in the symmetric C-N stretching mode (280 cm^{-1}) is observed in the electronic spectra. The spectrum of the most abundant isomer of the TPA-Ar (TPA-Kr) complex shows an anomalous *blue*-shift of 211 cm^{-1} (216 cm^{-1}) with respect to the spectrum of the free TPA molecule. The spectrum of the most abundant isomer of TPA complexed with two Ar atoms shows a regular 24 cm^{-1} red-shift with respect to the spectrum of TPA-Ar, so still an overall blue-shift relative to TPA itself.

High resolution (the resolution mainly being determined by the natural linewidth of the transition, i.e. 36 MHz) spectra are recorded using Laser Induced Fluorescence (LIF) in a cw molecular beam apparatus. The thus recorded origin of the $S_1 \leftarrow S_0$ transition is shown in Figure 2. Individual rotational transitions are resolved and the spectrum shows unambiguously that TPA is a symmetric top. The rotational constant B" in the S_0 state of TPA is equal to B"=(403.7 $\pm$ 0.5) MHz. Upon $S_1 \leftarrow S_0$ excitation both B and C increase with (7.4 $\pm$ 0.1) MHz and (2.8 $\pm$ 0.1) MHz, respectively. This indicates a decrease in torsion angle by 2 to 3 degrees and a shortening of the C–N bonds by 2 % upon electronic excitation. In Figure 3 the high resolution spectrum of the blue-shifted TPA-Ar isomer is shown. This spectrum is the spectrum of a symmetric top molecule as well, and therefore the Ar atom has to be located on the C_3 symmetry axis, either on top of or underneath the umbrella formed by the phenyl rings.

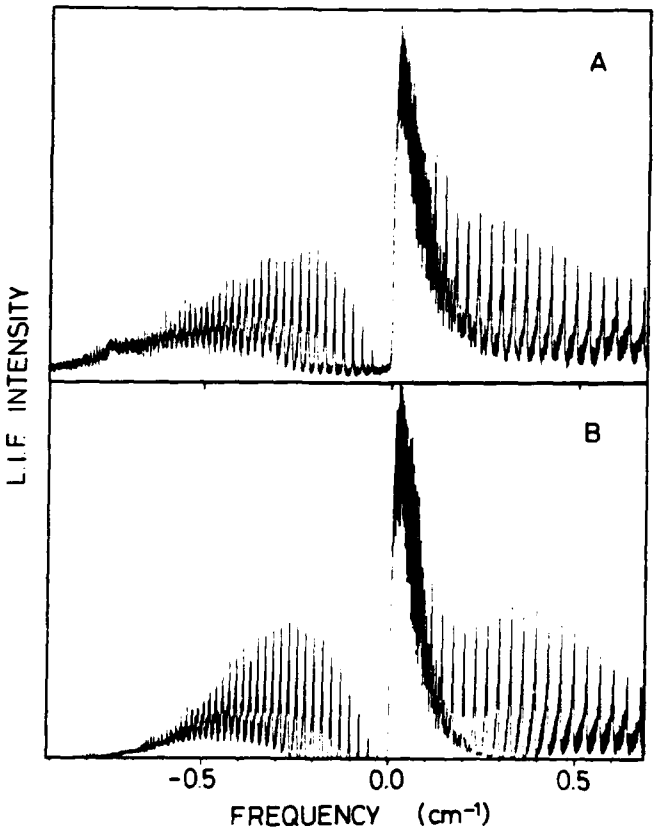

Figure 2:
High resolution LIF spectrum of the origin of the $S_1 \leftarrow S_0$ transition in jet-cooled TPA. The experimentally observed spectrum (A) can be fitted into the smallest detail, using the formulas for a rigid oblate symmetric top molecule, as shown in (B). Note the band head in the P-branch for large J",K" values.

It appears that when Ar or Kr forms a complex with TPA, the first Ar, Kr, atom goes preferentially in a position on the C_3 symmetry axis of TPA, a position which causes an abnormal blue-shift of the spectrum. With the first rare gas atom located in this special position, the second rare gas atom is forced into a "normal" position, i.e. above one of the phenyl-rings, causing a normal red-shift with respect to the TPA-Ar complex.

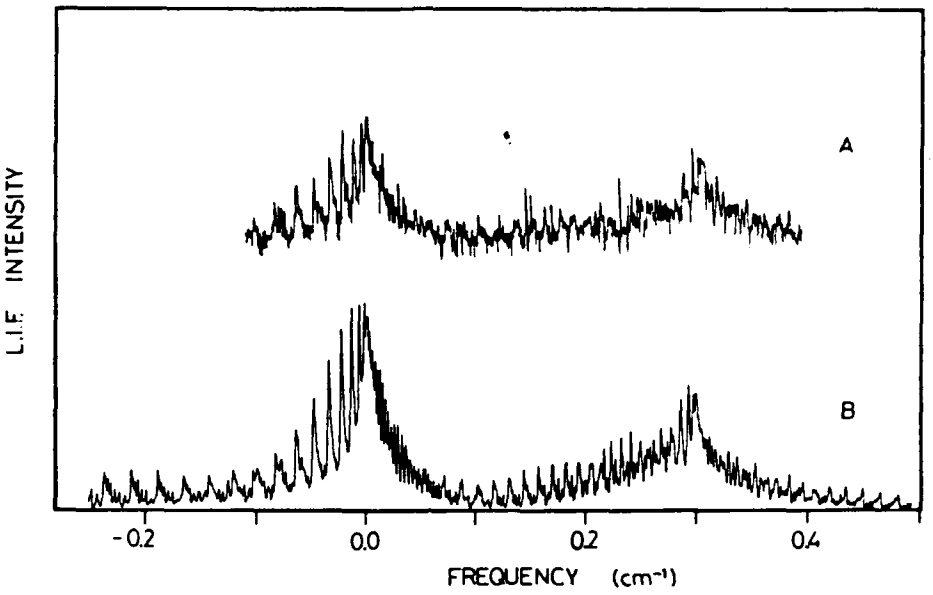

Figure 3:
Experimentally observed (A) and simulated (B) high resolution LIF spectrum of the origin of the 211 cm^{-1} blue-shifted TPA-Ar complex at 29731.2 cm^{-1}. The simulated TPA-Ar spectrum is for a van der Waals complex that is a symmetric top, i.e. a vdW complex in which the Ar atom is sitting on the c-axis. In the simulation the same rotational temperature (4.0 K), the same lineshape and the same values for C" and ΔC were taken as found for TPA. The simulated spectrum is for B" = 280 $\pm$ 5 MHz and ΔB = -8.5 $\pm$ 0.5 MHz. As now ΔB is negative, the R-branch has a band head, and the Q-branch degrades to the red.

MOLECULAR BEAM STUDY OF IR MULTIPHOTON EXCITATION WITH HIGH RESOLUTION

Sacco te Lintel Hekkert, Arjen Linskens and Jörg Reuss
Molecular and Laser Physics
University of Nijmegen, The Netherlands

A molecular beam of 5% SF_6 seeded in He is intersected by cw CO_2 lasers focused to a minimum waist of about 0.1 mm diameter. One of the lasers is chopped and the molecular beam signal is detected by a liquid-He-cooled bolometer, sensitive to the (chopped) excitation of the SF_6 molecules. In the laser interaction zone collisions can be neglected altogether.

The aims of the experiment are:

a) to determine the transition frequencies for one-, two- and three-photon transitions with an accuracy of 1 MHz,

b) to excite the SF_6 molecules by overlapping laser fields of different frequencies in order to explore new energy ranges for the final levels, e.g. accessible after absorption of $2\hbar\omega_1 + \hbar\omega_2$,

c) to study depletion of initial levels by multiphoton excitation through double resonance measurements,

d) to produce Rabi oscillations for $2h\nu$ transitions,

e) to produce Ramsey fringes for $2h\nu$ transitions,

f) to demonstrate population inversion by rapid adiabatic passage processes for $2h\nu$ and $3h\nu$ transitions, and

g) to produce ac Stark shifts and observe these in an inverse Λ-level scheme ($\sqrt{\ }$).

All of these aims have been realized, though with varying degrees of perfection. In figure 1 a three-photon transition is shown ($S(9)A_1$) which is surrounded by two-photon peaks. Since $2\hbar(\omega_1 + \Delta\omega) + \hbar(\omega_2 - 2\Delta\omega)$ leads to the same final level, the shift (Δ) of frequency ω_1 of the double-excitation laser leads to resonance for a double shift (2Δ) of the frequency ω_2. This is demonstrated in figures 1a and 1b. The shifts are plotted in figure 2. Note that for the laser powers used a detuning of about 10 GHz is permitted for intermediate levels, i.e. a frequency interval much larger than the tuning range of our cw lasers ($\pm$300 MHz). In this way we were able to determine which of our excitation peaks belong to three-photon transitions (see aim b), above).

The theoretical assignment of the observed transtions are based on work by Pierre et al. (Dijon) and Sartakov et al. (Moscow). The experimental observations also include hot-band transitions, which have eluded theoretical treatment so far. Depletion measurements (see c), above) show large effects for some of these unassigned transitions, whereas depletion of rotational levels of the vibrational ground state stayed below the detection limit (about 5% of the observed excitation signals).

Concerning g), figure 3 presents qualitatively the level scheme in a dressed-state picture. It serves to demonstrate the occurence of (strong) interference effects. N, $N+1$ and $N+2$ stand for the (small) number of uncoupled probe laser photons present in the system "molecule + pump laser field" which produces the $2h\nu$ absorption $|a> \rightarrow |c>$ (see insert). The strong pump laser is resonant with the transition $|a> \rightarrow |b>$. Its amplitude increases from left to right and causes the ac Stark shift indicated by the three-fold level arrangements.

Probe laser transitions are indicated by vertical arrows, (i) from the highest to the lowest and (ii) from the one-but-highest to the lowest level. Both of these transitions have three possible intermediate levels. Their detunings vary with the amplitude of the pump laser, $E = E_0$, the transition (i) passes through a resonance with zero detuning. For the corresponding laser power this transitions (i) assumes a steep maximum probability. For nearly the same laser power transition (ii) passes through a minimum, because the amplitudes for the path with negative detuning of the intermediate level interfere destructively to nearly zero with the two amplitudes belonging to paths with intermediate levels with a positive detuning.

The first results have been published in [1]

[1] A. Linskens, S. te Lintel Hekkert and J. Reuss, Infrared Phys. 32 (1991) 259

Figure 1
Relative shift of the three photon-transition S(9) A_1 (peak B) to the two-photon transitions R(7) E and Q21 F_2 (respectively peak A and C). Spectra taken with the pump laser (18 Watt) fixed on the 10P16 CO_2 laser line centre (upper spectrum), and with a 13 MHz shift of the pump laser (lower spectrum). The probe laser was scanned over the 10P14 CO_2 line (5,5 Watt). The distance between two fringes is 9 MHz. On the right, the energy level diagram of the three-photon transition is shown, utilizing two photons from the pump and one photon from the probe laser.

Figure 2
Plot of the shift of transition B (see fig.1) as a function of the shift of the two photon transition A (see fig.1) which is proportional to the shift of the pump laser. Transition B shifts twice as fast as transition A.

Figure 3
Interference effects for transitions (i) and (ii) arising from three possible intermediate levels (in a dressed level picture), for the two-photon transition $|a> \rightarrow |c>$, as a function of the pump laser amplitude. The pump laser is resonant for the transition $|a> \rightarrow |b>$. Level b is off-resonant by 80 MHz, for the two-photon resonance of the probing laser.

Figure 1

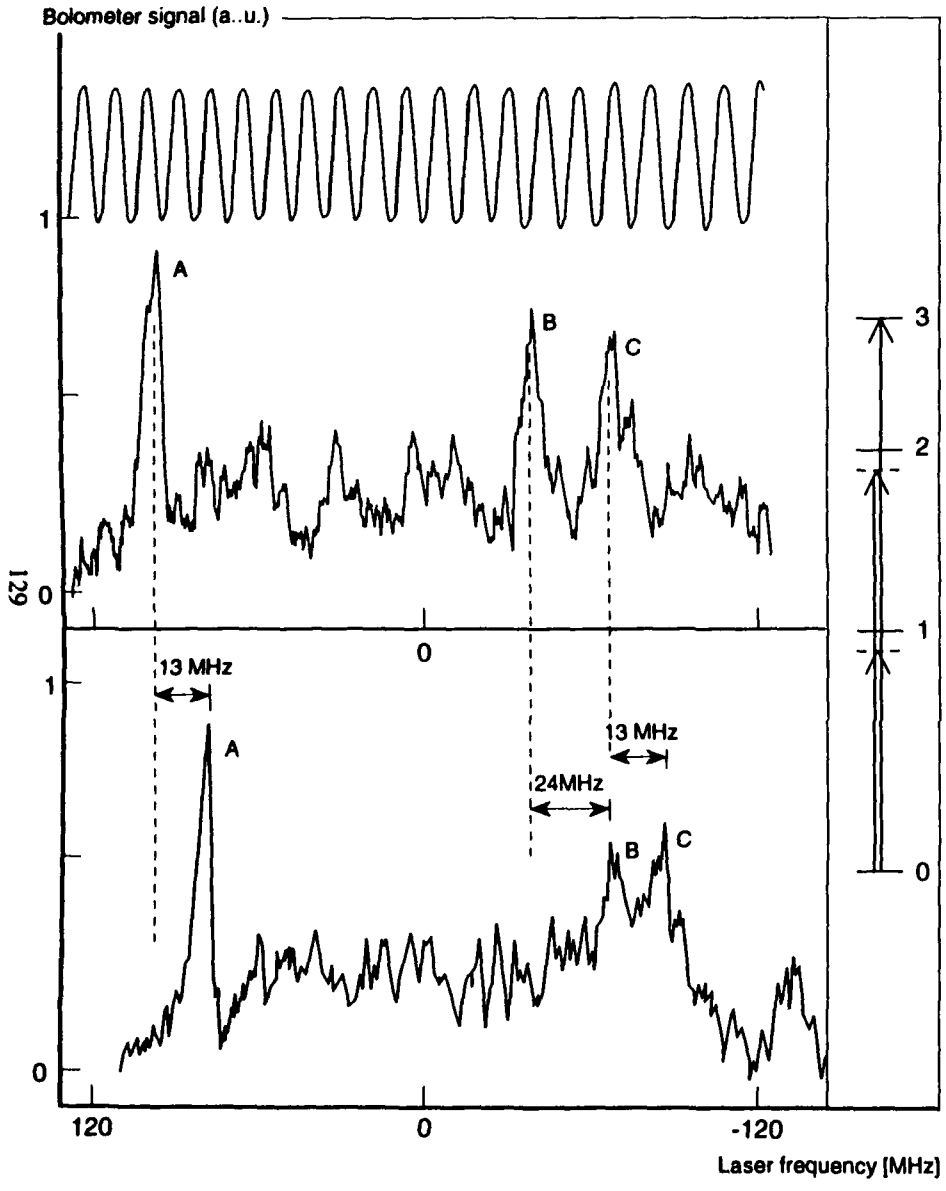

Figure 2

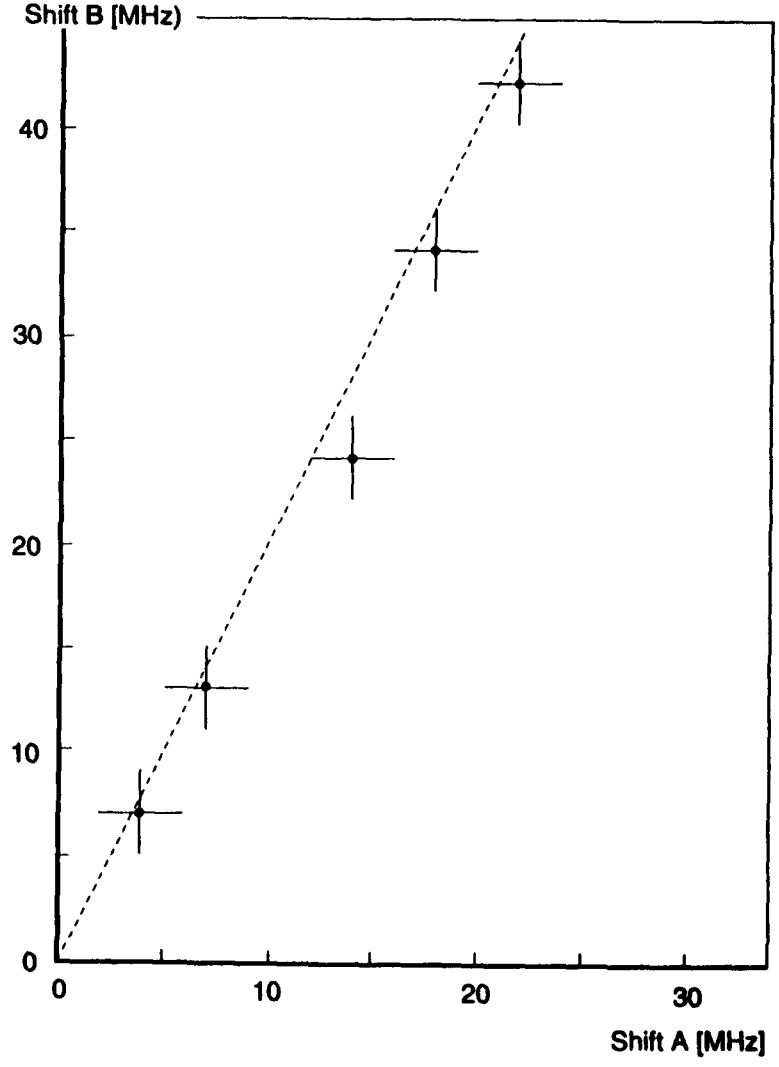

Figure 3

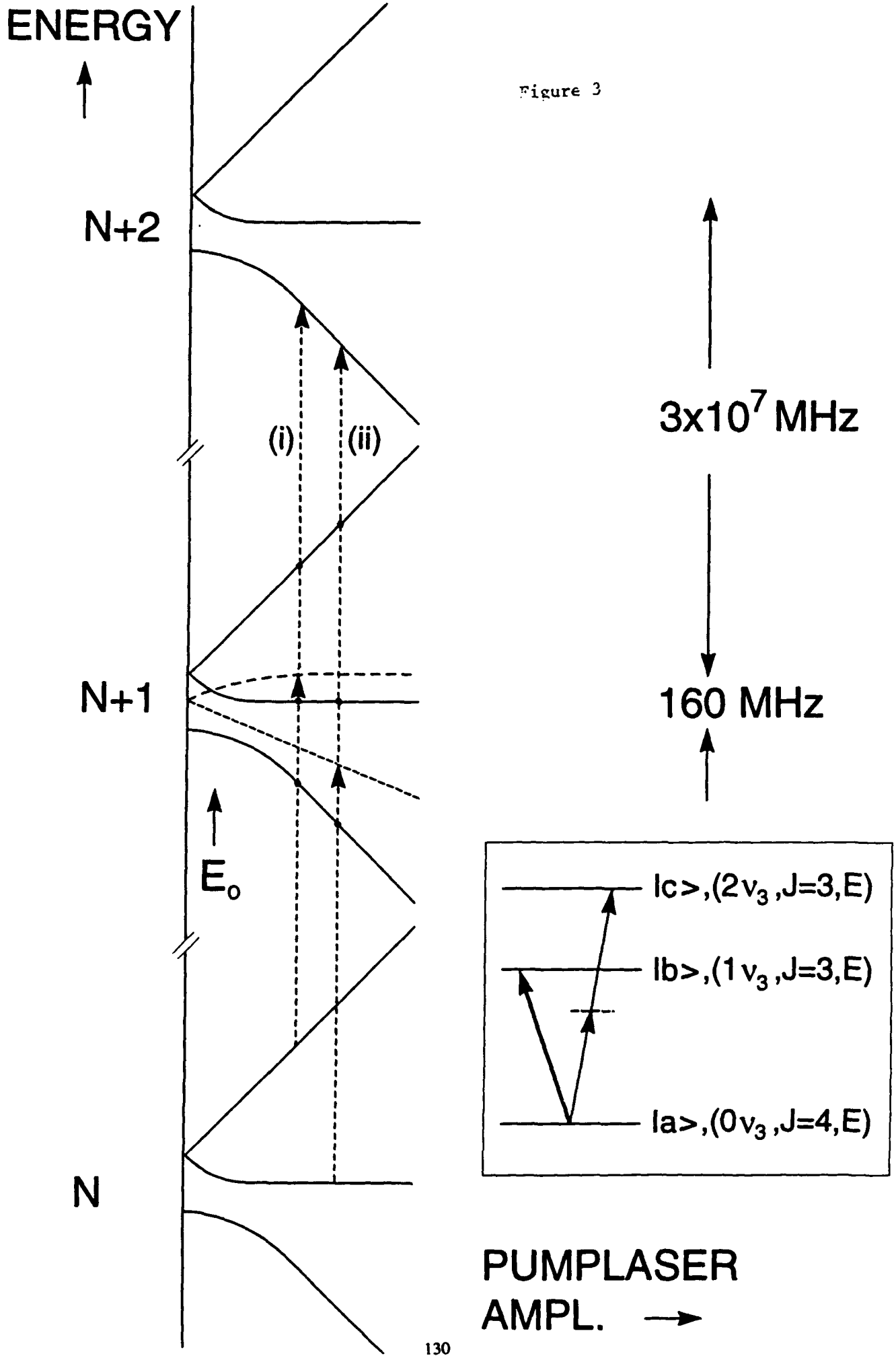
ENERGY
N+2
N+1
N
(i)
(ii)
E_o
$3x10^7$ MHz
160 MHz
|c>,(2v_3,J=3,E)
|b>,(1v_3,J=3,E)
|a>,(0v_3,J=4,E)
PUMPLASER
AMPL. →

Stimulated Emission Pumping of Acetaldehyde and Propynal: Influence of Molecular Structure on the High Resolution Vibrational Spectrum

J. M. Price, C.A. Rogaski, J. Mack, G. v. Helden, X. Yang[a], and A. M. Wodtke,
Department of Chemistry, University of California, Santa Barbara CA 93106

Since the beginning of research into infrared multi-photon dissociation of molecules, there has been a keen interest in the rate of intramolecular vibrational redistribution (IVR) in highly vibrationally excited polyatomics. While it has been recognized that the total vibrational state density is of crucial importance to the rate of IVR, it has not been clear what effect the gross *structure* of molecules has on the magnitude of coupling between vibrational states. Recent results showing heavy atom inhibition[1] and methyl-rotor acceleration[2] of IVR rates have given support to the intuitive notion that molecular structure may have a significant influence on vibrational state coupling, suggesting that state density may not be the sole arbiter.

In this work, we have applied the method of molecular beam stimulated emission pumping[3] (SEP) to obtain high resolution ro-vibrational spectra of the electronic ground state of two polyatomic molecules with comparable state densities: propynal (presented at another poster in this conference) and acetaldehyde. Both molecules are good examples of medium-sized polyatomics containing low frequency modes. Propynal's low frequency vibrations are distributed among a number of "skeletal" modes[4], while the low frequency motion in acetaldehyde is primarily confined to the methyl torsion[5,6]. Even though the density of vibrational states in propynal is actually slightly larger than that of acetaldehyde at the energies explored here, it is found that the spectrum of acetaldehyde is far more complex. The explanation for this phenomenon is couched in terms of the way the methyl rotor enhances vibration-vibration coupling in the molecule.

Both electronic absorption systems are believed to be $\pi^* \leftarrow$ n C-type ($\perp$) transitions, similar to formaldehyde. This would give rise to a large extension of the CO bonds in the excited electronic states. Evidence for this picture in propynal is supported by rotationally resolved UV spectrum[7,8], microwave data on the ground state[9] and dispersed fluorescence spectra which show a long progression in ν_4[10]. Unlike formaldehyde, the excited state of propynal remains planar because of the partial double bond character in the aldehydic-carbon to carbon linkage.

For acetaldehyde, little direct evidence on the nature of the transition has been obtained. Molecular beam excitation spectra have not yielded clear assignments of the expected strong CO progression in the excited state due to vibrational congestion above E_{vib} = 600 cm^{-1} and have only succeeded in resolving a handful of rotational transitions, precluding an accurate determination of excited state rotational constants[11]. Nevertheless, low resolution data indicate that the excited state is non-planar[12] and ab initio studies have suggested the excitation is analogous to formaldehyde[13]. Recent rotationally resolved excitation spectra from our laboratory give the excited state structure and confirm the $\pi^* \leftarrow$ n nature of the transition[14]. In addition to extension of the CO bond and puckering of the aldehydic chromophore, the methyl rotor moves from a carbonyl-eclipsed structure in the ground state[15,16] to a carbonyl-staggered structure in the excited state[17]. The barrier to internal rotation is also believed to increase from 415 cm^{-1} in the ground state[17] to 735 cm^{-1} in the excited state[17]. Acetaldehyde was chosen for these studies since it is the smallest molecule containing an internal rotor that may

be probed with SEP. Our hope was that these experiments would not only confirm or deny the importance methyl rotors in IVR, but would also lead to vibrational assignments of the emission spectrum of Acetaldehyde at least for low vibrational energies of the ground state. Unlike Propynal, the emission spectrum of this molecule has not lent itself to detailed analysis. Assigned spectra would prove very valuable in obtaining a clear picture of the dynamics of methyl rotor enhanced vibrational energy flow.

The experiments presented here were carried out in a small molecular beam chamber, specially designed to produce two nearly identical and simultaneous pulsed molecular beam, laser induced fluorescence experiments. Laser induced fluorescence was depleted in one of the molecular beams with a second DUMP laser allowing pulse by pulse fluorescence normalization, analogous to SEP cell experiments[18]. In addition, dispersed fluorescence spectra could be obtained with a 1 meter monochromator. Excimer pumped dye lasers were used for experiments on both molecules.

Figure 1 shows the dispersed fluorescence spectra of Acetaldehyde excited in the rotationally cold environment of a molecular beam. This molecule exhibits a very complex emission spectrum. A progression in ν_4 is clearly present, but the relative intensities of the combination bands with ν_4 are substantially greater, and there is also a dramatic "broadening" of these features that is *not* due to the limited resolution of the monochromator. This point is unambiguously supported by the large number of densely packed SEP transitions observed at high resolution, which are found to account for the broadening of the spontaneous emission structure. This is shown in fig. 2. Here, a portion of the resolved emission spectrum shown in fig. 1 is plotted over a 1000 cm^{-1} range. Also plotted is a 'stick' spectrum of measured SEP transitions over the same region. One can see that the width of the observed structures in emission can be justified in terms of the large number of active transitions within each band. Despite the fact that the vibrational density of states is less than half of that of propynal over this energy range, acetaldehyde's vibrational spectrum is much more complex.

Propynal, in contrast to acetaldehyde, is a very interesting example of a medium sized molecule whose emission spectrum, at least qualitatively, resembles that of a diatomic. The main progression is in ν_4 (the CO stretch). Combination bands with this ν_4 vibration associated with ν_6 (aldehydic C-C stretch) and ν_{10} (out-of-plane aldehydic C-H bend) are also apparent. The simple structure of the emission spectrum of this molecule is not however, due to some limitation imposed by a low density of states. We have performed direct harmonic count calculations[19] of the vibrational state density of both propynal and acetaldehyde. Propynal's vibrational state density is twice as high as that of acetaldehyde at every energy. Despite this, simple rotationally resolved SEP spectra can be obtained and molecular rotational constants derived. The simplicity of the propynal spectrum, is truly remarkable.

We hypothesize that this complexity in the emission spectrum is due to a structurally mediated enhancement of coupling between the available modes. The effect of this is to distribute the intensity derived from the favorable Franck-Condon factor normally associated with the isolated CO stretching vibration over many other vibrational states. We suggest that the "mediator" in this case is the methyl rotor.

REFERENCES:

1. E. R. Th. Kerstel, K. K. Lehmann, T. F. Mentel, B. H. Pate, G. Scoles, J. Phys. Chem. **95**(22) 8282 (1991)

2. Robert J. Longfellow, Charles S. Parmenter, J. Chem. Soc. Faraday. Trans. 2, **84**, 1499 (1988)

3. C. E. Hamilton, J. L. Kinsey, R. W. Field, Ann. Rev. Phys. Chem., **37**, 493 (1986)

4. G. W. King, D. Moule, Spectrochimica Acta, **17**, 286 (1961)

5. H. Hollenstein, Mol. Phys., **39**, 1013 (1980)

6. H. Hollenstein, F. Winther, J. Mol. Spectrosc., **71**, 118 (1978)

7. J. C. D. Brand, J. H. Calloman, J. K. G. Watson, Disc. Faraday Soc., **35**, 110 (1963)

8. J. C. D. Brand, W. H. Chan, D. S. Liu, J. H. Callomon, J. K. G. Watson, J. Mol. Spectrosc., **50**, 304 (1974)

9. C. C. Costain, J. R. Morton, J. Chem. Phys., **31**, 389 (1959)

10. J.M. Price, W. Pfieffer, G. Rumbles and G.H. Atkinson, Unpublished results.

11. M. Noble, E. K. C. Lee, J. Chem. Phys., **81**, 1632 (1984)

12. M. Baba, I. Hanazaki, U. Nagashima, J. Chem. Phys., 3938, **82**, (1985)

13. M. Baba, U. Nagashima, I. Hanazaki, J. Chem. Phys., **83**, 3514 (1985)

14. J. M. Price, J. Mack, X. Yang, G. v. Helden, A. M. Wodtke (to be published)

15. M. D. Harmony, V. W. Laurie, R. L. Kuczkowski, R. H. Schwendemann, D. A. Ramsey, F. J. Lovas, W. J. Lafferty, A. G. Maki, J. Phys. Chem. Ref. Data, **8**, 619 (1979)

16. R. W. Kilb, C. C. Lin, E. B. Wilson, J. Chem. Phys., **26**, 1695 (1957)

17. J. S. Crighton, S. Bell, J. Mol. Spectrosc. **112**, 315 (1985)

18. X. Yang, A. M. Wodtke, J. Chem. Phys., **92**, 116 (1990)

19. P. J. Robinson, K. A. Holbrook, "Unimolecular Reactions", Wiley-Interscience, London (1972) pp. 119-125

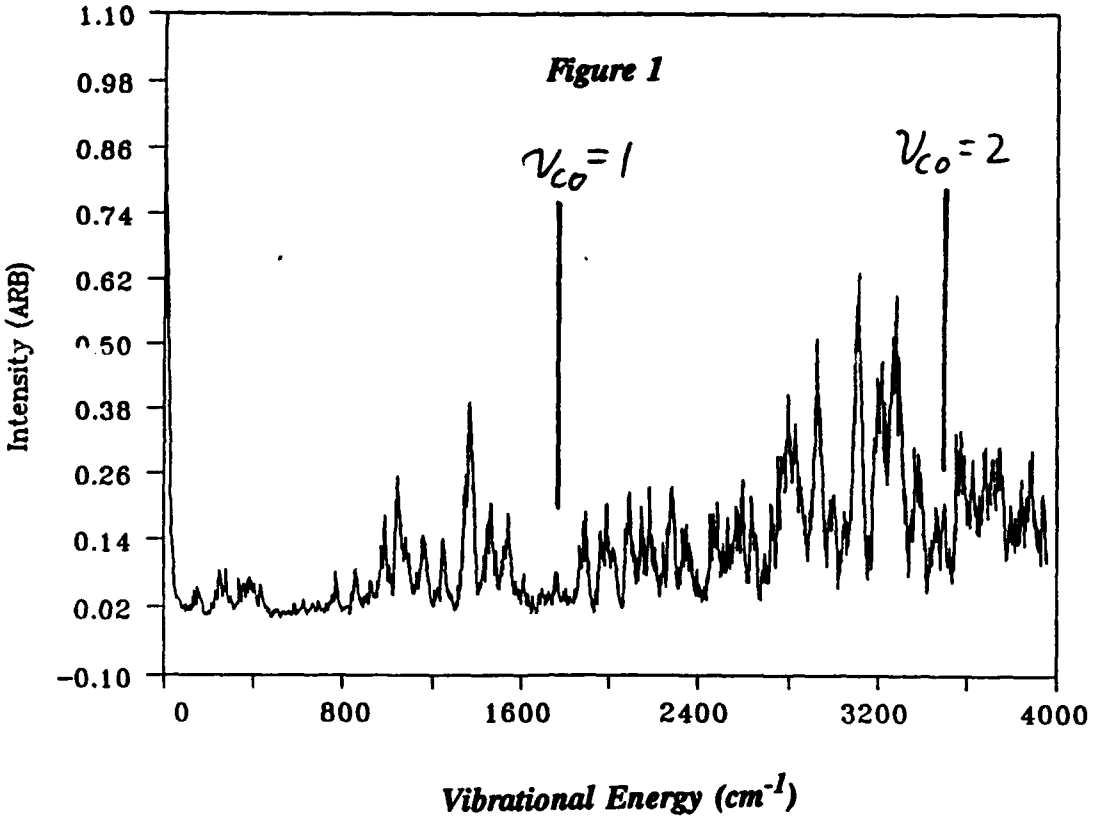
Figure 1
$\nu_{CO}=1$
$\nu_{CO}=2$
1.10
0.98
0.86
0.74
0.62
0.50
0.38
0.26
0.14
0.02
-0.10
Intensity (ARB)
0
800
1600
2400
3200
4000
Vibrational Energy (cm^{-1})

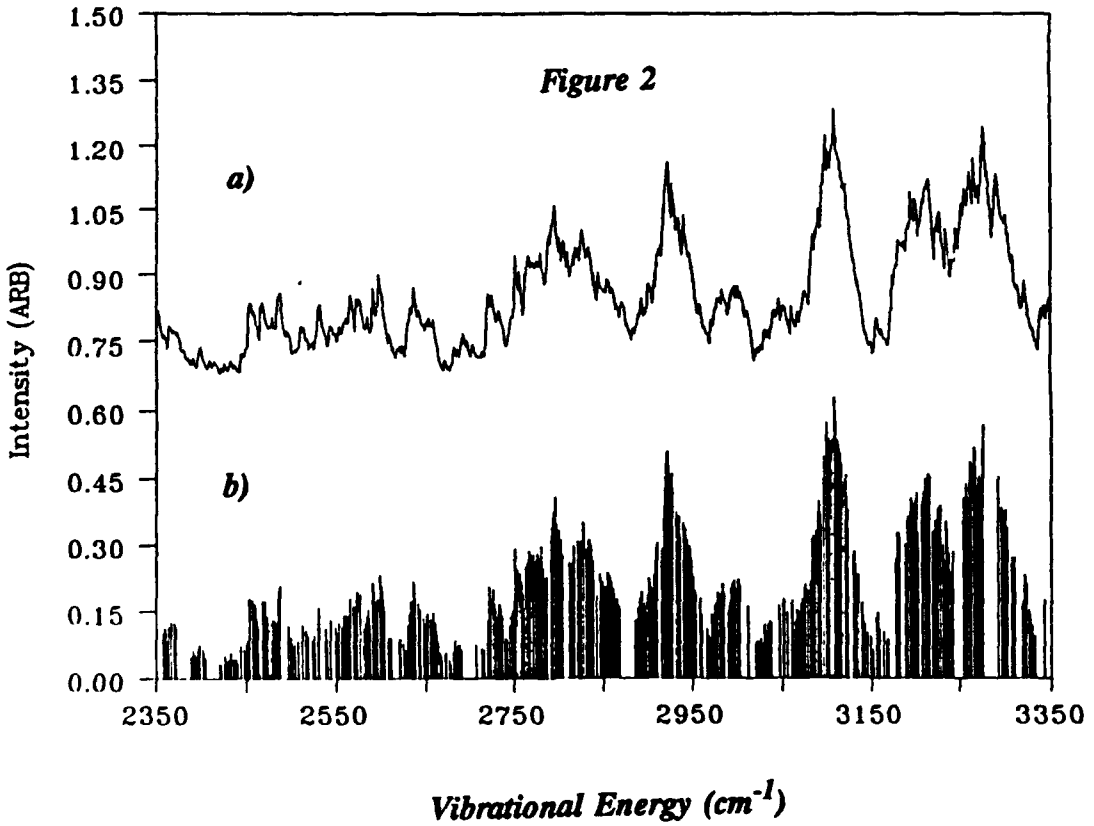
Figure 2
a)
b)
1.50
1.35
1.20
1.05
0.90
0.75
0.60
0.45
0.30
0.15
0.00
Intensity (ARB)
2350
2550
2750
2950
3150
3350
Vibrational Energy (cm^{-1})

Session VIII:

Photodissociation & Dynamics

Chemical Reaction Dynamics
Beyond the Born-Oppenheimer Approximation

Laurie J. Butler
The James Franck Institute and Department of Chemistry
The University of Chicago, Chicago, Illinois 60637

Much of our predictive ability for the branching between chemical reaction pathways has relied on statistical transition state theories or, in smaller systems, quantum scattering calculations on a single adiabatic potential energy surface. Yet, the chemical reaction dynamics evolves on a single potential energy surface only if the Born-Oppenheimer separation of nuclear and electronic motion is valid. Thus, the adiabatic approximation, though challenged at the inception of transition state theory,[1] is often now implicitly assumed to be valid for bimolecular and unimolecular reactions in the ground electronic state. Its shortcomings are only widely recognized for ion-molecule, charge transfer, and other reactions involving obvious electronic curve crossings. The experiments described here demonstrate the importance of nonadiabaticity at the transition state of any chemical reaction with a saddle point along the reaction coordinate and elucidate the role nonadiabatic transitions play in determining the branching between energetically allowed product channels.

The first series of experiments use molecular photodissociation to investigate nonadiabaticity in the transition state region of bimolecular reactions. In exact quantum reactive scattering calculations on benchmark systems like F + H_2 and I + HI, the nuclear dynamics is propagated on the adiabatic potential energy surface for the reaction, which includes a saddle point along the reaction coordinate. In the saddle point region the electronic wavefunction changes rapidly with nuclear coordinate, so the Born-Oppenheimer approximation may fail, resulting in nonadiabatic coupling to the upper adiabat[2] in the transition state region.

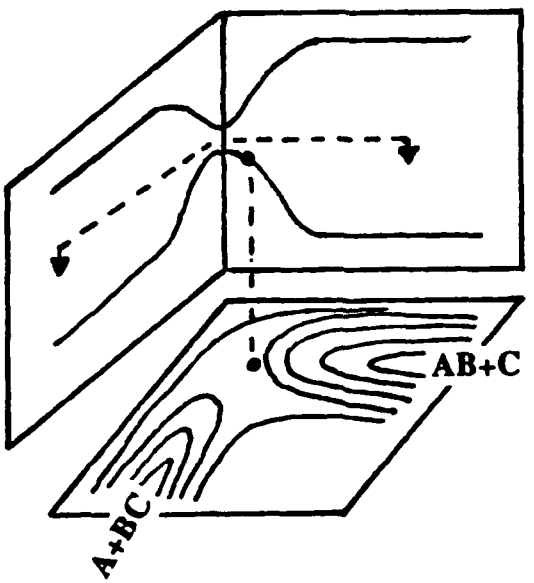

Our recent experiments[3] use molecular photodissociation to directly access both the upper and lower adiabats, respectively, near the transition state region of a bimolecular reaction to probe the influence of nonadiabatic coupling in chemical reaction dynamics. Photoexcitation in the lower energy absorption band of CH_3-S-H (A-B-C) promotes the

molecule from a bound ground state to an excited electronic state with a contour analogous to that shown in Figure 1 (bottom), accessing the Franck-Condon near the transition state for the A + BC → AB + C bimolecular reaction. Photoexcitation in the higher energy absorption band promotes the molecule to the upper bound adiabat, from which it dissociates via nonadiabatic coupling to the transition state region of the lower adiabat. Photofragment velocity and angular distribution measurements on CH_3-S-H show the nonadiabatic decay to the transition state region of the lower surface occurs in less than a picosecond and determines the branching between decay of the transition state complex to CH_3S + H or to CH_3 + SH. Complementary resonance Raman measurements probe the forces on the upper adiabat which result in accessing a region of the transition state that favors one exit channel over the other.

The second series of experiments[4,5] began with a naive question, can local electronic excitation of a molecule at, for instance, a carbonyl functional group induce selective fission of a strong alpha bond over a weaker bond beta to the functional group. The results go much deeper, demonstrating one of the simplest but most chemically important consequences of the failure of the Born-Oppenheimer approximation, the marked change in the expected branching between energetically allowed chemical bond fission channels due to nonadiabatic recrossing of a reaction barrier. The first experiment[4,5] measures the fragment velocity and angular distributions from the photodissociation of acetyl chloride and bromoacetyl chloride at 248 nm via the $^1n\pi^*$(C=O) transition, identifying the branching between bond fission channels and the fragmentation mechanism. The anisotropic angular distributions measured shows dissociation occurs on a time scale of less than a rotational period, resulting in primary C-X (X = Cl, Br) bond fission but no significant C-C bond fission. The data on bromacetyl chloride showed that excitation at the carbonyl group resulted in a competition between fission of the strong C-Cl bond alpha to the carbonyl and the weaker C-Br bond beta to the carbonyl, in a ratio of 1.0: 0.4. For comparison, the predicted branching is 1:30 for a statistical dissociation on the ground state potential energy surface, so the local electronic excitation induced preferential fission of the C-Cl over the C-Br bond, changing the branching by over a factor of 30. The highly anisotropic photofragment angular distributions (β=1.0 for C-Cl fission) are consistent with axial recoil upon $^1n\pi^*$(C=O) excitation in the Franck-Condon region, and shows that molecular dissociation occurs in too fast a time scale for internal conversion to the ground state or intersystem crossing to a triplet state. Consideration of the dissociation on the singlet excited potential energy surface shows that while selective fission of the C-Cl bond over the alpha C-C bond is easily predicted on the basis of the adiabatic potential energy surface, the preferential

fission of the C-Cl bond over the C-Br bond would not be predicted based on the relative barrier heights to each bond fission channel on the adiabatic potential energy surface. Because the barrier along the reaction coordinate for C-Br fission results from an avoided crossing between the (n,π^*(C=O)) and (n(Br),σ^*(C-Br)) electronic configurations, the electronic wavefunction changes rapidly near the barrier and the Born-Oppenheimer approximation can fail. We propose that the observed preferential fission of the C-Cl bond over the C-Br bond results from a decrease in the statistical rate of C-Br fission due to nonadiabatic crossing of the barrier to C-Br fission.

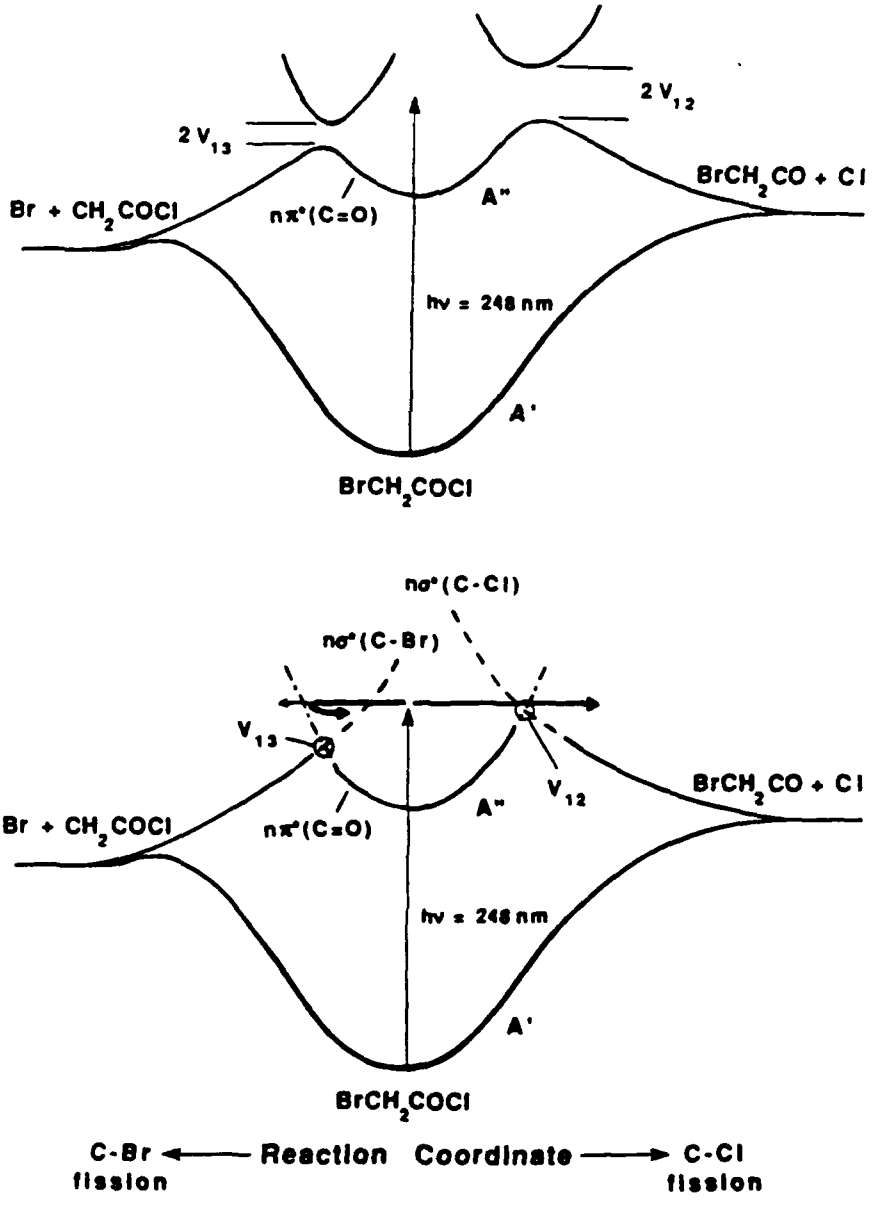

Our later experiments[5,6] test this conclusion by examining the branching between C-Cl and C-Br fission in bromopropionyl chloride, where the C-Br bond is separated from the carbonyl group by an additional CH_2 group. The separation should decrease the probability of crossing the barrier to C-Br fission adiabatically by reducing the coupling due to electron correlation between the $n\pi^*(C=O)$ and $n(Br)\sigma^*(C-Br)$ electronic configurations. The experiment confirmed this prediction, showing that the only C-Br fission observed was due to absorption in the tail of an overlapping transition to a surface repulsive in the C-Br bond. This experimental result is also consistent with our prediction based on previous intramolecular electron transfer experiments by Closs and coworkers,[7] which empirically determine the exponential decay in the coupling per number of intervening bonds. Thus the failure of the adiabatic approximation can be as important as the more thoroughly understood process of intramolecular vibrational energy redistribution in determining the branching between chemical reaction channels. These experiments demonstrate the need to go beyond the Born-Oppenheimer approximation to gain predictive ability for any chemical reaction with a saddle point along the reactive potential energy surface.

This work was supported by the National Science Foundation, The Office of Naval Research, and the Camille and Henry Dreyfus Teacher-Scholar Program.

1. The adiabatic assumption was briefly discussed in one of the first papers introducing transition state theory, M. G. Evans and M. Polanyi, Trans. Faraday Soc. **31**, 875 (1935)., and challenged by E. Rabinowitch in the discussion of the paper by M. G. Evans and M. Polanyi, Trans. Faraday Soc. **34**, 11 (1938). The following paper by E. Wigner, Trans. Faraday Soc. **34**, 829 (1938) also discusses the adiabatic assumption.

2. For a review, see J. C. Tully in *Dynamics of Molecular Collisions Pt. B*, W. H. Miller, ed. (Plenum, New York, 1976) p. 217.

3. J.S. Keller, P.W. Kash, E. Jensen, and L.J. Butler, J. Chem. Phys. **96**, 4327 (1992).

4. M.D. Person, P.W. Kash, S.A. Schofield, and L.J. Butler, J. Chem. Phys. **95**, 3843 (1991).

5. M.D. Person, P.W. Kash, and L.J. Butler, submitted to J. Chem. Phys. (1992).

6. P.W. Kash, G. C. G. Waschewsky, and L.J. Butler, in preparation (1992).

7. G. L. Closs and J. R. Miller, Science **240**, 440 (1988).

Differential Cross Sections for State-Selected Products by Direct Imaging: Ar + NO

A. G. Suits, L. S. Bontuyan, and P. L. Houston
Department of Chemistry
Cornell University
Ithaca, New York 14853-1301
U. S. A.

and

B. J. Whitaker
School of Chemistry
Leeds University
Leeds, LS2 9JT
United Kingdom

State-resolved differential cross sections provide detailed information about the mechanism and potential energy surface governing a chemical reaction, but they have heretofore been difficult to measure. This talk will describe a new technique for obtaining differential cross sections with both product state resolution and simultaneous detection of all scattering angles. The three-dimensional velocity distribution of state-selected reaction products is determined by ionizing the appropriate product and accelerating the ions onto a detector using a pulsed electric field. The resulting image is a two-dimensional projection of the three-dimensional velocity distribution. Visual inspection provides immediate qualitative information about the reaction, while mathematical analysis can provide detailed differential cross sections. We have used the technique to investigate the inelastic collision process Ar + NO($^2\Pi_{1/2}$,v=0,J=0.5) → Ar + NO($^2\Pi_{1/2}$,v=0,J') at a collision energy of 0.21 eV. Rotational rainbows in the product angular distribution are directly observed to change in position as a function of the final rotational state; the peak of the angular distribution moves toward the backward hemisphere and the angular distribution broadens with an increase in final rotational quantum number.

The collision dynamics of Ar + NO have been investigated previously at the total cross section level.[1-3] Using laser-induced fluorescence and two crossed beams, Joswig *et al.* found interference effects in the scattering of NO(v=0,J=0.5) by He, Ar, and Ne; the total cross section for scattering to NO product states displayed oscillations as a function of the final rotational quantum number. The oscillations also appeared in coupled-states calculations using the electron gas potential of Nielson *et al.*[4] The interference is due to scattering from the two different ends of the nearly homonuclear diatomic molecule.[5] Two potential surfaces are important, one in which the orbital of the unpaired electron is in the plane containing the three atoms (A'), and one in which it is

perpendicular to this plane (A''). As shown by Alexander,[6] multiplet changing collisions provide information about the difference between these two potentials, while multiplet conserving collisions provide information about the sum. Thus, state-resolved differential cross sections such as those made possible by the new method described here will be important in determining these two potential energy surfaces.

The new method for making these measurements is similar to that already used to determine the angular distribution of state-selected photofragments.[7-12] A variant of the method has also been used to investigate the $H + HI \rightarrow H_2 + I$ reaction,[13] although not in crossed molecular beams. In our configuration, a doubly differentially pumped primary beam is formed by expanding 7% NO in He from a total pressure of 1100 torr through a pulsed nozzle 85 cm from the interaction region. The expansion yields a rotational distribution in the beam given by $N_{J=0.5}=1$, $N_{J=1.5}=0.037$, $N_{J=2.5}=0.006$. The secondary Ar beam is formed by expansion of 1040 torr through a pulsed nozzle 15 cm from the interaction region. A pulsed laser beam at a wavelength near 226 nm was propagated counter to the Ar beam and used to ionize state-selected NO products on the axis of a Wiley-McLaren[14] time-of-flight mass spectrometer. The ions were accelerated in a direction perpendicular to the plane of the molecular beams by fields of ~800 volts/cm. After ~6 μs, the ions struck the first of two, 2"-diameter channelplate detectors, causing emission secondary electrons with a gain of $\sim 10^7$. Electrons from the channelplates were accelerated to a fast phosphor coated onto one end of a fiber-optic bundle mounted through a vacuum flange. A CID Camera (Xybion), gated according to the flight time for the mass of interest and equipped with a 480x512 pixel array, captured each image for averaging and analysis. A real-time video averager (Poynting RA-512) summed 256 images with 16 bit resolution. The most significant 8-bit slice of the resulting sum was normalized for laser power and stored in a computer. Alternate sets of images obtained with the Ar beam off were subtracted from those with both beams on. Roughly 300,000 laser shots were averaged for Figure 2 and Figure 3 shown below.

Figure 1 displays a superposition of two images obtained when a trace of NO is also seeded in the secondary Ar beam. In one of the two superimposed images the ionization laser propagates counter to the primary beam, while in the second it propagates counter to the secondary beam. The laser is tuned to ionize $NO(^2\Pi_{1/2}, v=0, J=0.5)$, the principal component of each beam, so the illuminated section of each of the molecular beams is visible in the figure. The intersection of the two beams is the collision region. The dark spots below and to the left of this intersection represent NO molecules that were ionized at the intersection of the beams and that traversed the intervening distance in the time between ionization and detection, ~6 μs. Measurement of distances and the delay time provides the velocity, dispersion, and size for each molecular beam. A "Newton" diagram for the collision can be easily constructed for elastic collisions; it is superimposed on Figure 1.

Figure 2 gives the image obtained when the probe laser (now propagating only counter to the pure Ar beam) is tuned to ionize NO($^2\Pi_{1/2}$,v=0,J=11.5). Despite some ionization of background room-temperature NO along the laser beam, the projection of the Newton sphere for the scattering is clearly visible. The scattering is actually symmetric about the relative velocity vector, but the detection sensitivity depends both on the velocity component perpendicular to the laser beam and on a center-of-mass to laboratory Jacobian. Qualitative analysis shows that the angular distribution is peaked at 30° with a FWHM of about 20°. This rotational rainbow in the scattering angular distribution is expected for atom-diatom collisions, even at the level of classical mechanics and hard ellipse scattering.[15]

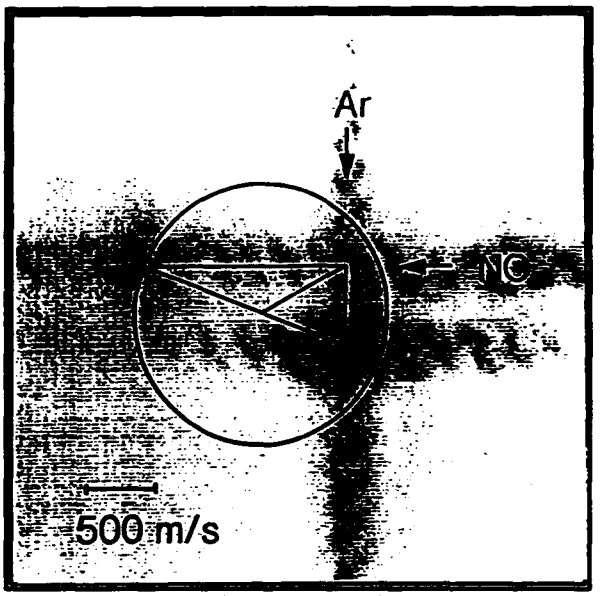

Figure 1 Image of beams obtained as described in the text, shown superimposed with a Newton diagram for elastic scattering.

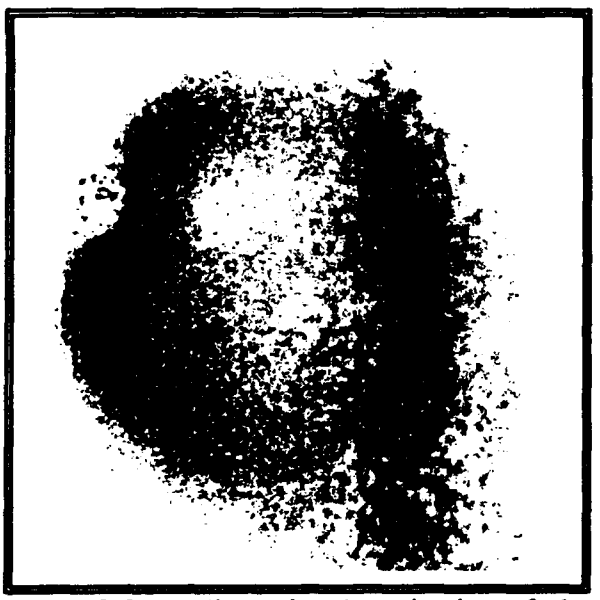

Figure 2 Two-dimensional projection of the scattering distribution for NO($^2\Pi_{1/2}$,v=0,J=11.5).

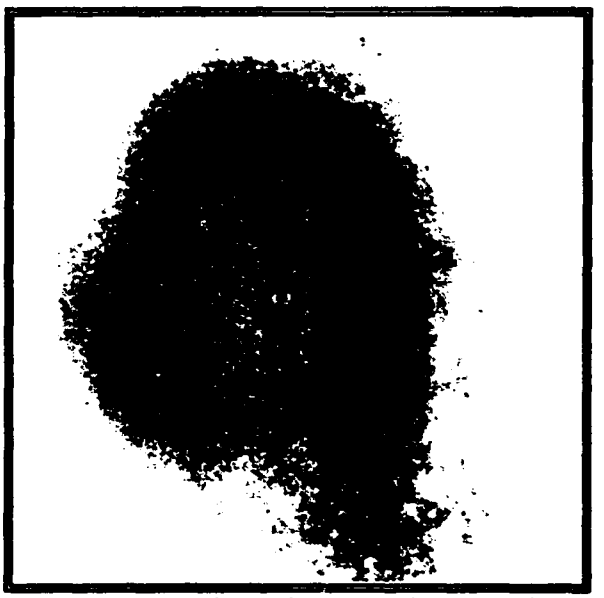

Figure 3 Two-dimensional projection of the scattering distribution for NO($^2\pi_{1/2}$,v=0,J=18.5).

Figure 3 displays the image obtained when NO($^2\Pi_{1/2}$,v=0,J=18.5) is ionized. The product scattering is more diffuse and is centered much further toward the backward hemisphere; qualitative analysis places the peak at 60° with a FWHM of 30°. In addition, the Newton sphere is measurably smaller, in accord with the lesser available energy for translation. Images were also recorded for J=9.5 (0±10°, FWHM=20°) and J=15.5 (40°, FWHM=30°).

The figures show that the imaging technique can provide direct qualitative information about the collision dynamics. Although a quantitative analysis of the images is not yet complete, it is clear to us that the detailed differential cross section can be obtained by a forward convolution technique which includes the density to flux transformation and the center-of-mass to laboratory Jacobian. The advantages of the technique are: *1)* that the state-resolution is limited only by the spectral resolution of the laser and the energy separation between molecular eigenstates, and *2)* that the entire angular distribution is recorded for each laser pulse. Potential disadvantages of the technique are that the molecule to be probed must be able to undergo state-selected multiphoton ionization. The data thus far provide encouragement that the state-selected differential cross sections needed to determine the two potential energy surfaces involved in the Ar+NO system can be obtained.

Acknowledgements

We are grateful to the U.S. Army Research Office for support under grant DAAL03-91-G-0125, to the Department of Energy for support under grant DE-FG02-88ER13934, to the Science and Engineering Research Council for the award of an Advanced Research Fellowship to BJW, and to NATO for the award of a Collaborative travel grant to BJW and PLH. We would also like to thank Dr. V. Hradil, Professor S. A. Hewitt, and Dr. T. Suzuki for early help in the design of the apparatus, and Dr. F. Suits for valuable suggestions concerning image acquisition and processing.

References

[1] A. S. Sudbo and M. M. T. Loy, Chem. Phys. Lett. **82**, 135 (1981).
[2] P. Andresen, H. Joswig, H. Pauly, and R. Schinke, J. Chem. Phys. **77**, 2204 (1982).
[3] H. Joswig, P. Andresen, and R. Schinke, J. Chem. Phys. **85**, 1904 (1986).
[4] G. C. Nielson, S. A. Parker, and R. T Pack, J. Chem. Phys. **66**, 1396 (1977).
[5] C. W. McCurdy and W. H. Miller, J. Chem. Phys. **67**, 463 (1977).
[6] M. H. Alexander, J. Chem. Phys. **76**, 5974 (1982).
[7] D. W. Chandler and P. L. Houston, J. Chem. Phys. **87** 1445 (1987).
[8] D. W. Chandler, J. W. Thoman, Jr., M. H. M. Janssen, and D. H. Parker, Chem. Phys. Lett. **156** 151 (1989).
[9] D. W. Chandler, M. H. M. Janssen, S. Stolte, R. N. Strickland, J. W. Thoman, Jr., and D. H. Parker, J. Phys. Chem. **94** 4839 (1990).
[10] J. W. Thoman, D. W. Chandler, D. H. Parker, M. H. M. Janssen, Laser Chem. **9** 27 (1988).
[11] D. P. Baldwin, M. A. Buntine, and D. W. Chandler, J. Chem. Phys. **93** 6578 (1990).
[12] T. Suzuki, V. P. Hradil, S. A. Hewitt, P. L. Houston, and B. J. Whitaker, Chem. Phys. Lett. **187**, 257 (1991).
[13] M. A. Buntine, D. P. Baldwin, and D. W. Chandler, J. Chem. Phys. **94** 4672 (1991).
[14] W. C. Wiley and I. H. McLaren, Rev. Sci. Instrum. **26** (1955) 1150.
[15] R. Schinke and J. M. Bowman, "Rotational Rainbows in Atom-Diatom Scattering," in *Molecular Collision Dynamics*, Chapter 4, J. M. Bowman, ed., (Springer-Verlag, Berlin, 1983), p. 61.

Observation of Transition State Vibrational Thresholds in the Rate of Dissociation of Ketene

Edward R. Lovejoy, Sang Kyu Kim, and C. Bradley Moore

Chemical Sciences Division of the Lawrence Berkeley Laboratory
and Department of Chemistry, University of California
Berkeley, California 94720

Rate constants for the dissociation of highly vibrationally excited ketene (CH_2CO), Fig. 1, have been measured at the threshold for the production of $CH_2(^3B_1)$ and $CO(^1\Sigma^+)$. The rate constant increases in a step-wise manner with increasing energy, consistent with the long standing premise that the rate of a unimolecular reaction is controlled by flux through quantized transition state thresholds, Fig. 2. The data give the energies of the torsional and C—C—O bending vibrations of the transition state.

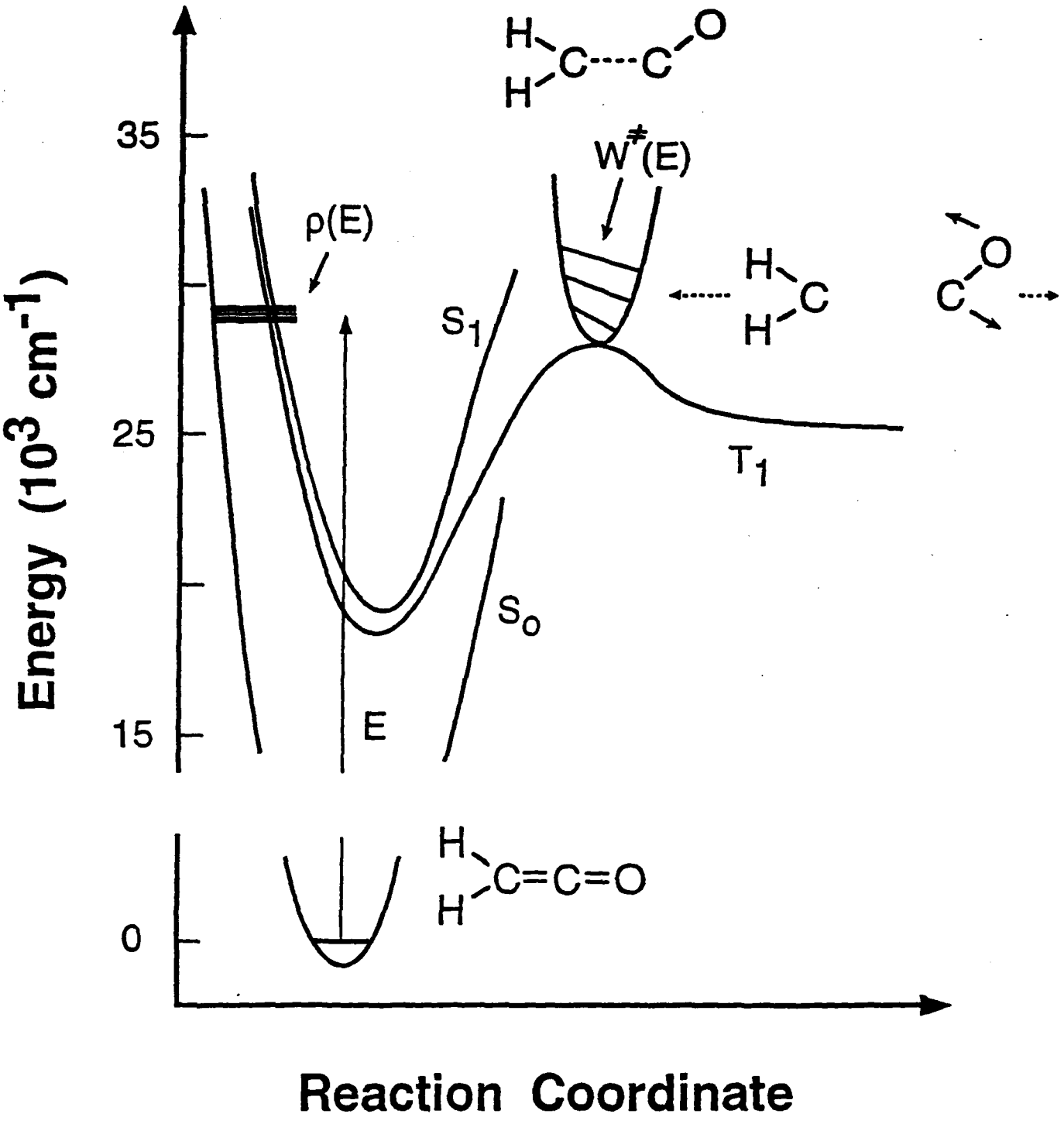

Figure 1. A schematic representation of the dissociation of triplet ketene. The reaction coordinate corresponds to the distance between the carbon atoms. The solid lines represent the potential energy for the ground singlet (S_o), the first excited singlet (S_1), and the first triplet (T_1) electronic states. The transition state, which separates the highly vibrationally excited reactant from the products, is depicted as a single potential well perpendicular to the reaction coordinate. This well is meant to represent the 8 bound vibrations of the transition state.

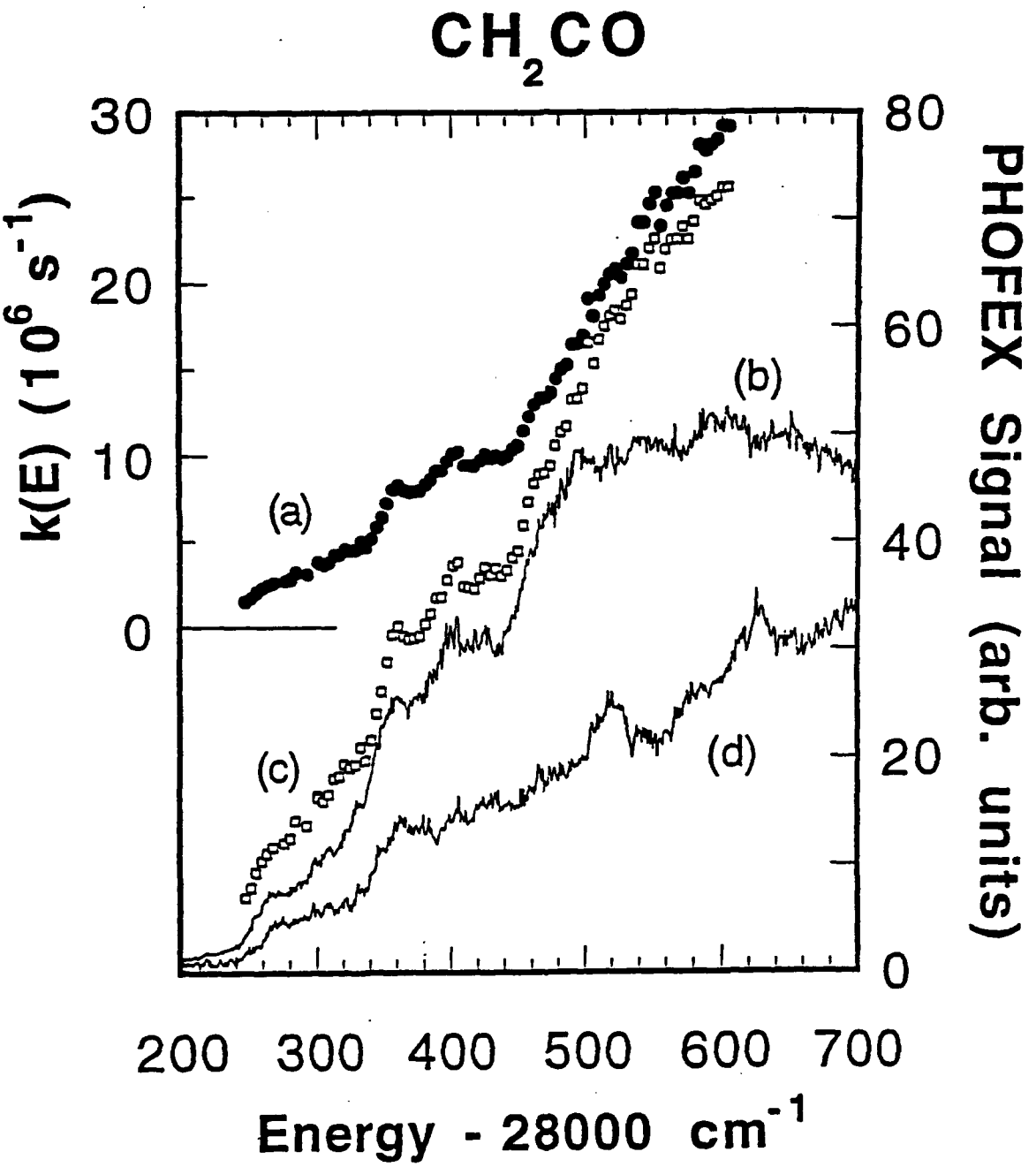

Figure 2. CH_2CO dissociation rate constant and PHOFEX data. (a) Experimental rate constants for the unimolecular decay of ketene. (b) CO($v=0,J_p=12$) PHOFEX signal. (c) PHOFEX spectrum calculated from the experimental rate constant data. (d) CO($v=0,J_p=2$) PHOFEX signal. The actual ratio of the yields of CO($v=0,J_p=12$) to CO($v=0,J_p=2$) is about 20:1 at 28,500 cm^{-1} for CH_2CO (7).

Real-Time Observation of a Step-Like k_{uni} vs. E Dependence for the Near Threshold Decomposition of NO_2

S.I. Ionov, G.A. Brucker, Y. Chen, C. Jaques and C. Wittig

Department of Chemistry
University of Southern California
Los Angeles, CA 90089-0482

The photoinitiated unimolecular reaction of NO_2 is presently the only documented case in which a stable triatomic species can be excited optically via an allowed one-photon transition to levels that lie above the reaction threshold and that have ground electronic state character. Despite a considerable interest in the near threshold photochemistry of this scientifically and technologically important molecule,[1-5] there has been no report to date of direct measurements of decomposition lifetimes. Thus, we have carried out time-resolved, subpicosecond-resolution measurements of photoinitiated NO_2 reaction rates using expansion-cooled samples.

The experimental measurements are performed on a set up consisting of (i) a dual-jet mode-locked dye laser (Coherent 702-1), synchronously pumped by the frequency doubled output of (ii) an actively mode-locked Nd:YAG laser (Spectron SL 903), (iii) two dye amplifiers pumped by (iv) a regenerative Nd:YAG amplifier (Continuum RGA 69-10), and (v) a vacuum chamber which is equipped with a pulsed nozzle for preparing a rotationally cold NO_2 sample, a quadrupole mass spectrometer for monitoring the supersonic jet, and accessories for detecting LIF. The laser system produces two tunable subpicosecond laser pulses which are used for initiating and subsequent probing of NO_2 decomposition. The pump pulse, tunable from 375 to 402 nm, is obtained by mixing in a BBO crystal the amplified 575-645 nm radiation from the mode-locked dye laser with the 1064 nm output form the RGA. This radiation excites NO_2 molecules in the supersonic jet to the $^2B_2$ electronic state, which is strongly coupled to the ground electronic state, $^2A_1$. Subsequent unimolecular decomposition of NO_2 via the ground electronic state surface is probed by the second pulse which excites LIF in the NO product. This 226 nm probe pulse is obtained by frequency doubling of an amplified 452 mn pulse which is filtered from a white continuum radiation generated in D_2O.

The NO LIF signal is preamplified, digitized and collected in an IBM AT computer simultaneously with both pump and probe pulse energies and a pump-probe cross-correlation signal. The cross-correlation is obtained by difference frequency generation in a 100 μm BBO crystal which is positioned shortly after the chamber. The pump, probe and difference frequency radiations are separated in a 60° quartz prism and detected by two UV-grade photodiodes and a PMT, respectively.

By changing the wavelength of the pump pulse, the NO_2 molecules are prepared on different levels above their reaction threshold and subsequent decomposition is measured on a real time scale by varying the delay between the pump and probe pulses. The experimental time dependences are fit assuming single exponential NO production after the

* Research supported by the U.S. Army Research Office.

(a) Present address: Department of Chemistry, University of California, Berkeley, CA 94720.

excitation event. The NO_2 dissociation rates obtained from the experimental delay time dependences are presented in the figure. Every point in the figure is an average of 8 to 16 rates, each obtained from independent scans at specific excitation wavelengths. Statistical uncertainties, i.e., standard deviations, are small, generally lying within the circles shown in the figure. It should be noted that independent measurements have been carried out for several excitation wavelengths near the reaction threshold with either one and two birefringent filters (BRF) in the mode-locked dye oscillator. With the single-plate BRF, a better time resolution (600 to 900 fs cross-correlation FWHM) but a lower spectral resolution of ca. 40-80 cm^{-1} is achieved, as compared to the double-plate BRF, which provides ca. 1.5 ps cross-correlations and 20-30 cm^{-1} spectral resolution. The experimental points obtained with the single and double plate BRFs are presented by open and closed symbols, respectively.

One aspect of the results presented in the figure is especially noteworthy. Namely, the measured variation of $k_{uni}(E)$ versus E is not a smooth ascending function of E, as is usually the case for unimolecular decompositions. For example, the reaction rate rises abruptly to ca. 1.6×10^{11} s^{-1} at reaction threshold, and then shows a moderate rise in the region $E - D_0 = 0 - 100$ cm^{-1}. The rate exhibits another steep rise to ca. 4×10^{11} s^{-1} near 100 cm^{-1} in excess of the reaction threshold, and then does not change from 120 to 210 cm^{-1}. At $E - D_0 = 220$ cm^{-1}, the rate climbs to ca. 5.5×10^{11} s^{-1} and then flattens again between 240 and 350 cm^{-1}. This step-like behavior cannot be dismissed as a S/N problem, i.e., each data point shown in the figure is the result of considerable signal averaging. Also, the reaction rate on the first step is roughly 1/2 and 1/3 of those on the second and third steps, respectively.

The simplest form of microcanonical RRKM theory uses Eq. (1) to compute $k_{uni}(E)$

$$k_{uni}(E) = \frac{N^{\ddagger}(E-E_0)}{h\,\rho(E)}, \qquad (1)$$

where $N^{\ddagger}(E-D_0)$ is the number of accessible states in the activated complex at energy E, E_0 is the reaction threshold, which in the present case is D_0 since rotation is minimal and there is no reverse barrier, and $\rho(E)$ is the density of states for the parent molecule. As is evident from its definition, $N^{\ddagger}(E-E_0)$ is a step function which is equal to zero if $E < E_0$, and which takes on the value 1 just above threshold when only one internal level of the activated complex is accessible. With increasing energy, $N^{\ddagger}$ changes from 1 to 2 when two channels become available, and so on. $\rho(E)$ changes much more slowly than $N^{\ddagger}(E-E_0)$. Equation (1) embodies a pretty elementary view, but has been shown to predict rates with uncanny success.

It is tempting to consider the possibility that the measured $k_{uni}(E)$ values shown in the figure can be rationalized in terms of Eq. (1). Although NO_2 reacts via its ground electronic state surface, it does not fit comfortably into the niche of standard unimolecular decomposition models. It has a complex electronic structure that derives from the conical intersection between the ground, $^2A_1$, and $^2B_2$ electronic state; it is a triatomic with a small density of vibronic states in the threshold region; reaction rates are quite rapid and may compete with intramolecular vibrational redistribution (IVR), and so forth. The above complexities notwithstanding, it is still worth comparing $k_{uni}(E)$ from Eq. (1) to the data.

The density of states $\rho(E) \approx 0.2$ cm near the decomposition threshold is estimated from the experimental spectra obtained by Miyawaki et. al.[5] These reported spectra lack rotational congestion since they have been obtained for NO_2 residing on the lowest rotational state 0_{00}. For estimating $N^{\ddagger}(E\text{-}D_0)$ we note that at the energies accessed in the present experiments, the transition state has only one vibrational frequency since the NO-stretch is at too high an energy, i.e., the vibrational frequency of free NO is 1876 cm^{-1}. The NO_2 fundamental bending frequency is 740 cm^{-1}, which will be lowered considerably at the transition state. Thus, evaluating $N^{\ddagger}(E\text{-}D_0)$ is simply a matter of choosing frequencies for the NO_2 bend at the transition state and counting the number of open channels, excluding one-dimensional reaction coordinate motion. For the threshold region of the unimolecular decomposition, where $N^{\ddagger} = 1$, we get $k = 1.5 \times 10^{11}$ s^{-1} which is very close to the experimental rate, $k = (1.6\text{-}2.4) \times 10^{11}$ s^{-1}, in the region $0 < E - D_0 < 90$ cm^{-1}.

From the above, it is clear that the unimolecular decay rate in the region $0 < E - D_0 < 90$ cm^{-1} can be attributed to dissociation via a vibrationless transition state having $N^{\ddagger} = 1$. The rise near $E - D_0 \sim 100$ cm^{-1} is associated with the opening of v=1 of the transition state bending mode, and likewise the step near $E - D_0 \sim 200$ cm^{-1} is associated with v=2 of the bend. These assignments are consistent with the relative rates on the first, second and third steps, i.e., k_{uni}(2nd step) ~ $2k_{uni}$(1st step), and k_{uni}(3rd step) ~ $3k_{uni}$(1st step). Finally, we note that the steps in $k_{uni}(E)$ vs. E are prominent only up to $E - D_0 \sim 350$ cm^{-1}. Two explanations may be offered. As seen from the figure, the steps disappear in the region where the reaction rates are fast compared to the experimental temporal resolution. It is possible that the deteriorating experimental accuracy hides fine details of the $k_{uni}(E)$ dependence in this region. Alternatively, it is plausible that the step pattern changes as a result of a transition from bending to internal rotation. We leave such questions for further investigations.

References

1. H. Zacharias, M. Geilhaupt, K. Meier and K.H. Welge, J. Chem. Phys. 74 (1981) 218.
2. H. Zacharias, K. Meier and K.H. Welge, in: Energy Storage and Redistribution in Molecules, ed. by J. Hinze (Plenum Press, New York, 1983), p. 107.
3. U. Robra, H. Zacharias and K.H. Welge, Z. Phys. D - Atoms, Molecules and Clusters 16 (1990) 175.
4. J. Miyawaki, T. Tsuchizawa, K. Yamanouci and S. Tsuchiya, Chem. Phys. Letters, 165 (1990) 168.
5. J. Miyawaki, K. Yamanouci and S. Tsuchiya, Chem. Phys. Letters, 180 (1991) 287.

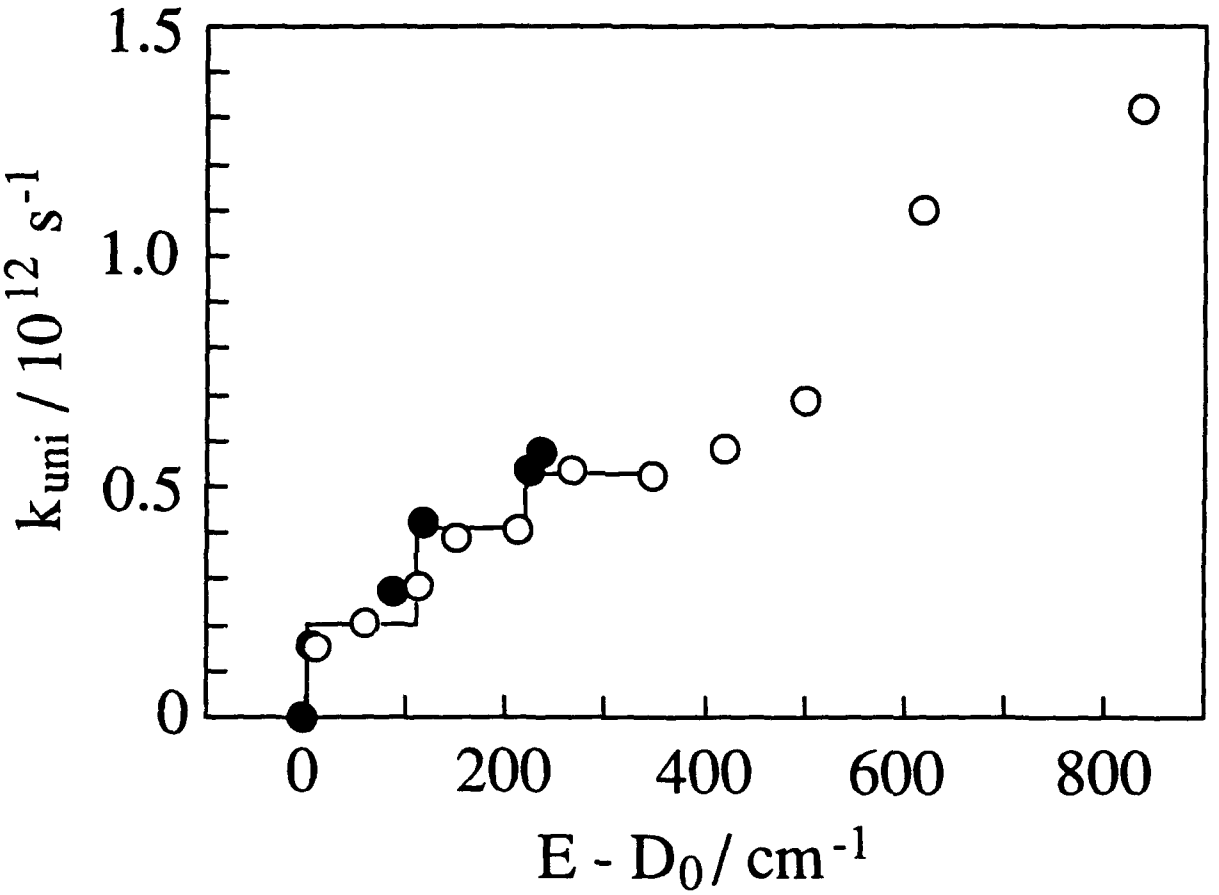
1.5
1.0
0.5
0
k_{uni} / 10^{12} s^{-1}
0
200
400
600
800
E - D_0 / cm^{-1}

Mode Specific Photodissociation Dynamics of OClO

H. Floyd Davis and Yuan T. Lee
Lawrence Berkeley Laboratory and
Department of Chemistry,
University of California, Berkeley
Berkeley, CA 94720

The photodissociation dynamics of bent triatomic molecules such as O_3 and NO_2 has been studied extensively over the past 20 years. These systems are particularly amenable to detailed study because the parent molecules possess only three vibrational degrees of freedom and their atom + diatom products are easily detected experimentally, and modelled theoretically. However, the apparent simplicity of these molecules is belied by a complex electronic structure and fast predissociation processes, leading to poorly understood features in their electronic absorption spectra.

The OClO ($A^2A_2 \leftarrow X\ ^2B_1$) absorption spectrum in the near UV, on the other hand, shows a well defined progression primarily resulting from excitation to the (ν_1,0,0),(ν_1,1,0),(ν_1,0,2), and (ν_1,1,2) levels[1,2]of the excited electronic state (Fig1).

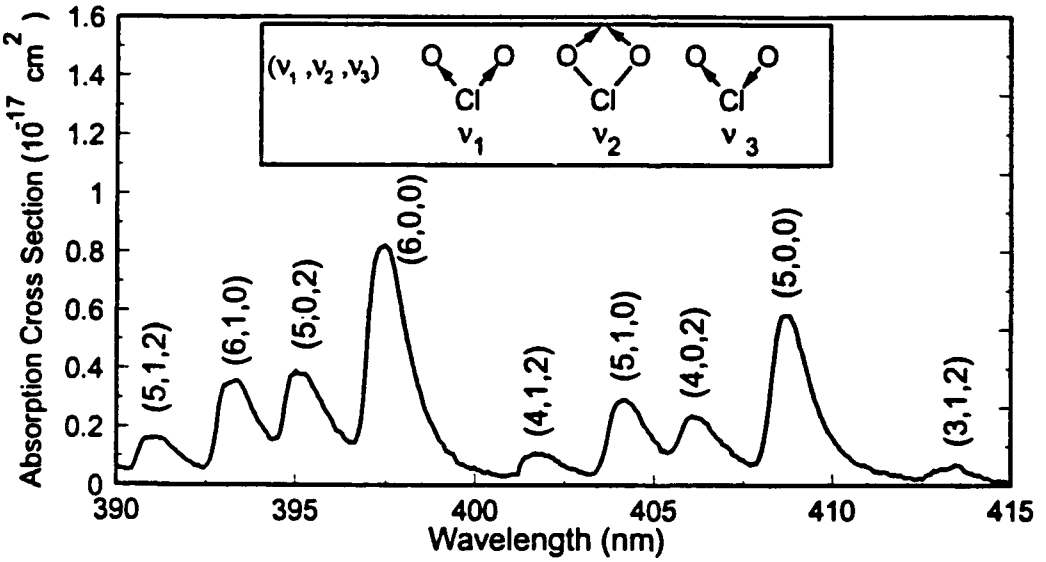

Figure 1: Absorption Spectrum of OClO[2]

This makes it possible to prepare the electronically excited molecule in various well defined initial vibrational levels-- all lie at energies above the thermodynamic threshold for dissociation:

$$OClO \rightarrow ClO(^2\Pi) + O(^3P) \quad \lambda_{thresh} = 496nm \qquad (1)$$

The narrow absorption linewidths observed throughout the spectrum indicate dissociation lifetimes in excess of several picoseconds even at excitation energies far above threshold.[1] Although it has generally been believed that channel 1 is dominant, a second possible channel has received considerable interest recently, since it could represent an additional mechanism for depletion of atmospheric ozone:[3,4]

$$OClO \rightarrow Cl(^2P) + O_2(^3\Sigma_g^-, ^1\Delta_g, ^1\Sigma) \qquad (2)$$

There has been no complete determination of the relative importance of channels 1 and 2.[3-5] We have studied the dynamics of these processes using photofragment translational energy spectroscopy with a tunable excitation laser and a mass spectrometer for product detection. We have clearly observed both fragment partners for both channels above and have obtained the branching ratios for channels 1 and 2 from different initial vibrational states of the electronically excited OClO molecule. We observe a considerable degree of state specificity in the photodissociation branching ratios. This is illustrated in the Cl^+ time of flight spectra shown in figure 2. The angle between the mass spectrometer and molecular beam was 20°. The large slower peak in each time-of-flight results from fragmentation of ClO from the ClO + O channel. The fast peak is Cl^+ from Cl + O_2. Excitation at wavelengths corresponding to symmetric bending or symmetric stretching modes of OClO (A^2A_2) leads to Cl + O_2 with a quantum yield of up to ~3%. However, excitation of an asymmetric mode having an absorption peak at wavelengths between those of the symmetric modes leads to a <0.4% yield of Cl + O_2. (Fig. 2) The Cl+ O_2 channel results from a concerted unimolecular process requiring simultaneous breaking of two Cl-O bonds and formation of O=O. This is strongly suppressed when electronic excitation is accompanied by asymmetric stretching. Both electronic states of O_2 are formed with comparable yields and a large fraction of the excess energy is channeled into relative translational motion.

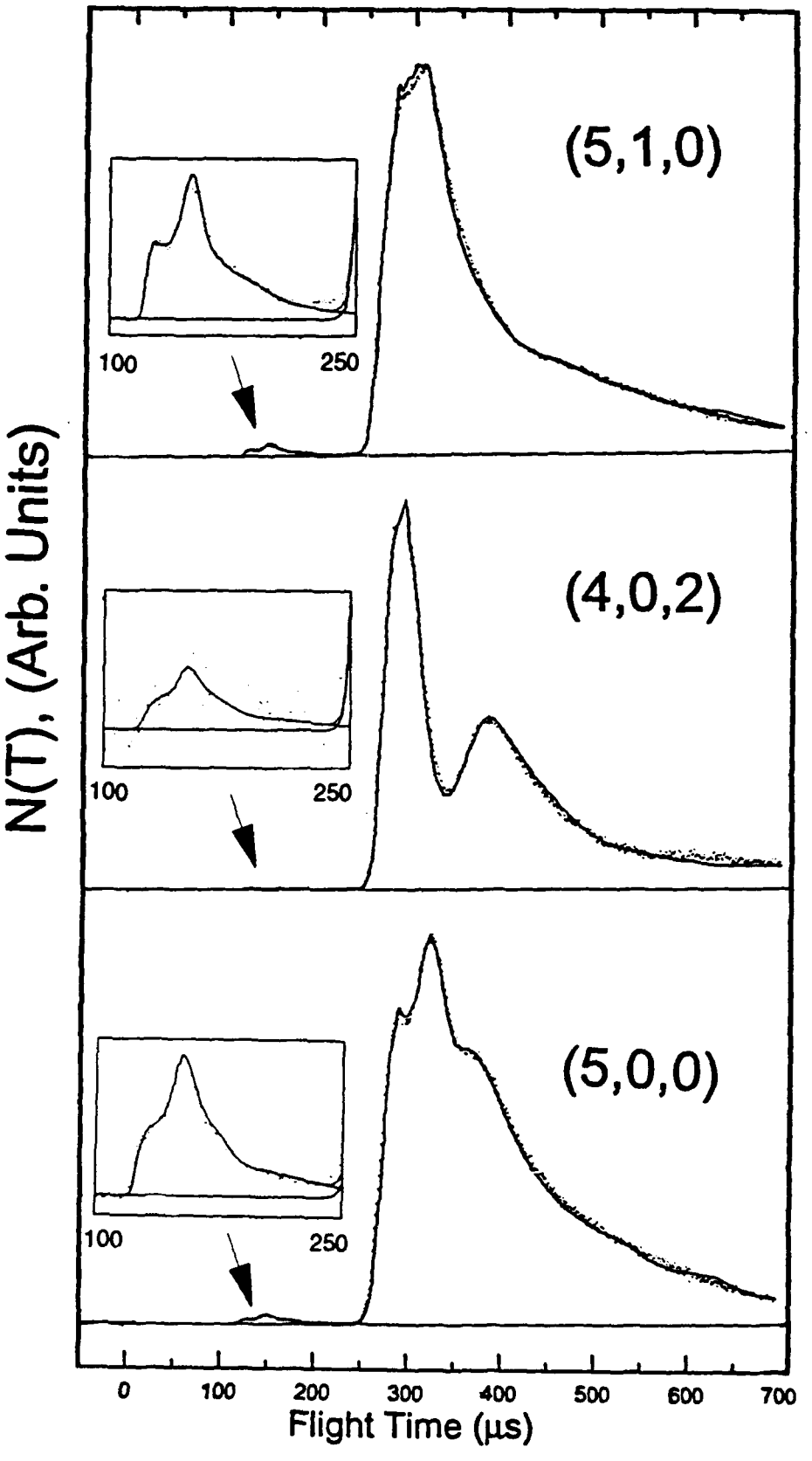

Figure 2: OClO Photofragment Time-of-Flight Spectra. Fast Peak is due to Cl from Cl + O_2 channel and slow peak results from fragmentation of ClO to Cl^+ in electron impact ionizer.

The ClO + O channel also exhibits highly localized dynamics- we are currently extracting the ClO vibrational state distributions as a function of initial OClO vibrational level. Because of the well defined nature of the initial excitation process and the low vibrational state density of the electronically excited state, mode specific behavior can be readily observed in this system. We hope that these detailed measurements will stimulate further theoretical work on the excited state potential energy surfaces of OClO.

References:

1. E.C. Richard and V. Vaida, J. Chem. Phys., 94(1), 153 (1991).
2. A. Wahner, G.S. Tyndall, A.R. Ravishankara, J. Phys. Chem., 91, 2734 (1987).
3. V. Vaida, S. Solomon, E.C. Richard, E. Ruhl, and A. Jefferson, Nature, 342, 405 (1989).
4. E. Bishenden, J. Haddock, and D.J. Donaldson, J. Phys. Chem., 95, 2113 (1991).
5. W.G. Lawrence, K.C. Clemitshaw, V.A. Apkarian, J. Geophys. Res., 95D, 18591, (1990).

Acknowledgement:

This work was supported by the Director, Office of Energy Research, Office of Basic Energy Sciences, Chemical Sciences Division of the U.S. Department of Energy under Contract No. DE-AC03-76F00098.

Photodissociation of Silane in a Supersonic Expansion

Th. Glenewinkel-Meyer[1], J.A. Bartz, and F.F. Crim
Dept. Chemistry, University of Wisconsin, Madison, WI 53706

We will report on the photodissociation of silane (SiH_4) in a pulsed supersonic molecular beam by means of mass spectrometric detection of the photofragments. Even though laser assisted decomposition of SiH_4 plays a major role in chemical vapor deposition of thin silicon films for semiconductors[1], information about the exact fragmentation processes is still scarce. The high lying SiH_4 states excited by the incident photons, which might lead to formation of silicon atoms for example through subsequent hydrogen ligand loss, are not very well characterized. Also very few experiments have actually been done utilizing the collision-free region of a supersonic molecular jet, where a single molecule may decay undisturbed by any collision partners.

In our experiments, we cross the molecular beam perpendicularly by two counterpropagating pulsed laser beams. The first laser pulse utilizes the doubled output from a Nd:YAG pumped dye laser in the 500 to 600 nm range. By frequency doubling and optional further mixing of those photons with the Nd:YAG fundamental, photons in the ultraviolet range between 210 and 300 nm are produced for photodissociation of the target molecules. Because of the high UV fluence, the dissociative excitation observed may be due to more than one photon. After a variable delay time of up to 1 μs the second laser pulse ionizes the photodissociation fragments using vacuum-ultraviolet photons of 125.1 nm wavelength. They are produced from another Nd:YAG/dye laser combination by resonant four-wave mixing in Hg-vapor using 625 nm light and its doubled output at 312.5 nm.

The fragment ions are then accelerated into a time-of-flight mass spectrometer and detected with an ion multiplier. The accelaration field is provided either by a DC potential difference, or an HV pulse, whose delay with respect to both lasers can be adjusted to suppress background signal, for example, produced by multiphoton ionization. In order get the fragment ion spectrum, we first run the two-laser experiment, followed by each of the one-laser experiments, where either the UV or the VUV-beam is blocked. The signal of the latter spectra must then be subtracted from the former one to map out only those peaks that are dependent on the photons of both lasers.

The energetics of the photodissociation of SiH_4 was thought to provide a very convenient scheme of detecting the products from fragmentation of the neutral molecule without interference from possible remnants of the parent ion SiH_4^+, which is known to be unstable[2]. Since the vertical ionization potential of SiH_4 is 12.36 eV[3], the adiabatic IP being 11.66 eV[3], no SiH_4^+ should be produced by VUV-ionization of the parent molecule. On the other hand the IP's of all possible neutral fragments SiH_3, SiH_2, SiH, and Si are 8.11 eV, 8.92 eV, 7.89 eV, and 8.152 eV, respectively[4]. Therefore it should be possible to ionize all of them with a single VUV-photon. Theoretical calculations have shown, however, that the electronically excited states of SiH_4 below its first ionization potential should be repulsive. Since they lie between about 9 eV and 12.4 eV above the $X\ ^1A_1$ ground state[5] with electron configuration $1a_1^2\ 2a_1^2\ 1t_2^6\ 3a_1^2\ 2t_2^6$, most of these would be accessible by two-photon excitation using our UV-radiation between 275 nm and 210 nm.

Nevertheless, first results of our experiments show some deviations from this expected, simple picture:

[1]Feodor-Lynen-Fellow of the Alexander-von-Humboldt Foundation

- Excitation with VUV–radiation only produces a strong signal of Si^+, SiH^+, and SiH_2^+ charged fragments, Fig. 1.

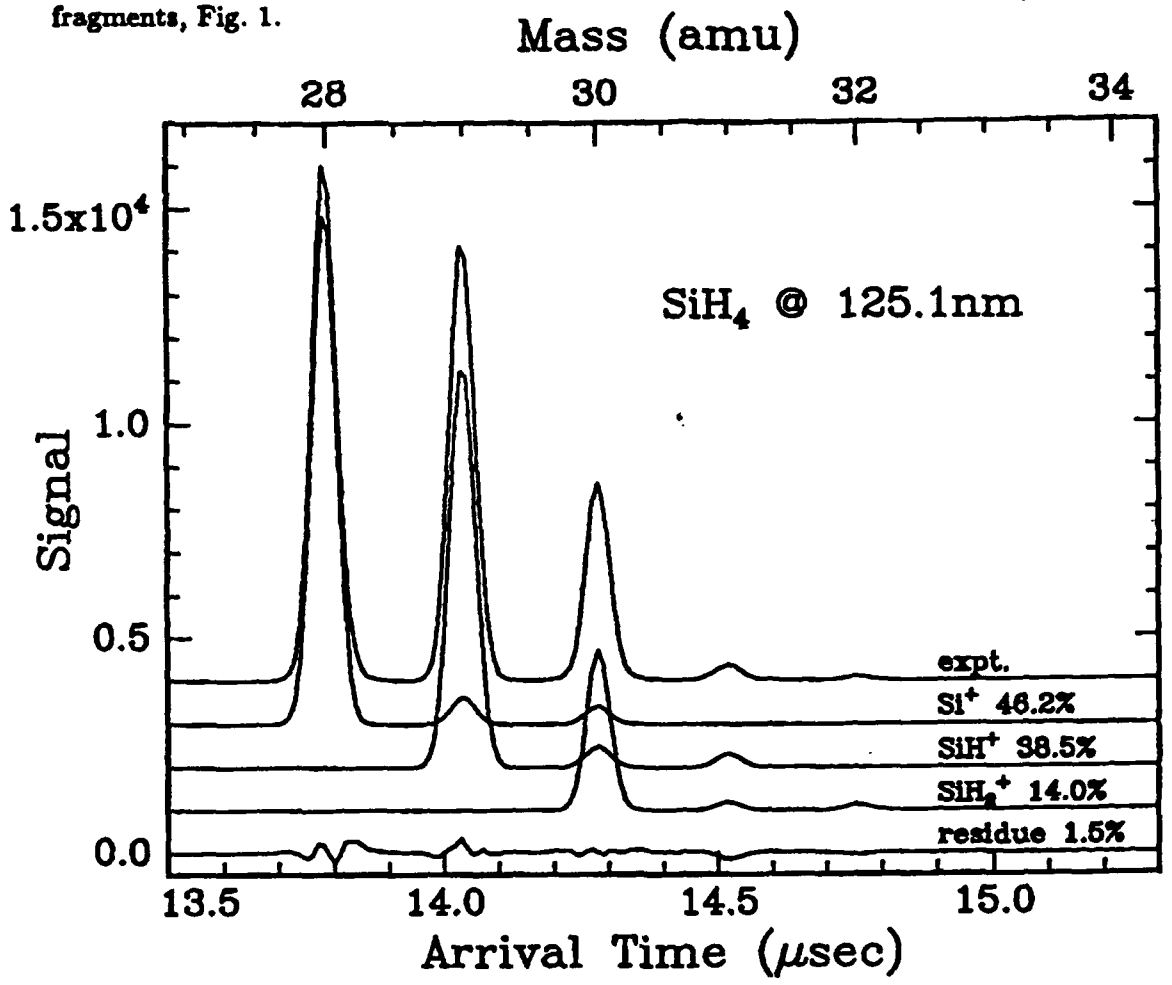

Figure 1: Mass spectrum of silane fragments for the VUV–only experiment, top curve. The three middle curves show the breakdown of the spectrum into the different fragments, by using the known isotope ratio for ^{28}Si : ^{29}Si : ^{30}Si of 92.2% : 4.7% : 3.1%. The bottom curve shows the residue after subtraction of these three fragment contributions from the experimental spectrum.

A power dependence indicates that these peaks are due to a resonant two–photon process. A reasonable mechanism involves the excitation of an electronically excited state near the VUV–photon energy of about 9.9 eV in the first step, with a cross section of about 0.5 $Å^2$[6]. This would either be a Rydberg or non–bonding valence state, which are known to lie in that region from several experiments[7], reached by promoting an electron from the outermost valence shell into the Rydberg orbital via $2t_2^{-1}$ 4p or a non–bonding valence orbital via $2t_2^{-1}$ $\sigma^*(t_2)$, forming either $^1T_2$ $(1a_1^2\ 2a_1^2\ 1t_2^6\ 3a_1^2\ 2t_2^5\ 4p)$ or $^1T_2$ $(1a_1^2\ 2a_1^2\ 1t_2^6\ 3a_1^2\ 2t_2^5\ \sigma^*(t_2))$. The second photon would account for the ionization step, which requires a cross section of again about 0.5 $Å^2$ for the observed amount of ion signal.

This proposed mechanism can be ascertained by comparison of our observed signal ratio

of Si^+ : SiH^+ : SiH_2^+ being 46% : 39% : 14% compared to data from the literature for Si^+ : SiH^+ : SiH_2^+ : SiH_3^+ given as 5% : 7% : 41% : 47%[8]. The latter signal is due to single photon excitation via light from a gas discharge lamp or synchroton radiation. The pronounced difference of our observed signal ratio indicates that in our case the dissociative ionization of SiH_4 is facilitated by a superexcited state above the second ionization potential (17.95 eV[8]) of silane, whose excitation would be dipole–forbidden from the ground state.

This process is, to our knowledge, the first observation of a two–photon excitation in the wavelength region at around 125 nm.

- By exciting SiH_4 in a two–color experiment, first with VUV–radiation and after some delay by UV–photons with 225.4 nm wavelength, a pronounced SiH^+ peak could be observed (Fig. 2), which depends on both lasers.

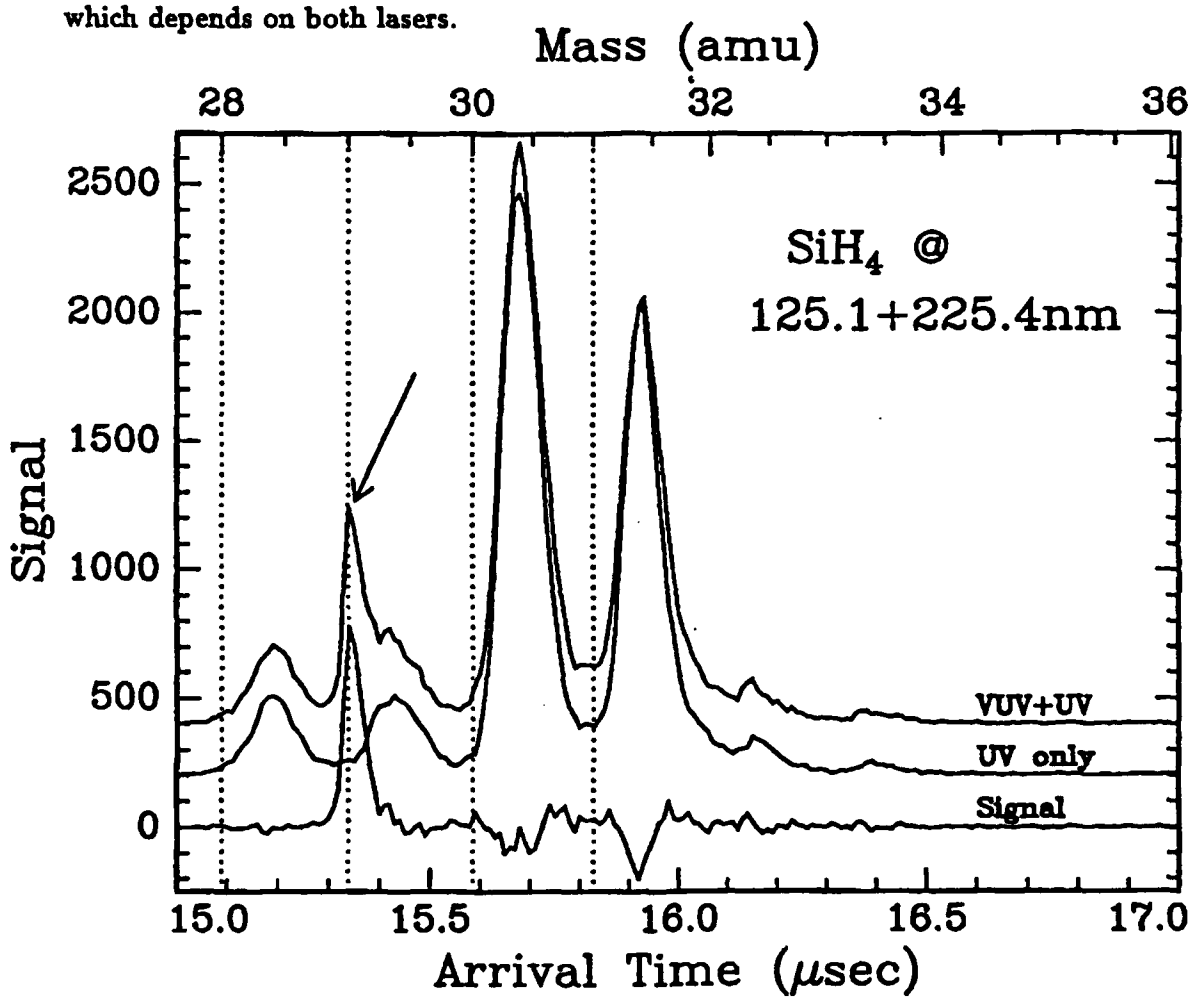

Figure 2: Mass spectrum for VUV and subsequent UV excitation. The arrow indicates the mass peak that depends on both lasers.

In this experiment the ion extraction is switched to the AC mode using a HV pulse. The pulsing scheme reverses the extraction voltage while the VUV–laser pulse excites the target molecules. Any signal due to the two–photon VUV process discussed above is then suppressed

by accelerating the ions onto the backing plate sitting in the direction opposite from the mass spectrometer. After about 300 ns, when all these ions have been destroyed, the extraction voltage is set to its normal value. After another 200 ns the UV–photons cross the molecular beam and cause, besides multiphoton ionization, the SiH^+ peak mentioned above.

In this case, the mechanism again involves excitation of the non–bonding valence state via $2t_2^{-1}\ \sigma^*(t_2)$ by the VUV–photon in the first step, as described in the section above. The second, UV–photon would then be able to promote an electron from an inner valence orbital into the vacant t_2–hole via $3a_1^{-1}\ 2t_2$. It would then correspond to a known valence state below the second ionization potential with the electron configuration $^1T_2\ (1a_1^2\ 2a_1^2\ 1t_2^6\ 3a_1\ 2t_2^6\ \sigma^*(t_2))$[7].

The peak could also be observed using 223 nm and 243 nm UV–photons, but not with those of 280 nm wavelength. This observation corresponds very nicely with the energy range of a photoionization band reported in the literature[8], which was attributed to this state.

In conclusion, we would like to point out that with different excitation schemes of SiH_4, by using more than one photon the dissociation pattern of the parent molecule can be changed distinctively towards production of fragment ions containing only small numbers of hydrogen atoms. Further experiments are in progress in order to map out the nature of these electronically excited states involved in the photodissociation.

References

[1] I.P. Herman, Chem. Rev. **89**, 1323–1357 (1989); J.M. Jasinski, B.S. Meyerson, and B.A. Scott, Ann. Rev. Phys. Chem. **38**, 109–140 (1987); J.M. Jasinski and S.M. Gates, Acc. Chem. Res. **24**, 9–15 (1991)

[2] M.S. Gordon, J. Chem. Phys. **69**, 4955–4961 (1978)

[3] B.P. Pullen, T.A. Carlson, W.E. Moddeman, G.K. Schweitzer, W.E. Bull, and F.A. Grimm, J. Chem. Phys. **53**, 768–782 (1969); A.W. Potts and W.C. Price, Proc. R. Soc. London A **326**, 165–179 (1972)

[4] B.H. Boo and P.B. Armentrout, J. Am. Chem. Soc. **109**, 3549–3559 (1987)

[5] M.S. Gordon, Chem. Phys. Lett. **59**, 410–413 (1978); D. Power, P. Brint, and T. Spalding, J. Mol. Struct., THEOCHEM **108**, 81–92 (1984)

[6] G. Cooper, T. Ibuki, and C.E. Brion, Chem. Phys. **140**, 133–145 (1990)

[7] see for example: M. Suto and L.C. Lee, J. Chem. Phys. **84**, 1160–1164 (1986); U. Itoh, Y. Toyoshima, H. Onuki, N. Washida, and T. Ibuki, J. Chem. Phys. **85**, 4867–4872 (1986); M.A. Dillon, R.-G. Wang, Z.-W. Wang, and D. Spence, J. Chem. Phys. **82**, 2909–2917 (1984)

[8] K. Börlin, T. Heinis, and M. Jungen, Chem. Phys. **103**, 93–100 (1986); T. Hayashi, T. Koizumi, T. Matsuo, T. Nagata, Y. Sato, H. Shibata, and Y. Yagishita, Chem. Phys. **116**, 151–157 (1987)

Double Photoionization Dynamics of Free Fullerenes

M. Fieber-Erdmann[1], T. Drewello[2], W. Krätschmer[3] and A. Ding[1]

1) Optisches Institut, Technische Universität, Berlin, Germany

2) Hahn-Meitner-Institut, Berlin, Germany

3) Max-Planck-Institut für Kernphysik, Heidelberg, Germany

Since the discovery of the fullerenes the investigation of the properties of this material have become a mayor task in physics and chemistry. Particularly interesting is the question, how many electrons can be removed from C_{60} and C_{70} and what the stability of this clusterion is after ionization.

We have therefore investigated the single and double photoionization efficiency of C_{60} and C_{70} which has been produced by evaporating a C_{60}/C_{70}-mixture from a quarz oven generating an effusive molecular beam. The experiments have been performed over the energy range between 20 eV and 120 eV and at different oven temperatures. Monochromatized light from the Berlin synchrotron facility BESSY served as the source for the VUV radiation.

The ionic products were analysed with the use of a time-of-flight mass spectrometer which allowed the separation of the singly and doubly charged C_{60} and C_{70} compounds. The threshold for double ionization as shown by Drewello et al. /1/ lies at 19.00 eV. Significant amounts of doubly charged ions, however, are not detected below E=30 eV. Above this energy the cross section rises steeply and exhibits somewhat reduced rising trend for higher energies. Spectra at different photon energies have been taken using He as a reference, see Fig. 1. It is clearly seen in Fig. 2 that the cross section depends strongly on the oven temperature, i.e. on the internal excitation of the cluster.

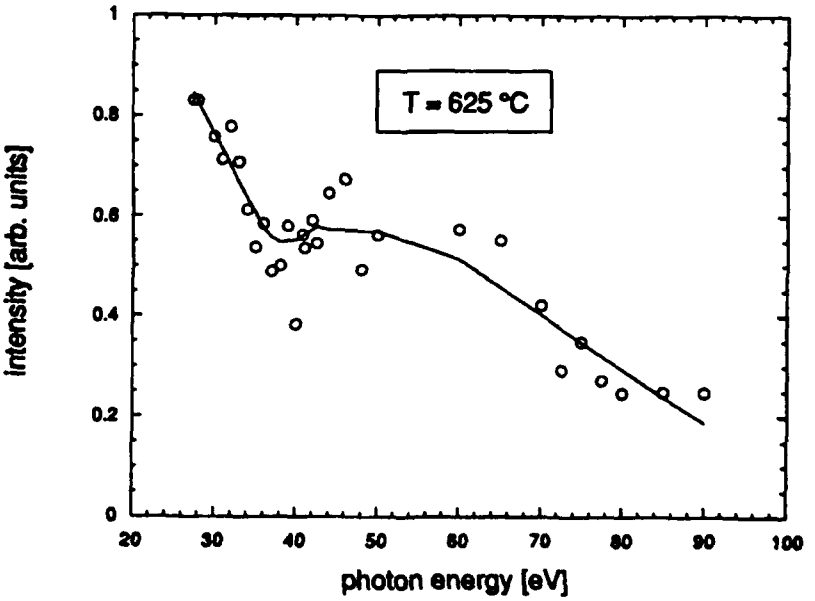

Fig. 1: C_{60}^{+} as a function of the photon energy using He as a reference.

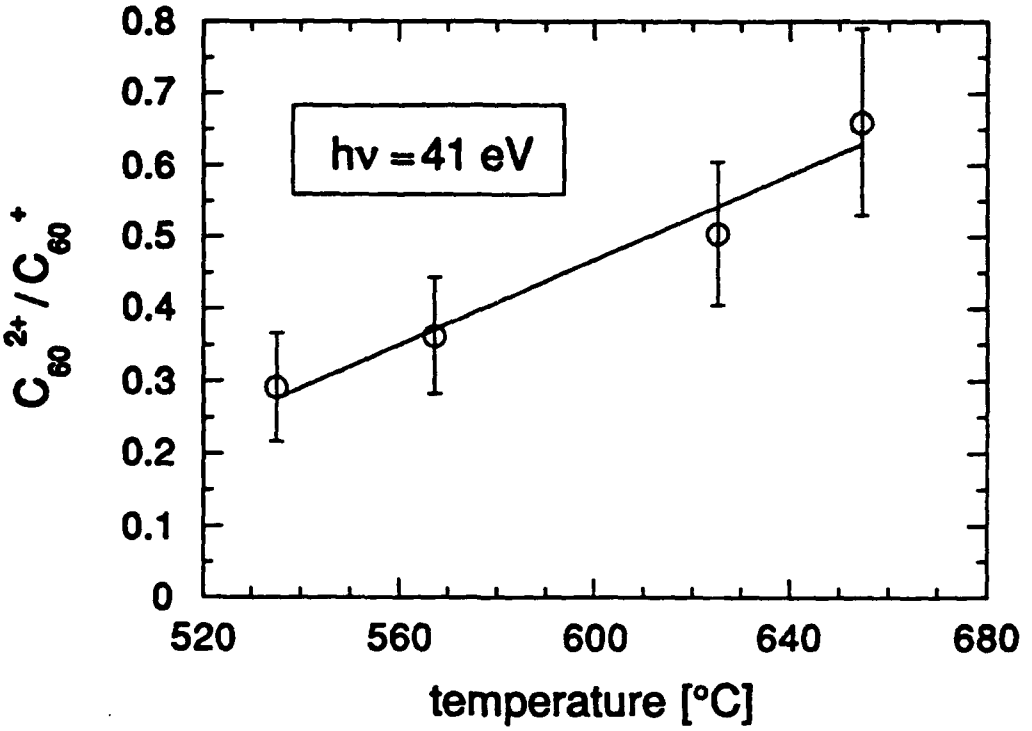

Fig. 2: C_{60}^{++} / C_{60}^{+} ration different oven temperatures.

Typical mass spectra are shown in Fig.3. At 40.8 eV both singly and doubly charged ions can be seen, but no fragmentation. In striking contrast to the total lack of singly charged fragment ions, the doubly charged species C_{58}^{++} and C_{56}^{++} have been observed but only in the limited energy range of about 65 eV to 77 eV . For the occurrence of these ions the

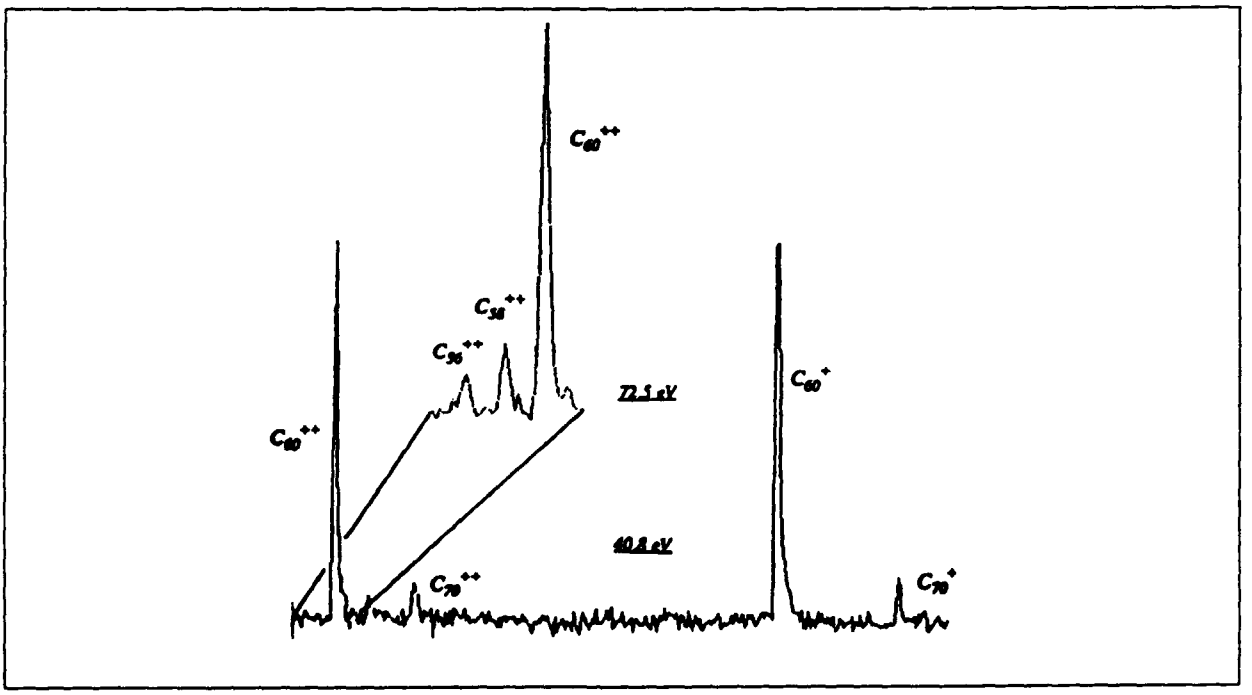

Fig. 3: Typical mass spectras at 40.8 and 72.5 eV.

present results seem to favour the existence of repulsive states located in this range of energies. The direct ionization of these fullerenes can be excluded, as these fullerenes are not present in the sample. In addition, C_{60}^{+++} for which an ionization threshold of 36.9eV has been measured recently /2/ is relatively abundant is this photon energy range as well. However, charge separation reactions of the triply charged ion leading to C_{58}^{++} and C_{56}^{++} appear not very likely, as the corresponding singly charged product ions could not be detected.

References:

/1/ H. Steger, J. de Vries, B. Kamke, W. Kamke, T. Drewello, submitted to Chem. Phys. Lett.

/2/ C. Lifschitz, M. Iraqi, T. Perez, J. E. Fischer, Rapid Commun. Mass Spectrm. 5 (1991) 238

Session IX:

SURFACES

THE CHEMISTRY OF HYDROGEN IN BULK NI

A. D. Johnson, S. P. Daley, A. L. Utz, S. T. Ceyer
Department of Chemistry
Massachusetts Institute of Technology
Cambridge, MA 02139 USA

Introduction to the Problem

The dissolution of hydrogen into the bulk of metals is pervasive. In such technologically important but diverse areas such as hydrogen embrittlement, plasma fusion and hydrogen fuel cells, it is a fundamental physical phenomenon. In the case of Ni metal, hydrogen dissolution occurs readily under high pressures of H_2 (>1 atm). However, if a Ni(111) crystal is exposed to 10^{-6} torr of H_2 in an ultrahigh vacuum surface science type of experiment, no hydrogen is observed to absorb into the Ni bulk. Instead, the H_2 incident on the surface dissociates and the resulting atomic H saturates the surface at one monolayer coverage whereupon the dissociative chemisorption stops. The Ni crystal does not take up any more hydrogen. The surface bound hydrogen is characterized by symmetric (A_1) and antisymmetric (E) stretching vibrations at 1170 and 955 cm^{-1}, respectively, as measured by high resolution electron energy loss spectroscopy (HREELS) and is observed to recombine and desorb between 340-380 K. There is no evidence for bulk H.

The potential energy diagram for the hydrogen-Ni system provides a plausible explanation for why hydrogen absorption is not observed under the low H_2 pressures of an ultrahigh vacuum experiment. In order for H_2 incident on a Ni crystal to dissociatively absorb, it has to overcome a barrier of approximately 26 kcal/mol. Since the average energy of gas phase H_2 at 300 K is 40 times lower, it is clear why H_2 dissociative absorption does not occur. However, the occurrence of absorption in the high pressure experiments seems inconsistent with these energetics! The explanation for this seeming contradiction is that at low pressure, there are too few molecules with energies high enough to overcome the barrier so as to make the absorption observable on a reasonable time scale. At high pressure, the absolute number of sufficiently energetic molecules in the Boltzmann tail is larger, making the rate of dissociative absorption sufficiently high to observe it. In principle, raising the energy of H_2 should circumvent the need for high pressures, but this is not the route chosen here. Instead, two more convenient methods for bulk H synthesis under low pressure conditions are presented.

Bulk H Synthesis by Atomic H Exposure and Detection of Bulk Hydrogen by High Resolution Electron Energy Loss Spectroscopy

Consider a H atom incident on the Ni crystal. Since the initial energy level of a H atom is far above any barrier to absorption into the bulk, exposure of a Ni(111) crystal to atomic H should result in bulk absorption. And it does. Exposure of the crystal to atomic H results in a new low temperature desorption feature at 185-215K. Unlike the high temperature feature, the low temperature feature can only be populated by atomic H incident on the crystal. Long exposures to atomic H have resulted in an equivalent of over 8 ML of hydrogen desorbing at low temperature. This significant increase in hydrogen uptake suggests bulk absorption. The HREEL spectrum also exhibits an additional vibrational feature at 800 cm^{-1}. Raising the crystal temperature to 273K results in the disappearance of the feature at 800 cm^{-1} concurrent with the low temperature desorption of H_2.

However, if this vibrational mode is really that of a bulk species, why is it observable with a technique that is usually considered sensitive to surface adsorbates only? The answer is twofold. First, the H vibration is not excited by the common dipole excitation mechanism but is excited by an impact excitation mechanism. Because impact scattering is a short range interaction (~1Å), the mean free path of the incident electron within the solid must be sufficiently long for it to reach the buried H and to scatter out of the metal without experiencing any inelastic collisions. The intensity of an inelastic transition from a bulk species can be shown to be directly proportional to the mean free path. We have found that by lowering the energy of the incident electron, we can increase the mean free path sufficiently to observe the vibration of a bulk species. It is also known that the mean free path decays with approximately an inverse quadratic dependence on the electron energy. To demonstrate that the 800 cm^{-1} loss feature is a result of electrons scattered inelastically from H embedded in the Ni, we have measured the intensity of this feature as a function of the incident electron energy. Indeed, we observe the intensity to decay to zero with an inverse quadratic dependence as the electron energy is increased from 3 to 20 eV. In contrast, the intensities of the two modes assigned to surface chemisorbed H are the same at 3 eV as at 20 eV. Therefore, the loss feature at 800 cm^{-1} is assigned to the vibration of H occupying a site beneath the Ni surface. This study has demonstrated the use of HREELS to detect bulk absorbates and to distinguish their vibrations from those of surface adsorbates.

Detailed measurements of the angular dependence of the intensity of this mode have also been carried out for the purpose of determining the site of the embedded H atom. The angular dependence is consistent with the selection rules for impact scattering from a site of octahedral symmetry. Therefore, the H is believed to occupy octahedral interstitial sites as it does in bulk Ni hydride. This is an important piece of information in understanding the unique chemistry of bulk H discussed below.

Bulk H Synthesis by Collision Induced Absorption

Now consider a H atom bound at a 3-fold hollow surface site. In order for this H atom to absorb, it has to acquire at least 24 kcal/mol to overcome the endoergicity and the barrier to bulk absorption. In principle, this energy could be provided by the impact of energetic inert gas atoms in a process called collision induced absorption. This proposed new mechanism for absorption is demonstrated in the following way. A monolayer of chemisorbed H is prepared by exposure of the Ni(111) crystal to H_2. A Xe beam with a kinetic energy of 87 kcal/mol is then directed normally at the surface covered with 1 ML of hydrogen. The resulting HREEL spectrum clearly exhibits the loss feature at 815 cm^{-1} associated with bulk H. The higher frequency of this bulk H mode than that following exposure to atomic hydrogen reflects the lower H absorbance. The frequency increases from 800 to 850 cm^{-1} as the H absorbance decreases from an equivalent of 1 to 0.4 ML. The decrease of the bulk mode frequency is found to correlate quantitatively with the increase in the lattice size with increasing absorbance.

The cross section for absorption of chemisorbed H induced by the impact of Ar, Kr or Xe atoms has been measured as a function of their incident energy and angle. The collision induced absorption cross section is observed to exhibit strict normal energy scaling in the inert gas atom energy and the cross section for absorption induced by Xe is significantly larger than that for Kr or Ar. These two observations suggest that the cross section for collision induced absorption is directly proportional to the energy transfer to the Ni lattice:

$$\Sigma(E_i,\varphi_i,m) = A\,\Delta E(E_i,\varphi_i,m)$$

where ΔE is the energy transferred from the inert gas atom to the lattice, E_i is the incident energy, φ_i is the incident angle, m is the mass of the inert gas atom and A is a proportionality constant.

In order to test whether the absorption cross section does correlate with energy transfer to the lattice, the incident energy, incident angle and mass dependence of the energy transferred from the inert gas atom to the Ni lattice are calculated and compared to that of the experimentally determined cross section. The energy transfer is calculated within a hard sphere-hard cube impulsive collision model which has been modified to include the multiple collisions that take place when a heavier gas atom is incident on a lighter substrate atom. The mass of the Ni atom is taken as its atomic mass. Motion of the Ni atom is only allowed normal to the macroscopic plane of the surface, which is known to be an excellent approximation in an atom-surface collision.

The energy transferred by Xe is then scaled to the experimental cross section for Xe, allowing the proportionality factor A to be determined. The proportionality factor is then used to predict the cross sections for absorption by Ar and Kr based on the energy transferred to the lattice by Ar and Kr. It is found that the experimental dependence of the cross sections on the mass and normal energy agrees very well with the predicted dependence of the cross sections based on the calculated energy transferred to the lattice. The one adjustable parameter in this model, the fraction of momentum with which the Ni atom recoils away from the lattice, is set at 0.8 but this parameter gives good agreement with the data over a wide range of values between 0.1 to 0.95 for a Ni mass of 58.7. This excellent correlation between the cross section for collision induced absorption and the energy transferred to the Ni lattice suggests a surface deformation mechanism. The incident atom collides with the surface either directly on top of or close to the adsorbed H atom. The impact of the collision transfers energy to the surface which momentarily distorts it so as to open up channels or holes into which the hydrogen can readily diffuse and enter the bulk.

Collision Induced Recombinative Desorption

In competition with absorption, recombinative desorption occurs. That is, the impacts of the inert gas atoms not only cause adsorbed H to penetrate into the bulk but also cause them to recombine and desorb as H_2. The cross section for recombinative desorption exhibits a complicated dependence on the incident angle and energy reflecting the competition between the angular dependence of the collision cross section and the normal energy transfer to the surface. The observation of collision induced recombinative desorption is significant because it is a new tool for the non-thermal removal of chemisorbed species without damage to the surface. For example, it is not possible to thermally desorb surface bound H without also desorbing bulk H because bulk H is less stable than surface H. Collision induced recombinative desorption enables the preparation of a crystal with a clean surface and with a bulk filled with H. Vacant surface sites are essential for a study of the chemistry of bulk H as shown in the next section.

The Chemistry of Bulk Hydrogen

The bulk hydrogen atom is found to undergo unique chemistry. An adsorbed methyl radical and an adsorbed hydrogen atom are shown to be unreactive but adsorbed CH_3 in the presence of bulk hydrogen is observed to readily produce CH_4.

The experiment is performed as follows. Exposure of the Ni(111) crystal to atomic H results in both bulk H and surface H. The surface H must be removed to make sites available for CH_3 adsorption. This is accomplished by collision induced recombinative desorption which sweeps the surface clean of hydrogen without perturbing the bulk H.

The clean surface is then exposed to CH_4 incident at 17 kcal/mol. The CH_4 dissociatively adsorbs, producing adsorbed CH_3 and adsorbed H. The surface temperature is then ramped at 2K/s and the partial pressures of hydrogen and methane are measured. At exactly the same temperature at which hydrogen desorbs from the bulk, 180K, there is very intense desorption of CH_4. In the case where the bulk is saturated with D, the only product observed is CH_3D. In the absence of bulk H, no CH_4 is observed.

The reaction proceeds by the direct reaction of an absorbed H atom with a CH_3 species which is known to be bound at a 3-fold hollow surface site on Ni(111). The absorbed H is bound in an octahedral interstitial site which is directly beneath the threefold hollow site. As the surface temperature is raised, the absorbed H atom moves up toward the threefold hollow site on the surface where it encounters a methyl radical. Because the H atom now has the correct orientation required by the transition state for sp^3 bonding, it reacts with CH_3 and immediately desorbs as CH_4. The reaction of CH_3 with an adsorbed H atom does not occur probably because access of the H atom to the Ni_3 -C bond is sterically hindered.

These observations document a new mechanism for a surface reaction, the reaction between an adsorbed and an absorbed species, and demonstrate for the first time the importance of bulk species to heterogeneous catalytic chemistry.

MOLECULAR BEAM STUDIES OF DISSOCIATION AT SURFACES

Brian E.Hayden

Department of Chemistry
The University of Southampton
Southampton, SO9 5NH
United Kingdom

The dissociation of a molecule at a surface is a critical first step in a large number of surface chemical processes. The dynamics of this step, which is often activated, is most accessible when the process is direct, and the transition state corresponds to a crossing of the weakly perturbed gas phase potential, and the potential of the dissociated state. Such a case is the dissociative adsorption of hydrogen on copper **[1]** which has now become a model system for the study of direct dissociation dynamics.

The activated dissociation of H_2 and D_2 on Cu(110) has been studied using pure and anti-seeded supersonic molecular beams. The barrier to dissociation is found to be accessible with translational energy, but a deviation from normal energy scaling **[2]** and enhanced sticking of H_2 over D_2 at any particular energy in the pure beam experiment **[3]** is interpreted as an indication of the importance of the vibrational co-ordinate in the dissociation dynamics. The relative contributions of vibrational and translational energy is accessing the barrier is separated in vibrationally hot, translationally cold seeded beams. The results for hydrogen indicate a translational onset for $H_2(v=1)$ of 130meV and for $D_2(v=2)$ of 60meV **[4]**. These results are consistent with a theoretically predicted barrier to dissociation of ca. 700meV which lies somewhat in the exit channel of a two dimensional potential energy surface. These results also provide consistency with results for desorption which demonstrated internal state distributions far from Boltzmann at the surface temperature, particularly in vibration **[5]**. A considerable effort to map the PES in more detail by vibrational state selection of hydrogen dissociation is now under way in other laboratories **[6]**.

We have also demonstrated that the direct dissociation of H_2 on Cu(110) can be promoted by adsorbed potassium **[7]**. The effect of the alkali metal is to enhance hydrogen adsorption, increase the activation energy to associative desorption, and reduce the activation energy for dissociative adsorption. This result is discussed in relation to the potential energy hypersurface for hydrogen dissociation over the co-ordinates of the Cu(110) unit cell.

In contrast to hydrogen dissociation on copper, which is not complicated by the existence of an intermediate resonant state **[8]**, oxygen dissociation on platinum and silver is complicated by the existence of an adsorbed molecular intermediate. In the case of O_2 on Pt(111) it has been shown **[9]** that the dissociation probability increases with kinetic energy above ca. 100meV, and this is interpreted as direct activated adsorption into the resonant O_2^- state prior to dissociation. In an attempt to study the dynamics of this particular step, the scattered fraction (angular distributions and translational energy) of the impinging molecules has been studied as a function of incident translational energy and incident angle **[10]**. The results suggest a transition from scattering from a flat potential to a corrugated potential at high energy. This manifests itself in a broadening of the direct inelastic lobe and a final translational energy which increases monotonically with final angle.

The results are compared to the direct inelastic channels for Ar scattered from Pt(111), and O_2 on Ag(111). The broadening observed in the direct inelastic lobes on both Pt(111) and Ag(111) at higher normal energies can be ascribed to the influence of the chemisorption precursor in the interaction potential. In the case of Pt(111), however, the direct inelastic distributions are additionally modified by the significant probability for dissociation.

References

1. B.E.Hayden in ***Dynamics of Gas Surface Collisions*** edited by M.R.Ashfold and C.T.Rettner (Royal Scociety of Chemistry, London, 1991) p.137.
2. B.E.Hayden and C.L.A.Lamont; Chem.Phys.Letts., 160 (1989) 331.
3. B.E.Hayden and C.L.A.Lamont; Surf.Sci., 243 (1991) 31.
4. B.E.Hayden and C.L.A.Lamont; Phys.Rev.Lett., 63 (1989) 1823.
5. G.D.Kubiak, G.O.Sitz and R.N.Zare; J.Chem.Phys., 81 (1984) 6397.
6. C.T.Rettner and D.J.Auerbach et.al.; (IBM, San Jose).
   A.Hodgson et.al.; (University of Liverpool).
7. B.E.Hayden and C.L.A.Lamont; Faraday Discuss.Chem.Soc., 91 (1991) 415.
8. J.K.Norskov; J.Chem.Phys., 90 (1989) 7461.
   J.Harris and S.Andersson; Phys.Rev.Lett., 55 (1985) 1583.
9. A.C.Luntz, M.D.Williams and S.D.Bethume; J.Chem.Phys., 89 (1988) 4381.
   A.C.Luntz, J.Grimblot and D.E.Fowler; Phys.Rev, B39 (1989) 12903.
   C.T.Rettner and C.B.Mullins; J.Chem.Phys., 94 (1991) 1626.
10. A.E.Wiskerke, F.H.Geuzebroek, A.W.Kleyn and B.E.Hayden; Surf.Sci., ***in press***.

Investigation of Homo- and Heteroepitaxial Growth on Ionic Insulators via He Atom Scattering.* S. A. Safron, J. Duan, G. G Bishop, E. S. Gillman, G. Chern and J. G. Skofronick, Departments of Chemistry and Physics and MARTECH, The Florida State University, Tallahassee, FL 32306.

Because of its high sensitivity to the state of surfaces, helium atom scattering (HAS) has become an important investigative tool in surface science.[1,2] In the work reported here three kinds of HAS experiments have been carried out: (1) Deposition curve measurements of the specular (and other Bragg) scattering intensities of the He atom beam as a function of deposition time or coverage; (2) Angular distribution measurements of the total He scattering intensity at selected coverages; and (3) Time-of-flight measurements of the inelastic scattering of the He atoms arising from single phonon interactions at the crystal surface for selected adsorbate coverages. These experiments allow one to follow the characteristics of the growth of the adlayers in real time; to determine the structure of the adlayers, including terrace widths and step and defect densities; and to compare the surface forces in the adsorbate layer with those of the corresponding cleaved crystal.

The design of this HAS instrument[3] uses a fixed 90° geometry between the beam source-target axis and the target-detector axis. In these experiments the He atoms were formed into a nearly monoenergetic beam with a velocity spread $\Delta v/v \approx 1\%$ (energy spread $\Delta E/E \approx 2\%$) over the range of incident wavevectors k_i from ~6-9 $Å^{-1}$, corresponding to a range of incident energies E_i from ~20-40 meV. The scattered He atoms are detected by a quadrupole mass spectrometer operated in a pulse-counting mode, interfaced with a computer-controlled data acquisition system.

Four different systems have been examined in this work: NaCl/NaCl[4], KBr/RbCl, KBr/NaCl[5] and NaCl/KBr. For every case the substrate alkali halide surface (right hand compound of each pair) was prepared by cleaving a single crystal of the alkali halide in air to obtain the (001) surface. After the HAS scattering chamber was baked to achieve ultra high vacuum (UHV) conditions, the target surface was cleaned by flashing to 500°C. The deposition was carried out by employing a sublimation source for the adsorbate alkali halide that included a beam flag shutter to stop the deposition at desired coverages. The deposition was also followed in many cases by a thickness monitor. In most of this work the target temperature was kept in the range of 200-225K.

The systems studied can be categorized by the degree of lattice matching. NaCl/NaCl is a case of homoepitaxy and the adsorbate and substrate have perfect lattice matches. For KBr/RbCl the surface lattice spacings are very close (4.661 Å for KBr, 4.654 Å for RbCl, ~0.2% mismatch), but the sizes of the pairing ions differ so that the first adlayer should be somewhat "rumpled". For the pair KBr/NaCl and NaCl/KBr there is a substantial mismatch in the lattice spacings (3.979 Å for NaCl, ~17% mismatch with KBr).

The deposition curves for the first two cases above showed oscillations in intensity corresponding to layer-by-layer growth, similar to the oscillations reported for the growth of metals on metals.[1,2] Variation in the depths of the minima in these oscillations with He wavevector were observed, which have been ascribed to the interference that arises between the coherently scattered beams from the new growing terraces and the exposed portion of the old surface.[1,2,6] This can be expressed as $|\Delta k_z| = N(2\pi/D)$, where Δk_z is the difference between the surface-normal components of the out-going and in-coming He atom wavevectors, D is the terrace step height and N = an integer for constructive inteference and = a half-integer for destructive interference. An important difference is found in these curves between the

NaCl/NaCl and the KBr/RbCl systems in that the variation with wavevector for the first oscillation of the latter system is out-of-phase with that of the other oscillations. This is interpretted as indicating that the terrace height of the first adlayer (KBr on RbCl) is different from that of the other layers (KBr on KBr) because the sizes of the individual ions of the KBr adsorbate differ from those of the RbCl substrate even though the lattice spacing is nearly a perfect match. For the third case, the large lattice mismatch results in a deposition curve with an oscillatory pattern with very much reduced intensity, an order of magnitude smaller than in the others. In addition, the first oscillation maximum is missing. Further, unlike the other two cases where the oscillation maxima gradually decrease with deposition time due to the build up of defects, here the maxima first grow in intensity for the first 6-8 layers and then gradually decline.

The angular distribution measurements of the clean substrates in all cases show the Bragg scattering peaks at angles corresponding to the positions where $\Delta\mathbf{K} = \mathbf{G}$, where ΔK is the difference between surface-parallel components of the out-going and in-coming He atom wavevectors ($\mathbf{k}_f = \mathbf{k}_i$) and G is a surface reciprocal lattice vector.[3,7] In the first two cases above the adsorbate and substrate have the same lattice spacing and the positions of these peaks do not change with deposition. However, the deposition causes a broadening of the widths of the Bragg peaks because of the smaller size of the terraces in the growing layer. For a fixed coverage of adsorbate the widths of the peaks are found to vary with He wavevector, which is consistent with the interference effects described above.[6] In addition, for the KBr/RbCl system we observe a variation in the relative heights of the Bragg peaks which is expected because of the modification of the surface corrugation due to the different ion sizes. In the NaCl-KBr pair of systems the angular distributions for the first two monolayers show only the Bragg peaks of the substrate, which are very much reduced in intensity from those of the clean cleaved crystals. The deposition of another layer results in angular distributions with satellite peaks that correspond to a superstructure of length $\approx$ 28 Å. (Seven NaCl lattice spacings, 27.85 Å, have very nearly the same length as six KBr lattice spacings, 27.97 Å). By the fourth monolayer one finds only the adsorbate Bragg scattering peaks along with the superstructure peaks and by the sixth or seventh monlayers only the adsorbate peaks remain. Thus, there appears to be an intermediate structure or "buckling" on the surface corresponding to a length scale where integer numbers of substrate and adsorbate units match up.

Time-of-flight experiments for the inelastic scattering of NaCl/NaCl with one or two monolayers deposited give spectra which are very similar to those of clean NaCl except that the single phonon peaks have been broadened, attributable to the comparatively poor surface quality. The energies (or frequencies ω) and surface wavevectors $\mathbf{Q}$ of the surface phonons can be calculated from these spectra from the relations $\hbar\omega = E_f - E_i$ and $\Delta\mathbf{K} = \mathbf{G} + \mathbf{Q}$, where E_f and E_i are the final and incident He atom energies, to construct the surface phonon dispersion curves.[3,7] The results are essentially the same as for the cleaved NaCl crystal. For one monolayer of KBr on RbCl the single phonon peaks corresponding to the Rayleigh wave (the lowest energy surface wave, a transverse acoustic mode polarized in the sagittal plane) yield a dispersion curve nearly the same as those for KBr and RbCl (which are very similar to each other). However, there are a number of peaks corresponding to higher energy surface modes which do not lie along the optical mode curves which had been measured for both KBr and RbCl crystals. These "anomalies" may arise as a result of the "mixed" ion pairs at the interface of the first KBr layer (i.e., one can think of the top RbCl layer and adjacent KBr layer as composed of regularly arranged stacks of RbBr's and KCl's). For the KBr/NaCl system the

mismatching lattice and ion masses appear to prevent good coupling between adsorbate and substrate vibrations. With two monolayers of KBr on NaCl, where the angular distribution shows only Bragg peaks of the substrate, the Rayleigh wave dispersion curve looks very much like that measured using a cleaved KBr surface, with the difference that for large wavelengths (small Q's) the phonon energies remain at finite energies rather than going to zero. With four monolayers, where the angular distributions still show the 28 Å superstructure peaks, all the previously measured branches of the surface dispersion curves except the longitudinal acoustic resonance are observed and are found to lie essentially on top of the curves that had been measured for the cleaved KBr crystal. The exceptions are again that the Rayleigh wave does not go to zero energy for small Q, although the values lie below those for the two monolayer curve, and the optical phonons in the center of the Brillouin zone lie at higher energies than those for the cleaved crystal. The absence of the longitudinal modes may just be due to the comparatively poor surface quality. The time-of-flight intensities of the scattering from NaCl/KBr were too low to permit a comparison with surface phonon measurements from clean NaCl. The very poor quality spectra are due in part to the very small coherent scattering intensities noted above and, probably, to the fact that the NaCl modes lie in the middle of the KBr bulk bands and thus may be obscured by a relatively large background signal.

• Supported by the U.S. Department of Energy under Grant DE-FG05-85ER45208

1. B. Poelsema and G. Comsa, Scattering of Thermal Energy Atoms from Disordered Surfaces, Springer, Berlin (1989).
2. H. Xu, Y. Yang and T. Engel, Surf. Sci. 255, 73 (1991).
3. G. Chern, J.G. Skofronick, W.P. Brug and S.A. Safron, Phys. Rev. B39, 12828 (1989).
4. J. Duan, G. G. Bishop, E. S. Gillman, G. Chern, S. A. Safron and J. G. Skofronick, J. Vac. Sci. Technol. A (in press).
5. J. Duan, G. G. Bishop, E. S. Gillman, G. Chern, S. A. Safron and J. G. Skofronick, Surf. Sci. (in press).
6. K. D. Gronwald and M. Henzler, Surf. Sci. 117, 180 (1982).
7. G. Brusdeylins, R. B. Doak and J. P. Toennies, Phys. Rev. B27, 3662 (1983).

Adsorption on Insulator Surfaces Studied by Helium Atom Scattering: Structure and Dynamics

Helmut Weiss[a)]

Institut für Physikalische Chemie und Elektrochemie der Universität Hannover, Callinstr. 3-3a, W-3000 Hannover 1

In the past few years an increasing number of experimental as well as theoretical studies was published on the topic 'adsorption of small molecules on alkali halide single crystal surfaces'. These adsorbate systems are generally assumed to be governed by electrostatic and van der Waals interactions, and were sometimes viewed as 'model systems' for physisorption. However, the number of systems studied, if compared to studies of chemisorption on metal and semiconductor surfaces, is small. To some extent this is due to the importance which is ascribed to chemisorption vs. physisorption. Another important reason is the sensitivity of alkali halides to electron beams which has hampered the experimental investigation so far. Therefore most of our present knowledge on adsorption on well-defined alkali halide single crystal surfaces originates from a non-destructive method, Fourier-transform infrared (FTIR) spectroscopy. Particularly the adsorption of CO and CO_2 on NaCl(001) was studied in much detail [1-6]. In the latter system the analysis of the vibrational spectra, the modelling of these spectra and the modelling of the adsorption potential allowed, for the first time, more than only guesses on the orientation, the adsorption site and the two-dimensional structure of adsorbate molecules on an insulator surface. It will be shown below that the drawn conclusions are in agreement with the Helium atom scattering (HAS) results as well as with a recent LEED study of CO_2 on NaCl(001) grown epitaxially on Ge(001) [7].
Although FTIR spectroscopy proved to be such a valuable tool for the study of adsorbates on insulator surfaces, it does not give immidiate access to the symmetry of the adsorbate lattice. For this purpose Helium atom diffraction is a much better suited technique. It is non-destructive, too, and absolutely surface-sensitive. As in LEED, the diffraction pattern is an image of the reciprocal surface lattice. Additional information can be obtained if the inelastic scattering of Helium atoms is monitored in a time-of-flight (t.o.f.) experiment. Sharp energy loss and gain features correspond to the excitation and deactivation of surface phonon modes or - in case of adsorbates on e.g. alkali halide surfaces - 'outer vibrations' of the adsorbed molecules. The energy of these motions (frustrated translations and rotations) is below about 20 meV (160 cm^{-1}) and not readily available to other experimental techniques. The knowledge of these energies is of importance for processes like surface diffusion, desorption and vibrational line-broadening.

The Helium atom scattering experiments were performed in the apparatus described in ref. [8]. In brief, the NaCl sample crystal is mounted to a manipulator with provisions for sample tilt, azimuthal rotation and polar rotation (i.e. rotation around an axis perpendicular to the sagittal plane). A highly monoenergetic Helium atom beam ($\Delta v/v \approx 0.5\%$) impinges onto the surface. Scattered atoms are detected at right angle to the incident beam. Different momentum transfers are probed by a change of the polar angle. The energy resolution in t.o.f. experiments, carried out with a chopped beam, is < 0.5 meV.
The sample surfaces were prepared by in-situ cleavage after bake-out under ultrahigh vacuum conditions. The surfaces were shown to be clean and of high quality by observation of sharp diffraction patterns as well as 'selective adsorption/desorption' features of Helium atoms. Sample temperatures were measured by means of a thermocouple embedded in the crystal; they could be adjusted between about 25 and 500 K. Adsorbates were generally prepared using methods developed for FTIR spectroscopy, under or at least close to adsorption/desorption equilibrium conditions. Most of the work done so far concentrated on CO/NaCl(001) and CO_2/NaCl(001); these are the presently

best-studied systems, and it seems like a good choice to test a new method on something not completely unknown. In the course of these first studies significant details could be contributed to the knowledge on these systems. Some of these results will be presented now.

Particularly the adsorption of CO on NaCl(001) single crystal surfaces was studied in recent years. From polarized monolayer infrared spectra a perpendicular orientation of the molecules was inferred, with one molecule per adsorbate lattice unit cell and a (1x1) structure. In the helium atom scattering experiments this (1x1) structure could be confirmed for sample temperatures of 45 K [9]. At this temperature diffraction spots are observed at exactly the same positions as and of equal width to those of the bare NaCl(001) substrate, indicating a well-ordered commensurate adsorbate. At $\leq$30 K additional strong half-order peaks can be observed, which can be attributed to domains of a (2x1) superstructure of the adsorbate lattice (see Fig. 1). Half-order spots are missing in the <110> direction, indicating a glide plane. The arrangement of the molecules in the (2x1) phase with respect to the high-temperature (1x1) phase can be (i) an oppositely directed shift of two adsorption sites, (ii) a tilt of the molecular axis away from the normal and (iii) a combination of both. FTIR experiments indicated molecules tilted antiparallel relative to the surface normal, demonstrating impressively the complementary information which can be obtained by these non-invasive methods [4].
Between 25 and 53 K the width of the specular and full-order peaks, which are present in the (1x1) as well as in the (2x1) adsorbate structure, is independent of temperature (see Fig. 2); the decrease in intensity with increasing T_{sample} can be explained by the decrease of the Debye-Waller factor. This is not the case for e.g. the [1 ½] superstructure peak: Above 30-35 K it becomes significantly broadened with increasing temperature and can barely be seen above 45 K. The temperature dependence of the peak width excludes Bragg diffraction from an ordered layer at temperatures above 30-35 K; it suggests critical scattering from the fluctuations of dynamically created clusters having locally the (2x1) structure of the low-temperature phase. The continuous increase of the intensity of

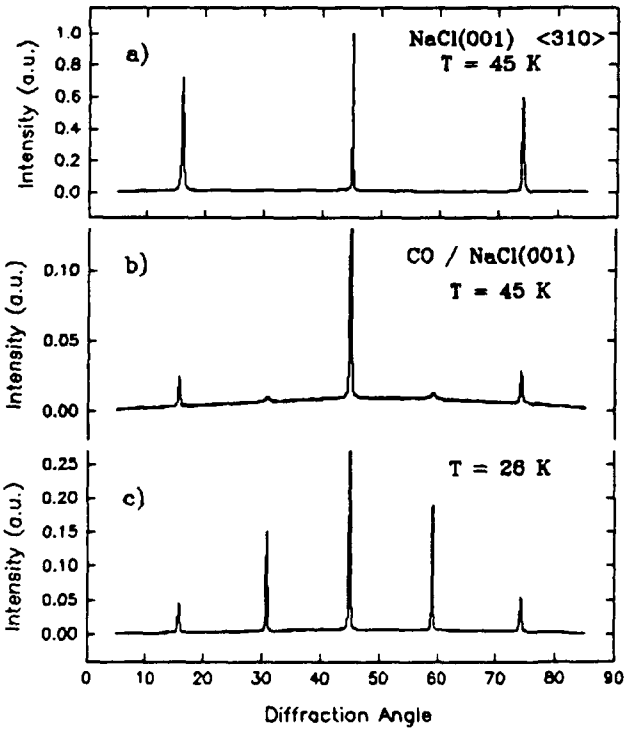

FIG. 1 Angular distributions for the bare NaCl(001) (a) and the monolayer CO/NaCl(001) (b,c), measured along the <310> direction for different temperatures. Incident wavevektor k_i=5.16 Å^{-1}. All specular intensities are normalized to 1.

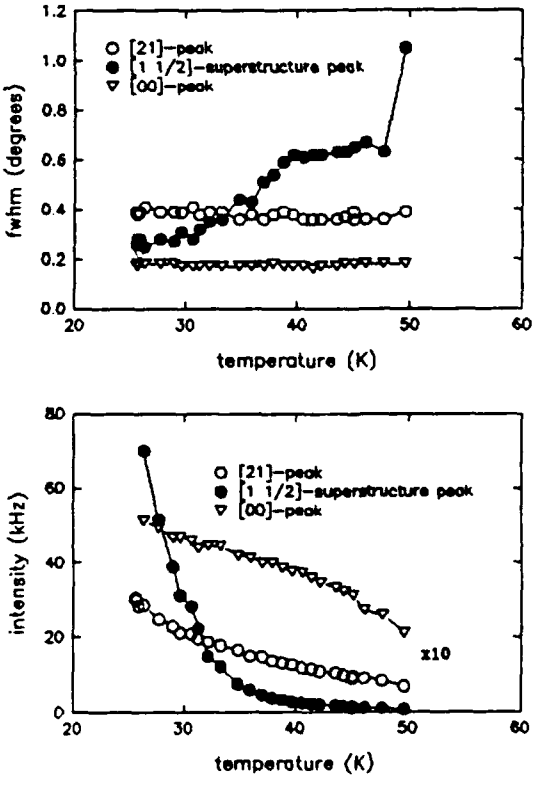

FIG. 2 Temperature dependence of width and intensity for different diffraction peaks of CO/NaCl(001), measured in the <310> direction.

all diffraction peaks with decreasing surface temperature strongly suggests a second-order phase transition. Below ~32 K the intensity of the [1 ½] superstructure peak decreases almost linearly with increasing sample temperature. Exptrapolation to zero intensity yields the transition temperature, $T_c \approx 34 \pm 2$ K.

First t.o.f. experiments from the monolayer CO/NaCl(001) indicate energies of about 7.5 and 15 meV (60 and 120 cm^{-1}) for external motions of the adsorbed molecules. Here further studies are necessary. The same is true for the clarification of the behaviour of submonolayers where island formation below about 35-40 K can be inferred from the appearance, intensity and width of the superstructure diffraction peaks. Plots of specular intensity vs. exposure show that at T_{sample}=40-45 K monolayer coverage is established not via the growth of large islands but probably via a statistical adsorbate.

The second system mentioned above, CO_2 on NaCl(001), was studied at monolayer coverage. In extensive infrared studies a two-dimensional (2D) first-order phase transition was observed [5,6]. Below about 2% of a monolayer a lattice gas exists, which is in equilibrium with large 2D islands at the transition pressure p_T. Above p_T a 2D solid (monolayer) is thermodynamically stable. From the monolayer FTIR spectra a (2x1) structure was deduced, with two molecules per surface unit cell which are arranged in a herringbone-like pattern and tilted by about 27° relative to the surface plane [2,5]. Helium atom diffraction from a monolayer CO_2/NaCl(001) at T=83 K and $p(CO_2)=10^{-9}$ - 10^{-8} mbar (i.e. under adsorption-desorption equilibrium conditions, where most of the FTIR spectra were collected) gave the following results: (i) All diffraction peaks observed for the bare NaCl surface are found in the adsorbate, too, in agreement with an adsorbate commensurate to the substrate. (ii) The width of the diffraction peaks is the same as for bare NaCl, indicating domain sizes in excess of about 450 Å. (iii) Additional half-order peaks are observed and in agreement with a (2x1) structure. As in case of CO/NaCl(001) the latter peaks are missing along the <110> and <110> directions, indicating a glide plane in the adsorbate lattice unit cell. It should be noted that these results are entirely in agreement with the results deduced from the FTIR spectra as well as from a recent LEED study, in which an NaCl(001) film epitaxially grown on Ge(001) was used as substrate [7].

In time-of-flight spectra of Helium atoms scattered from the monolayer CO_2/NaCl(001) low-energy loss and gain features were measured (see e.g. Fig. 3). For these experiments monolayer coverage was established at 80 K and than the sample temperature lowered to T_{sample}=30 K in order to suppress the inelastic background.

In the <110> direction five almost dispersion-free modes not present on the bare NaCl(001) surface were followed across the Brillouin zone, their energies being 3.6±0.2, 6±0.2, 7.5±0.2, 11±0.2 and 14.8±0.2 meV, respectively. The modes at about 3.6 and 7.5 meV are the strongest and probably have the largest component normal to the surface. For the (tentative) interpretation of these modes a normal coordinate analysis based on a potential energy calculation can be used [6]: The 3.6 meV loss may be attributed to a 'frustrated rotation', that one at 7.6 meV to a 'frustrated translation'.

First experiments with submonolayers (≥50% of a monolayer) as

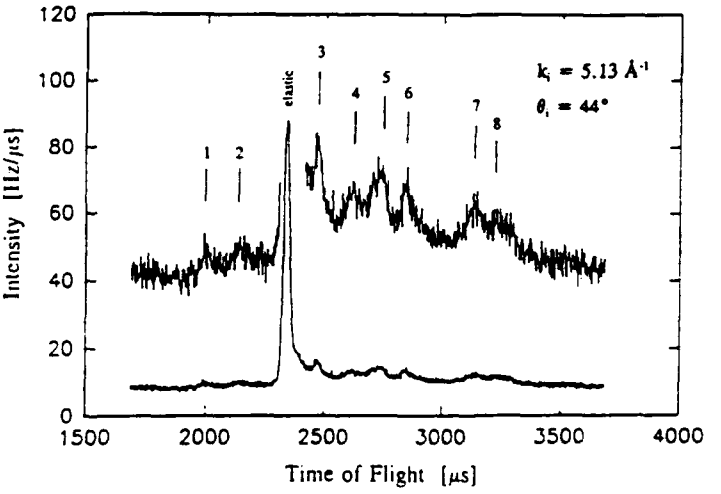

FIG. 3 Time-of-flight distribution of He atoms scattered from a monolayer CO_2/NaCl(001). <110> azimuth, T_{sample}=30 K, k_i = 5.14 Å^{-1}. Peak energies: 7.5 meV (1), 3.7 meV (2), -1.8 meV (3, Rayleigh mode), -3.5 meV (4), -4.6 meV (5), -5.4 meV (6), -7.2 meV (7) and -7.7 meV (8). 1,500,000 t.o.f. cycles.

well as multilayers were carried out, too. The intensity vs. exposure plots as well as diffraction patterns from submonolayers prove the growth of large CO_2 islands, with 450 Å or more in diameter. The CO_2 multilayer, grown on top of the monolayer CO_2/NaCl(001), forms a commensurate c(2x2) structure above an exposure to 170 Langmuir of CO_2. At lower exposures a superposition of the monolayer (2x1) and the multilayer c(2x2) structure can be observed, resulting in a p(2x2) structure.

This brief summary of selected results on adsorption of small molecules on well-defined alkali halide single crystals shall demonstrate that we still can (and have to) learn a lot about these only seemingly simple physisorption systems, which exhibit superstructures commensurate to the substrate, coverage- as well as temperature-dependent phase transitions, island formation and more. In particular, the interplay of two non-destructive methods, Helium atom diffraction and infrared spectroscopy, can widen our knowledge on these systems significantly.

[a] The Helium atom scattering experiments were carried out at the Max-Planck-Institut für Strömungsforschung, Göttingen, Germany. I would like to thank the Max-Planck-Gesellschaft and especially Prof. J.P. Toennies for the hospitality. Financial support by the Fonds der Chemischen Industrie is gratefully acknowledged.

[1] H.H. Richardson and G.E. Ewing, *J. Electron Spectrosc. Relat. Phenom.* **45** (1987) 99; H.H. Richardson, H. Chang, C. Noda and G.E. Ewing, *Surf. Sci.* **216** (1989) 93; C. Noda, H.H. Richardson and G.E. Ewing, *J. Chem. Phys.* **92** (1990) 2099

[2] O. Berg and G.E. Ewing, *Surf. Sci.* **220** (1989) 207

[3] J. Heidberg, K.-W. Stahmer, H. Stein and H. Weiss, *J. Electron Spectrosc. Relat. Phenom.* **45** (1987) 87; J. Heidberg, K.-W. Stahmer, H. Stein, H. Weiss and M. Folman, *Z. Phys. Chem. N.F.* **155** (1987) 223; J. Heidberg, E. Kampshoff, R. Kühnemuth, O. Schönekäs and M. Suhren, *J. Electron Spectrosc. Relat. Phenom.* **54/55** (1990) 945

[4] J. Heidberg, E. Kampshoff and M. Suhren, *J. Chem. Phys.* **95** (1991) 9408.

[5] J. Heidberg, E. Kampshoff, O. Schönekäs, H. Stein and H. Weiss, *Ber. Bunsenges. Phys. Chem.* **94** (1990) 118; J. Heidberg, E. Kampshoff, R. Kühnemuth, O. Schönekäs, H. Stein and H. Weiss, *Surf. Sci.* **226** (1990) L43

[6] J. Heidberg, E. Kampshoff, R. Kühnemuth and O. Schönekäs, *Surf. Sci.* **251/252** (1991) 314

[7] J. Schimmelpfennig, S. Fölsch and M. Henzler, *Surf. Sci.* **250** (1991) 198

[8] J.P. Toennies and R. Vollmer, *Phys. Rev.* **B 44** (1991) 9833

[9] D. Schmicker, J.P. Toennies, R. Vollmer and H. Weiss, *J. Chem. Phys.* **95** (1991) 9412.

Coverage Dependent Desorption Kinetics of CO and H_2 from Rh(111) Using Time-Resolved Specular Helium Scattering[1]

J. I. Colonell, T. J. Curtiss, K. A. Peterlinz, and S. J. Sibener

The Department of Chemistry and the James Franck Institute,
The University of Chicago, Chicago, Illinois 60637

Molecular beam measurements of surface chemical kinetics have traditionally focused on the low coverage regime, where changes in surface coverage during the measurement are necessarily small, so the kinetics are linear and the analysis is tractable. However, real world surface reactions often occur under conditions of finite coverage Also, the coverage dependence of the kinetics provides fundamental information about interadsorbate interactions. Rate constants measured under isothermal, isosteric conditions may be compared directly with calculated rate constants from simple models which incorporate interadsorbate interactions.

Isothermal, isosteric rate constants have been measured using a unique three beam apparatus. One beam is used to establish a steady state coverage on the surface. A second modulated beam perturbs the coverage slightly from the equilibrium value: the perturbation is kept small so that the kinetic response is linear, and Fourier analysis is practical.[1,2] The time-resolved specular signal from a third He beam monitors the coverage response to the perturbation, a method which offers a number of advantages. Fourier transform analysis of the He waveform yields the rate constant for desorption at the equilibrium coverage and given surface temperature.

The specular He signal is strongly dependent on the presence of adsorbates, as well as the structure of the overlayer, and thus acts as a non-destructive *in situ* probe of the coverage and phase behavior on the surface. In Figure 1, He reflectivity is plotted as a function of coverage for the CO/Rh(111) and H/Rh(111) systems. The rapid decay of the reflectivity with CO coverage is due to the large cross section of CO for diffuse He scattering. The data is well represented by the Poelsema-Comsa model for diffuse scatterers with repulsive interadsorbate interactions.[3] The hydrogen overlayer, in contrast, scatters He specularly as well as diffusely, and the reflectivity vs. coverage curve is dominated by interference effects between He reflected by the Rh substrate and the H

[1]This work was supported in part by the Office of Naval Research and by the NSF Materials Research Laboratory program at the University of Chicago

overlayer. In both cases, the sensitivity of the He reflectivity to small changes in coverage amplifies the kinetic response by up to two orders of magnitude: for example, in a typical measurement for the CO system, a 0.6% change in the CO coverage translates into a 20% change in the He reflectivity.[4] In addition, the high signal to noise ratio for He detection allows even very slow changes in the coverage to be measured, where the desorption rate is so small that measuring product waveforms is impossible.

Using this method, rate constants have been measured for the CO/Rh(111) system at a series of coverages and temperatures[4]: Arrhenius plots of these data are shown in Figure 2. These rate data compare well with theoretical calculations made using an imperfect two dimensional lattice gas model yielding quantitative estimates of interadsorbate interactions out to the third nearest neighbor.[5]

This method is currently being extended to the H/Rh(111) system. The large value of the He reflectivity for both the clean surface and the near saturation hydrogen overlayer allow sensitive coverage measurements over a very broad coverage range and tempertures ranging from 220 to 400 K. Preliminary results[6] indicate that the coverage dependence of the second order rate constant is much weaker than suggested by thermal desorption spectra[7]; however, the general trend of increasing rate constant with coverage, characteristic of repulsive interadsorbate interactions, is confirmed. Further extensions of the method to probe coverage dependent oxidation reactions are also underway.[8]

References

1. D. F. Padowitz and S. J. Sibener, J. Vac. Sci. and Technol. A 9 (1991) 2289.

2. H. H. Sawin and R. P. Merill, J. Vac. Sci. and Technol. 19 (1981) 40.

3. B. Poelsema and G. Comsa, *Scattering of Thermal Energy Atoms from Disordered Surfaces* (Springer, New York, 1989).

4. K. A. Peterlinz, T. J. Curtiss, and S. J. Sibener, J. Chem. Phys. 95 (1991) 6972.

5. S. H. Payne, H. J. Kreuzer, K. A. Peterlinz, T. J. Curtiss, C. Uebing, and S. J. Sibener, Surf. Sci. (in press).

6. J. I. Colonell, T. J. Curtiss, and S. J. Sibener, to be published.

7. J. T. Yates, Jr., P. A. Thiel, and W. H. Weinberg, Surf. Sci. 84 (1979) 427.

8. D. F. Padowitz, K. A. Peterlinz, and S. J. Sibener, Langmuir 7 (1991) 2566.

Fig. 1. (a) He reflectivity plotted as a function of CO coverage. The solid line is a fit to the data using the Poelsema-Comsa model: reflectivity = $(1 - m\theta_{CO})^{\Sigma_{CO}\eta/m}$ with Σ_{CO}= 148 Å^2, η = .13 Å^2 (known from Rh lattice spacing), and m = 3.163. (b) He reflectivity as a function of hydrogen coverage.

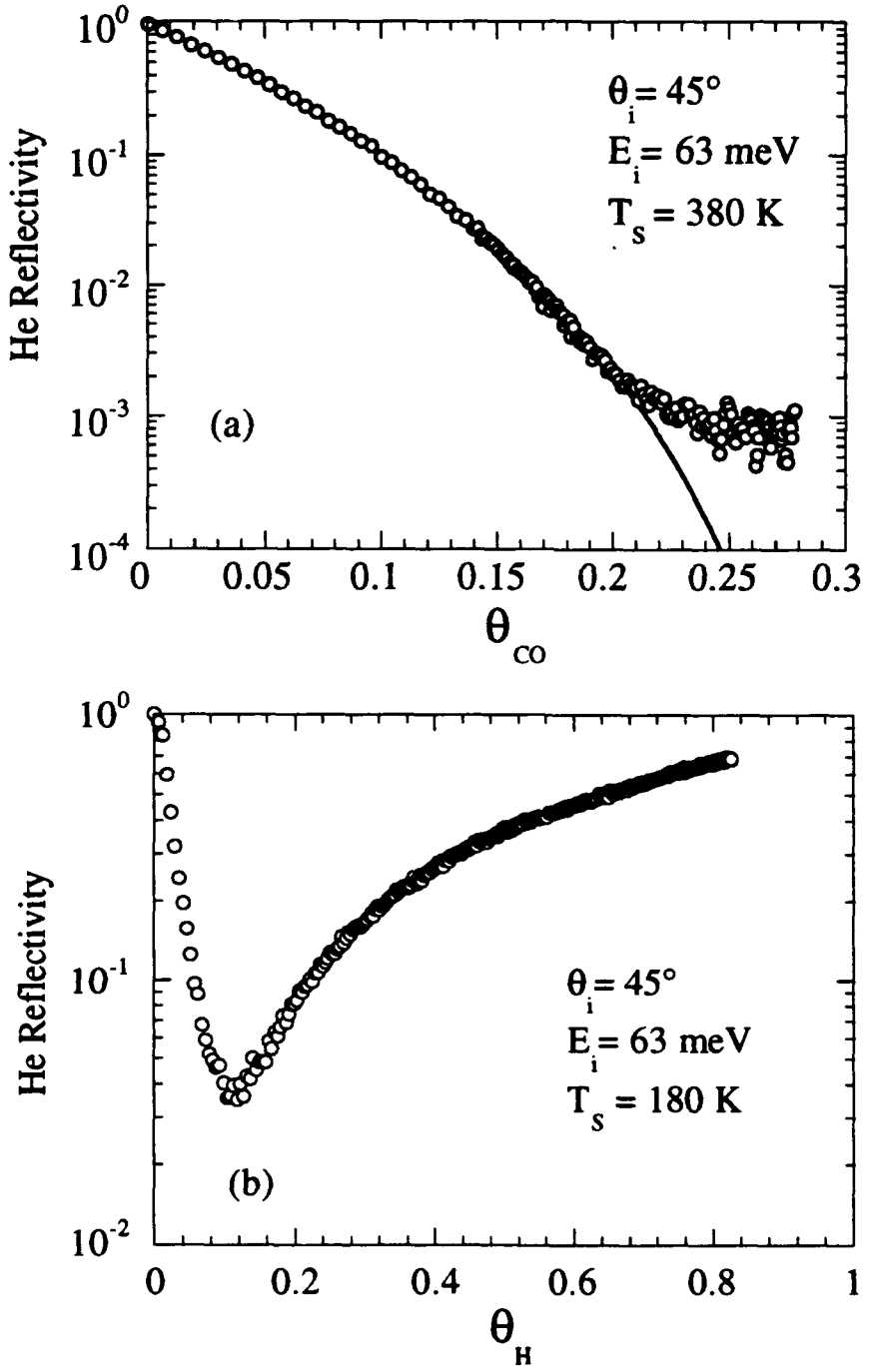

Fig. 2. Arrhenius plots of CO desorption rate constants derived from time resolved He scattering measurements.

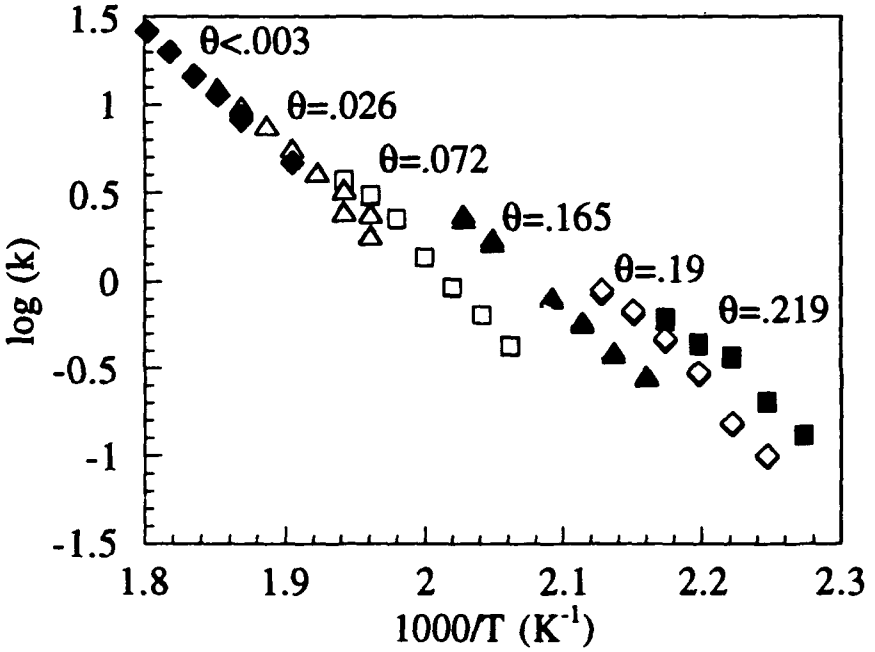

Aluminum Chemical Vapor Deposition and Surface Topographical Changes as Monitored by Helium Atom Diffraction.

B.J. Hinch[a], R.B. Doak[b] and L.H. Dubois[c].

[a] *Dept. of Chemistry and Laboratory for Surface Modification, Rutgers University, Piscataway, NJ 08855.*

[b] *Dept. of Physics and Astronomy, Arizona State University, Tempe, AZ 85287.*

[c] *AT&T Bell Laboratories, Murray Hill, NJ 07974.*

Aluminum was deposited by chemical vapor deposition (CVD) on an Al(111) surface, using trimethylamine alane (TMAA). He atom diffraction is a very surface and defect sensitive experimental technique and was used to look at this deposition system. In the past, layer by layer growth, step flow and 3-dimensional growth modes have been identified (using this experimental technique) for evaporation of metals on metal substrates[1-3]. More recently evaporated alkali halides have also been studied[4]. He diffraction is now applied to the study of *in situ* CVD processes.

The reaction kinetics of the growth of aluminum thin films from the pyrolysis of trimethylamine alane ($(CH_3)_3N{\cdot}AlH_3$ or TMAA) has received some detailed attention[5,6]. The reaction pathway is summarized in the following equations:

$$(AlH_3.TMA)_g \leftrightarrow (AlH_3.TMA)_{ads} \leftrightarrow (AlH_3)_{ads} + (TMA)_{ads}$$

$$\downarrow \qquad \downarrow$$

$$(Al)_s + \frac{3}{2} H_{2(g)} \leftarrow (Al)_s + 3(H)_{ads} \qquad (TMA)_g$$

The reaction proceeds by the dissociation of TMAA on the surface to TMA and adsorbed alane (AlH_3). The trimethylamine by-product ($N(CH_3)_3$ or TMA) desorbs easily from Al surfaces at T ≈ 320K. H_2 also desorbs readily at this temperature. At elevated temperatures the rate limiting step for aluminum deposition on aluminum is the dissociation of the Al-N bond. Al deposition is very clean at temperatures in excess of 350K.

All experiments were performed in an helium atom diffraction apparatus, which has been discussed in detail elsewhere[7]. TMAA exposures were made through a long 6mm stainless steel tube ending ~ 6cm from the crystal surface. Pressure rises in the sample

chamber, as measured by an ionization gauge, reached a saturation value of 2×10^{-6} torr. Although we could not ascertain the absolute exposures of the sample to TMAA, we are able to give an upper limit to the standard deposition rate at *high* surface temperatures (≥ 400K) of 15Å/min.

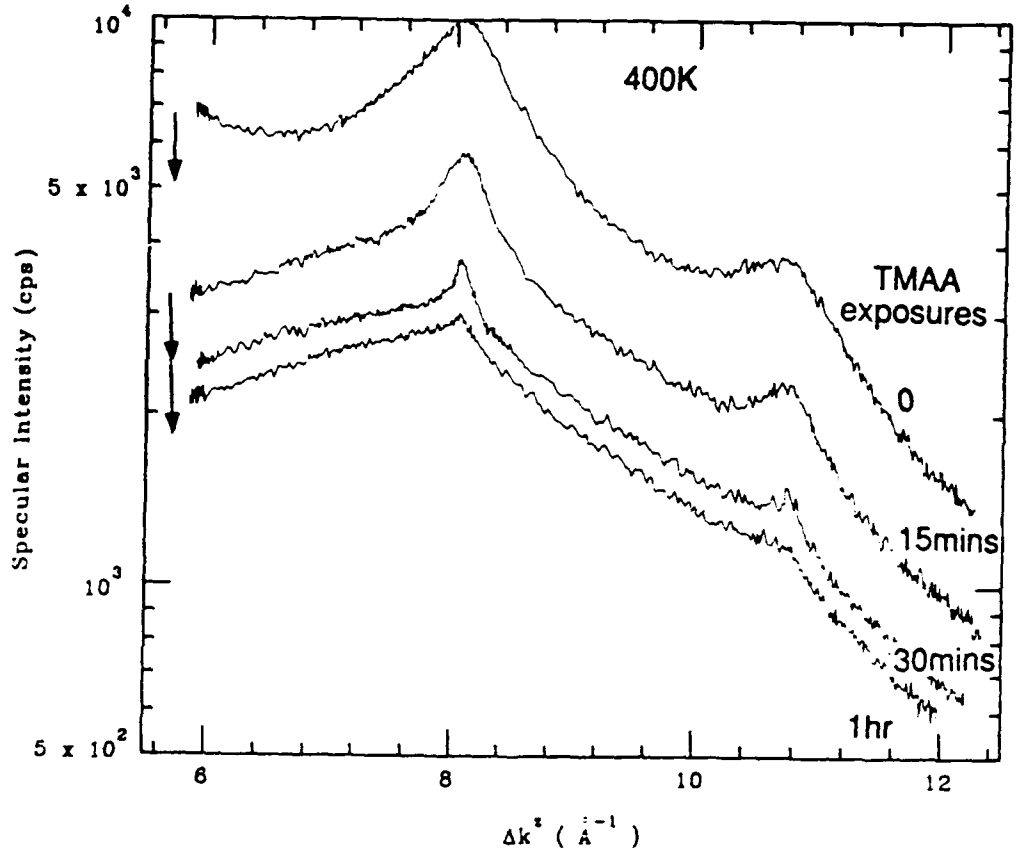

Fig. 1. Drift scans before and after TMAA exposures. The specularly reflected He atom intensities were measured from Al(111) at 400K. Each "drift" scan was taken with varying incident wavevector, ki, and/or perpendicular momentum transfer,. Δk^z, in the range $5.7\text{Å}^{-1} < k_i = \Delta k^z < 12.5\text{Å}^{-1}$. For clarity, each successive curve is offset (lowered) by a distance indicated by the arrows on the left. The upper curve was measured from the clean Al(111) surface. Lower scans were made after subsequent TMAA exposures (as indicated on the right). TMAA overpressures were identical for each exposure.

At 310K the chemical vapor deposition process was inhibited by adsorbed TMA on the surface. TMAA exposures produced an exponential decay in the specularly reflected He atom intensity. These intensity decays are indicative of a very slow surface contamination process with rates of order $\sim 10^{-3}$ MLmin^{-1}. This extremely low contamination rate decreases with increasing surface temperature.

At higher temperatures, when CVD is no longer inhibited, only very small specular intensity decays were observed. Intensity oscillations were not seen and a step-flow growth mode is implied.

The so called "drift" scans, illustrated in Fig. 1, show that terrace widths and step edge height distributions change during CVD film growth. At 400K, the characteristic shape of the drift scans, (plotted on a logarithmic scale), changes during exposure to TMAA.

The clean, "as prepared," Al surface always contains finite width terraces separated by steps of well defined step heights, nh_o, (where n is integral and h_o is the height of a monatomic step). Under the Bragg or in-phase kinematic conditions, the scattering between all adjacent surface terraces is coherent. These conditions show up as maxima in the drift spectra. At intervening Δk^z values the scattered helium from different terraces does not scatter in-phase and the net intensities are reduced.

Estimates of "one-dimensional" step densities were made by comparison with simulated drift spectra. For the modelling, one-dimensional geometric terrace length distributions and geometric step edge height distributions were assumed[8].

An equivalent one dimensional step density, for the upper curve in Fig. 1, is ~1/1700Å. This curve shows the broadest maxima implying that a large proportion of the steps were monatomic, of height h_o=2.338Å. The simulations suggest an average step height $\sim 1.7h_o$. The subsequent TMAA exposures, at 400K, increased the step height to $\sim 5h_o$, and the step density finally decreased to ~ 1/3100Å.

The clean, well-annealed Al surface is stepped and influenced strongly the observed Al growth mode. A step flow growth mode occurred as diffusion to a step edge (of either the reagent or an Al adatom) occurred more readily than nucleation of new Al islands.

The significant increase in average step height due to TMAA exposure data is the natural result of a step flow growth mode and step edge bunching, caused by non-uniform step-edge flow velocities. As steps of smali (perhaps monatomic) heights merge, fewer and higher step edges are formed. This represents the onset of microfacet formation.

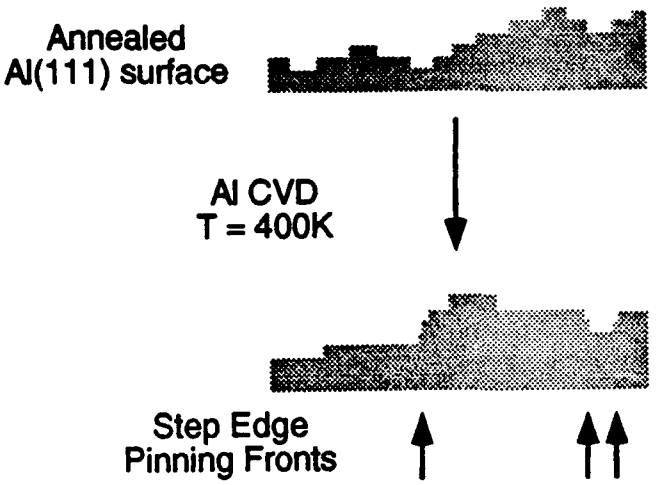

Fig. 2. Schematic topographical changes during CVD at 400K. N.B. The vertical scale is greatly exaggerated.

We believe that pinning of step edges at or around large fixed defects promotes the "piling up" of step edges during growth of Al(111) from CVD at 400K. Steps edges flow (at 400K) until they merge with the growing microfacets. Fig. 2 displays the results of CVD, *step flow growth* and a low density of step edge pinning centers. As drawn, three pinned step fronts are illustrated.

Annealing to 650 to 700K restores a TMAA-exposed Al surface to its initial surface topography. At temperatures of 500K or higher the unpinning of defects is initiated; the surface anneals out and more regularly spaced monatomic step edges are restored.

References

1. R. Kunkel, B. Poelsema, L.K. Verheij and G. Comsa; Phys. Rev. **B65** (90) 733.
2. J. Ferron, J.M. Gallego, A. Ceballada, J.J. de Miguel and S. Ferrer; Surface Science **211/212** (89) 797.
3. B.J. Hinch, C. Koziol, J.P. Toennies and G. Zhang; Euro. Phys. Let. **10** (89) 341.
4. J. Duan, G.G. Bishop, E.S. Gillman, G. Chern, S.A. Safron and J.G. Skofronick; private communication.
5. L.H. Dubois, B.R. Zegarski, C.-T. Kao and R.G. Nuzzo; Surface Science **236** (90) 77.
6. M.E.Gross, L.H. Dubois, R.G. Nuzzo and K.P. Cheung; Material Research Symposium Proceedings (90).
7. R.B. Doak and D.B. Nguyen; Rev. Sci. Instrum. **59** (88) 1957.
8. T.-M. Lu and M.G. Lagally; Surface Science **120** (82) 47.

Interaction Dynamics of Hydrogen at a Cu(111) Surface

D.J. Auerbach, C.T. Rettner, and H.A. Michelsen*
IBM Research Division, Almaden Research Center, San Jose, CA 95120, USA
* Dept. of Chemistry, Stanford University, Stanford, CA 94305, USA

The hydrogen/copper system has served as an important model system in the development and testing of a microscopic picture of surface chemical reactions. This system was first studied almost 150 years ago[1] and was used as an example by Lennard-Jones[2] in his classic paper on the "nature of" the adsorption process of molecules on metal surfaces. Hydrogen chemisorbs to copper surfaces as atoms, i.e it undergoes dissociative adsorption. Dissociative adsorption, quite common in the chemisorption of molecules at surfaces, is one of the simplest of surface chemical processes. It involves the breaking of a single intra-molecular bond and formation of new bonds between the surface and the resulting fragments.

Dissociative adsorption of hydrogen at copper surfaces is activated, i.e. there is an activation barrier between the molecular and chemisorbed states. The dynamical consequences of this barrier are dramatic. The probability for dissociative adsorption is a strong function of energy, angle, and internal state of incident molecules. Likewise, the energy, internal state and angular distribution of the products of the reverse reaction, associative desorption, are strongly non-statistical due to the influence of the barrier. Thus measurements of the energy requirements and energy disposal in this system bare directly on the underlying dynamics and provide a sensitive means for probing the size, location and nature of the barrier.

We use molecular beam and laser detection techniques to study the dynamics of both adsorption and desorption of H_2 and D_2 at a Cu(111) surface. These studies provide state specific information about dissociative adsorption. We will also report on progress towards the simultaneous measurement of angular, velocity and internal state distributions of the products of associative desorption.

Figure 1 shows measurements for the initial adsorption probability, S_0, of D_2 on Cu(111) at a surface temperature of 120 K for molecules with kinetic energies up to 0.85 eV, vibrational temperatures up to 2100 K, and incidence angles from 0° to 60°. S_0 is plotted as a function of the mean kinetic energy associated with motion normal to the surface $E_n = E_i \cos^2\theta_i$. S_0 increases by a factor of $> 3 \times 10^5$ over the range of conditions employed, which we believe is the largest such effect reported to date. The curves labeled with nozzle temperatures correspond to measurements with beams of pure D_2 and several anti-seeded mixtures of D_2 at four incidence angles, as indicated. For $T_n = 2100$ K, the results of two experiments with D_2 seeded in H_2 are also shown. The curve labeled "pure D_2" corresponds to measurements performed with nozzle temperatures ranging from 875 to 2100 K for beams at normal incidence.

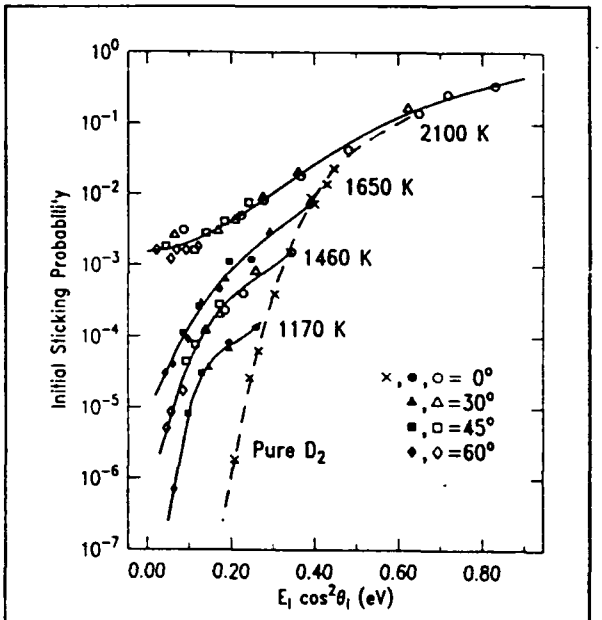

Fig. 1. Initial adsorption probability of D_2 on Cu(111) plotted as a function of the energy associated with motion normal to the surface for the incidence conditions indicated.

The dramatic dependence of S_0 on both E_n and T_n is a direct indication that both translational and internal energy play an important role in overcoming the barrier to adsorption. In principle, changes in T_n can affect the results through changes in both the vibrational and rotational state distributions of the beam. We expect, however, that the sticking probability is relatively insensitive to rotational energy based on detailed balance arguments[3] and the rotational state distributions that have been reported for recombinative desorption.[4] Thus we believe that the variation of S_0 with T_n at a given energy reflects the changing vibrational populations in the beam. The picture that emerges is that $D_2(v=3)$ determines S_0 at the lowest energies used here, and contributions from $D_2(v=2)$, $D_2(v=1)$, and $D_2(v=0)$ successively become significant as the energy is increased. A detailed analysis provides adsorption probability functions for molecules in individual vibrational states, $v=0$ to $v=3$.

We also measure the internal state distribution of molecules scattered from the surface, which provides direct state-resolved information on both adsorption and vibrational excitation. In these studies we use a molecular beam tailored to have a large spread in velocities. Information on the energy dependence of specific processes is gained by varying the delay of the laser pulse with respect to the mechanical chopping of the beam, so that high energy species are detected at early times. Time-of-flight (TOF) distributions recorded in this manner have a form derived from the kinetic energy distribution of the incident species folded with functions for the loss and gain of the specific quantum state as a function of energy. The form of the distributions is thus sensitive to losses due to dissociation and to vibrational excitation out of a given state and gains due to transitions into that state.

Such losses and gains are indeed observed as is illustrated in Fig. 2, which displays TOF distributions for D_2 recorded with the laser tuned to detect the $v=1$, $j=4$ state. To observe losses or gains, we compare the TOF distributions of the incident beam (Fig. 2a) with those recorded after scattering (Fig. 2b). Fig. 2a actually shows the TOF of the beam after scattering from a surface saturated with deuterium. We find such data to be indistinguishable from direct beam data recorded at the same total chopper to laser distance.

The TOF distribution after scattering from the bare surface (Fig. 2b) is clearly bimodal. This distribution shows dramatic examples of both loss and gain of intensity relative to the TOF distribution of the beam. For the lowest energies (longest times) the two distributions are similar. As the energy increases, a loss is seen above about 0.35 eV. Above about 0.6 eV a second peak in the TOF distribution emerges. *We attribute this additional peak to the excitation of high energy (early) $v=0$ species to the $v=1$ state.* Note that the $v=0$

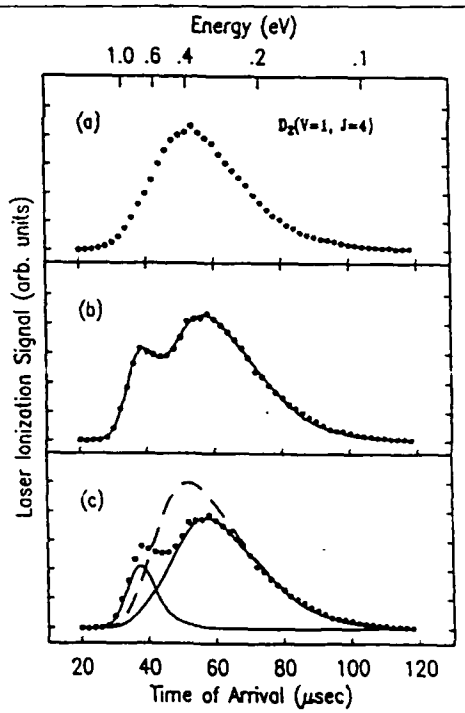

Fig. 2 Time-of-flight (TOF) distributions of $D_2(v=1, j=4)$ molecules detected after scattering from a Cu(111) surface: (a) scattering from a D-saturated surface which is indistinguishable from the incident beam; (b) scattering from the bare surface; (c) a comparison of (a) and (b) scaled to agree at long times.

population is much greater than that for v = 1 so that the excitation of a small fraction of the v = 0 species can result in a sizable v = 1 peak. This same behavior has been observed for many different beams with essentially the same result. The additional peak at early times has a constant energetic threshold and is only clearly apparent for beams with a high energy tail extending above ~1 eV.

Figure 2c shows a direct comparison of the beam TOF distribution (dashed curve) and the scattered TOF distribution, scaled to agree at low energy. The curve on Fig. 2b shows the result of a fit to the data, consisting of two components, which are displayed in Fig. 2c. The fitting procedure assumes that the v = 1 signal is composed of two terms: a term $(1 - P_{loss})f_i(t)$ representing loss via adsorption or inelastic scattering out of the v = 1 state, and a term $(P_{gain})\,F_B(T_s)f_i(t)$ representing gain via inelastic scattering from the v = 0 to the v = 1 state; $f_i(t)$ is the TOF distribution of incident species and $F_{(T_s)}$ is a Boltzmann factor giving the ratio of v = 0 to v = 1 species. We take the probability of both P's to be of the form[3]

$$P = \frac{A}{2}\left(1 + \tanh\left(\frac{E_i \cos^2\theta_i - E_0(v)}{W(v)}\right)\right). \qquad (1)$$

Here E_i and θ_i are the energy and angle of incidence. The fitting procedure involves a separate calculation for each measured point in the TOF distribution. It allows for the change in velocity that accompanies vibrational excitation and the fact that signals are proportional to the density, rather than flux, of scattered molecules. It also includes a convolution over the 6 μs chopper function. The parameters are adjusted by a non-linear least squares procedure to achieve the best overall agreement with the data.

This work has been complemented by studies of the desorption dynamics. Angular distributions for desorption have been measured for a range of surface temperatures. These distributions are found to be strongly peaked and symmetric about the surface normal. The temperature variation of desorption angular distributions gives information (via detailed balance) on the influence of surface temperature on the adsorption probability. We will also report on progress towards measuring the velocity distributions molecules desorbing in specific quantum states.

[1] J. B. A. Dumas, *Ann. de Chim. et de Phys. III* **8**, 189 (1843).
[2] J. E. Lennard-Jones, *Trans. Faraday Soc.* **28**, 333 (1932).
[3] H. A. Michelsen and D. J. Auerbach, *J. Chem. Phys.* **94**, 7502 (1991).
[4] G. D. Kubiak, G. O. Sitz, and R. N. Zare, *J. Chem. Phys.* **83**, 2538 (1985).

Poster Session

Molecular Beam Studies of the Photodissociation of Silane 157 nm

Deon S. Anex, Albert Stolow and Yuan T. Lee
Chemical Sciences Division
Lawrence Berkeley Laboratory and
Department of Chemistry, University of California
Berkeley, California 94720

ABSTRACT

The 157 nm photodissociation of silane beam was studied using photofragmentation translational spectroscopy. Silane, seeded in helium, was expanded to form a molecular beam and crossed with the output of an F_2 laser. By measuring the translational energy distributions of the SiH_n products, the primary reaction pathways were elucidated. The relative importance of H atom loss and H_2 molecular elimination are discussed, as well as the formation of silicon atoms. The present results are compared to previous bulk gas studies.

Quasiclassical state resolved cross sections for the reaction $D + H_2(v = 0, j = 0) \rightarrow HD(v', j') + H$. Evidence for classical collision complexes

F.J. Aoiz*, V.J. Herrero† and V. Sáez Rábanos‡

*Departamento de Química Física. Facultad de Química.
Universidad Complutense. 28040 Madrid, Spain.

† Instituto de Estructura de la Materia (CSIC).
Serrano 123. 28006 Madrid, Spain

‡ Departamento de Química General y Bioquímica. ETS Ingenieros de Montes
Universidad Politécnica. 28040 Madrid. Spain

The possibility of performing experimental measurements[1] that would demostrate the existence of scattering short lived complexes (resonances) in the $D + H_2(v = j = 0) \rightarrow HD(v', j') + H$ reaction, has awoken once more the interest in this proto-typic system.

The expected (broad) resonances should be manifest as structures in the evolution with energy of the rotationally (j') state resolved differential cross sections for low j'. These perspectives have stimulated us to carry out a detailed comparison of quasiclassical state resolved cross sections with exact quantum mechanical (QM) ones[3,4] in order to discern the purely quantum from the classical effects in these structures.

The (final) vibrationally state resolved cross sections from quasiclassical trajectory (QCT) calculations are qualitatively similar to the QM ones converged in the values of the total angular momentum (J). For the $v' = 0$ case, at collision energies higher than 0.6 eV the absolute values are 10–15% lower in the QCT case. As expected the well known resonance structure in the evolution of the reaction probability for $J = 0$ with energy is absent in the classical calculations.

The j' state resolved differential cross sections from QCT and QM calculations also show a similar trend with some differences (see Fig 1). The angular distributions for the lower j' are predominantly backward but they have forward tails, that become even small secondary maxima with increasing collision energy (E_T) (These forward components of the angular distributions are responsible for the resonance structure mentioned). With

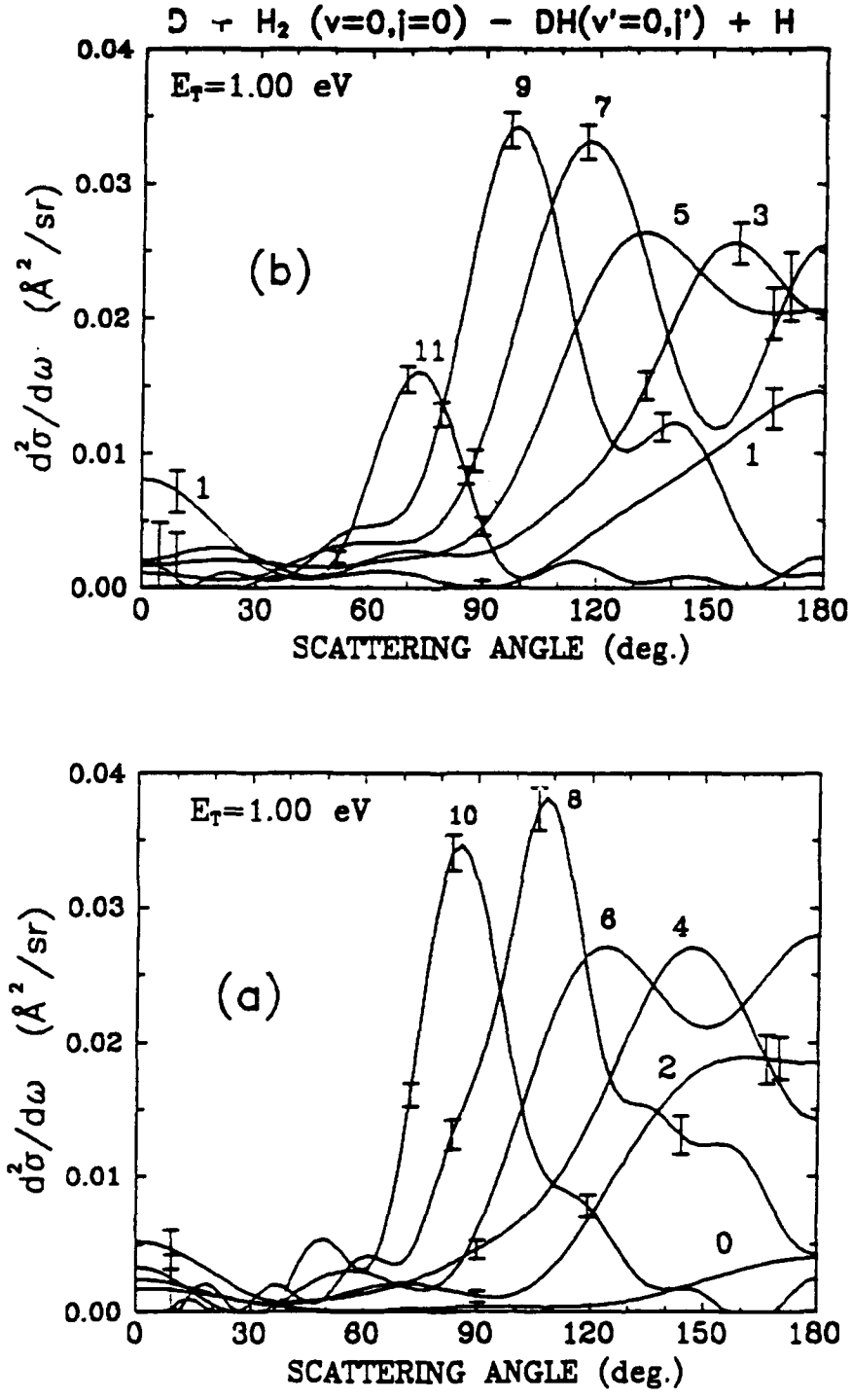

Fig 1 State resolved solid angle differential cross section at $E_T = 1.00$ eV for the title reaction. Cross sections for even (a) and odd (b) j' are displayed in separate panels for clarity. It is worth to notice the forward peak that is only present at low $j'(j' \leq 3)$. These results are to be compared with QM results at the same energy shown in fig 22 of ref. 3 and fig 9 of ref. 4.

growing j' the distributions become more sideways but loose the forward contribution. The QCT results correspond to j' distributions hotter by one or two quanta.

Most interesting, the QM "ridge" structure[2] present in the evolution of the rotationally resolved differential cross section for low j' with E_T, is also present though not so sharp in the QCT calculations[5].

An analysis of the classical trajectories leading to HD molecules in this "ridge" shows them to be associated with short lived (15–30 fs) "classical" complexes with large amplitude bending oscillations of the D–H–H angle during the reactive encounter.

References

[1] M.J.J. Vrakking, A.S. Bracker and Y.T. Lee, XIII International Symposium on Molecular Beams. El Escorial, Madrid, Spain, 2–7 June 1991. Book of abstracts p. 1–4.

[2] W.H. Miller and John Z.H. Zhang, J. Phys. Chem. 95, 12 (1991).

[3] J.Z.H. Zhang and W.H. Miller, J. Chem. Phys. 91, 1528 (1989).

[4] M. Zhao, D.G. Truhlar, D.W. Schwenke and D.J. Kouri, J. Phys. Chem. 94, 7074 (1990).

[5] F.J. Aoiz, V.J. Herrero and V. Sáez Rábanos, J. Chem. Phys. 95, 7767 (1991).

MAGNETIC ANALYSIS OF MOLECULAR BEAMS IN THE TRANSMISSION MODE: ZEEMAN EFFECT FOR DIATOMIC MOLECULES*

V.Aquilanti, R.Candori, D.Cappelletti, E.Luzzatti, and F.Pirani

Dipartimento di Chimica dell'Universitá, 06100 Perugia, Italy

Magnetic selection techniques have been applied to molecular beams since early days [1], but little of direct chemical interest has been done since then, in particular regarding the characterization of molecular properties [2]. Although magnetic deflection is considered an important state selection by nonoptical method [3], it has been applied only to a limited number of scattering experiments [4].

Our experimental apparatus, shown in Fig (1), employed this selection technique to obtain the magnetic sublevel population in open shell atomic beams, through the analysis of the beam transmittance across the magnetic selector [5]. Using this technique it has been possible to measure the total cross section, for scattering of open shell atomic beam with rare gases and simple molecules, under controlled populations of the involved magnetic sublevels: these studies have allowed to extend the characterization of the involved interactions also to their anisotropic component [6].

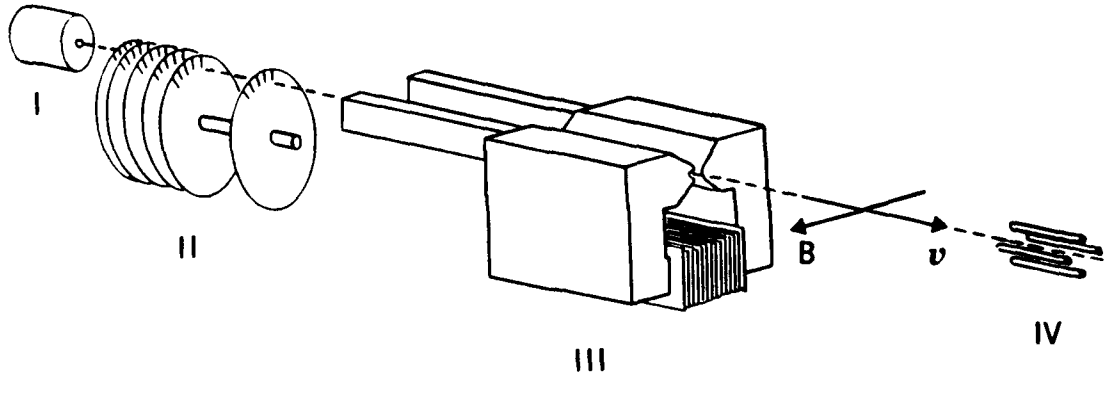

Figure (1) - Schematic view of the apparatus used in the present experiments: I source of the beam, II velocity selector, III Stern-Gerlach magnetic selector, IV quadrupole mass filter.

This work presents a novel application of the technique to study the magnetic properties of molecules under different rotational temperature conditions. In this experiments we measure the beam *transmittance*, across the magnetic selector, at different magnetic field strengths and as a function of the beam velocity. The use of molecular beam magnetic resonance spectrometers, which was operated in the flop-out method [7, 8], allowed the determination of rotational and spin-rotational temperatures of pure beams, after supersonic expansion conditions: from deflection patterns only low rotational states could be probed.

Results obtained on a test case, $O_2(^3\Sigma)$ are reported in Figs (1-2): the beam transmittances show slope changes as a function of both the magnetic field intensity B and the beam velocity v.

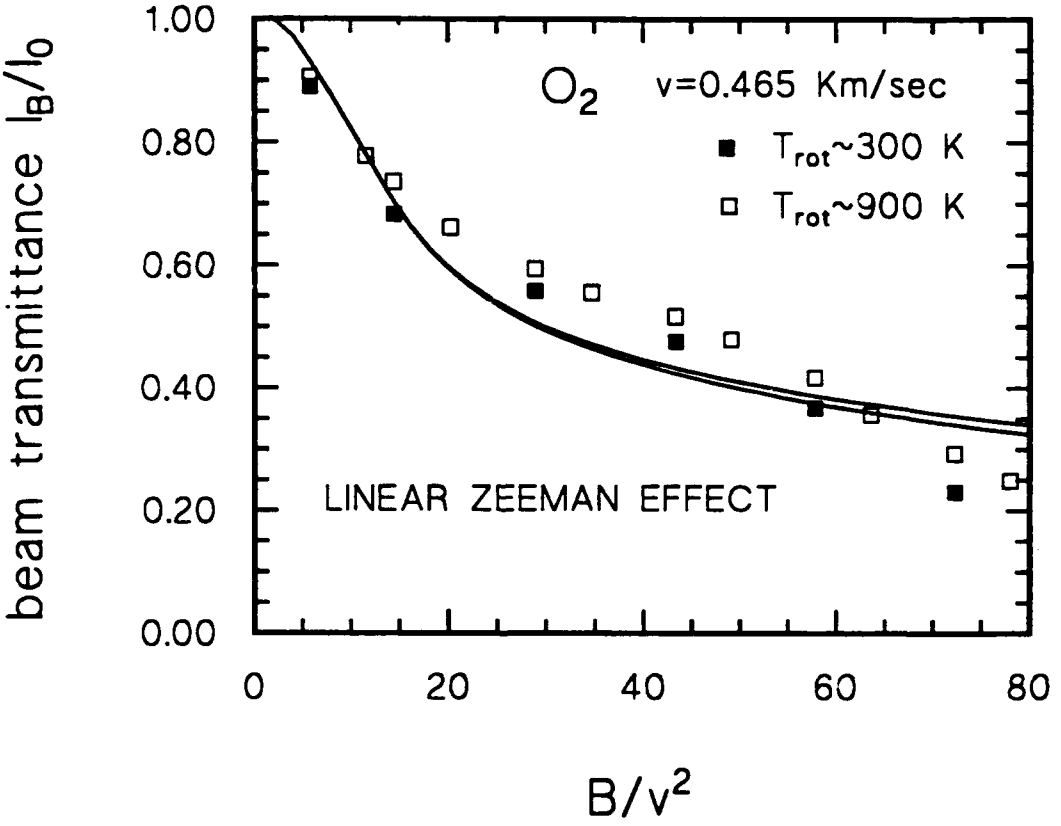

Figure (1) - Transmittance I_B/I_0 of a O_2 molecular beam, at two different rotational temperatures (900 and 300 K), as a function of the reduced parameter B/v^2. The experimental data are taken at a very low beam velocity and therefore at relatively low magnetic field intensities ($B \leq 2$ KG). The solid line is a calculation assuming only the linear Zeeman effect as obtained with a perturbative approach in ref. [9].

An analysis which takes into account the molecular magnetic moments depending on the Zeeman energies calculated using the formulas explicitly reported in ref [9] where they are obtained with a perturbative approach suggests that the different slopes are due to the change of relative contributions of linear and quadratic Zeeman effects as a function of the magnetic field.

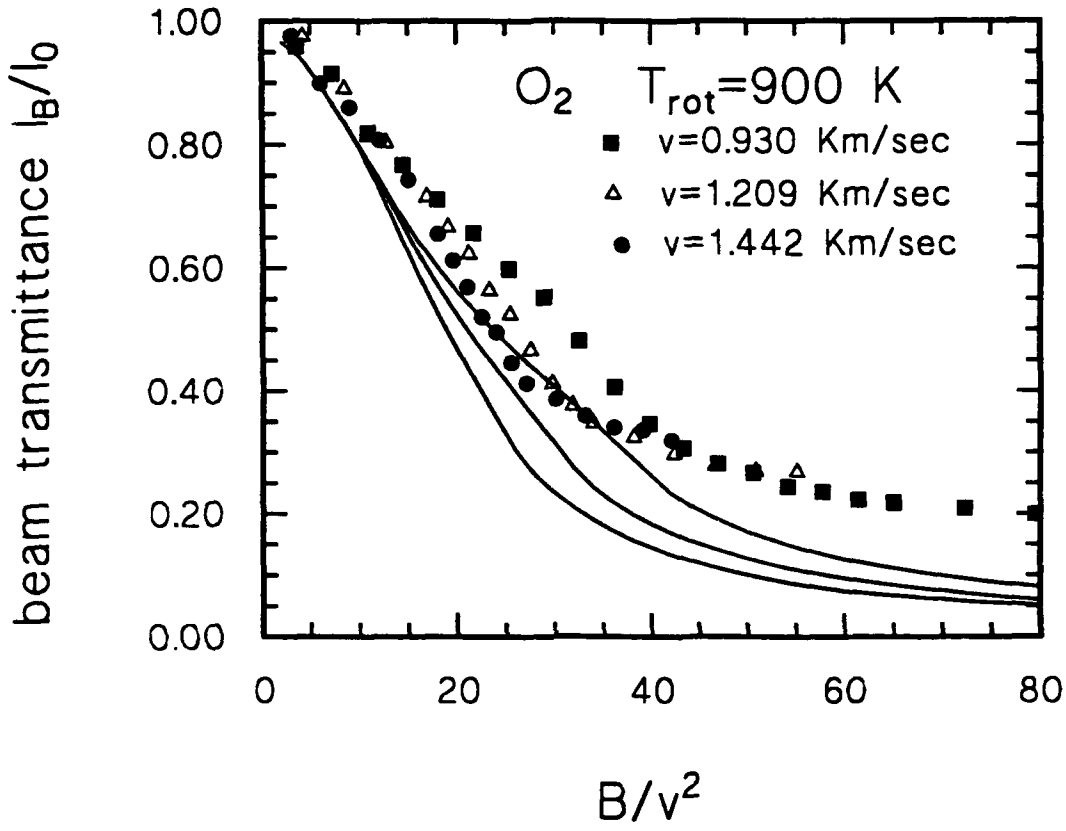

Figure (2) - Transmittance I_B/I_0 of a O_2 molecular beam, from a discharge in pure O_2 ($T_rot \sim 900$K), as a function of the reduced parameter B/v^2. The experimental data are taken at different beam velocities using magnetic field intensities up to 10 KG. The solid lines are calculations assuming the linear plus the quadratic Zeeman effects as obtained with a perturbative approach in ref. [9].

The poor quantitative agreement indicates that the assumed *diabatic* behavior of Zeeman energies is not adequate expecially when, as in our case, high rotational levels are involved: a more quantitative description must consider the *adiabatic* energies and include nonadiabatic effects.

This is in progress, and will permit to extend the technique to cases which cannot be studied otherwise, such as of excited molecular nitrogen produced in a microwave discharge and presumably in the metastable $^3\Sigma$ state.

References

[1] N.F.Ramsey , *Molecular Beams*, Clarendon Press, Oxford (1969).

[2] See for example D.R.Herrick, M.B.Robin, and A.Gedanken, *J.Mol.Spectry.* **133** (1989) 61.

[3] J.Reuss, in *Atomic and Molecular Beams Methods*, ed. G.Scoles (Oxford, New York, 1987), p.276, and references therein.

[4] S.Stolte, in *Atomic and Molecular Beams Methods*, ed. G.Scoles (Oxford, New York, 1987), p.631, and references therein.

[5] V.Aquilanti, R.Candori, D.Cappelletti, V.Lorent, and F.Pirani, *Chem.Phys.Lett.* in press (1992).

[6] V.Aquilanti, R.Candori, D.Cappelletti, G.Liuti, and F.Pirani, this book of abstract.

[7] A.Amirav and G.Navon, *Chem.Phys.* **82** (1983) 253.

[8] J.Mettes, B.Heigemen, J.Reuss, and D.C.Lainé, *Chem.Phys.* **87** (1984) 1.

[9] J.M.Hendrie and P.Kusch, *Phys.Rev.* **107** (1957) 716.

*Presented at the *XIV Symposium on Molecular Beams*, Asilomar, California, June 1992.

INTERATOMIC FORCES OF CHLORINE ATOMS WITH RARE GASES, HYDROGEN AND METHANE*

V.Aquilanti, D.Cappelletti, G.Liuti, V.Lorent and F.Pirani

Dipartimento di Chimica dell'Universitá, 06100 Perugia, Italy

The characterization of the structure and the dynamics of weakly bound complexes, involving open shell species such as oxygen and halogen atoms, is motivated by several reasons. For the rare gas oxides and halides, which are responsible for excimer laser action in the UV region, the electronically excited states are better known than the weakly bound ground states, in spite of the fact that their features affect the structure of the band emissions. In addition, the study of the low lying states of these molecular complexes is very interesting also to understand the peculiar nature of the involved bonds [1], the transport properties of open shell atoms in nonreactive baths and the selective role of long range forces in chemical reactivity [2].

Recent advances in the quantum mechanical treatment of open shell atom collisions [3, 4] allow to use scattering cross sections as fundamental data for the characterization of the involved interactions. Considerable experimental progresses in this direction are achieved by coupling molecular beam techniques and state analysis of the magnetic sublevels of the open shell atomic beam; in particular, for ground state atoms, the analysis using magnetic field is the technique of choice.

In general the state analysis is important to characterize and to change in a controlled way the weights of the magnetic sublevels of the open shell atom which correlate, at short interatomic distances, with different molecular states of the collision complex.

Elsewhere [5] we applied the magnetic selection technique to analyze halogen atom beams and exploited the possibility to obtain selected beams essentially composed by atoms in the upper fine structure level $J=1/2$. We are applying this selection method to measure integral cross section for scattering of chlorine atoms by rare gases and simple molecules.

In this paper we report experimental results for the $Cl(^2P_J)$-rare gases, $Cl(^2P_J)$-H_2 and

CH_4 systems. In Fig (1) are shown, as an example, the integral cross sections for the Cl-Xe case [6].

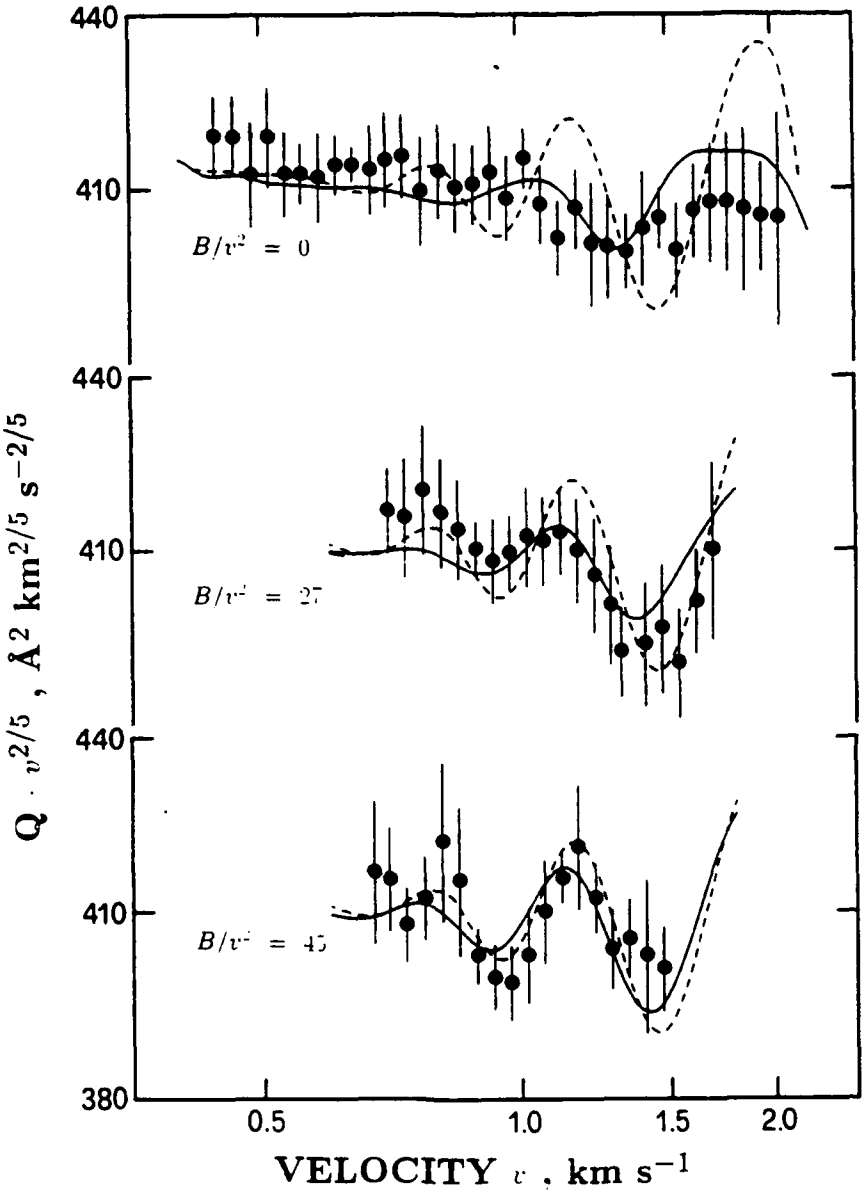

Figure 1 - Absolute integral cross sections $Q(v)$ for the Cl(^2P_J)-Xe system as a function of the beam velocity v, for three different values of B/v^2 (B in 10^2 G and v in km s^{-1}) and plotted as $Q \cdot v^{2/5}$ to emphasize the glory structure. The full lines represent the cross sections calculated for the scattering by the three adiabatic potentials involved using the proper weights for each state. The dotted lines are obtained using only the spherical component of the interaction.

COPY AVAILABLE TO DTIC DOES NOT PERMIT FULLY LEGIBLE REPRODUCTION

Their analysis is performed in terms of the three involved adiabatic potential energy curves which correlate with the different atomic sublevels of $Cl(^2P_J)$.

These curves are generated by the proper combination of the spherical $V_0(R)$ and the anisotropic $V_2(R)$ component of the electrostatic interaction. The results for the Cl-rare gas series are shown in Fig (2) together with nonadiabatic coupling matrix element derived from the same analysis. These interactions are being applied to several problems *e.g.* [7, 8]

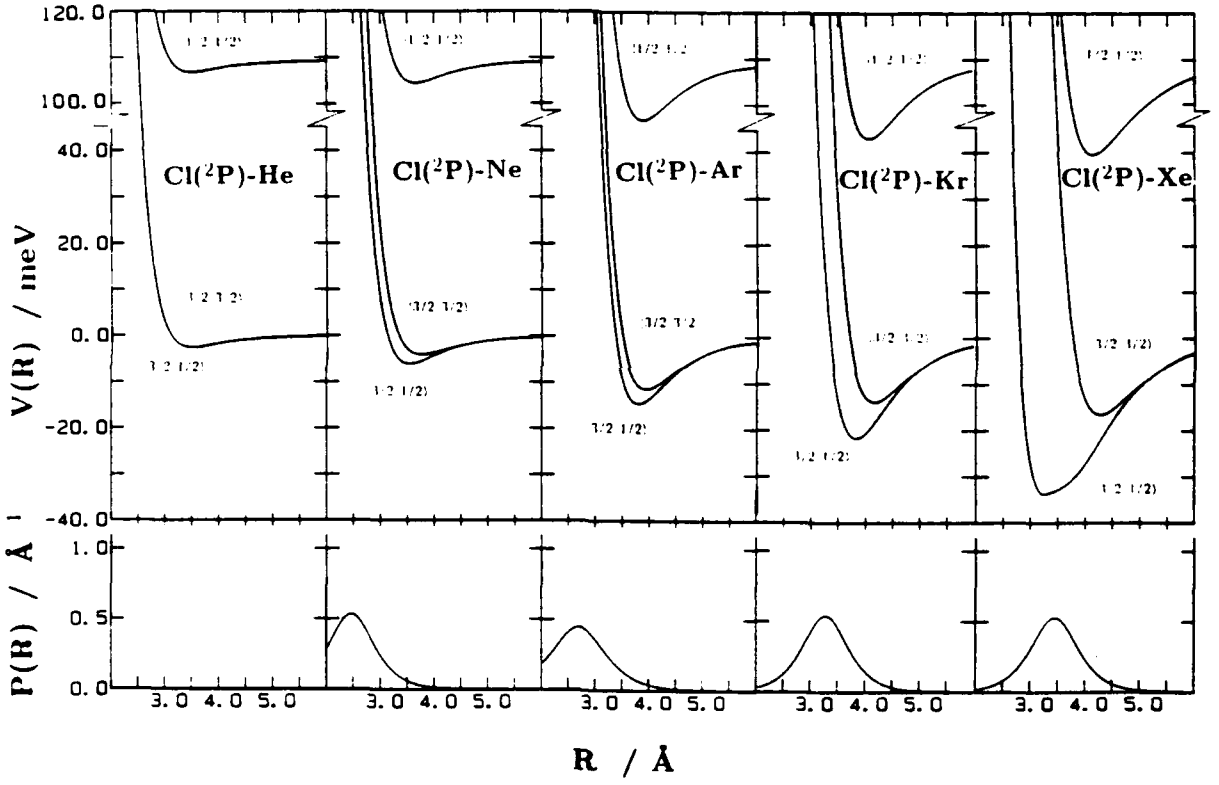

Figure 2 Adiabatic potential energy curves $V_{J\Omega}$ for the rare gas-Cl systems. In the lower panel is shown the nonadiabatic coupling matrix element P between the $|3/2\ 1/2\rangle$ and $|1/2\ 1/2\rangle$ states.

COPY AVAILABLE TO DTIC DOES NOT PERMIT FULLY LEGIBLE REPRODUCTION

The characteristics of the spherical V_0 term agree with the predictions from simple correlation formulas [9] between the potential parameters and the polarizzability of the interacting particles. This result confirms that the V_0 component of the interaction retains the meaning and maintains the features of a typical van der Waals interaction, as for other cases encountered earlier [2, 10].

The nature of the V_2 contribution (*i.e.* the $\Sigma\Pi$ splitting) can be interpreted as a configuration interaction effect among the lower electronic states and higher electronic states of the molecule. The results of these studies will amplify the systematics for understanding the nature and role of these weak bonds and specifically of the anisotropic interaction term V_2 [10].

References

[1] V.Aquilanti, G.Liuti, F.Pirani, and F.Vecchiocattivi, *J.Chem.Soc.Faraday Trans.*II **85** (1989) 955.

[2] V.Aquilanti, R.Candori, D.Cappelletti, E,Luzzatti, and F.Pirani *Chem.Phys.* **145** (1990) 293.

[3] V.Aquilanti and G.Grossi, *J.Chem.Phys.* **73** (1980) 1165.

[4] V.Aquilanti, P.Casavecchia, G.Grossi, and A.Laganà, *J.Chem.Phys.* **73** (1980) 1173.

[5] V.Aquilanti, R.Candori, D.Cappelletti, V.Lorent, and F.Pirani *Chem.Phys.Lett.*, in press (1992).

[6] V.Aquilanti, D.Cappelletti, V.Lorent, E.Luzzatti, and F.Pirani, *Chem.Phys.Lett.*, in press (1992).

[7] A.Garcia-Vela, R.B.Gerber, and J.J.Valentini, *Chem.Phys.Lett.*, **186** (1991) 223.

[8] J.G.McCaffrey, H.Kunz, and N.Schwentner, *J.Chem.Phys.*, **96** (1992) 155.

[9] R.Cambi, D.Cappelletti, G.Liuti, and F.Pirani *J.Chem.Phys.* **95** (1991) 1852.

[10] V.Aquilanti, D.Cappelletti, F.Pirani, L.Y.Rusin, M.B.Sevryuk, and J.P.Toennies, *J.Phys.Chem.* **95** (1991) 8248.

*Presented at the *XIV Symposium on Molecular Beams*, Asilomar, California, June 1992.

Halide Anion-Carbon Dioxide Clusters: From Electrostatic to Covalent Bonding

D. W. Arnold, S. E. Bradforth, E. H. Kim and D. M. Neumark
Dept. of Chemistry, Univ. of California, Berkeley, CA 94720

We present the results of experiments performed in our laboratory using anion photoelectron spectroscopy to study a series of halide anions clustered with carbon dioxide molecules. $X^-(CO_2)_n$ clusters are generated at the intersection of a pulsed molecular beam and a 1 keV electron beam. The clusters, which are cooled in the continuing molecular beam expansion, are mass selected and photodetached with a pulse of laser light. The resultant photoelectrons are energy analyzed providing a photoelectron spectrum for the neutral system. Cheshnovsky and co-workers[1] have obtained anion photoelectron spectra of $I^-(CO_2)_{n=1-7}$ and $Cl^-(CO_2)_{n=1,2}$ at low resolution (50 meV). While they obtained information about the solvation energies for these systems, our higher resolution experiment (8meV) uncovers vibrational structure in the spectra which results from interactions between the halide anions and the CO_2 molecules. The results of these experiments on $X^-(CO_2)_n$ (X = F, Cl, Br and I) provide information on the trend in chemical bonding of differing halogen anions with carbon dioxide molecules. Preliminary results indicate that the bonding ranges from being almost entirely due to electrostatic interactions for iodide to being a much more covalent bond in the case of fluoride. There is a charge-quadrupole interaction that is strong enough to bend the CO_2, forming a charge-induced dipole interaction that leads to a significant solvation stabilization in the case of Cl^-, Br^-, and I^-. As X^- goes from I^- to F^-, the decreasing atomic radius allows for an increasing interaction between anion and CO_2, leading to smaller OCO angles upon going from I^- to F^-. This interaction becomes a relatively weak quadrupole-induced dipole interaction in the neutral formed upon photodetachment (in the case of X = I, Br, and Cl). This weaker interaction should lead to a longer $X\cdots CO_2$ bond and a linear CO_2. This difference in geometry between the anion and the neutral is seen in our photoelectron spectra as an extended vibrational progression in the ν_2 mode of CO_2, the length of which is determined by the Franck-Condon factor for this process. In addition, the weakness of the neutral-neutral interaction combined with the ν_2 excitation of the CO_2 upon photodetachment leads to a dissociative process whose lifetime, if sufficiently short, is indicated by the width of the peaks in the spectrum.

As a first approximation, X^- (for X = Cl, Br and I) can be treated as a perturbation on the CO_2, bending the molecule from linearity. By using this simple model we can get an approximate estimate for

[1] G. Markovich, R. Giniger, M. Levin, and O. Cheshnovsky, Z. Phys. D. **20**, 69 (1991).

the angle of the CO_2 in the $X^-(CO_2)$ systems through the use of a simple Franck-Condon analysis. For FCO_2, a more rigorous analysis is required. A series of models is used to attempt to further describe the interactions involved in these clusters. A goal is to determine, qualitatively, how much of the change in geometry of the CO_2 can be explained in terms of a simple point-charge-at-a-distance electrostatics approach and how much of the interaction requires consideration of the chemical nature of the halide anion involved. The balance of these two contributions is studied as a function of the halide involved. Some of the models being considered are:

1) Simple electrostatic point charge and quadrapole,
2) Point charge along with a CO_2 treated quantum mechanically, and
3) Full quantum mechanical *ab initio* treatment of the $X^-(CO_2)$ complex.

CO_2 is one of the classic examples studied with the use of Walsh diagrams.[2] Upon going from the neutral molecule (22 electrons, $D_{\infty h}$ geometry) to the anion (23 electrons, OCO angle = 135°),[3] the molecule finds its most stable geometry changing from a linear to a bent form due to the stabilization of the $\pi_u(b_1/a_1)$ orbital achieved upon the change in OCO angle.

By studying larger clusters of the form $X^-(CO_2)_n$, information is learned about the interaction of the additional CO_2 molecules added to the anion clusters. The spectra provide details about the energies of solvation and the number of molecules present in solvation shells around the anions and demonstrate how the size of the solvent cages vary as a function of the halide ion. An interesting feature of these spectra is that not only does the vibrational structure remain when several CO_2 molecules are added to the X^- (i.e., $I(CO_2)_{13}$ shows resolved vibrational structure), but the extent of the vibrational progression increases with the addition of extra CO_2 molecules.

---

[2] A. D. Walsh, J. Chem. Soc. 2266 (1953).

[3] D. W. Ovenall and D. H. Whiffen, Mol. Phys. 4, 135 (1961); M. Krauss and D. Neumann, Chem. Phys. Lett. 14, 26 (1972).

Characterization of a Pulsed Uniform Supersonic Flow Reactor for Low Temperature Studies of Radical-Molecule Reactions

D. Atkinson, K. Cavanaugh and M. Smith
Department of Chemistry, University of Arizona
Tucson, Az 85721

We report the development of a pulsed uniform flow reactor for the study of radical-radical and radical-molecule reaction dynamics in the low to ultralow temperature regime (200 to 10 K). Laser photolysis is used to produce radicals which are expanded with a reagent in a uniform axisymmetric flow nozzle producing a well defined local density and temperature environment. Laser induced fluorescence is used to probe the radical concentration after nozzle exit as a function of time. By tuning stagnation conditions, the rate of reaction can be studied as a function of temperature continuously over large ranges. The temperature dependent reaction rates will be of great use in atmospheric modelling and will help to elucidate low energy reaction mechanisms, which may or may not be prevalent at higher temperatures. An example is the reaction of hydroxyl radical with methane, for which the rate has been a topic of controversy in atmospheric chemistry recently.

Flow reactors have been used extensively to study the kinetics of fast to very fast reactions ($k_{bimolecular}$ = 10^{-14} to 10^{-9} cm^3/sec), but problems are encoutered in measuring low temperature rates. The combination of the relatively high densities required to observe radical-radical and radical-molecule reactions and cryogenic cooling of the reactors may cause condensation problems. For this reason, some experimenters have opted for "free flow" reactors, where the flow is not enclosed by physical walls and the mechanism for cooling includes the natural cooling which is experienced by expanding flows. One example is our group's use of a pulsed free jet expansion to produce translationally and rotationally cold reactants for ion-molecule reactions.[1] Another is the group in Meudon, France who use a shaped Laval nozzle to produce a continuous uniform flow at low temperatures, also for the study of ion-molecule reaction dynamics.[2]

Measurement of radical-radical and radical-molecule reaction rates requires relatively high densities with respect to the ion-molecule studies. This prohibits the use of free jets, where the density drop is too great, and continuous uniform expansions, where the pumping and delivery requirements become prohibitive. We have decided to employ a pulsed uniform expansion for this purpose, where the density of the neutral reagents can be as high as 10^{17} cm^{-3}, without prohibitive pumping requirements. A second advantage of uniform high density flows is that a well defined isotropic temperature exists, which can be tuned over broad ranges. This breadth will allow measurement of radical reaction rates over a large range not currently accessible.

The core of our experiment is the shaped convergent-divergent (Laval) nozzle which is used to provide uniform high density flows at a specific mach number. These nozzles have been used to provide uniform flow test sections for wind tunnels for many years, but only recently has their application to flow reactors been considered. To get an idea of the extent of cooling in these expansions we can use the mach equation

$$\frac{T_0}{T} = 1 + \frac{\gamma-1}{2} M^2$$

where T_0 is the stagnation temperature, γ is the heat capacity ratio for the gas, and M is the mach number of the expansion. Note that in general mach number is not a constant for an expansion, it is the special nature of the uniform expansion which makes it so. The above expression also is the key to our temperature tunability; by varying stagnation temperature it is possible to change the final post expansion temperature in a simple continuous way. Our experiment varies stagnation temperature from cryogenic to near ambient via a liquid circulation system and from ambient to near 400 K using heaters. Using nozzles designed to give different terminal mach numbers, we can then cover the entire 10 to 200 K kinetic window continuously. We have designed nozzles with mach numbers of 1.5, 2, 3, 4, 5, and 8, which allow for access to

this full range. Our design method uses a program for the isentropic flow in Laval nozzles developed by Moger and Ramsay[3], coupled with a solution of the boundary layer problem by Potter and Carden.[4]

Figure 1 is a block diagram of the experimental setup. A pulsed valve is used to deliver a pre-cooled (or warmed) mixture of non-reactive molecular buffer gas, reactant, and radical precursor to the photolysis zone. An excimer laser is used to photolyze the radical precursor, and the nascent mixture is allowed to expand through the shaped Laval nozzle. While in this zone, the mixture accelerates to the final mach number and extensive collisional and expansive cooling allows the temperature to equilibrate at the final value. The entire nozzle assembly is cooled or warmed to the desired stagnation temperature so the nozzle does not contribute to the final temperature of the flow. The reacting mixture then travels into the vacuum chamber where it continues to flow in a uniform stream past the probe volume. At some distance, which corresponds to a reaction time, the flow is crossed by a tunable YAG pumped dye laser. The molecular or atomic fluorescence is collected by a camera system. The reaction distance (time) is scanned by moving the nozzle assembly with respect to the LIF zone.

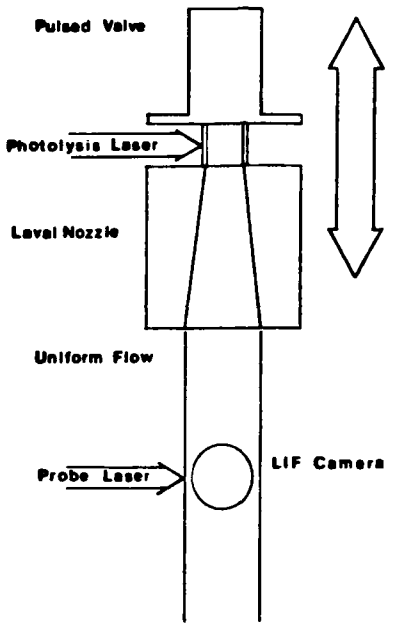

Figure 1 is a block diagram of the experimental appartus.
An explanation is given in the text.

Initially we have used NO_2 to determine the operational characteristics of the apparatus, since its fluorescence efficiency is high and its excitation spectrum in the visible (580-610 nm) is well known. By recording the spectrum and fitting the band contours it is possible the determine the temperature of the test gas in the N_2 buffer. Additionally the relative extent of vibrational and rotational relaxation in the flow can be measured. Finally, the profile of the jet can be mapped by scanning horizontally across the flow as well as vertically along the flow to determine the uniformity of the stream. The results of these studies will be presented, as well as some first results of radical reactions.

References

[1] M. Hawley, T. L. Mazely, L. K. Randeniya, R. S. Smith, X. K. Zeng, M. A. Smith, Int. J. Mass Spectrom. Ion Phys., *97*, 55, 1990.

[2] B. R. Rowe, *Rate Coefficients in Astrochemistry*, T. J. Millar and D. A. Williams (eds.), Kluwer Academic Publishers, 135-152, 1988.

[3] W. C. Moger and D. B. Ramsay, AEDC-TDR-64-110, 1964, Arnold Engineering Development Center, Tullahoma, Tenn.

[4] J. L. Potter and W. H. Carden, J. Spacecraft and Rockets, *5*, 1095, 1968.

193 nm Photodissociation of 1,1 and 1,2 Difluoroethylene

B.A. Balko[a], J. Zhang, and Y.T. Lee
Department of Chemistry, University of California at Berkeley and
Chemical Sciences Division, Lawrence Berkeley Laboratory
Berkeley, CA 94720

(a) Present address: Chemistry Department, University of Oregon, Eugene, Oregon 97403

Abstract:

The photodissociation of 1,1 and 1,2 difluoroethylene (DFE) at 193 nm was studied by measuring the translational energy distributions, $P(E_T)$'s, for the various product channels, specifically HF, H_2, H, and F elimination. The apparatus used to investigate the photodissociation was a modified fixed source/rotating detector molecular beam apparatus which has been described previously in connection with the photodissociation of acetylene [1].

The H_2 and HF molecular elimination was found to be similar to that observed in the H_2 elimination in ethylene, i.e. that three-centered elimination is preferred [2]. Detailed comparison of the $P(E_T)$'s for HF and H_2 three-centered elimination, however, reveals important differences in the nature of the transition states. The three-centered elimination of HF in the 1,2 DFE peaks very close to 0 kcal/mole showing that this fluorovinylidene channel has only a very small exit barrier. This should be compared with the three-centered elimination of H_2 in the 1,1 DFE which peaks at ~6 kcal/mole and that in ethylene at ~20 kcal/mole. These differences suggest that HF elimination occurs from a looser critical complex. In the four-centered H_2 elimination in the 1,2 DFE some H_2 + FCCF products were produced

with very little internal energy, something not seen in the ethylene photodissociation [2]. This difference could be attributed to there being less structural changes required to go from the transition state to the products in the DFE case.

The H atom elimination in the DFE's was found to be very much like that in ethylene [2] in that there is a large amount of secondary dissociation and the secondary fragments have only a very small percentage of their energy in translation. This suggests that the formation of an electronically excited state, most likely the lowest triplet, might be occurring. This involvement of a triplet is not unexpected based on Guillory and Andrew triplet quenching studies [3].

Guillory and Andrews believed that H elimination was preferred over F elimination in the DFE's [3] and this was confirmed in these studies. There was no evidence for any primary F atom elimination from 1,1 DFE. F atoms not from the cracking of HF, however, were detected in the 1,2 DFE photodissociation studies. The $P(E_T)$'s from this channel did not seem consistent with simple bond rupture. The exact mechanism to explain the F atom production, however, could not be determined from these studies.

References:

1. B.A. Balko, J. Zhang, and Y.T. Lee, J. Chem. Phys. **94**, 7958 (1991).
2. B.A. Balko, J. Zhang, and Y.T. Lee, submitted to J. Chem. Phys.
3. W.A. Guillory and G.H. Andrews, J. Chem. Phys. **62**, 3208 (1975).

A BENCHMARK GAS/SURFACE PES: XE/PT(111)

J. A. Barker and C. T. Rettner

IBM Research Division
Almaden Research Center K31/801
650 Harry Road, San Jose, CA 95120-6099.

We have determined an empirical potential energy function for the interaction of xenon with the Pt(111) surface which is consistent with a wide range of dynamical and equilibrium experimental data. These include scattering measurements at incidence energies from 0.5 eV to 14.3eV[1], measured desorption rates[2] and trapping probabilities[3], and the experimental "energy jump" at the transition from the commensurate to the uniaxially compressed incommensurate phase[4,5]. The potential also agrees with an experimental value for the frequency of vibration normal to the surface[6], and has the correct asymptotic behaviour at large distances from the surface ($V = -c_3/z^3$, with an experimental estimate[7] of c_3). The equilibrium position for a single xenon atom lies directly above a surface platinum atom; we shall refer to this as the "ontop" potential. The calculated equilibrium height of the Xe is 3.35 Å, reasonably close to the value 3.0 Å found by Müller [8] from an "ab initio" electronic calculation and within the range 3.1-3.5 Å suggested by Black and Janzen[9,10] . The calculated frequency of the normal vibration is 3.8 meV compared with the experimental value[6] 3.7 meV.

The chosen analytic form has sufficient flexibility to describe also potentials with equilibrium position over the threefold hollow site ("hollow" potentials). At first sight the hollow site seems a more likely choice for a system in which van der Waals interactions might have been expected to dominate. However potentials of this kind proved unable to reproduce all of the experimental data. In particular potentials which fitted all of the scattering data did not give agreement with the trapping measurements, and it was not possible to make the corrugation at the bottom of the attractive well sufficiently large to give agreement with the experimental "energy jump".

We represent the interaction between a xenon atom and the solid by a sum over all Pt atoms of nonspherical pairwise additive Xe-Pt interactions, together with an additional uncorrugated term which depends only on the normal distance (height) of the xenon atom from the local average surface. This term is intended to describe the interaction with the delocalized conduction electrons.

The nonspherical pair potential is modelled by a spherical part centered on the Pt atom, and a part centered at some distance above the Pt atom. The height of the "local average" surface is a weighted average of the heights of surface atoms, with a weighting function depending on the distance from the xenon atom. The Pt atoms were assumed to interact with a nearest neighbor central harmonic interaction.

Details of the form of the potential function and of the methods of calculation required to make contact with experiment are described by Barker et al [11]. who give a preliminary version of this work.

For "ontop" potentials the repulsion at low energies is provided by the uncorrugated potential, while for the "hollow" potentials it is provided by the pair potential. In both cases the repulsion at higher energies is provided by the central part of the pair interaction.

The "energy jump" at the commensurate to uniaxially compressed partially incommensurate phase was calculated by a method similar to that described by Gottlieb[12] and Gottlieb and Bruch [13], except that we used the finite temperature Monte Carlo method rather than energy minimisation.

These calculations used the Xe-Xe potential of Aziz and Slaman[14]. The calculations incorporated non-additive Xe-Xe interactions due to the substrate-mediated McLachlan interaction and the interaction of the adsorption-induced polarizable dipoles, as discussed by Gottlieb and Bruch[15,16], who give the necessary parameters.

The calculated value of the "energy jump" is 34.5 meV compared with the experimental[4,5] value 30 $\pm$ 15 meV. The calculated isosteric heat of the commensurate phase is 295 $\pm$ 5 meV, where the uncertainty derives primarily from that in the energy of adsorption at zero coverage[11]. This result agrees within the combined uncertainties with the experimental value[4,5] 311 $\pm$ 16 meV.

Our potential reproduces in a remarkable way the behaviour of the scattering angular distributions and the variation of average energy with angle for incident energies as low as 0.5 eV and as high as 14.3eV at a surface temperature of 800K. It also reproduces closely the variation of trapping probability with energy for incident energies from 0 to 0.3 eV at a relatively low surface temperature (85K). The agreement with the experimental "energy jump" and isosteric heat of the commensurate phase indicate that our values of the depth and corrugation at the minimum of the potential are close to the correct values.

References:

1. C. T. Rettner , J. A. Barker and D. S. Bethune, *Phys. Rev. Lett.*, **67** (1991) 2183.
2. C. T. Rettner, D. S. Bethune, and E. K. Schweizer, *J. Chem. Phys* , **92** (1990) 1442.
3. C. T. Rettner, D. S. Bethune and D. J. Auerbach, *J.Chem.Phys.*, **91** (1989) 1942.
4. K. Kern, R. David, R. L. Palmer and G. Comsa, *Surf. Sci.*, **175** (1986) L669.
5. K. Kern, R. David, P. Zeppenfeld, and G. Comsa, *Surf. Sci.*, **195** (1988) 353.
6. B. Hall, D. L. Mills, P. Zeppenfeld, K. Kern, and G. Comsa, *Phys. Rev. B*, **40** (1989) 6326.
7. P. A. Rejto, Ph. D. Thesis, Stanford University, 1991.
8. J. E. Müller, *Phys. Rev. Letters*, **65**, (1990) 3021.
9. J. E. Black and R. A. Janzen, *Langmuir*, **5**(1989) 558.
10. J. E. Black and R. A. Janzen, *Surf. Sci.*, **217**(1989) 199.
11. J. A. Barker, C. T. Rettner and D. S. Bethune, *Chem. Phys. Lett.*, **188** (1992) 471.
12. J. M. Gottlieb, *Phys. Rev. B*, **42** (1990) 5377.
13. J. M. Gottlieb and L. W. Bruch, *Phys. Rev. B*, **40**(1989) 148.
14. R. A. Aziz and M. J. Slaman, *Mol. Phys.*, **57** (1986) 825.
15. J. M. Gottlieb and L. W. Bruch, *Phys. Rev. B*, **44**(1991) 5750.
16. J. M. Gottlieb and L. W. Bruch, *Phys. Rev. B*, **44**(1991) 5759.

Exploring the Transition Region in Chemical Reactions

Michael D. Barnes, Philip R. Brooks, Robert F. Curl, & Peter W. Harland
Chemistry Department & Rice Quantum Institute
Rice University
Houston, Texas 77251

Chemical reaction is the process in which an old chemical bond breaks and a new one forms. Much has been learned about this process by monitoring the rates at which the reagents disappear or the products appear. Sophisticated chemical dynamics experiments reveal much more about reaction details, but even these experiments still interrogate the well-separated reagents or products. The fundamental event, the bond rearrangement process, is *not* directly observed and must be *inferred* by some theoretical means.

At some point in this bond rearrangement, one has neither reagents nor products, but rather a transient group of atoms in transition from reagents to products, which we call "transition region species (TRS's)".[1] Our goal has been to observe these species experimentally, and we believe that we have reasonably convincing evidence that we have been able to laser excite the TRS in the reaction

$$K + NaCl \rightarrow KCl + Na.$$

In order to probe TRS's *in the act of reacting*, we have studied reagents which react on nearly every gas-kinetic collision, K + NaX (X = Cl, Br, I). We cross beams in the cavity of a cw dye laser. These reagents react in the absence of the laser, and the TRS $[KXNa]^{\dagger}$ is known to live for about a rotational period, ≈ 1 ps. If the TRS is excited by a photon in the red, enough energy is available for the excited TRS to decay to Na*, and we observe the Na* in fluorescence. This process may be represented by the following kinetic mechanism:

$K + XNa \rightarrow [KXNa]^{\dagger}$	formation of the TRS
$[KXNa]^{\dagger} + h\nu_L \rightarrow [KXNa]^{\dagger *}$	laser excitation of the TRS
$[KXNa]^{\dagger *} \rightarrow KX + Na^*$	reactive decomposition of the excited TRS
$Na^* \rightarrow Na + h\nu_D$	fluorescence of the Na atom at the *D* line

The experiments so far have been restricted to "excitation spectroscopy" in which the beam intensities are kept constant and emission at the Na D line is monitored as the laser wavelength is swept. Despite the short lifetime of the TRS, and despite averaging over impact parameters inherent in full bimolecular collisions, we have observed *structured* excitation spectra for the reactions K + NaX (X = Cl, Br, and I). The KBrNa and KClNa spectra are shown in Fig 1; it is clear that the spectra are considerably different. (KINa is similar to KBrNa and is omitted for simplicity.)

Fig 1 shows two features for each molecule: a *blue* feature (steep rise near 600nm) which is similar for the three cases and a red feature (607 for KBrNa) which differs depending on the molecule. We believe these are features arising from excitation of the TRS. We suspect that the blue feature is the signature of an exit channel excitation and that the red feature arises as a consequence of some preferred nuclear configurations during the reaction.

Interpretation of these spectra is ambiguous and still incomplete, but some very broad conclusions can be drawn. A pictorial view of the potential energy surfaces (PES's) for the

[1] These are the set of real, transient nuclear configurations intermediate between the reagents and products, and include the "transition state" of some theories. See P. R. Brooks, *Chem. Rev.*, **88**, 407 (1988).

KClNa reaction is shown in Fig 2. The reagents are initially on the ground PES and a schematic trajectory is shown beginning on the ground surface[2]. A photon of given wavelength λ may connect the ground surface with the excited surface in regions where $\Delta E = hc/\lambda$. If a trajectory passes through a configuration in resonance with the photon, excitation to the upper surface is possible as suggested in Fig 2. If the wavelength of the photon were changed, *different* regions of the ground PES would be in resonance, and different ground state nuclear configurations would be excited. The ultimate fate of the TRS (decay to excited reagents or to excited products) depends on the nature of the upper surface, and this will also change as λ is changed.

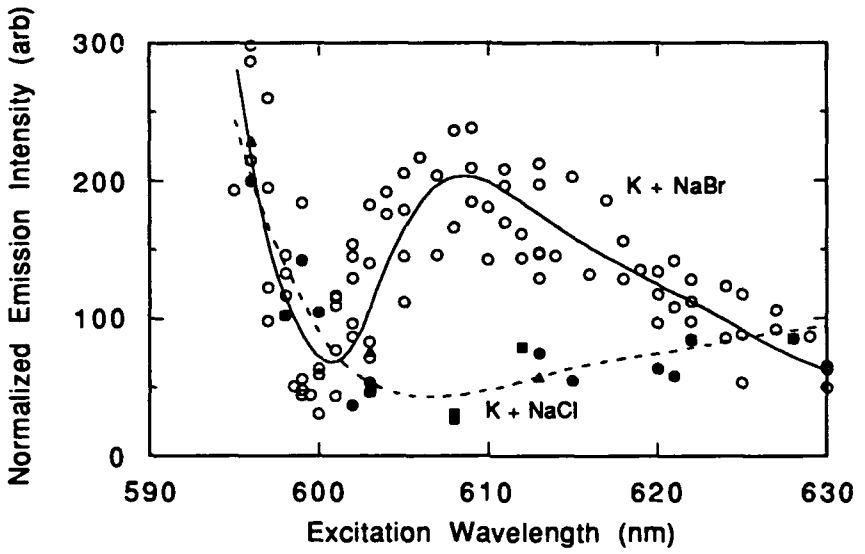

Fig 1. Excitation spectrum (emission at 589 nm Na D line vs laser wavelength) for KBrNa and KClNa systems. Curves are drawn through the points to guide the eye.

Using Fig 2 as a reference, we can draw some very general conclusions about the sort of spectra one might obtain in these experiments. These conclusions also follow from the results of line-broadening spectroscopy[1] and model calculations of the Polanyi group.[3] Some of these features are the following:

a) if the ground and excited potential surfaces are "parallel", a given λ will excite a relatively wide range of nuclear configurations. Many different configurations will absorb at $\lambda_{parallel}$ and a pile up of intensity will result in a "feature". For asymptotically large distances out in the exit and entrance channels, the ground and excited surfaces correspond to negligibly perturbed species. The surfaces ultimately become parallel with energy separation of the atomic line; the "feature" is the atomic line.

b) excitation of the TRS is expected to be most likely for λ's which can excite regions of greatest probability density on the lower state. Thus, if there are "bottlenecks" on the lower state through which most of the flux must pass, the absorption spectrum could

---

[2] K. Yamashita, K. Morokuma, *J. Phys. Chem.* **92**, 3109 1988) {potential energy surfaces} and *J. Chem. Phys.* **91**, 7477 (1989) {trajectory calculations}.

[3] J. C. Polanyi and R. J. Wolf, J. Chem. Phys., **75** 5951 (1981)

show a maximum when the laser is tuned to match the energy spacing between the surfaces at the bottleneck.

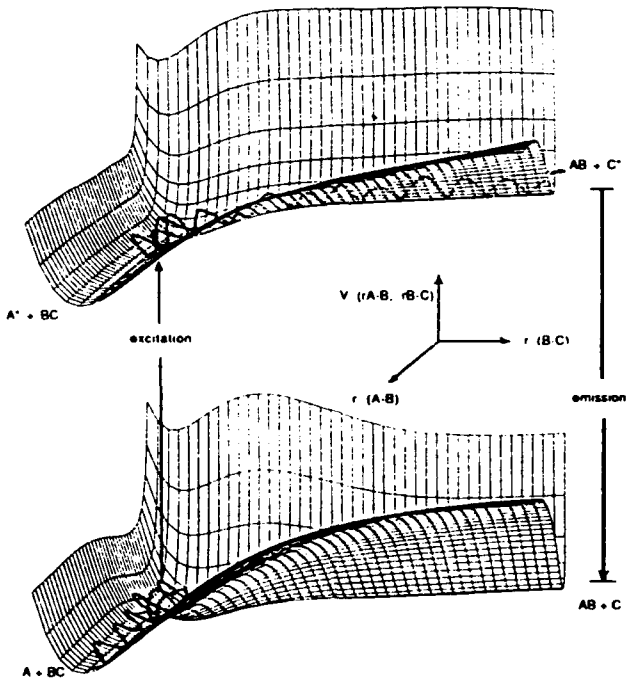

Fig 2. Fixed angle potential energy surfaces for the K + NaCl surfaces of Yamashita & Morokuma. A schematic reactive trajectory is shown to illustrate the formation of the TRS on the lower surface, excitation to the upper surface, and the reactive decay of the TRS on the upper surface.

c) if the TRS lives for several vibrations, "pools" of probability density might form on the ground surface, enhancing the probability of excitation and leading to spectral maxima.

Our preliminary interpretation of the steep rise in all the spectra for $\lambda < 600$ was that this feature represented type a) behavior, transitions between portions of the surfaces which were essentially parallel. As the products separate the lower surface will describe a ground state Na atom mildly perturbed by a KCl molecule, the upper state will describe a mildly perturbed Na*, and the difference will be roughly the energy of the Na D resonance line. This interpretation is not supported by the theoretical calculations available, however.

Yamashita and Morokuma (YM) have calculated ab-initio surfaces for the KClNa system and performed trajectory calculations on those surfaces. Some features of their surfaces are shown in Fig 3. The potential wells shown can be understood as the result of avoided crossings of the covalent (M--M'X) surfaces with the deeply attractive ionic (M^+--$M'X^-$) surfaces. The existence of a stable KClNa has been verified experimentally.[4] (The potential *curves* shown in Fig 3 are perhaps misleading; four dimensions are needed to represent the potential surfaces for this 3 atom system. The curves shown in Fig 3 represent minimum energies *permitting the angle to change.*)

---

[4] K. I. Peterson, P. D. Dao & A. W. Castleman, J. Chem. Phys. 79, 777 (1983); M. M. Kappes, P. Radi, M. Schaer & E. Schumacher, *Chem. Phys. Letters*, 113, 243 (1985)

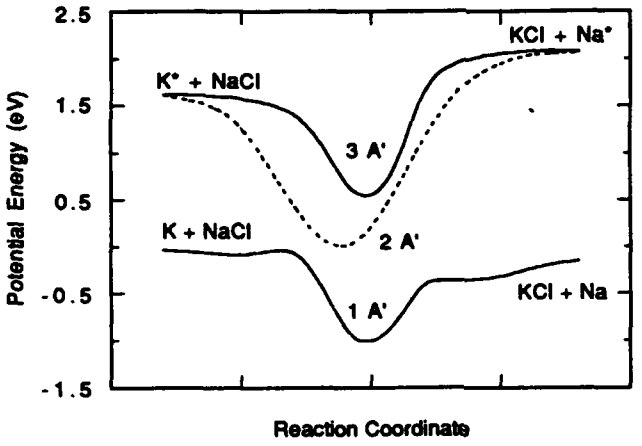

Fig 3. Calculated minimum potential energy paths (angle not restricted) on the Y-M surface for the 1 ^{2}A' and 3 ^{2}A' states. *(The path shown for the 2 ^{2}A' state is approximated.)*

The calculations suggest that the 3 A' state is populated for excitation in the visible, but inspection of the 1 A' and 3 A' surfaces shows that they are *not* parallel in the asymptotic product regions and these surfaces are thus not expected to show a feature at the sodium D line. The trajectory surface-hopping calculations of YM, extended in our laboratory,[5] confirm that the YM surfaces simply do *not* explain this blue feature. We suspect that the blue feature arises from excitation in the exit channel and that the disagreement between experiment and theory reflects the inadequacy of the surface in the asymptotic regions.

The surface-hopping trajectory calculations for KClNa show no evidence of any sort of feature, either red or blue. We calculated a spectrum using the trajectory-surface hopping approach of YM for the KBrNa system assuming the potential surface for the Br system is the same as that for the Cl system with the mass changed. The calculated spectrum still shows only a gradual monotonic decrease as the wavelength is increased. No indication of a feature is apparent. Thus the experiments cannot be interpreted in terms of the present KClNa surfaces for 1 A' and 3 A'.

There is another possibility: the 2 A' surface comes within a few kcal of the 1 A' for certain geometries,[6] and it has been suggested that diabatic "hops" from the 1 A' to 2 A' occur in reactions of vibrationally excited species.[7] If such a diabatic "hop" were to occur in KXNa, the system would not have enough energy to dissociate on the 2 A' surface and might be trapped in the 2 A' well long enough to enhance the likelihood of photon absorption to the 3 A' state. Thus the red feature might arise from pooling of probability density on the 2 A' surface. Differences among the intensities of the excitation spectra of various halides might thus reflect different probabilities of forming the 2 A' state, whereas differences in shapes would be indicative of different shapes of the 2A' and 3A' surfaces and different pooling regions. These possibilities are under study.

---

5 M. D. Barnes, PhD thesis, Rice University, Houston, Texas (1991)

6 A. C. Roach and M. S. Child, *Mol. Phys.*, **14**, 1, (1968)

7 S. K. Neoh & D. R. Herschbach, *J. Chem. Phys.*, **63**, 1030 (1975)

High Resolution Spectroscopy of Methylacetylene Clusters

R. D. Beck, T. A. Blake, D. Eggers, M. Lewerentz, S-H. Tseng, and R. O. Watts

Department of Chemistry
University of Washington
Seattle, Washington

F. J. Lovas

National Institute of Standards and Technology
Gaithersburg, Maryland

The rotationally resolved infrared spectra of the propyne (methylacetylene) clusters, propyne-Ar, propyne-N_2, and propyne-CO (Fig.1), as well as the corresponding acetylene complexes have been measured in a molecular beam using the optothermal technique.

In contrast to the linear structures found previously for the acetylene complexes[1,2] which were confirmed in the present study done under the same conditions as for the propyne complexes, we find that the propyne complexes are asymmetric tops with the added species located along the side of the propyne. The absorption spectrum of the propyne clusters is further complicated by the presence of the internal methyl rotor since both the m = 0 (A state) and m = ±1 (E-state) are populated, even at the very cold rotational beam temperature of about 1 K, due to the nuclear spin restriction.

With the help of microwave data obtained on an FT microwave spectrometer by Lovas, assignment of A state transitions can be done accurately using a Watson type asymmetric top Hamiltonian to yield the rotational constants and the band origin (Table 1 and 2). There are 42 A-state transitions with rms deviation of 0.00018 cm^{-1} and 43 E-state transitions with rms deviation of 0.00064 cm^{-1} assigned for propyne - Ar, 47 A state transitions out of about 90 lines observed assigned with rms deviation of 0.00034 cm^{-1} for propyne-CO, 80 A state transitions out of about 160 lines observed assigned with rms deviation of 0.00039 cm^{-1} for propyne-N_2. The b-type transitions are dominant in all the spectra, which reflects

the strong polarization along the b-axis. Most of the remaining absorption peaks for propyne-N_2 and propyne-CO are being fit to E state transitions where, in particular, one strong band ($\Delta J = 0$, $\Delta K_a = 0$, $\Delta K_c = 0$) is observed at around the band center. So far, no barrier height is added to the internal rotor.

A comparison between the band origins of these three propyne complexes reveals the increasing interaction strength from propyne and Ar to propyne and CO, as expected.

Table 1

	A" (cm^{-1})	A' (cm^{-1})	B" (cm^{-1})	B' (cm^{-1})	C" (cm^{-1})	C' (cm^{-1})
C_3H_4/Ar	0.2905*	0.2899	0.06056*	0.06039	0.04980*	0.04992
C_3H_4/N_2	0.2594*	0.2589	0.07403*	0.07398	0.05733*	0.05730
C_3H_4/CO	0.2690	0.2694	0.07092	0.07098	0.05615	0.05606

* from microwave data

Table 2

	C_3H_4 / Ar	C_3H_4 / N_2	C_3H_4 / CO
Band Origin (cm^{-1})	3334.5050	3333.9284	3333.3680

The structures for propyne - Ar and propyne - nitrogen are determined with the aid of microwave data provided by F. Lovas and shown as follows:

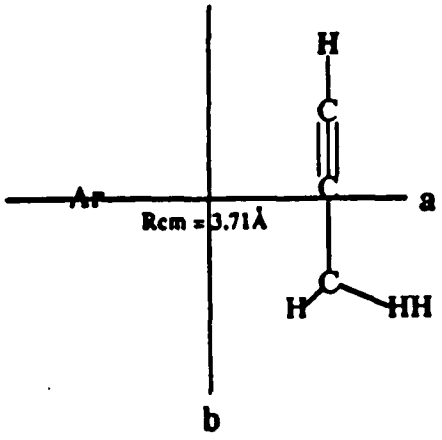

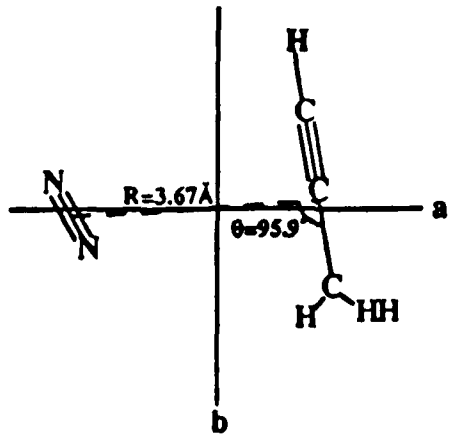

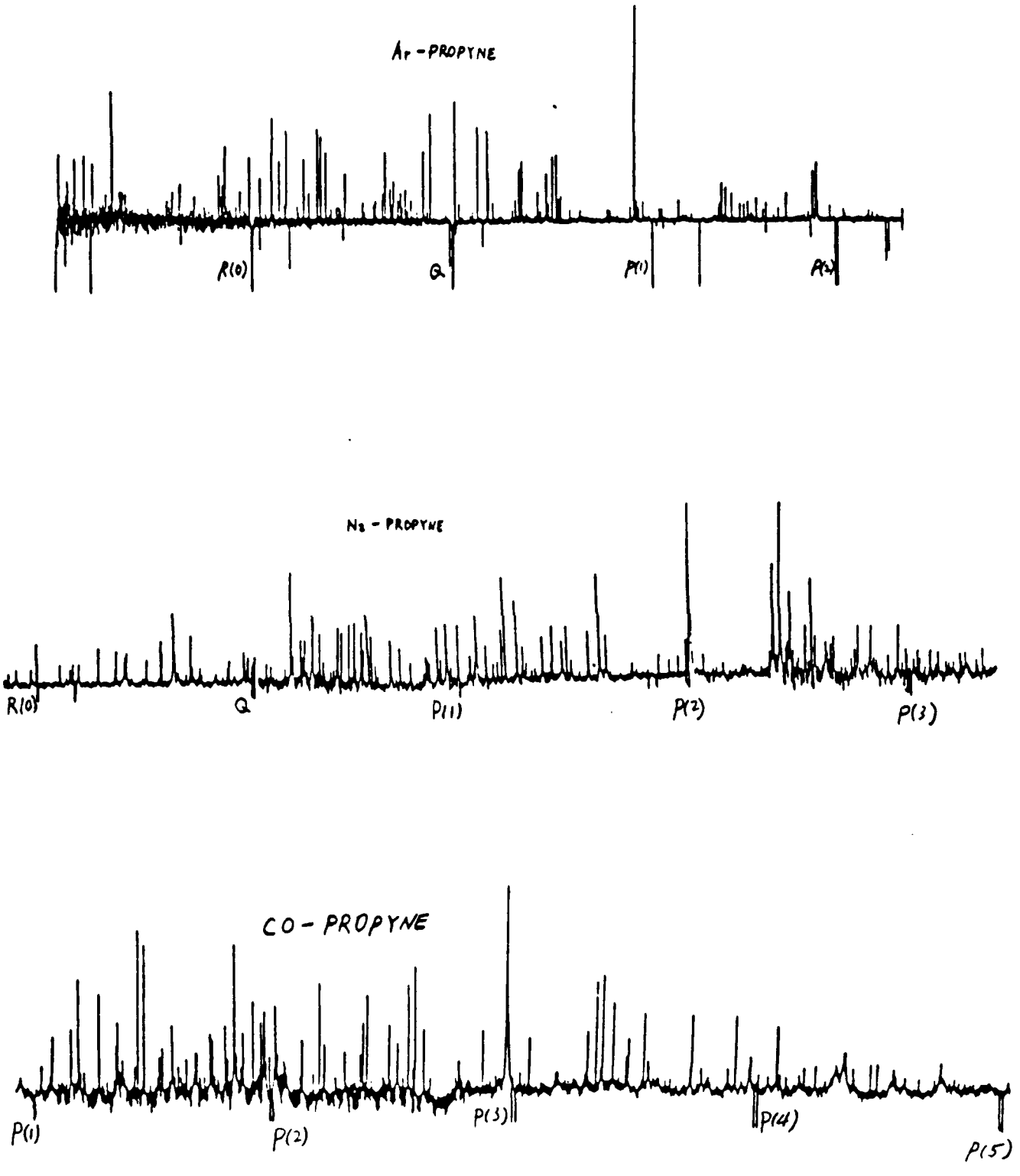
Ar - PROPYNE
R(0)
Q
P(1)
P(2)
N2 - PROPYNE
R(0)
Q
P(1)
P(2)
P(3)
CO - PROPYNE
P(1)
P(2)
P(3)
P(4)
P(5)

Fig. 1

Reference

1. M. D. Marshall, D. G. Prichard, and J. S. Muenter, J. Chem. Phys. **90**, 6049 (1989)
2. R. N. Nandi, D. G. Prichard, and J. S. Muenter, unpublished

PHOTOFRAGMENTATION OF MASS-SELECTED $(C_6H_6)_n^+$ AND $(C_6H_{12})_n^+$ CLUSTERS: SPECTRA AND MEASUREMENT OF MONOMER-CLUSTER BINDING ENERGY FOR n=7-15

S. M. Beck and J. H. Hecht

The Aerospace Corporation
P. O. Box 92957
Los Angeles, CA 90009

ABSTRACT

Benzene and cyclohexane cluster cations up to fifteen molecular units in size, produced in the throat of a supersonic nozzle by laser induced plasma formation, are studied by mass-selected photofragmentation spectroscopy.

Recent theoretical studies on neutral benzene and cyclohexane clusters, and experimental studies of benzene clusters, indicate that simple dispersion forces dominate the intermolecular interactions, and these non-polar clusters follow an icosahedral shell structure,[1-7] similar to that observed for rare gas clusters.[8] For instance, the cluster mass distribution for neutral benzene clusters formed in a supersonic expansion shows a local maximum at Bz_{13} which is proposed as a particularly stable icosahedral structure with a benzene molecule in the center.[4,5] When the clusters are positively charged the distribution maximum shifts one molecule to Bz_{14}^+. This is explained as an icosahedral structure with a dimer ion substituting for the central molecule in the neutral cluster.[1] The implication of this structure is a strongly bound dimer ion core, surrounded by neutral benzene molecules which are less strongly bound. Interestingly, we find that cyclohexane cation clusters maintain the "shell closing" at the 13 molecule cluster, indicating a more delocalized charge.

All of the clusters, both for benzene and cyclohexane, exhibit a strong, broad absorption which extends at least from 690 nm to 1064 nm. This absorption is assigned to the dimer based intervalence transition observed in solid state spectra of the benzene dimer ions. Excitation into this band produces prompt ejection of neutral benzene or cyclohexane molecules from the respective cluster ion. At low fragmentation laser intensities, a single daughter ion species is observed. We observe a simple dependence of the number of neutral molecules ejected on the fragmentation laser wavelength, strongly suggesting a sequential evaporation process of neutral molecules from the cluster ions.

Figure 1 shows a series of difference spectra for the fragmentations of Bz_{10}^{+} at four different wavelengths.

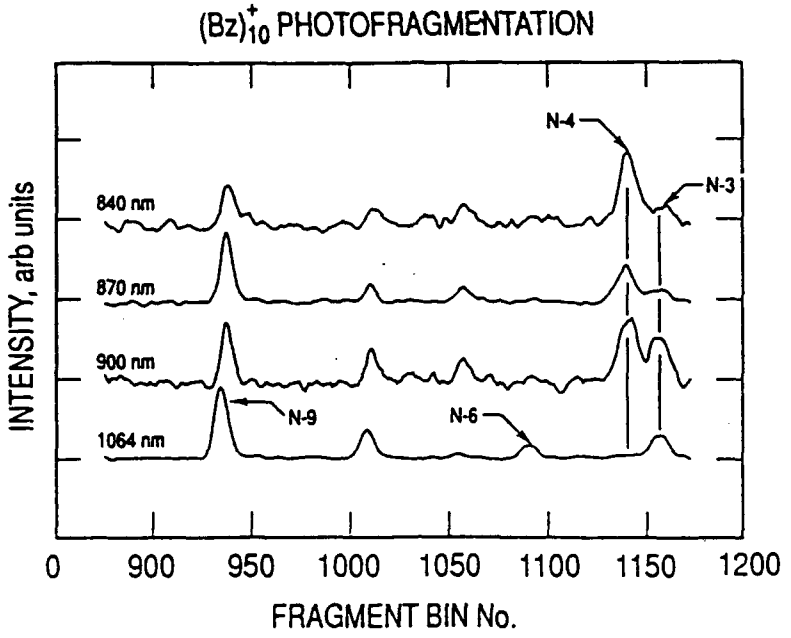

Figure 1

The top spectrum, obtained for a fragmentation wavelength of 840 nm, shows the dominant loss is four neutral molecules (n-4). The next two spectra, taken at 870 nm and 900 nm respectively, show an increase in the production of the n-3 peak at the expense of the n-4 peak. Finally, the bottom spectrum, taken at 1064 nm, shows predominantly n-3k loss, where k is the number of photons absorbed. Fragmentation laser intensity studies at 1064 nm have confirmed the photon dependence of the smaller mass fragments. At low fragmentation laser intensities the product distribution consists of a single n-3 daughter species. As the laser power is increased, the n-6 peak rises at the expense of the n-3 intensity, and then the n-9 increases at the expense of the n-6 peak. It is not known if the multiphoton process at higher laser intensities is direct or sequential, where the additional photons are absorbed by daughter ions.

Figure 2 shows the wavelength dependence, from 840-900 nm, for the production of the n-3 and n-4 fragments from three different parent cluster sizes, n=9, n=8, and n=7. There is a smooth transition from loss of three to loss of four neutral benzenes for all three parents. This occurs over a fairly broad energy range of approximately 100 meV. The origin of this width is not certain but is likely associated with the statistical disposition of the energy during the sequential fragmentation process. The proposed mechanism for the fragmentation is the following: The photon produces an initial excitation of a localized dimer core onto a dissociative potential. As the dimer begins to move apart, the dimer

mode is coupled to the van der Waals modes of the ground state potential, the cluster undergoes an internal conversion process, and the energy is quickly randomized throughout the intermolecular degrees of freedom of the ground state. The cluster then cools by sequential evaporation of monomers until the cluster temperature drops below the energy required to evaporate the next molecule within the observation time window. For each evaporation step there is a statistical distribution of kinetic energy release and internal excitation of the products. When this statistical variation is taken m times for m evaporation steps, the result is a broad energy region over which the initially excited cluster ensemble would loose m monomers.

For benzene cluster ions larger than six an average monomer binding energy ranges from 0.37 - 0.34 eV/molecule, quite close to the energy of vaporization for liquid benzene. The fourteen molecule cluster is found to have an anomalously high binding energy, providing strong evidence that it forms a stable icosahedral structure. The general trend of the benzene monomer binding energy with cluster size is well accounted for by a simple model based upon macroscopic constructs and liquid benzene dielectric constant, surface tension, and heat of vaporization values and is presented in figure 3.

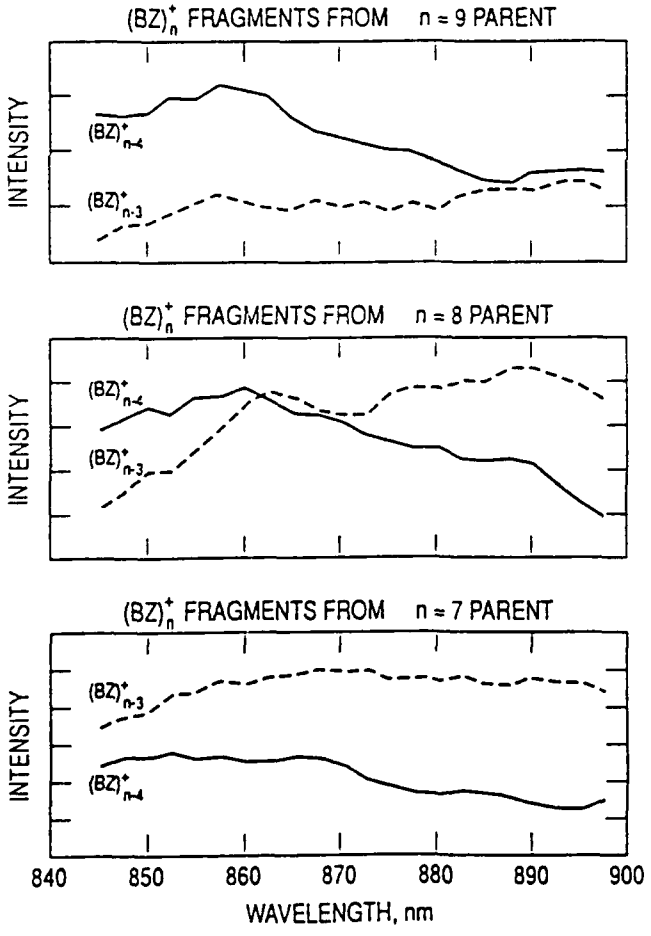

Figure 2

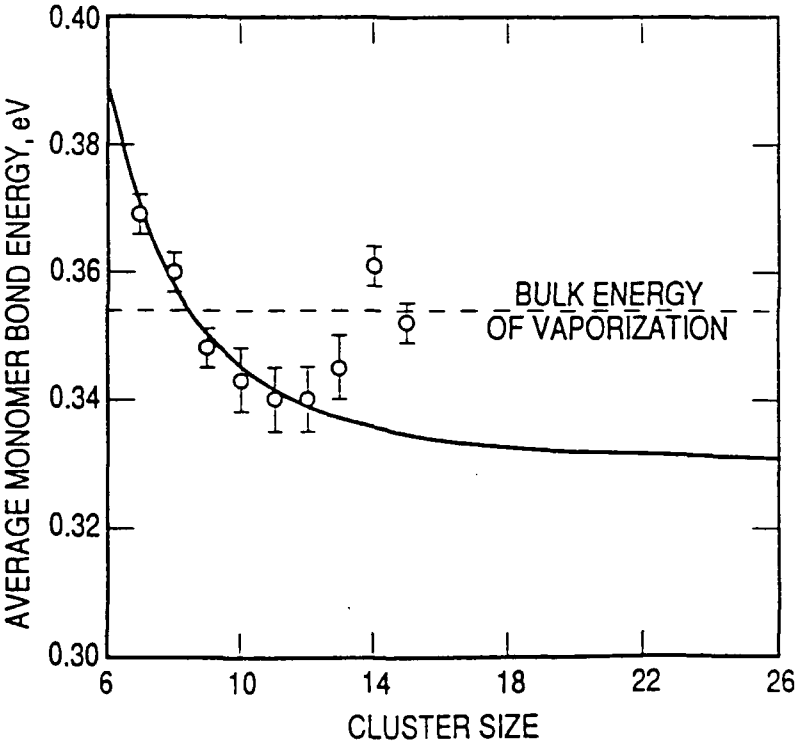

Figure 3

REFERENCES

1) D. C. Easter, R. L. Whetten, and J. E. Wessel, J. Chmem. Phys. 94, 3347 (1991).

2) K. E. Schriver, A. J. Paguia, M. Y. Hahn, E. C. Honea, A. M. Camarena, and R. L. Whetten, J. Phys. Chem. 91, 3131 (1987).

3) K. E. Schriver, M. Y. Hahn, and R. L. Whetten, Phys. Rev. Lett. 59, 1906 (1987).

4) M. Y. Hahn, K. E. Schriver, and R. L. Whetten, J. Chem. Phys. 88, 4242 (1988).

5) D. C. Easter, M. S. El-Shall, M. Y. Hahn, and R. L. Whetten, Chem. Phys. Lett.

6) B. W. Van de Waal, J. Chem. Phys. 79, 3948 (1983).

7) B. W. Van de Waal, Chem. Phys. Lett. 123, 69 (1986).

8) O. Echt, K. Sattler, and E. Recknagel, Phys. Rev. Lett. 47, 1121 (1981)

FRAGMENTATION ANALYSIS OF SIZE SELECTED NEUTRAL SODIUM CLUSTERS

L. Bewig, U. Buck, Ch. Mehlmann and M. Winter

Max-Planck-Institut für Strömungsforschung, D-3400 Göttingen, FRG

Weakly bound clusters fragment appreciably upon electron impact or photoionization. The reason is the structural change when going from the neutral to the strongly bound ionic configuration. Such a behaviour should not occur for systems with delocalized electrons so that, at least, the near threshold ionization of metal clusters is expected to be free of fragmentation. Detailed experimental information on this process is still rare, aside from one experiment with reneutralized cluster ions [1].

To get quantitative information on the fragmentation process, we recently developed a method [2], which is based on the different kinematic behaviour of the neutral clusters scattered by a target beam. By measurement of both angular and velocity distributions of the scattered cluster beam, the ion signal at a specific detection mass can unambigiously be attributed to the original neutral cluster. The experiments have been carried out in a crossed molecular beam machine, described in [3]. Details of the sodium cluster source will be found in [4]. In order to compare the fragmentation probability of the clusters for electron bombardment ionization and photoionization the setup has been extended by a second detection scheme for photoionization. The photons are generated from a Xe-arc lamp or an excimer pumped, pulsed and frequency doubled dye laser so that the scattered clusters could be detected simultaneously with photoionization and electron impact ionization in the two independent detection schemes. The different fragmentation probabilities of the sodium clusters which are caused by the distinct ionization processes can already be realized in the cluster abundance spectra shown in Table 1.

Aside from the overall smaller fragmentation due to the photoionization process, these data clearly indicate that sodium monomer and dimer ions form the main fragmentation channel under electron impact ionization. The full fragmentation analysis [2] yields in this

n	1	2	3	4	5	6	7	8	ionization method
	88946	90221	10000	2647	6838	1715	6053	3725	electrons (25 eV)
	1102	..03	10000	15210	6218	4278	8229	13929	photons (290 nm)

Table 1: Abundances of Na_n^+ cluster ions from different ionization methods

case for the neutral dimer a fragmentation probability to the monomer ion of $f_{21} = 0.28$. It also reveals that the trimers in the abundance spectrum for electron impact ionization result as ionic fragmentation products from larger neutral clusters, since $f_{33} = 0.0$, $f_{32} = 0.5$ and $f_{31} = 0.5$. The total fragmentation of the trimer under electron impact is also evident from the data in Fig. 1, which show the total differential cross sections for sodium clusters scattered from a helium beam and detected at the trimer mass with electron impact ionization and photoionization. In the first case, the differential cross sections for the trimer terminate at the maximum scattering angle corresponding to the tetramer, whereas for photoionization the trimer signal can be measured in the full kinematical allowed angular region. In the angular range below the maximum scattering angle for the pentamer, the different behaviour of the differential cross sections in Fig. 1 demonstrates also the reduced fragmentation upon photoionization.

For a detailed analysis of the fragmentation probability of photoionized sodium clusters we first used the unfiltered emission of a Xe-arc lamp, which contain photons with energies up to about 5.6 eV. Due to the low photon flux at this energies, the measured intensity for the sodium monomer is not high enough to give a reliable information in the time of flight spectrum, so this fragment channel is omitted in the data listed in table 2. The most striking result is the dominant fragment channel of the tetramer to the dimer ion Na_2^+, and not to Na_3^+, which is expected under energetic considerations [5]. This elucidates that the fragmentation process upon photoionization is not only governed by energetic concepts, but also dynamical processes come into play.

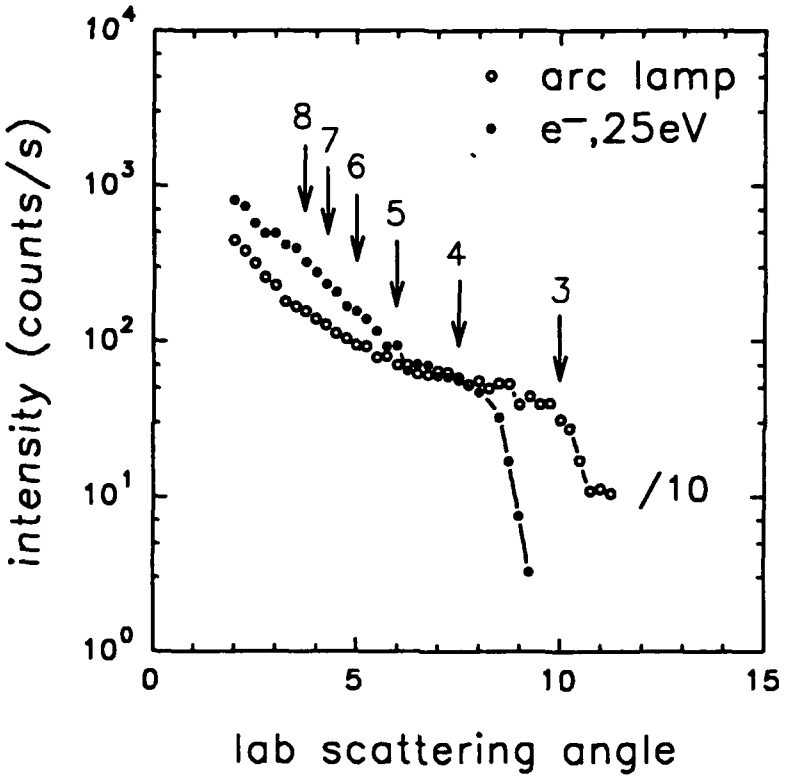

Figure 1: Differential cross sections for sodium clusters scattered from a Helium beam and detected at the trimer mass with electron impact and photoionisation

For a precise determination of the excess energy dependence of the fragmentation probabilities, investigations with several specific photon wavelengths have been carried out. These measurements corroborate the general trend, that the fragmentation of the cluster is reduced the closer the ionisation threshold energy is approached. As an example, the tetramer and the pentamer fragment only with a probability of less than 10% when ionized at 290 nm.

Na_4	f_{44}	f_{43}	f_{42}	f_{41}	Na_3	f_{33}	f_{32}	f_{31}
	0.29	0.07	0.64	—		0.37	0.63	—

Table 2: Fragmentation probabilities for the sodium trimer and tetramer under photoionisation with a Xe-arc lamp

References

[1] C. Bréchignac, Ph. Cahuzac, J. Leynier, R.Pflaum, J. Weiner *Phys. Rev. Lett.* , **61**, 314, (1988).

[2] U. Buck and H. Meyer *Phys. Rev. Lett.* **52**, 109, (1984).

[3] U. Buck, G. Hoffmann, J. Kesper, D. Otten and M. Winter Chem. Phys. , **126**, 159, (1988).

[4] L. Bewig, U. Buck, Ch. Mehlmann and M.Winter submitted to *Rev. Sci. Instr.*, (1992).

[5] C. Bréchignac, Ph. Cahuzac, J. Leynier and J. Weiner *J. Chem. Phys.* , **90**, 1492, (1989).

An investigation of non-equilibrium relaxation in free expansions. A Boltzmann solution for mixed atomic flow.

G.H.Bristow, T.L.Mazely and M.A.Smith
Department of Chemistry
University of Arizona
Tucson, AZ 85721

The flow dynamics of a multi-component atomic free jet are analyzed by solving the Boltzmann equation, utilising the method of moments.[1] A free jet expansion is an excellent media in which to study non-equilibrium relaxation including energy transfer and mass transfer (reaction). The theoretical approach to multi-component flow outlined here is necessary for an understanding of experimental results obtained from expansions and to gain further insight into the relaxation process itself.

For a continuous free jet there is no explicit time dependence of the distribution function and no external forces acting on the gases. The Boltzmann equation for a field free, continuous jet is then

$$\mathbf{v}_i \cdot \frac{\partial f_i}{\partial x} = \sum_j \mathbf{J}_{i,j}$$

where $\mathbf{J}_{i,j}$ is a collision integral representing changes in the distribution function due to collisions.

$$\mathbf{J}_{i,j} = \int_0^{2\pi} d\varepsilon \int_0^{\infty} b(\chi)\, db \int_{-\infty}^{\infty} dv_j\, (f'_i f'_j - f_i f_j) g_{i,j}$$

These collision integrals are nonzero in a non-equilibrium system and a knowledge of them at all positions in the expansion will directly give the gradient of the distribution function. By assuming the form of the distribution function this gradient will give us the gradient of all the dependent variables within the distribution function, i.e temperatures, number densities, velocities. It is common practice to assume the free jet possesses cylindrical symmetry which allows us to describe the distribution function with two temperature terms: one describing the random motion along the direction of flow and the other describing the motion perpendicular to this streamline flow. Thus the distribution function used here is an uncoupled ellipsoidal distribution function -

$$f_i = n_i \sqrt{\frac{m_i}{2\pi k T_{\parallel}}}\, \frac{m_i}{2\pi k T_{\perp}} \exp\left\{ -\frac{m_i}{2kT_{\parallel}} (v^2_{z,i} - u_i) - \frac{m_i}{2kT_{\perp}} (v^2_{x,i} - v^2_{y,i}) \right\}$$

The solution to the Boltzmann equation is obtained using the method of moments, the necessary moment equations being obtained by multiplying each side of the Boltzmann equation by some function of velocity, $\Phi(v_i)$, and integrating over all space -

$$\int_{-\infty}^{\infty} \Phi(v_i)\, \mathbf{v}_i \cdot \frac{\partial f_i}{\partial x}\, dv_i = \sum_j \int_0^{2\pi} d\varepsilon \int_0^{\infty} b(\chi)\, db \int_{-\infty}^{\infty} dv_i \int_{-\infty}^{\infty} dv_j\, \{\Phi(v'_i) - \Phi(v_i)\}\, f_i f_j\, g_{i,j}$$

To solve for multi-component flow we need 4N differential equations, where N is the number of species in the jet. The eight independent functions of velocity used for two component flow are n_i, n_j, $v_{\parallel,i}$, $v_{\parallel,j}$, $v_{\parallel,i}{}^2$, $v_{\parallel,j}{}^2$, $v_{\perp,i}{}^2$, $v_{\perp,j}{}^2$. These functions were chosen to simplify the collision integral calculations in that for a conserved property the collision integral goes to zero. This is the case for n_i and n_j due to conservation of number of particles and for $v_{\parallel}$ due to conservation of parallel momentum between identical collision partners.

To determine the form of the velocity moments on the right hand side of these equations it is necessary to understand how the velocity components change in a collision. The pre-collision and post-collision velocities are related by the following expression. [2]

$$\mathbf{v}_i' - \mathbf{v}_i = \frac{2\mu_{ij}}{m_i}\sin(\chi/2)(g_{i,j}\sin(\chi/2) + g_{i,j}\,\mathbf{k}_\perp)$$

The apse vector **k** is a unit vector parallel to the line of symmetry of a collision. Components of momentum and thus velocity parallel to **k** are reversed by collisions whereas the perpendicular components remain unchanged. So the apse vector is resolved into two components $\mathbf{k}_\parallel$ (=gsin(χ/2)) and $\mathbf{k}_\perp$,

$$\mathbf{k}_\perp = \begin{bmatrix} k_x \\ k_y \\ k_z \end{bmatrix} = -\cos(\chi/2) \begin{bmatrix} \cos\theta\cos\phi\cos\varepsilon + \sin\phi\sin\varepsilon \\ \cos\theta\sin\phi\cos\varepsilon - \cos\phi\sin\varepsilon \\ -\sin\theta\cos\varepsilon \end{bmatrix}$$

where ϕ,θ are the initial orientation of the relative velocity vector and ε,χ are the azimuthal and polar scattering angles. It now remains to integrate the expression for the velocity moments -

$$\int_0^{2\pi} d\varepsilon \int_0^{\infty} b(\chi)\,db \int_{-\infty}^{\infty} dv_i \int_{-\infty}^{\infty} dv_j \,\{\Phi(v_i') - \Phi(v_i)\}\, f_i f_j\, g_{i,j}$$

Assuming cylindrical symmetry the collisional cross section is independent of ε and ε is easily integrated over. To integrate over the other seven variables it is necessary to convert the distribution function into the center of mass frame where standard integrals are used to integrate over the centre of mass velocities. To integrate over the impact parameter,b, the following integral must be defined [3]

$$Q^{(l)}(g) = 2\pi \int_0^{\infty} (1 - \cos^l\chi)\, bdb$$

which has units of cross section. This integral quantifies the nature of the low energy collisions to the extent that they are controlled by the long range interaction part of a Lennard-Jones potential with l=1 relating to the transfer of momentum and l=2 relating to viscosity and energy transfer. The azimuthal angle, ϕ, is easily integrated over but the coupling between the polar angle, θ, and the relative velocity vector, g, which arises from velocity slip between different species in the expansion, prohibits an analytic solution to the final integration over g and θ. This integration is dealt with numerically using standard trapezoidal integration.

Having obtained a solution to the collision integrals the moment equations are now rearranged to obtain the spatial dependence of the density, n_i, hydrodynamic velocity, u_u, and translational temperatures, $T_{\parallel,i}$ and $T_{\perp,i}$ - see Table 1.

Thermal anisotropy develops as the expansion evolves, as also seen in a single component free jet.[4,5] In a multi-component free jet, however, the differing masses and interaction potentials between species complicate the thermal anisotropy by the presence of temperature slip between species. The possibility of temperature slip, especially in the parallel direction leads to energy anisotropy. This solution to the Boltzmann equation has naturally incorporated both velocity and temperature slip between chemically distinct colliding species in the calculation of the collision integral terms.

The technique is also applied to a slit nozzle for which results will be presented. Numerical results

for the integrated moments at various positions in a binary free jet and slit jet expansions will be presented.

Table 1 - spatial dependence for the observables of a binary atomic free jet.

$$\frac{d\ln(n_i)}{dz} = -\frac{2}{z} - \frac{3Z_i + \frac{2T_{\perp,i}}{z} - X_i}{\frac{m_i u_i^2}{k} - 3T_{\parallel,i}}$$

$$\frac{d\ln(u_i)}{dz} = \frac{3Z_i + \frac{2T_{\perp,i}}{z} - X_i}{\frac{m_i u_i^2}{k} - 3T_{\parallel,i}}$$

$$\frac{dT_{\perp,i}}{dz} = -\frac{2T_{\perp,i}}{z} + \frac{Y_i}{2}$$

$$\frac{dT_{\parallel,i}}{dz} = \frac{2T_{\perp,i}}{z} + \frac{3Z_i + \frac{2T_{\perp,i}}{z} - X_i}{\frac{m_i u_i^2}{k} - 3T_{\parallel,i}} \left[T_{\parallel,i} - \frac{m_i u_i^2}{k}\right] - 3Z_i$$

$$X_i = \frac{m_i}{n_i u_i k} \Delta[v_\parallel^2]_i$$

$$Y_i = \frac{m_i}{n_i u_i k} \Delta[v_\perp^2]_i$$

$$Z_i = \frac{m_i}{n_i k} \Delta[v_\parallel]_i$$

References

1.E.L.Knuth and S.S.Fisher, *J. Chem. Phys.*, **48** (1968), 1674
2.W.G.Vincenti and C.H.Kruger, Jr., Introduction to Physical Gas Dynamics (Robert E. Krieger Publishing Co., Huntington, NY, 1975)
3.J.O.Hirschfelder, C.F.Curtiss and R.B.Bird, Molecular Theory of Gases and Liquids (John Wiley & Sons, New York, 1954)
4.H.C.W.Beijerinck and N.F.Verster, *Physica C 111*,(1981) 327
5.L.K.Randeniya and M.A.Smith,*J. Chem. Phys.* ,**93** (1990), 661

IR -Depletion of Mixed Molecular Clusters, Probed with Resonant Two Photon Ionization Spectroscopy

B.Brutschy, Ch. Riehn, Ch. Lahmann, B. Wassermann
Freie Universität Berlin, Institut f. Physik.und Theoret. Chemie,Takustr.3, 1000 Berlin 33, Germany

Recently mixed clusters of organic molecules have attracted considerable interest as model systems to study ion-chemistry in tailor made microsolutes /1/. Evidence was presented, that already small clusters consisting of a subst.benzene cation with only few polar solvent molecules react differently observed in the gas phase /2/. The size of a reacting cluster system is characterized by the optical fingerprints of the solvated chromophore, deducible from the ion-yield curve of a cluster and of its product ions, measured with resonant two photon ionization (R2PI). The assignment of the size and structure of the solvent moiety is difficult if the clusters decays quantitatively into several product channels, since in that case the parent is not longer available for the mass identification of the fingerprints.

In the case of nucleophilic substitution reactions in (1:n) clusters consisting of a halobenzene cation and n polar solvent molecules like ammonia, methanol or water the reactions in 1:2 and 1:3 complexes are

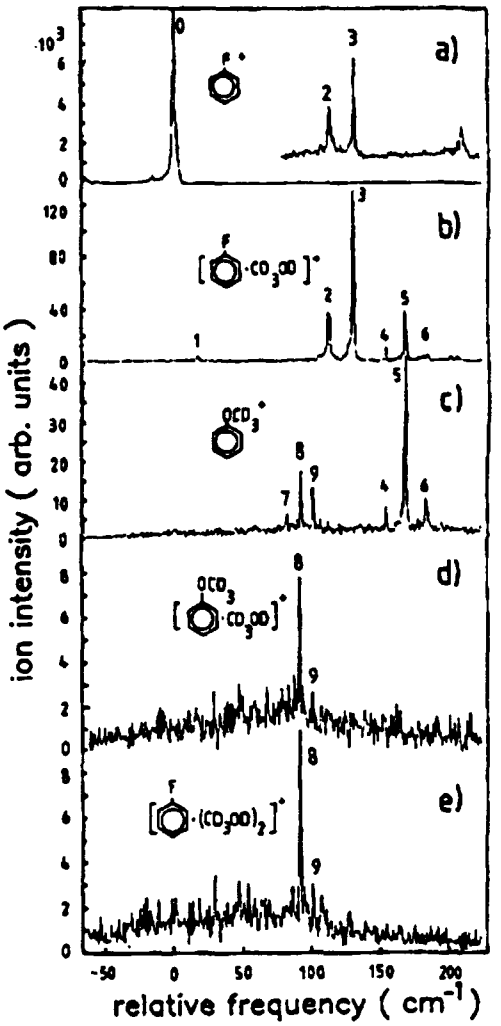

Fig.1 R2PI ion yield curves of some ions of an expansion of Fb and deuteromethanol ionized by R2PI near the $S_1 \leftarrow S_0$ transition of Fb.

very fast due to bifunctional catalysis by additional solvent molecules. An example is the reaction in mixed clusters of fluorobenzene$^+$ (Fb) with methanol. The ion-yield curves, measured with one color R2PI for several ions of this system are depicted in Fig. 1. Following assignment is made: bands 2,3 are assigned to the 1:1 precursor, bands 4-6 to the 1:2 complex. The latter should contain the solvent molecules as dimer, which decays quantitatively into two channels. One is the fragmentation to the 1:1 , the other the following nucleophilic substitution reaction:

$$Fb^+ \cdot (CD_3OD)_2 \longrightarrow anisole^+ + HF\cdot(CD_3OD) \qquad (1)$$

To corroborate the assignment of a (1:dimer) precursor, inferred from this particular reaction behavior, we developed a novel technique where the neutral precursors are analyzed by their IR depletion spectra probed by R2PI.

In this method, the cluster beam is irradiated by tunable IR laser light to excite intramolecular vibrations in a molecular subunit. The experimental setup is shown in Fig. 2.

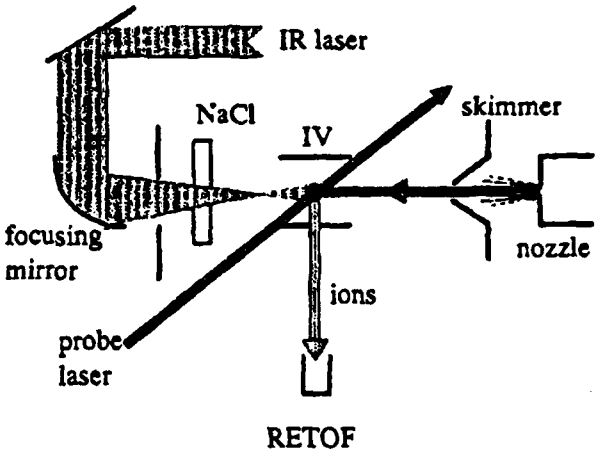

Fig.2 Experimental setup for the IR/R2PI depletion spectroscopy
RETOF=Reflectron TOF spectrometer
NaCl=NaCl window; IV=ionization vol.

After absorption of one or two vibrational quanta the cluster generally fragments by loss of one molecule. This IR predissociation of clusters was pioneered by Scoles and Miller in the early eighties. It is meanwhile applied by several groups and with different techniques to detect the depletion of the absorber. Buck et al./3/ and Huisken et al. /4/ for example measured the IR depletion spectra of several clusters of polar molecules size selected by using the scattering technique /3/.

These spectra measured by scanning the IR-laser, contains informations on the size and structure of the absorbing cluster. For

example in a methanol dimer the monomer's C-O stretching vibration is split up into two components due to the two nonequivalent absorbers, while clusters of 3 to 5 molecules exhibit only single bands /3/4/, indicating equivalent absorbers, probably forming planar rings. Similar IR-spectra are reported for clusters of ethylene, ammonia, water etc./

We probes the depletion of a cluster precursor with R2PI. To illustrate this new method Fig. 3 shows the depletion spectrum of $Fb^+ \cdot$(methanol) from Fig. 1b) probed via the fingerprint band 2 and and measured by scanning the CO_2 laser in the vicinity of the ν_8 C-O stretching mode of methanol at 1034 cm^{-1}. The spectrum contains two, very narrow bands (Fig. 3a). The red-shifted one (band I) is assigned to Fb. For other halobenzenes it is shifted. The second, more intense band II, blue-shifted by 7 cm^{-1} relative to ν_8 does not change its position with different chromophores. It is therefore assigned to the solvent. The weak shift relative to ν_0 in the free molecule indicates a weak interaction of the absorber with the π-electron system of Fb. Probing the depletion of anisole$^+$ by ionizing via the "reactive" band 5 (Fig. 1c) results in a depletion spectrum, consisting of two relatively broad bands (Fig. 3b) looking very similar to those observed for the free methanol dimer (Fig. 3c), as measured by Huisken et al./4/. The D band is assigned to the donor and the D band to the acceptor molecule in the linear H-bridge. In the free dimer the methanol donor is shifted by 8 cm^{-1} to the blue, the acceptor by 18 cm^{-1} to the red

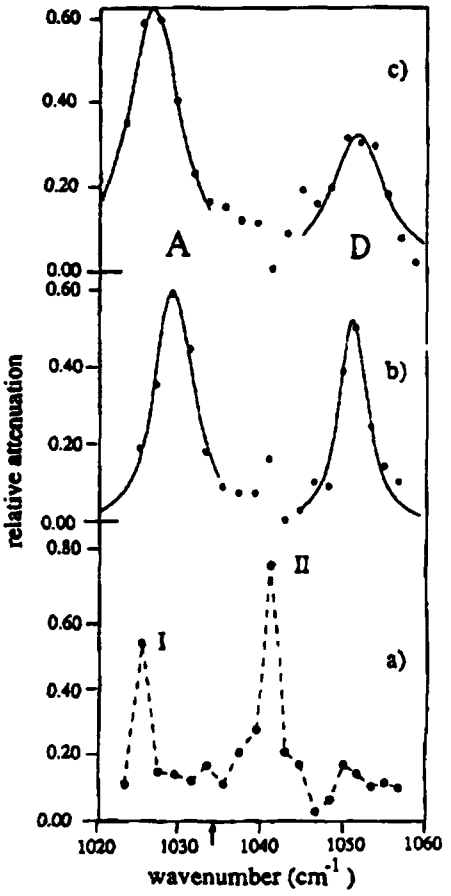

Fig.3 depletion spectrum of
a) the $(Fb \cdot (methanol))^+$
b) anisole$^+$ from eq. 1
c) $(methanol)_2$ measured by Huisken /4/
A = acceptor; D= donor
I = Fb II= methanol

side relative to ν_s, as discussed in the literature /4/5/. For comparison, a free trimer, due to its ring like structure, shows only a single band, shifted by 7 cm^{-1} /3/. In summary, the spectrum of the precursor of anisole$^+$ looks very similar to that of the free dimer, therefore the assignment of a (1:dimer) structure is justified. Some small changes have to be notified. The acceptor band in the associated dimer is blue-shifted by 4 cm^{-1} relative to the bands of the free dimer, while the donor band is unshifted. From this shift we deduce a weak H-bond between the acceptor molecule and the π-electron system, as already predicted by model calculations. The relative decrease of the acceptor intensity may also be due to its donor like interaction with the chromophore.

By this pump & probe depletion spectroscopy the structure of any small mixed cluster may be investigated if polar solvents associate in networks or subclusters and if the depletion spectra of the size selected free solvent clusters are known. A concluding assessment of the general applicability of this method is however not yet possible due to the scarcity of the results. With high resolution, tunable IR lasers, perhaps more size specific fine structure will appear in these spectra, allowing the unambiguous assignment of much larger solvent clusters. This structural informations may be crucial in understanding the reaction dynamics following ionization.

references

/1/ Brutschy, B. J. Phys. Chem. **1990**, *94*, 8637.

/2/ Brutschy, B.; Riehn, C.; Lahmann,C. J.Chem.Phys. **1992**, *96*,Apr.

/3/ Buck, U. in: Clusters of Atoms and Molecules; Haberland, H., Ed.; Springer Verlag: Heidelberg, **1991**, and references

/4/ Huisken, F.; Stemmler, M. Chem. Phys. Lett. **1988**, *144*, 391.

/5/ Buck, U.; Schmidt, B. J. Mol. Liqu. **1990**, *46*, 181.

EELS-Studies of Free Fullerenes Using Electron Energies between 10 eV and 1100 eV

A. W. Burose, T. Dresch and A. M. G. Ding

Optisches Institut, Technische Universität Berlin, Germany

Since the discovery of the new class of fullerenes/1/ and the development of its production techniques /2/ their properties have been the target of many investigations. High resolution energy loss spectra (EELS) on free fullerenes in the gas phase have been obtained in the electron energy range between 10 eV and 1100 eV using C_{60}/C_{70} mixtures as well as pure C_{60} . So far, EELS-spectra have only been taken in the forward direction covering energy losses between 1 eV and 100 eV. An experimental set-up used for EELS-experiments for free van-der-Waals clusters has been modified for this application and is displayed in Fig.1: electrons from a monochromatic source (ΔE = 30 meV) pass through an interaction region and are analyzed in a tandem electron spectrometer. In order to maintain high resolution the electron energies between 2 eV and 5 eV inside the electron spectrometers are kept at a fairly low level (2 eV to 5 eV); acceleration and deacceleration is being accomplished by specially designed electrostatic zoom-lenses. Electrons are detected using a channeltron electron multiplier.

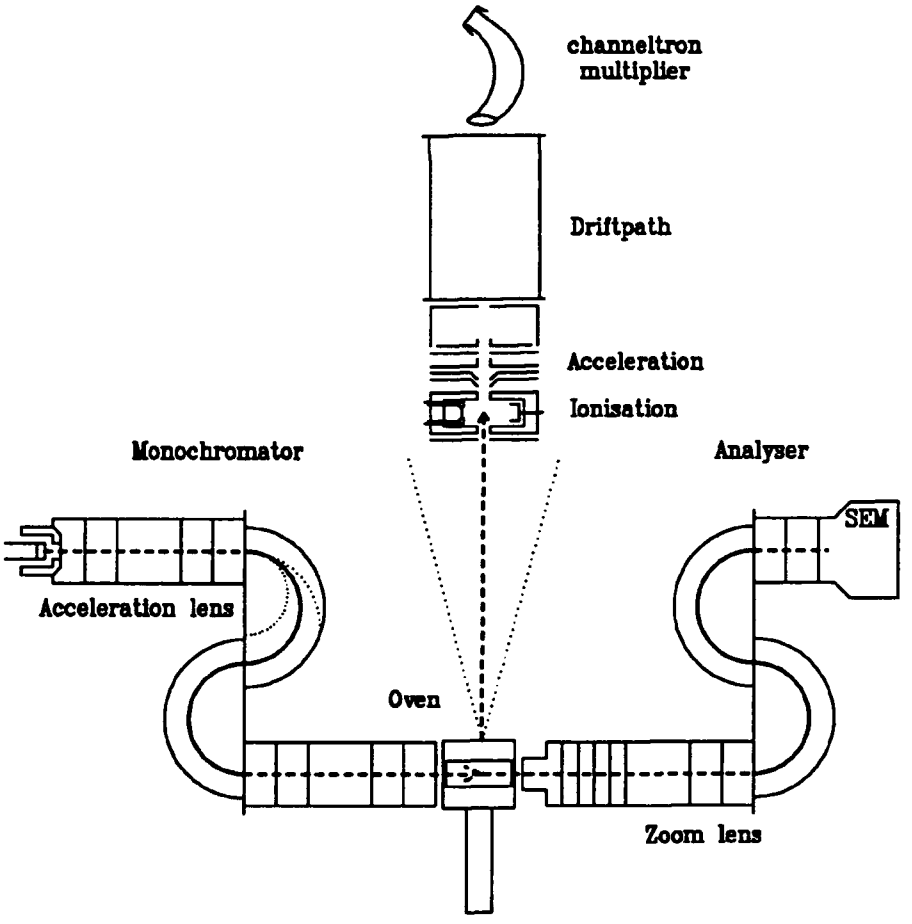

Fig. 1: Experimental arrangement for determining the electron energy loss spectra of free fullerenes

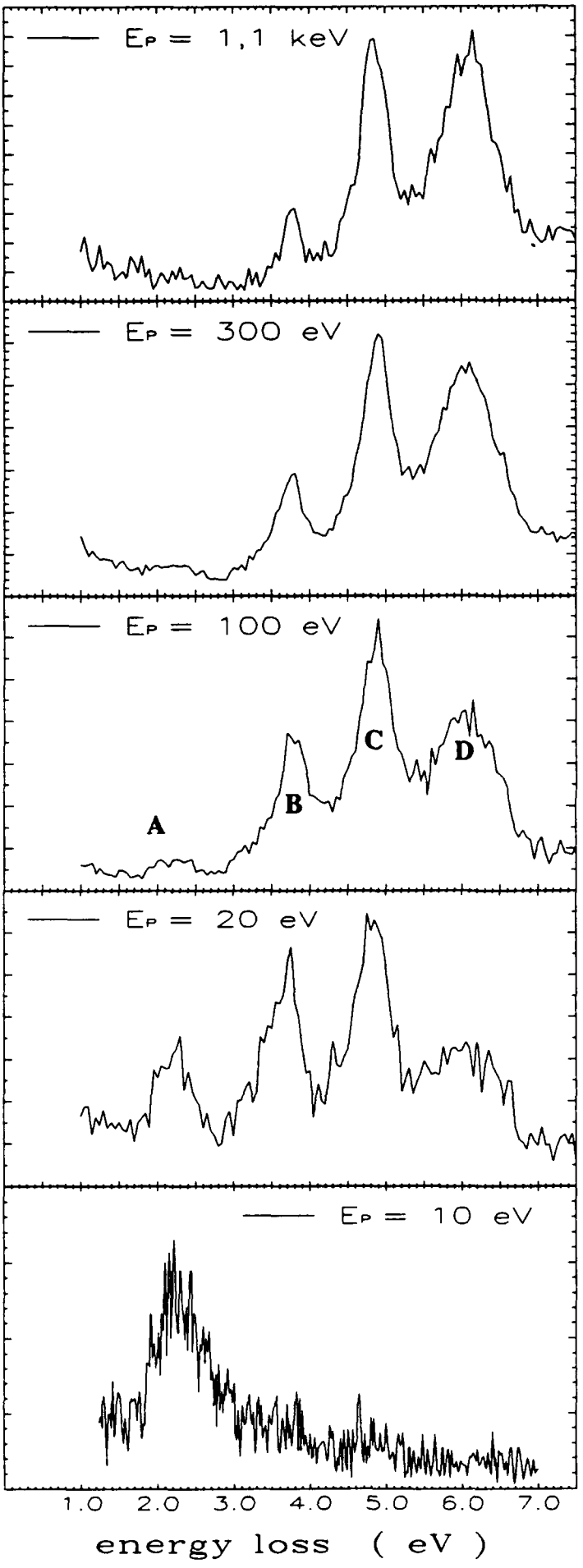

Fig. 2: EELS- spectra of pure C_{60} for different primary electron energies at constant temperature of 450°C.

An oven containing fullerene powder is placed in the interaction region which can be heated up to 600 °C. The oven caplsule has three apertures, one for the incoming electrons, one for the outgoing electrons and a third perpendicular to the electron beam axis for monitoring the composition of the beam using a simple time-of-flight mass spectrometer. TOF-mass spectra were taken simultaneously with the EELS-spectra in order to monitor the C_{60}/C_{70} ratio. At temperatures below 400 °C no significant amount of C_{70} was present in the beam although the C_{70} fraction was enriched with time when using higher oven temperatures.

Fig. 2 displays EELS-spectra of pure C_{60} taken at different primary electron energies. Four distinct features (denoted A to D in Fig. 2)arise in the energy loss intervall below 10 eV. The three higher transitions(B,C) are optically allowed, two of which have apoximately equal energies(C); they coincide approximately with the absorption spectra measured by Krätschmer et al./2/. According to Rosén et al. /4/ they are assigned to the h_u-t_{1g}(HOMO → LUMO+1), h_u-t_{2g}/h_g(HOMO → LUMO+2), and h_g-t_{1u}(HOMO-1 → LUMO)

transitions while the lowest one h_u-t_{1u}(HOMO → LUMO) corresponds to a optically forbidden transitions. The latter transition(noted A in Fig.2) increases in intensity when lowering energy of the primary electrons, which leads to a breakdown of the optical selection rules. It emerges as the strongest transition at $E_{el} = 10eV$.

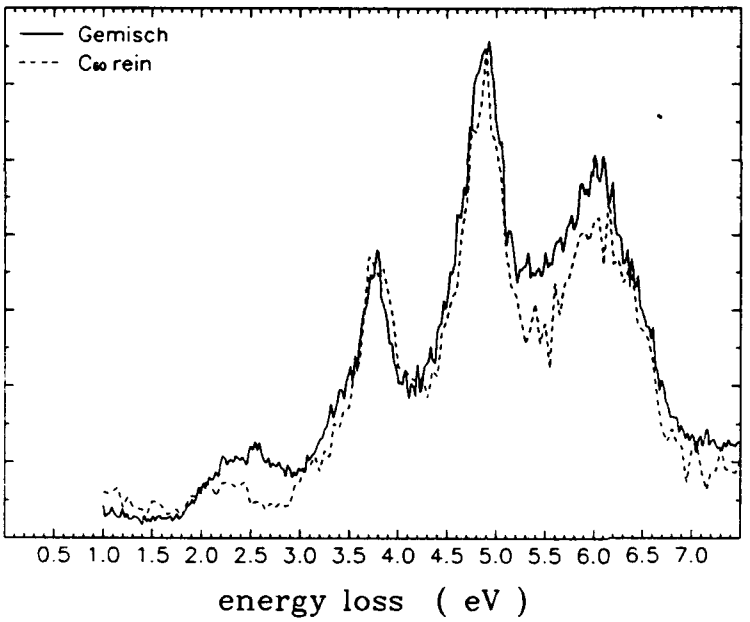

Fig. 3: Comparison between EELS-spectra of a mixture of C_{60}/C_{70} and pure C_{60} taken at an incident primary electron energy of 100eV and a temperature of 450 °C.

Using non purified fullerene mixtures it has to be kept in mind, however, that the interaction region contains also a non negligible amount of C_{70}. This depends mainly on the oven temperature and increases with time due to the preferential evaporation of the C_{60}. The spectral feature around 2.5 eV consists in fact of contributions from both C_{60}(2.3 eV) and C_{70}(2.6 eV), the latter structure disappearing with decreasing oven temperatures. This can be clearly seen when comparing EELS-spectra of mixed fullerenes with those of pure C_{60} as shown in Fig.3.

The peak at D shows also a dependance on electron energy, however in the opposite sense: While ist is practically absent at low E_{el} it increases strongly with electron energy. According to /5,6/ it is assigned to a pi-Plasmon resonance closely resembling the one found in solid graphite /7/. Compared with the optical spectra it is shifted to higher energies and

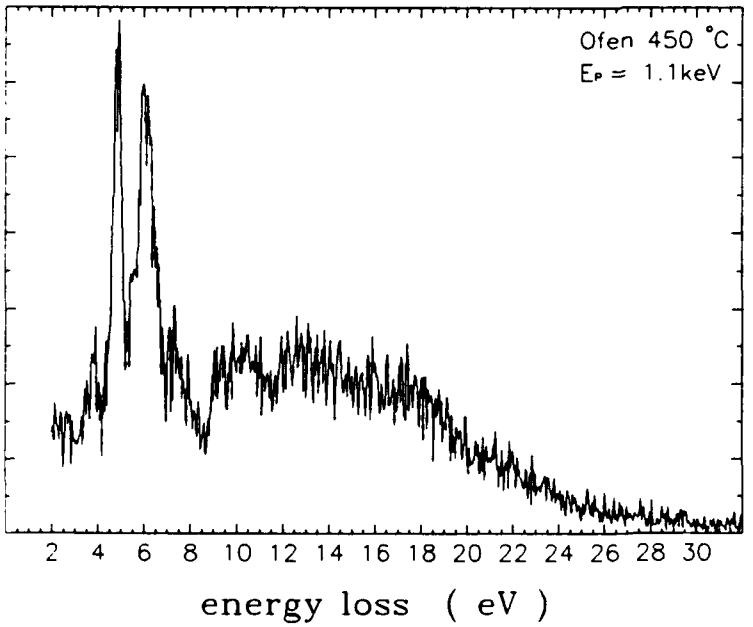

Fig. 4: Larger energy loss spectrum for pure C_{60} at a primary electron energy of 1.1keV.

shows a significant larger broadening which cannot be explained by the fact of additional underlying transitions of C_{70}.

Spectra taken over a larger energy loss interval show only weak features below $\Delta E = 24$ eV at $E_{el} = 1.1$keV in disagreement with experiments/5,6/ and calculations/8/ for solid fullerenes. As shown in Fig.4, these spectra display a very broad features with weak maxima at 7.5, 10, 13 and 17 eV and disappear altogether at lower electron energies. These maxima coincide approximately with those resulting from EELS experiments on solid fullerite layers, but are of much lower intensity compared with the main peaks around $E_{el} = 5$eV. This may partly be attributed to the dependence of the energetic position and the magnitude of the plasmons as a function of the scattering angle. Comparing our results with those of Lucas et al./6/ who observe very strong plasmon transitions around 25 eV it can only be concluded that features seen in the solid are strongly enhanced due to the solid state interaction in the fullerite crystals.

The authors thank Dr. W. Krätschmer for supplying fullerene mixtures and Dr. J. Fink and Dr. E. Sohmen for suplying pure C_{60}. The financial assistance of the German Research Council (DFG Sonderforschungsbereich 337) is greatfully acknowledged.

References:

/1/ H. W. Kroto, J. R. Heath, S. C. O'Brien, R. F. Curl, R. E. Smalley, Nature, **318**, pp. 162-163 (1985)

/2/ W. Krätschmer, L. D. Lamb, K. Fostiroupolos, D. R. Huffman, Nature, **347**, pp. 354-358 (1990)

/3/ C. Becker, A. Burose, A. Ding, Z. Phys. D - Atoms, Molecules and Clusters, **20**, pp. 35-38 (1991)

/4/ S. Larsson, A. Volosov, A. Rosén, Chem. Phys. Lett., **137**, 501 (1987)

/5/ E. Sohmen, J. Fink, W. Krätschmer, Z. Phys. B - Condensed Matter, **87**, pp. 87-92 (1992)

/6/ G. Gensterblum, J. J. Pireau, P. A. Thiey, R. Caudano, J. P. Vigneron, Ph. Lambin, A. A. Lucas, Phys. Rev. Lett., **67**, pp. 2171-2174 (1991)

/7/ S. Krummacher, S. Cramm, K. Szot, W. Eberhardt, W. Krätschmer, Europhys. Lett., **16**, pp. 437-442 (1991)

/8/ F. Bertold, A. Bulgerac, D. Tomanek, Y. Wang, Phys. Rev. Lett., **67**, 690 (1991)

PHOTOIONIZATION STUDIES OF THIOPHENE AND THIOPHENE CLUSTERS IN A MOLECULAR BEAM.

P. Cid-Aguero and E.A. Walters

Department of Chemistry, University of New Mexico, Albuquerque, NM 87131.

J.R. Grover

Chemistry Department, Brookhaven National Laboratory, Upton, NY 11973

Van der Waals complexes produced in a free jet expansion of C_4H_4S:Ar (1:9) and C_4H_4S:He (1:9) mixtures were studied by single-photon photoionization mass spectrometry. Two different photon sources were used: the tunable vacuum ultraviolet beam available at the U-11 beam line of the 750 MeV electron storage ring of the National Synchrotron Light Source (NSLS) at Brookhaven National Laboratory, and a laser system employing third-harmonic generation (THG) located at UNM.

Neutral cluster distributions were determined for thiophene homoclusters (dimers and trimers) for both the argon and helium expansions. The results are shown in Fig. 1. Dissociative photoionization fragments in the range m/e 40-320 resulting from the breaking of molecular bonds and intracluster reactions initiated by 584 Å (21.22 eV) light were studied as a function of pressure. At a nozzle pressure of 300 torr of C_4H_4S + Ar mixture, a system which probably contains large clusters, $(C_4H_4S)_n$, $n \geq 4$, substantial signals due to the following parent cluster ions and

fragmentation or intracluster reaction products were found: $C_4H_2^+$ (m/e 50), $C_4H_3^+$ (m/e 51), $C_2H_2S_2^+$ (m/e 90), $C_5H_5S^+$ (m/e 97), $C_8H_6S^+$ (m/e 134), $C_{10}H_8S^+$ (m/e 160), $(C_4H_4S)_2^+$ (m/e 168), $C_6H_6S_3^+$ (m/e 174), and $(C_4H_4S)_3^+$ (m/e 252).

The product $C_8H_6S^+$, (m/e 134), is observed in considerable abundance. Analysis of the pressure dependence of m/e 134 yields shows that the ion signal tracks the abundance of $(C_4H_4S)_3$ homotrimer. Therefore, the reaction leading to $C_8H_6S^+$ is:

$$(C_4H_4S)_3 + h\nu \rightarrow C_8H_6S^+ + C_4H_4S + H_2S + e$$

The photoion yield curve for $C_8H_6S^+$ is shown in Fig. 2; examination of the onset region gives $AP(C_8H_6S^+) = 15.5\pm0.1$ eV. These results are consistent with a $[C_4H_4S \bullet C_4H_2^+]$ complex structure for this ion.

Photoion efficiency functions at the NSLS for $C_4H_4S^+$ and $(C_4H_4S)_2^+$ revealed vibrational structures which were tentatively assigned to specific modes for these species. For the case of $(C_4H_4S)_2^+$, spectra obtained using the THG laser showed vibrational structure which corroborated results from the NSLS experiments for the homodimer ion and extended the observed vibrational progressions, Fig. 3 and Table I. C_4H_4S could not be ionized using the THG system and therefore was not studied using the laser.

Thresholds and onsets were measured: $C_4H_4S^+$, 8.867±0.006 eV; $(C_4H_4S)_2^+$, 8.27±0.04 eV; $(C_4H_4S)_3^+$, 8.17±0.04 eV; $C_8H_6S^+$, 15.50±0.07 eV; $C_2H_2S^+$, 12.03±0.01 eV; and CHS^+ 13.06±0.05 eV, The same data were used to calculate dissociation energies and heats of formation for the homodimer, homotrimer and $C_8H_6S^+$ ion, (assuming $D_o^o[(C_4H_4S)_2] = 2.5$ kcal/mol): $D_o[(C_4H_4S)_2^+] = 16.3\pm0.5$

kcal/mol; $D_o[(C_4H_4S)_3^+]$ = 4.8±0.5 kcal/mol; $D_o[C_8H_6S^+]$ = -44.6±0.5 kcal/mol; $\Delta H_{fo}^o[(C_4H_4S)_2^+]$ = 243±1 kcal/mol; $\Delta H_{fo}^o[(C_4H_4S)_3^+]$ = 265±1 kcal/mol; and $\Delta H_{fo}^o[C_8H_6S^+]$ = 412±2 kcal/mol.

TABLE I : Vibrational Frequencies of $(C_4H_4S)_2^+$ in cm^{-1}

Line	BNL[a] (±100 cm^{-1})	THG[b] (±20 cm^{-1})	Interpretation
1	0.0	-	-
2	81	-	ν_1
3	161	-	$2\nu_1$
4	403	-	ν_2
5	694	-	ν_3
6	1073	-	$\nu_2 + \nu_3$
7	1444	1485	ν_4
8	1726	1711	ν_5
9	1807	1865	$\nu_5 + \nu_1$
10	2065	1966	ν_6
11	2145	2094	$\nu_3 + \nu_4$
12	2290	2252	$2\nu_1 + \nu_3 + \nu_4$
13	2420	2409	$\nu_3 + \nu_5$
14	2524	2547	$\nu_2 + \nu_3 + \nu_5$
15	-	2673	-
16	-	2806	-
17	-	2967	-
18	-	3106	-
19	-	3223	-
20	-	3370	-
21	-	3497	-
22	-	3659	-
23	-	3872	-

a.- Brookhaven National Laboratory data
b.- Third Harmonic Generation data

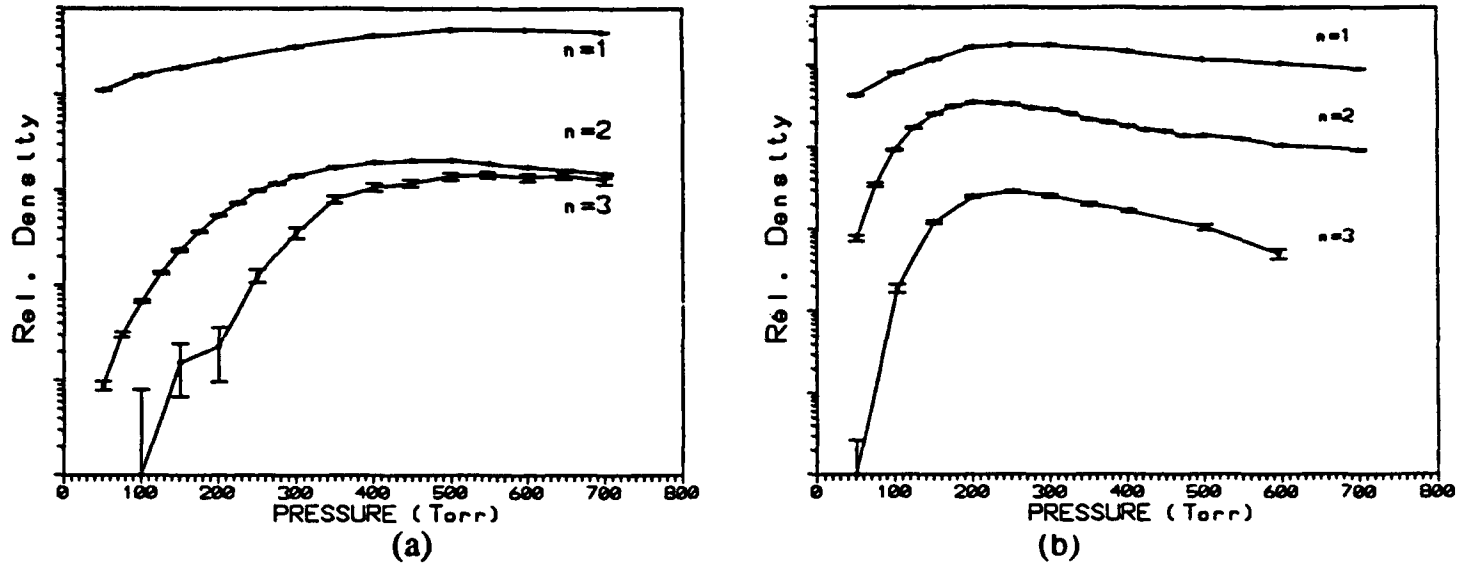

Fig. 1.- Neutral $(C_4H_4S)_n$, n=1-3 cluster distribution in free-jet expansion of: a) C_4H_4S : Hc (1:9) mixture, and b) C_4H_4S : Ar (1:9) mixture.

Fig. 2.- PIE curve of $C_8H_6S^+$ photoion over the range 450 - 1250 Å at 1 Å intervals from a 1:9 C_4H_4S : Ar mixture at 149 torr stagnation pressure.

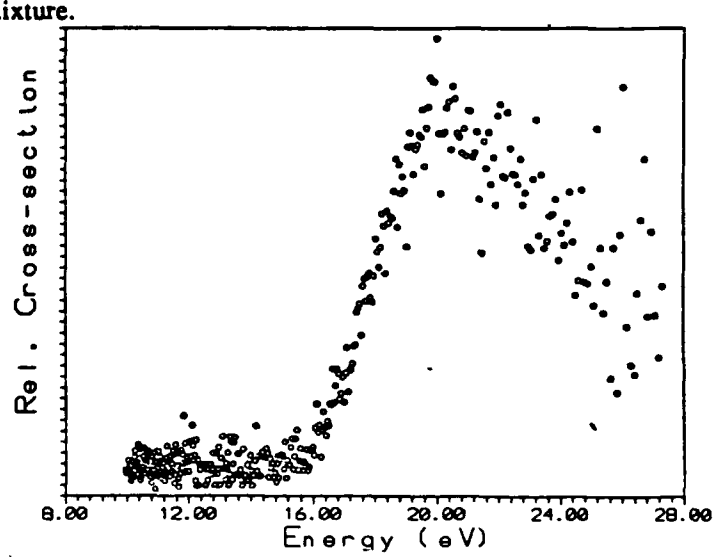

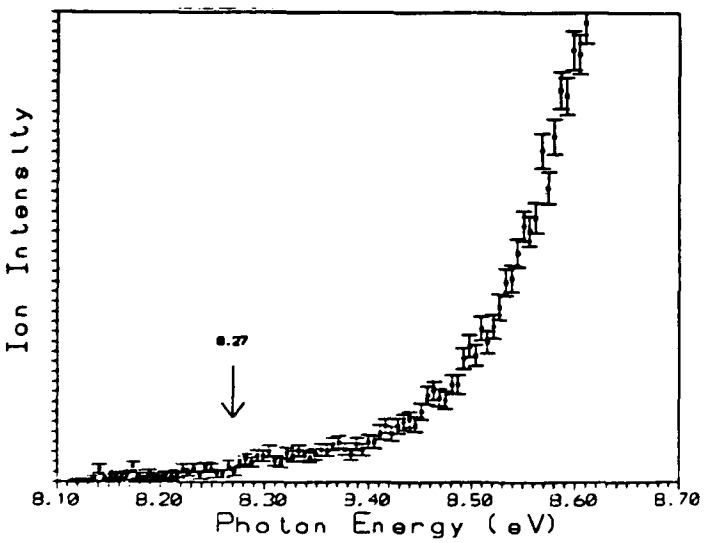

Fig. 3.- a) onset curve for $(C_4H_4S)_2^+$ ion from a 150 torr nozzle pressure of C_4H_4S+Ar mixture, over the energy range 8.10-8.70 eV. The arrow indicates the calculated threshold at 8.27±0.03 eV.

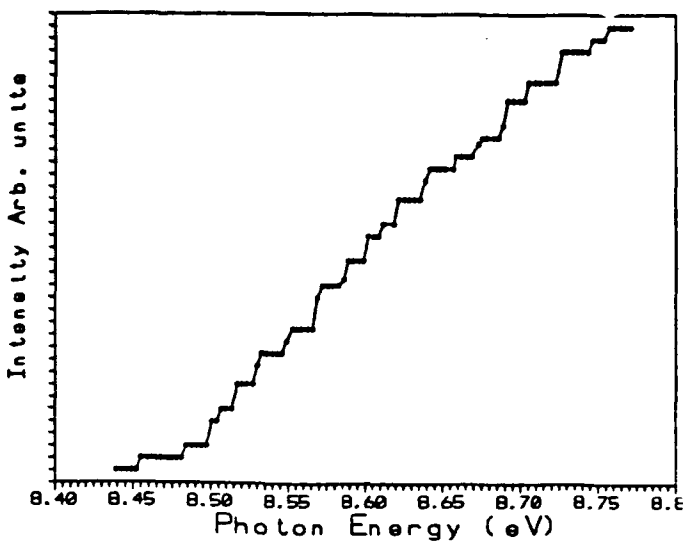

Fig. 3-b) The yield of $(C_4H_4S)_2^+$ ions produced by a THG photoionization experiment, in a 1:9 C_4H_4S + He mixture, at 200 torr stagnation pressure, over a 8.44-8.80 eV energy range.

HIGH RESOLUTION LIF STUDY OF A CAGE MOLECULE, DABCO.

D. Consalvo, G. Berden, M. Drabbels, W. Leo Meerts, D. H. Parker and J. Reuss

Molecular and Laser Physics, University of Nijmegen
Toernooiveld, 6525 ED Nijmegen, The Netherlands

One-and two-photon LIF excitation spectra with rotational resolution have been measured for 1,4-diazabicyclo [2,2,2] octane (DABCO, C_6 H_{12} N_2).

The first electronic excited state, S_1 (A_1') of the molecule under study lies at 280 nm above the totally symmetric ground state S_0 (A_1')[1].

Previous low resolution two-photon measurements allowed to access a_1' symmetry modes. The main contribution to the low resolution one-photon excitation results was concerned with e' modes [2]; a large number of one-photon measured transitions were not assigned.

A molecular jet has been formed by expanding DABCO, at room temperature, seeded in N_2 or He, with a backing pressure of 2.5 atmosphere, through a pulsed nozzle. The molecules are excited 5 cm downstream by a home built pulsed dye amplifier system with a bandwidth of 150 MHz in the visible [3]. The observed linewidth using N_2 as seeding gas is 400 MHz, with an estimated rotational temperature of 6 K, the Doppler broadening limiting the experimental resolution; in case of He as seeding gas the linewidth is 600 MHz and the rotational temperature 1K. When Ar is used as a seeding gas no spectra could be observed probably due to massive formation of DABCO-Ar clusters. The fluorescence signal has been imaged onto a photomultiplier tube by a quartz lens system.

A model of the molecule is depicted in Figure 1. Along the C_3 symmetry axis of the molecule, coinciding with the c-axes, two nitrogen atoms are placed. The presence of two lone pairs characterises the behavior of the molecule upon excitation. The symmetry of the molecule is D_{3h} and the transition dipole moment has E' symmetry along the a, b-axes and A_2'' symmetry along the c-axis; therefore also a_2'' vibrational modes could be accessed with 1-photon excitation.

High resolution measurements allow to re-examine the character of a measured band because in addition rotational selection rules play a finger print role.

From "parallel" bands information on the rotational constant B can be deduced since in all the spectra the P and R branches show a nearly constant spacing of 2B. In perpendicular bands extra information is present in adjacent features on the A rotational constant and on the ζ Coriolis parameter, e.g. in the Q branch, through $X_2 = 2[A'(1-\zeta) - B']$.

One- and two-photon measurements allow to access levels with different symmetries. Their comparison has allowed to clarify or revise some of the previous assignments. If a band measured with two photon excitation appears at exactly the same frequency as in the one photon spectrum the latter is a quadrupole transition. In particular the very intense 0-0 band, while symmetry forbidden in the one-photon spectrum, has in fact been observed, as a quadrupole band. In the spectrum, reported in figure 2a, the alternation in intensities typical of this "finger print" can be observed. Δ J= 0, $\pm$ 1, $\pm$ 2 are the selection rules for this type of transition with J=0$\not\rightarrow$ J=0 and J=0$\not\rightarrow$ J=1 [4]. The condition on

J explains the intensity pattern and the absence of two peaks adjacent to the Q branch. The two-photon spectrum, figure 2*b*, also shows the presence of two extra Q branches possessing a different shift with respect to the band origin. The blue shifted more intense peak belongs to the ^{13}C-isotopomer, while the red shifted weaker peak is probably due to the ^{15}N-isotopomer.

One-photon and two-photon transitions have been fitted to a nearly spherical top model in order to obtain relevant molecular parameters. In table 1 this set of independent parameters is reported for two different perpendicular bands, ν_{26} and ν_{27}. Figure 3*a* and 3*b* show the 26_0^1 and 27_0^1 one-photon bands, with 600 MHz resolution and 1K rotational temperature. It can be readily seen that the two spectral features, although being very different, both represent perpendicular transitions.

For a special choice of X_2, ($X_2 = 0$, for $\zeta = \zeta_{adhoc}$) a perpendicular band might even reproduce a parallel band "finger print". In table 2 all the observed bands with their relative assignment are reported.

Information concerning the molecular geometry of DABCO can be derived from the rotational constants. Assuming fixed distances betweeen neighbouring atoms [5], we have calculated the rotational constants as a function of α, the N-C-C angle. In the ground state S_0 the A constant amounts to 2665 MHz and B (=C) has the value 2496 MHz, for the tetrahedral angle $\alpha = 109°$. The molecule is therefore a prolate nearly spherical top, in its ground state.

From the analysis of the high resolution measurements $B'' \simeq B'$ and $A' \geq A''$ has been found. If the B constant remains unchanged and the A increases for the S_1 state it means that in the excited state the molecule shows a more compressed structure in the *a*,*b* plane. In order to keep B constant the distance between neighbouring carbon atoms has to increase along the *c*-axis. The molecule becomes thus slightly more prolate upon electronic excitation.

REFERENCES

[1] D. Consalvo, J. Oomens, D. H. Parker and J. Reuss, accepted for Chem. Phys.

[2] N. Gonohe, N. Yatsuda, N. Mikami and M. Ito, Bull. Chem. Soc. Japan 55 (1982) 2796

[3] J. Schleipen, L. Nemes, J. Heinze and J. J. ter Meulen, Chem. Phys. Lett. 175 (1990) 561

[4] G. Herzberg in *Molecular Spectra and Molecular Structure* vol. II Van Nostrand Reinhold Company, 1991

[5] P. Brüesch, Spectrochimica Acta vol. 22 (1966) 867

CAPTIONS

Figure 1 The DABCO molecule.

Figure 2*a* The 0-0 band, 1hν excitation spectrum, a quadrupole transition.

Figure 2*b* The 0-0, 2hν excitation spectrum, dominated by the central Q-branch with two red & blue isotopomer Q-branches.

Figure 3*a* The $\perp$ band at 823 cm^{-1}, due to excitation of the ν'_{26} (e')- vibration.

Figure 3*b* The $\perp$ band at 449 cm^{-1}, due to excitation of the ν'_{27} (e')- vibration.

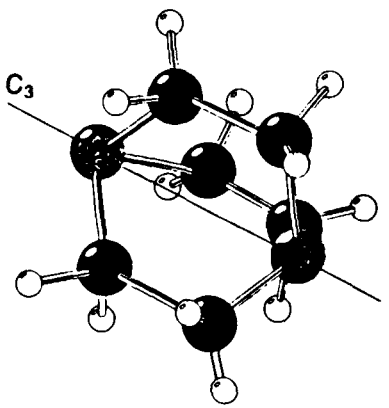

Figure 1

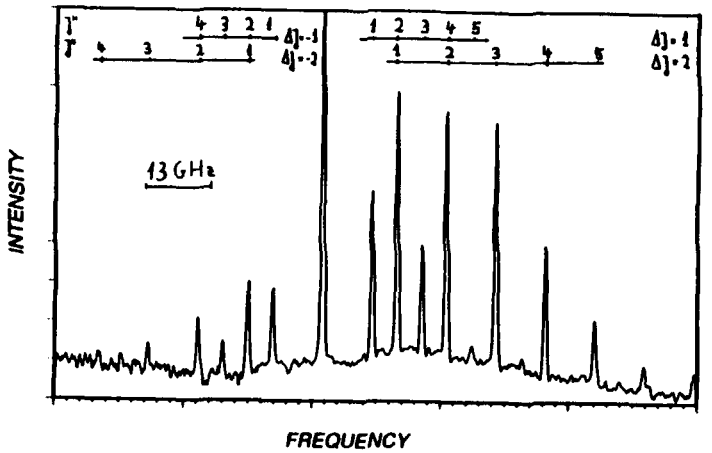

Figure 2*a*

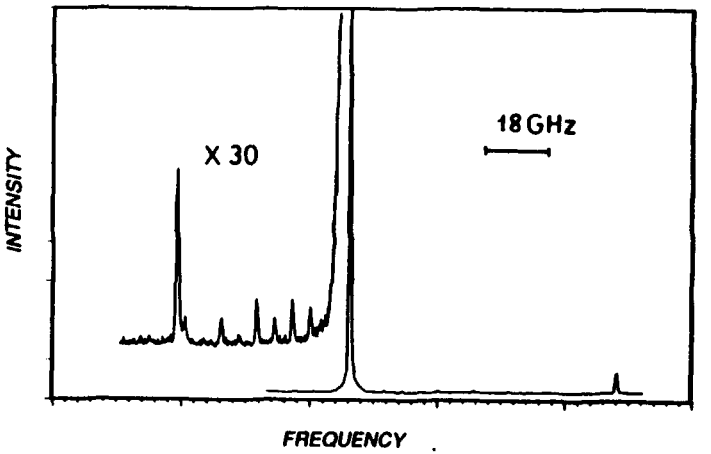

Figure 2*b*

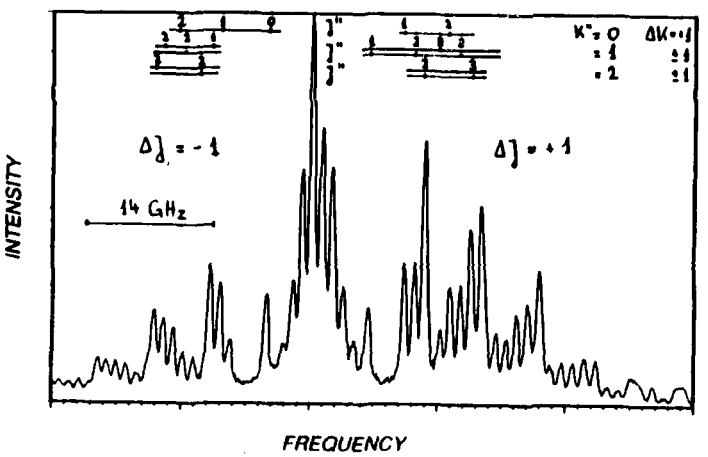

Figure 3*a*

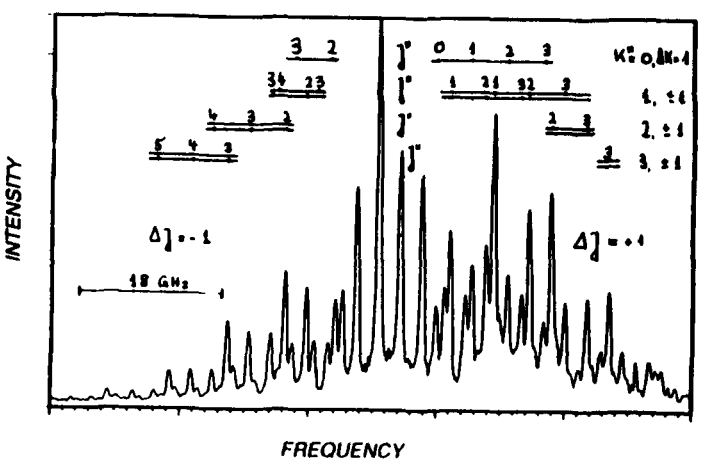

Figure 3*b*

Table 1: Parameters for two perpendicular bands.
$X_1 = \nu_0 + \nu'_z + [A'(1\text{-}2\zeta)\text{-}B']$ with $\nu_0 = 35783.26$ cm^{-1}.
X_2 is defined in the text; $X_3 = (A'\text{-}B')\text{-}(A''\text{-}B'')$

	ν_{26}	ν_{27}
Parameter	values [MHz]	values [MHz]
B″	2515 (4)	2505.0 (1.7)
B′	2515 (4)	2505.0 (1.6)
X_2	1109 (6)	3048 (5)
X_3	13 (3)	17.0 (1.4)
	[cm^{-1}]	[cm^{-1}]
X_1	36608.42 (0.02)	36232.46 (0.02)
ν'_z	825.16 (0.02)	449.20 (0.02)

Table 2: DABCO, the measured rotational transitions

band & position cm^{-1}	assignment	1hν band type (∥ , ⊥)	I arbs.	2hν band type (∥)	I arbs.	Remarks
0-0 0	origin	∥		∥		*a*
ν'_{13} 206	$4' \leftarrow 0''$	? & ?		∥		*b*
ν'_{27} 449	$1' \leftarrow 0''$	⊥		-		
ν'_{13} 670	$6' \leftarrow 0''$	∥	weak	∥		*d*, *e*
ν'_{36} 690	$2' \leftarrow 0''$	∥		∥		*c*, *d*, *e*
ν'_{6} 777	$1' \leftarrow 0''$	-		∥		
ν'_{26} 823	$1' \leftarrow 0''$	⊥		-		
$\nu'_{13}+\nu'_{27}+\nu'_{36}$ 889	comb.$\leftarrow 0''$	∥ & ∥		∥	strong	*a* & *c*
ν'_{27} 898	$2' \leftarrow 0''$	⊥		∥	weak	*f*
ν'_{5} 901	$1' \leftarrow 0''$	∥ & ?		∥		*a*, *g*
ν'_{17} 921	$1' \leftarrow 0''$	∥		-		
ν'_{24} 1007	$1' \leftarrow 0''$	⊥		-		

a : in the 1-photon spectrum the ∥ band is due to a quadrupole transition.
b : in the 1hν spectrum one of the two broad bands is shifted by + 0.8 cm^{-1} with respect to the ∥ 2hν band.
c : the 1-photon is a ⊥ band; appears like a ∥ band, due to $\zeta = \zeta_{adhoc}$
d : the 1-photon and 2-photon peaks are shifted.
e : the two 1-photon transitions, in Fermi resonance, are not yet assigned.
f : not shifted although of different symmetry.
g : the unassigned band is broad.

Resonant two photon ionization of aromatic molecules in a supersonic molecular beam

Marcello Coreno, Anna Giardini-Guidoni, Aldo Mele and Susanna Piccirillo

Dipartimento di Chimica, Università "La Sapienza"

Piazzale Aldo Moro 5

I-00185 Roma, Italy

Antonio Morone and Marcel Snels

Istituto per Materiali Speciali, CNR

Area industriale di Tito

I-85100 Tito (PZ), Italy

Nicola Lisi and Roberto Teghil

Dipartimento di Chimica, Università della Basilicata

Via N. Sauro 85

I-85100 Potenza, Italy

Abstract.

Recent advances in beams and laser technologies are making it possible to investigate molecular vibrational and electronic structure in powerful new ways in simple molecules and clusters [1].

In our laboratory a new molecular beam apparatus as been constructed recently, equipped with a pulsed valve and a time of flight mass analyzer. Two pulsed lasers are available for studying multi photon ionization processes in the visible and ultra violet. A excimer laser (Lambda Physik) operating on KrF provides about 150 mJ at 248 nm, a dye laser (Quantel) with doubling crystals and autotracker allows continuous scans from 210-320 nm, using different dyes. Both lasers are crossed perpendicularly with the supersonic beam, the ions produced in the multi photon ionization process are detected by a home built time-of-flight mass analyzer.

A supersonic molecular beam was produced by expanding mixtures of styrene in helium and styrene and ammonia in helium through a 0.4 mm diameter stainless steel nozzle, and crossed by a KrF laser in a second vacuum chamber. The multi photon ionization spectra showed a strong peak at the mass of the styrene parent ion and some weaker peaks at the masses of the mixed cluster ions styrene-$(NH_3)_n$ (n=1,..,4).

Using the tunable frequency doubled dye laser, a R2PI spectrum of jet cooled styrene (Fig. 1), in the wavelength region 279 nm- 284 nm ,at the styrene ion mass, was recorded, in excellent agreement with the excitation spectra obtained by ref [2] and with R2PI mass spectra of ref [3] which cover only part of the wavelength range observed by us. The assignments in Fig. 1 indicate several vibrational modes in the electronically excited state.

Further work is in progress on styrene-ammonia and styrene-benzene clusters.

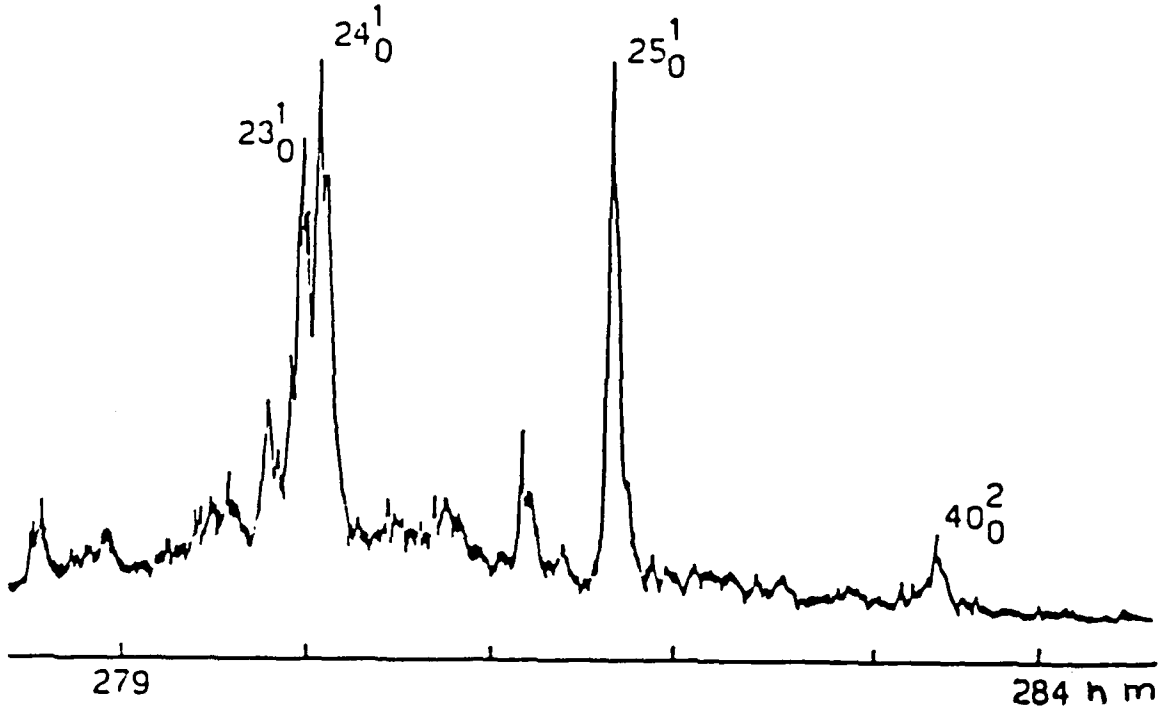

Figure 1. R2PI spectrum of an expansion of styrene in helium, excitation wavelength 279 - 284 nm.

References.

[1] "Atomic and Molecular Clusters", E.R. Bernstein ed., Elsevier, Amsterdam 1990

[2] J.A. Syage, F. Al Adel and A.H. Zewail, Chem. Phys. Lett. 103, 15 (1983)

[3] O. Dimopoulou-Rademann, U. Even, A. Amirav and J. Jortner, J. Phys. Chem. 92, 5371, (1988)

Photo-Initiated Intra-Cluster Dissociative Electron Transfer Reactions

D.M. Cyr, G.A. Bishea, M.G. Scarton, D.J. Lavrich and M.A. Johnson

Department of Chemistry, Yale University
225 Prospect St., New Haven, CT 06511

Ionized molecular beams provide an excellent medium in which to isolate intermediates trapped at local minima along the potential energy surface of ion-molecule reactions. We describe recent results from our efforts to characterize the classic $X^- + CH_3Y \rightarrow Y^- + CH_3X$ S_N2 ion-molecule reactions by selective preparation of the $X^- \cdot CH_3Y$ and $Y^- \cdot CH_3X$ ion-dipole complexes. Here we report the location and photophysics of electronically excited states and suggest that these states may be a useful way to photo-initiate charge transfer reactions within the clusters. Photoexcitation of the ion dipole complexes $I^- \cdot CH_3I$ and $I^- \cdot CH_2Br_2$ near the electron detachment threshold is observed to drive a dissociative intra-cluster electron transfer reaction yielding ionic products according to the scheme:

$$X^- \cdot CH_{4-n}Y_n + h\upsilon \rightarrow X \cdot [CH_{4-n}Y_n]^- \rightarrow X \cdot\cdot CH_{4-n}Y_{n-1} \cdot\cdot Y^- \rightarrow [X \cdot\cdot CH_{4-n}Y_{n-1}] + Y^-.$$

These reactions appear to proceed through charge transfer excited states, $I \cdot [CH_3I]^-$ and $I \cdot [CH_2Br_2]^-$, respectively, which correspond to the (diabatic) excited states implied by the double minimum potential energy surface for the gas phase S_N2 reaction.

The photofragmentation action spectra:

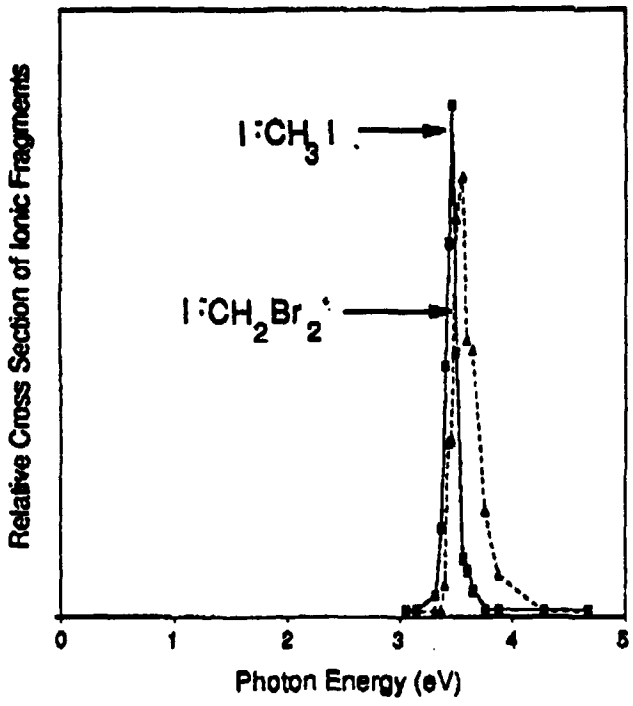

are rather narrow and appear within a few tenths of an electron volt above the detachment threshold of the complexes (determined independently by photoelectron spectroscopy). The shape of the spectra are consistent with a remarkably simple model in which low energy photoelectrons dissociatively attach to the methyl halides. While I^- is the only ionic product created by photoexcitation of $I^- \cdot CH_3I$, the dihalide IBr^- ion is the dominant photoproduct of the dibromide complex $I^- \cdot CH_2Br_2$. We rationalize the creation of this product by considering the recoil dynamics of the $[C\text{-}Br]^- \rightarrow C + Br^-$ bond dissociation in the presence of the iodine atom, which allows for recombination when the I-C-Br species have a non-linear arrangement in the complex. Efforts to extend these photo-induced charge transfer reactions to solvated anions, such as the $I^- \cdot (H_2O)_n \cdot CH_3X$ clusters are discussed.

A New Bolometer-based Surface Scattering Apparatus of Improved Sensitivity and Resolution

Maarten F. M. DeKieviet and Giacinto Scoles
Department of Chemistry, Princeton University, Princeton, N.J. 08544

We have recently built a bolometer-based atomic beam (He) surface diffractometer of improved performance with respect to the one presently operating in our laboratory* .

The main body of the machine consists of two differentially pumped vacuum chambers. In the source chamber a supersonic beam of atoms and/or clusters is generated, through a nozzle that can be cooled using a cryogenic liquid flow (4K, 77K). With typically 2000 psi behind a 10 micron nozzle, we sustain a vacuum higher than 10^{-4} Torr and obtain beam monochromaticity of better than $\Delta v/v=1\%$.

From the top of the scattering chamber two concentric cryostats, containing liquid nitrogen (77 K) and liquid helium (4 K), respectively, come down and slide precisely into a copper shielding mounted on the turret of the source chamber (see fig 1a). The inner cryostat can be rotated around its vertical axis and holds the detector: a semiconductor bolometer (operated at 1.6 K with an n.e.p of 10^{-12} W/√Hz and a responsivity of 10^5 V/W). The shielding (cooled to 50 K by a small refrigerator) allows for the insertion of a completely self-contained low temperature crystal manipulator, via the load-lock system described below. The volume thus enclosed is very effectively cryopumped and permits long experiments on cold surfaces, without appreciable surface contamination (as measured by specular beam attenuation).

In an effort to minimize the down time of the machine, due to sample changing, a cryogenic load-lock system was constructed. In both cryogenically pumped and "standard" UHV machines, breaking of the vacuum seriously delays further experimentation, either because the cryopumps have to be warmed up, or the UHV chambers need to be outgassed through baking.

Giving a side view of the scattering apparatus, figure 1a shows how the crystal manipulator is directly mounted onto the cold-head of a high power cryogenic refrigerator. The entire set-up is placed on a translational stage, enclosed by bellows and separated from the main vacuum system by a pneumatic, metal sealed gate valve. While the main body of the machine remains under vacuum and cold, the crystal can be retracted into the bellows, and the valve closed. The cold-head can be brought back up to room temperature relatively fast, while a 170 1/s turbo-molecular pump, backed by a small diffusion and rotary pump, frees the load-lock of any desorbing species. Subsequently, the load-lock can be vented with dry nitrogen and the specially designed quick-release conflat seal between the valve and the bellows can be broken. Under a continuous flow of nitrogen one can now change the crystal and repeat the above pro-

* L. Danielson, J.C. Ruiz, C. Schwartz, G. Scoles and J.M. Hutson, Faraday Discussion Chem Soc 80, 47 (1985)

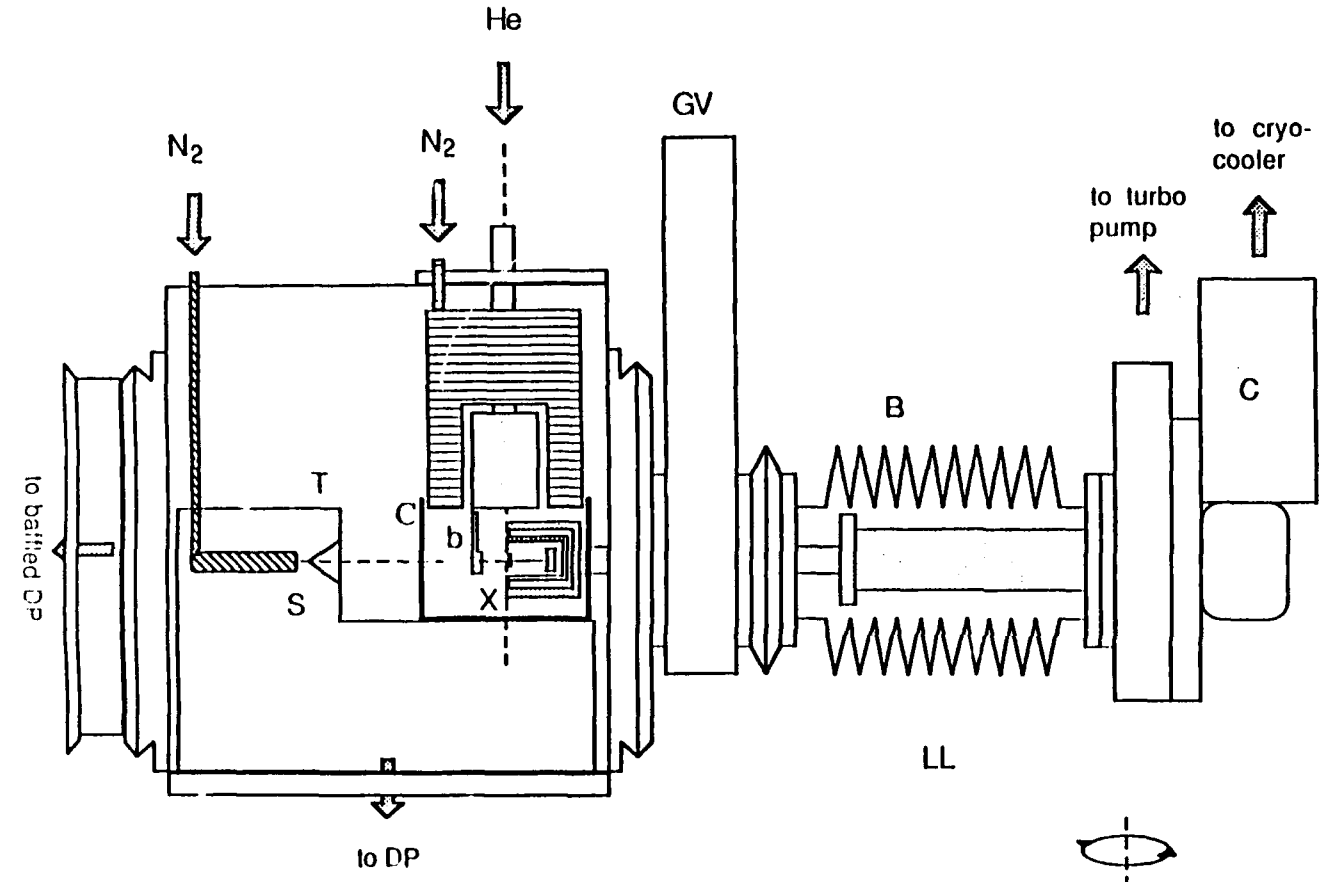

Figure 1a: Side View of Surface Scattering Machine: b - Bolometer, S - Supersonic Source, T - Turret, X - Crystal Manipulator, GV - Gate Valve, N_2 - Liquid Nitrogen Cryostat, C - Cold Shielding (50K), He - Liquid Helium Cryostat.

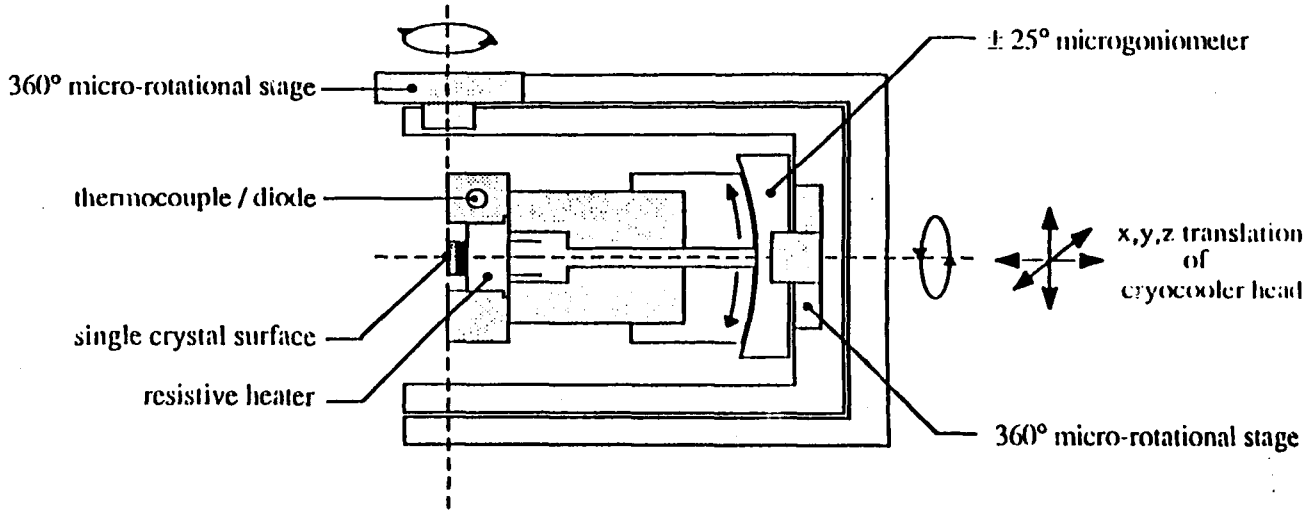

cedure in inverted order. The entire cryogenic load-lock is adjustable along three cartesian coordinates, so as to ensure that the crystal manipulator is properly positioned and aligned with respect to both the incoming atom/cluster beam and the arc described by the rotatable bolometer detector.

The crystal manipulator has three independent axes of rotation and is schematically shown in figure 1b. It is mounted on the cold-head, with a temperature buffer in between in order to smooth out temperature fluctuations due to the refrigerator. The cryopump establishes a 12 Watt heat sink, with a final temperature of 9 K. Using this manipulator experiments are currently being done with surface temperatures between 10 K and 550 K.

By going from a slit bolometer (2 x 0.2 mm^2) in our previous helium diffractometer to a circular geometry (0.3 mm ∅) in this machine we improved the azimuthal resolution by a factor of 7, while keeping the polar resolution virtually unchanged. The present machine has a resolution in both directions of circa 0.6 ° and a dynamic range that covers almost 6 orders of magnitude.

As a preliminary example of the new diffractometer's performance we show a typical calibration spectrum: the diffraction pattern of a room temperature He beam scattered off of the (001) face of a LiF crystal (kept at 70K) along the <110> azimuthal direction (fig 2).

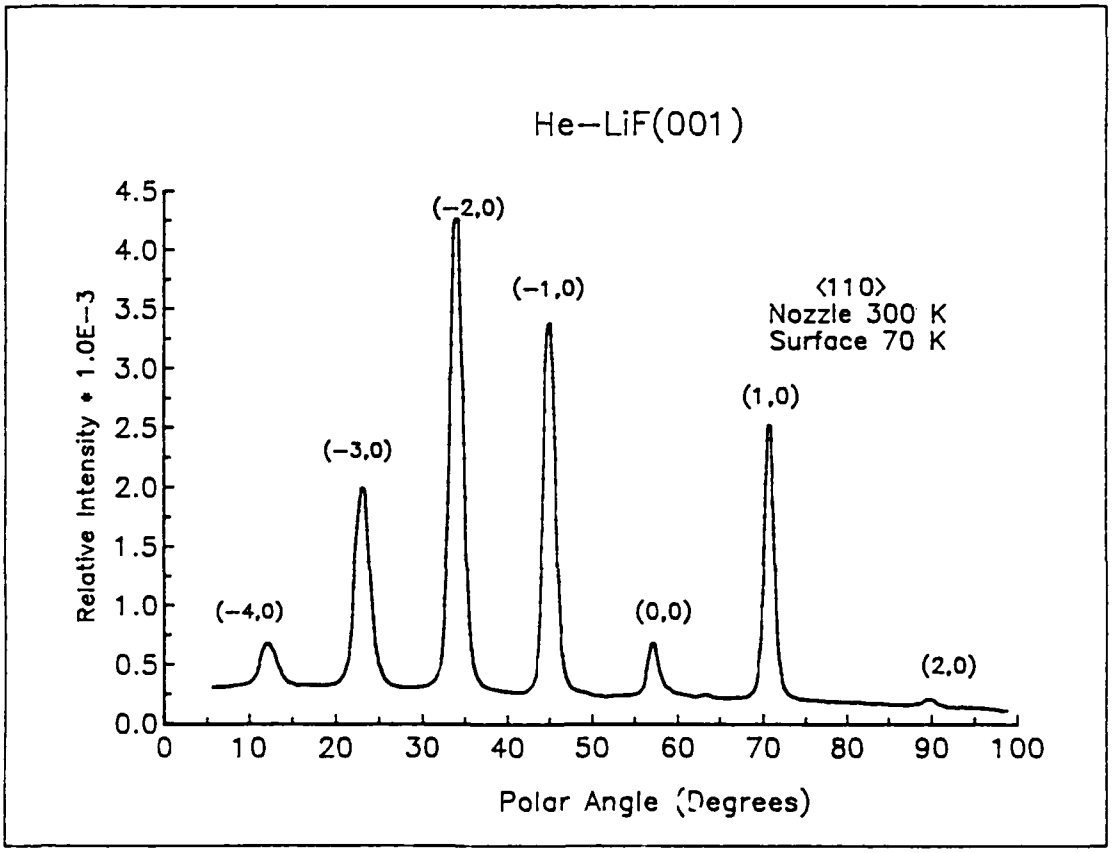

Figure 2: Diffraction Pattern of He atoms scattered from the (001) face of a LiF crystal. The intensity plotted is relative to the incoming beam (located at 0 degrees).

Multiphoton Ionization Photoelectron Spectroscopy of OCS

Ding Chuan-fan, Yang Da-lin, Zhou You, and Zhu Qi-he

State Key Laboratory of Molecular Reaction Dynamics
(Beijing Division)
Institute of Chemistry
Academia Sinica, Beijing 100080, China

We have built a TOF photoelectron spectrometer with a magnetic bottle parallelizer. The TOF path length is 2 m which gives a resolution better than 7 meV at photoelectron energy 0.55 eV. OCS was introduced from a pulsed molecular beam valve with a nozzle of 0.5 mm diameter. The stagnation pressure of neat OCS is 1.0 atm. The repetition rate of the pulsed valve is 30 Hz. The pulse width is 0.36 ms. A skimmer of 1 mm diameter is 20 mm apart from the nozzle. The pressure of beam chamber is 2.6×10^{-4} Torr and that of the ionization chamber is 1.6×10^{-6} Torr during experiment. A tunable dye laser was pumped by a YAG laser and the laser frequency was doubled by a WEX. The UV laser beam was focused by a lens of f = 45 mm. The photoelectrons were detected by multichannel plates and the signals were fed to a 100 MHz digital storage processor.

First, we used a TOF mass spectrometer for MPI spectra. We scanned the tunable laser with fixed mass number M = 60, 32, 28. These MPI spectra were shown in Fig. 1.

Then, fixing the laser wavelength at resonant peaks (1) 282.03, (2) 280.58, (3) 280.18, (4) 279.96, (5) 279.15, (6) 278.59 nm, we obtained the photoelectron spectra as shown in Fig. 2-7. As compared with the work of Yang et. al., we got more vibrational peaks for $X^2\Pi_{1/2,3/2}$ states of OCS. We have observed a new photoelectron peak at all wavelengths which corresponds to $B^2\Sigma^+$ state of OCS^+ from the 2+2 MPI.

Reference

Baorui Yang, Mohamad H. Eslami, and Scott L. Anderson, *J. Chem. Phys.* 89, 5527(1988).

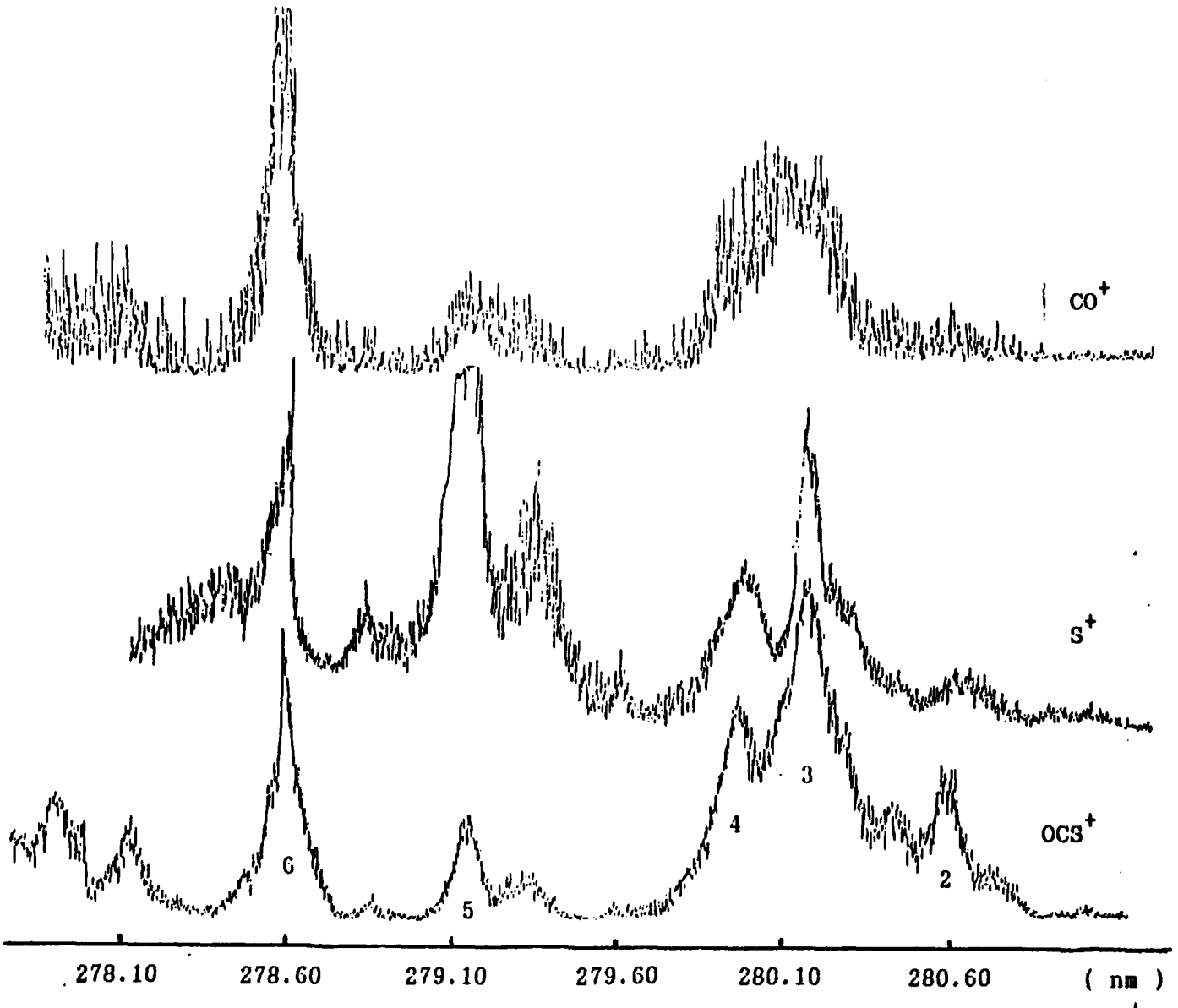

Fig. 1. Mass resolved MPI spectra of OCS.

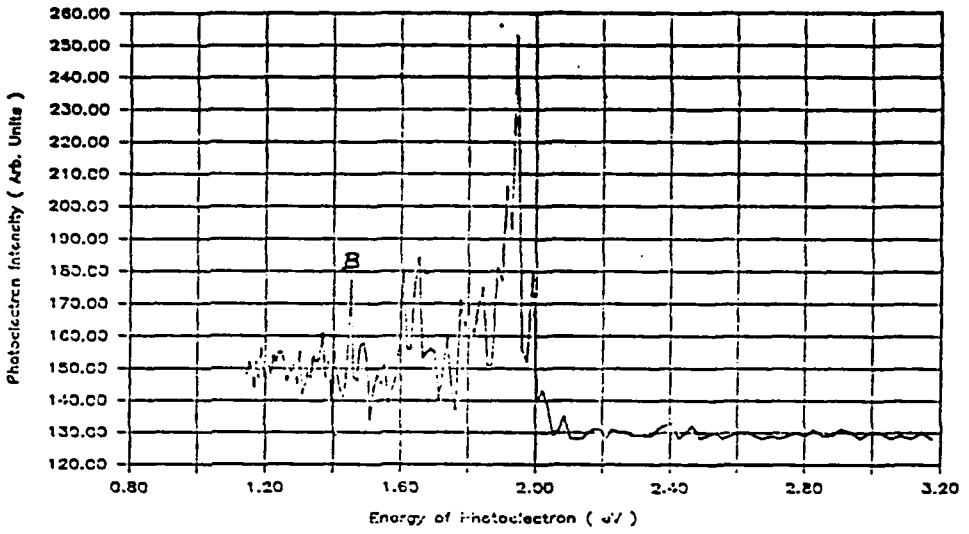

Fig. 2. OCS MPI-PES at 282.03 nm.

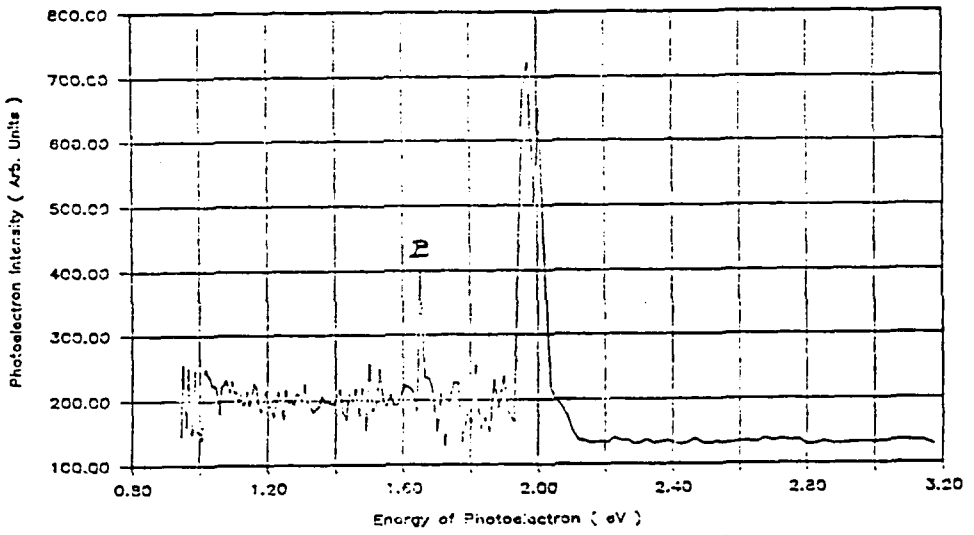

Fig. 3. OCS MPI-PES at 280.58 nm.

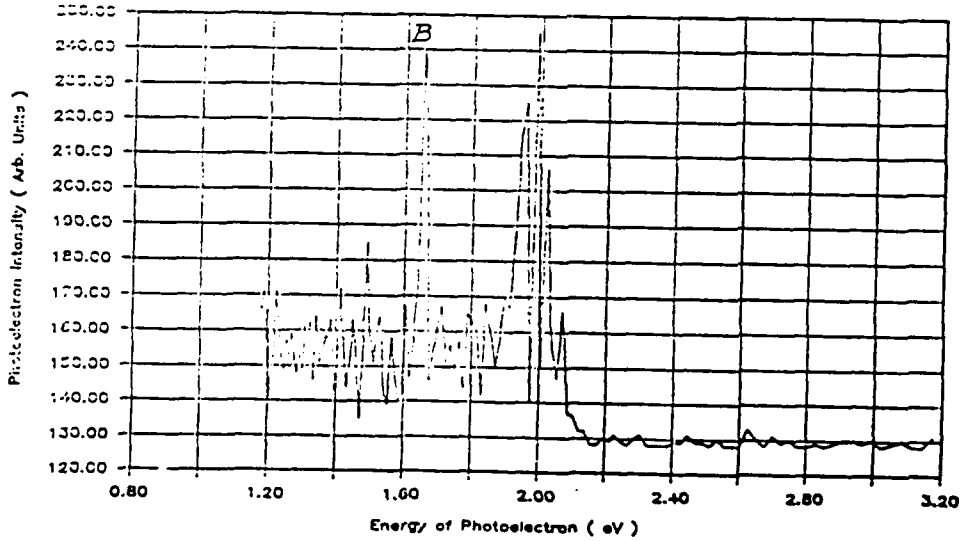

Fig. 4. OCS MPI-PES at 280.18 nm.

COPY AVAILABLE TO DTIC DOES NOT PERMIT FULLY LEGIBLE REPRODUCTION

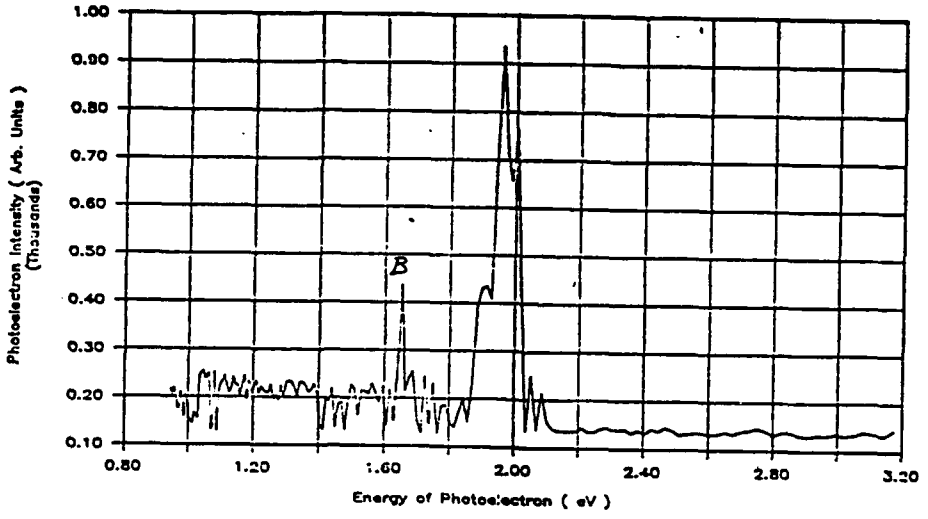

Fig. 5. OCS MPI-PES at 279.96 nm.

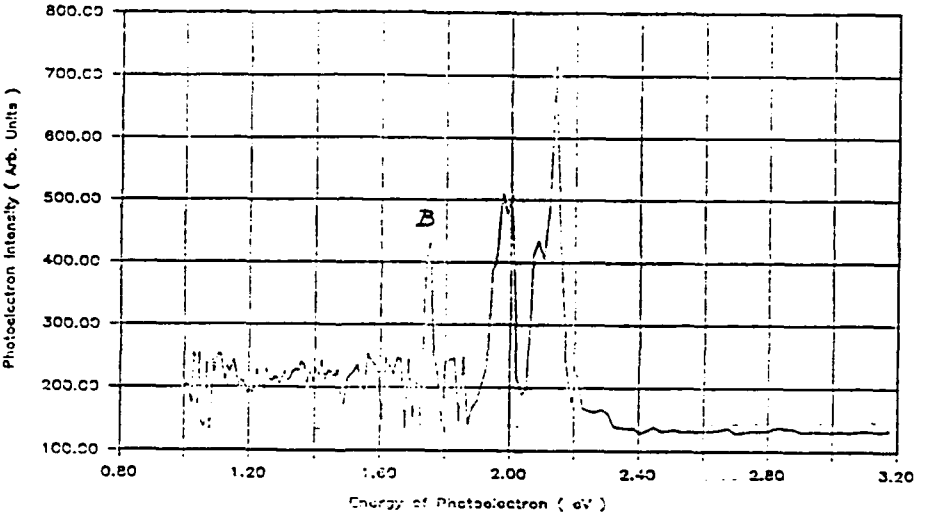

Fig. 6. OCS MPI-PES at 279.15 nm.

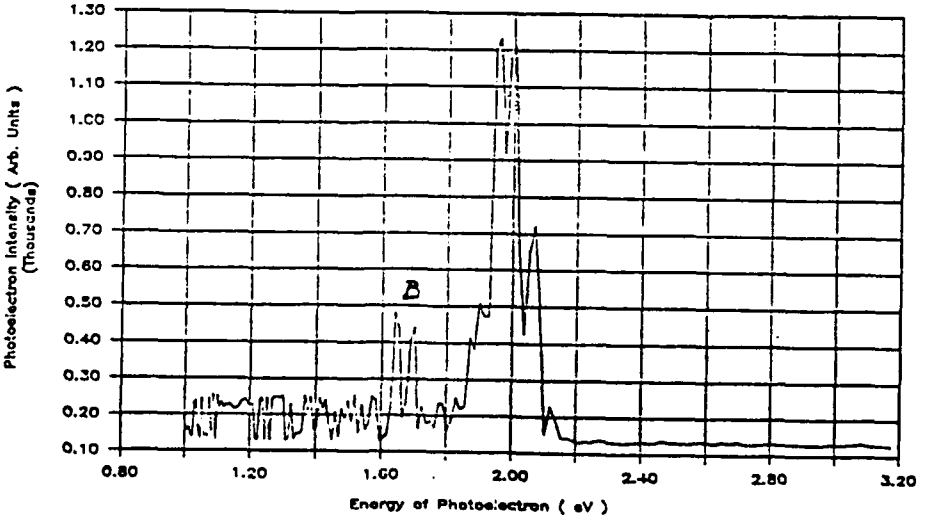

Fig. 7. OCS MPI-PES at 278.59 nm.

COPY AVAILABLE TO DTIC DOES NOT PERMIT FULLY LEGIBLE REPRODUCTION

SITE SPECIFICITY OF SOLVENT SHIFTS IN ANILINE-(ARGON)$_N$ CLUSTERS: A TWO-PHOTON TWO-COLOR RESONANT IONIZATION STUDY

Stéphane DOUIN, Patrice HERMINE, Pascal PARNEIX, Philippe BRECHIGNAC

Laboratoire de Photophysique Moléculaire, C.N.R.S,

Université de Paris-Sud, Batiment 213, F-91405 Orsay Cedex, France

and François G. AMAR

Department of Chemistry, University of Maine, Orono, ME 04469, USA

1. Introduction.

In the past ten years, clusters containing an aromatic molecule and several rare gas atoms have been studied by a number of groups. Two dominant motivations underly the great interest in these systems. First, the electronic spectra and ionization potentials of aromatic molecules such as benzene, its derivatives, and larger polycyclic aromatics are quite sensitive to the chemical environment. Mass selected clusters, therefore, provide an ideal testing ground for understanding size selective solvation and the transition to the bulk. Second, the sensitivity of the chromophore to the environment permits its use as a probe of cluster structure and dynamics. This second point will be stressed in the present paper.

Systematic spectroscopic studies in several polycyclic aromatics interacting with rare gases using multiphoton ionization to perform mass selection have recently suceeded, with the aid of numerical simulations, to identify many different isomers or isomer classes as well as isomerizations, side-to-side transitions, and possibly melting in these systems [1-7].

The presently reported investigations in clusters of argon interacting with a small aromatic molecule, specifically aniline, demonstrates the existence of different "binding sites", to which specific solvent shifts are associated for both the first allowed electronic transition [8] and the photoionization transition [9]. The observed sum rules are consistent with the additivity of van der Waals interactions.

2. Experimental.

The apparatus to perform the ResonantTwo-Photon Two-Color Ionization (R2P2CI) spectra or threshold profiles is made up as follows :

1) The aniline-Ar$_n$ clusters are synthesized in a seeded molecular beam, generated by expanding a mixture of Aniline/Argon/He through a pulsed nozzle in a first vacuum chamber ($P \cong 10^{-4}$ torr), skimmed and passed to a second vacuum chamber ($P = 10^{-5}$ to 10^{-6} torr).

2) Two anticollinear laser beams cross the molecular beam in the interaction region at the center of the first pair of electrodes of a (Jordan) reflectron time-of-flight mass spectrometer. The ion signal from a microchannel plate detector, after proper amplification, issent to a digital oscilloscope (Lecroy 9400) which displays the time of flight spectrum after adequate averaging. The signal corresponding to the cluster sizes of interest are gate-selected and recorded in a microcomputer as a function of laser wavelength. Two kinds of measurements can be performed : in the first case, the laser 1 is scanned in the region near the $\Pi \rightarrow \Pi^*$ transition [$X^1A_1 \rightarrow A^1B_2$] of Aniline (it is the resonant absorption of this beam which constitutes the spectrum), while the laser 2 wavelength is set to a value allowing to excite the cluster to just above the ionization threshold. In

the second case, the laser 1 is tuned to a resonance to optically select a given structural isomer of some cluster size, while the laser 2 is scanned through the threshold for appearance of ions (it allows to locate the ionization potential of the selected cluster with respect to the monomer value). Much care was taken during the experiments to reduce the intensity of the first laser beam to ensure that the 1C signal was much less than the 2C signal.

3) The laser system consists of a pulsed (rep. rate=10 Hz), Nd:YAG laser which pumps two dye lasers. The laser beam 1, which is used to excite the $S_0 \rightarrow S_1$ transition in the neighborhood of 300 nm, originates from frequency-doubling a 532nm-pumped Rhodamine-6G dye laser. The laser beam 2 , which is used to ionize near 350nm, is produced in two alternative ways: frequency-doubling a 532nm-pumped LDS698 dye laser, or mixing a 355nm-pumped Coumarine-540 dye laser with the fundamental Nd:YAG 1.06μm beam through a KDP crystal.

3. Results and discussion.

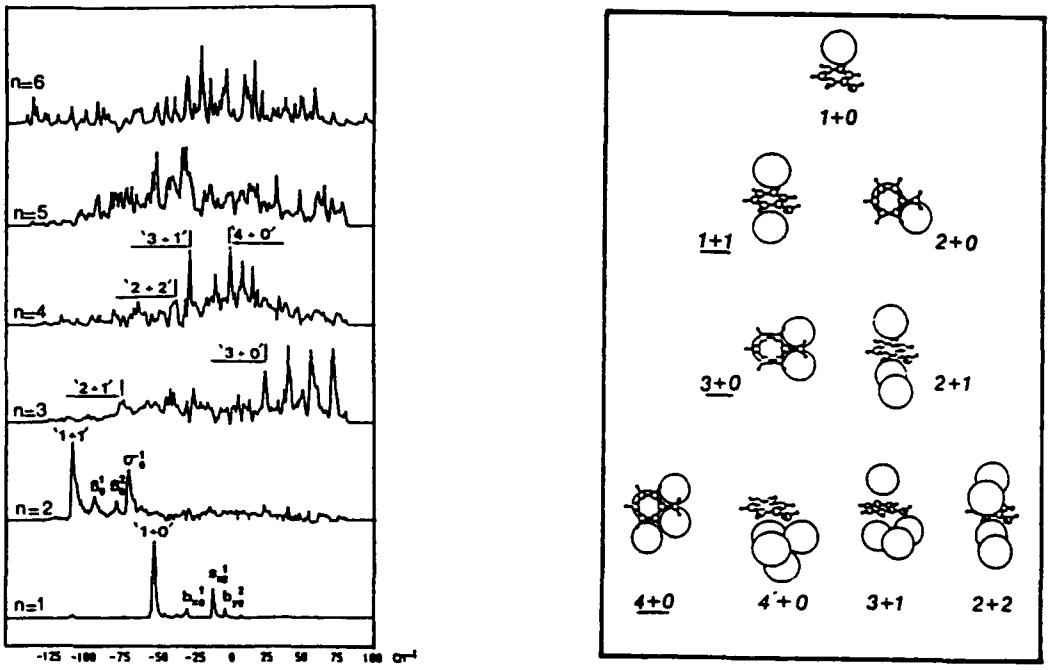

Figure 1 : R2P2CI spectra of An-Ar (n=1-6). Expansion conditions: room temperature vapor pressure of aniline in pure argon (P = 1.5 bar). The origin of the energy scale is the 0_0^0 band of the monomer. Assignments of vdW vibrations for n=1 and 2 and of band origins to different isomers are indicated.

Figure 2 : Isomer structures obtained from MD/quenching procedure using the potential model described in ref.[8]. The most stable isomer of each size is underlined.

Figure 1 shows a set of mass-selected spectra for different cluster sizes (n = 1 to 6). The most remarkable result is that some clusters (in particular n = 3, 5 and 6) exhibit absorption in a spectral range extending up to very far to the blue of the monomer band, in spite of the clear additive red shift observed for n =1 and 2. It is very unlikely that such spectra can be due to a single absorbing species. Indeed both experimental evidence (intensity changes with expansion conditions) and theoretical results (Molecular Dynamics calculations) have proven that several

conformers involving the same number of Argon atoms do contribute to an individual spectrum [8]. As a matter of fact it is possible to account for most of the clear features in the spectra by considering the various possible isomers of a given size. Moreover, introducing the notion of "site"-specific shift [9], this kind of analysis can be generalized through the so-called "modified shift additivity rule". Indeed two main binding sites appear to be important for these clusters (see Figure 2): the "ring" site where one Ar atom binds next to the "center of gravity" of the Π-cloud electron density, and the "nitrogen" site where one Ar atom binds next to the N atom in the $-NH_2$ substituent. Assigning a spectral shift of -53 cm^{-1} to the "ring" site and a spectral shift of +37 cm^{-1} to "nitrogen" site accounts for the assignments in Figure 1.

Figure 3 shows a set of spectra for different isomers (n=0 to 3) using both optical and mass selection, from which the appearance thresholds can be measured. The values of IP solvent shifts for the various clusters relative to the monomer are listed in Table I. For An-Ar3 MD calculations have provided the actual structure of the two most stable isomers (see Figure 2) : the "2+1" conformer (red-shifted by -74.5 cm^{-1} in the $S_1 \leftarrow S_0$ transition) has two "ring" sites and one "nitrogen" site occupied whereas the "3+0" isomer (blue-shifted by +22.5 cm^{-1} in the $S_1 \leftarrow S_0$ transition) has one "ring" site and two "nitrogen" sites occupied. The top two spectra in Figure 3 have been obtained after having tuned the $S_1 \leftarrow S_0$ laser to the origin band of each

Table I : Experimental values of the solvent shifts $\delta I(p+q)$ for p+q = 1 to 3 clusters relative to the monomer value IP(0) : $\delta I(p+q)$ = IP(p+q) - IP(0)

Species	This work (cm^{-1})
An-Ar : 1+0	-116 ± 10
$An-Ar_2$: 1+1	-226 ± 10
$An-Ar_3$: 2+1	-412 ± 15
: 3+0	-533 ± 15

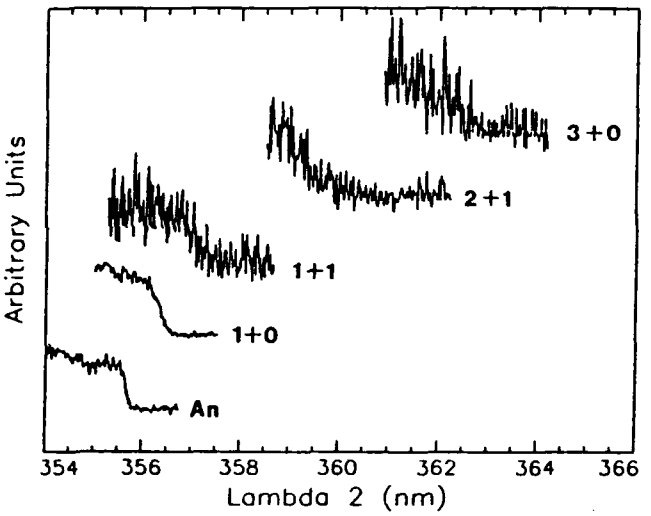

Figure 3 : Photoionization efficiency spectra for $An-Ar_n$ (p+q) clusters.

isomer. It is apparent from Table I that the IP exhibits a very large red-shift for this cluster size, revealing the special nature of the interaction when "nitrogen" sites are involved. Thus the data can be rationalized with a "ring" site IP shift being -114 cm^{-1} and a "nitrogen" site IP shift being -200 cm^{-1}. These simple sum rules are the same that in the case of the $S_1 \leftarrow S_0$ spectral shift above and can be used to extrapolate the results to so far unmeasured isomers of various cluster sizes.

To strengthen our demonstration of the site specificity of (additive) solvent shifts, it is quite interesting to remark that previously available results can be accounted for in the light of these new rules. A nice example is offered by the measurements on paraxylene-$(Argon)_n$ clusters reported by Dao, Morgan, and Castelman [10]. Assuming in the same way the existence of a "ring" site and a "substituent" (CH_3) site for Ar on paraxylene molecule, it is possible to assign the various peaks in the $S_1 \leftarrow S_0$ resonant spectra to different structural isomers. Table II is a comparison of the experimental

shifts to the values calculated on the basis of the model for both the $S_1 \leftarrow S_0$ transition and the ionization potential. The corresponding site-specific shifts are given in the caption. The overall agreement is extremly satisfactory. It is relevant to note that the tendency observed in these shifts when going from the ring to the substituent is similar to the case of aniline, in particular the blue spectral shift, and the increased stabiiization of the ion. This last observation calls for a similarity in the chemical processes thus probed. The origin of the blue shift is discussed more deeply in a separate work on Aniline-Argon interaction potential and bound states [11].

Table II : Comparison between experimental[3] and calculated values of the $S_1 - S_0$ and IP shifts for different (p+q) isomers of Paraxylene-(Argon) clusters. The calculated values are obtained by using the following site-specific shifts :

$S_1 - S_0$ transition : ring $-30\ cm^{-1}$, substituent $+17\ cm^{-1}$.
IP : ring $-110\ cm^{-1}$, substituent $-150\ cm^{-1}$.

n	(p+q) isomer	$\delta\nu(p+q)$ (cm^{-1}) calc.	exp.	$\delta I(p+q)$ (cm^{-1}) calc.	exp.
1	1+0	-30	-30.2	-110	-115
2	1+1	-60	-58.8	-220	-200*
	2+0	-13	-18.3	-260	-181
3	2+1	-43	-41.7	-370	-383
	3+0	+4	+2.7	/	/
4	3+1 or 2+2	-26	-28.5	-520	-509

* The poor agreement in that case could be due to experimental effects, like the superimposition of the 2+0 resonance feature with a van der Waals peak of the 1+1 isomer.

REFERENCES

1. A.Amirav, U.Even, and J.Jortner, J.Phys.Chem. 86, 3345 (1982); U.Even, A.Amirav, S.Leutwyler, M.J.Ondrechen, Z.Berkovitch-Yellin, and J.Jortner, Faraday Discuss.Chem.Soc. 73, 153 (1982).
2. U. Even, N. Ben-Horin, and J. Jortner, Phys. Rev. Lett. 62, 140 (1989).
3. J. Bosiger and S. Leutwyler, Phys. Rev. Lett. 59, 1895 (1987).
4. T.Troxler, R.Knochenmuss and S.Leutwyler, Chem.Phys.Lett. 159, 554 (1989)
5. S. Leutwyler and J. Bösiger, Chem. Rev. 90, 489 (1990).
6. M.Y. Hahn and R.L. Whetten, Phys. Rev. Lett. 61, 1190 (1988).
7. M. Schmidt, M. Mons, and J. Le Calvé, Chem. Phys. Lett. 177, 371 (1991).
8. P.Hermine, P.Parneix, B.Coutant, F.G.Amar and Ph.Bréchignac, Z.Phys.D 22, 529 (1992).
9. S.Douin, P.Parneix,and Ph.Brechignac, Z.Phys.D 21, 343 (1991); S.Douin, P.Hermine, P.Parneix, F.G.Amar and Ph.Bréchignac, J.Chem.Phys., submitted.
10. P.D.Dao, S.Morgan , and A.W.Castelman, Chem.Phys.Lett. 113, 219 (1985).
11. P.Parneix, N.Halberstadt, F.G.Amar, Ph.Brechignac, A.van der Avoird, and J.van Bladel, to be published.

C.A.R.S. MONITOR OF LASER INDUCED DISSOCIATION OF MOLECULES AND CLUSTERS IN A SUPERSONIC JET

R. FANTONI, M. GIORGI, K. LIPINSKA-KALITA*, M. SNELS#

ENEA, INN/SVIL, C.P. 65, I-00044 Frascati (Italy)

A pulsed molecular beam machine has been built in order to study laser induced dissociation of cold molecules and clusters in different wavelenghts regions from IR to UV. CARS diagnostics have been chosen both to characterize the molecular beam [1,2] and to measure parent decomposition as well as cluster dissociation from the attenuation of spectrally resolved Raman active vibrations, some fragments may be detected in the investigated wavelength range.

To this aim, a low resolution (6 cm^{-1}) C.A.R.S. spectrometer, built to detect single shot CARS signal in a wavelength range of about 40 nm in the blue spectral region [3], has been combined with the molecular beam machine. An overview of the experimental set up in sketched in Fig. 1, the photolysis (IR or UV) laser, not shown in the picture, is entering from the top window of machine after being focussed by a 20 cm lens of proper optical material crossing at rigth angle both the jet and the visible lasers used for CARS. The pulsed molecular jet is produced by an Newport Co. valve (BV-100V), a background pressure below 10^{-6} mbar is ensured by a 1500 l/s turbo molecular pump during the beam operation. Laser beams for CARS are produced by a Nd:YAG operated at the II harmonic and by a broad band dye laser (SOPRA) operated with a suitable mixture of dyes, typical laser energies are 30 mJ at 532 nm and 2.5 mJ in the red. As shown in Fig. 1 all electronics is triggered, after proper delays, by the computer control of the optical multichannel analyzer (OMA III EG&G) used for CARS signal detection and data acquisition. All the system is operated at 1 - 2 Hz.

Beam characterization has been initiated on He and CH_4 by detecting the beam profile at different distance from the nozzle on two fast vacuum gauges. Molecular velocities obtained corresponded to Mach number around 10, it has been deduced that translational temperatures about 15 K in the molecular flow region have been reached with a 0.5 mm nozzle and a backpressure of 2.5 atm.

CARS signal from a pure CH_4 jet have been measured at x/D= 5.8 . With 3 atm backpressure, single shot detection of the ν_1 Q-branch is possible. As shown in Fig. 2, where the CARS intensity of this peak is reported as a function of the delay between the laser and the valve, the molecular pulse is quite narrow (FWHM < 100 μs).

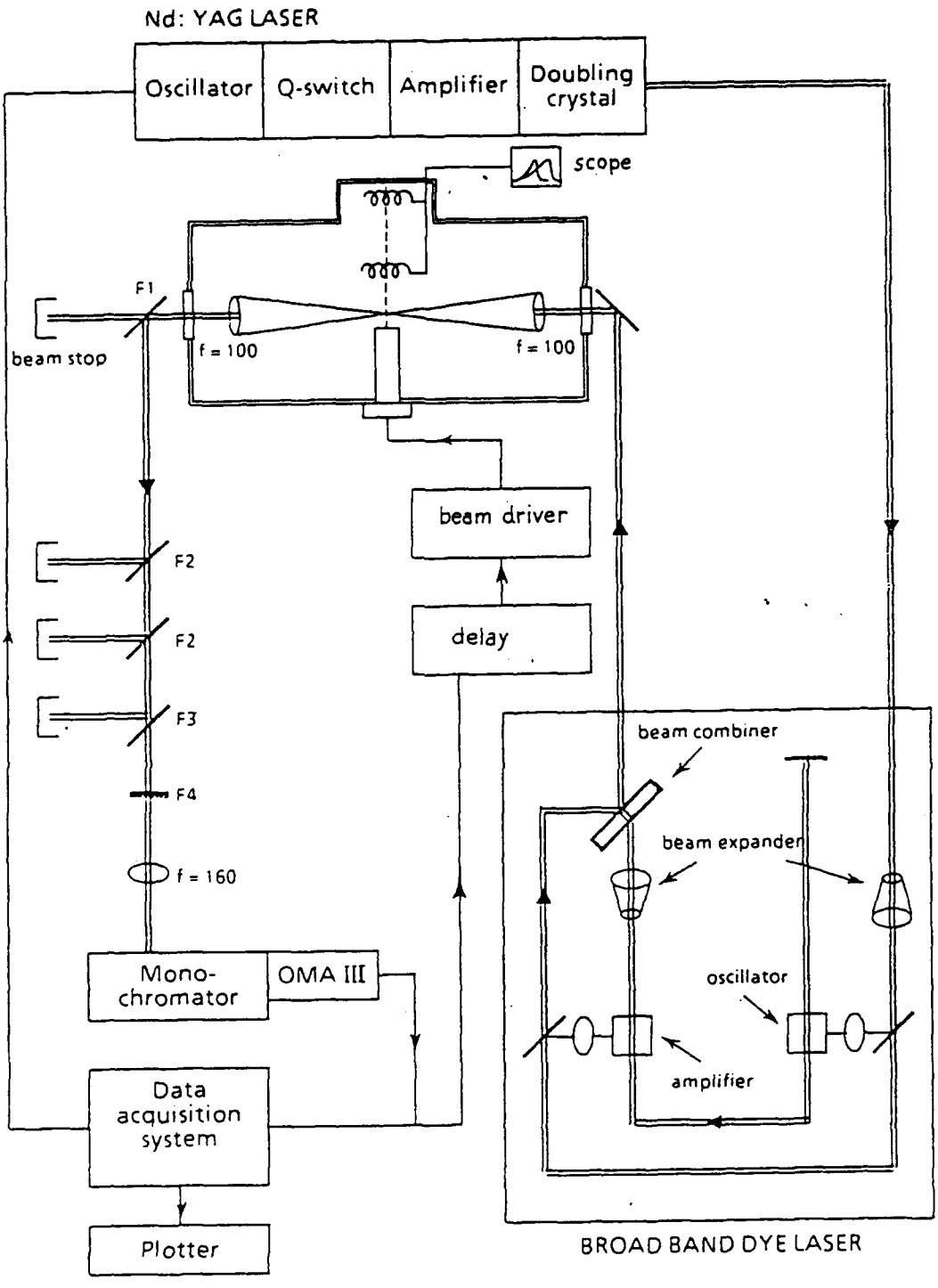

Fig. 1

Experimental set-up containing a CARS spectrometer combined with a pulsed molecular beam machine

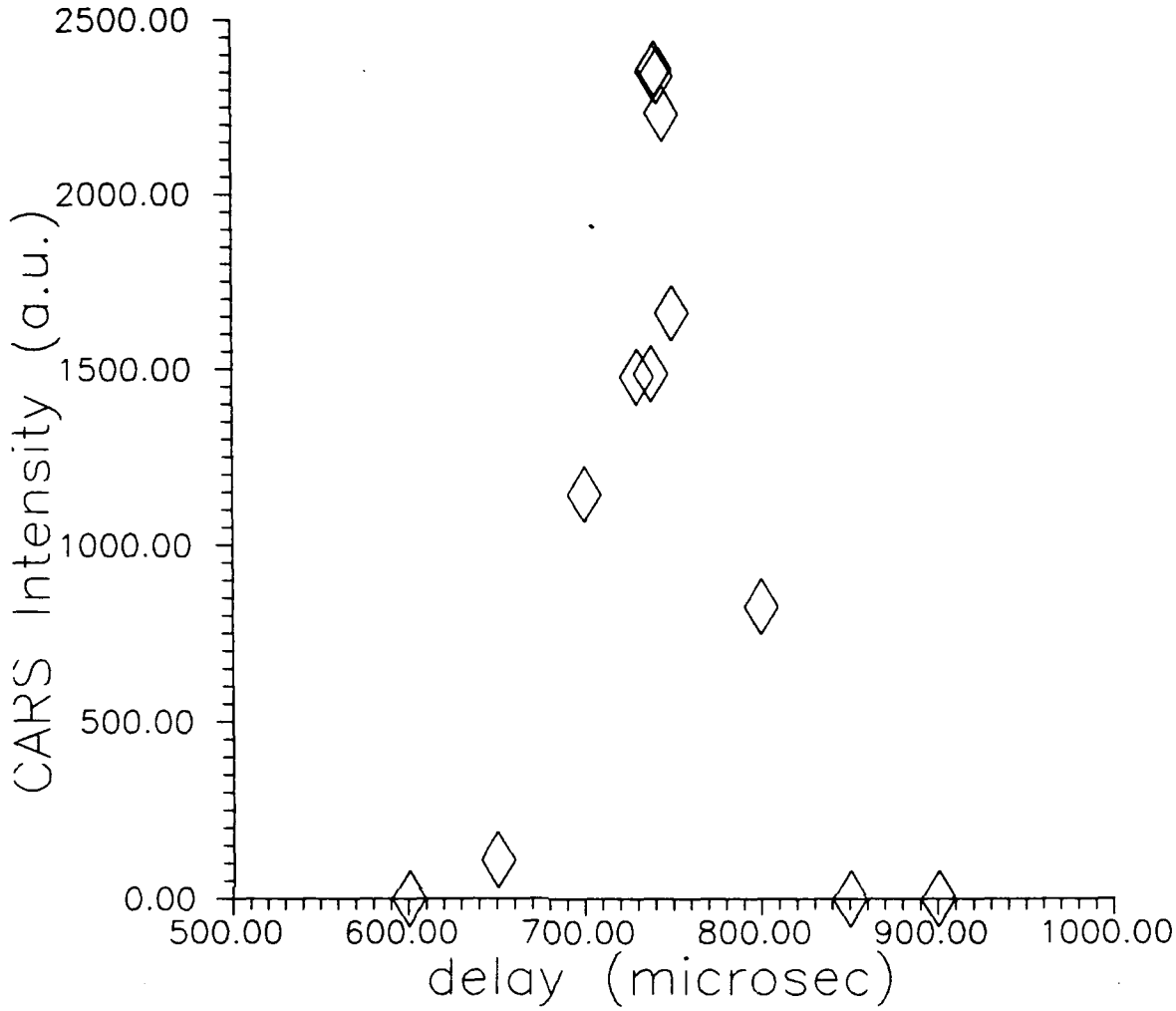

Fig. 2

Pulsed beam profile as measured on the v_1 CARS signal of CH_4

Fig. 3 shows the spectrum obtained after 1000 laser pulses, where also the perpendicular v_3 band of CH_4 is detected (expanded scale), which as shown in ref. [2] may be used to determine the rotational temperature.

Present data indicate that at least for high symmetric vibrations of small molecules (such as CH_4, NH_3, C_6H_6) it will be possible to perform this kind of measurements diluting the sample down to a few percent. This fact will allow to produce clusters, as observed in ref. [1], and to investigate their decomposition at different wavelengths.

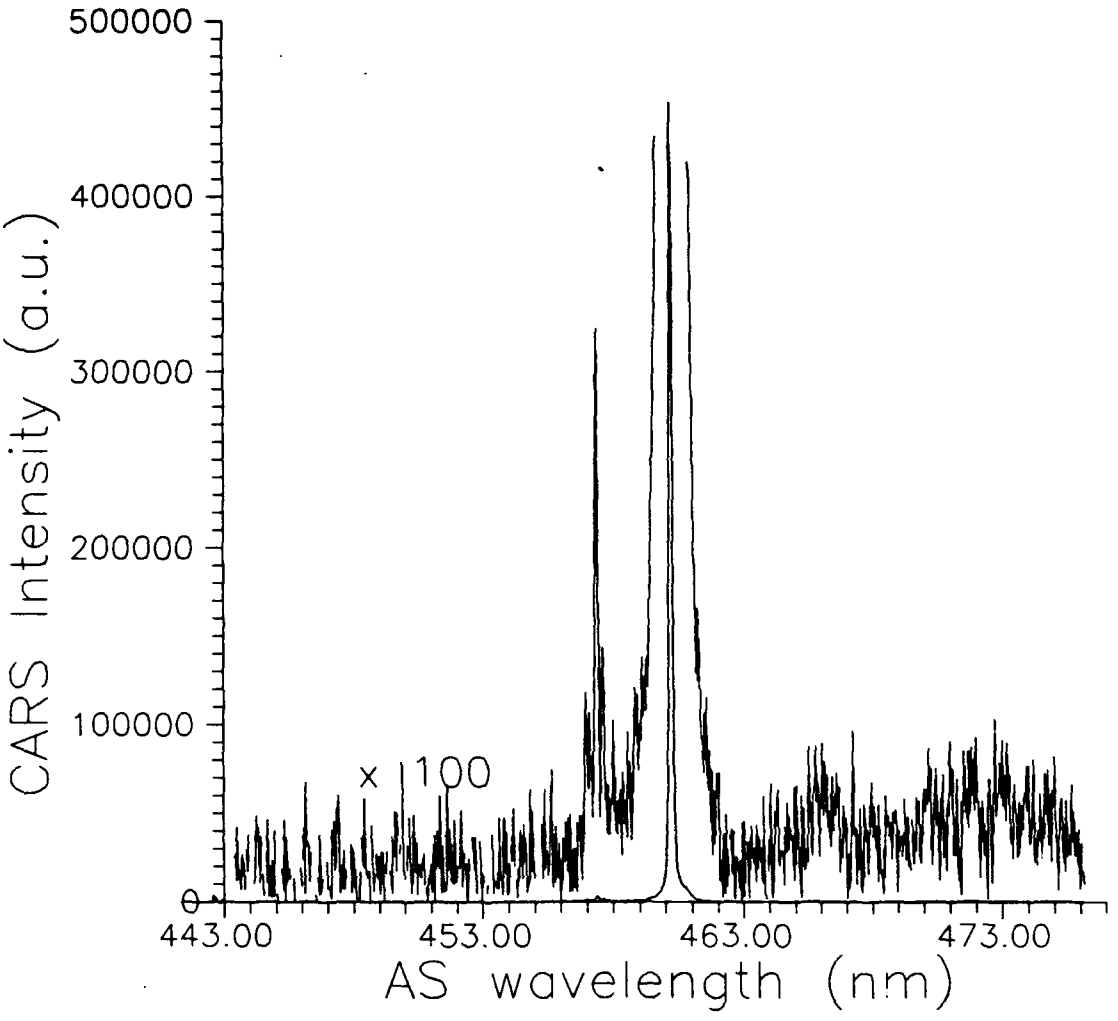

Fig. 3

CARS signal measured on a molecular jet of pure CH_4. The v_1 Q-branch dominate the spectrum, the v_3 weaker perpendicular band is detected with rotational resolution (see expanded spectrum).

Footnotes and references

(*) on leave of absence from Raman Lab., Jagiellonian University, Krakov (Poland)
(#) Istituto sui Materiali Speciali CNR, Potenza (Italy)

1] H.D. Barth, C. Jackschath, T. Pertsch, F. Huisken, Appl. Phys. B 45 (1988) 205.
2] F. Huisken, T. Pertsch, Appl. Phys. B 41 (1986) 173.
3] R. Fantoni, F. Bjinen, N. Djuric, S. Piccirillo, Laser Chem. 11 (1991) 13.

High Resolution Photoelectron Spectroscopy of NO and of the NO dimer

Ingo Fischer, Andreas Strobel, *Gereon Niedner-Schatteburg*,
Klaus Müller-Dethlefs, and Vladimir E. Bondybey
Institut für Physikalische und Theoretische Chemie
Technische Universität München
Lichtenbergstraße 4
8046 Garching
Germany

17 February 1992

Abstract

The high resolution photoelectron spectra of a homogeneous molecular cluster, the NO dimer, have been measured by means of the zero-kinetic-energy (ZEKE) method. A pulsed and skimmed molecular jet of a few percent NO in argon is crossed with the frequency-doubled output of an excimer pumped dye laser. Non-resonant two photon ionization yields photoelectrons which are pulse extracted after a suitable delay of about one microsecond discriminating kinetic electrons. Thus we allow for detection of zero-kinetic-energy electrons only and an energy resolution of about one wavenumber is achieved routinely. The rotationally resolved ZEKE photoelectron spectra of NO are obtained without involving an intermediate state into the ionizing transition. From the observed intensities one can extract propensity rules for the angular momentum with which a photoelectron is emitted. Photoelectron signal almost 5000cm^{-1} below the NO ionization threshold is attributed to the NO dimer. Clearly resolved vibrational structure is assigned to three vibrational modes of the cluster. Due to the observed long progression in an out of plane bending mode it is concluded that the planar neutral dimer twists out of plane upon ionization. Simple molecular electronic orbital considerations support this interpretation.

COPY AVAILABLE TO DTIC DOES NOT PERMIT FULLY LEGIBLE

Ethan Gallogly and
William M. Jackson
Department of Chemistry,
The University of California
Davis CA, 95616

Abstract:

Crossed Molecular Beam Studies of Buckminsterfullerene.

A crossed supersonic molecular beam machine for doing angularly resolved time-of-flight studies on the reaction dynamics of Buckminsterfullerene (C_{60}) has been constructed. The apparatus utilizes a quadrupole mass spectrometer as a detector, and has two perpendicular molecular beam sources which can be rotated with respect to the entrance aperture of the quadrupole. The initial scattering studies of C_{60} beams with seeded beams of rare gases and Halogens will be presented. The authors gratefully acknowledge the support of the National Science Foundation under grant # 9008095.

The Influence of Methyl Groups on the Rate of Intramolecular Vibrational Energy Relaxation.

J. Gambogi, K. K. Lehmann, B. H. Pate, G. Scoles and X. Yang
Department of Chemistry, Princeton University, Princeton, NJ 08542

Recently in our laboratory, the fundamental and first overtone of the acetylenic C-H stretch in a series of trimethyl substituted acetylenic compounds have been measured using high resolution, molecular beam optothermal spectroscopy[1]. These systems fall in the large molecule limit and thus their intramolecular vibrational energy redistribution (IVR) lifetime can be directly obtained from the Lorentzian linewidth observed in the frequency resolved spectra. A major motivation for carrying out this type of measurement is to understand the systematic variations of IVR rate with structure and composition. This in turn may lead to the design and synthesis of large molecules in which the IVR rates are comparable to the timescales required for bond selective chemistry.

The series of trimethyl substituted acetylenes, $(CH_3)_3X\text{-}C{\equiv}C\text{-}H$ (X = C, Si and Sn) was studied and unusually long lifetimes (up to a few nanoseconds) were measured[1]. A common feature of these molecules is the presence of hindered methyl rotors. It was expected, based on previous work, that deuteration of the methyl groups would result in a decrease in the IVR rate[2,3]. In order to more fully understand the effect of the methyl rotors on IVR, the high resolution spectra of 3,3-dimethylbutyne-d_9 (TBA-d_9) and (trimethylsily)acetylene-d_9 (TMSA-d_9) were measured. The IVR lifetimes obtained from the Lorentzian line shapes can then be compared to those of their undeuterated analogues[1].

For the fundamental of TBA-d_9 only the Q-branch was observed. This branch has a linewidth of 4 GHz and is observed to be a symmetric Lorentzian profile corresponding to an IVR lifetime of 40 psec. The first overtone region of TBA-d_9 was scanned and no evidence of any absorption was found, indicating a linewidth too broad to allow observation of the Q branch above the noise level. Based on the signal-to-noise of our

spectrometer, a reasonable estimate of the lifetime in this overtone is <20 psec. The corresponding lifetimes for the undeuterated TBA compound are 200 psec in the fundamental and 110 psec in the overtone.

The full spectrum of the fundamental C-H stretch of TMSA-d_9 from R(8) to P(9) was measured. Each P and R branch line consisted of a pure Lorentzian lineshape. For TMSA-d_9 and TMSA the linewidths are considerably narrower than in the carbon analogues and have a corresponding IVR lifetime of 850 psec for the deuterated silicon compound and 2000 psec for the undeuterated. In the overtone region of TMSA-d_9 the Q-branch was observed and a lifetime of 110 psec was obtained. This implies an eightfold increase in the IVR rate and contrasts the behavior of the undeuterated Silicon compound where the IVR rate decreases by a factor of two in going from the fundamental to the overtone.

In addition, the spectra was measured of the following compound, $(CF_3)_3C\text{-}C{\equiv}C\text{-}H$ (TBA-f_9), in which fully fluorinated rotors are present. Again, only the Q branch was observed in the fundamental showing a slightly narrower lineshape than TBA-d_9, implying a lifetime of 65 psec. The overtone spectrum was obtained only with marginal signal to noise, yielding a lifetime between 10 and 20 psec.

It is difficult to fully rationalize all the trends present in this series of compounds, although several conclusions can be established. The first is that in these compounds deuteration of the methyl groups causes an increase in the IVR rate, contrary to previous experimental observations[2] and theoretical predictions[3]. A second conclusion can be drawn about the importance of the methyl rotation in the molecules' IVR. Calculated density of states excluding the torsional modes show that for TBA, TBA-d_9, and TMSA the number of background states is too sparse to support statistical IVR and therefore some energy must flow into the torsional modes.

Finally, it is apparent from these and our previous results that IVR rates do not correlate with the total density of states. A correlation is present when comparing the

undeuterated to the deuterated analogue, but absent when going from C to Si or from v=1 to v=2. For all of these compounds, the density of states for the overtone is several orders of magnitude larger than for the fundamental. In order to explain the data set as a whole, a tier model is hypothesized where the C-H stretch is directly coupled by a small number of low-order resonances that transfer the C-H excitation into only 2 or 3 quanta of the other modes. These states are themselves coupled sequentially to other background states that have progressively more quanta distributed in the molecule. As one moves to "further tiers" the size of the direct coupling matrix element should fall rapidly, but the level density should increase rapidly. A reasonable ansatz is that the energy decays into the quasi-continuum of the distant tiers via a chain of low order couplings that go through virtual states in the first few tiers. In this case, the strength and density of the low order resonances determines the decay rate. By applying an analysis based only on the density of low order resonances, it is possible to explain many of the observed trends in the measured relaxation rates. The fluorinated compound does not fit well into this picture however, so a new and more powerful set of explanations must be found.

Acknowledgements

We thank Robert L'Esperance for the synthesis of the deuterated compounds. This work has been supported by the NSF under grants CHE 90-16491 and CHE 85-52757.

References

1. E.R.Th. Kerstel, K.K. Lehmann, T.F. Mentel, B.H. Pate, and G. Scoles, *J. Phys. Chem.*, **95**, 8282 (1991).
2. V.A. Walters, S.D. Colson, D.L. Snavely, K.B. Wiberg, and B.M. Jamison, *J. Phys. Chem.*, **89**, 3857 (1985).
3. (a) D.B. Moss, C.S. Parmenter, and G.E. Ewing, *J. Chem. Phys.*, **86**, 51 (1987). (b) C.C. Martens and W.P. Reinhardt, *J. Chem. Phys.*, **93**, 5621 (1990).

Complex resonances in the two-photon vibronic spectra of xenon dimers

David S. Green† and Stephen C. Wallace

Department of Chemistry, University of Toronto, Toronto, Ontario Canada M5S 1A1

ABSTRACT

We report the first observation of complex vibronic structure in the excitation spectra of xenon dimers formed in a supersonic molecular beam. Xe_2^* gerade states are populated by a two-photon excitation process in the energy range of the Xe $^1S_0$ + Xe* $6p\,[1/2]_1$ asymptotic limit. Two-photon resonant, three-photon ionization of the mass selected dimers reveal large isotope effects, erratic level spacings, and irregular intensity distributions. The interference between at least two deeply bound 1_g molecular states is discussed.

Among the many interests in supersonic molecular beams is the production of small van der Waals molecules and the possibility to determine their spectroscopic and dynamic properties. In this paper, we present results on the gerade states of Xe_2^* that correlate in the asymptotic limit with the lowest excited $6p$ atomic states Xe* $6p\,[5/2]_2$ and Xe* $6p\,[1/2]_1$.[1] These molecular states can not be populated via one-photon transitions from the ground state $X\,0_g^+$, but $g \longleftarrow g$ transitions are possible via two-photon processes. Since the ground state has a shallow minimum these transitions probe the long range potential of deeply bound upper states (i.e. at $R' \gg R_e'$). The information gathered from such beam experiments are complementary to studies of collision-induced processes.

Fig. 1 shows selected potential curves of the lowest excited molecular and atomic states after the empirical work of Mulliken.[2] Both the Xe* $6p\,[1/2]_1$ and Xe* $6p\,[5/2]_2$ atoms correlate with 1_g molecular states that are deeply bound. Molecules excited to these states can radiate to states that are derived from Xe* $6s\,[3/2]_1$ or Xe* $6s\,[3/2]_2$. Alternatively, the primary excited molecules can dissociate via curve crossing or coupling to underlying continua. The effective lifetimes of the molecules and the separated atoms are determined by the resonance trapping of the radiation to the ground state and collisions that govern the time behaviour with increased pressure.[3-7] Gas cell studies have shown that at pressures exceeding 10 Torr of Xe collisionally induced decay into lower lying states and two and three body recombination reactions of separated atoms are important kinetic and dynamic pathways.[3-7] In this case, decay processes of xenon after selective photoexcitation lead to excimer emissions at the wavelength of the two well known continua of Xe_2^* (1470 Å and 1700 Å). By contrast, the decay of dimers and atoms via collisions does not occur in the present studies because of the low downstream pressures in the gas expansion.

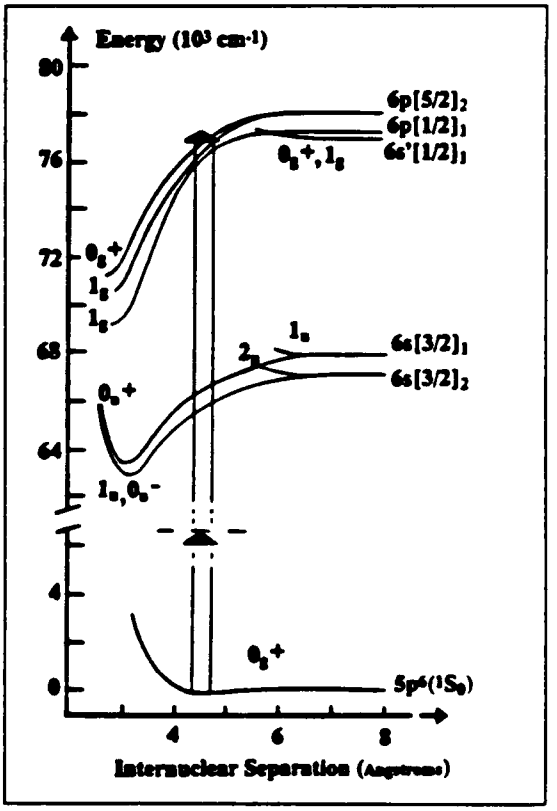

The Xe_2^* $6p$-Rydberg manifold includes a number of bound states that give rise to discrete two-photon vibronic spectra.[1,3-11] The kinetics and decay processes[2] in these states have been investigated under thermal collision conditions by Böwering *et al.*,[3,4] Moutard *et al.*,[5,6] and Ku and Setser.[7] To understand the energy structure in greater detail, spectra of cold Xe_2 in a supersonic expansion have been measured by Green,[1] Dehmer *et al.*,[8,9] Pratt *et al.*,[10] and Lipson *et al.*[11] The present study focuses on interferences between molecular states derived from Xe^* $6p$ that are kinetically important to relaxation pathways.[3-7]

The cold molecular beam is obtained by expanding Xe neat or diluted to 5 % in He through a commercial pulsed valve using stagnation pressures in the $10-30$ psi range and 500 μm nozzle. The nine stable isotopes of Xe generate some 45 possible isotopomers of the dimer that range in abundance from $\sim 10^{-4}$ to 17 %. Pulsed laser excitation provides a tunable source of intense radiation for resonant enhanced multiphoton ionization (REMPI). A linear polarizer followed by a Babinet-Soleil compensator is positioned in the laser path and the retardation adjusted to select excitation by either linear or circular polarized light. The laser beam is focussed and intersects the gas expansion at distance of approximately 5 cm downstream of the orifice. In conjunction with time-of-flight mass spectrometry (TOFMS) the experimental approach is sensitive to isotopomers and fragments. The dimer resonances are monitored by recording gated signals representing excitation of selected masses as a function of the dye laser wavelength. The laser has a linewidth of ≤ 0.1 cm^{-1} and is scanned through the fundamental wavelength range between 5090 Å and 5230 Å. This corresponds to a two photon excitation energy from 78563 cm^{-1} to 76461 cm^{-1}. The rotational constants of both Xe_2 ground state ($B_e'' = 0.013$ cm^{-1}) and excited states ($B_e' < 0.03$) are much smaller than the laser linewidth. Individual rotational lines are not resolved but most peaks are attributed to vibrational bands with a narrow contour from underling rotational branches.

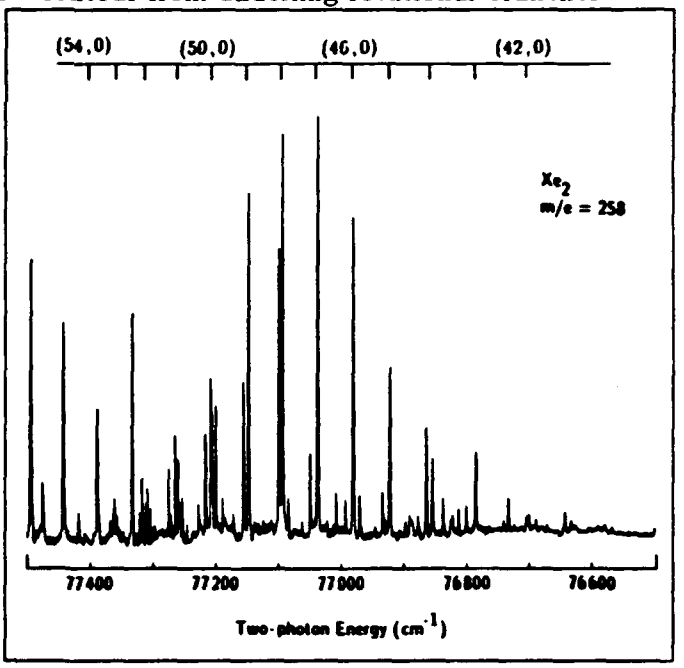

Fig. 2 shows a representative $(2+1)$ REMPI spectrum of Xe_2 in the vicinity of the Xe $^1S_0$ + Xe^* $6p\,[1/2]_1$ asymptotic limit, obtained using linearly polarized light and by monitoring the molecualr ion at m/e=258. Since two-photon atomic transitions to Xe^* $6p\,[1/2]_1$ from Xe $^1S_0$ are forbidden it was presupposed that the transition strengths to vibronic bands in this energy region would be vanishingly small. We find that the vibronic spectra of the 1_g states derived from Xe^* $6p[1/2]_1$ and Xe^* $6p[5/2]_2$ are relatively strong.[1] The spectra are heavily perturbed and we describe the progression as composed of *complex resonance structure.*

In the absence of mass discrimination the total ion yield spectrum below 77456 cm^{-1} is unassignable. By restricting the signal collection to discrete mass channels (for example m/e = 258 in Fig. 2 is 97% $^{129}Xe^{129}Xe$) it becomes obvious that the dominant spectral feature is a long vibrational progression with somewhat erratic intervals, $\Delta G'_{v+1/2} \approx 50$ cm^{-1}. The isotope shifts are large, on the order of 5 cm^{-1} between corresponding bands in adjacent mass channels (i.e. m/e = 258 to 268), and indicative of high vibrational numbering. Perhaps the most interesting and characteristic features are the intensity anomalies and the large density of satellite peaks superimposed on the stronger bands.

We rationalize the complex REMPI spectrum by considering interstate perturbations that can be best described as an interference phenomenon.[12] The two mixed eigenstates are considered a true superposition of the basis states. The resultant transition intensity is governed by the intensities to each of the individual states and carries an additional term, an interference term, that includes an appropriate phase relation. For transitions through two interfering states the transition probability amplitudes are additive. The observed signal intensity is then proportional to the average of the absolute square of the resultant amplitude.

By invoking moderate interstate mixing and intensity perturbations we can account qualitatively for the oscillator strength required to detect spectral transitions through the state derived from Xe* 6p $[1/2]_1$. We identify the symmetry and angular momentum of the excited state by considering the molecular states arising from the separated atom limit. In this instance, although both 0_g^- and 1_g molecular states are correlated with the Xe* $6p\,[1/2]_1$, only transitions to 1_g are two-photon allowed. We thus attribute a portion of the complex spectrum to $1_g \longleftarrow 0_g^+$ transitions. Mulliken[2] predicted this 1_g state to be the most strongly bound Rydberg state with the $A\,^2\Sigma^+_{1/2u}$ ion core. The observation of densely spaced satellite peaks is consistent with excitations through very high lying vibrational levels of such a deeply bound state. Further confirmation of this assignment is provided by the fact that the satellite peaks terminate abruptly at an energy of 77456 cm^{-1}. As shown in Fig. 3, this energy threshold corresponds to the Xe $^1S_0$ + Xe* $6p\,[1/2]_1$ asymptotic dissociation limit.

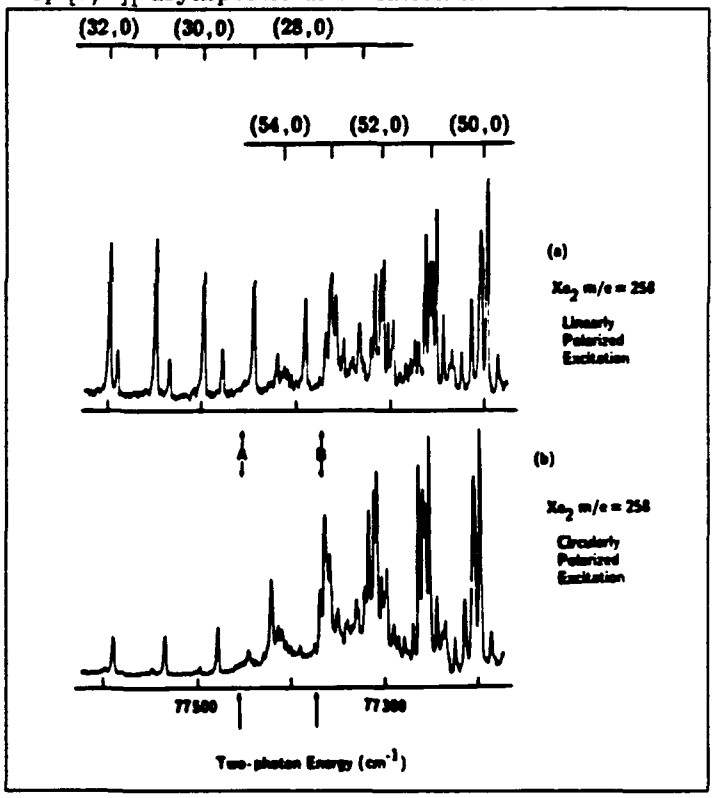

Fig. 3. (2+1) REMPI polarization selected spectra of Xe_2 in the vicinity of the Xe $^1S_0$ + Xe* $6p\ [1/2]_1$ asymptote (labelled A) and the Xe $^1S_0$ + Xe* $6s'\ [1/2]_1$ asymptote (labeled B), obtained using (a) linearly polarized light and (b) circularly polarized light, and by monitoring the molecular ion signal at m/e =258. Transitions through the vibrational levels of the deeply bound 0_g^+ state derived from Xe* $6p\ [5/2]_2$ diminish in strength on going from linear to circularly polarized excitation.

Strongly attractive gerade state potentials (1_g and 0_g^+) are associated with the Xe* $6p[5/2]_2$ level so that interactions with the 1_g potential derived from Xe* $6p\,[1/2]_1$ may be expected. From the polarization selected spectra, as represented in Fig. 3, we can readily distinguish between transitions through the upper 1_g and 0_g^+ states. The analysis of the $1_g \longleftarrow X\,0_g^+$ spectrum for selected dimer masses provides a vibrational numbering of the observed bands from $v' = 42$ through 54. The linear least-squares fit of the vibrational intervals yields an approximate vibrational frequency $\omega_e' \simeq 105.4(3.1)$ cm^{-1} and anharmonicity $\omega_e x_e' \simeq 0.5052(13)$ cm^{-1} for $^{129}Xe^{129}Xe$. From the expression $D_e' = \omega_e'^{\,2}/4\omega_e x_e'$ the potential well depth is estimated to be 5496 cm^{-1} which is consistent with a $A\,^2\Sigma_{1/2u}$ Rydberg state.

Excitation from the van der Waals ground state to regions near dissociation thresholds of excited electronic states provide a sensitive probe of interstate interactions. Understanding these interactions is a challenging problem, especially the detailed mechanism mixing states near the asymptotic dissociation limit. In this paper we have presented a case of complex resonances in the two-photon vibronic spectra of Xe_2 results from intensity perturbations involving a pair of deeply bound 1_g state. In particular, the interfering states are identified as two nested 1_g states correlating with the lowest $6p$ atomic states Xe^* $6p\,[1/2]_1$ and Xe^* $6p\,[5/2]_2$. Since collisional relaxation and decay pathways are important in excimer dynamics, the identification of these interstate interferences will impact on the interpretation of kinetic and dynamic data such as quenching rates and collision cross-sections.

†Current address: Department of Chemistry, Stanford University, Stanford California 94305.

References

1 D. S. Green, Ph.D. Dissertation, University of Toronto, Toronto, Ontario, Canada 1990, Chapter 6, pp. 380 – 458, and Appendix A2, pp. 515 – 551.

2 R. Mulliken, J. Chem. Phys. 52, 5170 (1970).

3 N. Böwering, M. R. Bruce, and J. W. Keto, J. Chem. Phys. 84, 709, (1986).

4 N. Böwering, M. R. Bruce, and J. W. Keto, J. Chem. Phys. 84, 715, (1986).

5 P. Moutard, P. Laporte, N. Damany, J. L. Subtil, and H. Damany, Chem. Phys. Lett. 132, 521 (1986).

6 P. Moutard, P. Laporte, J. -L. Subtil, N. Damany, and H. Damany, J. Chem. Phys. 88, 7485 (1988).

7 J. K. Ku, and D. W. Setser, J. Chem. Phys. 84, 4304 (1986).

8 P. M. Dehmer, S. T. Pratt, and J. L. Dehmer, J. Phys. Chem. 91, 2593 (1987).

9 P. M. Dehmer, S. T. Pratt, and J. L. Dehmer, J. Chem. Phys. 85, 13 (1986).

10 S. T. Pratt, P. M. Dehmer, and J. L. Dehmer, Chem. Phys. Lett. 165, 131 (1990).

11 R. H. Lipson, A. R. Hoy, and E. Chan, J. Chem. Phys. 90, 4664 (1989).

12 H. Lefebvre-Brion and R. W. Field, *Perturbations in the Spectra of Diatomic Molecules*, (Academic Press, Orlando, 1986) Chapter 5, pp 244 – 330.

Energy and Momentum Distributions and Projections in the Scattering of CO off Ag(111)

Thomas F. Hanisco,Chun Yan, and Andrew C. Kummel
Dept. of Chemistry, University of California, San Diego, La Jolla, CA, 92093

ABSTRACT

Here, we report a detailed comparison between monoenergetic, rotationally cold beams of 0.75 eV N_2 and CO scattering off the same Ag(111) crystal under identical conditions. The scattered flux was probed with resonantly enhanced multiphoton ionization detection (REMPI) to determine the cross correlations between the rotational state distributions, angular momentum alignment, and velocity distributions. For all conditions studied, the CO molecules channel a much larger fraction of their incident kinetic energy into rotational excitation and phonon excitation. However, both N_2 and CO leave the surface with angular momentum alignment and orientation. The interactions of N_2 and CO with Ag(111) differ because of the finite dipole moment of CO and the larger physisorption well for CO. The finite dipole moment of the CO may change the scattering by allowing the molecules to reorient prior to or post collision with the surface because the attractive gas-surface potential depends on the orientation of the molecules; for example on most metal surfaces CO is adsorbed carbon side down. In addition, because of its dipole moment, the gradient of the gas-surface potential with respect to molecular orientation should be larger for CO than for N_2. *This results in* greater rotational excitation and broader angular and velocity distributions for CO compared to N_2.

For normal incidence beams, the translational energies of the scattered CO and N_2 were measured and an inverse correlation between rotational energy and exit translational energy was found. In addition, for N_2 the rotational state selected velocity distributions are very narrow while for CO the rotational state selected velocity distributions are wide. This probably results from two competing effects: First, the gradient of the gas-surface potential with respect to the molecular orientation is larger for CO than for N_2, as evidenced experimentally by greater rotational excitation in the scattered CO molecules. Thus small differences in the initial molecular orientation and impact parameter result in much larger differences in exit velocity for CO scattering compared to N_2 scattering. Second, the increased width of the exit velocity distribution for CO may result from the C end first collisions transferring a different fraction of energy to the surface than O end first collisions that scatter into the same final J states. Thus a wider range of exit velocities are detected for each final J state. For both N_2 and CO, rotational excitation into high J states scales with the normal component of incident translational energy, but the phonons can be excited by both the parallel and normal components of the incident translational energy.

For normal incidence scattering, both CO and N_2 exhibit rotational rainbows at all exit angles and the CO rainbows are much more prominent than the N_2 rainbows; see Figure 1. However, the correlation between the rotational distributions and the exit velocity is much stronger for N_2 than

for CO. This results from the strong anti-correlation between rotational excitation and exit velocity for N_2 scattering and the wider velocity distributions for scattering into a given rotational state and exit angle exhibited by CO. The more prominent rainbows measured by our density sensitive REMPI detection for CO scattering is probably due to the molecules in the highest rotational states having a very small exit velocity for CO, and thus for a given flux, they have a higher density.

The most striking difference between the N_2 and CO rotational distributions for glancing incidence beams is that the CO rotational distributions are similar at specular and super-specular detection while the N_2 rotational distribution are consistently hotter at super-specular compared to specular detection; see Figure 2. The high correlation between exit angle and rotational distribution for N_2 results from conservation of parallel momentum. The similarity between the CO population distributions at specular and super-specular detection is probably due to the much broader lobular scattering distribution exhibited by CO which results from surface corrugation and the large gradient of the gas-surface potential with respect to both the gas-surface distance and the molecular orientation.

At glancing incidence, the low energy rotational peak for the medium exit velocity is much more prominent for N_2 than for CO. In contrast, for normal incidence, CO scattering has a more prominent low energy rotational population peak than N_2. Molecular modeling indicates that this low energy rotational peak is attributed to the large number of collisions with side-on molecular orientation and that at normal incidence the gas-surface impact parameter only has a modest influence on the final rotational state. We believe our data indicates that there is an increase in the influence of the impact parameter in determining the final rotational state for glancing incidence, side-on molecular orientation scattering.

There is 100% cartwheeling type alignment for N_2 in medium and high exit rotational states while for CO the alignment is weak except at the very highest rotational states where it is still less than 100% cartwheeling; see Fig 3. Our data can be interpreted as showing that the N_2 molecules at these relatively high energies collide with a slightly corrugated surface and have nearly linear trajectories. Conversely, the CO scattering data is consistent with scattering from a more corrugated surface. The CO molecules have a permanent dipole moment, therefore the gradient for the CO-Ag(111) gas surface potential with respect to molecular orientation is larger. In addition, CO has a deeper physisorption well on Ag(111). Thus, the CO molecules probe deeper into the corrugated repulsive portion of the potential and have a more inelastic collision that results in greater rotational and phonon excitation but lower exit translational energy. The lower alignment for CO scattering into high J states is consistent with the CO molecules having curved exit trajectories and/or multiple collisions with the surface. To further understand the role of molecular orientation in CO scattering, we have performed a series of measurements upon the angular momentum orientation of the scattered molecules; these measurements are now being interpreted using molecular modeling of gas-surface scattering so that we can better understand the importance of C-end first versus 0-end first molecular orientations.

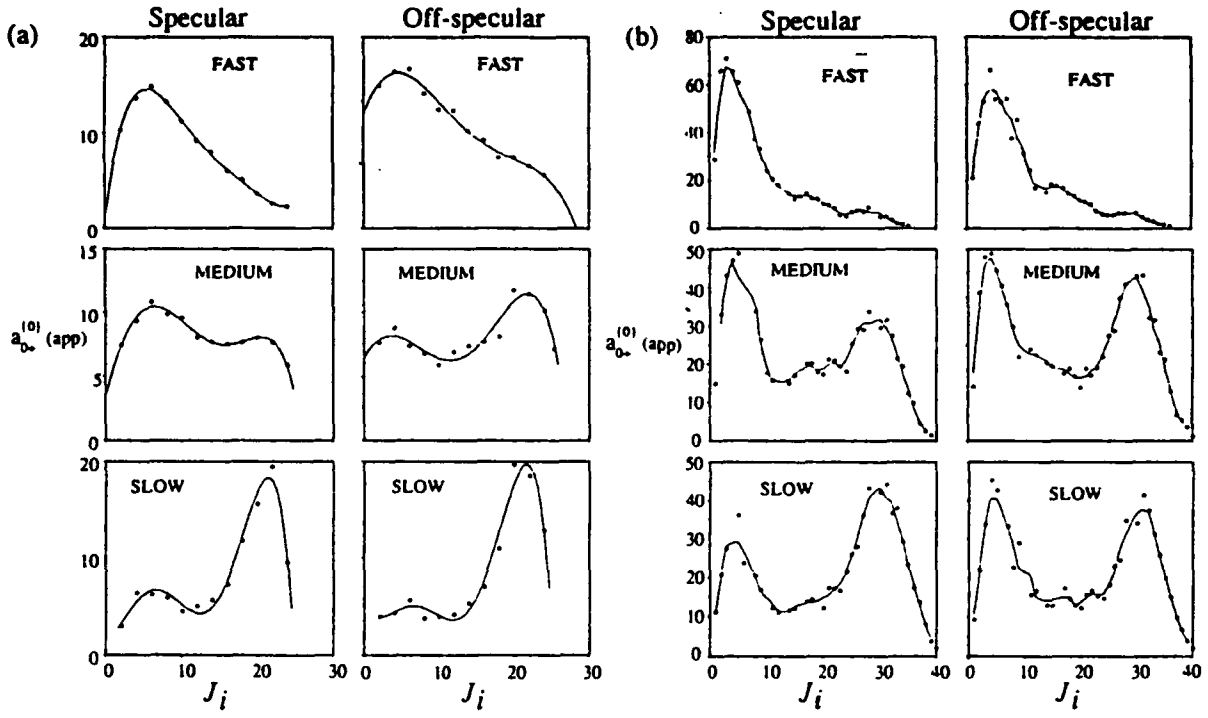

Figure 1: Exit velocity resolved populations versus ground rotational state and exit angle for (a) N_2 and (b) CO in a 0.75 eV beam, with 7 μsec long pulses, at normal incidence ($\theta_i = 0°$) scattered from Ag(111) at T_s = 300 K. The lines are smooth curve fits to the data. For N_2 the fast, medium, and slow velocities are (in m/sec): 2010 ± 330, 1530 ± 190, and 1060 ± 330. For CO the fast, medium, and slow velocities are (in m/sec): 1760 ± 300, 1300 ± 150, and 830 ± 300.

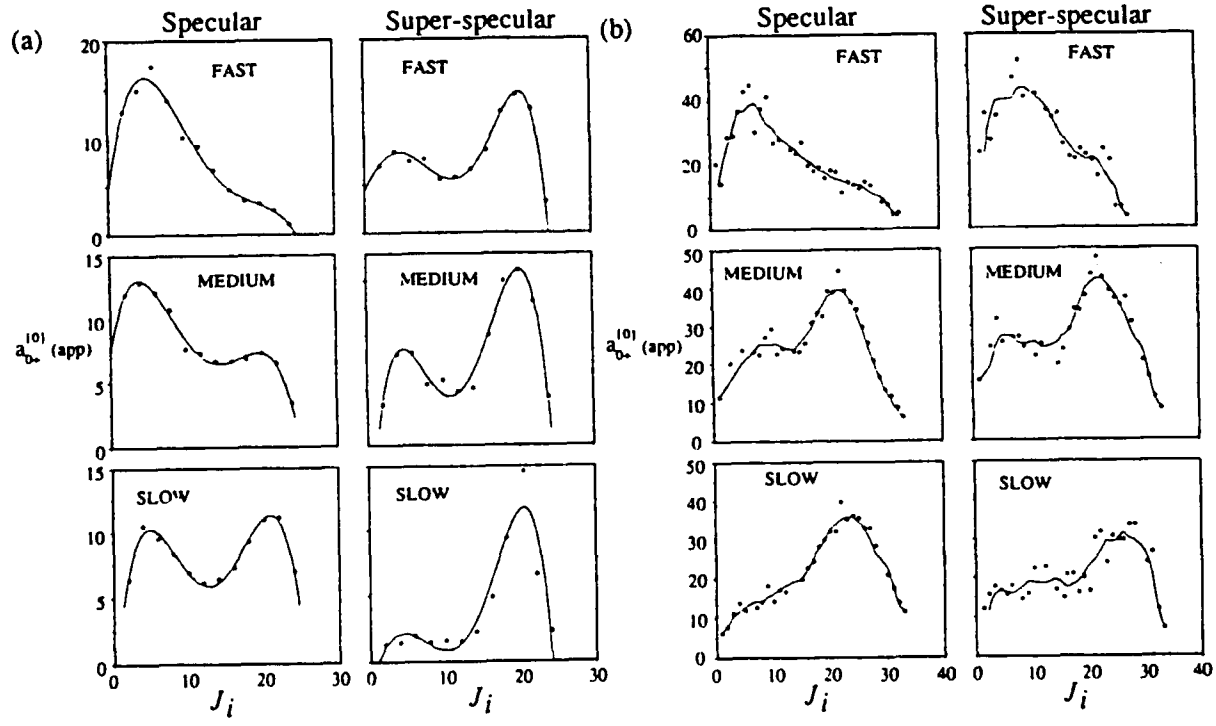

Figure 2: Exit velocity resolved populations versus ground rotational state and exit angle for (a) N_2 and (b) CO in a 0.75 eV beam, with 7 μsec long pulses, at glancing incidence ($\theta_i = 30°$) scattered from Ag(111) at T_s = 300 K. The lines are smooth curve fits to the data.

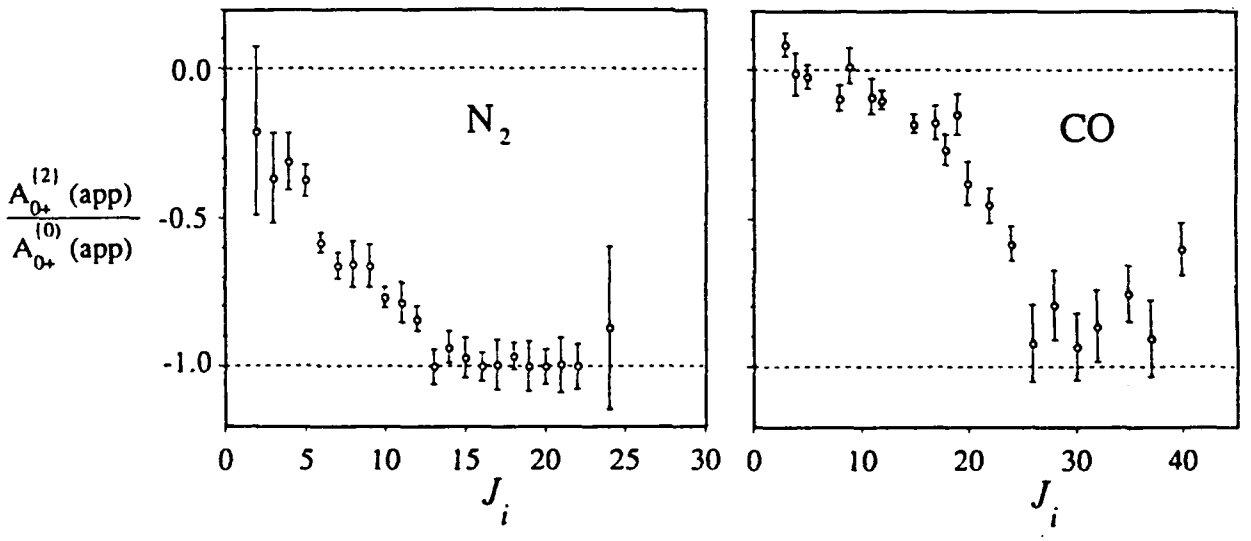

Figure 3: Angular momentum alignment, $A^{(2)}_{0+}$, versus ground rotational state, J, for E_i = 0.75 eV N_2 (left) and CO (right) scattered off Ag(111) at T_s = 300 K. The scattering was done at normal incidence and normal detection. For N_2 the alignment shows pure cartwheeling rotation (M_z = 0 where z = the surface normal) for J > 12. In addition, the alignment for N_2 is independent of exit velocity under these conditions. For CO, the molecules exhibit nearly pure (~90%) cartwheeling rotation for J > 26. At very high J's the alignment appears to decrease, *eg.* $A^{(2)}_{0+}$ = -0.6 for S(40), this is probably due to the break-down of cylindrical symmetry at very high J states. The alignment for CO is independent of exit velocity, exit angle, and ion channel.

Michael Hawley* and H. H. Nelson
Chemistry Division, Code 6111
Naval Research Labs
Washington, D.C. 20375

Detection of Methyl Fragment Internal State Distribution from the 193 nm Photodissociation of Dimethyl Sulfoxide in a Free Jet

The measurement of the internal state distributions of fragment species produced by laser induced photodissociation can be useful in elucidating the detailed mechanism of the photodissociation process itself. From the detailed state distributions obtained, information on the dissociating species can be deduced. For example, in the case of polyatomic molecules, where more than two fragments are produced, the state distributions of the photofragments can help to determine if the photodissociation process occurs via a stepwise mechanism or in one concerted step.[1] This general experiment can be performed on a precursor species which has been expanded in a free jet and is therefore rotationally cold. This will reduce the thermal energy in the precursor and in some cases allows for a more detailed analysis of the data.[1]

In this study we present the results of the methyl radical's vibrational and rotational state distribution produced from the photolysis of dimethyl sulfoxide, $(CH_3)_2SO$ at 193 nm in a free jet expansion and compare it to the photodissociation of the similar molecule acetone. The experimental apparatus is very simple, a free jet time of flight mass spectrometer. The precursor molecule, which is seeded into a buffer gas, is expanded through a pulsed beam valve (0.05 cm diameter, General Valve) and allowed to flow downstream about 5 cm to a point directly in front of the aperture of the mass spectrometer. At this point in the expansion the rotational cooling of the precursor species has ceased because the collison frequency is nearly zero. Here, an excimer laser is fired which dissociates the precursor molecule into its fragments. Photofragments can then be detected by REMPI spectroscopy. A tunable dye laser is triggered about 250 ns after the photolysis laser pulse, ionizing one of the fragment species, which is then mass specifically detected by the time of flight mass spectrometer at right angles to the free jet axis.

In the specific case discussed here, an ArF excimer laser dissociates DMSO at 193 nm into two methyl radicals and an SO molecule.[2] The REMPI laser used to detect the methyl radicals is a YAG pumped dye laser running on DCM dye. Frequency doubling this dye produces the tunable source from 325 to 335 nm necessary to detect CH_3 via the two photon $3p\ ^2A_2'' \leftarrow 2p\ ^2A_2''$ Rydberg transition.[3] This laser is focused through a 15 cm lens at a point in front of the entrance aperture of the mass spec. The two lasers counterpropagate collinearly through the extraction plates of the mass spectrometer to maximize the overlap of the beams.

The low temperature environments produced by free jet expansions make them ideal sources for clusters to form. To reduce possible interference from clusters in our study we have chosen helium as the inert carrier gas in the expansion. Furthermore, since the vapor pressure of DMSO is less than 1 torr at room temperature, our expansions are automatically very dilute in the precursor. Total backing pressures were also kept low to further reduce the possibility of clusters forming in the expansion. The backing pressures used were

* NRC/NRL Postdoctoral Associate

between 100 and 600 torr, and no systematic trend in the experimental results were observed as the pressured was varied.

Our experimental results are shown in Figure 1. This is a REMPI spectrum showing

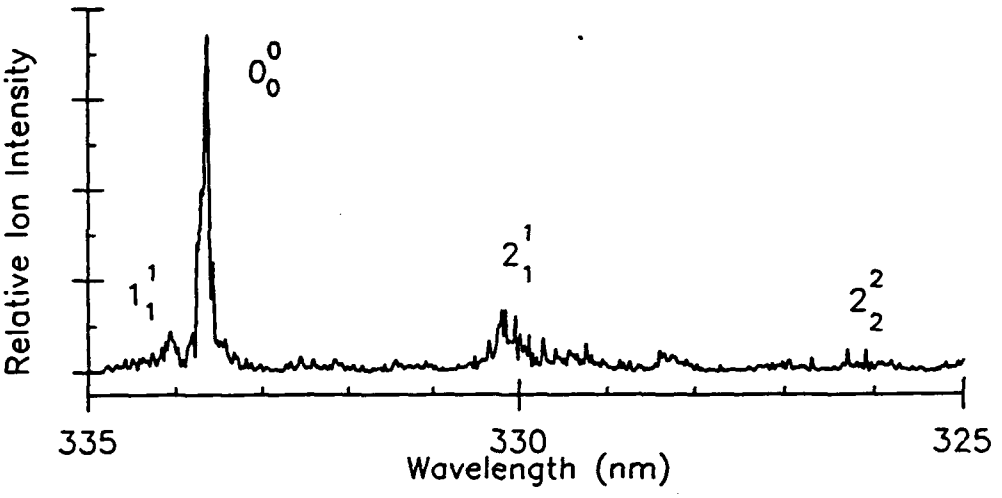

Figure 1: REMPI spectrum of the $3p\ ^2A_2'' \leftarrow 2p\ ^2A_2''$ transition in CH_3. The four observed vibrational bands are labeled on the figure. This spectrum is not corrected for laser energy.

the four different vibrational states of CH_3 that we observe populated in this process. The CH_3^+ signal we observe is linearly proportional to the power of the excimer laser and quadratically dependent on the power of the ionizing laser as would be expected for a single photon dissociation followed by a 2+1 REMPI process. After this spectrum is corrected for the laser intensity and Franck-Condon factors we determine that about 40 % of the methyl radicals are formed with vibrational excitation. Excitation is observed in both the symmetric stretching (ν_1) mode and the umbrella (ν_2) mode. From a fit of the rotational contour of the origin band we obtain an estimate of the rotational temperature of the methyl fragment to be a rather cold 150±100 K.

The total energy available to the photofragments at 193 nm is 44 kcal mol^{-1}. Previous experiments on the state distribution of the SO fragments have shown an inverted vibrational population with mild excitation, the SO possessing an average of 4.6 kcal mol^{-1} of vibrational energy.[2] The rotational energy distribution of these fragments is also relatively low in total energy, about 1.3 kcal mol^{-1}.

Figure 2 shows a Boltzmann plot of the umbrella mode (ν_2) of methyl, the slope corresponds to a vibrational temperature of 600±250 K. Figure 3 also shows the relative amount of excitation we observe in the high frequency symmetric stretch (ν_1) mode. No attempt has been made to correlate this observation with a Boltzmann temperature. From these observations it can be seen that the total average energy present in CH_3 vibration is about 4 kcal mol^{-1}.

Since the carbon-carbon bond energies are very similar in both DMSO and its carbonyl analog, acetone, the available energy to the photofragments is nearly the same in both cases, and allow a direct comparison. The vibrational distribution in the ν_2 modes of methyl from acetone are also observed to exhibit a Boltzmann distribution with a

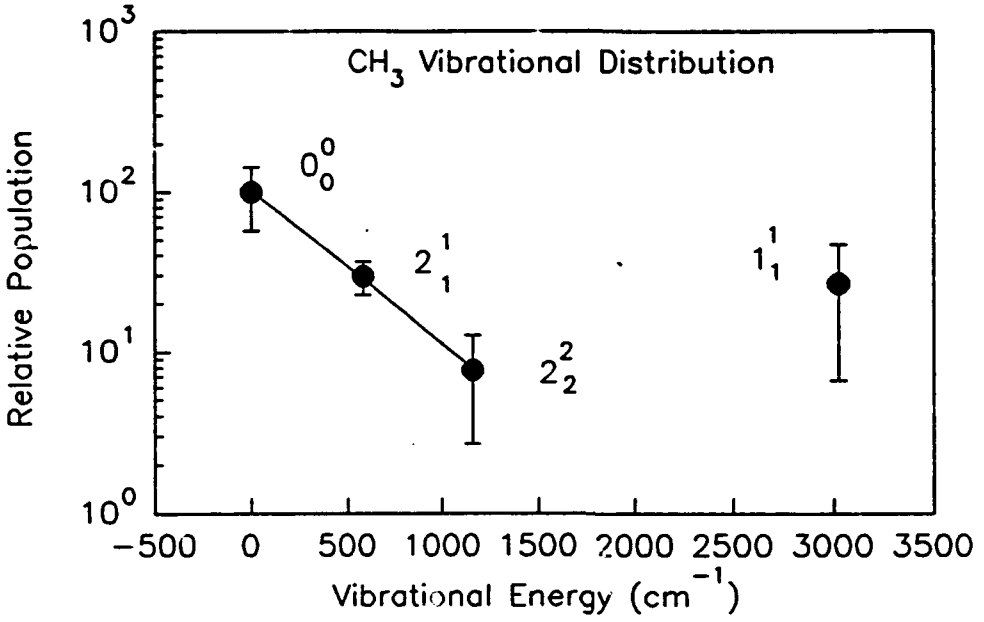

Figure 2: Boltzmann plot of the observed vibrational modes for CH_3 produced from 193 nm photolysis of DMSO. The line corresponds to a temperature of 600K for the ν_2 modes.

temperature of 800 K.[4] Our observed distribution is very similar to this, however we do observe much more excitation in the ν_1 mode. Our rotational distribution is also slightly colder than the 500 K observed for methyl radicals produced from acetone.[4] The CO fragment produced from acetone, much like the SO fragment exhibits substantial internal excitation.[4,5] However, nearly 70 % of the total available energy was still released as relative kinetic energy of the fragments in the case of acetone. Considering the distributions for DMSO, by conservation of energy we observe about 75 % of the total energy in translation. In the case of acetone, the dissociation has been successfully modeled using an impulsive mechanism for a nonsynchronous stepwise dissociation through a bent CH_3CO intermediate. It would appear that our mechanism is very similar, with first a bond fragmentation to produce a metastable CH_3SO molecule which subsequently dissociates. Further studies are in progress to quantify this dissociation mechanism more precisely.

References:

(1) R. Bersohn, "Molecular Photodissociation Dynamics", M.N.R. Ashfold and J.E. Baggott, eds., Royal Society of Chemistry, London, p. 1-30 (1987).
(2) X. Chen, F. Asmar, H. Wang and B.R. Weiner, J. Phys. Chem., 95, 6415 (1991).
(3) J.W. Hudgens, T.G. DiGiuseppe and M.C. Lin, J. Chem. Phys., 79, 571 (1983).
(4) K.A. Trentleman, S.H. Kable, D.B. Moss and P.H. Houston, J. Chem. Phys., 91, 7498 (1989).
(5) E.L. Woodbridge, T.R. Fletcher and S.R. Leone, J. Phys. Chem., 92, 5387 (1988).

Molecular beam studies of the reactions of alkaline earth metal atoms with halogenated hydrocarbons

Guozhong He Nanquan Lou

State Key Laboratory of Molecular Reaction Dynamics
Dalian Institute of Chemistry Physics
Chinese Academy of Sciences
Dalian 116023, P.R. China

The main purpose of this work is to investigate the configurational dependence of the different halogenated hydrocarbons on the reactivity of these compounds reacting with alkaline earth metal atom.

The CL and LIF spectra of MX (M=alkaline earth metal atom; X=halogen atom) produced under single collision condition from the reactions of alkaline earth metal atom with halogenated hydrocarbon have been obtained. The vibrational distributions, the fractions of the available energy going into vibrational energy (fv) of the products MX have been calculated by means of the computer simulation.

The results presented here represent some definitive though preliminary observations of the configuration and mass effects on reactivity of the reagent molecules and product internal energy distributions.

(A) Alkaline earth metal atom + halogenated alkane

** $Ba(^1S)$,$Ca(^1S)$ + halogenated methane

(1) For a given halogenated methane, fv of MX increases as alkaline earth metal atom becomes more heavier.

(2) For a given alkline earth metal atom, fv of MX increases as halogen atom in halogenated methane becomes more heavier.

(3) For a given alkline earth metal atom, fv of MX increases as the number of halogen atoms in the halogenated alkane increases.

(4) The chemiluminescent reactions

$Ba(^3D) + CH_{4-n}Cl_n \text{ -----> } BaCl(X,A,B,C) + CH_{4-n}Cl_{n-1}$ (n=2,3,4).

The relative chemiluminescent cross section is larger for BaCl (A,B-->X) emission but smaller for BaCl (C-->X) emission while the number of Cl atom in the halogenated alkane increases.

(5) The chemiluminescent reactions

$Ca(^3P) + CH_{4-n}Cl_n \text{ -----> } CaCl(X,A,B) + CH_{4-n}Cl_{n-1}$ (n=2,3,4).

The results are similar to those of the Ba series.

(6) $BaCl_2^*$ can be formed directly from the $Ba(^3D) + CCl_4$.

** $Ba(^1S)$,$Ca(^1S)$ + halogenated ethane

(1) For a given halogenated ethane, fv of MX increases as alkaline earth metal atom becomes more heavier.

(2) For a given alkaline earth metal atom, fv of MX increases as the number of halogen atom in halogenated ethane increases.

(3) For a given alkaline earth metal atom and a given number of halogen atoms, fv of MX for halogenated methane reaction is larger than those for halogenated ethane reactions.

(4) $Ca(^1S) + CH_2Cl_2 \text{ -----> } CaCl + CH_2Cl$ --1--

$Ca(^1S) + CHCl_3 \text{ -----> } CaCl + CHCl_2$ --2--

$Ca(^1S) + CCl_4 \text{ -----> } CaCl + CCl_3$ --3--

$Ca(^1S) + (1,1)C_2H_4Cl_2 \text{ -----> } CaCl + C_2H_4Cl$ --4--

$Ca(^1S) + (1,1,2)C_2H_3Cl_3 \text{ ----> } CaCl + C_2H_3Cl_2$ --5--

$Ca(^1S) + (1,1,2,2)C_2H_2Cl_4 \text{ ----> } CaCl + C_2H_2Cl_3$ --6--

In contrast to the corresponding reactions (1), (2), (3), the reactions (4),(5),(6) have smaller reaction cross sections. But the vibrational population distributions of the CaCl of the reactions (4) and (6) are similar to reactions (1) and (2). However, the vibrational population distribution of the CaCl product of the reaction (5) is equivalent to the combination of those the reaction (4) and (6). $P_5(v) = 0.25\ P_4(v) + 0.75\ P_6(v)$, where $P_4(v)$,$P_5(v)$,$P_6(v)$ are the vibrational distributions of the reactions (4),(5),and (6) respectively.

**$Ba(^1S)$ + halogenated alkane

(1) $Ba(^1S) + n\text{-}C_nH_{2n-1}Br$, (n=2,3,4,5)

The average vibrational energies of the products BaBr increase slightly as the length of carbon chain in those halogenated alkane increase and can be described as a linear function of the mass factors of these reaction systems.

(2) $Ba(^1S)$ + dibromoalkane

For the reactions Ba + CH_2Br_2, 1,2-$C_2H_4Br_2$, 1,3-$C_3H_6Br_2$, the vibrational excitation of the product BaBr decrease obviously when the number of the carbon atoms increase.

(3) $Ba(^1S) + (n,i,s,t)\text{-}C_4H_9Br$

There are no big differences among those reactions.

(B) Alkaline earth metal atom + unsaturated halogenated hydrocarbon.

Compared to Ba + 1-Bromopropane reaction, the Ba + 1-Bromopropylene produced more strongly inverted vibrational population of BaBr.

(C) Alkaline earth metal atom + halogenated benzene

(1) For a given alkaline earth metal atom, fv of MX decrease as halogen atom becomes more heavier (Cl-->Br-->I). This tendency is just opposite to the reactions of halogenated alkane.

(2) The vibrational excitation of the product BaI and the reactive cross section of Ba + p-$C_6H_4INH_2$ are bigger than those of the reaction Ba + C_6H_5I.

(3) The vibrational excitation of the product BaBr (BaCl) and reactive cross sections of the reactions Ba + m-$C_6H_4BrCH_3$ (m-$C_6H_4ClCH_3$) are smaller than those of the reaction Ba+C_6H_5Br(C_6H_5Cl).

(4) The vibrational excitation of the product BaCl and reactive cross sections of the reactions Ba + o-,m-,p-$C_6H_4Cl_2$ are almost the same.

(5) The vibrational excitation of the product BaCl of the reactions Ba(^1S) + o-,m-,p-$C_6H_4ClCH_3$ are almost the same, But for the reactive cross section, the reaction Ba + o-$C_6H_4ClCH_3$ is larger.

(6) In the reactions of Ba(^3D) + o-,m-,p-$C_6H_4Cl_2$ and reactions Ba(^3D) + o-,m-,p-$C_6H_4ClCH_3$, the relative chemiluminescent cross sections depend on the site of the Cl atom on the benzene ring. For o-$C_6H_4Cl_2$ and o-$C_6H_4ClCH_3$, the relative chemiluminescent cross sections are larger for BaCl(A,B-->X) emission but smaller for BaCl(C-->X) emission.

In the report, we will show up the data and give some explanations of the results.

Acknowledgement

The research works are supported by National Natural Science Foundation of China. Co-workers are Han Keli, Xu Dali, Mo Yuxiang and He Guoxin et al.

STERIC EFFECTS IN GAS-PHASE REACTIONS OF $Ca(^1D_2)$ + CH_3X(JKM) (X = F,Cl)

M.H.M. Janssen[a], D.H. Parker[b], A. van der Avoird[c] and S. Stolte[a]

(a) Laser Centre, Department of Chemistry, Vrije Universiteit, Amsterdam, The Netherlands
(b) Dep. of Molecule and Laserfysics, Catholic University Nijmegen, Nijmegen, The Netherlands
(c) Institute of Theoretical Chemistry, Catholic University Nijmegen, Nijmegen, The Netherlands

The steric effect and total yield of the electronically excited $CaF(A\ ^2\Pi)$ channel from the reaction $Ca(^1D_2)$ + CH_3F(JKM) → CaF + CH_3 has been investigated using a state selected and oriented CH_3F-molecule beam. The total chemiluminescent cross section of the CaF(A) → CaF(X) + hν product is found to decrease monotonically with collision energy. Meanwhile the steric effect turns out to increase with increasing translational energy. This surprising behaviour of the steric effect was postulated to reflect the occurrence of an orientational steering of the molecular axis by long-range forces between the reactants. Suggesting even stronger the importance of the presence of long range forces are the more puzzling observations for the reaction $Ca(^1D)$ + CH_3Cl(JKM) → $CaCl(B\ ^2\Sigma)$ + CH_3. The potential energy surfaces for the 'long-range' interaction between CH_3X and $Ca(^1D)$ have been calculated invoking the $Ca(^1D)$ (quadrupole) and CH_3X (dipole + quadrupole) moments. A comparison between the experimental data and the calculated results on the five different potential surfaces between $Ca(^1D)$ and CH_3X will be presented and their importance for the occurrence of orientational steering of electronic energy transfer will be discussed.

Effect of Molecular Orientation in Electron Ionization of Oriented Chlorometane in the (111) Eigenstate

Toshio Kasai, Tadanori Matsunami, Tohoru Fukawa, Hiroshi Ohoyama, and Keiji Kuwata

Department of Chemistry, Faculty of Science, Osaka University
Toyonaka, Osaka 560 Japan

Considerable attention has been directed recently to studies on stereodynamics of chemical reactions at the molecular level[1-2]. Kaesdorf and co-workers have observed stereo-asymmetric ejection of photoelectrons from oriented CH_3I molecules[3]. For collisional ionization, Harland and co-workers have detected K^+ ions in the oriented molecule reactions of CH_3I and CF_3I with fast K atoms[4]. The result revealed the favored collisional ionization at the I end of the molecule even though the electrical polarity of the I end is different for CH_3I and CF_3I. It is thus an open question whether or not the electron attacks at a particular site of the reagent molecule.

There has been no direct study conducted using oriented molecules for a category of reactions involving charged particle as "reagent", such as the electron. A basic experimental difficulty appears to be an unavoidable interference of the orienting field with the charged particles at the beam intersection. This study aims at elucidation about effect of molecular orientation in electron ionization.

Experimental

A pulsed beam with 3-ms duration of 1% CH_3Cl seeded in helium emerged from a supersonic pulse valve at a stagnation pressure of 850 Torr. The (111) eigenstate of the molecule was selected and focused by a 2-m electrostatic hexapole field. Then the focused beam passes through a guiding field of 50 cm in length which upholds the adiabiticity of the rotational eigenstate of the molecule if a field

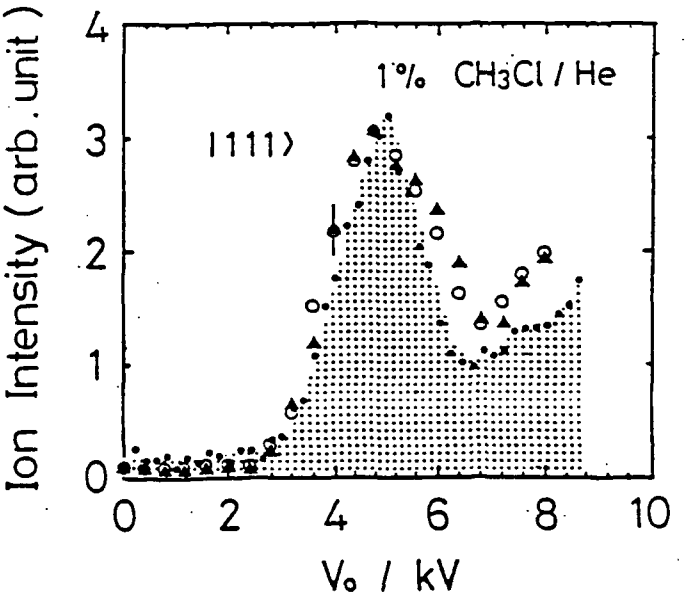

Figure 1. Dependence of beam intensity on V_0. Closed circles (shaded area) represents primary beam intensity obtained using the MS ionizer. Triangles and open circles are neutral products which are formed by impact of the electrons and which are field ionized in the MS. The MS ionizer is turned off for those points.

of - 400-70 Vcm^{-1} is applied. The molecules lose their quantization axis when the field is grounded (the random orientation). The molecules can be oriented parallel (the Cl end orientation) or antiparallel (the CH_3 end orientation) with respect to the incident electron beam.

A modified rotary quadrupole mass spectrometer(MS) was used to measure the CH_3Cl beam and to detect highly excited neutral species produced at the beam intersection. Ions are not detected because they are deflected out of the beam by the field in the collision zone. Figure 1 shows the dependence of the beam intensity on the hexapole voltage, V_0. Monte Carlo trajectory simulations[5] assigned the first peak at 5 kV as the (111) eigenstate of CH_3Cl. A typical focusing curve of the incident CH_3Cl beam directly measured is also shown with the filled circles and the dots. Nice agreement between these two curves demonstrated adequate crossing of the two beams in the orienting field.

Results and discussion

Figure 2 represents angular distributions of the product of the electron beam impact. The orienting field strength, E, was varied from 0 to 35 Vcm^{-1}. The polarity of the field is indicated as "CH_3 end" in the figure where the methyl end of the molecule points towards the incoming electrons and as "Cl end" where the Cl end points towards the incoming electrons. The peak heights decrease in both polaries but the shapes of the angular distributions do not change very much with E and they are almost the same distributions of the reagent CH_3Cl beam. This result indicates that the nascent product after impact is neutral and is ionized by subsequent small perturbations such as by collision or by electrostatic fields in the mass spectrometer. This fragile species is most likely to be the CH_3Cl molecule in highly excited Rydberg states.

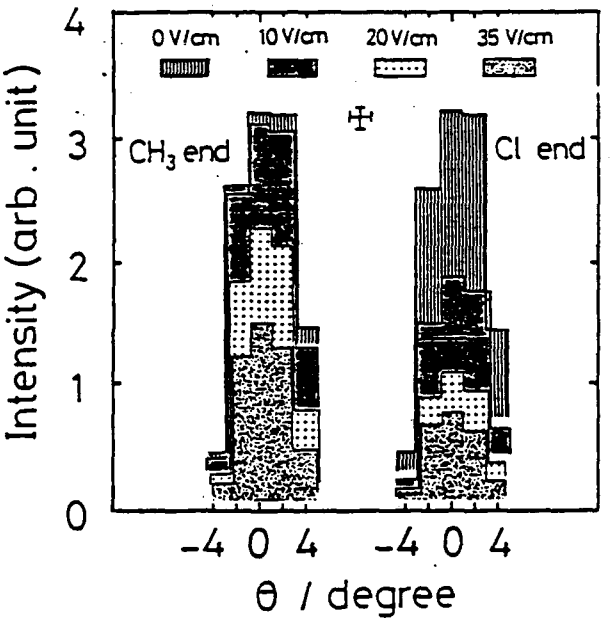

Figure 2. Angular distributions of the product from the beam intersection. Experimental inaccuracies for angular resolution and intensity of the product are indicated by the cross bars. The numbers given at the top of the figure are the strength of the orienting field.

As seen in figure 2, the total yield of the product decreases with E regardless of the field polarity. This tendency indicates unavoidable intervention from the orienting field. To extract real signals due to steric effects, one has to cancel this interference from the orienting field and for this reason the apparent intensity should be normalized at each E.

Figure 3 shows the E-dependence of those normalized yields. The open circles of I_+^0 denote the product signals for the Cl end orientation and the filled circles of I_-^0 for the CH_3 end orientation. I_+^0 and I_-^0 begin to show opposite behaviour after ~10 Vcm^{-1}. The plots appear to reach asymptotic values at higher E and the yield in the Cl end orientation gave a larger asymptotic value than that in the CH_3 end orientation. This behaviour on I_+^0 and I_-^0 should be interpreted by a mixed contribution from orientation and from alignment of the molecule. In photoionization alignment of the molecule plays a prime role[5]. Since it is not likely that inner electrons of molecule give much stereo-anisotropy, outer electrons of the molecule such as the $3a_1$ bonding orbital of CH_3Cl could be responsible for this orientation dependence[6].

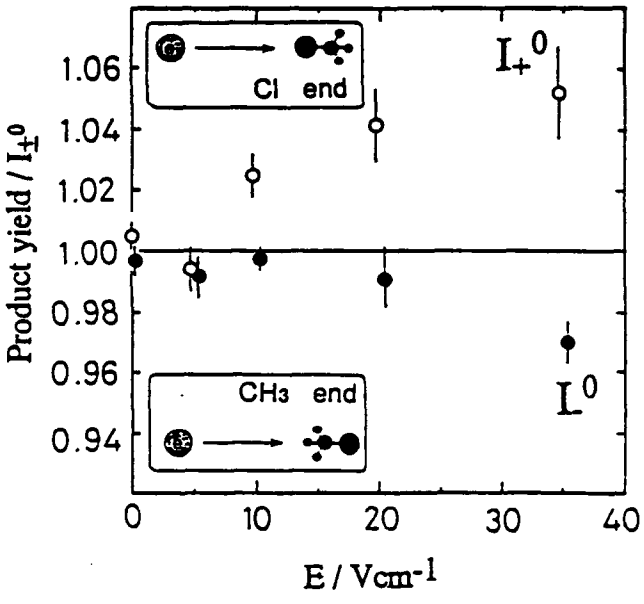

Figure 3. Dependence of I_+^0 and I_-^0 on the orienting field, E.

A brief analysis using Legendre expansion showed that contribution of alignment of molecule may not be negligible in this collisional ionization. The effect of molecular orientation in the present electron ionization provides further steps toward a deeper insight into reaction dynamics at molecular level understanding.

References

1) P. R. Brooks, Science, 193, 11 (1976); R. B. Bernstein, D. R. Herschbach, R. D. Levine, J. Phys. Chem.(Dynamical Stereochemistry Issue), **91**, 5365 (1987); D. H. Parker, R. B. Bernstein, Annu. Rev. Phys. Chem., **40**, 561 (1989); R. D. Levine, A. Zewail, M. A. El-Sayed, J. Phys. Chem. (Bernstein Memorial Issue on Molecular Dynamics), **95**, 7961 (1991).

2) K. Ohashi, T. Kasai, D-C Che, K. Kuwata, J. Phys. Chem., **93**, 5484 (1989); H. Ohoyama, T. Kasai, K. Ohashi, K. Kuwata, Chem. Phys. Lett., **136**, 236 (1987).

3) S. Kaesdorf, G. Schonhense, U. Heinzmann, Phys. Rev. Let., **54**, 885 (1985).

4) P. W. Harland, E. S. Carman, Jr., L. F. Phillips, P. R. Brooks, J. Chem. Phys., **90**, 5201 (1989).

5) " Electron Impact Ionization", Ed. by T. D. Mark, G. H. Dunn, Springer - Verlag (1985).

6) A. Minchinton, J. P. D. Cook, E. Weigold, Chem. Phys., **113**, 251 (1987).

The Optical Response of Small Niobium Clusters

M.B. Knickelbein and W.J.C. Menezes
Chemistry Division, Argonne National Laboratory
Argonne, Illinois 60439 USA

The measurement of size-specific optical absorption spectra of small, unsupported clusters of metal atoms (M_n) is a technically challenging task. Because these transient species are typically generated in molecular beams only at very low densities, direct absorption measurements are not possible. Furthermore, common methods of gas phase metal cluster generation (e.g. oven and laser vaporization sources) usually produce a broad size distribution, ranging from dimers to clusters containing hundreds or thousands of atoms. Most gas phase optical absorption studies to date have been performed on weakly bound systems such as neutral or ionic alkali metal clusters[1] and the cluster ions of copper[2] and aluminum,[3] in which photon absorption by M_n results in fragmentation to M_{n-1} + M. The extent of fragmentation is monitored mass spectrometrically as a function of wavelength, thus yielding the *photodissociation action spectrum* for M_n. Because this method relies on the photodissociation of the cluster under study, it can only provide a spectrum at wavelengths to the blue of its photodissociation threshold.

For transition metal clusters, dissociation threshold energies are considerably higher than those of alkali metal clusters. For small niobium clusters (Nb_n), the dissociation thresholds lie in the 5-6.5 eV range,[4] thus severely restricting the spectral range which may be investigated using the photodissociation technique described above. However, by forming rare gas van der Waals (vdW) complexes of the metal clusters, this energetic limitation may be circumvented. We have generated Nb_nAr_m species by supersonic expansion from a cooled (77 K) laser vaporization source. In a crossed laser-molecular beam configuration the photodissociation action spectra of argon atom loss following photoexcitation of these Nb_nAr_m vdW species have been recorded for n = 7-20: $Nb_nAr_m \xrightarrow{h\nu} Nb_n + mAr$. Because the threshold for this process is expected to be of the order of 50 meV per argon atom, action spectra can in principle be recorded at wavelengths extending far into the infrared with this technique.

A laser photoionization time-of-flight (TOF) mass spectrum of Nb_n and Nb_nAr_m (λ_{ion} = 193 nm) is shown in the top trace of Figure 1. The

bottom trace of Figure 1 shows a TOF spectrum in which a dye laser at 410 nm, copropagating with the ionization laser, irradiates the cluster beam 100 ns prior to the the ionzation pulse, under otherwise identical experimental conditions. A depletion of each of the argon complex mass peaks and an increase in "bare" cluster intensity are observed when the dye laser is on, indicating that the Nb_nAr_m species in this size range possess nonzero absorption cross sections at 410 nm. Absolute absorption cross sections are readily calculated once the fractional depletion and laser fluence are known. Using this method, we have measured the absorption cross sections of Nb_nAr_m (n = 7-20) at 2 nm intervals from 394 to 594 nm. The action spectrum for Nb_7Ar is shown in Figure 2. Our results thus far indicate that all clusters in this size range display broad, featureless action spectra spanning the visible region similar to that shown for Nb_7Ar, with absorption cross sections which increase with photon energy and exceed 10^{-16} cm^2 at the shortest dye laser wavelengths employed. In contrast to the measured optical response of small clusters of nearly-free electron metals (e.g. Na_n, K_n, Ag_n etc.), no surface plasmon resonances are observed in the visible region for niobium clusters in this size range. Our results for these small niobium clusters are in qualitative accord with the monotonically increasing absorption cross sections predicted to occur with decreasing wavelength for small niobium spheres by classical electrodynamic theory using the optical constants of bulk niobium. We are currently extending these cross section measurments further into the ultraviolet.

This work is supported by the U.S. Department of Energy, Office of Basic Energy Sciences, Division of Chemical Sciences, under contract W-31-109-ENG-38.

References

1. W.A. de Heer *et al.* Phys. Rev. Letters 59, 1805 (1987); C. Bréchignac *et al.* Chem. Phys. Letters 164, 433 (1989); C.R.C Wang, S. Pollack and M.M. Kappes, Chem. Phys. Letters 166, 26 (1990).

2. M.F. Jarrold, U. Ray, J.E. Bower and K.M. Creegan, J. Chem. Soc. Faraday Trans. 86, 2537 (1990).

3. U. Ray, M.J. Jarrold, J.E. Bower and J.S. Kraus, Chem. Phys. Letters 159, 221 (1989).

4. D.A. Hales, L. Lian and P.B. Armentrout, Int. J. Mass Spec. Ion Proc 102, 269 (1990).

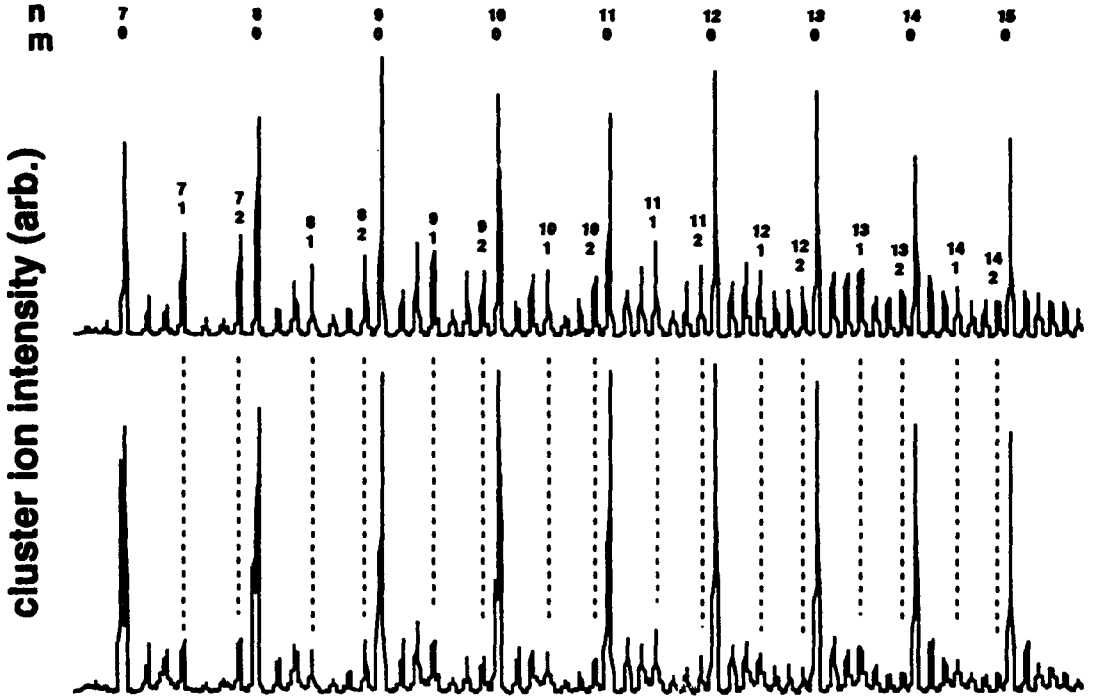

Figure 1. TOF mass spectra of Nb_nAr_m from n = 7 to 15. Top trace: ArF ionization laser only. Bottom trace: dye laser (410 nm) fired 100 nsec prior to ionization laser. Peaks for m = 0,1, and 2 are labeled.

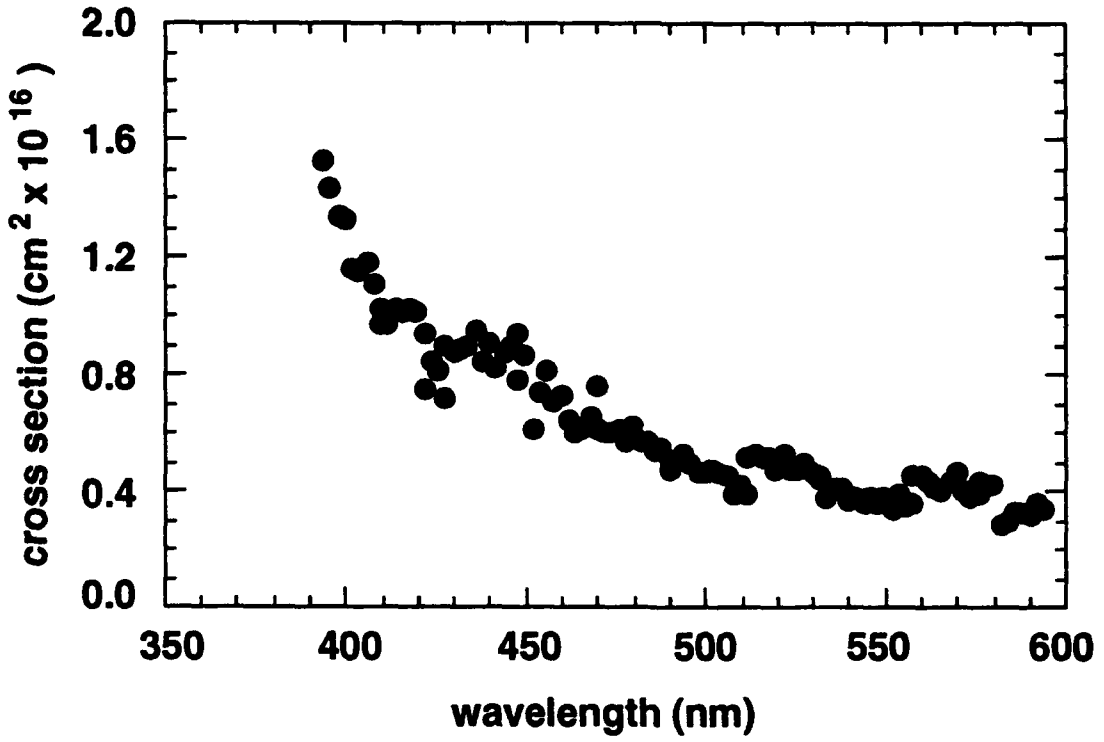

Figure 2. Photodissociation action spectrum of Nb_7Ar from 394 nm to 594 nm.

Inelastic and Relaxation Processes in Ion–Molecule Collisions at Very Low Temperatures.

D.R. Latimer*, M. Hawley, N. Melosh and M.A. Smith
Department of Chemistry, University of Arizona, Tucson, AZ 85721

Ion–neutral chemistry is recognized to play an important role in molecular synthesis in interstellar clouds [1] where the temperatures are of the order of 10—50 K. There are several theoretical models describing ion–neutral interactions which predict similar behaviour at ambient and elevated temperatures yet differ significantly from each other at low temperatures. Using a pulsed supersonic expansion it is possible to study ion–molecule reactions in the gas phase at translational temperatures in the range of 0.5—30 K. The ability to study the interactions between ions and molecules at very low translational temperatures provides a sensitive tool to test ion–molecule interaction theories and to provide fundamental information in the very low collision energy regime.

Although there exist several techiniques to study ion–neutral reactions at ambient and elevated temperatures only four other groups have been able to study ion–molecule reactions at temperatures below 80K: Böhringer and Arnold developed a selected ion drift tube which operates in the 20—420 K temperature range [2]; Dunn *et al.* [3] and Gerlich and Kaefer [4] have cryogenically cooled RF traps enabling them to study reactions in the 10—100 K temperature regime, in addition, Gerlich *et al.* have recently developed a merged beam technique with collision energies adown to 1 meV [5]; and Rowe *et al.* have developed the CRESU technique to allow study of reactions at discrete temperatures in the range 8—163 K [6]. Reactant condensation at the lower temperature extremes introduces experimental difficulties in the drift tube and RF trap techniques making the study of gases other than He or H_2 difficult. The CRESU technique uses computer optimized convergent-divergent Laval nozzles to produce gas flows of uniform temperature and density but requires large volumes of reactant and buffer gases and has not allowed continuous variation of temperature.

In our free jet flow reactor it is possible to produce translationally cold reaction mixtures, which under appropriate conditions will not suffer from condensation (clustering), in a technique which consumes only small amounts of reactant and buffer gases [7]. The ion–neutral reaction is initiated by expanding a premixed sample of buffer, ion precursor and reactant neutral through a pulsed molecular beam valve and once the expansion has reached terminal velocity and internal state distribution the ion precursor is state selectively ionized by an appropriate resonantly enhanced multiphoton ionization scheme. The ion–neutral packet is allowed to evolve under field free conditions for a predetermined reaction time upon when all positively charged ionic species are extracted and analyzed by time of flight mass spectrometry. In contrast to the CRESU technique, all degrees of freedom are not thermally equilibrated in the free jet, which may be important in rotationally or vibrationally driven processes, however, the core of the free jet expansion is understood sufficiently well (particularily the translational degrees of freedom) to enable

kinetic analysis [8, 9].

The hydrogen abstraction reaction $C_2H_2^+ + H_2 \longrightarrow C_2H_3^+ + H$ has long been considered to be 2 kcal mol^{-1} endothermic, and a positive temperature dependence for temperatures above 80 K is consistent with a thermally driven endothermic process. In the low temperature limit below 3 K the rate coefficient is greater than the room temperature rate coefficient by an order of magnitude and the rate coefficient shows a strong negative temperature dependence ($k(T) = 5.6 \times 10^{-11}$ T^{-2} cm^3 s^{-1}). The reaction cannot be endothermic and the negative temperature dependence suggests that a long lived complex is formed prior to the hydrogen abstraction. At very low collision energies the collision intermediate lifetime is expected to be long for a statistical intermediate due to the high density of states above the >2 eV deep attractive potential well.

The rate coefficient for the hydrogen abstraction reaction is well below the collision limit suggesting the presence of a barrier to the exit channel. If the barrier is a potential energy barrier it cannot be high (high temperature data suggests ~0.1 eV). The negative temperature dependence as well as isotope scrambling rate coefficients in isotopically labelled reactants are consistent with a mechanism where the $C_2H_2^+ + H_2$ collision complex tunnels through the barrier to products. However, the bimolecular rate coefficient does not appear to be affected by incoming rotational energy of H_2 indicating the intermediate is not behaving as an ethenyl ($C_2H_4^+$) statistical complex. These observation may be reconciled by proposing two competitive channels; one intermediate statistical in nature expected to dominate the isotopic scrambling and three body association processes and a second more loosely bound, $C_2H_2^+ \cdot H_2$, *complex which maintains* local H_2 angular momentum and is responsible for bimolecular atom transfer [10, 11].

More recently we have turned our attention to vibrational and electronic relaxation processes in atomic and molecular ions in order to further study the effects of complex formation on inelastic collisions. The vibrational relaxation of NO^+(v=1) by He, Ar, and N_2 have been measured using a monitor technique whereby a neutral that will charge transfer only with the NO^+(v=1) state is added to the expansion mixture and competes with the vibrational relaxation of NO^+ by He, Ar or N_2 [12]. Argon and N_2 are found to quench NO^+(v=1) with unit efficiency below 5 K. Surprisingly, vibrational quenching by He has a negative temperature dependence and is extremely efficient below 2 K, again indicating the importance of long lived collision complexes. Currently we are using the monitor technique to determine the distribution of spin–orbit states of the atomic rare gas ions Kr^+ and Xe^+ produced by resonantly enhanced multiphoton ionization. Results for this as well as the electronic relaxation of the $^2P_{\frac{1}{2}}$ spin orbit state by atomic and molecular collision partners will be presented.

References

1. G. Winnewisser and E. Herbst, *Top. Curr. Chem.*, **139**, 119 (1987).
2. H. Böhringer and F. Arnold, *Int. J. Mass. Spec. Ion. Proc.*, **49**, 61 (1983).

3. S.E. Barlow, J.A. Luine and G.H. Dunn, *Int. J. Mass. Spec. Ion. Proc.*, **74**, 97 (1986).

4. D. Gerlich and G. Kaefer, *Astrophys. J.*, **347**, 849 (1989).

5. D. Gerlich, H.J. Jitschen and O. Wick, *Abstract, Symposium on Atomic and Surface Physics*, Trentino, Italy, 1992.

6. B.R. Rowe and J.B. Marquette, *Int. J. Mass. Spec. Ion. Proc.*, **80**, 239 (1987).

7. M. Hawley, T.L. Mazely, L.K. Randenyia, R.S. Smith, X.K. Zeng and M.A. Smith, *Int. J. Mass. Spec. Ion. Proc.*, **97**, 55 (1990).

8. T.L. Mazely and M.A. Smith, *J. Chem. Phys.*, **89**, 2048 (1988).

9. L.K. Randeniya and M.A. Smith, *J. Chem. Phys.*, **93**, 661 (1990).

10. M. Hawley and M.A. Smith, *J. Chem. Phys.*, **96**, 1121 (1992).

11. E Herbst, private communication.

12. M. Hawley and M.A. Smith, *J. Chem. Phys.*, **95**, 6662 (1991).

XIVth International Symposium on Molecular Beams, Asilomar Conference Grounds, Pacific Grove, California, June 7-12, 1992

Geometric mechanics and molecular reaction dynamics

F. J. Lin and J. E. Marsden
Department of Mathematics
University of California
Berkeley, CA 94720 USA

The purpose of this paper is to introduce molecular reaction dynamicists to some potentially useful ideas in geometric mechanics. Geometric mechanics is a coordinate-free approach to classical dynamics. Applied to classical molecular dynamics, geometric mechanics describes not only the dynamics of rotating, vibrating molecules but also the dynamics of molecular collisions with their respective phase spaces distinguished by their distinct topological types. Further, the geometric approach can be applied to describe the corresponding quantum molecular dynamics and to computationally examine the respective classical and quantum molecular dynamics.

1. Geometric mechanics. Classical mechanics is based on Newton's laws, the conservation theorems (of linear momentum, angular momentum, and energy) for a single particle and for a system of particles, Lagrange's equations, and Hamilton's equations. These can be expressed in Cartesian or, more generally, curvilinear coordinates. Further, geometric mechanics gives a more general, coordinate-free formulation of Hamilton's equations in terms of symplectic manifolds describing the phase space and Hamiltonian vector fields describing the time evolution corresponding to Hamilton's equations.

2. Classical molecular dynamics. a. Application to atomic clusters. With an application to rare-gas clusters, Jellinek and Li (1989) have shown that the total kinetic energy of any nonrigid N-body system can be expressed as the sum of uncoupled terms. For a nonrigid system, let $\mathbf{L}$ be the angular momentum, $\mathbf{I}(t)$ be the instantaneous moment of inertia, m_i and $\mathbf{r}_i$ be the mass and coordinate of the i-th particle, respectively, and $V(\mathbf{r}_1,...,\mathbf{r}_N)$ be the potential energy. One defines the instantaneous angular velocity $\omega_{\mathbf{L}}^{\text{"rb"}}(t)$

$$\mathbf{L} = \mathbf{I}(t)\cdot\omega_{\mathbf{L}}^{\text{"rb"}}(t) \quad , \tag{2.1}$$

the rigid body momentum $\mathbf{p}_i^{\text{"rb"}}$

$$\mathbf{p}_i^{\text{"rb"}} = m_i(\omega_{\mathbf{L}}^{\text{"rb"}} \times \mathbf{r}_i) \quad , \quad i = 1,...,N \quad , \tag{2.2}$$

and the difference $\Delta\mathbf{p}_i$ between it and the momentum $\mathbf{p}_i$

$$\Delta\mathbf{p}_i = \mathbf{p}_i - \mathbf{p}_i^{\text{"rb"}} \quad , \quad i = 1,...,N \quad . \tag{2.3}$$

Then the total kinetic plus potential energy of the nonrigid system is

$$\sum_{i=1}^{N} \frac{\mathbf{p}_i^2}{2m_i} + V(\mathbf{r}_1,...,\mathbf{r}_N) = \sum_{i=1}^{N} \frac{(\Delta \mathbf{p}_i)^2}{2m_i} + \sum_{i=1}^{N} \frac{(\mathbf{p}_i^{\text{"rb"}})^2}{2m_i} + V(\mathbf{r}_1,...,\mathbf{r}_N) \quad . \tag{2.4}$$

2.b. Reduction of Hamiltonian phase spaces with symmetry. (Simo, Lewis, and Marsden, 1991; Lin and Marsden, 1992) The separation of energies can be expressed geometrically as a reduced Hamiltonian on a reduced phase space. Let $\mu = \mathbf{J}(z_e)$ be the value of a generalization of the momentum, the momentum map $\mathbf{J}$, at a relative equilibrium z_e of the (original) phase space. Let $p_{\mathbf{J}}$ be the relevant conserved momentum associated with the momentum map $\mathbf{J}$

$$p_{\mathbf{J}}(z) = \mathbf{FL}[\xi(z)_Q(q)] \quad , \tag{2.5}$$

where ξ is the relevant velocity, $\xi(z)_Q$ is the infinitesimal generator of the action on the configuration space Q, and $\mathbf{FL}$ is the Legendre transformation. Let p_μ be the shifted momentum

$$p_\mu = p - p_{\mathbf{J}} \quad . \tag{2.6}$$

Let g be the relevant fundamental metric tensor, $\mathcal{I}$ be the relevant instantaneous mass factor, V_μ be the amended potential

$$V_\mu(q_\mu) = V(q_\mu) + \frac{1}{2}\mu\mathcal{I}^{-1}(q_\mu)\mu \quad , \tag{2.7}$$

and G_μ be a symmetry group of the Hamiltonian corresponding to μ. Then the reduced Hamiltonian H_μ on the reduced phase space $z_\mu = (q_\mu, p_\mu) \in P_\mu = \mathbf{J}^{-1}(\mu)/G_\mu$ separates into the following terms

$$H_\mu(z_\mu) = \frac{1}{2}\|p_\mu\|^2_{g^{-1}} + V_\mu(q_\mu) \quad . \tag{2.8}$$

The dynamics on the original and reduced phase spaces (P,ω) and (P_μ,ω_μ), respectively, are both determined by Hamilton's equations, which can be expressed

$$i_{X_H}\omega = dH \tag{2.9}$$

and

$$i_{X_{H_\mu}}\omega_\mu = dH_\mu \quad , \tag{2.10}$$

respectively, in terms of the respective Hamiltonian vector fields X_H and X_{H_μ} and the respective symplectic forms ω and ω_μ (not to be confused with the angular velocity). Here i denotes the interior product, and μ is the value of a conserved quantity generalizing the momentum and corresponds to a symmetry of the Hamiltonian. Such a reduction determines the internal phase space for the dynamics. The linearized dynamics near a relative equilibrium are expressible in a normal form.

2.c. Topology of phase spaces. The reduced phase space is furthermore foliated by leaves. For the case of the molecular two-body problem, a leaf is of one of the following topological types (Lin and Marsden, 1992):

(i) the empty set, corresponding physically to a classically forbidden trajectory;

(ii) a single point, corresponding to a bound trajectory describing a rigid, possibly rotating molecule;

(iii) a circle, corresponding to a bound trajectory describing a rotating and vibrating molecule;

(iv) the disjoint union of a circle and a point, corresponding to a bound trajectory describing a rotating and vibrating molecule or to an unbound system with particles at large separation;

(v) the disjoint union of a circle and a line, corresponding to a bound trajectory describing a rotating and vibrating molecule or to a scattering trajectory that is grazing;

(vi) the union of a circle and a tangent line, corresponding to a scattering trajectory that is possibly eventually orbiting; and

(vii) a line, corresponding to a scattering trajectory that is rebounding.

This places both the bound and scattering molecular trajectories in a single geometrical framework. The previously derived geometrical results can now also be applied to unbound molecular trajectories, including molecular scattering.

2.d. Application to molecular beam scattering. (Lin and Marsden, 1992) *i. Molecular reaction dynamics.* For the molecular three-body problem, the scattering trajectories can be either *reactive*, i.e., $A + BC \rightarrow AB + C$ or $A + BC \rightarrow AC + B$, or *nonreactive*, i.e., $A + BC \rightarrow A + BC$. Within each of these categories, the scattering trajectory can correspond to a collision that is either *direct* or *complex* (also called *compound*). The Hamiltonian reduction described above applies naturally to the complex trajectories.

2.d.ii. Lagrangian reduction. In addition to Hamiltonian reduction, there is another type of reduction relevant to molecular dynamics. The Newton diagram describes the required transformation of the velocity phase space from the laboratory frame (assumed for simplicity to be inertial) to the center of mass frame. This transformation motivates the definition of a Lagrangian reduction **LR** in terms of the Hamiltonian reduction **HR** (just mentioned in 2.*b*), e.g.,

$$\begin{array}{ccc} q_1, \ldots, q_{3N}, v_1, \ldots, v_{3N} & \xrightarrow{\mathbf{LR}} & q_1, \ldots, q_{3(N-1)}, v_1, \ldots, v_{3(N-1)} \\ \Big\downarrow \mathbf{FL} & & \Big\downarrow \mathbf{FL} \\ ((q_1, \ldots, q_{3N}, p_1, \ldots, p_{3N}), \omega) & \xrightarrow{\mathbf{HR}} & ((q_1, \ldots, q_{3(N-1)}, p_1, \ldots, p_{3(N-1)}), \omega_\mu) \end{array} \quad . \tag{2.11}$$

3. Quantum molecular dynamics. a. Geometric approach. (Lin, 1991a; Lin and Marsden, 1991) The Schrödinger equation

$$i\hbar \frac{\partial \psi}{\partial t} = H\psi \tag{3.1}$$

is a Hamiltonian dynamical system. Its solution is an integral curve of a Hamiltonian vector field on a phase space. The dynamics of the wave function on the original and reduced phase spaces (P_ψ, ω_ψ) and $((P_\psi)_{\mu'}, (\omega_\psi)_{\mu'})$ are related by a gauge symmetry and a conserved quantity μ'

$$(\psi, \omega_\psi) \xrightarrow{\mathbf{HR}} ((\Re\psi_{\mu'}, \Im\psi_{\mu'}), (\omega_\psi)_{\mu'}) \quad , \tag{3.2}$$

where ψ is a wave function in the Hilbert space of solutions of the Schrödinger equation.

Moreover, the relationship between reduction and geometric quantization of the classical phase space determine the reduced configuration space for the wave function, e.g.,

$$\begin{array}{ccc} ((q_1,...,q_{3N},p_1,...,p_{3N}),\omega) & \xrightarrow{\mathbf{HR}} & ((q_1,...,q_{3(N-1)},p_1,...,p_{3(N-1)}),\omega_\mu) \\ \Big\downarrow quantize & & \Big\downarrow quantize \\ (\psi(q_1,...,q_{3N}),\omega_\psi) & \xrightarrow{reduce} & (\psi(q_1,...,q_{3(N-1)}),\omega_{\mu\psi}) \quad . \end{array} \tag{3.3}$$

These phase spaces can then each be further reduced as described in Eq. (3.2),

$$\begin{array}{ccc} (\psi(q_1,...,q_{3N}),\omega_\psi) & \xrightarrow{reduce} & (\psi(q_1,...,q_{3(N-1)}),\omega_{\mu\psi}) \\ \Big\downarrow \mathbf{HR} & & \Big\downarrow \mathbf{HR} \\ ((\Re(\psi_N)_{\mu'},\Im(\psi_N)_{\mu'}),(\omega_\psi)_{\mu'}) & \xrightarrow{reduce} & ((\Re(\psi_{N-1})_{\mu'},\Im(\psi_{N-1})_{\mu'}),(\omega_{\mu\psi})_{\mu'}) \quad , \end{array} \tag{3.4}$$

where $\psi_N = \psi(q_1,...,q_{3N})$ and $\psi_{N-1} = \psi(q_1,...,q_{3(N-1)})$. These diagrams outline the steps in the derivation of a reduced phase space of the wave function on a (reduced) configuration space.

3.b. Computational approach. (Lin, 1991a) A symplectic integrator is a difference scheme that preserves the form of Hamilton's equations at each time step. The use of such an integrator allows the determination of numerical results for classical and quantum molecular dynamics. Further, it is more advantageous to first derive the reduced phase space, if possible, before implementing a symplectic integrator.

4. Concluding remarks. These geometric techniques are relevant to both the classical and quantum mechanical molecular dynamics. They are applicable not only to rotating and vibrating molecules, but also to other examples such as elastic, inelastic, and reactive molecular scattering, and laser-induced molecular excitation and dissociation.

References

J. Jellinek and D. H. Li, *Phys. Rev. Lett.* **62**, 241 (1989).

F. J. Lin, Geometric approach to computational quantal molecular dynamics, *Bull. Am. Phys. Soc.* **36**, 1796 (1991a).

F. J. Lin, Geometric mechanics and molecular dynamics, Differential Geometry Seminar, Department of Mathematics, University of California, Berkeley, November 1, 1991b.

F. J. Lin and J. E. Marsden, Geometric approach to the quantal cumulative reaction probability for $O + H_2 \rightarrow OH + H$, Conference on the Dynamics of Molecular Collisions, Lake George, NY, July 7-12, 1991.

F. J. Lin and J. E. Marsden, Symplectic reduction and topology for applications in classical molecular dynamics, *J. Math. Phys.* **33**, to appear (1992).

J. E. Marsden, *Lectures on Mechanics*, London Mathematical Society Lecture Note Series, (Cambridge University Press, New York, to be published (1992)).

J. C. Simo, D. Lewis, and J. E. Marsden, *Arch. Rational Mech. Anal.* **115**, 15 (1991).

N. Woodhouse, *Geometric Quantization*, (Clarendon Press, Oxford, 1980).

The Solvation of Iodine Anions In Water Clusters:PES Studies

Gil Markovich, Stuart Pollack, Rina Giniger, and Ori Cheshnovsky
School of Chemistry, Tel-Aviv University, 69978 Tel-Aviv University, Israel

The microscopic details of ion-cluster interaction are of great importance for the understanding of solvation phenomena. Alkali metal cations and halogen anions solvated in clusters have served as model systems for both experimental[1] and theoretical[2] studies of this problem.

High pressure mass spectrometry and flow-tubes, (the traditional techniques) are limited tc the study of small clusters (n<8). These studies probe thermodynamic properties, resulting in the inseparable energetics of ion-solvent and solvent-solvent interactions. *PhotoElectron-Spectroscopy* (PES) studies of anions solvated in clusters enable the investigation of ion-solvation in clusters containing up to hundreds of ligands. These studies specifically probe the electrostatic anion-solvent interactions.

Recently we have reported about PES solvation studies of iodine anion in up to 15 water molecules[3]. In this report we present the extension of these studies to 30 water molecules.

The anion-clusters are produced by a pulsed electron-beam in the early stages of a pulsed supersonic expansion. The newly formed charged clusters are cooled by further flow in the expansion, and mass separated by a reflecting time-of-flight mass-spectrometer. The mass-selected ions are impulse decelerated to ~20 eV kinetic energy, to reduce Doppler-broadening.

The highest photon energy of the photodetachment-laser is 7.1 eV (the H_2 7th AS of the 3rd harmonic of a Nd:Yag laser). The kinetic energy of the electrons is analyzed with a magnetic TOF photoelectron spectrometer[4]. The resolution is ~50 meV at 1.5 eV electron energy. The spectrometer is calibrated with PES of the halogen anions (Cl^-, Br^-, I^-).

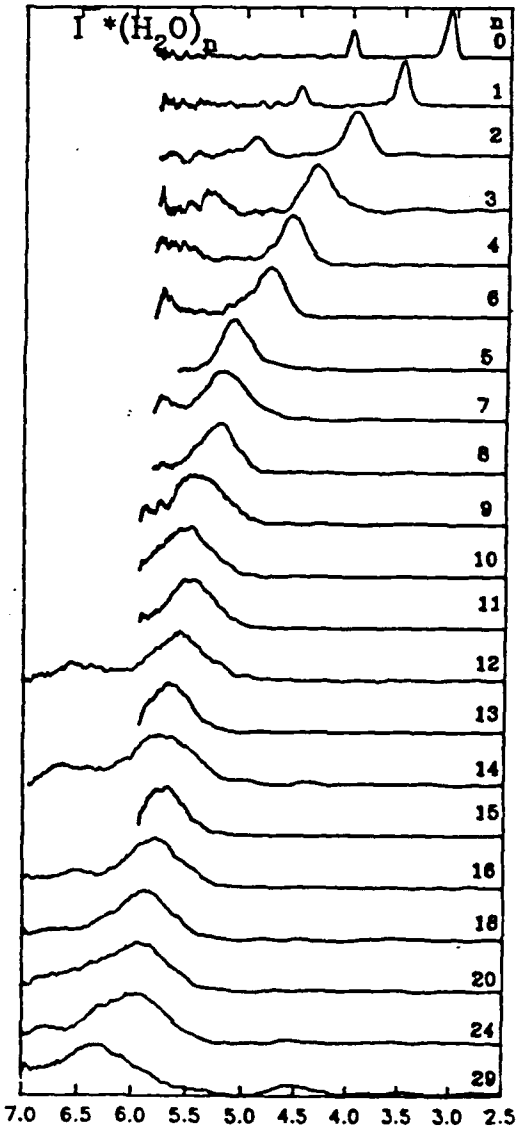

Fig 1

Fig. 1 displays representative photoelectron spectra of iodine anion bound to *n* water molecules where *n* = 1-30. Note, that the typical spin-orbit peaks of the bare iodine anion are shifted to higher binding energies with the cluster size. We assign the lowest binding-energy peak of each spectrum to the vertical photodetachment energy. The difference between this vertical photodetachment energy and the electron affinity of the bare ion, E_{stab}, is essentially the electrostatic stabilization of the solvated ion in its equilibrium configuration. This is true, since the interaction between the bare atom (with its smaller diameter) and the solvent cluster is small. Solvent-solvent interactions are identical in the initial and final states in the photodetachment process, and do not influence E_{stab}.

Fig. 2 presents E_{stab} as a function of cluster size. The increase in E_{stab} with *n* becomes moderate in clusters containing more then six water molecules. This is a strong indication that six water molecules form the first solvation layer around the iodine anion. The addition of subsequent solvent molecules into the second solvation layer results in a smaller interaction with the ion. This observation is inconsistent with finite temperature simulations of Lin and Jordan, which predict three water molecules in the first solvation layer around I^-.

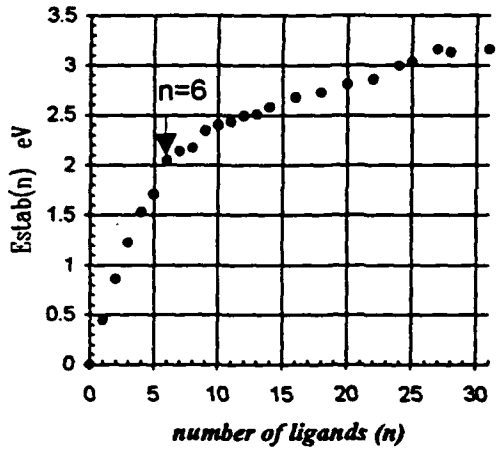

Fig. 2

The detailed analysis of E_{stab} as a function of the cluster size yields higher values then expected from theoretical models. One possible explanation could be that the outcoming photoelectron loses energy by inelastic scattering off the solvent water molecules. We are now in the process of including these effects in the analysis of the PES data.

References:

[1] P. Kebarle, *Ann. Rev. Phys.* **28**, 445 (1977); T. D. Mark and A. W. Castleman, *Advances in Atomic and Molecular Physics* **20**, 65 (1985); A. W. Castleman, and R. G. Keese, *Acc. Chem. Res.* **19**, 413 (1986); A. W. Castleman, and R. G. Keese, *Chem. Rev.* **86**,589 (1986).

[2] S. S. Sung, and P. C. Jordan, *J. Chem. Phys.* **85**, 4045 (1986); S. Lin, and P. C. Jordan, *J. Chem. Phys.* **89**, 7492 (1988) and references mentioned there;. L. Perera, and M. L. Berkowitz, *J. Chem. Phys.* **95**, 5793 (1991).

[3] G.Markovich, R. Giniger, M. Levin, and O. Cheshnovsky, *Z. Phys. D.* **20**, 69 (1991);G. Markovich, R. Giniger, M. Levin, and O. Cheshnovsky, *J. Chem. Phys.* **95**, 9416 (1991).

[4] O. Cheshnovsky, S. H. Yang, C. L. Pettiette, M. J. Craycraft, and R. E. Smalley, *Rev. Sci. Instru.* **58**, 2131 (1987); P.Kruit, and F. H. Read, *J. Phys. E. (Sci.Instrum.)* **16**, 313 (1983).

Effect of Incident Vibrational and Translational Energies on the Reaction of $NO^+(v)$ with GaAs(110)

J. Scott Martin, J. Neil Greeley and ***Dennis C. Jacobs***
Department of Chemistry and Biochemistry
University of Notre Dame
Notre Dame, IN 46556

The interaction of molecular ions with semiconductors surfaces has significant practical importance to device fabrication in the microelectronics industry. The dynamics governing these processes, however, remain largely unknown. The experiments reported here exploit a tunable laser to prepare incident molecular ions in a particular vibrational level of the ground electronic state. By having the ability to independently select the exact amount of internal and translational energy, we can uniquely determine the role that each of these variables plays on the dynamics, i.e. the relative branching into different product channels and the disposal of energy into translational degrees of freedom.

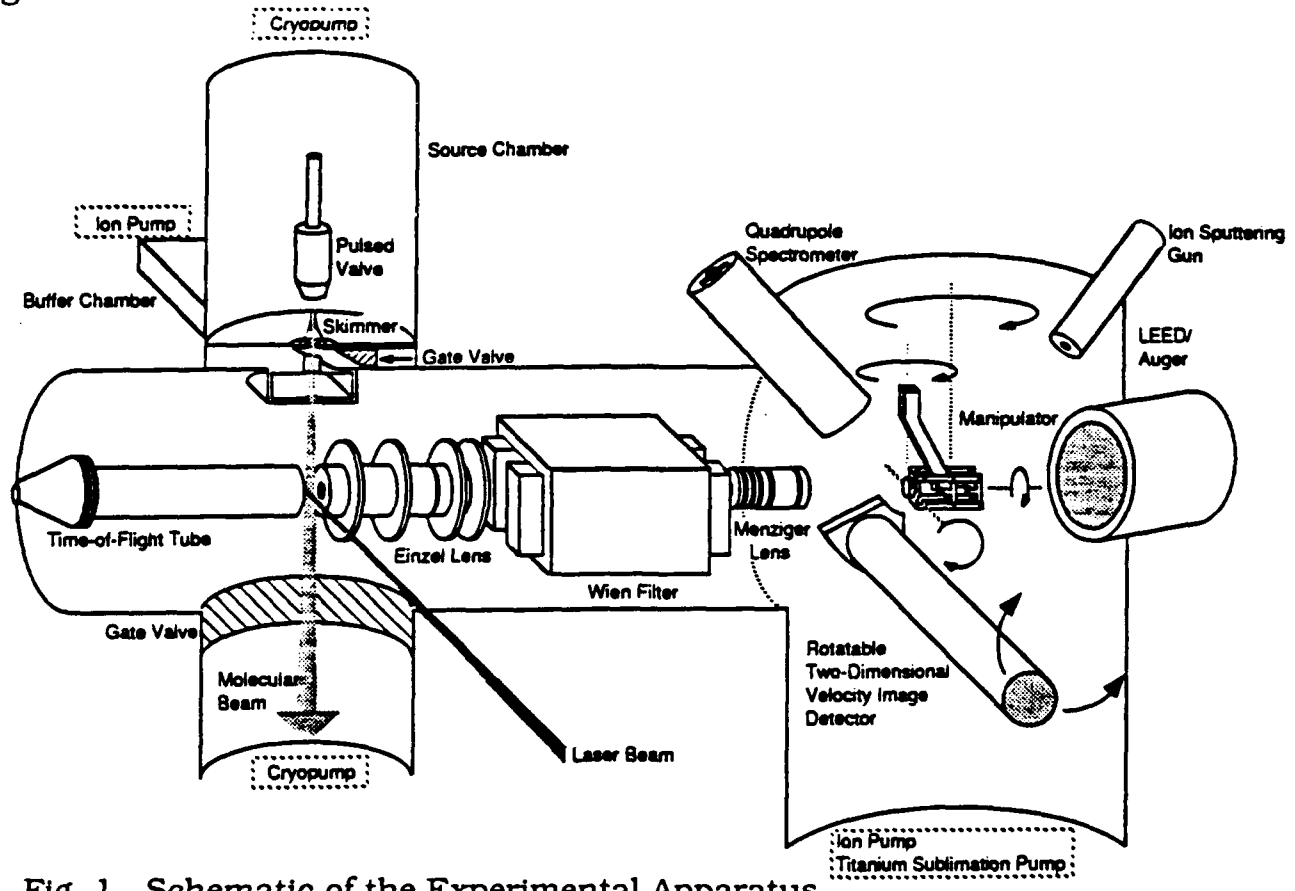

Fig. 1. Schematic of the Experimental Apparatus.

Figure 1 shows the ultrahigh vacuum scattering chamber for studying the interaction of hyperthermal molecular ions with single-crystal metal and semiconductor surfaces. The state-selected, pulsed ion beam is initiated at

the intersection of a supersonic molecular beam of NO and a tunable ultraviolet pulsed laser. Here, resonance enhanced multiphoton ionization (REMPI) through the $C^2\Pi$ or $E^2\Sigma^+$ states prepares NO^+ ions in a select vibrational level (v=0-6) of the $X^1\Sigma^+$ state.[1] These ions are extracted, accelerated, and focused onto a clean well-characterized GaAs(110) surface. The mass- and angle-resolved time-of-flight distributions for scattered ionic products are measured with a two-dimensional velocity image detector (See Fig. 2).[2]

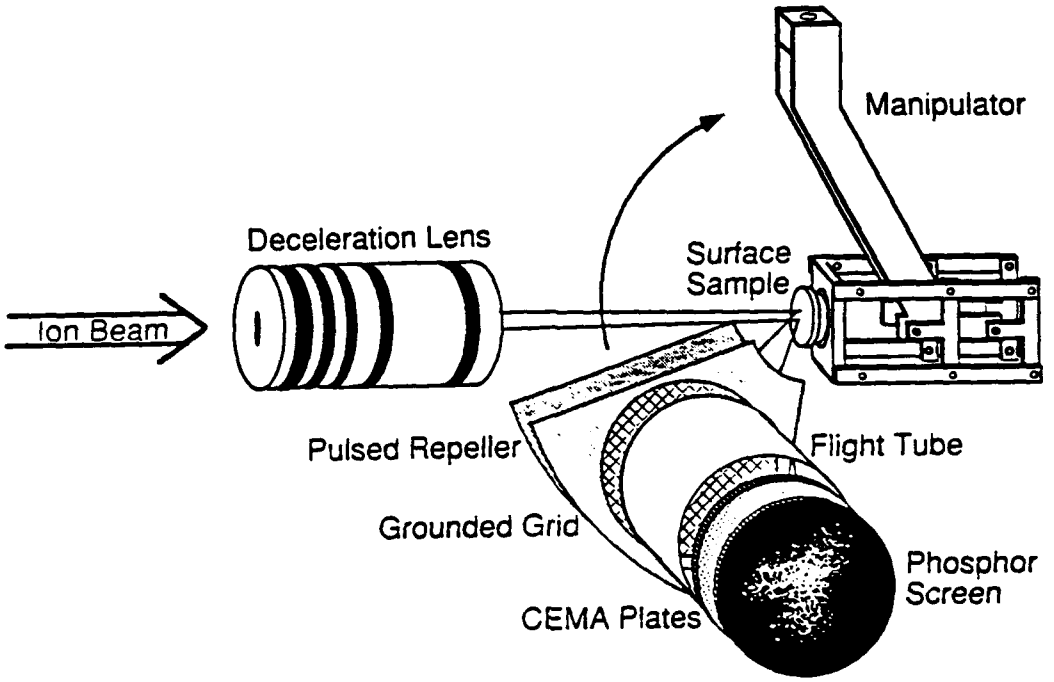

Fig. 2. A schematic of the two-dimensional velocity image detector. The ion beam exits the Menzinger deceleration lens and is directed toward the surface sample manipulator. The detector can be rotated around the surface center ±45° relative to the ion beam axis.

We have investigated reactive collisions of hyperthermal (2-80 eV of translational energy) state-selected NO^+(v=0-6) ions with GaAs(110). The survival probability for NO^+ scattering from this surface is quite low ($<10^{-6}$). The scattered products are predominantly neutral; however we have also observed NO^- and O^- formed at higher incident translational energies. The yield of O^- ions, as a function of incident translational energy, shows distinct threshold behavior. It is believed that the mechanism may involve two distinct charge transfer steps as well as collision induced dissociation of the molecule.[3] We are currently measuring the effect that vibration in the incident NO^+ molecule has on the various scattering channels.

---

[1] T. Ebata and R. N. Zare, *Chem. Phys. Lett.* **130**, 467 (1986).

[2] D. Corr and D. C. Jacobs, *Rev. Sci. Instrum.*, will appear in March 1992.

[3] P. H.F. Reijnen, AP. J. Van Den Hoek, A. W. Kleyn, U. Imke and K. J. Snowdon, Surf. Sci. **221**, 427 (1989).

These experiments represent the first time that one has probed isolated collisions between hyperthermal state-selected molecular ions and a well-characterized surface. The conclusions of this work will reveal general principles about ion-surface interactions, provide information on various features of the relevant potential energy surfaces (eg., state-specific barrier heights, effect of topology on surface reactivity, etc.), and help identify the more reactive species that might contribute to plasma etching at semiconductor surfaces.

Stability of very small doubly charged clusters: experiment and theory

S. Martrenchard-Barra, C. Lardeux-Dedonder, C. Jouvet, D. Solgadi
Lab. Photophysique Moléculaire du CNRS, Bat. 213, Université de Paris-Sud 91405 Orsay (France)

V. Brenner, P. Millié
CEA-CE Saclay, DSM/DRECAM/SPAM, 91191 Gif sur Yvette (France)

The stability of doubly charged clusters [1] except for those where a real chemical bond is expected [2] are usually well interpreted by the liquid drop model proposed by Echt and coworkers [3]. In this model, the binding energy of a cluster is calculated as the sum of cohesive energy (modelized by Lennard-Jones potentials) and coulomb repulsion of the two charges. A doubly charged cluster can be observed when it reaches a critical size for which the cohesive forces overcome the coulombic repulsion. In many experiments, the observed critical size of appearance of molecular doubly charged clusters agree with this model. An example is benzene where $(Benzene)_{23}^{++}$ is the smallest doubly charged cluster observed by Whetten and coworkers [4] whereas the droplet model predicts a critical size of 18.

Up to now, two significant exceptions to this model have been reported: the first by Peifer and Garvey [5] on $(1,1\text{-difluoroethylene})_n^{++}$ (observed for n=9) and the second on 1,4-difluorobenzene [6]: PDFB. The first doubly charged cluster produced in a supersonic expansion by multiphoton ionization is $PDFB_3^{++}$. Its observation in the TOF mass spectrometer implies that its lifetime is on the microsecond time scale.

In order to estimate the stability of benzene and para difluorobenzene clusters we have performed calculations [7]with the semi-empirical method of Claverie [8] which takes into account intermolecular interactions between neutral and ionic species in the cluster. We have found that $PDFB_3^{++}$ is metastable versus the dissociation in two singly charged moieties with a barrier to dissociation of 1 kcal/mol for a geometry where the three PDFB

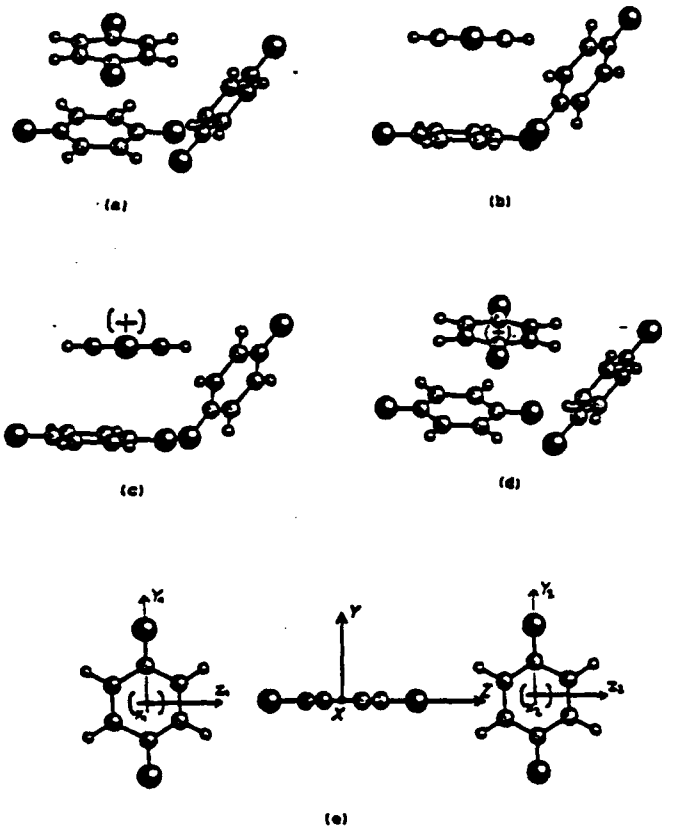

Figure 1: *Most stable structures of $PDFB_3$, $PDFB_3^+$ and $PDFB_3^{++}$*

molecules are aligned (see figure 1). For benzene clusters, the cluster.

The question that arises immediately is why $PDFB_3^{++}$ is observed experimentally while $(Benzene)_6^{++}$ is not. The formation mechanism may be the clue to this question.

Can $PDFB_3^{++}$ be formed directly by Franck-Condon excitation? The differences in geometry between neutral, singly and doubly charged trimers (shown on figure 1) indicate that this process is highly unprobable, and this is confirmed by calculations. Another mechanism is thus considered: formation of larger doubly charged clusters which evaporate neutral molecules.

In a very simple description where the PDFB are considered as spheres, three molecules of PDFB must be aligned in the neutral cluster to reach the metastable well of the doubly charged one. This can be easily found in neutral clusters of PDFB which involve about ten molecules. In the case of benzene, six molecules within the cluster must be found in a "linear" configuration. This can be only observed for large clusters sizes which can be treated by the

liquid drop model.

In order to check our assumption on the formation process of these small doubly charged clusters by evaporation of larger ones, we have undertaken Molecular dynamics simulations. In a zero order model, PDFB are considered as spheres and intermolecular interactions are estimated by one dimension potentials deduced from the full calculations developped previously [7]. For different clusters sizes we have performed the following simulations:

we start from a singly charged $PDFB_n^+$ cluster with various excess energy and we let it explore the potential surface during about 100 psec. Periodically a charge is added, defining the t=0 time and we look at the evolution of the system. After a certain time t_{max} three types of behavior are observed:

1) coulomb explosion
2) evaporation of a neutral molecule to give $PDFB_{n-1}^{++}$
3) nothing happens, $PDFB_n^{++}$ still subsists.

For an energy excess E_T above the metastable well of $PDFB_n^{++}$, we get a set of runs . The lifetime $\tau(E_T)$ associated to this excess energy can be calculated as

$$N_o/N_T = e^{-tmax/\tau}$$

where N_o is the number of $PDFB_n^{++}$ still present at time $t=t_{max}$ and N_T is the total number of runs. $\tau(E_T)$ is calculated for various E_T for which the dissociation time is less than 1 nsec (limitation of the computation). If E_b is the barrier to dissociation, the lifetime is given by

$$\tau = 1/\nu[1 - E_T/E_b]^{s-1}$$

in the RRKM theory, where s is the number of degrees of freedom and ν the frequency along the dissociation coordinate.

ν and E_b from the above formula are fitted from $\tau(E_T)$ data for small times (*i.e.* high energy E_T). As an example, figure 2 shows the lifetime as a function of excess energy E_T for $PDFB_6^{++}$. Arrow 1 shows the energy obtained by a direct ionization of $PDFB_6^+$: the cluster shows a short lifetime (≅ 100 psec). At the opposite, if $PDFB_6^{++}$ is produced by the evaporation process

$$PDFB_7^{++} \text{ --> } PDFB_6^{++} + PDFB$$

the lifetime reaches the microsecond time scale (arrow 2), as observed experimentally.

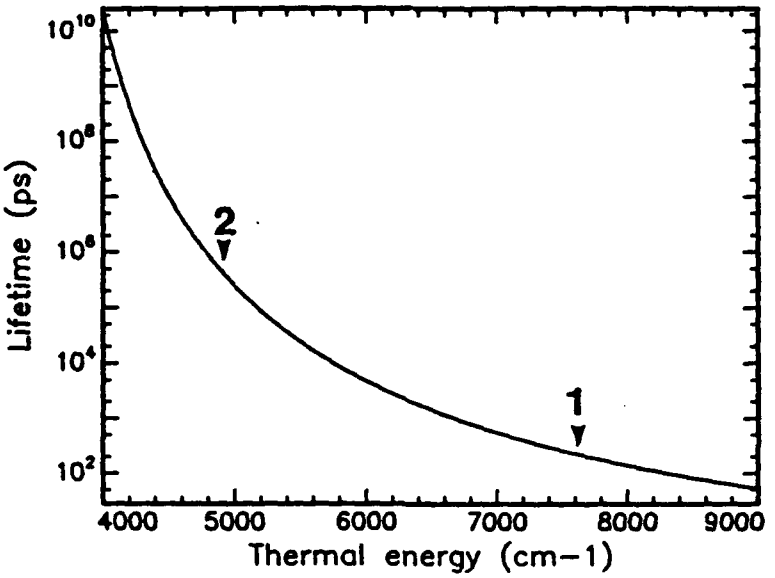

Figure 2 *Lifetime of $PDFB_6^{++}$ cluster as a function of excess energy*

References

1) T.D. Märk, Int. J. Mass Spectrom. Ion Process, 79, 1 (1987)

2) see for example:

a) H. Heln, K. Stephan, T.D. Märk, D.L. Huestis, J. Chem. Phys., 74, 3844 (1981)

b) P.P. Radi, G. von Helden, M.T. Hsu, P.R. Kemper, M.T. Bowers, Chem. Phys. Lett., 179, 531 (1991)

3) O. Echt, D. Kreisle, E. Recknagel, J.J. Saenz, R. Casero, J.M. Soler, Phys. Rev., A38, 3236 (1988)

4) M.Y. Hahn, K.E. Schriver, R.L. Whetten, J. Chem. Phys., 66, 4242 (1988)

5) W.R. Peifer, J.F. Garvey, J. Chem. Phys., 91, 1940 (1989)

6) S. Martrenchard, C. Jouvet, C. Lardeux-Dedonder, D. Solgadi, J. Chem. Phys., 94, 3274 (1991)

7) V. Brenner, S. Martrenchard, P. Millié, C. Jouvet, C. Lardeux-Dedonder, D. Solgadi, Chem. Phys. (1992) to be published.

8) P. Claverie, Intermolecular interactions: from diatomics to biopolymers; Pullman, B. Ed., Wiley: New-York, (1978); chapter 2.

Solvation of Hg_{1and2} by clusters of argon, dimethylether, ammonia and water

S. Martrenchard-Barra, C. Lardeux-Dedonder, C. Jouvet, D. Solgadi, A. Tramer

Laboratoire de Photophysique Moléculaire du CNRS, Bât. 213, Université de Paris-Sud 91405 Orsay (France)

The ionization potentials of many metallic clusters decrease as the size increases. However, in some cases, solvated clusters, for example $Ag_n(H_2O)_\infty$, show an opposite behavior. We have studied the solvation of mercury atom and mercury dimer step by step in various $[Hg_n(solvent)_m]$ clusters produced in a supersonic expansion in order to understand the nature of metal-ligand interaction.

Three kinds of experimental studies can be performed [1]:

1)spectroscopy of the first excited state: in the case of $Hg(solvent)_m$ clusters, 1-1 complexes have been previously studied [1] and present two states in the vicinity of mercury: a Π state in which the 6p orbital of mercury is perpendicular to the diatomic axis and a less stable Σ state in which it is parallel. In the case of water and ammonia, the spectra of $Hg(solvent)_n$ show the same behaviour as the 1-1 complexes (see figure 1b): two states can be observed. At the opposite in $HgAr_n$, one of the states disappears for $n \geq 3$ (see figure 1a).

2) Ionization thresholds measurements through resonance enhanced two color two photon ionization: for example, Hg_2 dimer in the ionic state is well stabilized by dimethylether while the ionization potentials of $Hg_2(H_2O)_n$ and $Hg_2(NH_3)_n$ are about the same as that of free Hg_2.

3) Fragmentation pattern in the ionic state can also be studied: the weakest bond usually breaks. In the case of mercury dimer complexed with ammonia, the main dissociation channel is the evaporation of neutral solvent molecules whereas in the case of $Hg_2(DME)_n^+$, the mercury bond breaks.

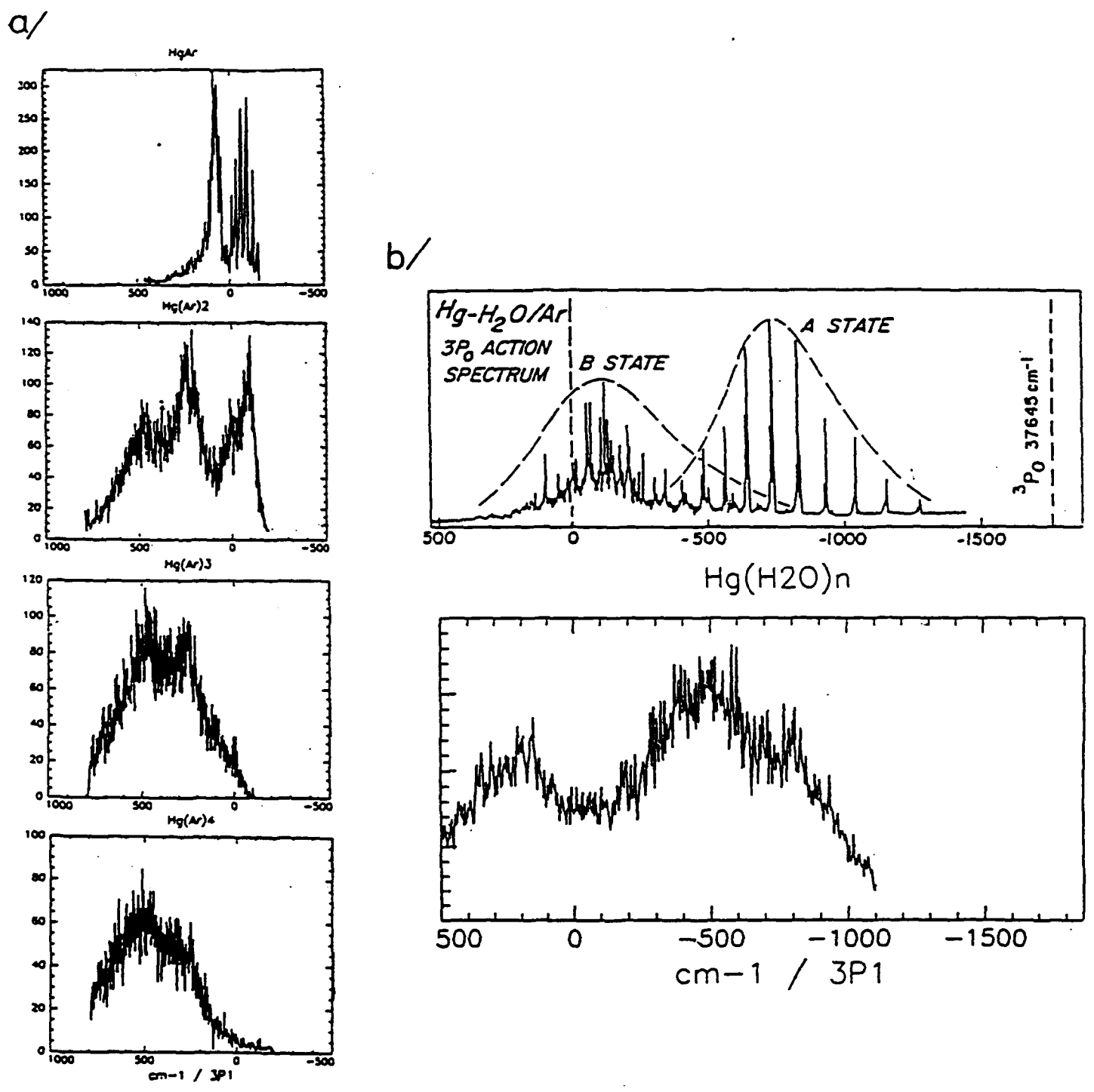

Figure 1: Excitation spectra of $Hg(Solvent)_n$ clusters

a) - $HgAr_n$ with n=1-4

b) - $Hg(H_2O)$ [2a]
- $Hg(H_2O)_n$

All the experiment can be understood in terms of geometries of neutral clusters, assuming that excitation and ionization processes are governed by Franck-Condon rule. Two kinds of geometries are involved: either mercury is on the surface of a solvent cluster - this is the case for NH_3 and H_2O -, or mercury can be solvated in the cluster - this is the case for Argon and DME -.

The comparison of binding energies of metal-solvent versus solvent-solvent justifies this classification. In the case of H_2O and NH_3 the solvent-solvent bond is much stronger than the ligand-solvent bond, whereas in the case of Argon and DME the binding energy are of the same order of magnitude, which enables mercury to interact with more solvent molecules.

Molecular dynamics simulations (with quenching), which enable to explore the whole potential surface and to find the main equilibrium geometries in the ground state, have been performed. These simulations agree with the above assumption: for hydrogenated solvents (NH_3 and H_2O), the calculated structure is Hg_n on the surface of the cluster (see figure 2a), whereas for argon and DME the calculated structure shows the solvation of Hg_n in the cluster (figure 2b).

References

1 a) C. Dedonder-Lardeux, C. Jouvet, S. Martrenchard, D. Solgadi and A. Tramer
Z. Phys. D at.,mol. and clusters 20, 73 (1991)

b) C. Dedonder-Lardeux, C. Jouvet, M. Richard-Viard and D. Solgadi Chem. Phys. Letters 170, 153 (1990)

2 a) M.C. Duval, O. Benoist d'Azy, W.H. Breckenridge, C. Jouvet and B. Soep
J. Chem. Phys. 85, 6324 (1986)

b) M.C. Duval and B. Soep
J. Phys. Chem. 95, 9077 (1991)

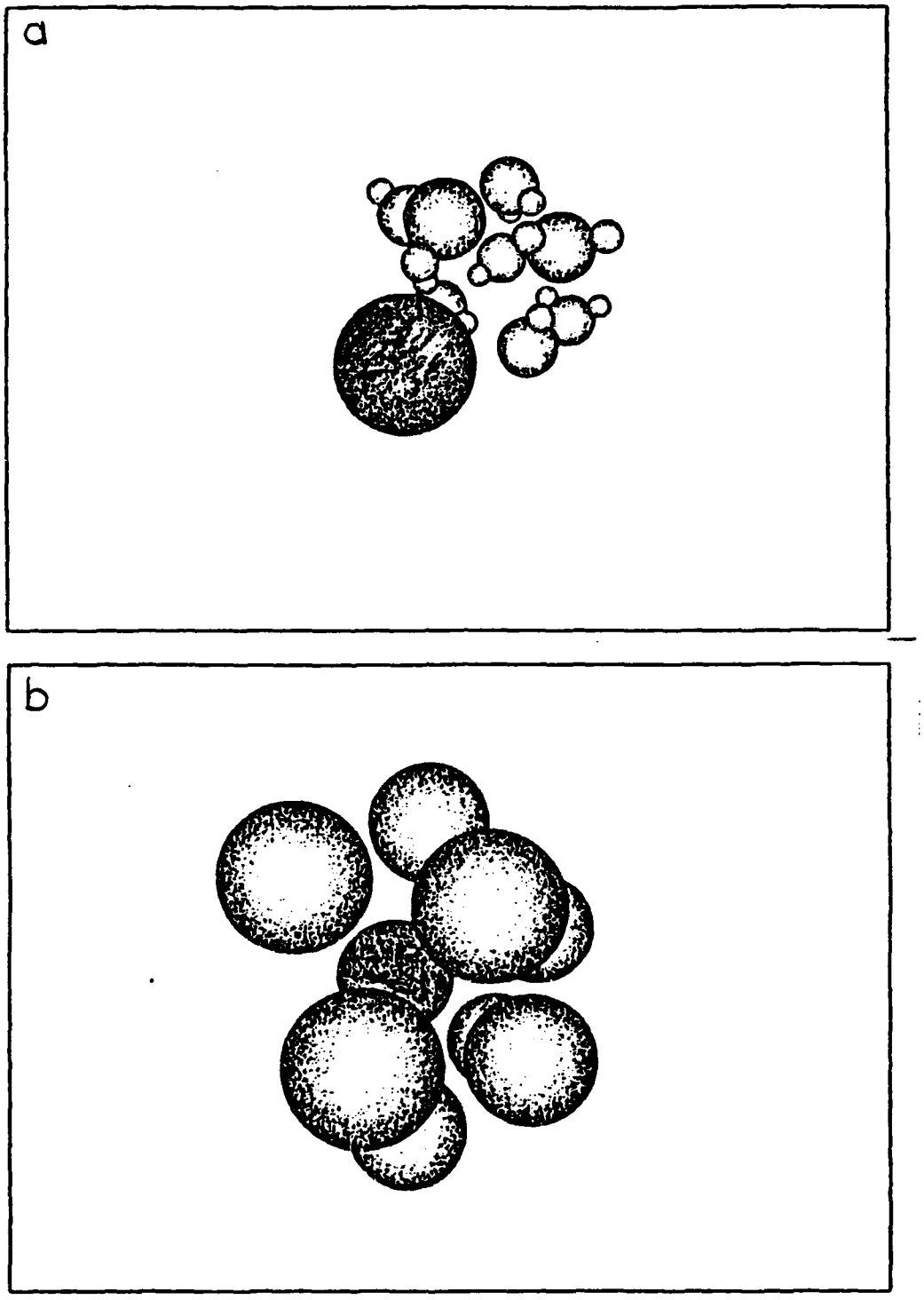

Figure 2: Most stable geometries found by Molecular dynamics simulations: a) $Hg(H_2O)_8$ b) $HgAr_8$

Molecular Beam Studies of Alkane Adsorption Dynamics on Clean and Adsorbate-Modified Pt(111)

Mark C. McMaster, James A. Stinnett, Stephanie A. Soulen
and Robert J. Madix

Understanding alkane reactions on platinum is important both academically and industrially. The first step in furthering this understanding is investigating the adsorption dynamics of alkanes on a platinum surface. By use of molecular beam techniques, this area has been examined in our laboratory: 1) Dissociative adsorption dynamics of alkanes of varying molecular weight on a clean Pt(111) surface, and 2) Molecular associative adsorption dynamics of ethane on an adsorbate-prepared Pt(111) surface.

The activation of alkanes on platinum surfaces is an important industrial process since there it offers the possibility of using the dissociated product(s) to construct more valuable hydrocarbons through subsequent reforming, isomerization and oxidation reactions. In industrial heterogeneous catalytic processes utilizing alkanes as reactants, dissociative alkane adsorption is often identified as the rate-limiting step. Our objective was to determine what gas and surface dynamical parameters are important to activate these otherwise inert molecules and by what mechanism dissociation occurs.

We have used supersonic molecular beam techniques to study the dissociation dynamics of alkanes on Pt(111). The adsorption probability on the clean surface was measured as a function of incident translational energy and angle, energy in vibrationally excited states and surface temperature for CH_4, C_2H_6 and C_2D_6. For translational energies above 55 kJ/mol, alkane dissociation occurs via direct collisional activation. Over the entire range of incident translational energy and angle, direct alkane dissociation depends only upon the component of the ethane translational energy directed along the surface normal. The initial dissociation probabilities of CH_4 and C_2H_6 are nearly identical for similar incident normal translational energies. The dissociation of C_2H_6 and C_2D_6 displays a significant kinetic isotope effect, decreasing from 2.7 and 1.6 as the translational energy increases from 75 to 108 kJ/mol. The dramatic dependence 'of the initial dissociation probability on incident normal translational energy is accounted for using a model in which alkane dissociation occurs via the tunneling of a hydrogen (or deuterium) atom in the incident alkane through the barrier to dissociation. Using an Eckart barrier to model the alkane-platinum interaction and accounting for translational energy dissipation to the lattice during the alkane-platinum collision process, similar barrier heights and widths for methane and ethane activation are extracted suggesting that ethane dissociation occurs via C-H rather than C-C bond rupture. Differences in the zero point energy for C-H and C-D stretching motion can account for the 5 kJ/mol larger barrier height extracted for C_2D_6 relative to C_2H_6.

The independence of the initial dissociation probability for methane and ethane on nozzle temperature suggests that excited vibrational motion in the incident alkane does not play an important role in the direct dissociation process. However, we can only conclusively state that vibrational motion involving modes other than C-H (or C-D) stretching motion do not significantly promote alkane dissociation under these experimental conditions. Over the range of nozzle temperatures employed, the change in the fraction of incident molecules occupying the first excited state for C-H (or C-D) stretching modes does not exceed our experimental error in the measurement of the initial dissociation probability. Finally, the similar dissociation probabilities for direct ethane dissociation on Pt(111), Ni(100)[1] and Ir(110)-(1x2)[2] suggest that the electronic properties of these metal surfaces play a secondary role in the direct dissociation of ethane compared to the dynamical parameters in the incident ethane.

In addition to the study of alkane activation, the investigation of the effect of adsorbates on the associative trapping of ethane is also important industrially. Industrial catalytic hydrogenation processes often occur at high pressure under which conditions the catalytic surface may be partially covered by adsorbates. For this reason, our laboratory has recently investigated the molecular adsorbation dynamics of ethane on adsorbate-prepared Pt(111) surfaces to gain insight on energy dissipiation mechanisms. Adsorbates of comparable mass to that of ethane such as sulfur, ethylidyne, and ethane were employed for this study. Simple hard cube models predict that energy transfer is maximum when the two colliding species are of the same molecular weight.[3] Thus, by using adsorbates of similar molecular weight to that of ethane, the effect of different energy loss mechanisms can be examined. In addition, an adsorbate of significantly different molecular weight, hydrogen, was also used.

For each adsorbate-prepared system, the initial trapping probability of ethane was obtained as a function of incident translational energy and incident angle. By comparing both the absolute magnitude of the initial trapping probability and the energy scaling for the system, the efficiency of energy transfer as well as the effect of corrugation is examined.

Figure 1 presents the initial trapping probability of ethane on each of the adsorbate-modified surfaces as a function of inicident translation energy for an incident angle of 0° and a surface temperature of 95 K. Relative to the clean surface, all of the adsorbate-modified surfaces, with the exception of the hydrogen-modified surface, result in an increased magnitude of the initial trapping probability. This observation is consistent with the concept that an increase in the mass ratio of the colliding partners results in more efficient energy transfer. In addition, the relative magnitude of the trapping probability for each of the adsorbate covered surfaces can be explained by the surface vibrational properties. For the hydrogen-adsorbate surface, the decrease in the magnitude of the trapping probability relative to the clean surface could be due to a surface "stiffening," as reported by other laboratories.[4]

The effective corrugation of the gas-surface potential can be examined by determining the energy scaling of the system. Ideally, for a perfectly "flat" surface, only the normal component of momentum should contribute to the trapping probability. Thus, the trapping probability should scale as the square of the cosine of the incident angle. This scaling is referred to as "normal"

energy scaling. On the other hand, for a highly corrugated surface, both parallel and normal momentum dissipiation should contribute equally. Hence, the trapping probability should be independent of the incident angle, or exhibit "total" energy scaling. Experimentally, the trapping probability usually scales between these two extremes. Although no physical meaning can be attributed to an energy scaling between these two extremes, it is useful as a relative indication of the corrugation of the gas-surface potential.

Figure 1. Initial Trapping Probability of Ethane on Adsorbate-Modified Pt(111)

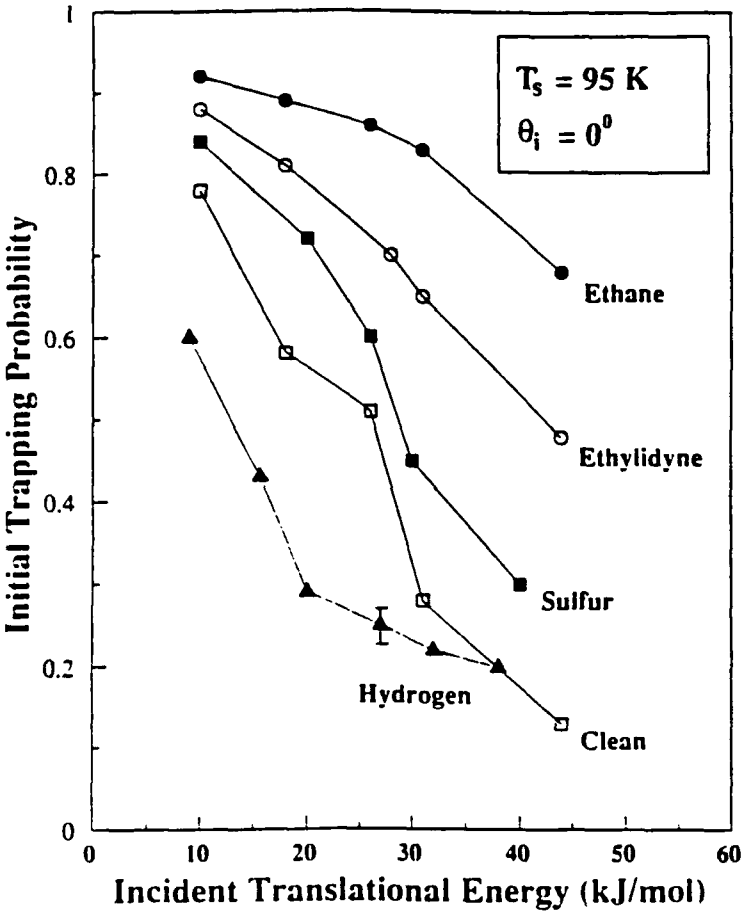

Table I presents the energy scaling for the various ethane-surface systems. For the adsorbates of sulfur, ethylidyne, and ethane, the gas-surface potentials appear to be highly corrugated as these systems exhibit "total" energy scaling. For the hydrogen-modified surface, however, the gas-surface potential appears to be less corrugated than that of the clean surface as the energy scaling is shifted towards "normal" energy scaling.

Table I. Energy Scaling for Ethane Associative Adsorption

Surface	Energy Scaling Exponent
Pt(111)-Hydrogen	1.1
Pt(111)	0.6
Pt(111)-Ethane	0.0
Pt(111)-Ethylidyne	0.0
Pt(111)-Sulfur	0.0

In conclusion, the ethane associative adsorption study indicates that the presence of adsorbates alters the adsorption dynamics. In general, the increase in the trapping probability from the clean to the adsorbate-modified surfaces follows the predictions of the simple hard cube model. However, the energy scaling of the adsorbate systems indicates that a simple one-dimensional model does not apply. In regards to the hydrogen system, the trapping probability results can not be explained by an increase in the "effective" mass of the colliding species; but, rather, must be described more precisely with surface phonon energy dissipiation mechanisms.

References

1. A. V. Hamza and R. J. Madix, Surface Science 179 **25** (1987).

2. A. V. Hamza, H.-P. Steinruck and R. J. Madix, Journal of Chemical Physics **86** 6506 (1987).

3. R. M. Logan and R. E. Stickney, Journal of Chemical Physics, **44** 195 (1966).

4. V. Bortolani, A. Franchini, G. Santoro, J. P. Toennies, Ch. Woll, and G. Zhang, Physical Review B, **40** 3524 (1989).

SEARCHING FOR RESONANCES IN THE TOTAL REACTION CROSS-SECTION: A CROSSED BEAM STUDY OF THE $Ca(^1D) + HCl \rightarrow CaCl(A) + H$ REACTION*

by

M. Menéndez, M. Garay, E. Verdasco,
J. Castaño and A. González Ureña

Departamento de Química Física
Facultad de Químicas
Universidad Complutense de Madrid
28040-Madrid

and

Centro de Láseres y Haces Moleculares
C/ Isaac Peral s/n
Universidad Complutense de Madrid
28040-Madrid

ABSTRACT

The $Ca(^1D) + HCl \rightarrow CaCl(A) + H$ reaction is studied using the time-of-flight technique under crossed beam conditions. The collision energy effect in the title reaction dynamics is reported showing a smooth oscillation in the excitation function.

The experimental setup

The crossed molecular beam technique main details have been reported elsewhere[1] and therefore its description is omitted. Essentially a pulsed discharge produces an intense beam of electronically excited Ca (^1D, ^3P) atoms. The pulsed beam collides with a supersonic HCl beam formed by nozzle expansion with He as carrier. The pulsed CaCl (A) produced by the

$$Ca^*(^1D) + HCl \rightarrow CaCl\ (A) + H$$

reaction is detected, at the scattering center, in coincidence with the pulse of the Ca^* atoms. The experimental technique allows us to measure the chemiluminescence yield as a function of: (i) the metastable $Ca(^1D$ or $^3P)$ concentration, (ii) the collision angle of both beams, (iii) the time arrival of the Ca^* atoms for fixed (i) and (ii) conditions. Therefore the collision and electronic energy effects in the chemiluminescence yield can be measured.

---

* This work received financial support from CICYT of Spain (grant PB88/140) and EEC grant SCI-0006C.

Results and discussion.

As described elsewhere[2] changing the discharge conditions one can modify the ratio of the $^1D/^3P$ metastable concentration and so to determine the reaction cross section for each metastable reaction. A two state model analysis[2] has been reported to account for these two reactant contributions. In this model any chemiluminescence band I_{chem} is described as a linear combination of each metastable reaction, namely

$$I_{chem} = \{\sigma_{^3P} \cdot n_{^3P} + \sigma_{^1D} \cdot n_{^1D}\}\, n_{HCl} \cdot \bar{v}_R \qquad [1]$$

where $n_{^3P}$ and $n_{^1D}$ are the metastable ^3P and ^1D densities, respectively. The a coefficients contain the respective reaction cross-sections as well as the reagents' velocity and other experimental parameters. Equation [1] leads to linear plots from which both metastable reaction cross-sections σ_D and σ_P can be obtained in relative units. The present experiments were carried out for collision energies below $E_T \leq 0.4$ eV to guarantee that the Ca^1D is the only possible metastable reaction since that of Ca^3P is endoergic in $\Delta E_0 = 0.4$ eV.

Once the time-of-flight of the Ca^1D, $n_D(t)$, is measured as well as the time profile of the nascent CaCl, $S_{CaCl}(t)$, produced from the crossed-beam reaction, the time and so collision energy dependent reaction cross-section can be obtained via the equation

$$\sigma_{chem}(t/E_T) = \frac{S_{CaCl}(t)}{n_{^1D}(t) \cdot n_{HCl} \cdot v_R(t)\,\Delta V}$$

Since both n_{HCl} and ΔV are held constant during the experiments relative values of $\sigma_R(E_T)$ can be obtained by the experimental $S(t)/n_D(t)$ ratio over the relative velocity $v_R(t)$ which can be calculated from the experimental conditions. Figure 1 shows preliminary data of the excitation function for the CaCl(A) production obtained using this procedure, over the low collision energy regime.

This excitation function shows an apparent energy threshold around the ^1P potential energy surface (0.20 eV above that of ^1D because our $E_{int} = 0.02$ eV) and a smooth oscillation that could be interpreted as bending excitation of the Ca^* - HCl complex as the collision energy increases. This local model excitation has been studied by laser excitation of the excited van der Waals Ca - HCl complex[5]. In our crossed beam experiment (collision energy resolution $\Delta E = 25$ meV) the van der Waals bending mode excitation would correspond to an increase of the impact parameter range leading to reactive trajectories.

REFERENCES

1. E. Verdasco and A. González Ureña, J. Chem. Phys. 93, 426 (1990).

2. E. Verdasco, V. Sáez Rábanos and A. González Ureña, Laser Chem. 10, 51 (1989).

3. A. González Ureña, Adv. Chem. Phys. 66, 213 (1987).

4. C. T. Rettner and R. N. Zare, J. Chem. Phys. 77, 2416 (1982).

5. B. Soep and C. J. Whitham, A. Keller and J. P. Visticot. Far. Dis. Chem. Soc., 91, 191 (1991).

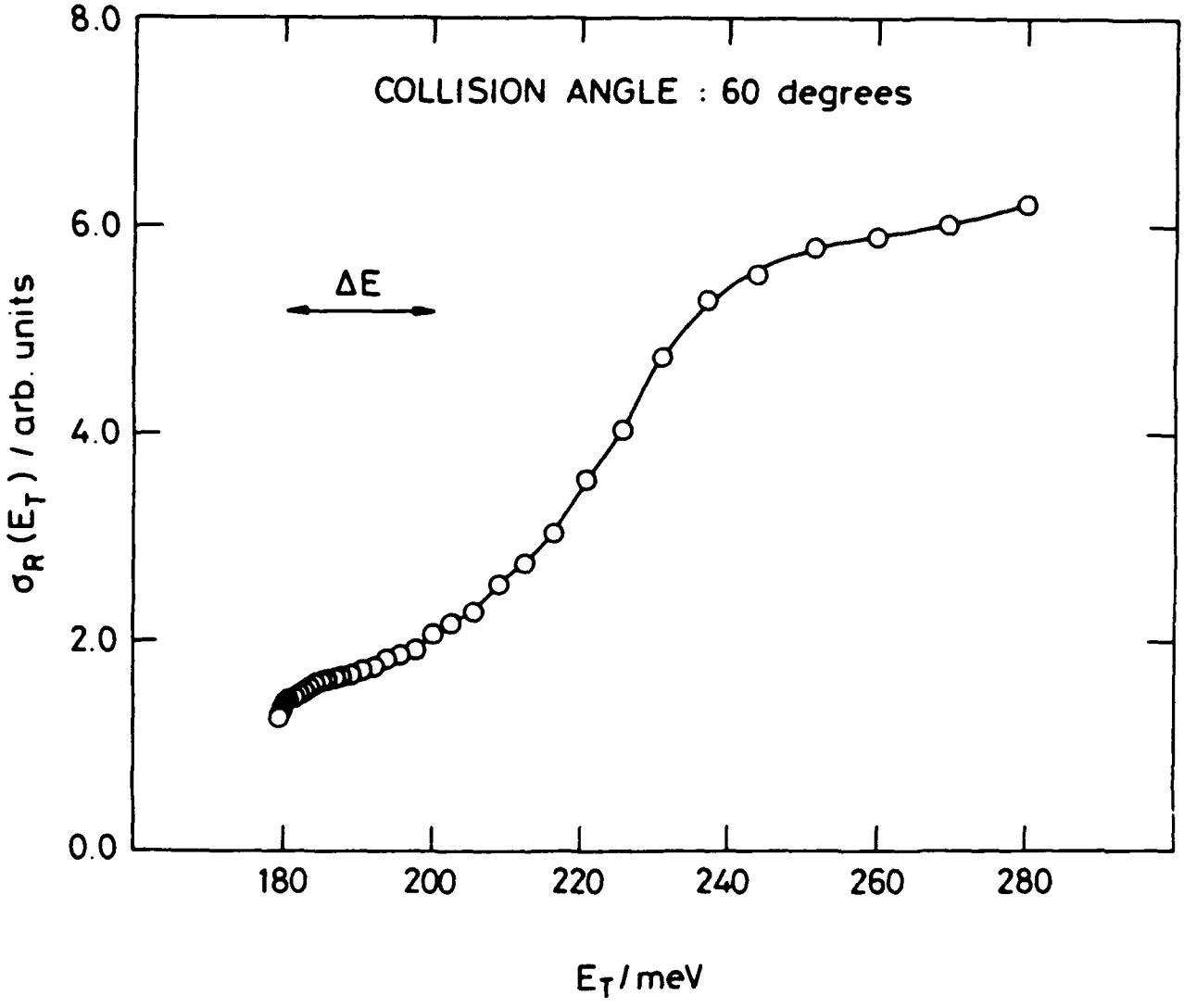

Figure 1. *Excitation function for the Ca(^{1}D) + HCl → CaCl(A) + H chemiluminescent reaction.*

Electrospray Ionization - A New Window on the Solution Scene

C.K. Meng, T. Nohmi, S.D. Fuerstenau, J.B. Fenn
Yale University, New Haven, CT, and

Shida Shen and J.F. Banks, Jr.
Analytica, Inc., Branford CT.

Introduction. Electrospray (ES) ionization consists in electrostatically dispersing volatile solutions as a fine spray of highly charged droplets in a bath gas at or near atmospheric pressure. As the droplets evaporate their surface charge density increases until Coulomb repulsion and surface tension become equal. At or near this Rayleigh limit a droplet becomes violently unstable and breaks up into smaller droplets, an event sometimes referred to as a "Coulomb Explosion." These smaller droplets continue to evaporate until they too reach the Rayleigh limit and the process repeats. Some combination of evaporation and explosions, yet to be very well characterized, finally results in the formation of free ions in the ambient gas from solute species in the liquid phase. Two scenarios for ion formation have been proposed. In the Charged Residue Model (CRM) first suggested by Dole et al [1], Coulomb explosions lead to ultimate droplets so small that they contain only one solute molecule. As the last of the solvent evaporates that residual molecule retains some of the droplet charge to become a free ion in the bath gas. In the Ion Evaporation Model (IEM), proposed later by Iribarne and Thomson [2], at some intermediate stage in the shrinking process a droplet's radius of curvature becomes so small that at a surface charge density below the Rayleigh limit the surface electrostatic field is strong enough to desorb a solute ion from the droplet into the ambient gas. The end product of either model is a dispersion of solute ions in bath gas. By techniques now routine in molecular beam studies, some of this ion-bearing gas enters a small orifice to expand as a supersonic free jet into the first stage of a vacuum system. A core portion of that ion-bearing free jet passes through a skimmer into one or more vacuum stages in tandem, the last of which houses a mass analyzer for "weighing" the ions.

Literally hundreds of investigators are now practicing ES ionization in the mass spectrometric (MS) analysis of fragile and non-volatile species, but very few are addressing the question of how ions are formed. As yet there is no unanimity on whether more reality is embodied in the CRM of Dole, the IEM of Iribarne, or some other mechanism yet to be formulated. In our view the IEM scenario is favored by accumulating evidence that the nature and abundance of observed ions depends strongly on the composition of the starting solution. It follows that examination of these features of ES ions might cast light not only on the mechanism of their formation but also on solution properties and processes. Here we sketch some scenes that have been glimpsed through this new window on solutions.

Apparatus and Procedures. Figure 1 shows a schematic diagram illustrating the essential features of an ESMS apparatus. Solution emerging from the needle tip at flow rates generally from 1 to 10 uL/min is dispersed into charged droplets by the field due to a potential difference of 3 to 5 kV between the needle and the metallized front surface of the glass capillary. Evaporating as they go the droplets drift down the field toward the capillary through a

counter-current flow of dry bath gas. By some mechanism not yet entirely clear (vide supra) ions are formed from the evaporating droplets and are entrained in the gas entering the capillary. When for convenience and safety the needle is at ground potential, the ions entering the capillary are in a potential well. Gas flow through the dielectric capillary drags the ions up the potential gradient out of this well to emerge in the free jet at almost any desired potential up to 15 or more kV above ground. By a combination of gas-dyanmic and electrostatic forces the ions are directed into the mass analyzer, a quadrupole filter (VG1212) in our system.

Results and Discussion. ES ions can always be identified as solute cations or anions (depending on the polarity of the field), or adducts of such ions with solvent molecules or solute species not ordinarily regarded as ionic in solution. Ions of a large solute species show extensive multiple charging and produce mass spectra comprising a coherent sequence of peaks in which the ions of any one peak differ from those of adjacent peaks only by one adduct charge. To the extent that ES ions are formed by the ion evaporation mechanism, one would expect their observed composition, abundance and charge to reflect both their state in the solution and the rate at which they leave. As in any activated process, that rate for any species depends on both the change in its free energy from solution to gas and its concentration, i.e. on its fugacity. Following are some observations that seem to reflect the influence of one or both of these factors. Additional examples and more detailed discussion will be presented in the full account.

The solid curve in Fig. 2 shows a nearly linear dependence of MS signal for ES cations on concentration in 1:1 methanol-water of tetrabutylammonium bromide up to about 40 umolar. We think the change in slope there is due to solute saturation in the vaporizing droplets. Adding acetic acid decreases signal and shifts the break to higher concentration (dashed curve). The higher solubility (lower fugacity) of TBAB in acid solutions can explain this behaviour.

The solid curve in Fig. 3 shows MS signal of ES cations for several tetra-alkyl ammonium bromides in 1:1 methanol:water. Solute molecular weight Mr (abscissa) increases as the alkyl groups go from tetramethyl to tetrahexadecyl. We attribute the initial rise in ion current to increasing fugacity of the ion as its solvophobicity increases with hydrocarbon chain length. Above Mr's of 400 solvophobicity is so strong that solubility decreases, thus lowering solute concentration and therefore MS signal. Adding isopropanol (dashed line) increases solubility so ion current remains high.

Figure 4 shows the ES ion signal (ordinate) for 0.45 mmolar solutions of adenine, thymine, cytosine and guanine. Abscissa scale is pKa (-log dissociation constant for BH+, B being the nucleo base.) For pure water (lower curve) signal decreases with pKa. Low pH (upper curve) suppresses BH+ dissociation so its concentration and thus MS signal are nearly the same for all bases.

Figure 5 shows selected ion currents obtained with equimolal solutions of the peptides gramicidin S (grcS) and cyclosporin A (cspA) at total micromolarities from 0.1 to 100. Noteworthy is that the doubly protonated grcS is always more abundant than the singly charged ion. For cspA the converse is true. The higher solubility of the former means it likes the solvent and requires more charge to desorb from the droplet at a high rate. Chromatographic retention times confirm the higher solvophobicity of cspA. The high abundance of the doubly-charged grcS-cspA dimer is surpris-

solubility of the former means it likes the solvent and requires more charge to desorb from the droplet at a high rate. Chromatographic retention times confirm the higher solvophobicity of cspA. The high abundance of the doubly-charged grcS-cspA dimer is surprising. Its two charges imply high solvophilicity so the high ion current indicates very high concentration in solution. The unexpectedly high affinity of these species may have biochemical implications.

Reminiscent of the ability of free jets to produce clusters of almost any vaporizable species, evaporating charged droplets can also produce clusters of non-volatile solute species over a wide range of sizes. As droplets reach supersaturation, solute fugacity becomes so high that it flees the solution by precipitating in a new phase. An alternative escape route from a highly charged droplet is desorption as a cluster ion. The formation of the grcS-cspA dimer shown in Fig. 5 is one aspect of such escape. Figure 6 shows clearly that aggregation can go much further for arginine solutes. The number of molecules per cluster increases strongly with initial solute concentration. (Note: 6+ means 6 molecules in a cluster with a single positive charge.) Expansion of the bottom spectrum reveals clusters with up to 24 molecules and 4 charges.[3] Similar results with other species imply new worlds for cluster research to conquer.

The spectra in Fig. 7 obtained by Chait and colleagues [4] show interesting changes in charge state distribution for ions of the protein cytochrome. The solution pH is 2 in panel (a), 2.6 in panel (b) and 3.1 in panel (c). The signal and average charge state are highest in (a) lowest in (b) and intermediate in (c). It is known that the conformation is most open at pH 2, most compact at pH 2.6 and intermediate at 3.1. The inviting prospect: charge state distribution on ES ions of large molecules may provide information on their conformation (tertiary structure) in solution.

References

1. M. Dole, L.L. Mach, R.L. Hines, R.C. Mobley, L.P. Ferguson, M.B. Alice, J. Chem. Phys. 49, 2240 (1968)
2. J. V. Iribarne, B. A. Thomson, J. Chem. Phys. 64, 2287 (1976)
3. C.K. Meng, J.B. Fenn, Org. Mass Spectrom. 26, 542 (1991)
4. S.K. Chowdhury, V. Katta, B.T. Chait, JACS 112, 9012 (1990)

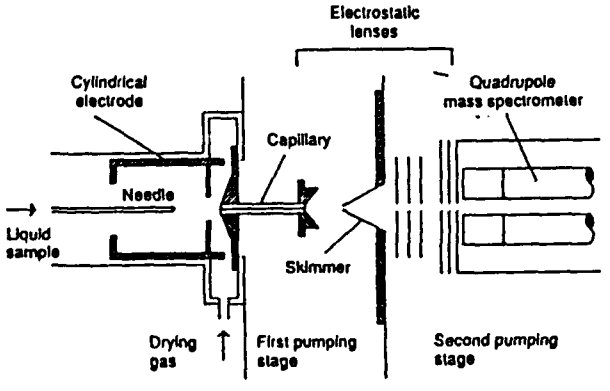

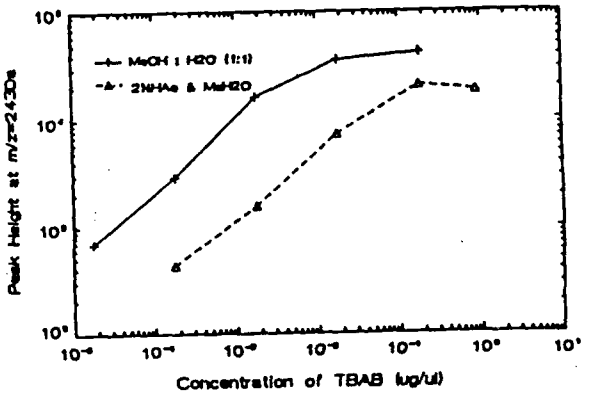

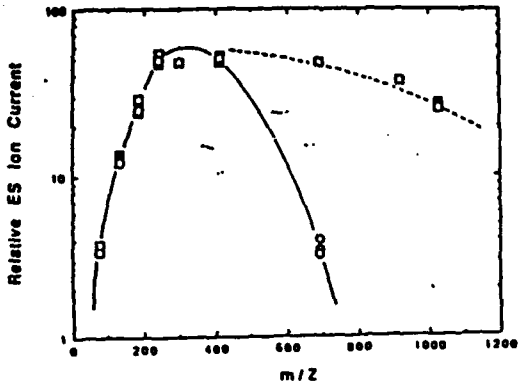

Figure 3

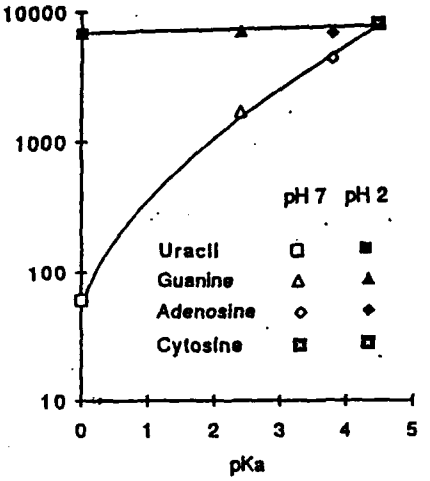

Figure 4

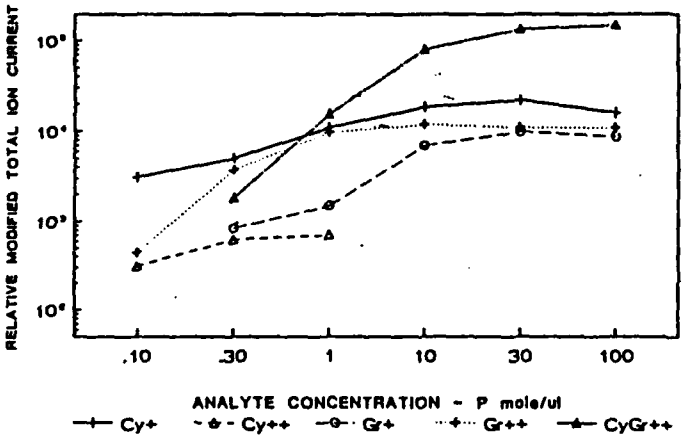

Figure 5

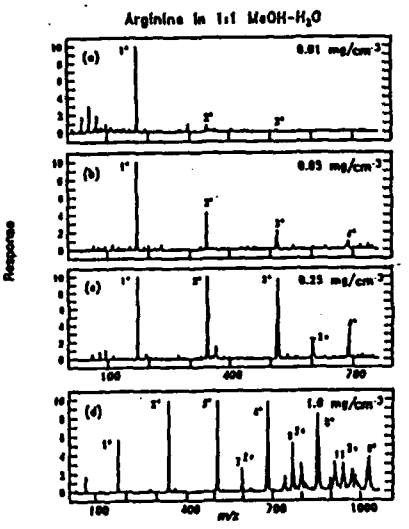

Figure 6

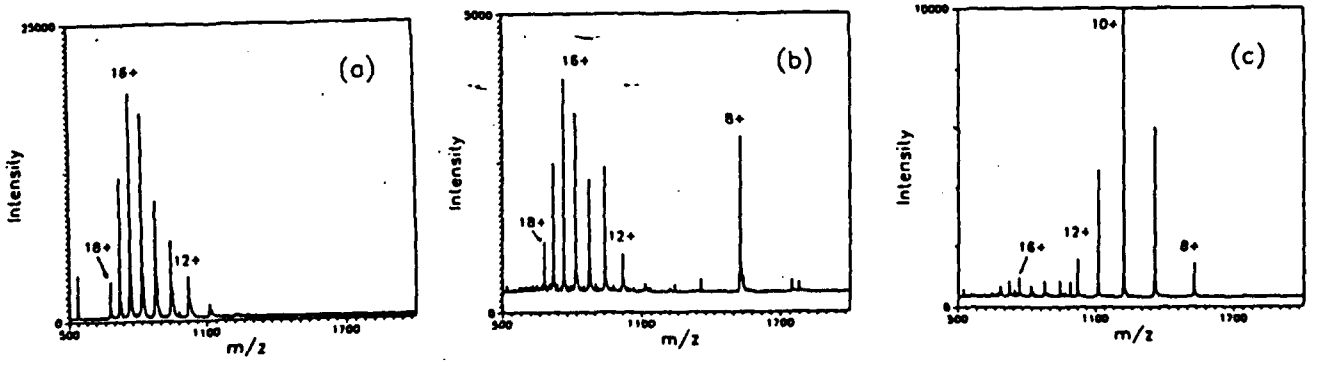

Figure 7

COPY AVAILABLE TO DTIC DOES NOT PERMIT FULLY LEGIBLE REPRODUCTION

Direct Observation of ClO from Chlorine Nitrate Photolysis

Timothy K. Minton
Jet Propulsion Laboratory, M.S. 67-201
California Institute of Technology
4800 Oak Grove Drive
Pasadena, CA 91109

Christine M. Nelson, Teresa A. Moore, and Mitchio Okumura
Department of Chemistry, M.S. 127-72
California Institute of Technology
Pasadena, CA 91125

Although the mechanisms for polar ozone depletion are believed to be well understood, our recent investigation of the photodissociation of chlorine nitrate ($ClONO_2$) in a molecular beam indirectly raises questions about the presumably dominant ozone destruction cycle involving ClO:

$$\begin{aligned} ClO + ClO + M &\longrightarrow ClOOCl + M \\ ClOOCl + h\nu &\longrightarrow ClOO + Cl \\ ClOO + M &\longrightarrow Cl + O_2 + M \\ 2(Cl + O_3 &\longrightarrow ClO + O_2) \\ \text{Net:}\quad 2O_3 &\longrightarrow 3O_2 \end{aligned}$$

A crucial assumption made in the second step of this cycle is that ClOOCl photodissociation leads to atomic chlorine. This assumption requires the Cl-O bond (21 kcal/mol) to break preferentially over the weaker O-O bond (18 kcal/mol), and it is based on the argument that excitation of an n$\rightarrow \sigma^*$ transition localized on the chlorine yields selective dissociation of the Cl-O bond. This idea arose from previous photolysis experiments on $ClONO_2$ in a flow cell. The concensus from these experiments is that the quantum yield for Cl atoms is ~ 0.9.[a] Recently, a very similar study on ClOOCl reported a quantum yield of 1.0 for Cl atoms produced from the primary photochemical reaction (step 2).[b]

However, our results (see, for example, Fig. 1) show conclusively that in the photodissociation of $ClONO_2$ at 193 and 248 nm the ClO + NO_2 channel is significant, accounting for about 45 percent of the dissociation events. The only other channel observed was Cl + NO_3. Our experiments were carried out on a crossed molecular beams apparatus and employed the technique of photofragment translational spectroscopy. All primary photoproducts were observed directly with a rotatable mass spectrometer detector, and their time-of-flight and angular distributions have been measured. A photodissociation experiment was also performed on Cl_2O, which fragments to Cl + ClO and thus provides a means to calibrate the mass spectrometer detector so that the branching ratio between the two dissociation pathways in $ClONO_2$ can be accurately determined.

Even though the weaker O-N bond (26 kcal/mol) does break 45 percent of the time, the dominant channel is still Cl-O bond fission, which requires 40 kcal/mol. This result is

[a] *Chemical Kinetics and Photochemical Data for Use in Stratospheric Modeling*, JPL Publication 90-1, edited by W.B. DeMore, et al. (Jan. 1, 1990).

[b] M.J. Molina, A.J. Colussi, L.T. Molina, R.N. Schindler, and T.-L. Tso, Chem. Phys. Lett. **173**, 310 (1990).

consistent with the picture of a transition localized on the Cl-O moiety. Nevertheless, the large fraction of ClO product was not seen in the previous photolysis studies. Therefore, the report of only Cl atoms from ClOOCl photolysis becomes questionable. If ClO is in fact an important product of ClOOCl photodissociation, then the catalytic cycle above may not account for as much ozone destruction as currently believed.

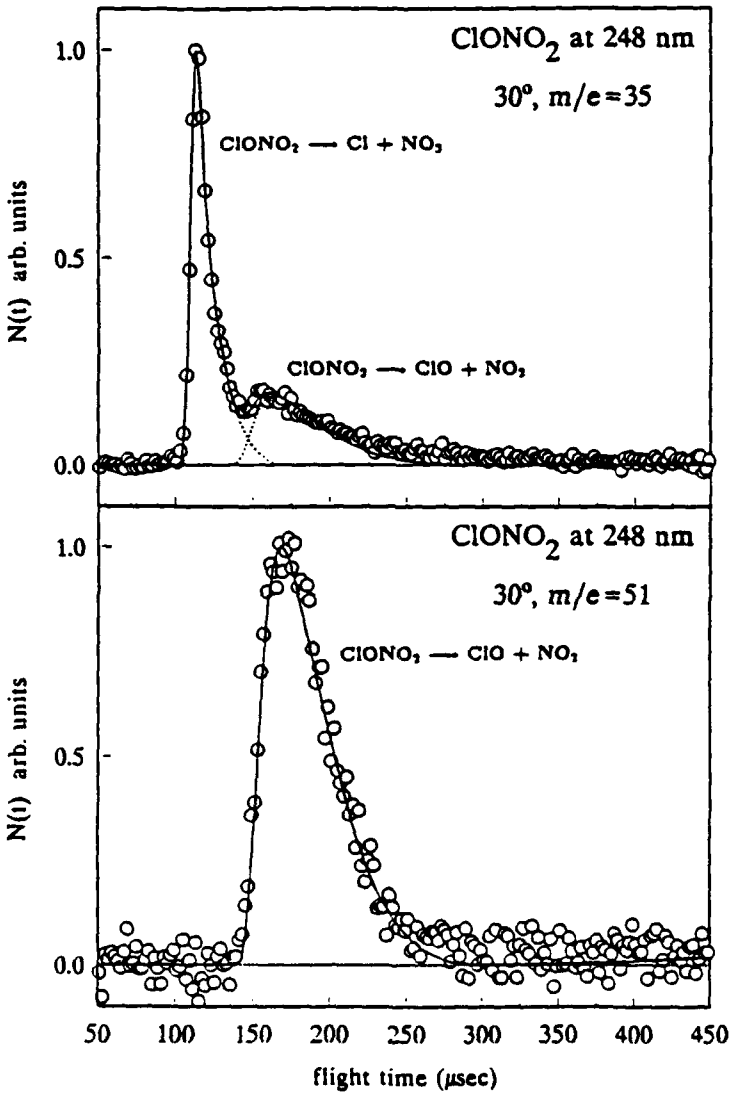

Figure 1. Laboratory time-of-flight (TOF) distributions for $ClONO_2$ photoproducts detected at m/e=35(Cl^+) and m/e=51(ClO^+) following excitation at 248 nm. The m/e=35 TOF distribution shows two components which are assigned to Cl atoms from the Cl + NO_3 channel and to ClO from the ClO + NO_2 channel. The parent ClO, detected at m/e=51, shows a single peak that corresponds in time and shape to the slower component in the m/e=35 TOF distribution. Also shown with the TOF data are fits that were calculated from optimized center-of-mass angular and translational energy distributions.

STRUCTURE-DEPENDENT INTRAMOLECULAR VIBRATIONAL REDISTRIBUTION IN THE BENZENE-Ar_n COMPLEXES.

Michel MONS, Martin SCHMIDT and Jacques LE CALVÉ,

CEA, Service des Photons, Atomes et Molécules,
Centre d'Etudes de Saclay, Bât 522,
91191 GIF-SUR-YVETTE Cedex,
France.

Recent two-color resonant two-photon ionization (R2PI) experiments, combined with Monte Carlo simulations, have shown that the first benzene-Ar_n (Bz-Ar_n) clusters exhibit a large variety of isomeric forms /1-3/.

In the two-color R2PI spectrum of the $S_1 \rightarrow S_0$ 6_0^1 Bz transition of the Bz-Ar_2 complex, two distinct bands are easily observed /1/. The different ionization efficiency spectra obtained from these bands (Fig.1)

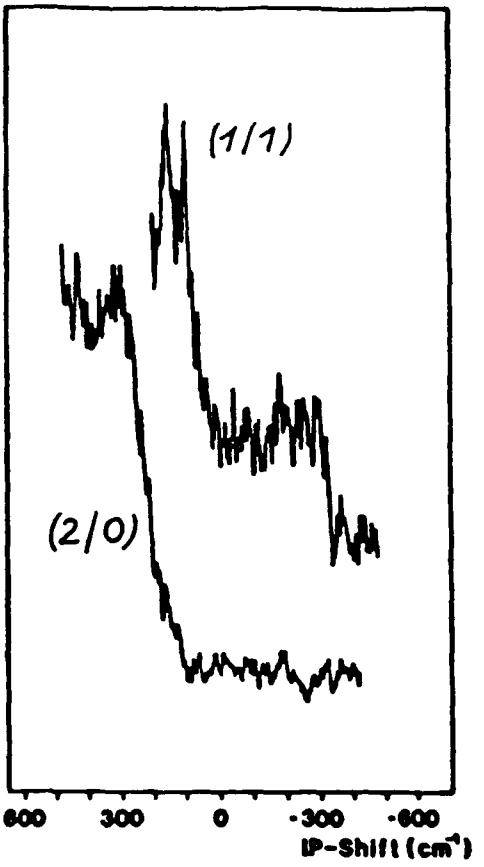

Fig. 1 : Mass-selected two-photon ionization efficiency spectra of the two isomeric forms ((1|1) and (2|0)) of the Bz-Ar_2 complex. The IP scale is relative to the monomer IP.

allows us to assign them to two different species: the expected two-sided form (noted (1|1)) and a one-sided (2|0) conformer. Similarly for the Bz-Ar_3 complex, three forms are observed: one two-sided (2|1) and two one-sided (3|0), only differring by the position of the triangular argon trimer above the benzene ring (Fig. 2): in one case, the trimer occupies a symmetric position ((3s|0) form); in the other case ((3c|0) form), one argon atom occupies a central position close to the Bz C_6 axis and the others are in peripheral sites, which is a structure similar to that of the (2|0) form.

The possibility to selectively excite species corresponding to different arrangements of argon "solvent" atoms around the Bz molecule allows us to study the influence of the microsolvation characteristics upon the dynamical properties of the solvated molecule.

The dynamics of the S_1 state of the first Bz-Ar_n clusters has been investigated in a two-color R2PI experiment.

The ionization efficiency spectra of each isomeric form of these clusters have been recorded: two kinds of spectra are obtained depending on the species studied:

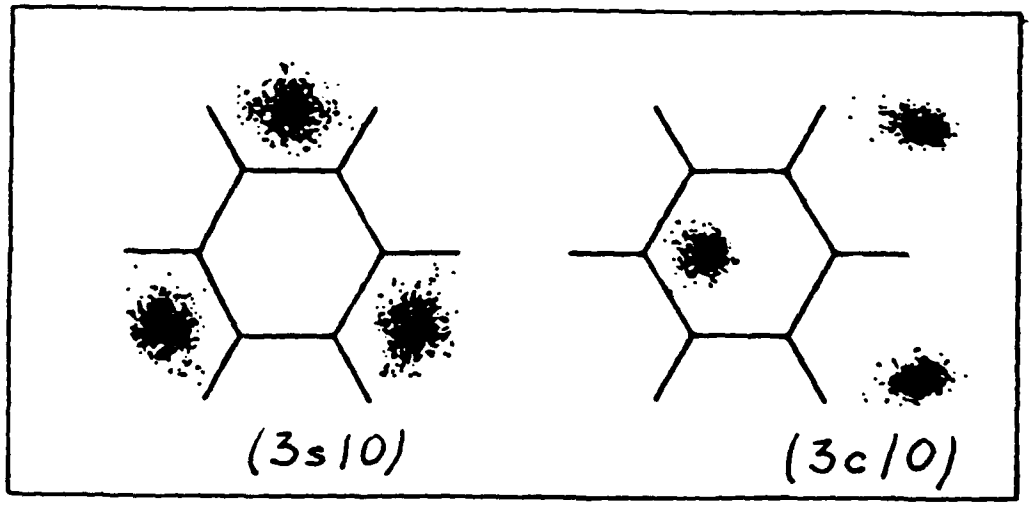

Fig. 2 : Top view of the Monte Carlo simulation, at 3K, of the two "one-sided" isomeric forms of the benzene-Ar_3 cluster.

- The symmetric species, (1|0), (1|1), (3s|0) pumped to the S_1 6^1 level of the benzene chromophore (520 cm^{-1} vibrational energy) exhibit ionization behaviors similar to that obtained on the monomer (Fig. 1): the ionization curves, consisting of successive steps, reflect the vibronic structure of the benzene cation.
- The other species (2|0), (2|1), (3d|0), excited in the 6^1 level present an anomalous ionization spectrum, characterized by a wide ionization threshold, blue-shifted (~ 500 cm^{-1}) relative to the corresponding symmetric species (Fig. 1). The same behavoir is also observed for the (1|1) species, when excited in the $6^1 1^1$ level of the S_1 state (1444 cm^{-1} excess energy in the chromophore).

These results show that, in the second case, the direct ionization process is not observed. Ionization takes place after an energy-dependent dynamical process occuring in the excited vibrational S_1 levels of these complexes, which is assigned to the IVR within the cluster /4/. The vibrationally excited chromophore relaxes towards a less excited vibrational S_1 level and the excess energy flows into the intermolecular degrees of freedom. Such a process fairly accounts for the higher energy IP observed (Fig. 1), because of the $\Delta v=0$ vibrational propensity rule expected for both molecular and intermolecular vibrations in the ionization step.

The originality of the present results consists in the dependence of the IVR rate with the structure of the complex. In spite of their similar density of intermolecular vibrational states, the (1|1) and (2|0) species have very different behaviors during the time delay (typically 30 ns) between the lasers of the two-color experiment. But the most striking example arises from the comparison between the two one-sided isomers of the $Bz-Ar_3$ complex, for which final intermolecular states are nearly identical.

This strongly structure-dependent IVR process is interpreted in the classical frame of the Fermi golden rule /../, by taking into account:
i) the increase of accessible vdW final states due to the less constraining selection rules, in the complexes of lower symmetry, ii) the difference in the coupling between molecular and intermolecular vibrations for different isomeric forms.

References:

/1/ M. Schmidt, M. Mons and J. Le Calvé, Chem. Phys. Lett. 177 (1991) 371.

/2/ M. Schmidt, M. Mons, J. Le Calvé, P. Millié and C. Cossart-Magos, Chem. Phys. Lett. 183 (1991) 69.

/3/ M. Schmidt, M. Mons and J. Le Calvé, J. Phys. Chem. (1992), in press.

/4/ G.E. Ewing, J. Phys. Chem 91 (1987) 4662.

Photodissociation of Cyclopentadiene at 193 nm

James D. Myers and Yuan T. Lee
Chemistry Department
University of California at Berkeley

The dissociation of cyclopentadiene (C_5H_6) to H atom and cyclopentadienyl radical (C_5H_5) requires only 78 kcal/mol. This is due to resonance stabilization of the radical electron in the cyclopentadienyl fragment. However, the most thermodynamically stable dissociation pathway is opening of the ring and formation of methyl acetylene and acetylene (66.1 kcal/mol). The barrier to this reaction is not known. Several other channels, such as H_2 loss from the ring, or fragmentation to CH_2 and C_4H_4 , or C_2H_3 and C_3H_3, are within 55 kcal/mol of the lowest energy channel. Again, the barrier heights are not known.

Kinetics data have shown that H atom elimination is the major dissociation pathway at temperatures around 1000 K. Dean[1] has modeled the autocatalytic production of ethane and larger hydrocarbons during methane pyrolysis and found that C_5H_6 is largely responsible for the autocatalytic effect. Once C_5H_6 is formed, unimolecular dissociation, followed by abstraction of hydrogen from methane by the C_5H_5 radical, yields a catalytic route to the production of CH_3 and H from methane. The high concentration of radicals leads to rapid production of larger hydrocarbons and eventually to soot. Dean found no evidence for the existence of other C_5H_6 dissociation channels.

Glassman et. al. have suggested that ring opening may compete with H atom loss. They have studied the oxidation of many aromatic hydrocarbons in a turbulent flow reactor[2,3]. In studies of C_5H_6 oxidation[4], they noted anomolously early production of CO and CO_2. To account for this, they suggested dissociation of C_5H_6 to CH_2 and C_4H_4 followed by oxidation of the CH_2 to CO_2. Dissociation of C_5H_6 to acetylene could also produce CO and CO_2. Another mechanism that included only H atom loss was proposed, but none of the models satisfactorily explained the data.

An investigation of the unimolecular dissociation of C_5H_6 with 193 nm excitation and hydrogen atom laser induced fluorescence detection was done by Yi et. al. They found a quantum yield of .85 +/- .07 for H atom loss. It was speculated that H_2 elimination accounted for the rest of the dissociation yield, though this could not be determined by their technique.

We have investigated the photolysis of C_5H_6 at 193 nm using molecular beam Photofragment Translational Spectroscopy (PTS) in an attempt to understand the unimolecular reactions of C_5H_6 and C_5H_5. PTS allows us to determine all of the dissociation channels, the branching ratios between them, and

the translational energy distribution for each individual channel. It also allows us to distinguish between primary and secondary dissociation.

To study C_5H_6, we crossed a cold molecular beam of 8% C_5H_6 seeded in helium with <5mJ/cm2 of 193 nm light at right angles. Mass and angle resolved time of flight spectra were recorded using an electron bombardment ionizer, quadrupole mass filter, and ion counting detector. The kinetic energy distributions of the fragments were calculated by iterative forward convolution of an assumed distribution with the instrument response to fit the observed time of flight spectra. Conservation of linear momentum in the center of mass frame was used to identify conjugate fragments. As expected, the dominant dissociation channel was hydrogen atom loss (~90%). However, several other channels were observed:

$$C_5H_6 \text{ ---> } \begin{array}{l} CH_2 + C_4H_4 \\ C_2H_2 + C_3H_4 \\ C_2H_3 + C_3H_3 \end{array}$$

No evidence was found for H_2 elimination. Power dependence studies show that these channels are all one photon processes. Comparison of the maximum experimentally observed translational energy release with the limit imposed by thermodynamics in the CH_2 channel identifies the C_4H_4 fragment as vinyl acetylene. Similarly, the C_3H_4 fragment could be allene or methyl acetylene but it cannot be cyclopropene. Calculation of more accurate branching ratios for all of the products are in progress.

We also repeated the experiment at higher laser fluences and observed the stimulated secondary dissociation of the cyclopentadienyl radical. Analysis of these data will also be presented. At the highest laser fluences (~250 mJ/cm2), we observed a stepwise increase in the maximum translational energy for masses 63 and 62 relative to 65 and 64, mass 61 relative to 63 and 62, and mass 60 relative to 61. This suggests that it is possible to strip all of the hydrogens off of C_5H_6, with no C-C bond cleavage except for ring opening, to produce C_5. The stepwise increases suggest that the dissociation sequence is either H, H_2, H_2, H, or a sequence of fast and slow H atoms. It should be possible to distinguish these two pathways with further analysis. The possibility of stripping off all hydrogen atoms while leaving the carbon skeleton intact (except for ring opening) would continue a trend seen in smaller hydrocarbons[6]. This, and the astronomical observation of C_5H and C_3[7], suggests that C_5 may exist in interstellar space.

References:

(1) A. M. Dean, J. Phys. Chem. **94**, 1432 (1990)

(2) K. Brezinsky, F. N. Egolfopoulos, J. L. Emdee, C. K. Law, I. Glassman Prepr. Pap., Am. Chem. Soc., Div. Fuel Chem **36**, 1478 (1991)

(3) K. Brezinsky, G. T. Linteris, T. A. Litzinger, I. Glassman, Twenty-first Symposium on Combustion/The Combustion Institute, 833 (1986)

(4) R. G. Butler, K. Brezinsky, I. Glassman, Eastern States Section Meeting of The Combustion Institute, December 1990
(5) W. Yi, A. Chattopadhyay, R. Bersohn, J. Chem. Phys **94**, 5994 (1991)
(6) W. M. Jackson, D. S. Anex, R. E. Continetti, B. A. Balko, Y. T. Lee, J. Chem. Phys. **95**, 7327 (1991)
(7) B. L. Turner, Space Science Reviews **51**, 235 (1989)

A Simple Method for Product Rotational Distribution in Atom-Diatom Chemical Reactions

Masato Nakamura†
Institute for Solid State Physics, University of Tokyo, Roppongi, Minato-ku, Tokyo 106 Japan

A very simple method for the product rotational distribution in atom-diatom chemical reactions is presented. This method gives an overall product rotational state distribution for a given reactive vibrational transition with a considerable accuracy.[1,2] It is applicable to low energy collinear-favored reactions. Particular, it is effective when the collision energy is lower or a little higher than the potential barrier height where the classical trajectory method fails.

The rotational transition in a chemical reaction is induced by the two different mechanisms. One is the rotationally inelastic half collision in both reactant and product channels essentially the same as that in the non-reactive collisions. The other, which is inherent to rearrangement collisions is the coordinate transformation from the reactant channel to product channel in the reaction zone. Then, the cross section from initial rotational state j_i to final rotational state j_f may be written as[3,4]

$$\sigma_R(j_i \to j_f) = \sum_{j'_f} P_f(j'_f \to j_f) \sum_{j'_i} \sigma_{re}(j'_i \to j'_f) P_i(j_i \to j'_i), \qquad (1)$$

where $P_\alpha(j_\alpha \to j'_\alpha)$ is the rotationally inelastic transition probability from j_α to j'_α in an α-arrangement channel ($\alpha = i$ for reactant and f for product) half collision, while $\sigma_{re}(j'_i \to j'_f)$ represents the cross section due purely to the rearrangement. Effects of the coordinate transformation are involved in the latter.

Rotational transition probabilities in a half collision can be usually calculated using the infinite-order-sudden (IOS) approximation. On the other hand, the 'rearrangement' cross section should be represented within the framework of the distorted-wave (DW) approximation. Although the computation of the DW cross section is time consuming in

† present address: Aono Atomcraft Project, ERATO, JRDC, Kaga, Itabashi-ku, Tokyo 173 Japan

general cases, I found that it can be reduced into a simple analytical form for collinear-favored reactions.[1] Since many chemical reactions are collinear-favored, the formalism is expected to be practical. The cross section is given by

$$\sigma_{re}(j_i \to j_f) \sim \sum_{l_f l_i j} (2l_f+1)(2l_i+1)|\langle l_i 0 l_f 0|j0\rangle\langle j_i 0 j 0|j_f 0\rangle|^2 Q_{j_i j_f l_i l_f}, \quad (2)$$

where l_α is the orbital angular momentum, $\langle ...|..\rangle$ is the Clebsch-Gordan coefficient and Q is a factor representing the reaction probability for each angular momentum transfer. Further details about this expression including the explicit formula of Q are stated in ref. 1. The expression involves no numerical integral and we can obtain the product rotational distribution easily.

In many cases, the effect of rotationally inelasticities is less important than that of the coordinate transformation. Then, one may often approximate as

$$\sigma_R(j_i \to j_f) \cong \sigma_{re}(j_i \to j_f). \quad (3)$$

In what follows we show some illustrative examples to demonstrate the effectiveness of the method.

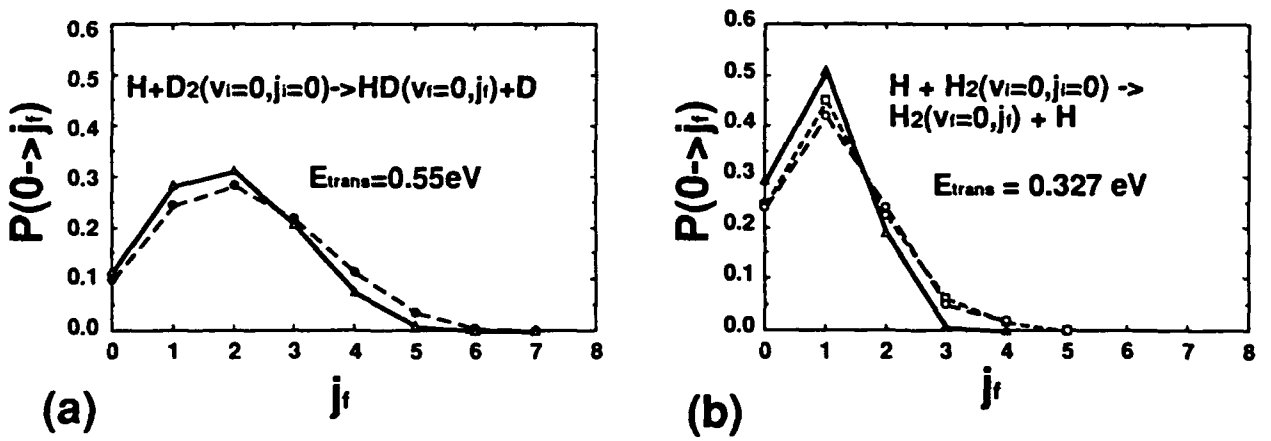

Fig. 1 : (a) Product rotational state distribution in H + D_2 ($v_i = 0, j_i = 0$) $\to$ DH($v_f = 0, j_f$) + H at E_{trans} = 0.55 eV; Δ : from eq.(2)[1], ● : the DW calculation of Connor and Southall.[5] (b) Product rotational state distribution in H + H_2 ($v_i = 0, j_i = 0$) $\to$ H_2 ($v_f = 0, j_f$) + H at E_{trans} = 0.327 eV; Δ : from eq.(2) and eq.(3), □ : from eq.(1) and eq.(2), ○ : from the close coupling calculation.[6]

The H + H_2 reactions and its isotopic variations have been extensively studied. First, we will demonstrate that eq.(2) is a good approximation to the original DW approximation. Figure 1(a) shows the product rotational state distribution in the H + D_2 → HD + D reaction at the collision energy of 0.55 eV. The distribution obtained from the original DW[5] approximation and that from our formalism (eq.(2)) agree quite well.

In Fig. 1(b), calculated rotational distributions in the H + H_2 reaction are plotted together with that from an accurate calculation.[6] Among two calculations, one includes the effects of rotational inelasticity (using eq.(1) and eq.(2)) and the other does not (using eq.(2) and eq.(3)). We recognize that the simple methods reproduce an accurate distribution surprisingly well. The difference between two our calculations is small. This means that effects of rotationally inelasticity are small in this system.[3,4]

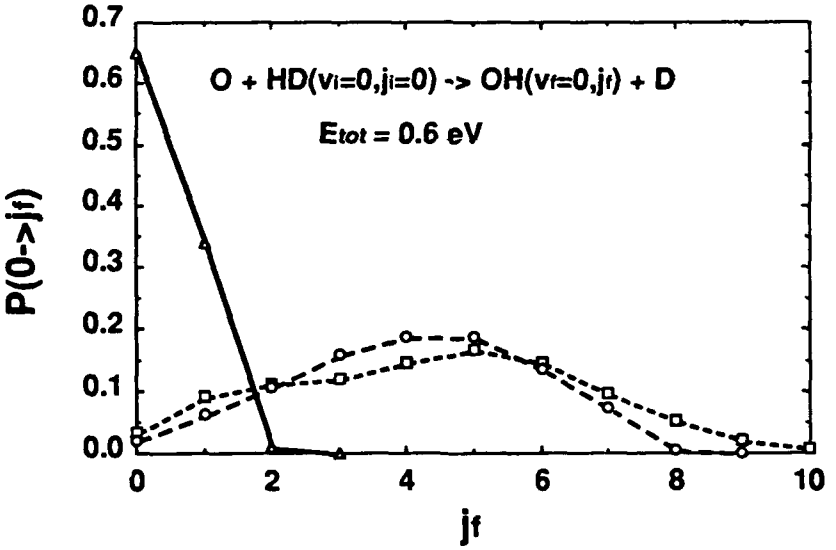

Fig. 2 : Product rotational state distribution in O + HD(v_i=0, j_i = 0) → OH(v_f=0,j_f) + D; △: from eq. (1) and eq.(3), □: from eq. (2) and eq.(3), ○: from the CSDW[7] calculation.

Next, we present an example in which the rotationally inelastic scattering plays a significant role. Figure 2 shows the product rotational distributions in the O + HD → D + OH reaction at E_{total} = 0.6 eV. Distributions obtained in two manners are plotted together with that from an accurate CSDW (coupled-state distorted-wave) calculation.[7] We find that the accurate distribution cannot be reproduced without including

the effects of rotational inelastic half collisions. This fact means that effects of rotationally inelastic scattering are quite important in the systems with a large asymmetry like this one. In fact, the high-j_f peak seen in the distribution is due to the rotational rainbow effect in the final half collision.

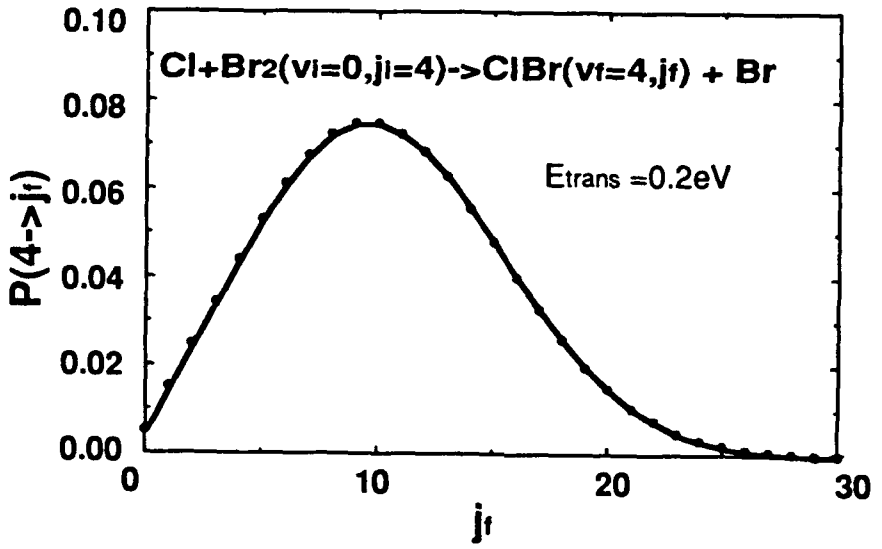

Fig. 3 : Product rotational state distribution in Cl + Br_2 ($v_i = 0, j_i = 4$) $\rightarrow$ ClBr($v_f = 4, j_f$) + Br at $E_{trans} = 0.20$ eV.

Because of its simplicity, the formalism is applicable to reactions in which a number of the rotational states are open and hundreds of partial waves contribute to the cross section. So far, calculations of a quantum mechanical rotational distribution in such a reaction would be practically impossible. Such an example is shown in Fig. 3 in the case of the Cl+Br_2 reaction at the collision energy of 0.2 eV.

[1] M. Nakamura: J. Chem. Phys. **95**, 4102 (1991).
[2] M. Nakamura: J. Chem. Phys. **96**, (1992) (in press).
[3] M. Nakamura and H. Nakamura: J. Chem. Phys. **90**, 4835 (1989).
[4] M. Nakamura and H. Nakamura: Chem. Phys. **143**, 271 (1990)
[5] J. N. L. Connor and W. J. E. Southall: Chem. Phys. Lett. **123**, 139 (1986)
[6] G.C.Schatz and A.Kuppermann: J.Chem.Phys.**65**,4668(1976)
[7] G. C. Schatz, J. Chem. Phys. **83**, 5677 (1985)

Computer Simulations on Interaction of Low Velocity Rare Gas Beams with Solid Surfaces

Masato Nakamura[†], Masaru Tsukada[*] and Masakazu Aono[**†]

[†] Aono Atomcraft Project, JRDC, ERATO, Itabashi-ku, Tokyo 173 Japan

[*] Faculty of Science, University of Tokyo, Bunkyo-ku, Tokyo 113 Japan

[**] RIKEN, Institute for Physical and Chemical Research, Wako, Saitama 351-01 Japan

Scatterings of rare gas atoms (ions) from solid surfaces have been extensively studied both experimentally and theoretically. So far, most of the works have been focused to either high energy ($E > 1$ keV) or thermal energy ($E < 0.1$ eV) regimes. There have been relatively small amounts of works on the hyperthermal energy (1 ev$< E <$100 eV) scatterings.

To clarify the mechanisms of beam-surface interactions in this energy region, the molecular dynamics (MD) calculation has been performed. As an illustrative example, scatterings of He atom from an oxygen-covered Rh(111) surface are presented here. Here each adsorbate O atom is assumed to locate above the first-layer Rh atom (A-site).

The calculation has been carried out systematically in the energy range of 5-50 eV at normal incidence. The interaction potential used in the computation is built by slightly modifying the pairwise additive form proposed by Garrison et al.[1] Surface is represented by a slab of seven layers of 25 atoms each and the periodic boundary condition is employed. There, we observe a drastic change of the profile of scattering particles by the variation of the collision energy.

Figure 1 (a)-(c) shows the intensity of scattered He particles as a function of the scattering angle θ and final energy E_f. The intensity is integrated over the azimuthal angle ϕ. The translational energies of the beam are set to be (a) 5 eV, (b) 15 eV and (c) 50 eV, respectively. The contours representing the equipotential surfaces of these energies are drawn in Fig. 2. From this figure, we can easily recognize that the surface behaves like a wall at low energy ($E = 5$eV) while it behaves as an aggregate of individual atoms at high energy ($E = 50$eV).

As shown in Fig. 1 (a), we have a very sharp distribution accompanied by the rainbow peaks[2] at low energy. One can interpret the dis-

tribution as scattered from a 'corrugated wall'; the both ridge line and rainbow position are well explained by the hard-cube model[3] or wash-board model.[4]

As increasing the energy, the profile changes drastically. When the collision energy is increased as much as 15 eV, both the penetrations from adsorbate layer to the first layer and the sputterings of adsorbate oxygen atoms begin to be observed. In this intermediate energy, we have double-scattering peaks in lower E_f region than the primary peak corresponding to the binary collision with an oxygen atom. The profile is somewhat similar to those observed by Tenner et al.[5] in K^+ scattering from W(100) surface at $E = 35$ eV.

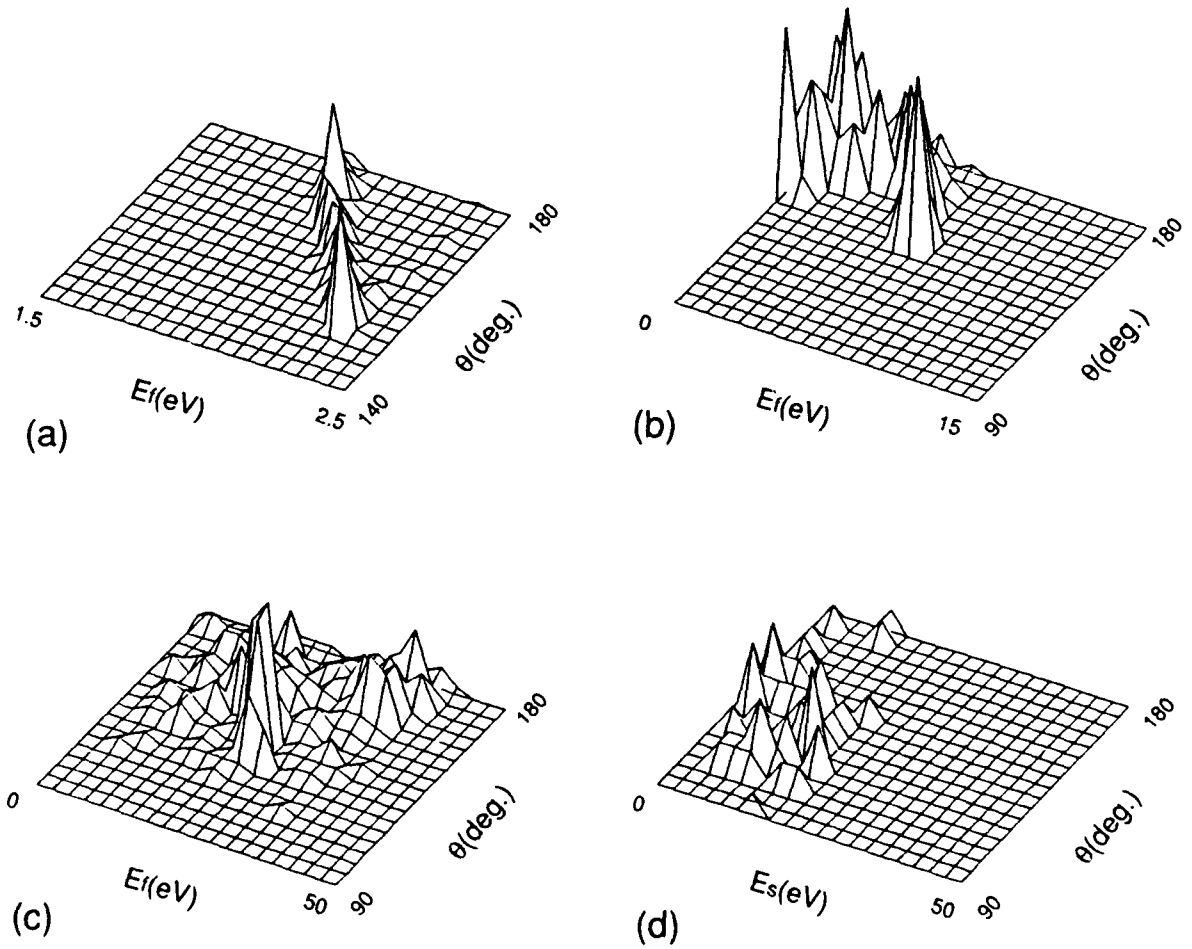

Fig. 1 : Intensity of scattered He particle from O/Rh(111) surface as a function of E_f and θ at (a) $E = 5$ eV, (b) $E = 15$ eV and (c) $E = 50$ eV. (d) Intensity of sputtered oxygen atoms by impacts of He beam of $E = 50$ eV.

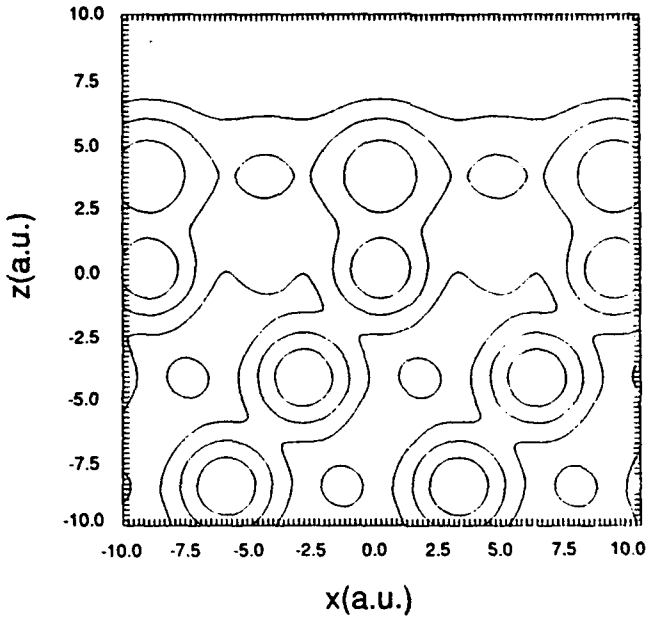

Fig. 2 : Equipotential energy map for He - O/Rh(111) system as a function of He position along the $\{1\bar{1}0\}$ azimuth. The potential contours are 5, 15 and 50eV.

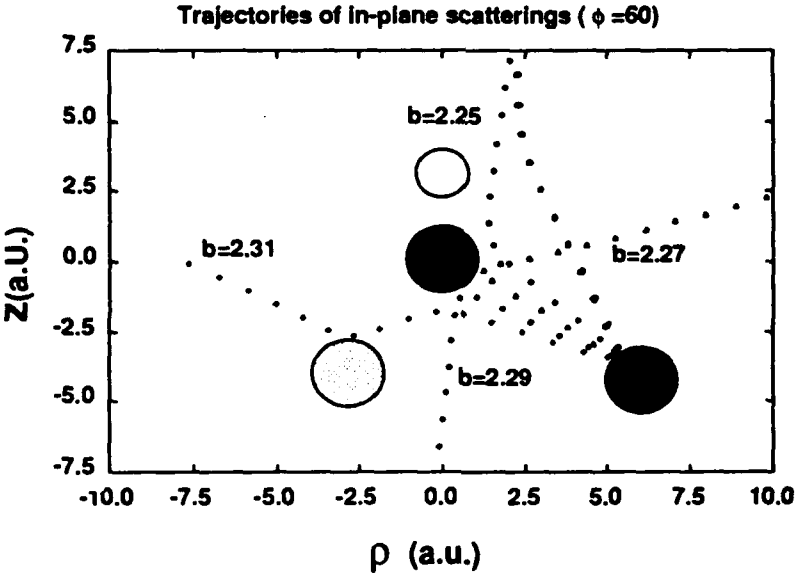

Fig. 3 : Variations of the trajectory of an incident He particle penetrated into the crystal for slight changes of impact parameter b . The white spot represents adsorbate oxygen atom; filled and hatched spots represent, respectively, in-plane and out-plane Rh atoms.

In high energy scattering (E = 50 eV), the distribution becomes much broader although we still observe the ridge corresponding to the binary collision and a huge rainbow peak. Lower mountains in higher E_f region are due to binary collisions with the second- and third- layer Rh atoms. On the other hand, a diffuse structure in lower E_f regions arises mainly from the multiple collisions inside the crystal. Figure 3 (a) shows the motions of a particle penetrated inside the crystal in the case of in-plane scattering for azimuthal angle $\phi = 60^{\circ}$. We see that a slight change of the impact parameter leads a drastic variation in the scattering angle due to the multiple collisions inside the crystal. This quasi-chaotic behavior produces a diffuse structure in low energy regions.

Due to the channeling, the intensity of scattered He particle at E = 50 eV is much weaker than that at lower energies. On the other hand, the intensity of sputtered oxygen particle becomes fairly strong. Figure 1 (d) represents an angle-energy distribution of sputtered O atoms at E = 50 eV. They have broad distribution because oxygen atoms are ejected by both direct and indirect impacts of He particles which are moving stochastically inside the crystal.

[1] B.J.Garrison, C.T.Reimann, N.Winograd, and D.E. Harrison: Phys. Rev. **B36**, 3516 (1987).

[2] A.W.Kleyn and T.C.M.Horn: Phys. Rep. **199**, 191 (1991) and references cited therein

[3] R. M. Logan and R. E. Stickney: J. Chem. Phys. **44**,195 (1966).

[4] J. C. Tully: J. Chem. Phys. **92**, 680 (1990).

[5] A.D.Tenner, K.T.Gillen, T.C.M.Horn, J.Los and A.W.Kleyn: Surf. Sci. **172**, 90 (1986), A.D.Tenner, R.P.Saxon, K.T.Gillen D.E.Harrison Jr., T.C.M.Horn and A.W.Kleyn: Surf. Sci. **172**, 121 (1986)

Photodissociation of Methyl Radicals at 193 nm

Simon W. North, Pamela Chu, Yuan T. Lee
Department of Chemistry, University of Califonia, Berkeley, California 94720

We have recently studied the photodissociation of methyl radical using photofragmentation translational spectroscopy (PTS) to determine the fate of CH_3 after excitation to the 3s rydberg state. Our interest was in understanding the dynamics the dissociation and the extent to which the elimination of molecular hydrogen (1) competes with atomic hydrogen elimination (2,3). Since methyl radicals are not known to undergo radiative relaxation from the 3s state we need only consider non-radiative processes. Following absorption of a 193 nm photon, CH_3 can dissociate via three thermodynamically accessible pathways[1],

$$CH_3 + 193\ nm \longrightarrow CH\ (X\ ^2\Pi_r) + H_2 \qquad (1)$$

$$CH_3 + 193\ nm \longrightarrow CH_2\ (X\ ^3B_1) + H \qquad (2)$$

$$CH_3 + 193\ nm \longrightarrow CH_2\ (a\ ^1A_1) + H \qquad (3)$$

The photochemistry of methyl radical upon 216 nm excitation of the $B\ ^2A_1' \leftarrow X\ ^2A_2''$ transition was recently investigated by Chen et. al.[2]. Broadening of the transition, corresponding to a subpicosecond excited state lifetime was attributed to either predissociation or rapid internal conversion[3,4,5]. Ab initio results[6] suggest that the potential energy surface from which the dissociation originated should be evident from the observed product branching ratios. These calculations predict that dissociation from the excited ($B\ ^2A_1'$) state of CH_3 should lead almost exclusively to CH_2 ($a\ ^1A_1$) + H. Although there exist some possible pathways to H_2 elimination from the excited state, the process is expected to be unfavorable[6]. RRKM analysis suggests that dissociation from a highly vibrationally excited ground state will favor production of CH ($X\ ^2\Pi_r$) + H_2 over CH_2 ($X\ ^3B_1$) + H [2].

Product time-of-flight distributions measured by PTS are consistent with the elimination of atomic hydrogen. Figure 1 shows the time-of-flight data of m/e 14 (CH_2^+) and m/e 13 (CH^+). The smaller fast peak in both spectra is from the photodissociation of residual azomethane, our methyl radical precursor, that dissociates via a sequential process at 193 nm to yield two methyl radicals with similar time-of-flight distributions[7]. The dissociation dynamics of azomethane have been taken into account in obtaining a total fit to the data. The forward convolution[8] fit to the m/e 13 spectrum was obtained considering contributions from only the CH_2 + H channel and residual azomethane dissociation indicating that, within the signal-to-noise, we are observing predominately H atom elimination. This is in agreement with the theoretical results if the dissociation occurs from the excited electronic state.

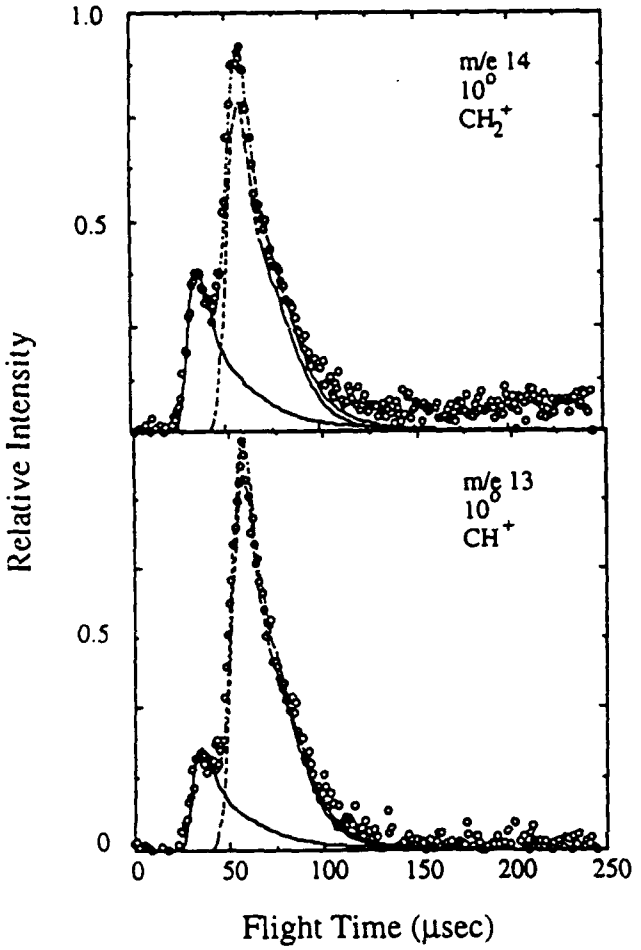

Figure 1. Time of flight spectra for m/e 14 and 13 at 10° The points are data and the solid line is the fit considering contributions from azomethane (CH_3 precursor) and the CH_2 + H channel.

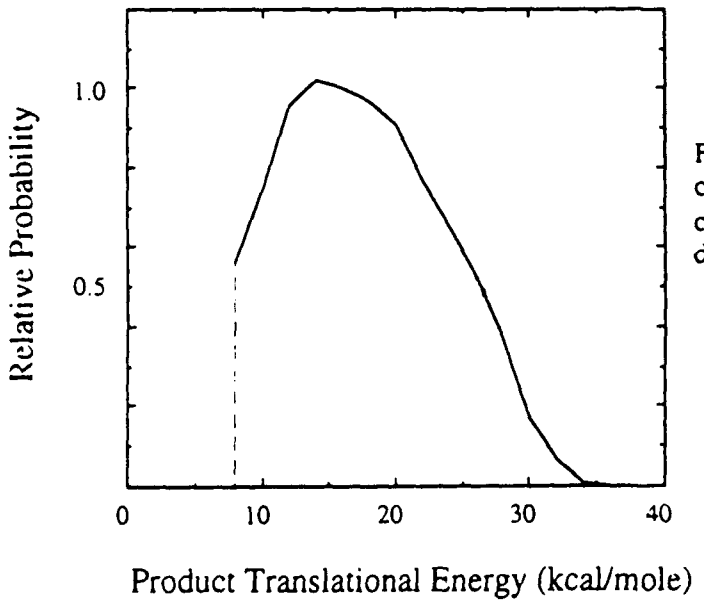

Figure 2. Translational energy distribution curve $P(E_T)$ for the CH_2 + H channel. The curve was used to fit the time of flight data shown in figure 1.

The translational energy distribution $P(E_T)$ used to fit the time-of-flight data for the CH_2 fragment is shown in figure 2. The distribution indicates that a significant release of the available energy from the dissociation goes into translation of the product fragments. This suggests that the dissociation occurs rapidly from the excited state potential energy surface. The $P(E_T)$ peaks at 15 kcal/mole and extends out to 34 kcal/mole. From the known thermodynamic heats of formation for CH_2 ($a\ ^1A_1$), H, and CH_3 ($X\ ^2A_2''$)[1] and the 34 kcal/mole maximum translational energy release, a C-H bond energy of $\leq 114 \pm 3$ kcal/mole was estimated. Because we are detecting the heavier fragments of the dissociation event, the recoil velocity of the products from the molecular beam is not sufficient to detect all the slower moving species. The dashed line in the $P(E_T)$ indicates the limit of our sensitivity to the product fragments with low translational energies (< 8 kcal/mole).

In summary, it appears that dissociation of methyl radical after excitation to the 3s rydberg state proceeds directly from the $B\ ^2A_1'$ state producing predominately CH_2 ($a\ ^1A_1$) + H. This is important not only in understanding the photochemistry of CH_3 but also in describing the A state photochemistry of NH_3, H_2O, and CH_4[6].

REFERENCES:

1. D.R. Stull, H. Prophet et. al., JANAF Thermochemical Tables, 2nd ed., Natl. Stand. Ref. Data Ser. Natl. Bur. Stand. (U.S. GPO, Washington, D.C. 1971)

2. P. Chen, S.D. Colson, W.A. Chupka, *Chem. Phys. Letters*, **147**(5), 466 (1988)

3. G. Herzberg, *Proc. Roy. Soc.*, **A 262**, 291 (1961)

4. S.G. Westre, P.B. Kelly, Y.P Zheng, L.D. Ziegler, *J. Chem. Phys.*, **94**(1), 270 (1990)

5. J. Danon, H. Zacharias, H. Rottke, K.H. Welge, *J. Chem. Phys.*, **76**, 2399 (1982)

6. H.T. Yu, A. Sevin, E. Kassab, E.A. Evleth, *J. Chem. Phys.*, **80**, 2049 (1984)

7. S.W. North, P. Chu, Y.T. Lee, unpublished results

8. X. Zhao, Ph.D. thesis, University of California, Berkeley, UCLBL Report No. LBL-26322 (1988)

LINE-TUNABLE SUPERSONIC BEAM IODINE LASER IN THE VISIBLE AND NEAR-INFRARED*

S.M. O'Shaughnessy and D.C. Lainé

Physics Department, Keele University,
Keele, Staffordshire, ST5 5BG, U.K.

The operation of a supersonic I_2 beam laser pumped with an argon ion laser was first reported by Hefter, Eichert and Bergmann [1] in 1985, with operation on the strong line B, v' = 43 -> X, v'' = 83 at 1338 nm. For this laser transition, the Franck-Condon factor is rather high, at 0.45. Subsequently, Jones and Lainé [2] extended the spectral range of the laser to cover 526 nm to 735 nm (v'' = 2 to 30, except v'' = 22, 27 and 29), with oscillation on 26 lines despite the fact that the Franck-Condon factors of these transitions are two orders of magnitude lower than for the 1338 nm line. Multiline power output was 45 mW and at 556 nm (v'' = 7) the output was 15 mW single line.

Operation of the iodine beam laser at 1338 nm clearly benefitted from the large Franck-Condon factor, and the inversion gain dominated over Raman gain as evidenced by the bidirectional laser output from the ring laser cavity employed. The preferred direction was the same as the laser pump beam. Hefter et al [1] obtained a backward-forward anisotropy ratio of the output power of 0.1. In the visible spectral region the lower Franck-Condon factors reduces inversion gain. However, the Raman gain is higher than at 1338 nm, since the ratio of the wave-vectors k_p/k_d (where the subscripts relate to pump and I_2 beam laser respectively) are close to unity. Therefore, the lower inversion gain which results from lower Franck-Condon factors is compensated by higher Raman gain.

The possibility of extending the operational wavelength of the I_2 beam laser to bridge the hitherto unexplored range 735-1320 nm in a beam laser is not immediately obvious, since (i) the FCFs are low (relative to that of the 1338 nm line) especially at wavelengths below 1105 nm (i.e. $< 8.17 \times 10^{-3}$ for v'' = 62 and below) although for some lines the FCFs grow in successively larger steps up to 60.31×10^{-3} (v'' = 81) at 1320 nm, and finally jump to 454×10^{-3} (v'' = 83) at 1338 nm and (ii) the Raman gain in this midband region will be significantly lower than in the visible. Here, the successful extension is reported of I_2 molecular beam laser operation over the spectral range 735-1338 nm with as many as 24 lines giving rise to laser oscillation so far.

The experimental system comprised of a ring resonator system with argon ion laser pumping of the I_2 beam, as shown in Fig. 1. Two sets of mirrors were used; the first to cover the spectral range 700-1000 nm, the second to cover 1000-1400 nm. The input couplers were dichroic with respectively 94% and 74% transmission of the 514.5 nm pump laser radiation for each of the two near-infrared ranges investigated. As mirrors, they possessed > 99.8% reflectivity over most of the spectral range covered. The other mirrors of the ring resonator were > 99.0% reflecting over the spectral range 654-963 nm and 99.5% over 1060 - 1400 nm, with slightly reduced values between these wavelength ranges.

To effect variable output coupling, a rotatable glass wedge placed intracavity was used as shown in Fig. 1 which could extract between 3.0

* Work supported by RSRE, Malvern, under Agreement No. 2098/09.

to 14.0% of the intracavity power. The I_2 beam nozzle was constructed as shown in Fig. 2, with type 316 stainless steel to withstand iodine corrosion. Two nozzle lengths have been used: 24 mm and 40 mm, with a slit spacing of 80 μm. The nozzle was demountable for cleaning purposes, and for slit width adjustment.

The demountable iodine reservoir, shown in Fig. 2, was made with type 316 stainless steel. In operation the nozzle temperature was set at 430 K and kept 30 K hotter than the reservoir to avoid nozzle clogging problems. The iodine was cryopumped by means of a liquid air trap placed under the molecular beam nozzle system, aided by a rotary pump. Up to 1.5 kg of iodine was used for a single experimental run of three hours. Typically three such runs could be made before the iodine needed to be reclaimed from the cryotrap, when pumping efficiency became somewhat impaired. The length of the expanding molecular beam perpendicular to the plane of the slit was as little as 2 mm, so a relatively high background pressure between 10^{-3} and 10^{-2} torr could be tolerated, which was reached at high beam flux.

In operation, the molecular beam iodine laser produced the results presented in Table 1. The number of molecular beam laser lines made to oscillate is actually greater than the number contributing to the laser power values listed when the laser cavity is heavily loaded for maximum power output. Single line tunability was obtained by the use of a birefringent filter. This enhanced the laser output power on single lines. Through the reduction of competition between lines, some of the weaker lines were also found to support laser oscillation. In the visible, the laser gain was so high that oscillation continued even when the cavity mirrors were grossly misaligned. TEM modes up to TEM_{80} for v'' = 7, 9, 11, and 15 appeared with one-plane cavity misalignment; indeed at the surface of the resonator mirrors, a ribbon of laser oscillation as wide as 1 cm was observed under these conditions. For v'' = 7 and 9, TEM_{88} modes could be produced with a two-plane misalignment, thereby producing a laser beam of effectively square cross section. On the strong 1338 nm line observed with an infrared viewer, the ribbon of laser oscillation was seen intracavity for one-plane misalignment.

Wavelength range (nm)	No. of osc. lines contrib. to output power	Pump power (mW)	Beam laser power (mW)	Optical conversion efficiency (%)
540- 680	7	800	64	8
740-1000	9	1000	50	5
1000-1340	14	1000	65	5

Table 1. Molecular beam laser I_2 laser: multiline operation. Output coupling 5-11% for maximum power output.

The relatively high power output of the I_2 molecular beam laser of between some 50-65 mW multiline, and up to 15 mW single line for the v'' = 7 line at 556nm as already noted was obtained with the 40 mm long source. Further power improvements are expected by careful optimization of the laser parameters. Power scaling seems to be feasible, since pump

power saturation at the one watt level does not occur. To date 50 lines have been observed to support laser oscillation over the spectral range 526nm to 1338nm.

References

[1] Hefter,U., Eichert,J. and Bergmann, K., Optics Communications 52 (1985) 330.

[2] Jones, D.R. and Lainé, D.C. XII International Symposium on Molecular Beams, Perugia, Italy, 29 May - 2 June (1991) 64.

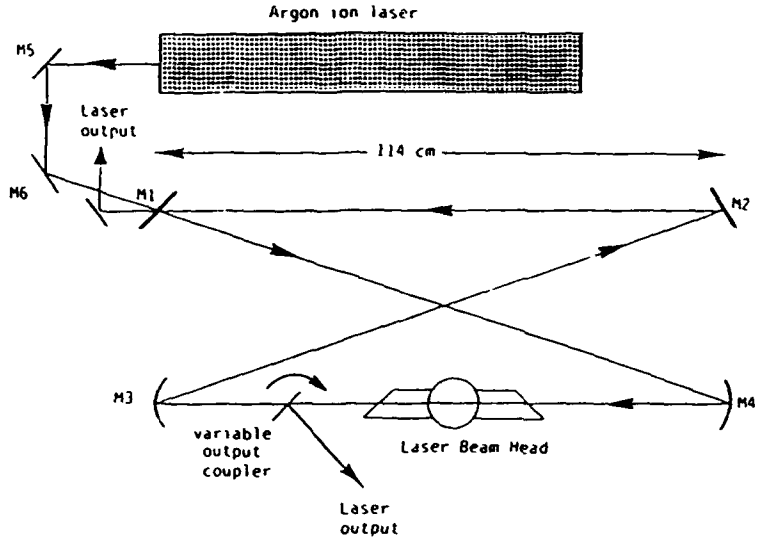

Fig. 1 Experimental scheme for the molecular beam iodine laser.

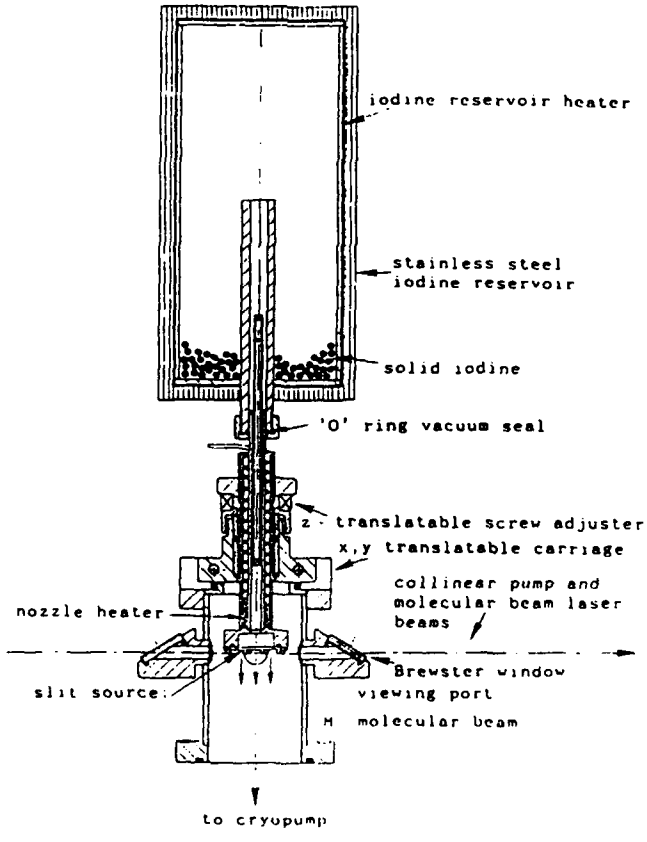

Fig. 2 Molecular beam I_2 laser head: experimental system.

ACCURATE NON-ADIABATIC COUPLINGS: PREDISSOCIATION OF H_3

A. E. Orel and J. L. Krause, Department of Applied Science, UC Davis, Livermore, California 94550 and B. H. Lengsfield III, Theoretical Atomic and Molecular Physics Group, Lawrence Livermore National Laboratory, Livermore, California, 94550.

Though H_3 is unstable in its ground electronic state, its Rydberg states are bound and decay either by predissociation or photon emission to the ground dissociative state. Recent experiments have studied this dissociation process yielding detailed data about the 2-body/3-body dissociation ratio[1] and the vibrational/rotational final state distributions of the H_2 product produced by predissociation of a selected Rydberg state.[2]

Theoretical studies of this system present special difficulties since the energy of the Rydberg states is quite high (7-8 eV above the dissociation limit) and because the three-body channel is open and quite important in the scattering. We have chosen to study this system using a time-dependent wave packet method. This proceeds by direct integration of the time-dependent Schrodinger equation,

$$i\frac{\partial}{\partial t}\Psi(r,R,\theta) = H\,\Psi(r,R,\theta)$$

Our first calculations were performed in two-[3] and later three-[4] dimensions. These calculations employ an initial wave packet at t=0 of the form:

$$\Psi_0(r,R,\theta) = F(r,R,\theta)\phi_0(r,R,\theta)$$

where $\phi_0(r,R,\theta)$ is the initial vibrational wave function on the Rydberg state surface, and $F(r,R,\theta)$ are the non-adiabatic couplings between the initial state and the dissociating states. In our earlier study of this process, the non-adiabatic couplings of the relevant states were assumed to be constant.

These couplings have been difficult to calculate accurately. Most treatments were approximate, or relied on finite difference methods which are difficult to apply for accurate wavefunctions, even for diatomic systems. Recently, a theory has been developed that allows the application of analytic gradient techniques to the study of

electronically nonadiabatic matrix elements.[5] Therefore, the derivative couplings to be calculated even when the electronic states are represented as large-scale multireference configuration-interaction (CI) wavefunctions.

We have applied these techniques to obtain the non-adiabatic couplings that induce predissociation of the Rydberg states of H_3. We have calculated energies and the dipole and non-adiabatic couplings between the two lowest states of H_3, and the 2s, 2p, 3s, and 3d Rydberg states. Varandas *et al* [6] have calculated the energies of, and the non-adiabatic coupling between, the two lowest states of H_3. Our results are in good agreement with their calculations.

The potential energy surfaces and the non-adiabatic couplings we calculated have been used to generate the correct initial state wave function for the time-dependent wave packet calculation. We will discuss the effects of these couplings on the predissociation from these states.

ACKNOWLEDGEMENTS

This work was performed under the auspices of the U.S. Department of Energy at Lawrence Livermore National Laboratory under contract number W-7405-Eng-48. Computer time was supplied by the San Diego Supercomputing Center.

REFERENCES

1. J. R. Peterson, P. Devynck, Ch. Hertzler, and W. G. Graham, submitted
2. P. C. Cosby and H. Helm, Phys. Rev. Lett., 61, 298 (1988)
3. A. E. Orel and K. C. Kulander, J. Chem. Phys., 91, 6086 (1989)
4. J. L. Krause, K. C. Kulander, J. C. Light, and A. E. Orel, J. Chem. Phys., XX, XXXX (1992)
5. B. H. Lengsfield III and D. R. Yarkony, J. Chem. Phys., 84, 348 (1986)
6. A. J. C. Varandas, F. B. Brown, C. A. Mead, D. G. Truhlar, and N. C. Blais, J. Chem. Phys., 86, 6258 (1987)

Vibrational Population Inversion in Aniline Scattered from Various Organic Surfaces.

Y. Paz, M. S. de Vries[a], and R. Naaman

Department of Chemical Physics
Weizmann Institute of Science, Rehovot 76100, Israel.

In general, vibrational excitation upon collision of a molecule with a surface is not an efficient process. When it occurs, it is attributed to coupling to an electron-hole deexcitation in the metal surface (1). In this process an electron is transferred from the metal surface to a colliding molecule having high electron affinity. The mechanism has been discussed theoretically (2), and formation of the anion was also found to be important for rationalizing the vibrational excitation in associative molecular desorption (3-5) and dissociative scattering (6). It has been demonstrated that when the surface is nonmetallic, no vibrational excitation is observed (7).

We investigated the scattering of aniline from amorphous C_{60} and C_{70} films, from single crystal C_{60} surfaces and from surfaces covered with organized organic monolayers. The scattered molecules were state selectively detected using resonant ionization. Vibrational population inversion was observed in some of the surfaces and it can be rationalized by the specific surface-molecule interaction.

Aniline was chosen for this investigation because of its relatively low ionization potential (7.7 eV) and its well documented spectroscopy. In addition, comparison is possible with previous studies in which the energy content in aniline scattered from various non metal surfaces has been documented (8).

The experimental setup has been described before (9). It consisted of a two stage differentially pumped beam machine. A pulsed nozzle (Jordan Inc.) with a nozzle diameter of 0.5 mm was used for producing 100 μsec long pulses of aniline seeded in various gases. Ar, He and H_2 were used as carrier gases in order to vary the aniline velocity. The organized organic monolayers were prepared by spontaneous absorption as discribed in references 8,9 from two type of amphiphiles: n-octadecyltrichlorosilane (OTS) and perfluorodecanoic acid (PFDA). The fullerenes were produced with the carbon arc method (10), followed by chromatographic separation. Amorphous surfaces were produced by sublimation of the purified material onto aluminum substrates, to create 1000 A films. Crystals of C_{60} about 1 mm in size, were grown from a supersaturated vapor, after successive sublimation steps. An unfocused laser beam was used for the Resonance Enhanced Two Photon Ionization (RETPI) process and a michrochannel plate monitored the resulting ions.

Figure 1 shows the RETPI spectra of the cold aniline in the molecular beam (A), aniline scattered from OTS (B), from PFDA (C), from LiF single crystal surface (D), aniline scattered from a C_{60} single crystal surface (111) (E). Two spectral features are especially important for our discussion, the origin and the I_1^1 bands. The I mode is the -NH_2. inversion mode which has a frequency of 40.9 cm^{-1} in the ground electronic state. Since the Franck-Condon factors for exciting the origin and the I_1^1 transition are about the same (11), the ratio (R) of the relevant two lines in the spectra represents the relative population of the I_1^1 state versus the ground state. For all fullerene surfaces investigated, the ratio, after correction for the laser intensity, was found to be 1.7 ± 0.5. For comparison, R is less than one for a LiF single crys-

tal surface. No change in the ratio could be observed when the incident collision energy was varied from about 100 meV up to 800 meV, or when the surface temperature was changed between 260K to 360K. Furthermore, the ratio did not depend on the flight time of the scattered molecules, as measured by changing the delay between the molecular beam pulse and the detection laser pulse. In the time of flight studies it was found that all molecules are scattered with a translational temperature identical to the surface temperature and independent of the collision energy. Some of the molecules may reside on the surface for up to ten microseconds. These observations, as well as the independence of the vibrational population on the collision energy and scattering velocity imply that the molecules have time to fully accommodate with the surface. It must also be noted that the experimental geometry was such that a large solid angle was probed by the detection laser; therefore any possible dependence of the ratio on scattering angle would not be observed. The large error bar for the ratio R results from the need to integrate the band contour in order to obtain the J independent ratio. The congestion of the spectral lines at the I_1^1 region did not allow a more precise evaluation of the ratio. The ratio of 1.7 is a conservative lower limit for the population ratio, deduced after all the experimental difficulties were taken into account.

In the organic monolayers a distinct difference in R is observed between the all alkyl chain (OTS) and the perfluorinated one (PFDA). While in the former population inversion is observed with a ratio of about 1.5, in the PFDA $R \approx 1$.

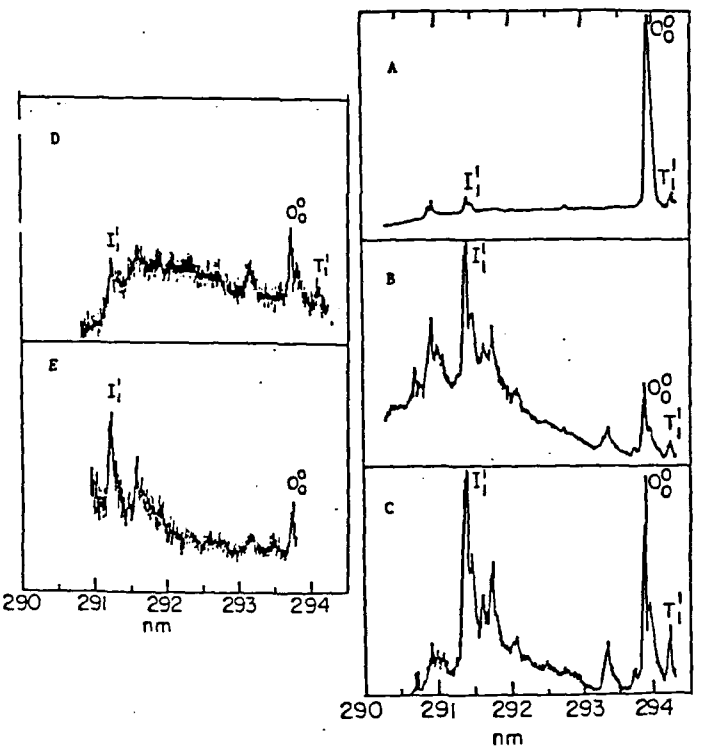

Figure 1: Resonance enhanced two photon ionization spectrum of aniline in (A) the cold beam (B) aniline scattered from OTS, (C) from surfaces covered with PFDA, (D) from LiF surface and (E) from C_{60} single crystal surface.

The results obtained with the fullerene surfaces, can be rationalized assuming a charge transfer process. Because of the relatively low ionization potential of aniline and the large electron affinity of the fullerene surfaces (e.g. for C_{60} $EA_{surface} = EA_{molecule} = 2.62$ eV) (12) a crossing between the covalent and the ionic interaction potentials can occur at a distance of about 3

angstroms from the surface. From this point in its approach, the molecule can transfer charge to the surface. The aniline cation is planner with a $^2B_1$ ground state (13), while the neutral species electronic ground state is A_1. Its inversion (I) mode has a symmetry of b_1 with a double minimum in the ground electronic state. Therefore conservation of symmetry requires that the ground state neutral will become an vibrationally excited ion, upon electron transfer to the surface. For the same reason, an ion in its ground state will produce a vibrationally excited neutral (in the v = 1 state) when neutralized.

When the colliding species leaves the surface, a second potential crossing occurs and neutrals are formed. If we assume that, when colliding with the surface, the vibrationally excited ions are quenched and return mainly to their ground state, then on the second crossing, the neutrals are formed in the vibrationally excited state. If the only effect of the surface is reversal of momentum, leaving the internal energy intact, then the initial vibrational population formed upon the first curve crossing remains when the molecule is leaving the surface. In that case, on reneutralization, occurring on the way out from the surface, the neutral aniline is formed in the ground vibrational state.

The probability for charge transfer P_c may depend on the orientation of the aniline relative to the surface. However if the molecule resides on the surface for a long time, relative to its rotational time, this probability approaches unity.

Regarding the electronic transition between the neutral aniline and its cation, we denote the probability for the transition between the covalent vibronic state, c, and the vibronic state of the ion, as a_{cf}. For simplicity we shall focus only on the vibrational ground state and the I(v = 1) mode, denoted as 0 and i, respectively. In what follows, f represents the fraction of excited cations that undergo vibrational relaxation to the ground state at the surface.

The ratio between the population in the two modes can now be written as:

$$R=\frac{P_c[a_{0i}a_{ii}(1-f)+a_{i0}(a_{00}+fa_{0i})]}{1+P_c[a^2_{00}+a^2_{0i}(1-f)+a_{0i}a_{00}f-1]} \qquad (1)$$

Since $P_c \approx 1$ and $a_{00} \approx a_{ii} < a_{0i} \approx a_{i0}$ and if $f \approx 1$, then the expression for R becomes:

$$R \approx \frac{a^2_{0i}f}{a^2_{0i}(1-f)+a_{0i}a_{00}f} \approx \frac{a_{0i}}{a_{00}} > 1 \qquad (2)$$

The above description indicates that even those molecules that are fully accommodated with the surface can come out vibrationally excited. In fact, with small a_{ii}, accommodation would be a prerequisite for excited products. That, in turn, implies that in the present experiment, the fraction f, of accommodated molecules is the same for all incident energies, as well as for all scattered velocities. This suggests a strong interaction between the fullerene surface and the aniline ion.

If the propose mechanism is correct, it indicates that the OTS surface has high electron affinity, while the electron affinity of the PFDA surface is smaller. The high electron affinity may be due to the silane head group and the ability of electrons to tunnel through the alkyl chain. One does expect that the barrier for tunneling will be higher in the case of perfluorinated surfaces.

The present work suggests a new mechanism that may result in extensive vibrational excitation in molecules desorbed or scattered from surfaces. This non-thermal vibrational population is

counter intuitive and provides an indication for strong interaction between the generally inert fullerene surfaces and molecules which are good electron donors.

Acknowledgements

This work was partially supported by the Fund for Basic Research, operated by the Israel Academy of Science and by the MINERVA foundation, Munich, Germany. The authors thank D.J. Elloway, and H.R. Wendt for help with growing crystals, and C.A. Brown for chromatographic separation of the fullerenes.

References

a) Permanent address: IBM Almaden Research Center, San Jose, CA 94120-6099 USA.

1) C.T. Rettner, F. Fabre, J. Kimman, and D.J. Auerbach, Phys. Rev. Lett. 55,1904 (1985).

2) See for example: J.W. Gadzuk, J. Chem. Phys. 86,5196 (1987).

3) R.P. Thorman, D. Anderson, and S.L. Bernasek, Phys. Rev. Lett. 44,743, (1980).

4) S. Bernasek and S.R. Leone, Chem. Phys. Lett. 84,401 (1981).

5) G.D. Kubiak, G.O. Sitz, and R.N. Zare, J. Chem. Phys. 83,2538 (1985).

6) E. Kolodney, A. Amirav, R. Elber, and R.B. Gerber, Chem. Phys. Lett. 111,366 (1984).

7) E. Kolodney, D. Baigh, P.S. Powers, H. Reisler, and C. Wittig, Chem. Phys. Lett. 145,177 (1988).

8) Y. Paz and R. Naaman, J. Chem. Phys. 94,4921 (1991).

9) S.R. Cohen, R. Naaman and J. Sagiv, J. Chem. Phys. 88,2757 (1988).

10) W. Kratschmer, L.D. Lamb, K. Fostiropoulos, D.R. Huffman, Nature 347, 354 (1990).

11) M. Quack and M. Stockburger, J. Mol. Spectrosc. 43,87 (1972).

12) F.H. Yang, C.L. Pettiette, J. Conceicao, O. Cheshnovsky and R.E. Smalley, Chem. Phys. Lett. 139,233 (1987).

13) J.T. Meek, E. Sekreta, W. Wilson, K.S. Viswanathan amd J.P. Reilley, J. Chem. Phys. 84,1741 (1985).

Fractal Structure in Cluster Growth

Anthony Pearson and Roger W. Anderson
Department of Chemistry, University of California, Santa Cruz, California 95064

Atomic and molecular clusters may grow by kinetically or thermodynamically controlled mechanisms, and it is important to have experimental techniques to distinguish them. X-Ray scattering which is is based upon the transform of pair correlation functions is one such method. We seek to understand these correlations at both short and long range distances. The pair correlation function at short range for any type of cluster can be expressed as r^{D-1}, as characterized by many workers,[1] where D is the fractal dimension. Thermodynamic control will yield compact crystalline or amorphous clusters which can be characterized by a constant density where D=3. However kinetic control may result in mass fractal clusters where D is less than 3. However the radius of gyration, R_g, is primarily determined by the long-range structure of the cluster. The short range correlation function can be modified to give long range information by introducing a cutoff function, f(r): $p(r) = r^{D-1}f(r)$.

The form of the pair correlation function associated with an aggregate can be probed with SAXS measurements. It can be shown[2] if f(r) approaches zero sufficiently quickly for large r, that the small angle scattering intensity decreases as q^{-D} in the fractal region: $1/R_g<q<1/r_0$, where r_0 is the minimum atom-atom distance. This simple dependence is only found for large clusters, and a mild or pronounced oscillation is often superimposed on the q^{-D} scattering.

Guinier scattering ($q \leq 1/R_g$) is often used to determine size and particle shape. The scattering in the Guinier region is always determined[3] by R_g:

$$I(q) \approx I(0)(1 - R_g^2q^2/3 + \cdots).$$

Where: $q = 4\pi\sin(\theta)/\lambda$.

Here we propose simple methods to extract the short range correlation information, D, and the long range information, f(r), from the SAXS of clusters with 10^3 to 10^5 atoms. The size (R_g or the spanning length, a) and the cutoff shape is also to be determined. This technique describes any monodisperse system of homogeneous spherically symmetric random aggregates.

We have calculated synthetic diffraction spectra for computer grown random clusters of size from 5000 to 100,000 atoms. We have used diffusion limited aggregation (DLA)[4], Eden[5], ballistic[6], and dielectric breakdown (DBM)[7] models for the encounters that lead to solid phase growth. The calculations use cubic lattices with unit cell lengths. The first three models use Monte Carlo methods to choose and follow the trajectories leading to growth. A DBM calculation solves the Laplace equation in two or three dimensions to generate the probabilities for the addition of particles.

For each cluster synthetic SAXS is calculated from the Debye sum, and we wish to find a continuous p(r) that will reproduce the data. The scattering is now determined by the expression:

$$I(q) = 4\pi \int_{r=0}^{\infty} p(r)\frac{\sin(qr)}{qr}dr.$$

We use four simple models for the pair correlation function to compare with the synthetic scattering. The first has an exponential f(r): $p(r) = r^{D-1}\exp(-r/\lambda)$, that has often been used by other workers[8,9]. The

parameter λ is a measure of the size of the cluster. The second has a Gaussian f(r): $p(r) = r^{D-1}\exp(-r^2/\xi^2)$. Here ξ is a size parameter. The third is the power law correlation function: $p(r) = r^{D-1}(1-r/a)^{\mu}$. Here the parameter "a" is the spanning length and μ is a shape parameter. The fourth is a modified power-law function where μ is constrained to be D–1.

These correlation functions result in analytic functions for the scattered intensity. The result for the exponential f(r) is

$$I(q) = \frac{4\pi\lambda^{D-1}\Gamma(D-1)}{q(1+q^2\lambda^2)^{(D-1)/2}}\sin((D-1)\tan^{-1}(\lambda q))$$

For the Gaussian function:

$$I(q) = \frac{4\pi\xi^D\Gamma(D/2)}{2}\,{}_1F_1(D/2;\,3/2;\,-\xi^2q^2/4).$$

For the power law function:

$$I(q) = \frac{4\pi a^{D-1}\Gamma(D-1)\Gamma(\mu+D)}{2iq\Gamma(\mu+2D)}[\,{}_1F_1(D-1;\,\mu+D;\,iaq) - {}_1F_1(D-1;\,\mu+D;\,-iaq)]$$

We fit the parameters of each pair correlation to the synthetic diffraction data by a nonlinear least squares. The best fits are presented in Figures 1, 3, and 4 for three computer grown clusters. Clearly the power law function always fits the Guinier region much better than the exponential function. Only the power law function can reproduce the oscillations in some of the synthetic diffraction patterns. In all cases, the commonly used exponential function provides the worst fits.

We make the following observations about the correlation functions. The simple exponential function gives the worst estimate for the shape of the correlation function and thus very poor size results. The Gaussian function has a better shape, but cannot yield the fine structure in the fractal region. These two models never give the proper fine structure due to the absence of a size cut-off in these models. The power laws we propose combine both size cut-off and shape as variable parameters and hence provides a good representation of the fractal region.

The power law function provides excellent values for R_g and the fractal dimension. The Table compares the fitted R_g that determined directly from the coordinates of the cluster. Although not shown in the Table the R_g values from the power law fit are always superior to those from the other models.

In discussing the idea of fractals and scale invariance it's important to note that any fractal, size, and shape information contained in the real-space coordinates through the actual pair correlation function must be preserved in the Fourier transform to q-space. The q-space of all the aggregates we have examined has been determined by the analog of a Fourier transform of their spatial pair correlation functions. This principle constitutes Debye scattering and all other scattering phenomena. We have shown by example that any of our pair correlation functions can reproduce the fractal dimension with q^{-D} scattering in the fractal region, for: $D < 3$. We also have shown that the Guinier scattering and transition regions before the fractal region are reproduced only with a realistic f(r) such as the power law function, regardless of the fractal dimension, or size of the structure. Due to Fourier reciprocity, we would expect that all models should behave similarly in the fractal region. In reality all models exhibit q^{-D} behavior except in the case of D=3, where the behavior is related to the first derivative of f(r) at r=0.

Figure 2 shows the actual averaged pair correlation function for the clusters and the correlation function for the best power law fits. Fractal structures with D near 3 can be almost exactly reproduced. Other fractal structures with much lower D (especially DLA) are well reproduced in the region

$r < R_g$, but not in the region $r > R_g$. It appears that only the integrated areas beneath the curves are similar and not their shapes. Part of the problem with the DLA and DBM (α=1) clusters is that our spherical symmetry assumption is problematic. Since there is no structure for very small q, all information about the very long range tail of the correlation function must be found in the oscillatory behavior just before the fractal region. This transition region is always evident to some degree for all clusters grown in three dimensional space, but never for clusters grown in two dimensional space.

Acknowledgement: We wish to thank the National Science Foundation for supercomputer time at Illinois and San Diego under grant CHE900022N.

References

1. P. Meakin, *Phase Transitions and Critical Phenomena*, (Academic Press, New York), Vol. 12, 1987.
2. T. Vicsek, *Fractal Growth Phenomena*, (World Scientific, Singapore, 1989) p. 74.
3. A. Guinier and G. Fournet, *Small-Angle Scattering of X-Rays*, (Wiley, New York, 1955) pp. 24-25.
4. T.A. Witten and L.M. Sander, Phys. Rev. B **27**, 5686 (1983).
5. M. Eden, in *Proceedings of the Fourth Berkeley Symposium on Mathematical Statistics and Probability*, Berkeley, Los Angeles, 1960, J. Neyman, ed. (University of California, Berkeley, 1961), Vol. IV, p. 223.
6. P. Meakin, J. Colloid Interface Sci. **105**, 240 (1985).
7. L. Niemeyer, L. Pietronero, and H. J. Wiesmann, Phys. Rev. Lett. **52**, 1033 (1984).
8. Ph. Mangin, B. Rodmacq, and A. Chamberod, Phys. Rev. Lett. **55**, 2899 (1985).
9. J. Teixeira, New J. Chem. **14**, 217 (1990).

Table
Power Law Pair Correlation Fits to Small Angle Scattering

Cluster	Size	D	a	μ	R_g (fit)	R_g (actual)
DBM α=0.0	5000	3.07	25.9	2.36	9.4	9.2
DBM α=0.1	5000	3.02	25.2	1.97	9.6	9.6
DBM α=0.25	5000	2.96	26.0	1.77	10.2	10.5
DBM α=0.5	5000	2.88	31.4	1.81	12.0	12.1
DBM α=0.6	5000	2.84	31.2	1.64	12.2	12.4
DBM α=0.75	5000	2.80	32.5	1.59	12.8	13.4
DBM α=1.0	5000	2.64	37.9	1.43	15.0	15.2
DBM α=0.0	100000	3.02	65.5	2.13	24.3	23.1
Eden	100000	3.00	59.7	1.91	22.9	22.6
DLA	10000	2.44	73.0	1.35	28.4	26.8
OFFDLA	10000	2.48	66.1	1.17	26.8	25.3
DLA	100000	2.52	128.9	0.91	55.3	58.8
Ballistic	100000	2.92	67.2	1.58	26.9	27.3
TSAW (Polymer)	18500	2.12	665.6	13.63	70.2	69.1
DLA-2D	10000	1.67	232.4	0.39	98.5	104.7
Eden-2D	10000	2.00	112.5	1.37	40.2	40.4

α for DBM is the power of the perimeter potential used to assign probabilities for addition of particles.

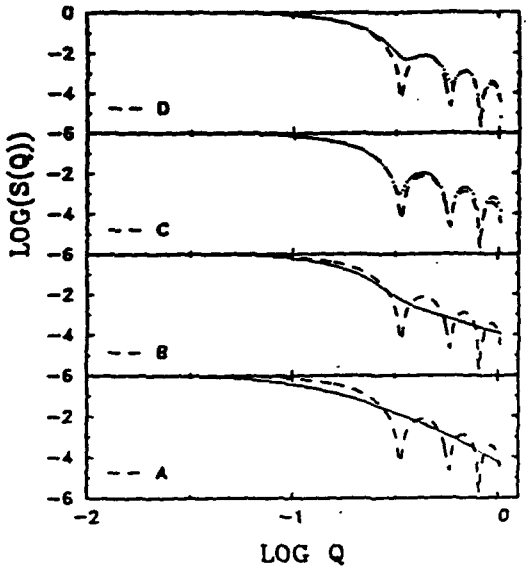

Fig. 1. Fits to the small angle scattering for a spherical cluster of 10000 atoms. The dashed line represents the Debye Sum scattering in each case. Panels A,B,C,D, present exponential, gaussian, power, and modified power fits.

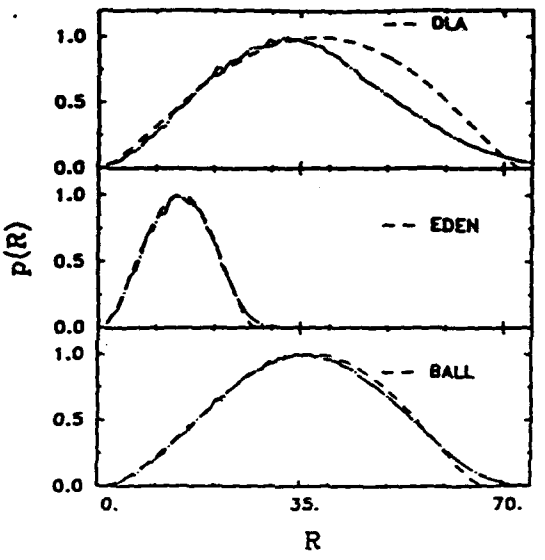

Fig. 2. Comparison of the fitted power law pair correlation function and the actual pair correlation function for the clusters shown in Figures 3 and 4, and a 100000 atom ballistic cluster. The actual function has been averaged over a small range of r to remove severe oscillations caused by the non-allowed distances on a cubic lattice..

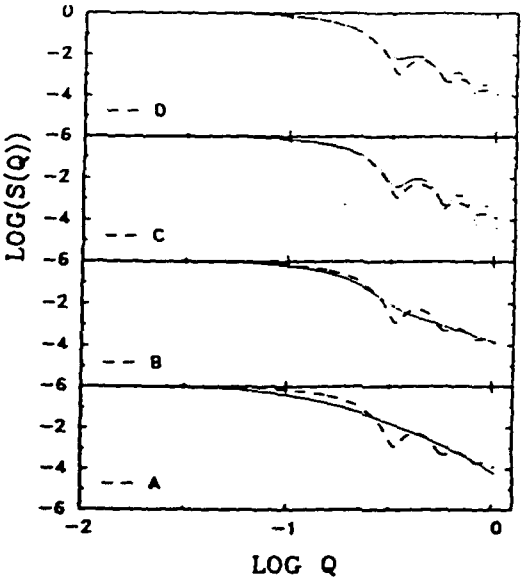

Fig. 3. As Figure 1 but for an Eden cluster of 10000 atoms.

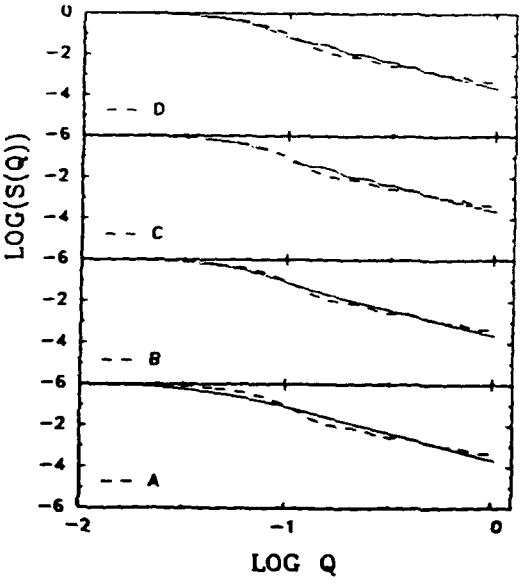

Fig. 4. As Figure 1 but for a DLA cluster of 10000 atoms.

The Structure of Acetaldehyde in its First Excited Singlet State: Experiment and Theory

J.M. Price, J.A. Mack, G.v. Helden, X. Yang, and A.M. Wodtke, Department of Chemistry, University of California, Santa Barbara CA 93106

The role of molecular structure is one of the central driving forces in modern chemical research and it is for this reason that so much of molecular spectroscopy has strived for rotationally resolved results, from which molecular structures can be experimentally derived. One class of molecules that has received a great deal of attention is the carbonyl-containing aldehydes and ketones. Because of their photochemical activity, the first excited singlet and triplet states are of substantial significance.

Surprisingly, one of the simplest examples of an aldehyde, acetaldehyde or CH_3CHO, has eluded spectroscopic analysis of its first excited electronic state. As for, essentially, all aldehydes and ketones, the UV absorption system for acetaldehyde is *assumed* to be $\pi^* \leftarrow$ n C-type ($\perp$) transition, similar to formaldehyde. This would give rise to a large extension of the CO bond in the excited electronic state, and a puckering of the CCOH portion of the molecule from a planar to a pyramidal structure. Low resolution data suggest that the excited state CCOH group is non-planar[1] and ab initio studies have indicated the nature of the excitation is analogous to formaldehyde[2]. In reality, there is little or no *direct* evidence for the $\pi^* \leftarrow$ n picture for acetaldehyde. Molecular beam excitation spectra have not produced the expected CO stretch progression in the excited state due to spectral congestion above $E_{vib} = 600$ cm^{-1} [3]. Additionally, because of the rotational congestion in the spectrum, rotationally resolved spectra have only been obtained for beam conditions where only a single rotational state is present. Molecular constants derived from such a spectrum are certainly not good enough for a structure determination.

As a prelude to Stimulated Emission Pumping experiments on acetaldehyde (presented at another poster in this conference), rotationally resolved fluorescence excitation spectra were recorded for acetaldehyde (H_3CCHO) and the fully deuterated analog (D_3CCOD) seeded in a pulsed molecular beam (1% in He). Under these conditions, the rotational temperature of the molecule is $\sim$2K for the J distribution and $\sim$11K in K-quantum number distribution.[4] Figure 1a shows a recently obtained rotationally resolved excitation spectra from our laboratory[5]. The temperature in the beam is warm enough that many rotational states are populated and the information content from this, as well as isotopic variants is expected to yield the structure. The experimental structural determination would unambiguously settle the question of the nature of the electronic excitation in this molecule. Figure 1c shows a calculated spectrum for a rigid asymmetric top molecule optimized fit to the experimental line positions. The standard deviation of the fit of the transition frequencies was $\sim$0.035 cm^{-1} and the electronically excited state rotational constants obtained from the fit are: A= 1.596 B= 0.334 C= 0.304 cm^{-1}. Figure 1b is the convolution of the calculation in figure 1c with a linewidth function to simulate the appearance of the experimental data. Preliminary results for the structure are given in table 1.

The data is most sensitive to the positions of the heavy atoms. A full analysis of the isotopic data is in progress and will lead to unambiguous results on the positions of the light atoms. Nevertheless, these results are already enough to conclude that the aldehydic Carbon must be pyramidal (since the CCO angle is much reduced from the 120° expected for sp^2 hybridization) and that the CO bond is significantly lengthened over that of the ground electronic

TABLE 1

Lengths and Angles[a)]	Experimental[b)]	Theoretical
C-O (Å)	1.331	1.36
C-C (Å)	1.530	1.50
C-C-O (degrees)	113.4	114.1

a) other structural parameters were held at the values determined by ab inito calculation
b) this structure gave A = 1.597 (1.596); B = 0.338 (0.334); C = 0.300 (0.304), compared to experimental values in parentheses

state (1.21 Å). This is the first experimental confirmation of the nature of the $\pi^* \leftarrow$ n C-type ($\perp$) nature of the acetaldehyde $S_1 \leftarrow S_0$ absorption.

In order to establish the uniqueness of this structure, ab initio calculations of the excited electronic state of acetaldehyde were carried out at the SCF level (Restricted Open Shell Hartree Fock, 6-31G(d,p) basis). Similar calculations on the excited state of propynal, which can be compared to experiment gave results accurate to within 0.03 Å in the bond lengths and 3° in the bond angles. The theoretical results for acetaldehyde are also shown in table 1. The comparison suggests the experimentally determined structure is indeed unique. Finally, figure 2 shows the theoretically calculated excited state geometry. Acetaldehyde exhibits a pyramidal structure for the CCOH portion of the molecule in the S_1 excited state in contrast to the planar ground state structure. The methyl hydrogens also move to a staggered configuration relative to the C=O bond from the eclipsed conformation in S_0. We conclude that the molecular orbital picture for the excitation of acetaldehyde is, as was expected, correct.

REFERENCES:

1. M. Baba, I. Hanazaki, U. Nagashima, J. Chem. Phys., 3938, **82**, (1985)

2. M. Baba, U. Nagashima, I. Hanazaki, J. Chem. Phys., **83**, 3514 (1985)

3. M. Noble, E. K. C. Lee, J. Chem. Phys., **81**, 1632 (1984)

4. NB: The use of the symmetric top "K" is not strictly correct for this asymmetric rotor, but has some meaning in the light of the fact that acetaldehyde is a near symmetric top with $\kappa = -0.9545$. κ is Ray's asymmetry parameter, and ranges from -1 to +1 for prolate and oblate tops, respectively.

5. J. M. Price, J. Mack, X. Yang, G. v. Helden, A. M. Wodtke (to be published)

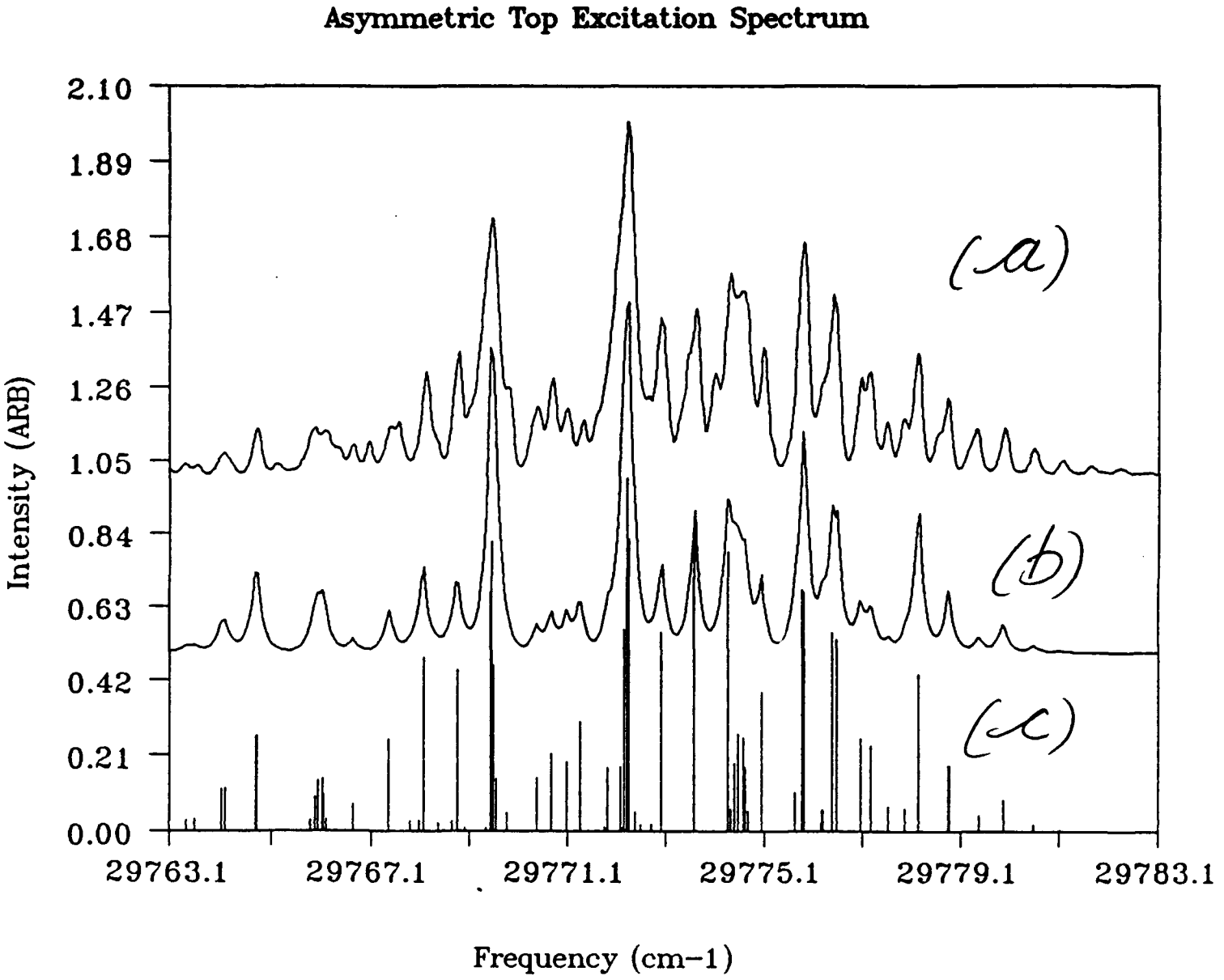

Figure 1: ***Rotationally Resolved Molecular Beam Excitation Spectrum of Acetaldehyde***: a) observed spectrum; c) stick spectrum determined by optimization with respect to twenty assigned transitions; b) convolution of stick spectrum with a realistic laser bandwidth function

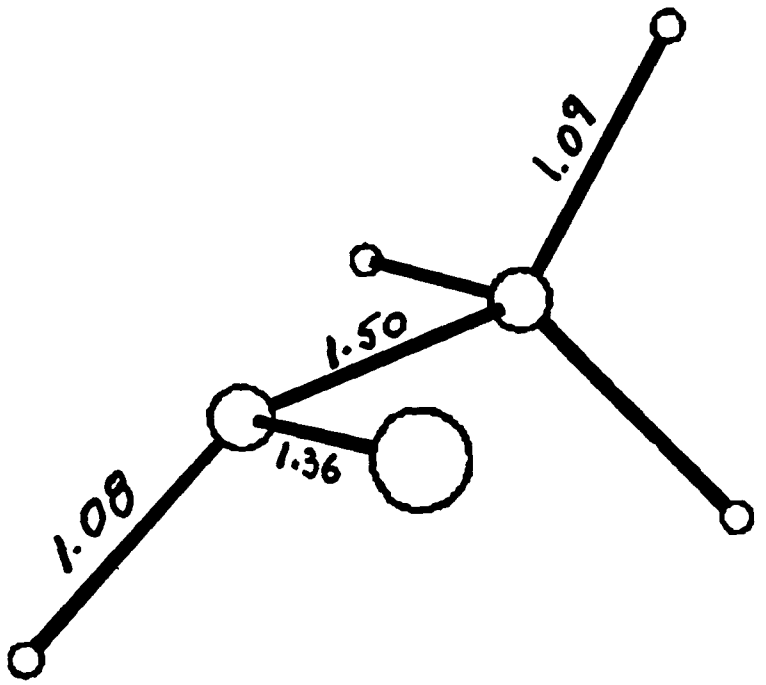

Figure 2: ***Theoretically Calculated structure for the first excited singlet state of acetaldehyde:*** Bond lengths are given in Å.

A MOLECULAR BEAM STUDY OF THE O_2/Ag(111) INTERACTION.

Age Raukema, Frieke M.A. Box and Aart W. Kleyn.
FOM-Institute for Atomic and Molecular Physics, Kruislaan 407, 1098 SJ Amsterdam, Netherlands.

The interaction between O_2 and a Ag(111) surface has been studied using a molecular beam with energies in the range from 0.4 to 1.7 eV (40 to 165 kJ mol^{-1}). Both scattering and sticking experiments were performed giving complementary information about the O_2/Ag(111) interaction. Earlier measurements in our group have shown an onset of surface corrugation [1,2] and a clear dependance of the initial sticking coeffient s_0 on incoming energy in the range mentioned above [3]. Thermal desorption measurements carried out by Campbell [4] showed that O_2/Ag(111) is a triple well system having a shallow physisorption state, a more strongly bound molecular chemisorbed state and an atomic chemisorbed state (dissociative chemisorption). Desorption from the latter state occurs at about 600 K.
Our aim is to deduce the dynamics of the interaction leading to both sticking and scattering. An important question is if the oxygen molecule sticks dissocitively upon impact with the surface or if it proceeds via one (or more) so-called precursor states as e.g. in the case of O_2/Pt(111) [5,6].

Our experimental system consists of a three stage differentially pumped molecular beam line connected to an UHV scattering chamber [7]. The Ag(111) crystal is mounted in the center of this chamber on a 2-axis goniometer. A differentially pumped quadrupole mass spectrometer, mounted on the rotatable top flange of the UHV chamber, can be rotated in the scattering plane around the crystal. A high speed chopper is mounted in the last stage of the molecular beamline which enables us to perform Time-Of-Flight (TOF) measurements. Our quartz nozzle can be heated resistively to about 1100 K. The measurements that will be presented were taken using a gas mixture of 2% O_2 and 98% He.

TOF measurements were taken using a chopperblade with 2 narrow slits (0.5% duty cycle). TOF-spectra were measured for the scattered molecules for incoming angles from 38° to 60°, measured with respect to the surface normal, and a whole range of scattering angles and of the beams not intersected by the crystal (direct beams). The experiments were carried out at a surface temperature of 600 K, just above the desorption temperature of dissociatively adsorbed oxygen [4,8]. A deconvolution scheme was carried out yielding a value for the mean beam energy before and after collision and a measure for the incident and (fraction of the scattered) flux. In this scheme the finite opening time of the mechanical chopper is explicitly taken into account. This

leads to lower values of the final energy of the scattered molecules than if the convolution effect is ignored, as was done by Spruit et al.

For the sticking measurements the 0.5% chopper was replaced by a 50% duty cycle chopper. We employed Thermal Energy Atom Scattering (TEAS) [9] to monitor the sticking coefficient. This means that we used the reflectivity of the lighter He carrier gas as a probe for the surface coverage (Mixed Beam TEAS) [3]. Because of the large scattering cross section of dissociatively adsorbed oxygen for He we are very sensitive to small surface coverages, an advantage because of the low sticking probability of oxygen on Ag(111). The initial slope of the He-reflectivity as function of surface coverage is a measure of the initial sticking probability. These experiments were carried out at a surface temperature of 400 K and for incoming angles from 32° to 60°.

Some experimental results for an incoming angle of 38° are shown in figure 1. Figure 1A shows the scattered flux as a function of scattering angle and normalized to the maximum of the scattered flux for E_i=0.59 eV. A tail in the distribution towards the surface normal is seen, becoming more pronounced for the higher incident energies. The scattered flux decreases also for these higher energies. This last effect is also shown in figure 1C and seems to have reached a minimum value above about 1.2 eV.
Figure 1B shows the relative energy after the collision. The points labeled 'conservation' show the behaviour if parallel momentum should be conserved. Clearly this is not the case at the scattering angles measured. The trend of decreasing energy with increasing scattering angle for the case of parallel momentum conservation is more or less present towards the lower impinging energies. This trend is reversed towards smaller scattering angles. The scattering angle of the turning point of this trend is increasing towards the higher incoming energies. For the highest energy the trend is fully reversed. This behaviour is an indication of increasing surface corrugation with increasing incident energies [10]. The observed decrease of the scattered flux in the scattering plane with increasing incident energy (figure 1A) is compatible with this explanation. An increase in corrugation will cause an increase of scattering out of the scattering plane; the solid angle in which the flux is scattered increases with increasing corrugation.
The values of the initial sticking coefficient shown in figure 1D are still preliminary but it seems to come up quite sharply at an incoming energy where the maximum corrugation is about reached. If a different part of the potential energy hypersurface (the repulsive wall of another well) of the O_2/Ag(111) would be sampled at the energy where the initial sticking coefficient comes up one would also expect a change in the scattering behaviour. This is not really the case and suggests a direct mechanism to dissociation rather than a mechanism via a

precursor at these energies. A measurement of the initial sticking probability at Θ_i=32° and E_i=1.29 eV shows no dependance on surface temperature in the range from 350 K to 600 K which also suggests a direct mechanism.

This work is part of the research program of the Stichting voor Fundamenteel Onderzoek der Materie (Foundation for Fundamental Research on Matter) and was made possible by financial support from the Nederlandse Organisatie voor Wetenschappelijk Onderzoek (Netherlands Organisation for the Advancement of Research).

References.

[1] M.E.M. Spruit, P.J. van den Hoek, E.W. Kuipers, F.H. Geuzebroek and A.W. Kleyn, Surf.Sci. 214 (1989) 591.
[2] M.E.M. Spruit, P.J. van den Hoek, E.W. Kuipers, F.H. Geuzebroek and A.W. Kleyn, *Phys.Rev.* B 39 (1989) 3915.
[3] M.E.M. Spruit and A.W. Kleyn, Chem.Phys.Lett. 159 (1989) 342.
[4] C.T. Campbell, Surf.Sci. 157 (1985) 43.
[5] A.C. Luntz, M.D. Williams and D.S. Bethune, J.Chem.Phys. 89 (1988) 4381.
A.C. Luntz, J. Grimblot and D.E. Fowler, Phys.Rev. B 39 (1989) 12903.
[6] C.T. Rettner and C.B. Mullins, J.Chem.Phys. 94 (1991) 1626.
[7] M.E.M. Spruit, E.W. Kuipers, M.G. Tenner, J. Kimman and A.W. Kleyn, J.Vac.Sci.Technol. A 5 (1987) 496.
[8] P.H.F. Reijnen, A. Raukema, U. van Slooten and A.W. Kleyn, Surf.Sci. 253 (1991) 24.
[9] B. Poelsema and G. Comsa, Scattering of Thermal Energy Atoms, Springer Tracts in Modern Physics, Springer-Verlag (1989).
[10] C.T. Rettner, J.A. Barker and D.S. Bethune, Phys.Rev.Lett. 67 (1991) 2183.

Figure 1A.
Scattered flux as function of scattering angle at an incoming angle Θ_i=38° and different incoming energies.
Figure 1B.
Relative energy after the collision as function of scattering angle at an incoming angle Θ_i=38° and different incoming energies.
Figure 1C.
Maximum scattered flux as function of incoming energy at an incoming angle Θ_i=38°.
Figure 1D.
Initial sticking coefficient as function of incoming energy at an incoming angle Θ_i=38°.

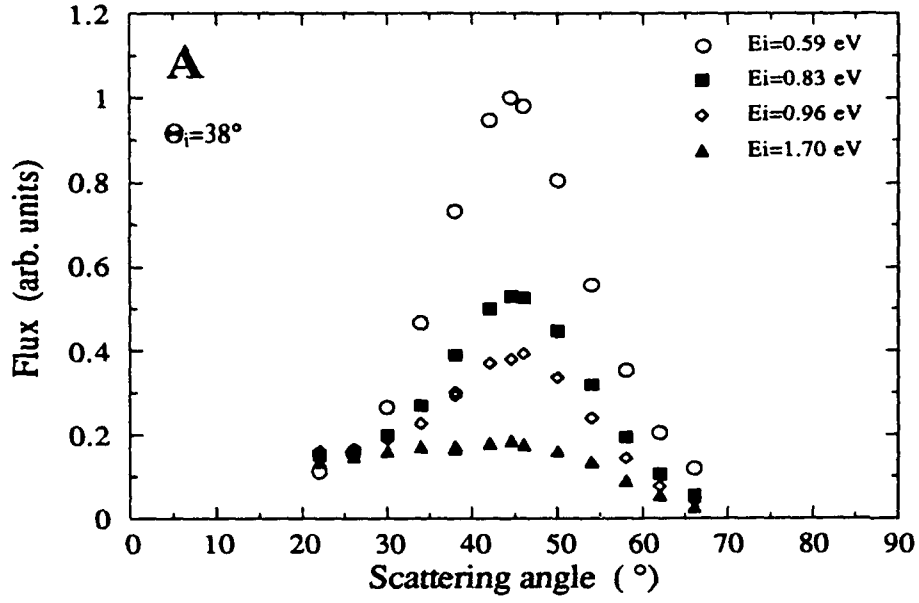
A
Θ_i=38°
Ei=0.59 eV
Ei=0.83 eV
Ei=0.96 eV
Ei=1.70 eV
Flux (arb. units)
Scattering angle (°)

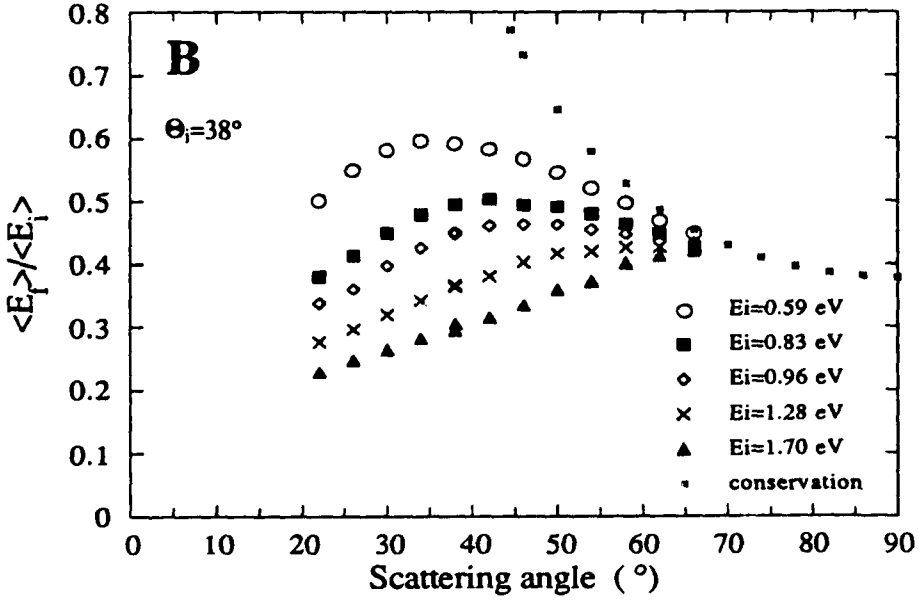
B
Θ_i=38°
Ei=0.59 eV
Ei=0.83 eV
Ei=0.96 eV
Ei=1.28 eV
Ei=1.70 eV
conservation
$<E_f>/<E_i>$
Scattering angle (°)

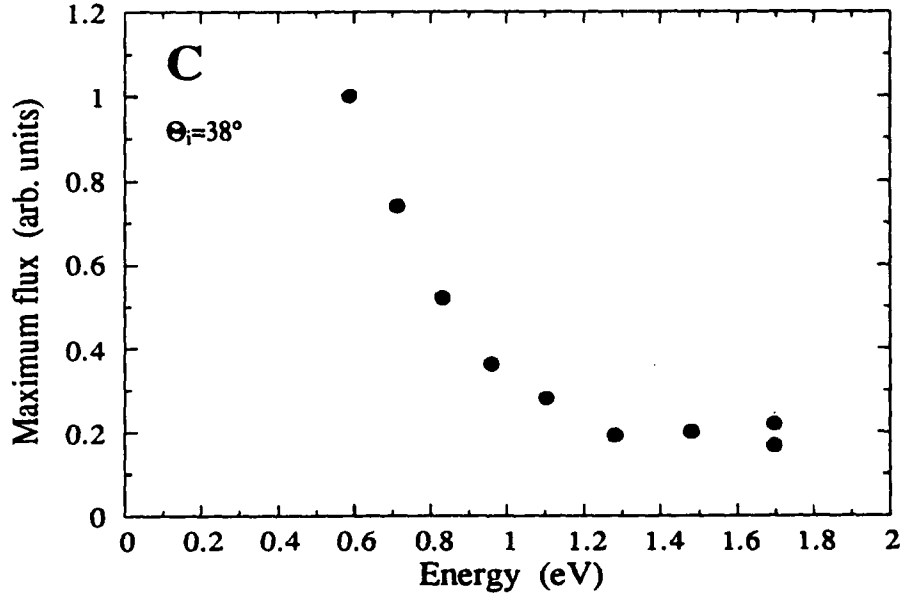
C
Θ_i=38°
Maximum flux (arb. units)
Energy (eV)

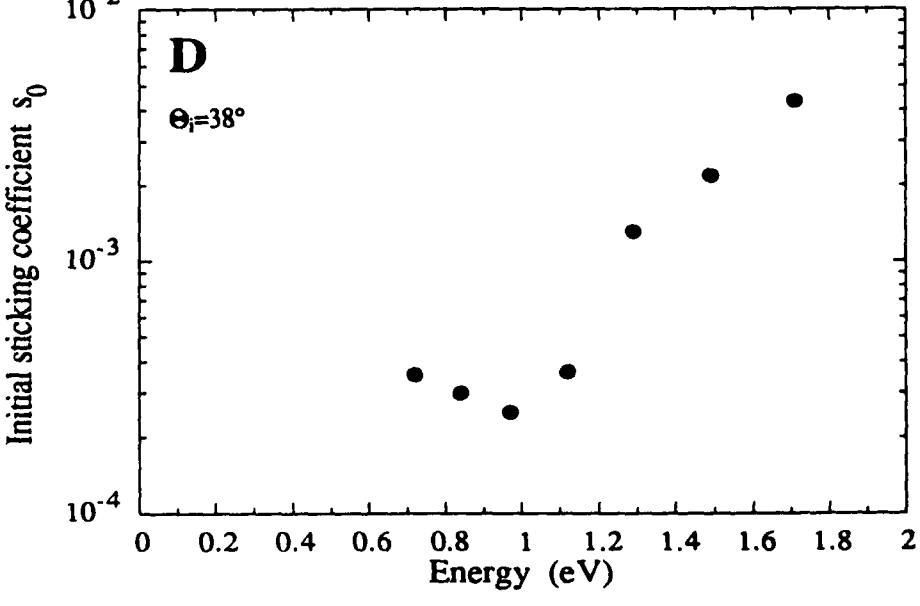
D
Θ_i=38°
Initial sticking coefficient s_0
Energy (eV)

INELASTIC SCATTERING of HYDROGEN FLUORIDE by ARGON: COMPARISON of EXPERIMENT to THEORY

Leslie J. Rawluk,[a] Mark Keil,[a] Millard Alexander,[b] Howard R. Mayne,[c] and J. J. Barrett[c]

[a] *Department of Chemistry, University of Alberta, Edmonton, Alberta T6G 2G2, Canada*

[b] *Department of Chemistry, University of Maryland, College Park, Maryland 20742*

[c] *Department of Chemistry, University of New Hampshire, Durham, New Hampshire, 03824*

We compare rotationally-resolved differential cross section (DCS) measurements for crossed-beam scattering of HF by Ar[1] to exact quantum scattering calculations on a variety of potential energy surfaces at a collision energy of 121 meV.

Experimentally, the initial HF rotational distribution is generated by a nozzle expansion, without further state selection. Its composition is mostly $J = 0$ and $J = 1$, with small admixtures for $1 < J \leq 5$. The DCS for each final state J' is measured using a stabilized cw HF chemical laser, in conjunction with a rotatable liquid He-cooled bolometer. The chemical laser operates in a single-mode configuration, and is locked onto the Lamb dip of the HF vib-rotational transition within the lasing medium. We obtain a power of $\sim 50-80$ mW within a linewidth of $\lesssim 15$ MHz, for a dozen lines in the $P_1(J)$- and $R_1(J)$-branches. These laser characteristics yield saturated absorptions for the scattered HF beam within the scattering apparatus, and may be maintained indefinitely. We estimate that the apparatus achieves a sensitivity of $\sim 5 \times 10^4$ HF molecules/sec per quantum state.

Theoretically, we complement the experimental results with fully-converged close-coupling (CC) calculations. State-to-state DCS's within $v = 0$ are calculated in the center-of-mass co-ordinate frame for each initial $0 \leq J \leq 5$ at four different collision energies required for properly averaging over the beam velocity and angular distributions. This requires 24 different total energies in the range of $82 - 242$ meV. The state-to-state DCS's are then transformed to the laboratory frame and summed over the distribution of initial rotational states, weighted by the measured rotational population. This accurately reproduces the experimental conditions of detecting one particular rotational state after the collision.

Currently, four different HF+Ar potential energy surfaces (PES) are available in the literature. Three of these are based primarily on spectroscopic observations of the HF•Ar van der Waals complex.[2-4] The fourth PES is based on Hartree–Fock calculations for the repulsive wall and is adjusted for agreement with the spectroscopic observations.[5] We centre our efforts on the Hutson (1992) surface, which is presumably the most accurate in its attractive well region.

The experimental measurements and the CC calculations using the Hutson (1992) PES are presented below. The calculations reproduce all qualitative features of the experiment:

— the strong forward peak for all J', entirely from elastic scattering for $J' > 1$;
— the broad shoulder at $\sim 30°$ for $J' = 0$;
— the flattening out of the wide-angle DCS's for $J' = 2$ and 3;
— the increase in the DCS's at high angles for $J' = 4$ and 5.

The scattering experiments complement the spectroscopic results in providing sensitivity to the repulsive wall of the PES, which would appear to require improvements for better quantitative agreement, especially for $J' = 4$ and 5.

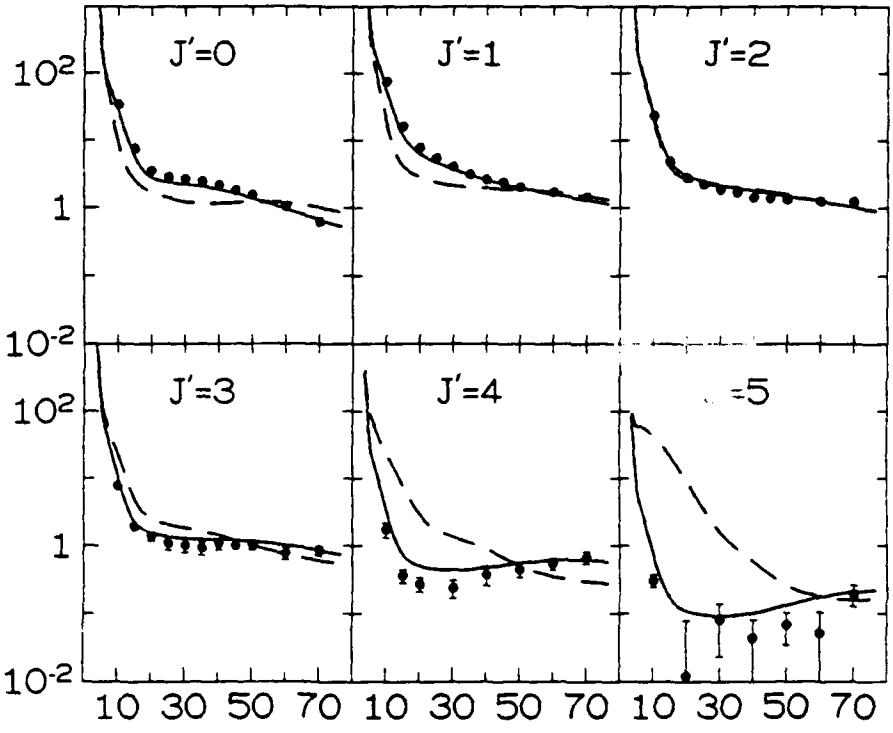

HF+Ar experimental and calculated DCS's (Å²/sr) vs. lab angle (deg); PES is Hutson (1992)[4]. Dashed line is IOSA; solid line is CC; data points from Rawluk et al.[1] Experimental data is least squares normalized to the CC calculation.

Fully-averaged dynamical calculations using the infinite order sudden approximation (IOSA) are also presented in the figure above. The IOSA is unable to reproduce any of the above features (agreement for $J' = 2$ is fortuitous), as might be expected for a system with such a large rotational constant. For example, the $J = 0 \rightarrow J' = 5$ transition requires transfering $\sim 60\%$ of the available energy, and is clearly detrimental to the IOSA.

We have also completed similair comparisons for the Douketis *et al.*[5], Hutson-Howard[2] and Nesbitt *et al.*[3] potential energy surfaces. At the IOSA level, we have not seen clear distinction as to the quality ranking for these four potentials in predicting the experimental data. However, at the CC level the Hutson (1992)[4] potential definitely provides the best agreement to the experiment. Details will be provided in the poster.

The CC results also provide insight into the composition of the experimental signals. Firstly, it is gratifying that we are reproducibly measuring DCS's as small as $\sim 0.2\,\text{Å}^2/\text{sr}$. Secondly, although the measured DCS's do not distinguish between elastic and inelastic contributions, the CC calculations do, and their relative contributions may be ascertained from the figure below.

The left-hand panel of the figure below shows that the elastic $J = 4 \rightarrow J' = 4$ DCS exceeds any inelastic DCS at all scattering angles. However, the right-hand panel, where the state-to-state DCS's are weighted by the rotational distribution in the incident HF beam, the elastic contribution dominates only at small scattering angles, dropping to only $\sim 10\%$ at the widest angles. The contribution of $J > 5 \rightarrow J' = 4$ DCS's is completely negligible, as evident by the $J = 5 \rightarrow J' = 4$ DCS contributing $< 2\%$ at all scattering angles. Hence, our calculations are fully-converged with respect to initial rotational states. Over half of the DCS at high scattering angles is due to the $J = 0 \rightarrow J' = 4$ and $J = 1 \rightarrow J' = 4$ transitions. Transferring almost 40% of the available kinetic energy, these highly inelastic collisions probe the repulsive wall. This observation is likely the first time a rotational rainbow is observed for transitions on such an attractive PES [$\epsilon(0°) = -27.3\,\text{meV}$].

We are currently conducting fully-averaged classical trajectory simulations for the HF+Ar scattering experiment in attempts to elucidate the origin of the broad shoulder at $\sim 30°$ for $J' = 0$ and the increase in the DCS's at high angles for $J' = 4$ and 5, two of the most prominent features of the experimental DCS's noted earlier.

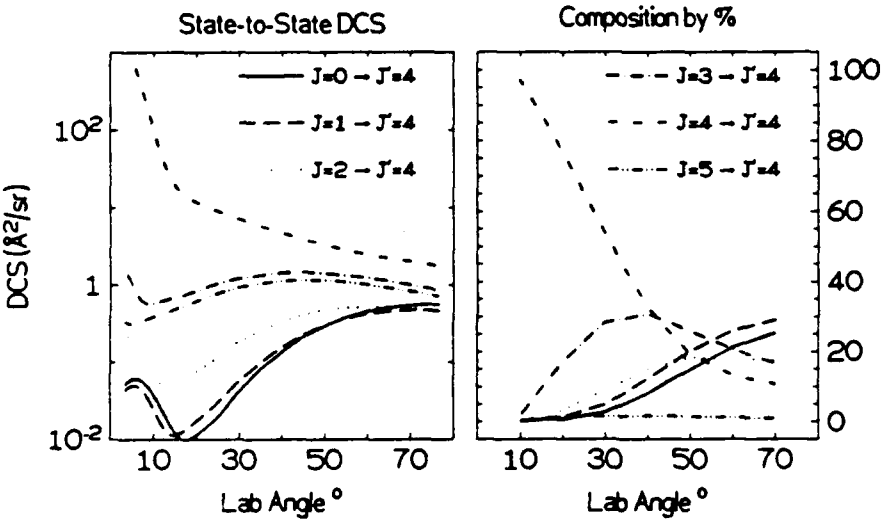

CC results decomposing the calculated $J' = 4$ DCS on the Hutson (1992) surface into its state-to-state components, fully averaged and transformed into the laboratory frame. Inelastic maxima below $\sim 10°$ are kinematic in origin, and are not present in the centre-of-mass DCS's. The DCS's in the left-hand panel have been weighted by the initial rotational population to obtain the DCS's shown in the right-hand panel.

References:

1. L. J. Rawluk, Y. B. Fan, Y. Apelblat, and M. Keil, *J. Chem. Phys.* **94**, 4205 (1991).
2. J. M. Hutson and B. J. Howard, *Mol. Phys.* **45**, 791 (1982).
3. D. J. Nesbitt, M. S. Child, and D. C. Clary, *J. Chem. Phys.* **90**, 4855 (1989).
4. J. M. Hutson, *J. Chem. Phys., in press* (1992).
5. C. Douketis, J. M. Hutson, B. J. Orr, and G. Scoles, *Mol. Phys.* **52**, 763 (1984).

Rotationally Resolved Circular Dichroism in Photoelectron Angular Distributions from NO($A^2\Sigma^+$)

Katharine L. Reid, David J. Leahy, Hongkun Park, and Richard N. Zare
Department of Chemistry, Stanford University, Stanford, CA 94305

For some time we have been concerned with probing the detailed dynamics of molecular photoionization. To this end, we have performed (1+1') resonance-enhanced multiphoton ionization (REMPI) on the NO molecule and observed photoelectron angular distributions with sufficient energy resolution to determine the rotational states of the ion formed in the photoionization process [1,2,3]. Our experimental apparatus consists of a molecular beam of NO which is perpendicular to the direction of our counter propagating laser beams. To obtain sufficient energy resolution (~2.5 meV), we generate slow photoelectrons and detect them at the end of a 50 cm field-free time-of-flight tube. To map out the angular distributions, we rotate the laser polarization vectors.

In our previous experiments both the excitation laser and the ionization laser were linearly polarized; in the work presented here, the ionization laser is circularly polarized. This provides us with additional information because we are now sensitive to the handedness of the photoionization process. This is illustrated in Fig 1 where we show photoelectron angular distributions for three ion rotational states after photoionizing NO($A^2\Sigma^+$, v=0, N=22).

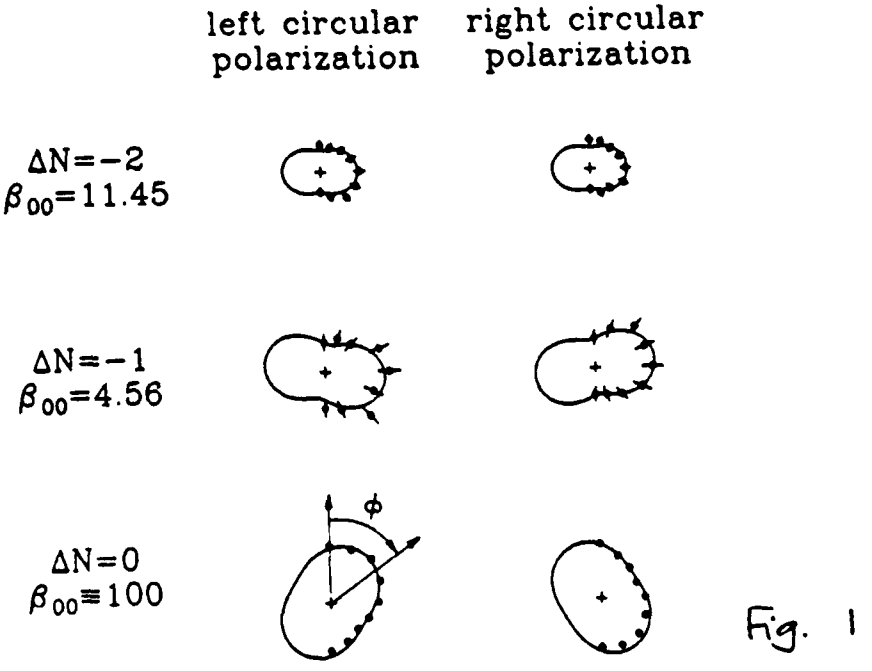

Fig. 1

Here we see that we observe different angular distributions depending on whether we ionize with left circularly polarized or right circularly polarized light. In other words there is a circular dichroism in the angular distributions [4].

The general expression for the angular distribution of photoelectrons can be written as follows:

$$I(\theta,\phi) = \sum_{LM} \beta_{LM} Y_{LM}(\theta,\phi) \tag{1}$$

where

$$\beta_{LM} = \sum_{\ell\lambda\ell'\lambda'} C_{\alpha\ell\lambda\ell'\lambda'} r_{\ell\lambda} r_{\ell'\lambda'} \left[\cos(\eta_{\ell\lambda} - \eta_{\ell'\lambda'}) + i\sin(\eta_{\ell\lambda} - \eta_{\ell'\lambda'})\right]. \tag{2}$$

The $r_{\ell\lambda}$ and $\eta_{\ell\lambda}$ quantities in Eq. (2) are the dynamical parameters of interest; they represent the magnitude and the phase of the radial dipole matrix elements that connect the intermediate level to each photoelectron partial wave $\ell\lambda$. The $\sin(\eta_{\ell\lambda}-\eta_{\ell'\lambda'})$ terms in Eq. (2) only arise when circularly polarized light is used. Only in this instance are we sensitive to the *sign* of $(\eta_{\ell\lambda}-\eta_{\ell'\lambda'})$.

Using Eq. (2), we fit all our angular distributions together to determine the values of $r_{\ell\lambda}$ and $\delta_{\ell\lambda-\ell'\lambda'}\equiv(\eta_{\ell\lambda}-\eta_{\ell'\lambda'})$. These compare well with the ab initio calculations of Rudolph and McKoy [5]. This has enabled us to make a "complete description" of the photoionization of $NO(A^2\Sigma^+)$, by which we mean that we are able to predict all quantities of the final system state, such as the alignment of the NO^+ ion.

[1] S.W. Allendorf, D.J. Leahy, D.C. Jacobs, and R.N. Zare, *J. Chem. Phys.* **91**, 2216 (1989).
[2] K.L. Reid, D.J. Leahy, and R.N. Zare, *J. Chem. Phys.* **95**, 1746 (1991).
[3] D.J. Leahy, K.L. Reid, and R.N. Zare, *J. Chem. Phys.* **95**, 1757 (1991).
[4] R.L. Dubs, S.N. Dixit and V. McKoy, *Phys. Rev. Lett.* **54**, 1249 (1985).
[5] H. Rudolph and V. McKoy, *J. Chem. Phys.* **91**, 2235 (1989).

PROTON TRANSFER IN MIXED MOLECULAR CLUSTERS

Ch. Riehn, Ch. Lahmann, B. Brutschy and H. Baumgärtel.
Freie Universität Berlin
Institut für Physikalische und Theoretische Chemie
Takustr. 3, D 1000 Berlin 33, Germany

Introduction, Experimental

Mixed molecular clusters, consisting of a chromophore A and a small number of solvent molecules B, associated as $A:B_n$, may show a complex variety of relaxation reactions after ionization /1/ . Among these are:

- -evaporative loss of neutral molecules (van der Waals-fragmentation)
- -dissociative electron or proton transfer (dET,dPT,resp.)
- -ion-molecule reactions /2/ .

The efficiency of different reactions competing in a given system depends not only on the chemical nature of the components but also strongly on the size of the cluster/3/. Suitable energetics provided, there are remarkable changes in the product yield distribution already in small clusters with $1<n<3$. These systems are preferably analyzed with the described method, because the relationship between the precursor cluster and its products can be assigned. Fig. 1 gives a schematic representation of the experimental setup. Mixed clusters are produced in a supersonic beam expansion using the

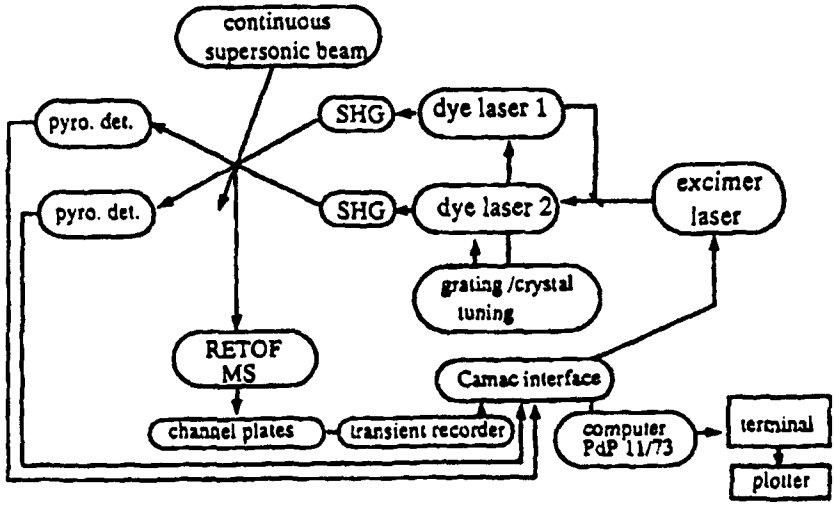

Fig. 1
Scheme of the experimental setup
RETOF MS = reflectron mass spectrometer; SHG = frequency doubling crystals; pyro. det. = energymeter

seeded beam technique. The gas mixing unit provides control over the beam composition within certain limits and is used to suppress larger clusters ($n < 5$). The aggregates are ionized by one color resonant two photon ionization, "1C-R2PI" of A and mass analyzed by a reflectron-type time-of-flight mass spectrometer (RETOF). The ion yield curve (R2PI spectrum) of an ion is measured by tuning the laser in the vincinity of the $S_1 \leftarrow S_0$ transition of A at low intensity ($I = 10^4 - 10^5$ W/cm^2). The R2PI spectra are recorded with a 200 MHz transient recorder and the ion yield values are normalized to the square of the laser intensity. Since the absorption of the first photon is a resonant process, it represents the absorption spectrum of the chromophore A, characteristically modified by the influence of the solvation environment. Product ions from chemical reactions in the ionized cluster show the same absorption peaks in the R2PI spectrum as their precursor clusters, allowing to assign reactant-product relationships by their identical spectroscopic fingerprints.

Results

We report here on a study of systems, that show dPT after R2PI among the other reactions mentioned above.

Proton transfer is probably the most important class of reactions from the standpoint of thermochemistry. We found two mechanisms leading to the occurence of protonated product ions. In the case of fluorobenzene/ammonia-clusters electron transfer from the ionized chromophore to the solvent moiety occurs as the first step, followed by an intrasolvent proton transfer. This is a general process in clusters with a larger number ($n > 2$) of solvent molecules. The second type of protonation reactions takes place for instance with toluene/ ammonia - clusters. Here the cation may act as an acid, inducing direct proton transfer to the solvent. This process starts already in the smallest possible mixed cluster, the (1:1)-aggregate.

The dissociative proton transfer (dPT) reaction may be summarized as follows:

$$R^{\cdot}H^+ * B_n \longrightarrow (R^{\cdot} * B_nH^+) \longrightarrow R^{\cdot} + B_nH^+$$

Besides the evidence provided by analyzing the spectroscopic fingerprints of the relevant species, both reaction types can clearly be distinguished by using deuterated compounds/3 /.

If both, a chlorine and a methyl-group are present in the cation as in the case of chlorotoluene$^+$, direct proton transfer competes with a nucleophilic substitution reaction. In the latter case, o-methylaniline$^+$ and HCl are produced. Fig.2 shows the TOF mass spectrum of the o-chlorotoluene/ ammonia cluster system. Besides reaction products from nucleophilic substitution (m/z=107), one observes a relatively intense peak at m/z=18 (protonated ammonia), which corresponds to m/z=21 when the same spectrum is measured using ND_3.

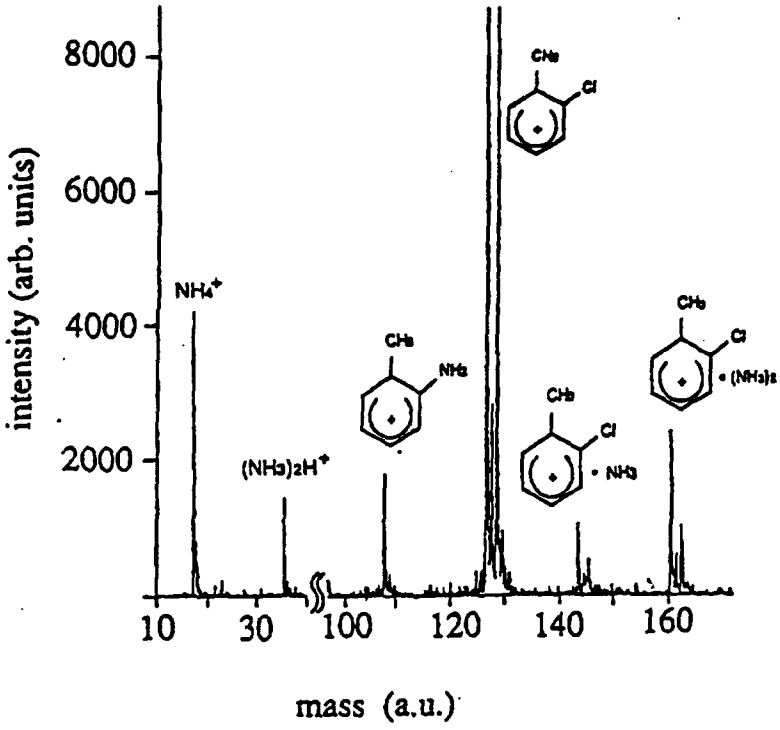

Fig.2
TOF-mass spectrum of an o-chlorotoluene/ ammonia/He expansion

Fig.3 shows the 1C-R2PI spectra of the most important ions from Fig.2. The spectrum of the monomer (Fig.3a) shows a dominant ν_{00} band and some tiny, blue shifted bands. The latter are tentatively assigned, as in the case of toluene, to the rotation of the methyl-group/4/. Comparing the spectroscopic fingerprints, it turns out, that bands 2-6 of the (1:1)-cluster have coincident peaks in the spectrum of the protonated ammonia cation and also tiny ones in the spectrum of o-chloroaniline+. The relative intensities, displayed in arbitrary units, indicate, that the proton transfer plays the major role, compared to the low efficiency of the substitution reaction.

Looking at bands 7-9 assigned to the (1:2)-cluster, the situation changed remarkebly: The "fingerprints" in the spectra of the protonated ammonia dimer and of o-methylaniline are almost the same and do not correspond to the spectrum of the detected (1:2)- clusterion (not shown in Fig.2).

From these results, it can be deduced, that the (1:2)- cluster decays quantitatively and the

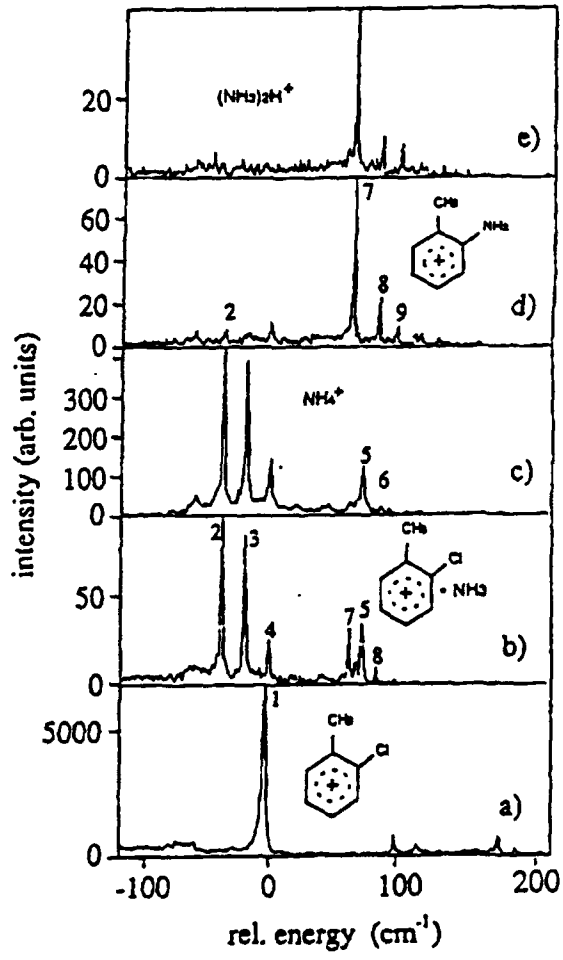

Fig.3
R2PI spectra for some ions of a o-chlorotoluene/ ammonia/He expansion

detected (1:2)-cluster is due to fragmentation of larger clusters. Comparing the relative intensities of the decay channels of the (1:2)-cluster, the S_N - reaction efficiency has increased considerably with regard to the dPT. The efficiency of both channels is now almost the same. That means, that the S_N - reaction is enhanced by two orders of magnitude when the solvent moiety is changed from one to two ammonia molecules.

To explain these findings, we postulate a concerted mechanism, composed of a nucleophilic attack at the ipso carbon together with a PT to the chlorine substituent. For the (1:2)-cluster, this mechanism requires a second PT within the ammonia-dimer which can easily be performed in H-brigded systems. In the case of the (1:1) - cluster, the S_N - reaction is obviously much slower and the dPT channel dominates. Fig. 4 illustrates the assumed transition states in the reactive complexes of both, the (1:1)- and the (1:2)-cluster. The geometrical requirements for an efficient proton transfer to the chlorine group are met in b), where the system is able to adapt to a more favourable reaction path.

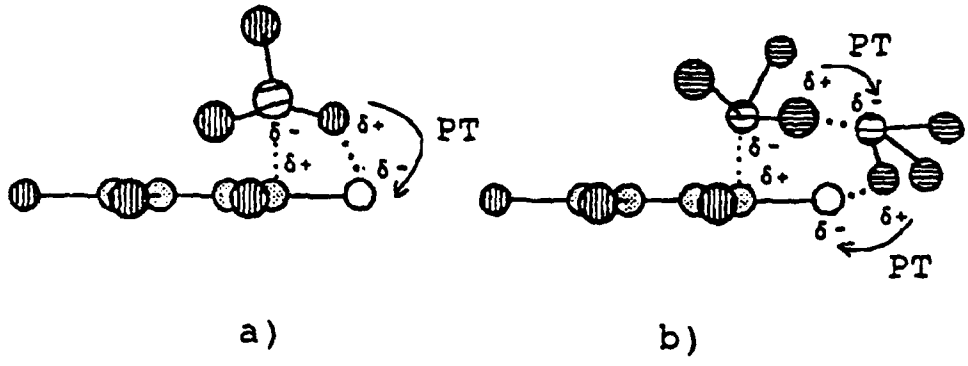

Fig.4 Schematic representation of the activated comlexes of the S_N2 - reaction in the a) (1:1) and b) (1:2)-cluster of o-chlorotoluene/ammonia

The system o-chlorotoluene/ammonia provides an instructive example of bifunctional catalysis in microsolvates and shows the capability of the described method to get some insight in the general aspects of solvation on a microscopic scale.

References

/1/ J.Eggert, C.Janes, B.Brutschy, H. Baumgärtel, Ber.Bunsenges.Phys. Chem., 94, 1282-1287 (1990)
B.Brutschy, J.Phys.Chem., 94, 8637-8647 (1990) and references therein.

/2/ T. Maeyama, M. Mikami, J.Am.Chem.Soc. 110, 7238, (1988)
T. Maeyama, M. Mikami, J.Phys.Chem. 94, 6973, (1990)

/3/ B.Brutschy, C.Janes, J.Eggert, Ber.Bunsenges.Phys.Chem., 92, 74-81, (1988)

Pulsed Molecular Beam Microwave Measurements On The HCCH-CO van der Waals Complex

M.A. Roehrig and S.G. Kukolich

Department of Chemistry,
University of Arizona,
Tucson Az, 85721

The infrared spectrum of acetylene-carbon monoxide van der Waals complex was recently observed in the 3μ region by Marshall, Pritchard and Muenter[1]. The IR experiment established the general orientation and the separation of the center of masses for the two monomer subunits, but accurate values for the structure of the complex were not obtained. Pulsed beam microwave measurements provide more precise values for rotation and distortion constants which can be used to calculate additional parameters which describe the complexs' structure and inertial dynamics. Data was obtained for HCCH-CO and HCCH-^{13}CO and new results for HCCD-CO, DCCD-CO, and DCCH-CO isotopomers. All of the isotopomers and isomers could be observed in a neon-helium ('first run neon') expansion gas as well as in argon, but, only the DCCH-CO isotopomer was *not* found in the argon expansion. This could be due to the low barrier for rotation of the acetylene molecule about its center of mass combined with a facilitation of this rotation in argon. It is expected the HCCD-CO isomer would be more stable than the DCCH-CO isomer since most hydrogen bonds are stronger for D than for H due to reduced 'zero point' vibrational motion of D relative to H.

All measurements were made using a Flygare-Balle type pulsed beam Fourier transform microwave spectrometer[2]. The present spectrometer[3] has had many modifications improving frequency range, signal reliabilty, and sensitivity. Spectra for the five isotopic species of the HCCH–CO van der Waals complex were collected in the 4-18 GHz range. Four of the isotopic forms of the HCCH–CO complex were observed by pulsing a 1-2% mixture of acetylene and carbon monoxide in 1 atm of argon buffer gas into an evacuated (10^{-6} - 10^{-7} torr) Fabry-Perot cavity. The DCCH–^{12}CO isotopomer was observed using the same ratios of sample, but, neon was used as the carrier gas, since initial searches for this isotopomer in argon yielded no observable signals. The carrier gas was changed to neon and a signal belonging to this isotopomer was found at 7986.806 MHz. The other isotopomeric species were also observed in the neon buffer gas.

The acetylene-carbon monoxide spectrum is that of a linear rotor, $\nu = 2B(J+1) - 4D_J(J+1)^3$, and all spectral fits were made using linear regression algorithm with the observed transition frequencies.

It is well known that van der Waals molecules undergo large amplitude motions about an equilibruim geometry, which, in the present case is linear. The

observed moments of inertia will then be a function of the structural parameters induced by these vibrational motions. By taking into account these motions, the pseudodiatomic model for van der Waals complexes can be modified to include the vibrationaly averaged projections of the moments to yield an effective moment of inertia,

$$I_b^{complex} = \mu_{PD} R_{cm}^2 + \langle 1 - \frac{sin^2\theta}{2} \rangle I_b^{HCCH} + \langle 1 - \frac{sin^2\phi}{2} \rangle I_b^{CO} \qquad (1)$$

where

$$\mu_{PD} = \frac{m_{HCCH} m_{CO}}{(m_{HCCH} + m_{CO})}$$

and R_{cm} is the distance between the centers of mass of the monomer units. The bracketted quantities are the average values for the projections on the R_{cm} axis with vibrational motion about the linear equilibrium goemetry; the angles θ and ϕ represent the vibrational amplitudes, not an equilibrium value. The reported value of R_{cm}^* in Table 1 is the corrected R_{cm} distance corresponding to the parent isotopic species HCCH–^{12}CO since this must be taken into account for the corresponding shifts in centers of mass upon isotopic substitution. The angles θ and ϕ are the angles of the acetylene and carbon monoxide subunits respectively with R_{cm}.

Table 1. Parameter values from the fit to the observed rotational constants. Indicated uncertainties are 2 standard deviations.

parameter	value
R_{cm}^*	5.018(6) Å
$\frac{sin^2\theta}{2}$	0.06(6)

The fit results to equation (1) in which R_{cm}, $\frac{sin^2\theta}{2}$ and $\frac{sin^2\phi}{2}$ are the fit parameters, are shown in Table 1. The R_{cm}^* distance of 5.018(6) Å is in good agreement with the R_{cm} distance of 5.011 Å obtained by Marshall *et.al.*[1]. The parameter $\frac{sin^2\theta}{2}$ yields a value of $\approx 21°$ for the angle θ and is consistent with other linear hydrogen bound carbon monoxide complexes[4,5,6,7,8]. The parameter $\frac{sin^2\phi}{2}$ was fixed 0 since there was only one data point which was sensitive to this

parameter, e.g. the HCCH–^{13}CO isotopomer. Fits which included this parameter did not yield a statistically significant value for $\frac{sin\phi^2}{2}$.

D_J values combined with some structure data, can be used to calculate the stretching force constant k_s for changing the separation of centers of mass of the monomers (R_{cm}) and to estimate the binding energy. The normal experssion for D_J for a diatomic molecule is modified[10] for a polyatomic linear dimer to give

$$D_J = \frac{4B^3}{\omega_s^2}\left(1 - \frac{B}{B_{HCCH}} - \frac{B}{B_{CO}}\right) \tag{2}$$

where B is the rotational constant of the complex and the stretching frequency (for the hydrogen bond) is such that

$$\omega_s^2 = \frac{4\pi^2 k_s}{\mu_{PD}}.$$

Using these relations k_s values for the various isotopomers were calculated and listed in Table 2.

Table 2. Calculated k_s, ν_s, r_e and ϵ values derived from measured distortion constants D_J and R_{cm} values. The r_e values are the equilibrium centers of mass separation for the complexs.

isotopomer	k_s(mdyne Å^{-1})	ν_s(cm^{-1})	r_e(Å)	ϵ(cm$^-$1)
HCCH--^{12}CO	0.0171	46.4	5.0011	299
HCCH--^{13}CO	0.0174	47.9	4.9788	301.5
HCCD--^{12}CO	0.0185	47.8	4.9078	311.5
DCCD--^{12}CO	0.0185	47.8	5.0006	323.4

The Lennard-Jones potential has only two adjustible parameters; the binding energy ϵ and the equilibrium internuclear separation r_e. This potential has been used, with pseudo- diatomic model for complexes to estimate the binding energy ϵ, given the derived force constant k_s and interpreting r_0 as the measured value for r_{cm}. First an 'equilibrium' rotational constant is obtained from the measured rotational constant for the complex B_0 using

$$2B_e = \frac{\nu_s}{18} - \left[\left(\frac{\nu_s}{18}\right)^2 - 4\left(\frac{\nu_s}{18}\right)B_0\right] \tag{2}$$

and

$$2\pi\nu_s = \omega_s$$

r_e is then the equilibrium value for R_{cm} obtained from B_e using the pseudo-diatomic model given earlier. The well depth is obtained from expanding the Lennard- Jones potential in a Taylor series about r_e and identifying the coefficient of the $(r - r_e)^2$ term with the calculated force constant to obtain an expression for the estimated dissociation energy $\epsilon = k_s r_e^2/72$. The values obtained are listed in Table 2.

The lack of any observable signals for the DCCH-CO isomer in argon carrier gas was quite unexpected, since signals for the other isomers were easily observed with a single beam pulse. It is likely that most of the DCCH-CO isomers formed were isomerized to the lower energy HCCD-CO isomer in the presence of the argon. This would require a low barrier for rotation of the acetylene molecule within the complex. We may speculate that since argon forms stronger complexes with other molecules than neon does, three-body collisions involving argon would facilitate the isomerization more readily than neon would. It would be helpful and interesting to have results of *ab initio* calculations on this complex with energies for various values for θ, the angle of rotation of acetylene relative to r_{cm}.

References

1. M.D. Marshall, D.G. Prichard and J.S. Muenter, *J. Chem. Phys* **90**, 6049 (1989); M.D. Marshall, J. Kim, T.A. Hu, L.H. Sun and J.S. Muenter, *J. Chem. Phys.* **94**, 6334 (1991).

2.T.J. Balle and W.H. Flygare, *Rev. Sci. Instrum.* **52**, 33 (1981).

3. R.E. Bumgarner and S.G. Kukolich, *J. Chem. Phys* **86**, 1083 (1987).

4. A.C. Legon, P.D. Soper and W.H. Flygare, *J. Chem. Phys.* **74**, 4944 (1981).

5. P.D. Soper, A.C. Legon and W.H. Flygare, *J. Chem. Phys.* **74**, 2138 (1981); R.S.Altman, M.D. Marshall, W. Klemperer and A. Krupnov, *ibid.* **79**, 52 (1985).

6. M.R. Keenan, T.K. Minton, A.C. Legon, T.J. Balle and W.H. Flygare, *Proc. Natl. Acad. Sci.*, **77**, 5583 (1980).

7. F.J. Goodwin and A.C. Legon, *Chem. Phys. Lett.* **87**, 81 (1984).

8. A. Suckley, Z. Wang, G. Bandarage, R.R. Lucchese, A.C. Legon and J.W. Bevan, *46th Ohio State University international Symposium on Molecular Spectroscopy, June 17-21, 1991.* Paper TF'8.

9. D.J. Millen, *Can. J. Chem* **63**, 147 (1985).

High Resolution Molecular Beam Spectroscopy of Highly Vibrationally Excited Propynal(C_3H_2O) : Structural Immunity to IVR

C.A. Rogaski and A.M. Wodtke
Department of Chemistry
University of California, Santa Barbara, California, 93106

With the development of spectroscopic techniques that allow the study of highly vibrationally excited molecules [1], the study of the dynamics of intramolecular vibrational redistribution (IVR) in polyatomics has become experimentally accessible. It has been recognized for some time that the vibrational state density is one of the most important factors in determining the IVR rate. However, recent results showing heavy atom inhibition[2] and methyl-rotor acceleration[3] of IVR, indicate that molecular structure has a significant effect on the magnitude of the *coupling matrix elements* even in regions of high vibrational state density. In our experiment, stimulated emission pumping (SEP) spectra of highly vibrationally excited propynal have been measured. The spectra can be easily assigned and rotational constants can be obtained for overtone states of the CO stretch. So far such spectra have been obtained at energies where the vibrational state density is as high as 20 vibrational states / cm^{-1}. This work will be extended to energies with more than 300 states / cm^{-1}. This work presents the observation of a molecule which is, at least in comparison to other molecules, "immune" to IVR.

Propynal, like formaldehyde, is a planar near symmetric top (κ=-0.9897) in its ground state and undergoes a near UV n—>π^* electronic transition

---

[1]C.E. Hamilton, J.L. Kinsey, R.W. Field, Ann. Rev. Phys. Chem. 37, 493(1986)
[2]E.R.Th. Kerstel, K.K. Lehmann, T.F. Mentel, B.H. Pate, and G. Scoles, J. Phys. Chem., vol. 95 No. 22, 8282(1991)
[3]Robert J. Longfellow, Charles S. Parmenter, J. Chem. Soc. Faraday. Trans. 2, 84,1499(1988)

significantly lengthening the CO bond. Unlike formaldehyde, propynal retains its planarity in the S_1 excited state. Dispersed fluorescence spectra are very simple, resembling that of a diatomic molecule, and show a long progression in the ν_4 C=O stretching mode out to $\nu_4 = 5$. Using SEP, rotational constants for several vibrational states have been measured.

The experiment proceeds as follows. A double molecular beam of propynal, seeded in helium, is formed in a small molecular beam chamber. Each molecular beam is overlapped with part of the PUMP laser exciting propynal to its lowest excited singlet state. The fluorescence from each beam is imaged onto a separate PMT. One of the two molecular beams is also exposed to the DUMP laser and florescence dips are observed with pulse by pulse pump laser normalization. This is analogous to many cell experiments[4] . Two excimer pumped dye lasers are used for the experiments. Fluorescence dip spectra are recorded for a series of rotationally resolved PUMP transitions and rotational term energy plots are constructed, from which rotational quantum number assignments are possible. Assignments lead to optimized A, B and C rotational constants for the excited vibrational levels of Propynal. A typical fluorescence dip spectrum for $\nu_4 = 2$ is shown in figure 1. A direct harmonic count of vibrational states shows that there are about 3 vibrational state/cm^{-1} at this level of vibrational excitation. This is comparable to that of Acetylene in the region where intrinsically unassignable spectra were observed[5]. Similar results are found at higher vibrational energy where the state density is 20/cm^{-1} . The fact that simple SEP spectra are observed in Propynal even when the state density is 40 times greater than in the example of Acetylene is remarkable. This indicates that the rate of IVR for propynal is much slower than acetylene at comparable levels of state density. Propynal is therefore the latest example of how molecular structure can inhibit IVR .

---

[4]Xueming Yang, C.A. Rogaski, A.M. Wodtke, J. Opt. Soc. Am. B, Vol. 7 No. 9(1990)
[5]Y. Chen, D.M. Jonas, J.L. Kinsey, R.W. Field, J. Chem. Phys., **91**, 3976(1989)

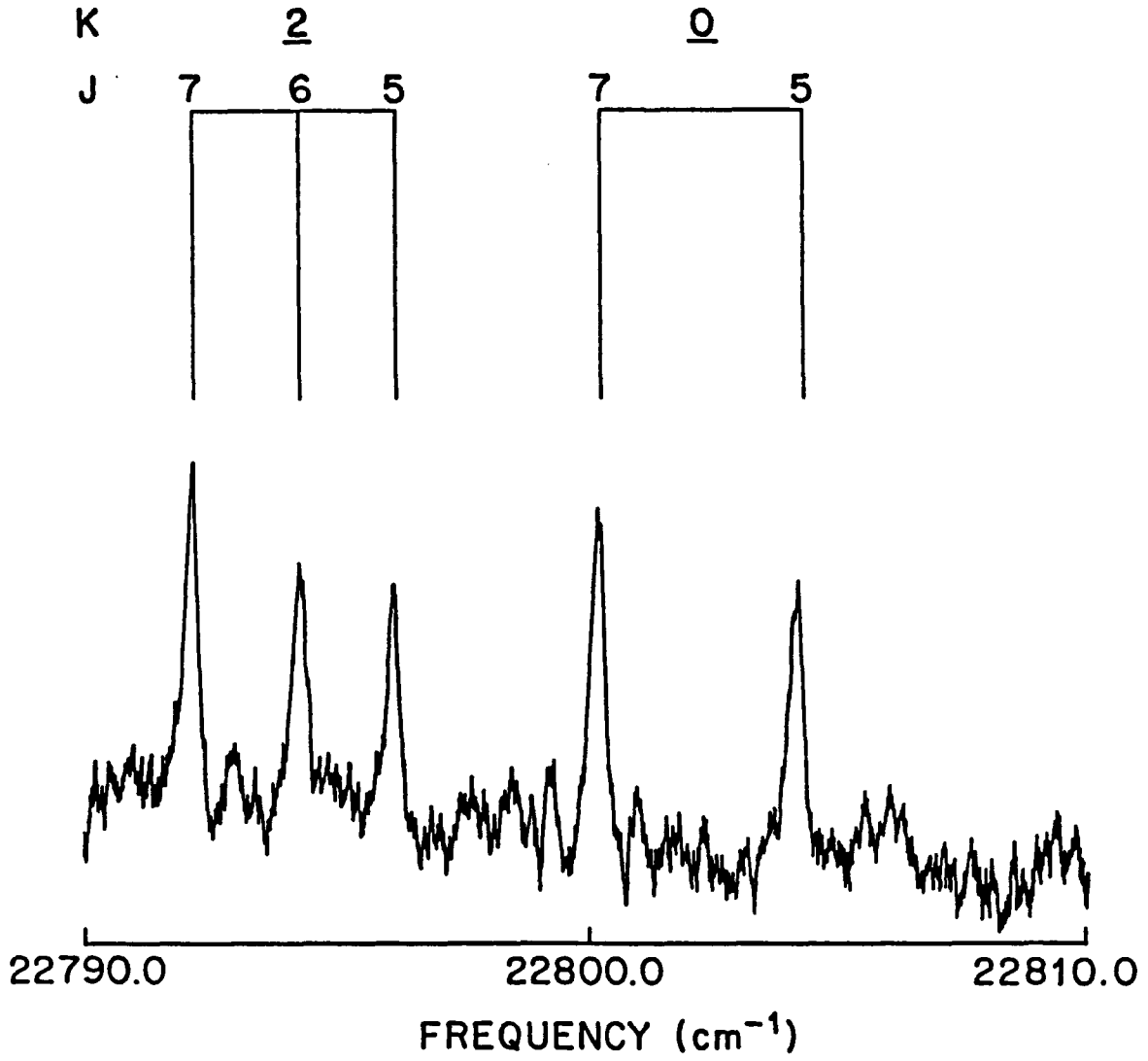

Figure 1: ***Fluorescence Dip Spectrum of $^{r}P_{0}(7)$ PUMP line of Propynal (v_4= 2)*** : Rotational Structure is characteristic of a $\perp$ transition. The $^{p}Q_{1}$ branch is missing in all of the SEP spectra. We believe this to be due to asymmetric top Hoenl-London factors.

TABLE 1: Rotational analysis of SEP data for $\nu_4 = 2$ in propynal

OBS.	CALC.	OBS-CAL
3369.189	3369.047	0.142
3369.472	3369.360	0.112
3369.849	3369.985	-0.136
3370.921	3370.924	-0.003
3372.185	3372.175	0.010
3373.740	3373.739	0.001
3375.586	3375.616	-0.030
3377.831	3377.805	0.026
3378.137	3378.203	-0.066
3379.050	3379.142	-0.092
3380.314	3380.393	-0.079
3381.940	3381.957	-0.017
3383.827	3383.834	-0.007
3386.062	3386.023	0.039
3389.428	3389.414	0.014
3390.750	3390.665	0.085

Standard Deviation = 0.079

Vibrational Term Energy =	3,369.05	+/- 0.04
0.5*(B + C) =	0.1564	+/- 0.0011
A-0.5*(B+C) =	2.0545	+/- 0.0065

units are wavemumbers

Rudich

Energy Distribution In HCl(v=1) Following the Vibrational Predissociation of C_2H_2-HCl Complex

Y. Rudich and R. Naaman
Department of Chemical Physics
Weizmann Institute, Rehovot, Israel

High resolution infrared spectroscopy of van der Waals (vdW) molecules is an important tool in understanding their structure and the interaction potential energy surfaces (PES) near the equilibrium configuration[1,2,3]. To gain comprehensive knowledge about vdW molecules, dynamical properties such as predissociation lifetimes and state distributions after dissociation are required. Rotational energy distribution following IR vibrational excitation, has been studied for only a few systems[4,5].

Several models for vibrational predissociation (VP) of vdw molecules have been proposed[6,7,8]. All these models predict that the excess available energy will redistribute mainly in the fragments' internal degrees of freedom rather than in translational motion. The importance of the vibrational modes in VP, taking place on the ground electronic PES, was deduced indirectly in absorption studies[9,10,11] from line broadening.

We report the detection of vibrationally excited HCl, emerging from the photodissociation of C_2H_2-HCl, in an IR pump - Resonance Enhanced Multiphoton Ionization (REMPI) probe experiment.

From microwave[12], matrix isolation[13] and IR[9] spectroscopy it is known that the C_2H_2-HCl complex is T-shaped with the HCl hydrogen bonded to the Π cloud of the acetylene. In high resolution IR spectra[9], the C_2H_2-HCl absorption lines are broadened compared with those of C_2H_2-DCl, suggesting that the near resonant V-V dissociation channel to the HCl subunit shortens the lifetime of the excited state. This model predicts that the HCl fragment will emerge vibrationally excited and the dissociation energy was estimated to be less than 390 cm^{-1}.

Clusters are formed by expanding HCl (5%), acetylene (5%) and Ne (90%) from a 0.5 mm diameter pulsed nozzle, at a total pressure of about 1000 torr. Infrared photons are generated by frequency subtracting 1.06μm from the output of a dye laser, operating at ~789 nm, in a

$LiNbO_3$ crystal. IR pulses of ~200μJ, 8 ns long with a bandwidth of 0.5 cm^{-1} FWHM are obtained. After a short delay (0-600ns), the rotational distribution of HCl in v=1 is probed by 2+1 REMPI via the v'=16 of the V electronic state[14,15]. The UV light is produced by doubling the output of a dye laser and then mixing it with 1.06μm in KDP. Pulses of about 500μJ at ~240 nm are obtained. The two laser beams counter propagate collinearly, each focused by a 250mm focal length lens. The two beams are perpendicular to the molecular beam. Ions are collected and amplified by microchannel plate. The delay between the pump and probe is controlled by direct triggering of the probe laser's Q switch from the pump laser's variable Q switch synchronous output. This scheme allows delays of 0-600 ns with a jitter much smaller than the length of the laser pulse. By continuously varying the delay between the pump and probe lasers, the lifetime of the vibrationally excited complex can be probed.

The symmetric CH stretch of acetylene is excited to v=1 by IR absorption at ~3270 cm^{-1} [9]. The signal of the emerging HCl(v=1,J) was monitored as function of the delay between the pump and probe lasers. The intensity of the signal showed no variation for delays at the range of 10-100ns. This indicates that the lifetime of the vibrationally excited complex is shorter than the experimental resolution of 10 ns. The rotational energy distribution in HCl(v=1) was probed at a delay of 20 ns and averaged over 500 laser shots for each rotational level. Only rotational states between J=0 to J=3 were populated and no signal could be detected at J=4. The error in the signal for J=1 is large due to the background from transition from J=5 in the vibrational ground state. The distribution was fitted to a Boltzman distribution (Fig 1.) with a temperature of 53 ± 5 K. This is indicative of the slow dissociation process.

From this rotational distribution the calculated new upper limit for the dissociation energy of the complex is ≤ 260 cm^{-1}. Since J=3 is populated, but no population is observed at J=4, the dissociation energy must be between $260 > D_0 > 170$ cm^{-1}. This is lower than the 350cm^{-1} which has been calculated using atomic charges[16]. For the system studied, less than 10% of the energy is deposited in relative translation of the fragments. Such a low deposition into translation is predicted by models and some experiments[17], but is markedly different from $(NO)_2$, where 75% of the energy appeared in translation[4]. The rotational distribution of HCl(V=1) and the short lifetime of the excited state (T<10ns) support the model proposed by Dayton et. al.[9] of near

resonant V-V energy transfer in the vibrational predissociation of C_2H_2-HCl and are direct evidence for the role of vibration as a very efficient sink for the excess energy in VP of vdW molecules.

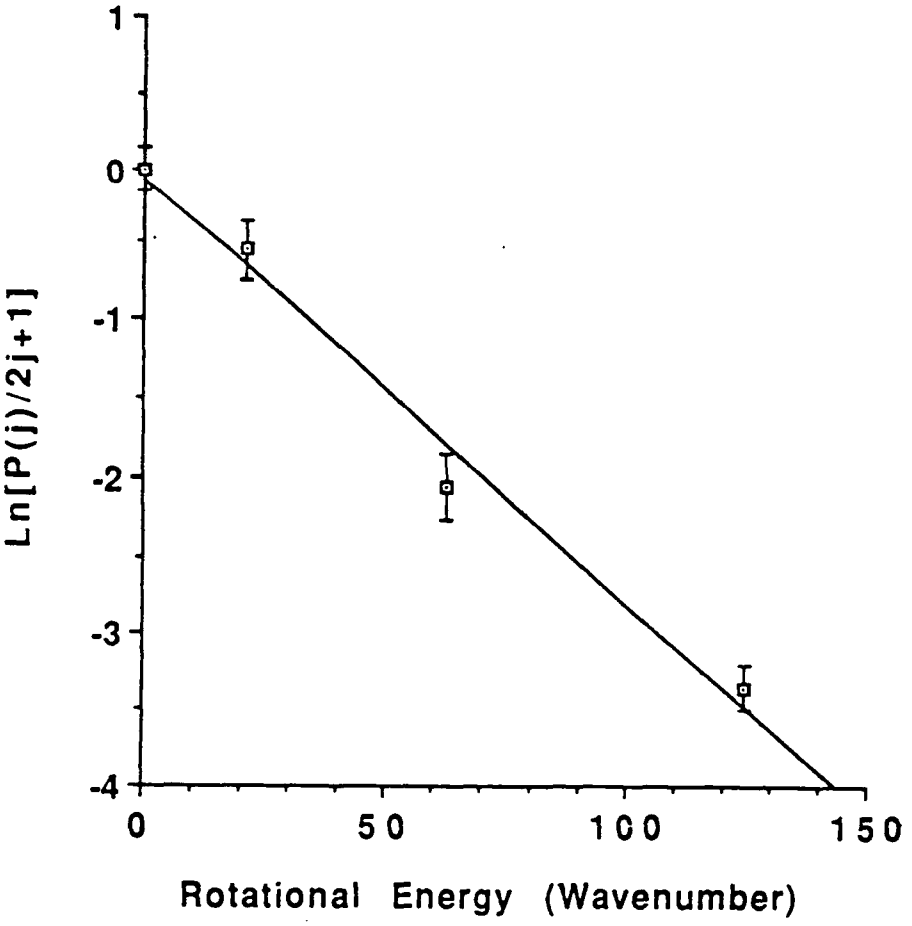

Figure 1. Boltzman fit to the observed rotational energy distribution in HCl(V=1). Slope fits a temperature of 53±5 K.

References:

1. R.E. Miller, J. Phys. Chem. **90**, 3301 (1986) and references therein.

2. D.J. Nesbitt, Chem. Rev. **88**, 843 (1988). and references therein.

3. K.C. Janda, Adv. Chem. Phys., **60**, 201 (1985).

4. M.P. Cassasa, J.C. Stephanson and D.S. King, J. Chem. Phys., **89**, 1966 (1988). J. Chem. Phys., **85**, 2333 (1986).

5. D.C. Dayton, K.W. Jucks and R.E. Miller, J. Chem. Phys., **90**, 2631 (1989).

6. J.A. Beswick and J. Jortner, Adv. Chem. Phys. **47**, 363 (1981).

7. G.E. Ewing, J. Phys. Chem. **91**, 4662 (1987), Faraday Discuss. Chem. Soc. **73**, 325 (1982).

8. J. Huston, D. Clary and J.A. Beswick, J. Chem. Phys., **81**, 4474 (1984).

9. D.C. Dayton, P.A. Block and R.E. Miller, J. Phys. Chem. **95**, 2881 (1991).

10. G.T Fraser, A.S. Pine and R.D. Suenram, J. Chem. Phys., **88**, 6157 (1988).

11. C.H. Lovejoy, D.S. Nelson Jr. and D.J. Nesbitt, J. Chem. Phys., **89**, 7180 (1988).

12. A.C. Legon, P.D. Aldrich and W. H. Flygare, J. Chem. Phys. **75**, 625 (1981).

13. L. Andrews, G.L. Johnson, B.J. Kelsall, J. Phys. Chem., **86**, 3374 (1982).

14. T.A. Spiglanin, D.W. Chandler and D.H. Parker, Chem. Phys. Lett., **137**, 414 (1987).

15. Y. Rudich, R.J. Gordon, E.E. Nikitin and R. Naaman, J. Chem. Phys., in press.

16. M. Gussoni, C. Castiglioni and G. Zerbi, Chem. Phys. Lett., **99**, 101 (1983).

17. D.S. Bomse, J.B. Cross and J.J. Valentini, J. Chem. Phys., **78**, 7175 (1983).

Inelastic Electron Scattering by Alkali Clusters

Adi Scheidemann*, Vitaly Kresin**, and Walter D. Knight
Department of Physics
University of California, Berkeley, CA 94720

We have measured absolute inelastic scattering cross sections for collisions of low energy (0.1-30 eV) electrons with sodium clusters. Prior to this work [1, 2] studies of electron metal cluster collisions have been limited to metal dimers [3], or focused on ionization threshold measurements [4]. The study of the electron-cluster interaction will lead to deeper understanding of metal cluster polarization, and of electron cloud spill-out in metallic systems. Furthermore, the common use of electron impact ionizers also provides motivation for a quantitative study of the electron cluster interaction.

The experiment employs the technique of beam depletion spectroscopy. A supersonic free jet of neutral sodium clusters is intersected perpendicularly by low energy electron beam. The electron gun is based on a design described in Ref [5]. The gun assembly is placed in a uniform magnetic field (B=1400 G) directed parallel to the electron beam. The electron current density (J_e) in the collision region (length l= 24.5 mm) is approximately 1.2 mA/cm^2 for electron energies above 1 eV. After passing through the collision region, the metal clusters are ionized with broadband UV light (240-420 nm), mass-selected in a quadrupole field, and detected using a Daly detector unit. The electron beam is pulsed (3 Hz), and the corresponding change in the counting rate of the detected cluster ion mass is measured. This depletion ratio ($\Delta N/N$) has been measured for Na_8, Na_9, Na_{20}, and Na_{40}. The scattering cross section is given by:

$$\sigma = \Delta N/N \cdot v_{cluster} / (J_{el} \cdot l)$$

The removal of clusters after an inelastic electron collision occurs via three different scattering channels:

Electron Attachment: $Na_X + e^- \rightarrow Na_X^-$, for $E_{col} < E_{binding} \cong 1$ eV.

Electron Induced Fragmentation: $Na_X + e^- \rightarrow Na_{X-n} + n\,Na + e^-$, for $E_{col} > E_{binding} \cong 1$ eV.

Electron Induced Ionization: $Na_X + e^- \rightarrow Na_X^+ + 2\,e^-$, for $E_{col} > E_{threshold} \cong 3$ eV.

The contribution of elastic collisions to the total cross section is approximately 25% for Na_8, and Na_9, while it is negligible for larger clusters. For the case of electron attachment or ionization, the clusters are driven out of the beam by the Lorentz force of the magnetic field of the electron gun. Electron-induced fragmentation removes the clusters via the recoil of the fragments out of the narrow collimated beam.

The total absolute inelastic scattering cross sections for the closed shell clusters Na_8, Na_{20}, and Na_{40} are shown in Fig.1. The results presented were obtained by averaging data points measured in a series of experimental runs. The determination of the cross

sections is limited by the low depletion ratios (0.2%-0.5%); we estimate an uncertainty of ±20% for Na_{20} and Na 40 and ±%50 for Na_8.
The open shell cluster Na_9 has been studied as well, and to within experimental accuracy, the results are similar to those of Na_8. Our finding is in strong contrast to the photoabsorption spectra of Na_8 vs. Na_9, where both the surface plasmon resonances and the photoionization thresholds reflect the shell closing/opening of the metal clusters [6, 7].

The experimental data given in Fig.1. show three major features:

1) For Na_8 and Na_{20}, we observe a strong increase of the cross section for collision energies below 0.5 eV. This increase in the cross section corresponds to the 1/v-law for S-wave scattering [8]. Since the impact energy is lower than the binding and the ionization energies of the cluster, we conclude that electron attachment removes the cluster from the beam.

2) The inelastic collision cross section shows a plateau region above 0.5 eV. (However, narrow spectral features may have been averaged over due to the limited resolution.) For $E_{collision} > 1$ eV, angular momenta up to $l = k \cdot A$ will contribute to the cross section. Here A describes the maximal range of the cluster-electron interaction, and k gives the wave number of the electron. In this case, an upper bound of the inelastic cross section is given by [8]:

$$\sigma_{max} = \pi \cdot A^2.$$

In addition to cluster fragmentation, electron induced ionization becomes possible for energies above approximately 3 eV. However, we do not see a marked ionization threshold in our cross section measurements. For Na_{40} cross sections have been measured for energies up to 30 eV; their values are similar to the results in the 1.0-5.0 eV range [2]. This indicates that in this energy range, the electron-induced ionization is a minor channel compared to collision-induced cluster fragmentation.

3) The measurements allow us to determine the inelastic interaction range of the electron cluster collision. It is found that the cross sections scale with the cluster size:

$$A \equiv (1.4 - 1.7) \cdot R.$$

R is the radius of the positive cluster background in the framework of the jellium model [7]:

$$R = a_0 \cdot r_s \cdot N_e^{1/3}.$$

Here a_0 is the Bohr radius, r_s is the Wigner-Seitz radius, and N_e is the number of valence electrons in the cluster. This large value for A exceeds the range of the electron spill-out and reflects the influence of the attractive long-range polarization interaction between an electron and a metal cluster [9].

We would like to thank K. Selby and M. Vollmer for valuable help and discussions. This work was supported by the U.S. National Science Foundation under grand No. DMR-89-13414. A. S. thanks the Deutsche Forschungsgemeinschaft for financial support.

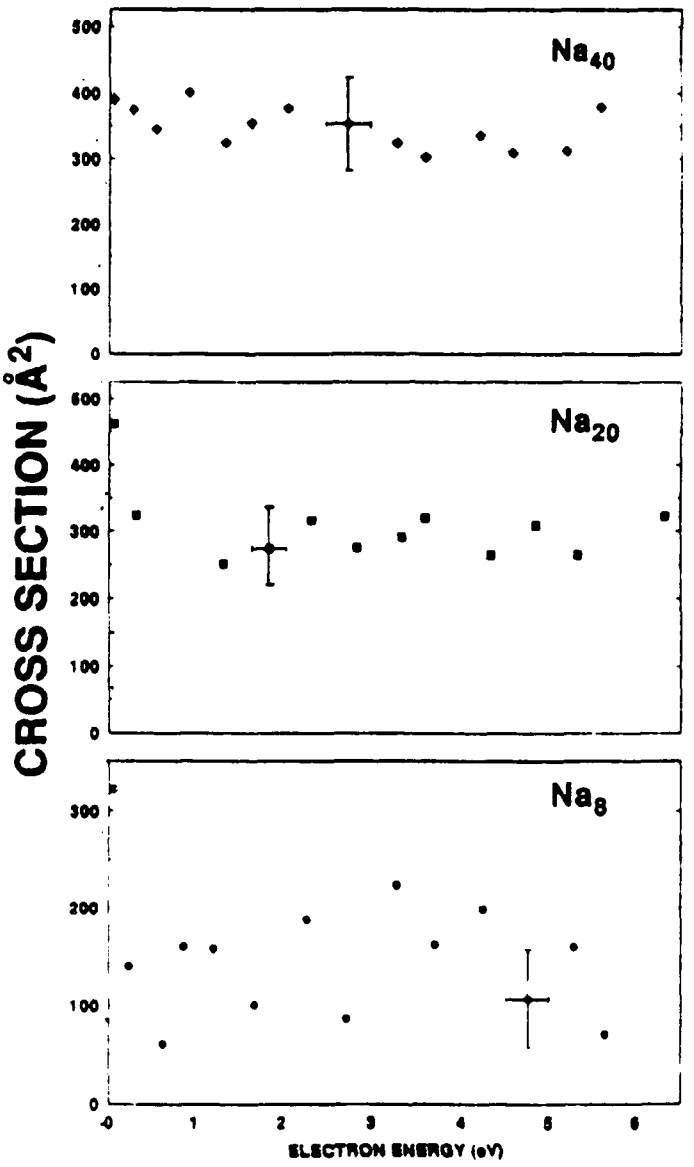

Figure 1. Absolute electron-impact depletion cross sections for the spherical clusters Na_8, Na_{20}, and Na_{40} in the energy range from 0.1 to 6.0 eV; the uncertainty in the cross section is ±50% for the Na_8, and ±20% for the Na_{20}, and Na_{40}. The electron energy has an uncertainty of ±0.3 meV below 1.0 eV, and ±0.5 eV at higher energies.

Present address: * University of Washington, Department of Chemistry, Mail Stop BG 10, Seattle,WA 98195.
Present address: ** Lawrence Livermore National Laboratories, Mail Stop L-268 Livermore, CA 94550.

1 V. V. Kresin, A. Scheidemann, W. D. Knight, Phys. Rev. A, **44**, R4106, 1991.
2 V. V. Kresin, A. Scheidemann, W. D. Knight, Proceedings of the Int. Conf. on Physics and Chemistry of Finite Systems, Richmond, VA, Oct., 1991, ed. by P. Jena, S. N. Khanna, B. K. Rao, to be published.
3 K. Franzreb, A. Wucher, H. Oechsner, Z. Phys. D **19**, 77, 1991.
4 T. D. Märk, Int. J. Mass Spectrom. Ion Proc. **79**, 1, 1987
5 R. E. Collins, B. B. Aubrey, P. N. Eiser, R. J. Celotta, Rev. Sci. Instrum. **41**, 1403, 1970
6 K. Selby, V. Kresin, J. Masui, M. Vollmer, W. A. de. Heer, A. Scheidemann, W. D. Knight, Phys. Rev. B **43**, 4565, 1991
7 W. A. Heer, W. D. Knight, M. Y. Chou, M. L. Cohen, in *Solid State Physics, Advances in Research and Applications*, ed. H. Ehrenreich, D. Turnbull, Academic, New York, 1987, Vol. 40.
8 N. F. Mott and H. S. W. Massey, *The Theory of Atomic Collisions*, 3rd. ed. Oxford University, Oxford, 1965, Chap. XII.
9 C. Joachain, *Quantum Collision Theory*, North-Holland, Amsterdam, 1975, Chap. 20.

Spectroscopic Study of Solvated Sodium Atoms

C.P. Schulz, C. Nitsch, C. Hüglin, G. Unger, and I.V. Hertel

Fakultät für Physik, Albert–Ludwigs–Universität
D–7800 Freiburg, Germany F.R.

The interaction of alkali metal atoms with polar solvent molecules is of great importance for many fundamental chemical processes. Usually the first step in these processes is the charge separation of the alkali valence electron and the formation of the so–called solvated electron. To get some detailed insight into this solvation process we have studied spectroscopic properties of $Na(H_2O)_n$ and $Na(NH_3)_n$ clusters. Two quantities are of special interest to follow the charge separation from small aggregates to the bulk: first the overall electron binding energy, i.e. the ionization potential (IP) of these clusters and second the photo excitation of the valence electron, i.e. photo absorption of the clusters.

Experimentally, these clusters are formed in a pickup source [1] where a cloud of Na atoms collides with an expanding pulsed beam of water seeded in Argon or neat ammonia gas. The clusters are excited and ionized further downstream by pulsed lasers. A time–of–flight arrangement provides a mass analysis of the ionized clusters. Typically, aggregates containing one Na atom and more than 80 solvent molecules are observed.

It has been predicted and later confirmed by experiments [1], that the ionization potentials of $Na(H_2O)_n$ and $Na(NH_3)_n$ are shifted to lower energies with respect to the ionization limit of the Na atom. This can be easily understood – at least for very small clusters up to $n = 4$ – by the difference in the binding energy for the neutral and the ionic complex: While the neutral Na atom is bound by a dipole–induced dipole interaction the binding energy of the cluster ion is dominated by the much stronger

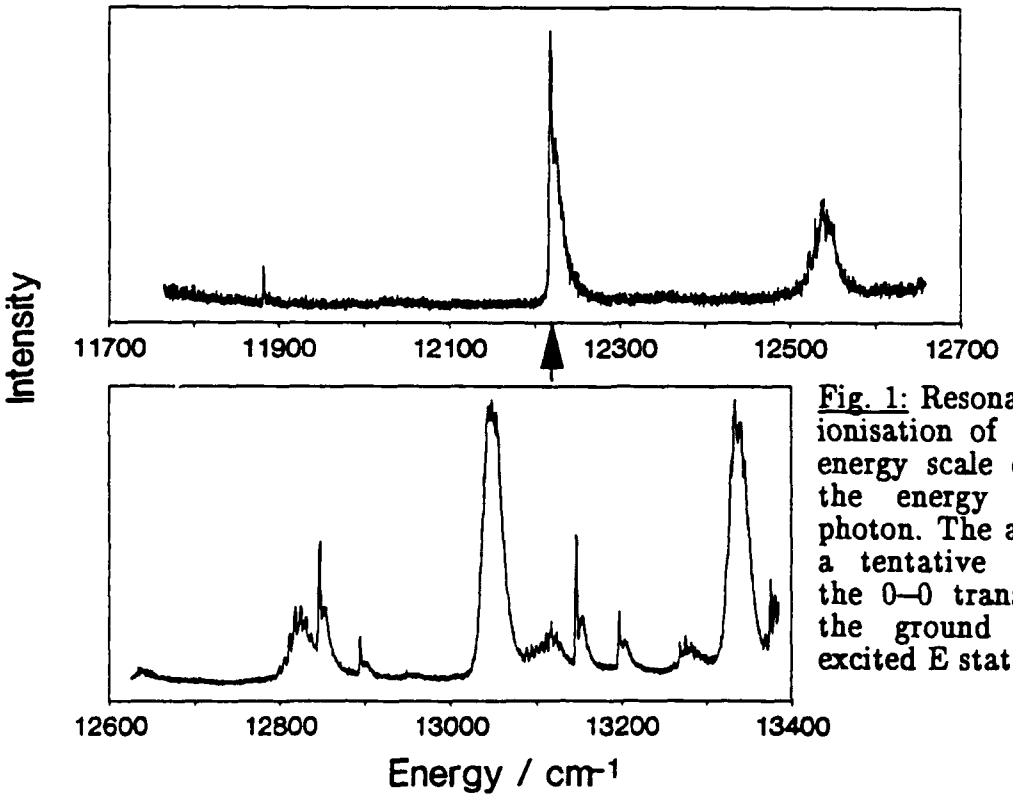

Fig. 1: Resonant two photon ionisation of $Na(NH_3)$. The energy scale corresponds to the energy of the first photon. The arrow indicates a tentative assignment of the 0–0 transition between the ground A_1 and the excited E state.

ion–dipole force. For larger clusters this picture is no longer valid because of the solvation effect. Large differences in the size dependence of the measured ionization potentials have been found for H_2O and NH_3 as solvent molecules [2]. While the IP for $Na(NH_3)_n$ decreases more or less monotonically with increasing cluster size the IP for $Na(H_2O)_n$ stays constant for all clusters with $n \geq 4$. The formation of a solvated electron bound to the surface of the cluster has been postulated for this surprising feature [2].

To get more information on the electron localisation we have recently started to measure the photoabsorption of the first excited state which asymptotically corresponds to the Na(3p) excitation. The two colour two photon technique has been used so far. An example of such a measurement is shown in fig. 1, where $NaNH_3$ is excited by laser light with variable wavelength as denoted by the horizontal axis. A second photon fixed in energy at 417 nm (24009 cm^{-1}) ionizes the excited $NaNH_3$ complex. We have tentatively assigned the strong line near 12220 cm^{-1} (arrow) as the 0–0 transition since no strong line was observed at lower photon energies. This assignment is given further support by a SCF calculation by the same authors, which gave a value of 12178 cm^{-1} for the 0–0 transition. A rich yet unassigned vibrational and rotational structure is observed above this energy. One should note that by attaching only one ammonia molecule to the sodium atom the excitation energy is already lowered by 0.6 eV compared to the 2.1 eV for the 3p excitation of the bare Na atom.

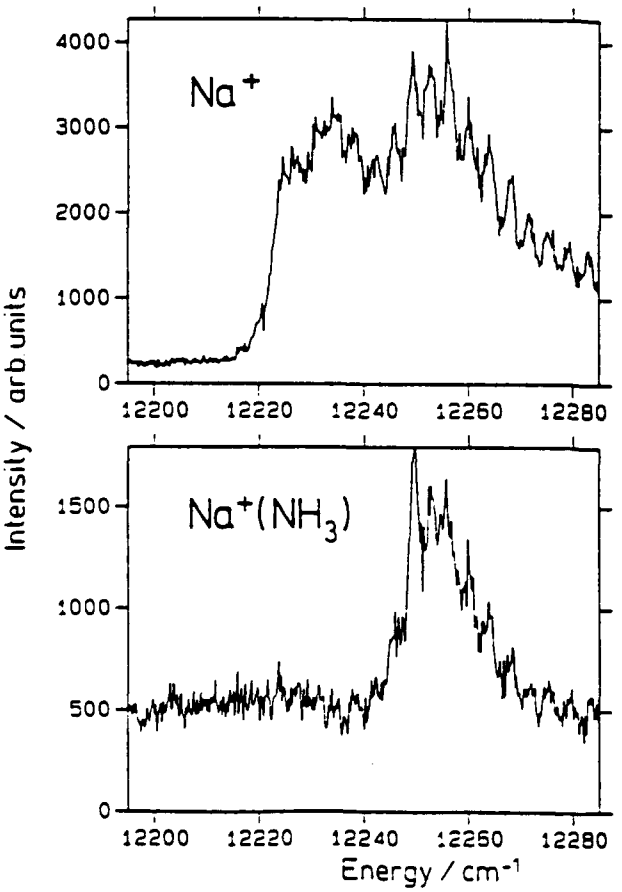

Fig. 2: Fragmentation of $NaNH_3$ after multi photon ionization (see text)

An interesting observation was made when the intensity of the red laser light (near 820 nm)was increased by a factor of 10 to 130 mJ/cm^2: even without the second laser sodium ions are detected, which are produced by a fragmentation process of the $NaNH_3$ complex after multi photon absorption. Fig. 2 shows the multi photon ionization signal as a function of the laser wavelength near 12250 cm^{-1}. In the upper trace the Na ion signal is reproduced while in the lower part the intensity of the $NaNH_3$ ion is shown. Two regions can be distinguished: between 12220 cm^{-1} and 12240 cm^{-1} only Na ions are detected while for larger photon energies up to 12280 cm^{-1} both ions ($NaNH_3^+$ and Na^+) are observed with an oscillatory structure. The period of 3.9 cm^{-1} is somewhat smaller than expected for the rotation of the three hydrogen atoms about the N–Na axis. In order to give an explanation of the excitation steps and the fragmentation path leading to the observed features further experiments have to be made.

References:

1. C.P.Schulz, R.Haugstätter, H.U.Tittes, I.V.Hertel: Z.Phys.D 10, 279 (1988)
2. I.V.Hertel, C.Hüglin, C.Nitsch, C.P.Schulz: Phys.Rev.Lett. 67, 1767 (1991)

OPTO-THERMAL SPECTROSCOPY OF BENZENE C-H STRETCH OVERTONES

Mario SCOTONI, Cristina LEONARDI,
Loris MENEGOTTI and Davide BASSI
Dipartimento di Fisica and I.N.F.M., Unità di Trento
Università degli Studi di Trento
I-38050 Povo, Trento, Italy

Supersonic beams are a powerful tool for high resolution spectroscopy. Molecular beam experiments are characterized by the rotational cooling of molecules which leads to a dramatic simplification of the absorption spectrum, especially in the case of polyatomic molecules. This is particularly useful in the study of vibrational overtones, where it is important to separate the inhomogeneous rotational broadening from the homogeneous contribution originated by the intramolecular vibrational energy redistribution processes (IVR).

We have investigated the overtone absorption of the benzene C-H stretch mode by means of an opto-thermal spectrometer [1]. The results for the $\Delta v_{CH} = 4$ overtone [2] are shown in Fig.1. The room-temperature $\Delta v_{CH} = 4$ cell spectrum [3] is not shown in Fig.1. It is characterized by the presence of a broad absorption band centered around ≈ 11498 cm^{-1} with a FWHM of 82 cm^{-1}. The molecular beam spectrum shows two "main" peaks centered around 11490 and 11509 cm^{-1} respectively and several other vibrational transitions which are partially resolved. The observed spectrum has been fit (full line in Fig.1) by means of ten Lorentzian curves having a FWHM of 17 cm^{-1} (about a factor 5 less than the room-temperature cell result). The result of the fit demonstrates that several vibrational transitions contribute to the overtone spectrum. Their spacing is lower than the rotational broadening at room-temperature and this explains the origin of the 82 cm^{-1} nearly "homogeneous" linewidth reported in ref. [3]. Moreover it should be pointed out that our fitting procedure is somewhat arbitrary and that our result of 17 cm^{-1} FWHM is only an upper limit for the homogeneous broadening of the $\Delta v_{CH} = 4$ overtone.

It is interesting to compare our measurements with the recent investigation of the C-H stretching predissociation spectrum of *t*-butil hydroperoxide carried out by Flemeing and Rizzo [4]. They used a high-resolution three-color technique for measuring the C-H spectrum subsequent to the $\Delta v_{OH} = 4$ excitation at about 13303 cm^{-1}. Fleming and Rizzo found a linewidth of about 17 cm^{-1}, exactly the value of our upper estimate for the direct excitation of the $\Delta v_{CH} = 4$ benzene overtone. This coincidence is probably casual because the two experiments are very different and experimental results cannot be directly compared. However results of ref. [4] suggest the possibility that our upper estimate of the $\Delta v_{CH} = 4$ linewidth is not too far from the true homogeneous limit.

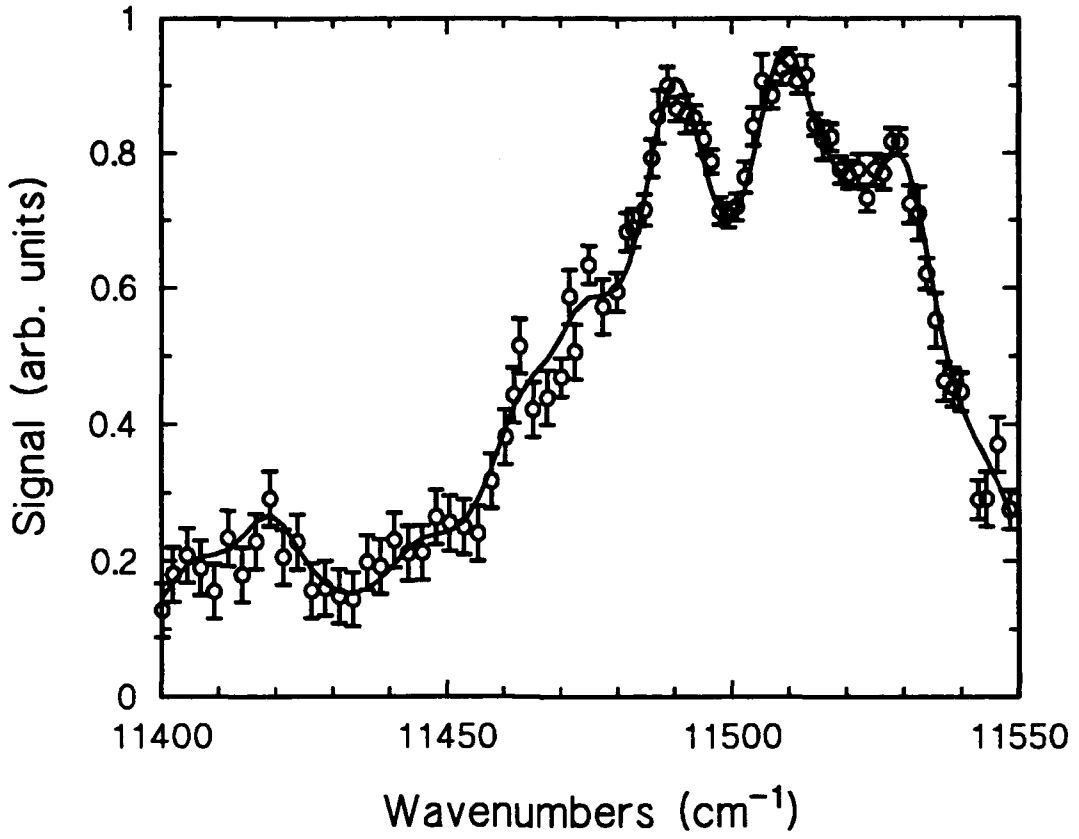

Fig. 1 : Opto-thermal spectrum of the $\Delta v_{CH} = 4$ benzene overtone (open circles). The full line is a fit based on ten Lorentzian curves with a linewidth of 17 cm^{-1} [2].

An attempt to detect the presence of a fine structure in our opto-thermal spectrum was unsuccessful, at least within the present limits of detection sensitivity (≈ 10^{-24} cm^2) and frequency resolution. Measurements of the fundamental spectrum [1] have demonstrated that our actual frequency resolution is far from the limit set by the laser source. In fact the laser linewidth (≈ 0.08 cm^{-1}) is higher than the typical resolution needed for resolving the rotational structure of benzene (≈ 0.01 - 0.02 cm^{-1}) [5] and adjacent vibrational transitions cannot be resolved if their separation is narrower than the width of the rotational envelope. This rotational broadening is ≈ 30 cm^{-1} FWHM at room-temperature and decreases to ≈ 8 cm^{-1} FWHM at the rotational temperature of ≈ 20 K corresponding to the overtone spectrum shown in Fig. 1. In order to investigate the effect of rotational broadening we measured the opto-thermal spectrum using two different molecular beam source conditions. The lower rotational temperature reached in our experiment is ≈ 10 K corresponding to a rotational broadening of ≈ 5 cm^{-1} FWHM (measured at the fundamental benzene transition around 3048 cm^{-1}). Measurements of the overtone spectrum in the 11480 - 11520 cm^{-1} range do not show any significantly change when the rotational broadening is reduced from 8 to 5 cm^{-1}. Of course we cannot exclude the presence of closely spaced vibrational transitions which are not resolved in both our measurements.

Further experimental work is in progress to extend this measurements to deuterated and partially fluorinated benzene.

REFERENCES

1) M.Scotoni, A.Boschetti, N.Oberhofer and D.Bassi, J.Chem.Phys. **94**, 971 (1991).
2) M.Scotoni, C.Leonardi and D.Bassi, J.Chem.Phys. **95**, 8655 (1991).
3) K.V.Reddy, D.F.Heller and M.J.Berry, J.Chem.Phys. **76**, 2814 (1982).
4) P.R.Flaming and T.R.Rizzo, J.Chem.Phys. **95**, 1461 (1991).
5) a) J.Pliva and A.S.Pine, J.Mol.Spectr. **93**, 209 (1982);
   b) J.Mol.Spectr. **126**, 82 (1987).

A preliminary investigation of the $O(^1D)+H_2,D_2,HD$ reactions: Chemical laser determination of the nascent product vibrational distributions and the $O(^1D)+HD$ macroscopic branching ratio

Junlong Shao, Li Yuan, Hongyi Yang, Yukun Gu,
Kaiba Li, Ke Wang, Yusheng Tao

(Dalian Institute of Chemical Physics, Chinese Academy of Sciences, Dalian China)

Abstract

Concentric Xe flashlamp pumped chemical lasers of different lengths were built to study the $O(^1D)+H_2,D_2$ reaction. $O(^1D)$ was produced by photolyzing high purity ozone to ensure the successful operation of the $OD^\dagger$ vibrotational chemical laser. The times to threshold of lasing were found to be decreasing with increasing of the reactants pressure or of the discharge voltage of the flashlamp. Thirty three vibrotational laser emissions were identified under free-running chemical laser operations. In addition, fifteen new $OH^\dagger$ laser emissions were identified.

The nascent product vibrational distributions of the reactions

$$O(^1D)+H_2(^1\Sigma_g^+,v=0,J)\rightarrow OH(^2\pi_i,v',J')+H(^2S_{1/2}),\Delta H_{300}=-181.6KJ/mol \quad (1)$$
$$O(^1D)+D_2(^1\Sigma_g^+,v=0,J)\rightarrow OD(^2\pi_i,v',J')+H(^2S_{1/2}),\Delta H_{300}=-180.8KJ/mol \quad (2)$$
$$O(^1D)+HD(^1\Sigma_g^+,v=0,J)\rightarrow OH(^2\pi_i,v',J')+D(^2S_{1/2}),\Delta H_{300}=-178.2KJ/mol \quad (3)$$
$$O(^1D)+DH(^1\Sigma_g^+,v=0,J)\rightarrow OD(^2\pi_i,v',J')+H(^2S_{1/2}),\Delta H_{300}=-184.9KJ/mol \quad (4)$$

were studied with a four meter Xe flashlamp pumped grating selection chemical laser. The preliminary results obtained were as follows:

reaction	reactants ratio	total pressure	vibrational distributions			
			N_1/N_0	N_2/N_1	N_3/N_2	N_4/N_3
(1)	$O_3:H_2:He=$ 1:3:50	54 torr	0.72±0.01 (1.02)*	0.90±0.12 (0.99)*	0.82±0.02 (0.96)*	0.52±0.06 (0.40)*
(2)	$O_3:D_2:He=$ 1:6:10	34	<0.69	0.95±0.07	0.71±0.03	0.87±0.01**

(3)	O_3:HD:He= 1:3:50	54	0.76±0.10***	0.83±0.09	0.90±0.15
(4)	O_3:DH:He= 1:6	28		0.94±0.08	

* figures in the parenthesis are the results of modelling calculation based upon experimental time to threshold and relaxation rate constants of OH(v') by various species involved in the reaction.
** $N_5/N_4 > 1.0$
*** O_3:HD:He=1:3:30, total pressure=34 torr

The effect of the thermalization of $O(^1D)$ before reaction and the rotational equilibrium of $OH^\dagger$ or $OD^\dagger$ product on the vibrational distribution were taken into consideration and believed to be of minor influence on our results. Our results are compared with the experimental results of infrared chemiluminescence and laser induced fluorescence and also the results of theoretical calculation based upon different potential energy surfaces.

The macroscopic branching ratio of $O(^1D)$+HD reaction was studied by varying the concentration of hydrogen in the $O(^1D)+H_2$ reaction, so that the times to threshold were identical for the same laser transition of both reactions. The macroscopic branching ratio thus obtained was 1.8±0.2, which is different from the result obtained by the H(D) atomic detection with laser induced fluorescence by Bersohn. Our results authenticated that the theoretical calculation based upon SL (Schincke-Lester)-type surface is better than those based upon either Murrel-Carter or diatomic in molecules surfaces.

The chemical laser technique is a valuable method for the determination of the nascent product vibrational distributions, especially when it is complemented by modelling calculation if all the necessary relaxation rate constants are available. The potentiality for the improvement of the chemical laser grating selection technique to obtain more accurate results is finally elucidated.

References:

(1) C. Amiot, J. P. Maillard and J. Chauville
J. Mol. Spectro. 87, 196 (1981)

(2) J. E. Butler, R. G. MacDonald, D. J. Donaldson and
J. J. Sloan
Chem. Phys. Lett., 95, 183 (1983)

(3) J. E. Butler, G. M. Jursich, I. A. Watson, J. R. Wiesenfeld
J. Chem. Phys., 84, 5365 (1986)

(4) P. M. Aker and J. J. Sloan
J. Chem. Phys., 85, 1412 (1986)

(5) C. B. Cleveland, G. M. Jursich, M. Trolier and
J. R. Wiesenfeld
J. Chem. Phys., 86, 3253 (1987)

(6) K. Tsukiyama, K. Katz and R. Bersohn
J. Chem. Phys., 83, 2889 (1985)

(7) M. S. Fitzcharles and G. C. Schatz
J. Phys. Chem., 90, 3643 (1986)

A Proposal to Produce Velocity-Selected and State-Selected Molecular Beams Using The Ballistic Effect.

J.M.Sindoni, Yap Analytics Inc., 594 Marrett Road, Lexington, Ma.02173
R.D.Sharma, Optical Environment Division, Phillips Laboratory, Hanscom AFB, Ma.01730

The study of chemical reactions and energy transfer processes using molecular beams has revolutionized our understanding of the mechanisms underlying these processes[1]. Still, except for a few fortunate instances[2], most of the processes studied involve reactants with low internal excitation[3] or with Boltzmann distributions at the oven temperature[4-6]. In this letter we propose a method for producing molecule beams in a desired internal state and travelling with a desired velocity. The rates of chemical reactions are known to depend, sometimes strongly, upon the initial state of the reactants. One should expect greatly improved understanding of the chemical reactions and the possibility of studying many more reactions using the ideas presented here. We illustrate the method by describing the circumstances leading to the production of a desired N_2 beam resulting from collisions of N_2 with Li^+ in crossed beams - a system studied extensively by Toennies and co-workers[3].

The method is based upon the ballistic effect discovered about 19 years ago[4-6]. Herschbach and co-workers studied the collisions between an alkali halide molecule and an Ar atom at about 1 eV relative translational energy by crossing two beams and measuring the laboratory recoil velocity of the alkali halide molecule as a function of the laboratory scattering angle. In addition to a peak centered at the recoil velocity of elastically scattered alkali halide molecules (pseudoelastic peak, formerly called elastic peak[7]), another equally strong peak centered at the recoil velocity corresponding to the motion of the center-of-mass (ballistic peak) was observed. Obviously, the ballistic peak is contributed to only by those alkali halide molecules which are almost stationary in the center-of-mass (c.m.) frame and have nearly all of the collision (relative translational) energy converted into the internal (vibrational and/or rotational) energy.

A theory of ballistic collisions[8] gives excellent agreement with the measured results for the CsF-Ar system at the laboratory scattering angles of 30 and 60 degrees. According to this theory, when the differential cross section for the scattering of alkali halide molecules is measured along the direction of the c.m. velocity, only a few transitions contribute to the ballistic peak. This is in contrast to several hundred inelastic transitions making up the pseudoelastic peak. Further, when the relative translational energy equals the energy of one of the rotation-vibration transitions (resonant T-(V,R) process), this transition may have a differential cross section which is larger than that of any other neighboring transition by as much as an order of magnitude. This gives us a state-selected beam travelling at the speed of the c.m. It should be pointed out that the differential cross section of the resonant transitions in the c.m. frame is nearly equal to the nearby nonresonant transitions. The resonant transition has a much larger differential cross section in the laboratory frame because of a greater Jacobian of transformation from the c.m. to the laboratory coordinates.

Physically it means that, for the correct viewing geometry, the signal from the entire 4π steradian solid angle in the c.m. frame may be collected by a small solid angle in the laboratory frame.

The differential cross sections are calculated using an exact formulation of a three-dimensional quantum-mechanical impulse approach (IA) calculation described earlier[9]. Physically, one may use the impulse calculation when the time duration of the collision is much shorter than the periods of vibrational and rotational motion of the diatom. The nuclei constituting the diatom may then be considered stationary during the collision and the intramolecular potential is the generator of the momentum distribution of the constituent nuclei. The atom-molecule potential, in the IA, is written as the sum of the atom-atom potentials and the atom-atom scattering amplitudes are added to obtain the atom-molecule scattering amplitudes. The atom-atom potential, in the present study, is described by a hard core interaction. Following the previous study[9], the hard core radius for the Li^+-N interaction is taken to be 1.62 Å.

Figure 1 is a plot of the calculated laboratory differential cross section for the excitation of $N_2(v=0,j=0)$ during a collision with Li^+, with a relative translational energy of 0.8825 eV, as a function of the laboratory recoil velocity at the laboratory scattering angle of $48.0(\pm 0.125)$ degrees. A beam of N_2 molecules in the state $v=3$, $j=10$ travelling at 1440 m/s may be obtained by filtering out velocities lower than 1350 and higher than 1550 m/s. The character of ballistic scattering in this calculation is qualitatively different from that in the previous work[8] where, when the scattering is viewed along the c.m. velocity, several ballistic transitions are calculated although one transition is still dominant. For the Li^+-N_2 system there is only one ballistic transition. Because of the small rotational constant and low frequency of the vibration of the diatomic molecules studied in the earlier work[8], several rotation-vibration transitions could be nearly-resonant ($\Delta E/E \sim 1$) and appear ballistic. Because of the large rotational constant and high vibrational frequency of N_2 only one transition can be nearly-resonant. It is seen from figure 1 that if one interested in defining only the vibrational level, one may obtain a beam of N_2 molecules in $v=3$ by filtering out molecules with recoil velocities below 920 and higher than 1750 m/s. It should be noted, however, that defining only the vibrational level leads to an increase of signal by only a factor of about 2. Figure (2) demonstrates the feasibility of producing velocity-selected N_2 beams in the $v=6,j=0$ state. Lower values of the recoil velocities in the figures correspond to small c.m. scattering angles, resulting in transitions to only a few rotational levels having small quantum numbers. The transitions to different vibrational levels are well separated. Large values of recoil velocities, on the other hand, correspond to large c.m. scattering angles leading to large changes in the rotational quantum number during the collision. The rotational transitions are therefore not as neatly bunched within each vibrational level.

A beam containing molecules in nearly any final state may be prepared by giving the appropriate energy to the collision partners provided the c.m. cross section for the particular transition is not too small ($< 10^{-22}$ cm^2/sr). The velocity of the beam is equal to the c.m. velocity of the collision partners. The possibilities are limitless.

Part of this research was done while R.D.S. was visiting the Theoretical Institute for Atomic and Molecular Physics in Cambridge, Massachusetts. The research was in part funded by the Air Force Office of Scientific Research.

REFERENCES

1.R.D.Levine and R.B.Bernstein, *Molecular Reaction Dynamics*, 2nd ed. (Oxford University Press, New York, 1987).
2.F.F.Crim, M.S.Chou and G.A.Fisk, *Chem. Phys.* , 2,271(1973).
3.R.Bottner, U.Ross and J.Peter Toennies, *J.Chem.Phys.* 65, 733 (1976).
4.H.J.Loesch and D.R.Herschbach, *J.Chem. Phys.* 57,2038 (1972).
5.D.L.King, H.J.Loesch and D.R. Herschbach, Discuss. Faraday Soc. 55, II-34 (1973).
6.D.L.King, *Ph.D.Thesis* (Chemistry Department, Harvard University, 1974).
7. Elastic peak was so named because it has the maximum intensity where one would detect the elastically scattered alkali halide molecules. This peak was later shown[8] to consist mainly of inelastically scattered alkali halide molecules. This was causing some confusion. At the suggestion of Dudley Herschbach the elastic peak was renamed pseudoelastic peak. The new name is very appropriate because it describes the location of the peak and carries the warning label.
8.J.M.Sindoni and R.D.Sharma, *Phys. Rev. A, Rapid Communication,* (In Press).
9.R.D.Sharma, P.M.Bakshi and J.M.Sindoni, *Phys. Rev. A* 43, 189 (1991).

FIGURE CAPTIONS

Figure 1. Differential Cross Section (cm^2/sr) in the laboratory frame for the scattering of N_2(initial state v=0,j=0; velocity= 1200 m/s, 90°) upon colliding with Li^+(velocity= 5377 m/s, 0°) with a relative translational energy of 0.8825 eV as a function of the laboratory recoil velocity of N_2 at the laboratory scattering angle (48°±0.125°) coincident with the direction of the c.m. velocity vector (48.3°). The lone ballistic transition to the final state of N_2(v'=3,j'=10), ΔE/E= 0.99987, can be clearly seen.

Figure 2. Differential Cross Section (cm^2/sr) in the laboratory frame for the scattering of N_2(initial state v=0,j=0; velocity= 1200 m/s, 90°) upon colliding with Li^+(velocity= 7506 m/s, 0°) with a relative translational energy of 1.68 eV as a function of the laboratory recoil velocity of N_2 at the laboratory scattering angle (57.5°±0.125°) coincident with the direction of the c.m. velocity vector (57.46°). The lone ballistic transition to the final state of N_2(v'=6,j'=0), ΔE/E= 0.99994, can be clearly seen.

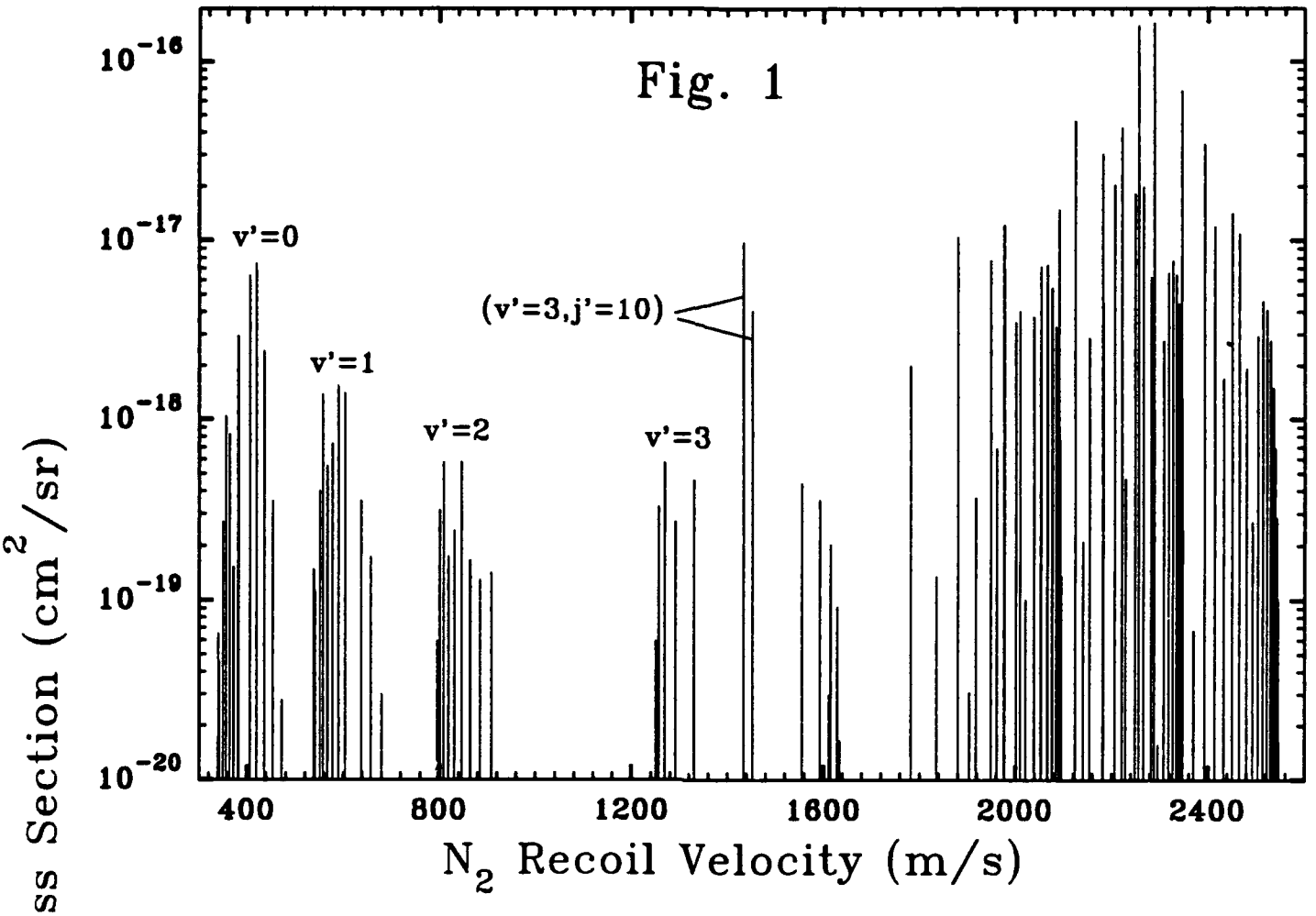
Fig. 1
Differential Cross Section (cm^2/sr)
10^{-16}
10^{-17}
10^{-18}
10^{-19}
10^{-20}
v'=0
v'=1
v'=2
v'=3
(v'=3,j'=10)
400
800
1200
1600
2000
2400
N_2 Recoil Velocity (m/s)

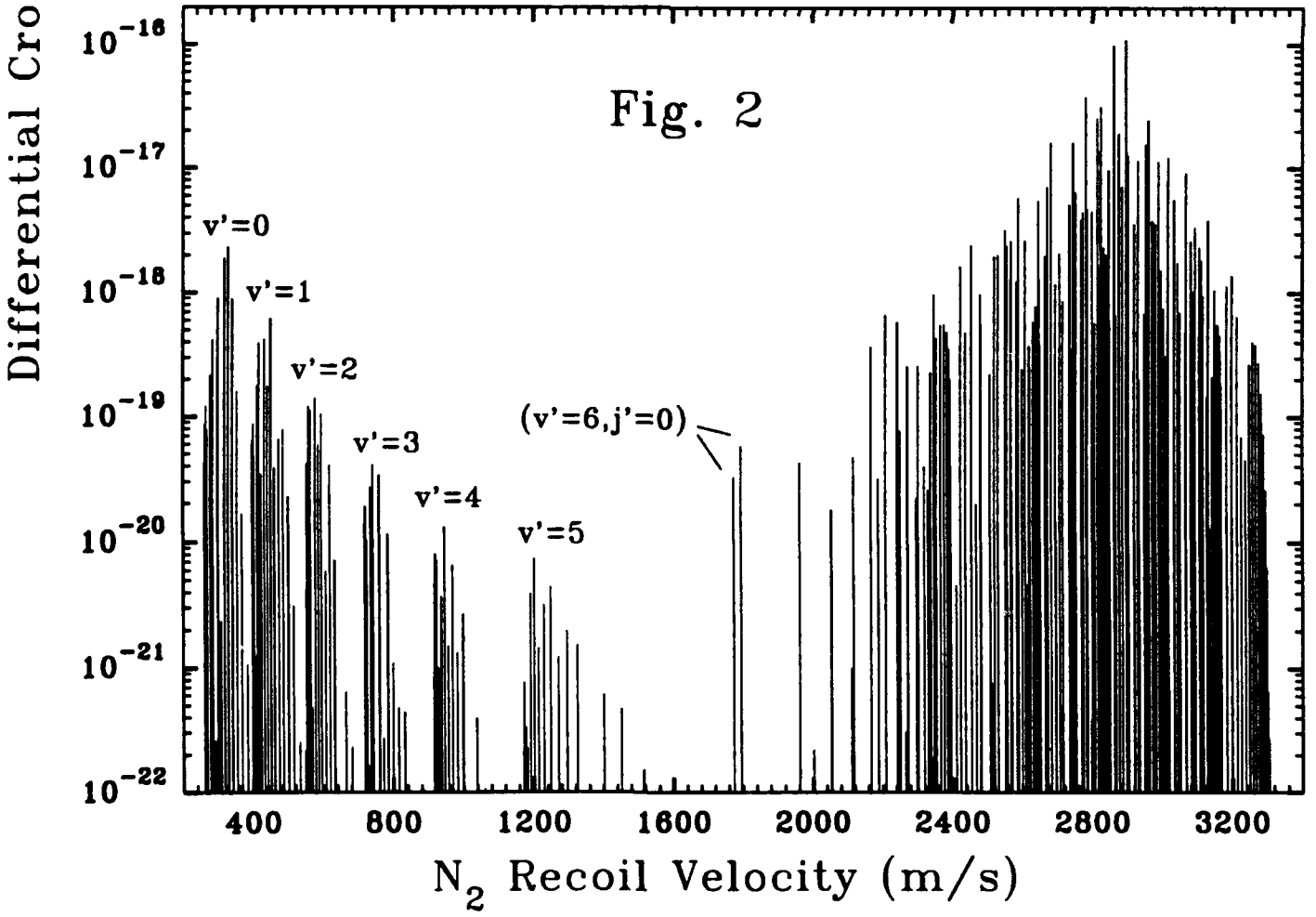
Fig. 2
Differential Cross Section (cm^2/sr)
10^{-16}
10^{-17}
10^{-18}
10^{-19}
10^{-20}
10^{-21}
10^{-22}
v'=0
v'=1
v'=2
v'=3
v'=4
v'=5
(v'=6,j'=0)
400
800
1200
1600
2000
2400
2800
3200
N_2 Recoil Velocity (m/s)

Molecular Beam-Surface Scattering: Investigations of Energy Transfer in Impulsive Collisions

Laura Smoliar, Deon Anex, and Yuan T. Lee

Department of Chemistry, University of California and Chemical Sciences Division, Lawrence Berkeley Laboratories, Berkeley, California 94720.

Molecular beam-surface scattering has been a useful tool for studying the dynamics of gas-surface interactions including phonon excitation, trapping, sticking, and energy transfer.[1] Our research will use this technique to study the role of collision energy and energy transfer in chemical processes such as etching, catalysis, and thin film deposition. As a first step, however, the dynamics of a relatively simple system have been explored to show the capabilies and power of this technique.

The Gas-Surface Machine (GSM) has a fixed source-detector angle of 90 degrees, with the crystal mounted on a rotating manipulator. The detector measures the time-of flight (TOF) of scattered products, mass selected by a quadrupole mass filter, at each of the angles allowed by rotation of the manipulator. The GSM design also has a fast ion gauge facing the incident beam, chopped by a four-slot wheel, so that the initial beam velocity will eventually be measured directly. At present, we calculate the beam velocity based on the nozzle temperature, measured by optical pyrometry. Thus, by measuring incident and final beam energies, we learn about energy transfer from the gas-surface interaction.

As an initial experiment, we chose to look at scattering of He and Ne off a cleaved LiF (100) surface. High kinetic energy beams were generated by combining seeding and nozzle heating to allow for a range between 2 and 140 kcal/mole. By seeding 1% Ne in H_2 and 5% He in H_2, we gain a factor of 9.08 and 1.90 in translational energy, compared to running a neat beem at the same temperature. A high temperature rhenium nozzle run at 250 watts (nozzle temperatures up to 2800 K) allows for beam energies as high as 140 kcal/mole (Ne mixture) and 35 kcal/mole (He mixture). The source can also be used to generate

hydrogen atoms from H_2 since a few percent dissociation is achieved at this temperature.

The results will be compared to those predicted from the gas phase model of hard sphere impulsive collisions, where energy transfer is dependent on the masses of the atoms in the colliding species:[2,3] In addition, the angular distribution of products will be used to describe the dynamics of the inelastic scattering seen in the case of Ne at incident energies greater than 78 kcal/mole. Finally, some evidence for reactive scattering with hydrogen and deuterium atoms will be presented.

In the future we will extend this study to a CsF surface where the impulsive model can be tested over a wider range of masses. We also plan to look at reactive systems, such as H-atom etching of graphite, once we add another section of differential pumping around the crystal to provide a cleaner environment for the surface.

1. J. A. Barker and D. J. Auerbach, Surf. Sci. Rep. 4 (1985) 1-99.
2. F. P. Tully, N. H. Cheung, H. Haberland, and Y. T. Lee, J. Chem. Phys. 73, 4460 (1980).
3. Bruce H. Mahan, J. Chem. Phys., 52, 5221 (1970).

MASS SPECTROSCOPIC MEASUREMENTS OF MOLECULAR BEAMS FORMED FROM HYDROCARBON ARCJET PLASMAS THAT DEPOSIT DIAMOND THIN FILMS*

Kenneth R. Stalder

Molecular Physics Laboratory

SRI International

Menlo Park, CA 94025

Thin diamond films, which can be deposited by a variety of methods, hold great promise for a variety of technological applications.

We have been studying the deposition of polycrystalline diamond by arcjet plasmas impinging on silicon and tantalum substrates. Using this technique, we have observed diamond growth rates of approximately 1 μm/min when a 1 kW arc plasma is maintained with 1% CH_4 in hydrogen gas at 200 Torr and 10 slm. This rate, comparable to that observed in the oxy-acetlyene flame deposition method, is approximately 2 orders of magnitude greater than that reported in low-rate deposition systems, such as in the hot filament method. The strongest deposition occurs near the stagnation point for the normal incidence flow as it strikes the surface.[1]

Optical emission spectroscopy of an unobstructed jet shows strong emission in the C_2 Swan bands and CH (A-X, B-X, C-X) transitions.[2] Detailed emission measurements of the C_2 Swan bands and comparisons with synthetic spectra show that these molecules are well thermalized both rotationally and vibrationally. The apparent temperature of the jet is approximately 5000 K at the exit orifice and drops to below 4000 K in just 1 cm. Independent laser induced fluorescence measurements of the ground state temperatures of CH in the jet are somewhat contradictory in that they indicate temperatures of around 2200 K downstream of the orifice.[3]

In order to study molecules that do not radiate, we are currently forming molecular beams at the stagnation point where the flow strikes a tantalum surface. A diagram of the apparatus is shown in Figure 1. The hot gas effuses through a small orifice into a region pumped by a high-speed roots pump, then is skimmed by a second orifice and enters a high vacuum analysis region where it enters a quadrupole mass spectrometer. A tuning fork chopper and lock-in amplifier enables us to discriminate against the background residual gases.

Mass spectra of the molecular beam indicates that significant chemistry is induced in the high temperature arc plasma. The mass spectrometer does not resolve hydrogen atoms efficiently, which are expected to be the dominant species.[4] Of the higher mass species, acetylene (C_2H_2) predominates. In some models of diamond growth, acetylene is thought to be an important growth species.[5] As shown in Figure 2, the acetylene concentration increases linearly with increasing CH_4 flow. Methyl radicals, CH_3, which others suggest are important precursors to diamond formation[6] are also observed, but the signal is erratic, indicative of some turbulent boundary layer phenomena or other effect.

Figure 1

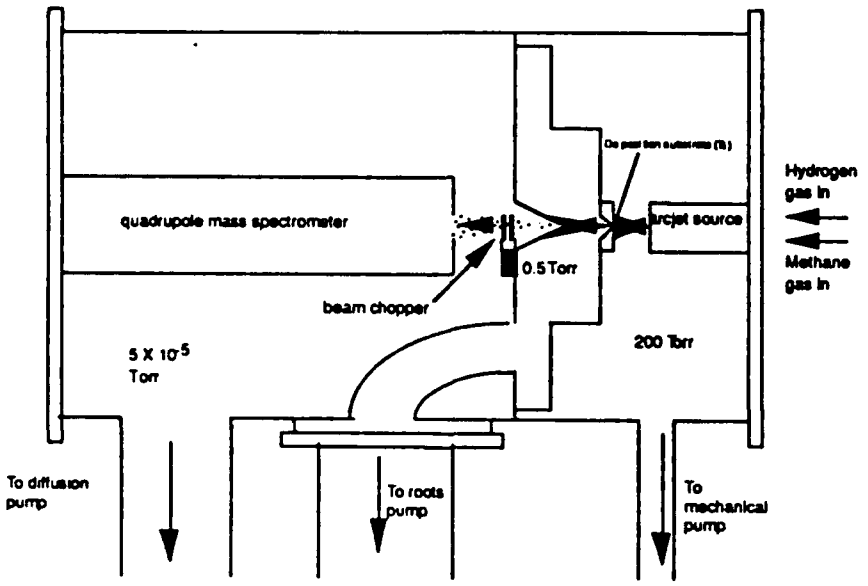

We also observe several features that are not predicted in the models. Specifically, we observe significant amounts of M/e = 29, which we attribute to either C_2H_5 or HCO (the latter must be a consequence of a small, persistent leak). The former may be naturally present in the arcjet, a fragmentation product of C_2H_6, or it may form from recombination of methyl radicals in the first expansion orifice from the reaction. These effects are under continuing investigation.

Also predicted by Goodwin[4] is an abundance of carbon atoms. He postulates that this species might play an important role in the arcjet synthesis of diamond. However, in our experiments, no significant peak at M/e = 12 peak is observed.

This presentation will describe our work on the arcjet-produced molecular beams and planned experiments on the deposition of diamond by this molecular beam.

Figure 2

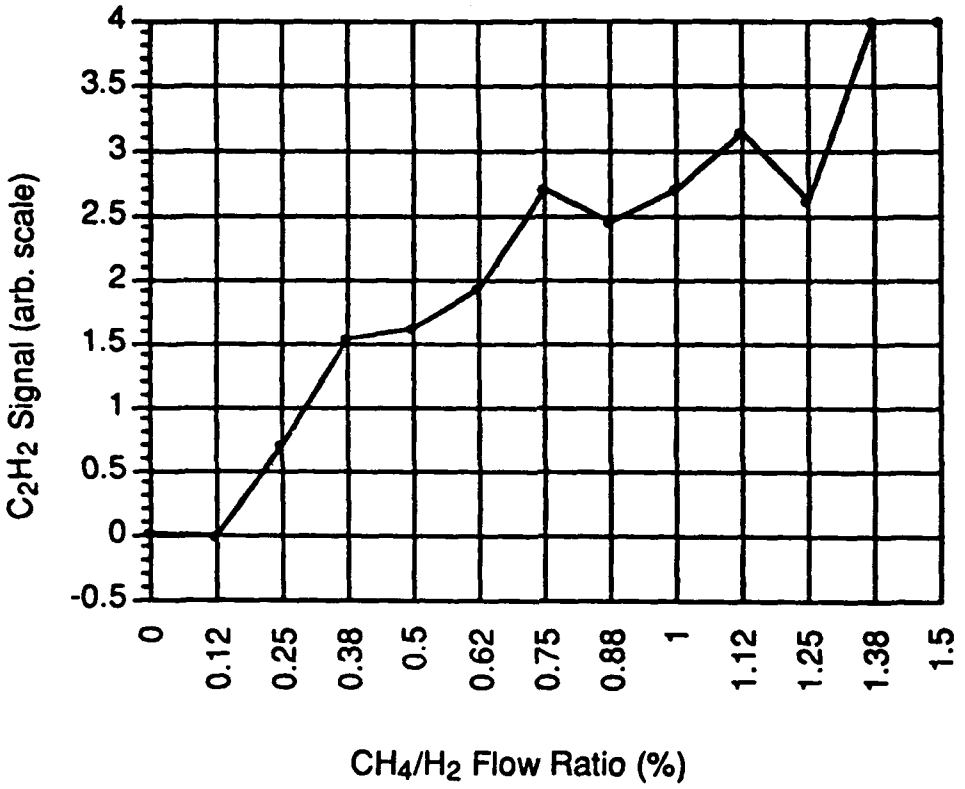

* This work is supported by the Army Research Office, Contract Number DAAL03-89-K-0157.

REFERENCES

1. A. W. Phelps and K. R. Stalder, Appl. Phys. Lett. **57**, 1090 (1990).

2. K. R. Stalder and R. L. Sharpless, J. Appl. Phys. **68**, 6187 (1990).

3. G. A. Raiche, G. P. Smith and J. B. Jeffries, Proc. 2nd Int. Conf. on New Diamond Sci. and Tech., ed. R. Messier and J. J. Glass, Mat. Res. Soc. (1990).

4. D. G. Goodwin, Appl. Phys. Lett. **53**, 277 (1991)

5. D. Huang, M. Frenklach, M. Maroncelli, J. Phys. Chem. **92**, 6379 (1988).

6. S. Harris, Appl. Phys. Lett. **56**, 2298 (1990).

Asilomar abstract I

Mode Specific Photodissociation of the $^1B_2$ State of CS_2

C. Starrs, M.N. Jego, A. Mank, and J.W. Hepburn
Department of Chemistry
University of Waterloo
Waterloo, Ont. N2L 3G1
CANADA

In this paper we discuss results of a study into the spectroscopy and photodissociation dynamics of the predissociating $^1B_2$ state of the CS_2 molecule. This study used photofragment spectroscopy on CS_2 molecules cooled by supersonic expansion, using a tunable photolysis laser (200nm to 216nm) to excite several vibrational bands of the predissociating $^1B_2$ state. The photofragment spectrometer used tunable vacuum ultraviolet light to detect the atomic sulfur products resulting from the CS_2 photodissociation. For the photolysis wavelengths used, there are two possible product channels:

$$CS_2 + h\nu \rightarrow CS_2^*(^1B_2) \rightarrow CS(X^1\Sigma^+) + S(^1D_2)$$

$$\rightarrow CS(X^1\Sigma^+) + S(^3P_J)$$

These channels can be probed separately by excitation of S resonance lines at 144.8nm for the $^1D_2$ channel, and between 147.4nm and 148.7nm for the three spin orbit sublevels of the ^3P_J channel.

Two different types of experiments have been carried out. In the first, the detection wavelength was fixed to detect a specific product channel and an excitation spectrum for that channel was measured. In this way, we have mapped out the absorption spectrum for jet cooled CS_2, and we are using a semi-rigid bender treatment to analyse the spectrum, which is very complicated in this case. Once bands were identified, the second type of experiment was to fix the photolysis laser on one of these vibrational bands, and then scan the VUV probe

laser to probe the dynamics, through a combination of Doppler spectroscopy and relative product yield measurements.

The most interesting result from this work has been the observation of a strong product channel selectivity resulting from exciting different vibrational levels in the $^1B_2$ state. As an example, figure 1 shows excitation spectra for one group of vibrational bands around 208nm in the CS_2 $^1B_2 \leftarrow X^1\Sigma^+_g$ spectrum, recorded for $S(^1D_2)$ and $S(^3P_2)$ product formation. It can be seen that the branching ratio between these two channels is a strong function of which band in the CS_2 spectrum is excited, a result confirmed by fixed photolysis wavelength experiments. The difference is in the K quantum number, with the bands labelled Σ_0 being K=0, and those labelled Π_1 being K=1.

Figure 1: Action spectra for CS_2 around 208nm

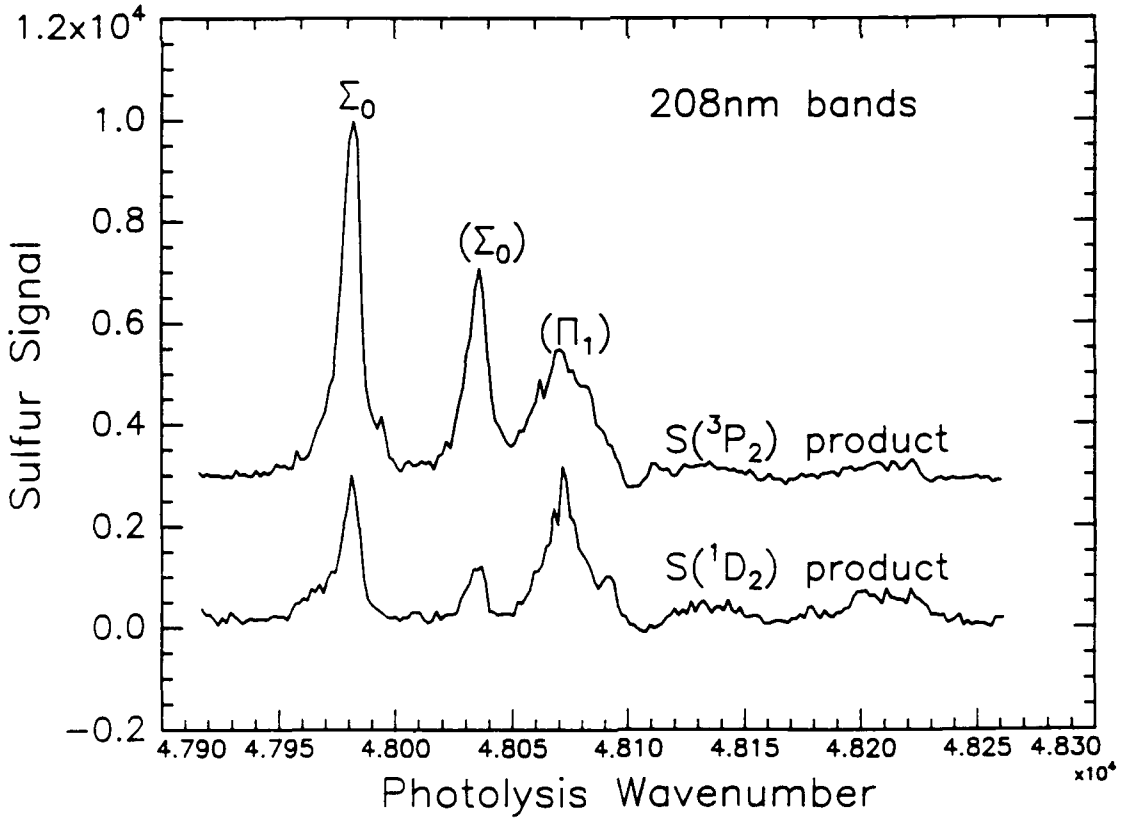

In fact, the product channel selectivity is very specific, with the $S(^3P_2)$ product being favoured very strongly over all other possible products ($S(^1D_2)$, $S(^3P_1)$, and $S(^3P_0)$) for K=0 levels in the $^1B_2$ state, and a more democratic product distribution being observed for K=1 levels.

Although this selectivity is general for the $^1B_2$ state, it appears that it gets stronger for lower vibrational levels in the $^1B_2$ state. This can be seen in Figure 2, were the $^3P_2$ and $^1D_2$ excitation spectra are shown for a group of CS_2 bands around 210nm. The dynamics is affected in many ways as a function of vibrational excitation, with the predissociation lifetime decreasing steadily as v increases, and the S atom singlet:triplet branching ratio changing from 1:30 for 210nm to 1:2.8 for 193nm excitation[1].

Figure 2: Action spectra for CS_2 around 210nm

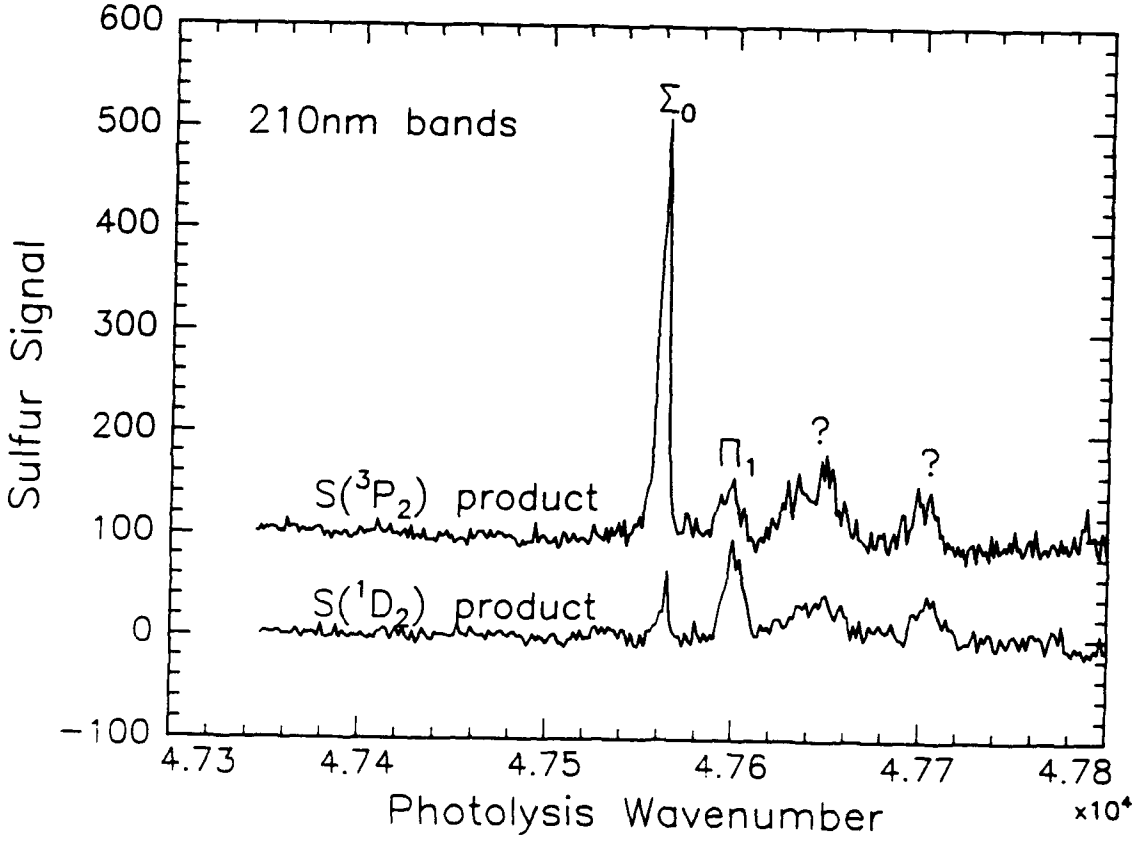

All of these results on CS_2 provide detailed insight into the predissociation dynamics in this important model system, and we will present some conclusions on the role of singlet triplet curve crossing in this case.

1. I.M. Waller and J.W. Hepburn, *J. Chem. Phys.* **87**, 3261 (1987)

Acknowledgements

This work was supported by NSERC(Canada), and the Canadian national networks of centres of excellence program, administered by NSERC. Some additional support was provided by the Ontario Lasers and Lightwaves Research Centre. MNJ was supported by a Canada-France exchange fellowship.

MOLECULAR-STATISTICAL DERIVATION OF THE ARRHENIUS LAW FOR HOMOGENEOUS BIMOLECULAR DILUTED GAS-PHASE REACTIONS

W. Stiller

Theoretical Kinetics Group, Permoserstr. 15, D-O-7050, Leipzig
Germany

INTRODUCTION

Let us consider a diluted (carrier)gas C in which reactants of the kinds i = X, Y are dispersively distributed leading to a bimolecular (forward) reaction:

$$X + Y \xrightarrow{(C)} \text{products} \qquad (1)$$

A method commonly used in kinetics is to describe the temperature behavior of the velocity of the reaction (1) by a rate coefficient $k^{(A)}$ according to the following (modified) Arrhenius Law [1]:

$$k^{(A)}(T) = A_{(n)} T^n \exp(-E_A/k_B T) \qquad (2)$$

$A_{(n)}$ preexponential constant; n parameter; E_A Arrhenius activation energy; k_B Boltzmann constant; T temperature.

In this paper it is intended to give some molecular-statistical criteria under which physicochemical conditions an ansatz, Eq. (1) is justified. From the statistical point of view we have to differ between - thermodynamical equilibrium situations - in which the time-dependent velocity distribution functions $f_X(\vec{v}_X,t)$ and $f_Y(\vec{v}_Y,t)$ of the reactants X and Y are Maxwellians and - nonequilibrium situations - in which the $f_i(\vec{v}_i,t)$, i = X, Y have to be calculated from so-called kinetic equation systems (e. g. coupled Boltzmann kinetic equations) containing the statistical information on all kinds of elastic, inelastic, and reactive collisions between the reacting and/or non-reacting particles (here X, Y, C).

EQUILIBRIUM THEORY: f_i's are Maxwellians

It is well-known, that in this situation the (equilibrium) rate coefficient $k^{(eq)}$ has the general form [2]:

$$k^{(eq)}(T) = \left(\pi m [k_B T]^3/8\right)^{-1/2} \int_0^\infty E\sigma_R(E)\exp(-E/k_B T)dE \qquad (3)$$

$m^{-1} = m_X^{-1} + m_Y^{-1}$, reduced mass; $E = mv^2/2$, kinetic energy of the relative motion of the particles X and Y with their relative velocity (magnitude) $v = |\vec{v}_X - \vec{v}_Y|$; σ_R, total reactive cross section.

In order to determine what function $\sigma_R(E)$ in Eq. (3) can reproduce the Arrhenius Law for $k^{(eq)}(T)$ we identify the Eqs. (2) and (3). This leads to a linear Laplacian integral equation for $y(E) = E\sigma_R(E)$ with the "product kernel" βE, where $\beta = 1/k_B T > 0$, in the form:

$$\int_0^\infty \exp(-\beta E) y(E) dE = f(\beta) \qquad (4)$$

with

$$f(\beta) = B_{(n)} \beta^{-(n+3/2)} \exp(-\beta E_A), \quad B_{(n)} = A_{(n)} (\pi m/8)^{1/2} k_B^{-n} \qquad (5)$$

The solution of integral equation (4) gives

$$\sigma_R^{(A)}(E-E_A) = \sigma_{(n+1/2)}^{(R)} E^{-1} (E-E_A)^{n+1/2} \quad \text{for } E \geq E_A \qquad (6)$$

and $\sigma_R^{(A)} = 0$ for $E < E_A$. Results similar to Eq. (6) were obtained with different methods e. g. by Karplus, Porter and Sharma [3], Lin and Eyring [4], Perwušin [5], Ureña [6], and Polak and Chačojan [7]. For $n = 0$ ("pure" Arrhenius Law with $k^{(A)} = A_{(o)} \exp(-E_A/k_B T)$) Eq. (6) goes over into $\sigma_R^{(A)}(E-E_A) = \sigma_{(1/2)}^{(R)} (E-E_A)^{1/2}/E$ (peculiar case a)) and if additionally $E_A = 0$ (no activation barrier) we obtain $\sigma_R^{(A)} \sim E^{-1/2}$, i. e. $k^{(A)} = A_{(o)} = \text{const}$.

NONEQUILIBRIUM THEORY: f_i's are non-Maxwellians

To find the conditions for the validity of an Arrhenius Law under nonequilibrium situations (f_i's non-Maxwellians) is more difficult than the equilibrium case. The rate coefficient $k^{(non)}$ can be expressed for moderately diluted gas-phase reactions as follows:

$$k_{(t)}^{(non)} = n_X^{-1}(t) n_Y^{-1}(t) \iint_{33} d\vec{v}_X d\vec{v}_Y v \sigma_R(v) f_X^{(non)}(\vec{v}_X, t/\sigma_{el}, \sigma_R) \cdot f_Y^{(non)}(\vec{v}_Y, t/\sigma_{el}, \sigma_R) \qquad (7)$$

σ_{el}, elastic cross sections for all elastic collisions between X, Y and C; σ_R reactive cross section for a (X,Y)-reaction; n_X, n_Y, number densities of X and Y, resp.

For simplicity we ignore the internal degrees of freedom of

the reactants and the inert component. The question is now under which functional combination of σ_R, $f_X^{(non)}$, and $f_Y^{(non)}$ the sixfold integration will result in an Arrhenius Law, Eq. (2). To answer this question the functions $f_X^{(non)}$ and $f_Y^{(non)}$ must be calculated from kinetic equations. For moderately diluted gases these are (coupled) Boltzmann equations, i. e. nonlinear integrodifferential equations in general. This problem can be solved by direct Monte Carlo simulation[8]. Let us discuss an analytically and a numerically solved particular cases:

case c) $\sigma_R \sim v^{-1} \sim E^{-1/2}$

In this case Eq. (7) gives as a result ("normalization solution") $k^{(non)} = \text{const.}$, i. e. $k^{(non)} = k^{(A)}$ ($n = 0$, $E_A = 0$) which coincides with the peculiar case b) under equilibrium conditions whatever had been calculated for $f_X^{(non)}$ and $f_Y^{(non)}$.

case d) reative Lorentz gas; σ_R as in the peculiar case a) with $\sigma_{(1/2)}^{(R)} = 4 \cdot 10^{-18}$ cm^2 and $T = 300$ K

Requiring $m_X/m_C \ll 1$, $m_Y/m_C \ll 1$ (mass relations), $n_X/n_C \ll 1$ and $n_Y/n_C \ll 1$ (number density relations), i. e. Lorentz gas conditions and put $m_X/m_Y = 1/50$ we find in the large time limit: The greater the relation $\sigma_{(1/2)}^R/\sigma_{el}$ the stronger is the deviation from an Arrhenius Law. In the paper also variations with the activation energy are discussed.

DISCUSSION

Under equilibrium (f_i's Maxwellians) the validity of an Arrhenius Law for bimolecular homogeneous gas-phase reactions ($X + Y \longrightarrow$ products) can be reduced to a particular choice of the total reactive cross section. Under nonequilibrium conditions (f_i's non-Maxwellians) an Arrhenius Law is only valid in singular situations (e. g. $\sigma_R \sim v^{-1}$, f_i's arbitraryly chosen). Under Lorentz gas conditions it can be shown by direct MC simulation that the deviation from the Arrhenius Law is considerably if the reactive cross section comes into the order of magnitude of the elastic one.

REFERENCES

[1] S. Arrhenius, Z. phys. Chemie (Leipzig) 4 (1889) 226

[2] M. A. Eliason, and J. O. Hirschfelder, J. chem. Phys. 30 (1959) 1426

[3] M. Karplus, R. N. Porter, and R. D. Sharma, J. chem. Phys. 43 (1965) 3259

[4] H. Lin, and H. Eyring, Proc. Natl. Acad. Sci. US 68 (1971) 402

[5] J. V. Perwušin, Zurn. fiz. Chim. 51 (1977) 1682

[6] A. G. Ureña, Adv. Chem. Phys., vol. 66 (1987) pp. 213-335

[7] L. S. Polak, and A. V. Chačojan, Chim. vys. Energ. 15 (1981) 26

[8] W. Stiller, Arrhenius Equation and Nonequilibrium Kinetics, Teubner, Stuttgart, Leipzig 1989, chapts. 5 and 6

Dynamics of the Ba + HI Reaction: BaI(v) Rotational Distributions and Specific Opacity Functions

A. A. Tsekouras, C. A. Leach, K. S. Kalogerakis, and R. N. Zare
Department of Chemistry, Stanford University, Stanford, CA 94305, USA

The reaction Ba + HI → BaI + H is the prototypic example of a bimolecular, kinematically constrained system. The low exoergicity of the reaction and the high rotational constant of HI justify the simplification of the expression for the conservation of angular momentum to the form

$$\mu_{Ba\text{-}HI}\, v_{rel,Ba\text{-}HI}\, b_{Ba\text{-}HI} = J_{BaI} \qquad (1)$$

where we have the reduced mass, the relative velocity, and the impact parameter of the reagents on the lefthand side and the rotational angular momentum of the BaI product on the righthand side. This expression has the potential to reveal information on the impact parameter - a quantity which defies direct control or observation in reactive collisions.

Detailed spectroscopic measurements of BaI - made difficult by its reduced mass - provide its rotational excitation. Standard beam measurements supply the other needed quantity in Eq. 1, viz. $v_{rel\ Ba\text{-}HI}$.

The experimental apparatus[1] consists of three parts: the reaction chamber, the probe laser source and the detection system. A supersonic beam of HI seeded in N_2 intersects at right angles a slightly supersonic, neat Ba beam emerging from an oven source maintained at 1300 K. The reaction products are electronically excited by a high-resolution ring dye laser beam. The resulting fluorescence is imaged on a photomultiplier tube directly or via a monochromator[2]. The photocurrent is monitored using phase-sensitive detection or photon counting and recorded by the computer that also controls the frequency scan of the laser.

The same detection scheme is used to record the Doppler-shifted spectrum of Ba. A chopper - quadrupole mass spectrometer combination in conjunction with a boxcar amplifier allows the determination of the time-of-flight (TOF) profile of the HI beam.

The raw data from the experiment are TOF distributions for the HI beam, sub-Doppler and Doppler-broadened spectra of Ba, and, most importantly, detailed scans of the BaI $C^2\Pi$ - $X^2\Sigma^+$ band system with rotational resolution. The exact transmission spectrum of the monochromator which corresponds to a set of BaI scans is also recorded by scattering the laser beam off a suitably located target inside the chamber.

Monochromator transmission spectra are fit to an empirical formula to facilitate parametric representation. BaI spectra are processed to yield assigned[3] line intensities. These are combined with transition line strengths and transmission probabilities through the monochromator to give BaI $X^2\Sigma^+$ rotational population distributions for different vibrational levels.

The Ba ^3D - ^1S line profile is convoluted in a fit with a parameterized velocity distribution to construct the experimental Doppler profile of the same transition. Similarly, the HI velocity distribution is determined in a fit where the parameterized distribution is convoluted with the gas pulse profile and the mass spectrometer response function to yield the experimental TOF signal.

The relative velocity distribution is easily established from the known beam velocity distributions and their relative geometry.

Specific opacity functions, $P_v(b)$, i.e., the reaction probability for given product vibrational states as a function of impact parameter, are also determined with a convolution fit. A certain functional form of $P_v(b)$ is convoluted with the relative velocity distribution under the energetic and kinematic constraints to simulate the observed rotational distributions.

Experiments were done under crossed-beam[4,5] and beam-gas conditions. The former gave rise to narrow rotational distributions which were recorded for the three lowest vibrational levels. These distributions peaked at J values as high as 420. The corresponding relative velocity values were approximately 950 m s^{-1}. In the beam-gas experiments rotational distributions were recorded for v=0, 4, 8, 12, and 16. These were wider and displayed a very clear trend for the most populated rotational levels, $J_{max,v}$: J_{max} dropped from 410 for v=0 to 150 for v=16.

At the simplest level of approximation each vibrational level is assumed to have a very narrow Gaussian-shaped opacity function. The only adjustable parameter is the peak position of $P_v(b)$. The result is a sequence of evenly spaced Gaussian peaks located from 4.5 Å for v=0 to 2.1 Å for v=16. These values can be compared with the equilibrium bond length of BaI, viz. 3.08 Å, which remains largely the same at the vibrational or rotational levels under consideration.

Although the velocity dependence of the reactivity has not been studied, the picture that emerges shows that the collision impact parameter controls the vibrational level of the BaI product. Furthermore, a 1:1 mapping is found in which reactive collisions with large impact parameters correspond to BaI product in low states of vibrational excitation.

Support by the US National Science Foundation is gratefully acknowledged.

References

1 P. H. Vaccaro, D. Zhao, A. A. Tsekouras, C. A. Leach, W. E. Ernst, and R. N. Zare, *J. Chem. Phys.* **93**, 8544 (1990).

2 D. Zhao, P. H. Vaccaro, A. A. Tsekouras, C. A. Leach, and R. N. Zare, *J. Mol. Spectrosc.* **148**, 226 (1991).

3 C. A. Leach, A. A. Tsekouras, and R. N. Zare, *J. Mol. Spectrosc.* **153**, xxx (1992).

4 C. A. Leach, A. A. Tsekouras, P. H. Vaccaro, R. N. Zare, and D. Zhao, *Faraday Discuss. Chem. Soc.*, **91**, 183 (1991).

5 P. H. Vaccaro, A. A. Tsekouras, D. Zhao, C. A. Leach, and R. N. Zare, *J. Chem. Phys.* **96**, 2786 (1992).

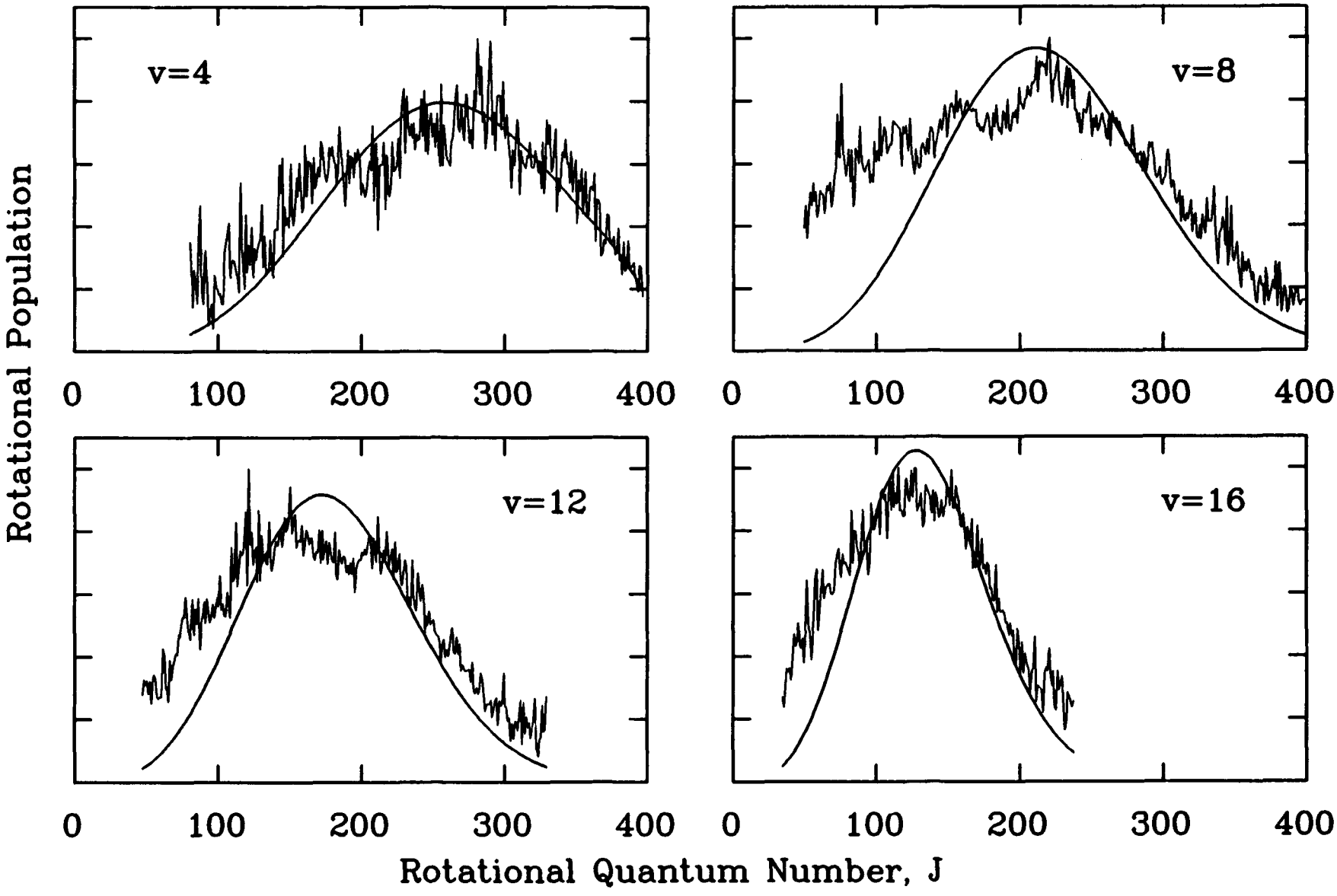

Figure 1. BaI(v) rotational population distributions recorded under beam - gas conditions. The smooth lines are simulations where the specific opacity functions used have Gaussian shape with peaks and widths as indicated in Fig. 2.

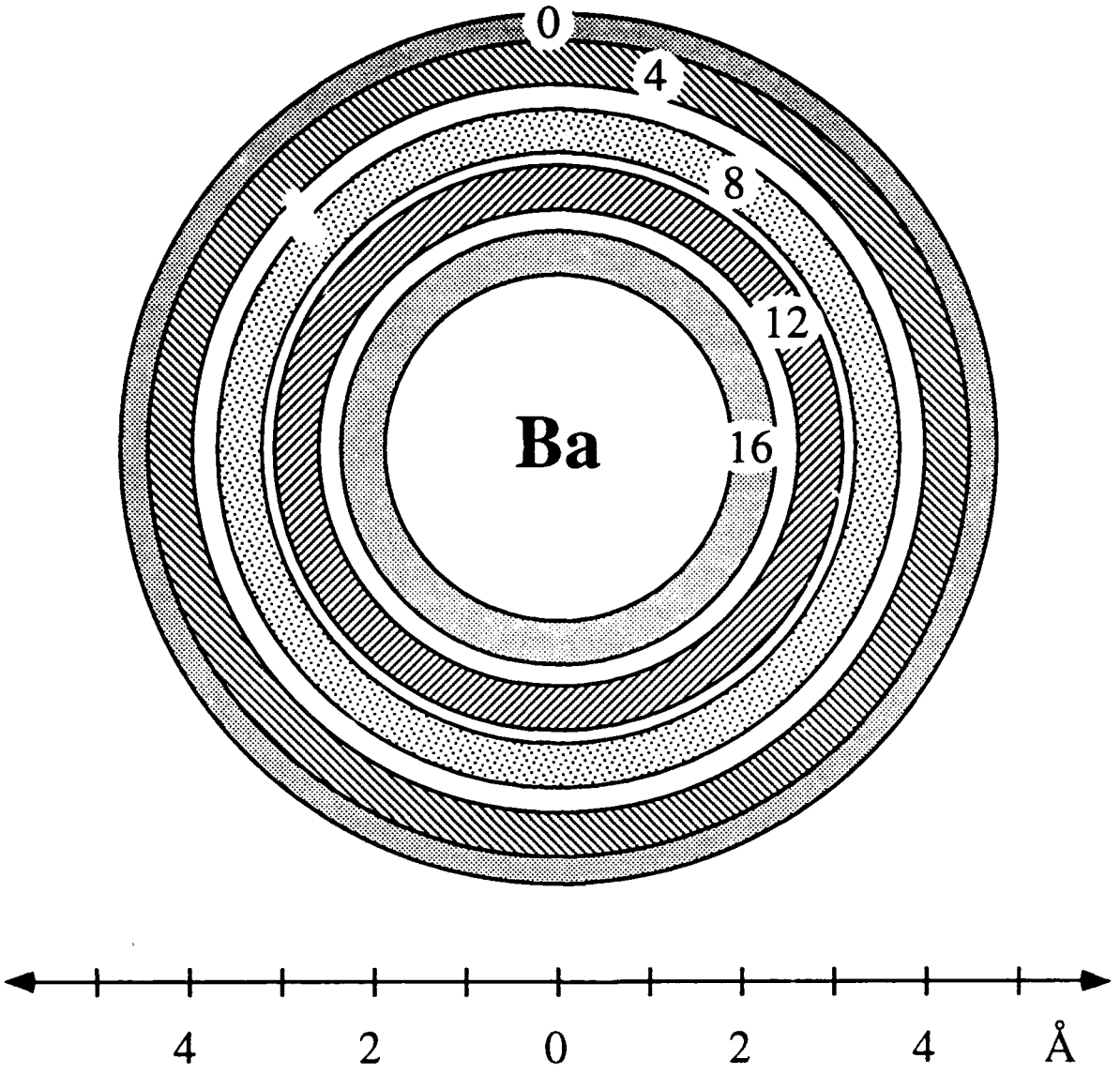

Figure 2. Specific opacity rings for the reaction Ba + HI → BaI(v) + H. The vibrational level of the reaction product is indicated for each ring.

Structure and conformation in the photofragmentation dynamics of large molecules

Jeffrey L. Tomer, Mark C. Wall, D. Scott Tonner, and Joseph I. Cline
Department of Chemistry/216
University of Nevada
Reno, NV 89557-0020

Recent experimental work has shown that dynamical data can be used to explore the role of molecular geometry[1] and conformation[2] in photodissociation dynamics. This paper describes experiments that focus on the role of molecular geometry in the dissociation dynamics of alkylnitroso compounds. Unlike molecules that undergo direct photodissociation, the relatively slow dissociation of S_1 excited nitroso compounds can be dictated by molecular structures not directly involving the breaking bond.[3] Information about the initial excitation event is scrambled in these systems and energy redistribution can greatly influences fragment trajectories. Under certain excitation conditions, dissociation takes place across a barrier with little excess energy. In these experiments we explore the relationship between structure and dynamics under these conditions with a particular interest in how low frequency motions effect NO product rotational excitation.

Experimental Strategy:

Pump-probe type pulsed (ns) laser spectroscopy is conducted on nitroso compounds seeded in a skimmed, pulsed supersonic expansion. The pump laser pulse at 600-700 nm crosses the molecular beam 30 cm from the nozzle and excites the $S_1 \leftarrow S_0$ ($\pi^* \leftarrow n$) transition of the jet-cooled molecules. A temporally delayed, spatially overlapped probe laser pulse measures the rovibronic quantum state population distribution of the nascent NO product by 1+1 resonance-enhanced multiphoton ionization (REMPI) at 226 nm through the $A^2\Sigma^+ \leftarrow X^2\Pi_{1/2,3/2}$ transition. Pulsed-extraction time-of-flight mass spectrometry will be used to determine the center-of-mass velocity of the photodissociation products. Careful control of the pump and probe laser intensities permits any NO signal from probe laser induced dissociation of the parent molecule to be completely eliminated.

Results and Discussion

The 1+1 REMPI spectrum of $NO(X^2\Pi_{1/2}, v''=0)$ from the 680 nm photofragmentation of 2-chloro-2-nitrosopropane ($(CH_3)_2ClCNO$) seeded in He is shown in Fig. 1a. The probe laser pulse is delayed approximately 10 ns from the pump pulse. Fig. 1b shows a simulated NO spectrum for a best fit to a Boltzmann rotational population distribution characteristic of a rotational temperature of 220 K. The distribution is not truly Boltzmann and the relatively low temperature is consistent with a dissociation mechanism involving rapid intersystem crossing and direct dissociation across a barrier on the T_1

electronic surface as has been proposed for excitation of $(CF_3)_3CNO$ above the T_1 barrier.[4] However, in contrast to $(CF_3)_3CNO$, preliminary experiments on 2-chloro-2-nitrosopropane do not show the anomalously cold spin-orbit population distribution characteristic of dissociation on the T_1 surface.

The effect of the substitution of a chlorine atom for a methyl group on this system and the resulting change in the dynamics along the dissociation and C-N-O torsional coordinates will be discussed in terms of their effect upon rotation, spin-orbit population, and kinetic energy release. Data for the photofragmentation of 1-chloro-1-nitrosocyclohexane will be interpreted, focussing on any role that molecular conformation plays in directing the NO fragment trajectory.

References:

1. E.F. Cromwell, D.J. Liu, M.J.J. Vrakking, A.H. Kung, and Y.T. Lee, *J. Chem. Phys.* **95**, 297 (1991).
2. H.J. Hwang and M.A. El-Sayed, *J. Chem. Phys.* **94**, 4877 (1991).
3. H. Reisler, M. Noble, and C. Wittig in M.N.R. Ashfold and J.E. Baggot, Eds., *Molecular Photodissociation Dynamics* (Royal Society of Chemistry, London, 1987), Chapt. 5.
4. M. Noble, C.X.W. Qian, H. Reisler, and C. Wittig, *J. Chem. Phys.* **85**, 5763 (1986).

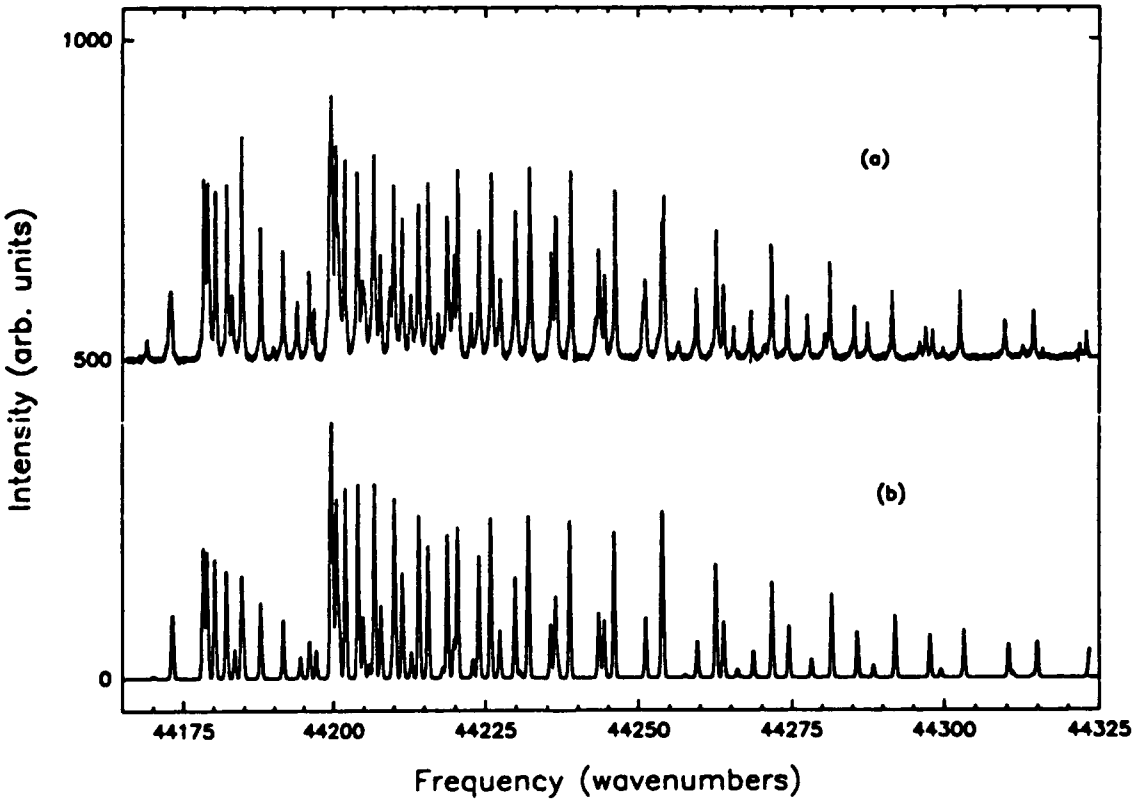

Figure 1

MOLECULAR COLLISIONS STUDIED BY LIGHT-INDUCED DRIFT

G.J. van der Meer, H.I. Bloemink, P.L. Chapovsky*and L.J.F. Hermans
Huygens Laboratory, Leiden University,
P.O. Box 9504, 2300 RA Leiden, The Netherlands

Traditionally, information on molecular collisions is obtained either from molecular beam experiments or from gas kinetic effects. A direct comparison between data from these two types of experiments is often difficult, because, in classical gas kinetic effects, a wide range of molecular internal states and velocities is involved.

Recently a new type of gas kinetic effect - Light-Induced Drift (LID) - was predicted [1], which can provide detailed information about the dependence of molecular collisions on molecular vibrational and rotational quantum states as well as on molecular velocity. Thus, information obtained from LID is largely analogous to that obtained from molecular beam experiments. It is the purpose of this paper to review the latest LID experiments, which illustrate the extremely high sensitivity of LID as a tool to study molecular collisions. The principle of LID is explained in Fig. 1.

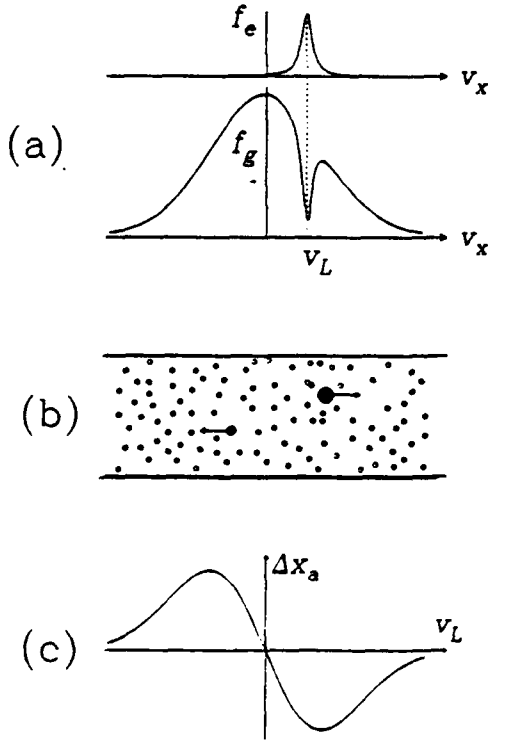

Figure 1: The principle of Light-Induced Drift schematically.
(a) Ground-state and excited-state velocity distribution for excitation by radiation propagating along the positive x-axis and tuned slightly above resonance: $(\omega_L - \omega_o)/k \equiv \Omega/k = V_L$.
(b) If the excitation modifies the interaction of the molecules with respect to the buffer gas particles, a net flux will result. In a closed tube this will give rise to a concentration gradient.
(c) The resulting concentration difference Δx_a as a function of V_L if $\Delta\nu/\nu$ is assumed constant.

*Permanent address: Institute of Automation and Electrometry, 630090 Novosibirsk, Russia

Using the Doppler effect, narrow band laser radiation excites molecules in a velocity selective way. This gives rise to a flux of excited-state particles with a well defined velocity component along the wave vector, and an opposing flux of ground state particles. If the collision cross sections, or the transport collision rates for excited (ν_e) and ground state (ν_g) particles with respect to a buffer gas are different, the two fluxes will experience different friction forces, and a net flux will result. In a closed tube this will give rise to a concentration gradient of the light-absorbing particles. This can be measured either by a mass-spectrometric technique [2], or by a thermal conductivity method [3].

The difference in absorbing particle concentration along the tube is connected with the relative difference in transport collision rate $\Delta\nu/\nu \equiv (\nu_e - \nu_g)/\nu_e$ by

$$\Delta x_a = -\frac{\Delta\nu}{\nu}\frac{2\Delta P_L}{\pi R^2 n\hbar\omega_L}\frac{V_L}{V_o^2},$$

where x_a is the volume fraction of light-absorbing particles, $V_o = \sqrt{2kT/m}$ is the thermal speed, ΔP_L is the absorbed laser power, R is the radius of the tube, ω_L is the laser frequency and n is the total number density.

Since LID arises only if $\Delta\nu/\nu \neq 0$, the sensitivity for measuring $\Delta\nu/\nu$ is very high. Experiments [2,3] have shown that for rovibrational transitions with reasonable light absorption values of $\Delta\nu/\nu$ of 10^{-6} can be easily measured. Typically, one finds that $\Delta\nu/\nu$ is on the order of 1×10^{-2} for vibrational excitation [2,3].

LID also provides the possibility to observe the dependence of $\Delta\nu/\nu$ on the rotational quantum numbers. The rotational-state dependence of $\Delta\nu/\nu$ for the same vibrational transition can be quite strong as is shown in Fig. 2.

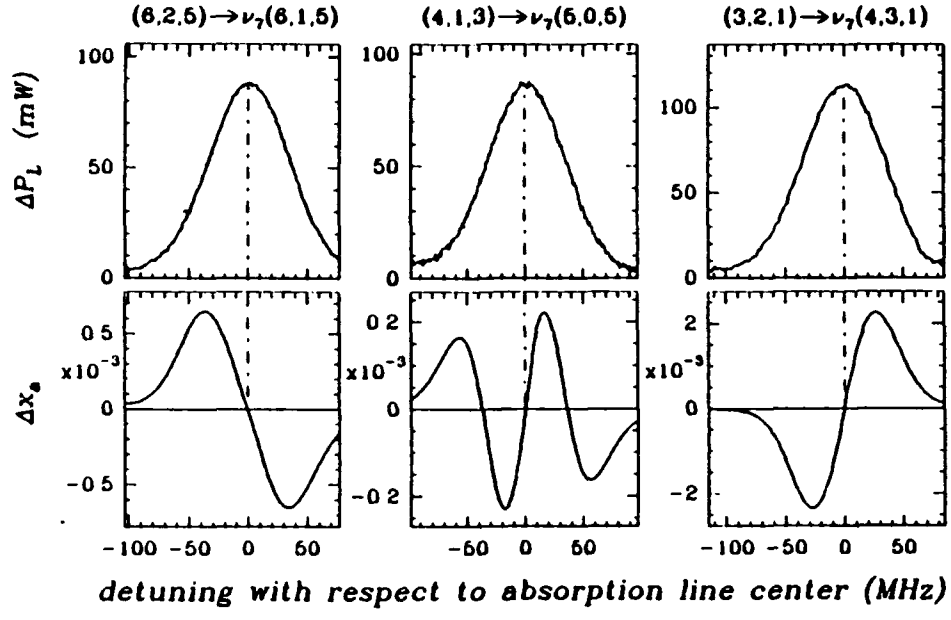

Figure 2: Experimental data for a C_2H_4/Kr mixture, for various rotational transitions (J,K_a,K_c)→ $\nu_7(J',K_a',K_c')$ in C_2H_4 as a function of laser frequency detuning. The upper panels show the absorbed laser power; in the lower panels the LID concentration differences are plotted. The lower middle panel shows that the value of $\Delta\nu/\nu$ changes sign as a function of detuning.

In similar measurements with different buffer gases (e.g. Kr, SF_6 and CH_3Cl), dramatic buffer gas dependences of $\Delta\nu/\nu$, both in sign and in magnitude, were observed.

Also the velocity dependence of $\Delta\nu/\nu$ can be studied with LID . By tuning the laser frequency through the Doppler profile, molecules with various velocity components along the wave vector are excited. As a result, $\Delta\nu/\nu$ can be determined for various values of the relative velocity between light-absorbing and buffer gas particles. In addition, the relative velocity can be varied through the gas temperature at fixed laser frequency. Examples of such measurements at four temperatures are given in Fig. 3 for the (4,1,3) $\rightarrow \nu_7(5,0,5)$ transition of C_2H_4 immersed in Xe. Preliminary results of $\Delta\nu/\nu$ as a function of the average relative velocity as derived from these data are shown in the lower panel of Fig. 3.

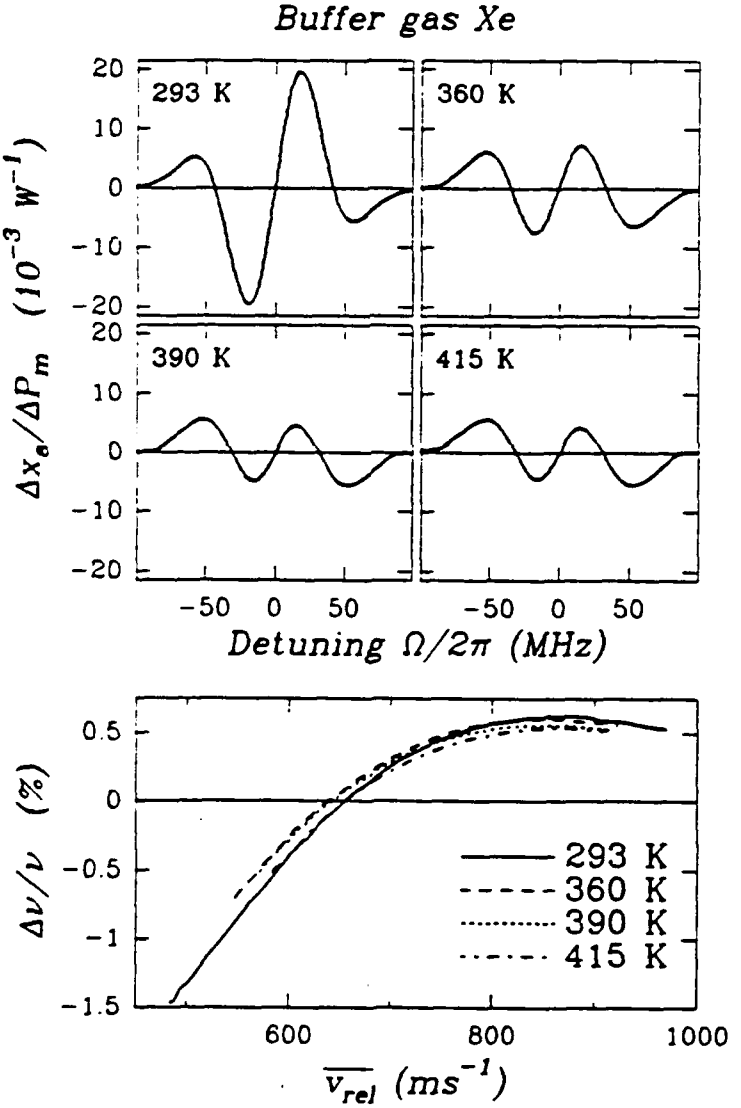

Figure 3: Results for LID in a C_2H_4/Xe mixture at various temperatures. The rovibrational transition (4,1,3) $\rightarrow \nu_7(5,0,5)$ of C_2H_4 is excited. Shown is the observed concentration difference, normalized with the absorbed laser power at line center, as a function of laser frequency detuning. The lower panel shows preliminary results of $\Delta\nu/\nu$ as a function of average relative velocity.

In conclusion, the data presented in this paper show that the difference in the transport collision rate between two rovibrational states can be measured with very high sensitivity using LID. Dependences of transport collision rates on molecular vibration, rotation and molecular velocity as well as the type of collision partner can be determined.

References

[1] F.Kh. Gel'mukhanov and A.M. Shalagin, Pis'ma Zh.Eksp.Teor.Fiz. **29**, 773 (1979) [JETP Lett. **29**, 711 (1979)].

[2] V.N. Panfilov, V.P. Strunin and P.L. Chapovsky, Zh.Eksp. Teor.Fiz. **85**, 881 (1983) [Sov.Phys.JETP **58**, 510 (1983)].

[3] G.J. van der Meer, R.W.M. Hoogeveen, L.J.F. Hermans and P.L. Chapovsky, Phys.Rev. **A39**, 5237 (1989).

Structures of Carbon Cluster Ions from 3 to 60 Atoms: Linears to Rings to Fullerenes

Gert von Helden, Ming-Teh Hsu, Paul R. Kemper and Michael T. Bowers

Department of Chemistry
University of California
Santa Barbara, CA 93106

Introduction:

The first (and perhaps only) carbon clusters that can be isolated in macroscopic quantities are the recently synthesized carbon clusters C_{60}, C_{70} and C_{84} (1). Structures for these species can be examined by standard techniques such as NMR and X-Ray diffraction. Results validate the "Fullerene" structures proposed by Kroto, Smalley and Curl (2). Little is known about the structures of clusters other than these fullerenes. For some small carbon clusters with less than 10 atoms, spectroscopic data is available (3), and at least some structures have been determined. High level ab initio calculations for clusters with up to 10 atoms have been undertaken by Raghavachari and Binkley (4). Results show that in this size range the cluster ground state is either linear or monocyclic.

We are investigating properties of positively charged carbon clusters in the gas phase. By measuring the gas phase mobility of these cluster ions we obtain information on the geometrical "size" of a particular cluster and on the existence of structural isomers. Possible carbon cluster structures are calculated using various semi-empirical or ab-initio quantum mechanical methods. These candidates for structures are then tested for consistency with experiment by computer modeling of their mobility.

Experimental setup:

Carbon cluster ions are generated in a standard pulsed laser vaporization - supersonic expansion cluster source. Helium is used as a buffer gas. An intense beam of positively charged clusters exits the source and no further ionization is needed. The cluster ions are accelerated to 5 keV , mass/charge selected by a double focussing reverse geometry mass spectrometer, decelerated and injected into a high pressure drift cell. The drift cell is 4 cm long and usually Helium at 5 Torr is used as a buffer gas. A small drift field (13 V/cm) is used to gently pull the ions through the cell. Under these conditions collisions between clusters and Helium in the cell are entirely thermal. A small portion of the ions exits through an exit aperture, passes through a quadrupole mass filter and is detected by standard ion counting techniques.

In the mobility experiment, a 1-10 μs pulse of ions is injected into drift cell. The arrival time distribution (ATD) of ions exciting the cell is then recorded on a multichannel scaler. For a single ion species, the so obtained time distribution is almost Gaussian in shape with a width of 10 - 100 μs and a residence time of 200 - 1000 μs

Results and Discussion:
a) Mobility Experiment

Figure 1 shows ATD's for C_{29}^+, C_{30}^+, C_{31}^+ and C_{32}^+. Multiple peaks are clearly resolved. We interpret these different peaks as different structural isomers of these clusters. By integrating the peak areas, relative abundances of these isomers can be obtained.

Fig.1 Arrival time distributions (chromatograms) for C_{29}^+, C_{30}^+, C_{31}^+ and C_{32}^+.

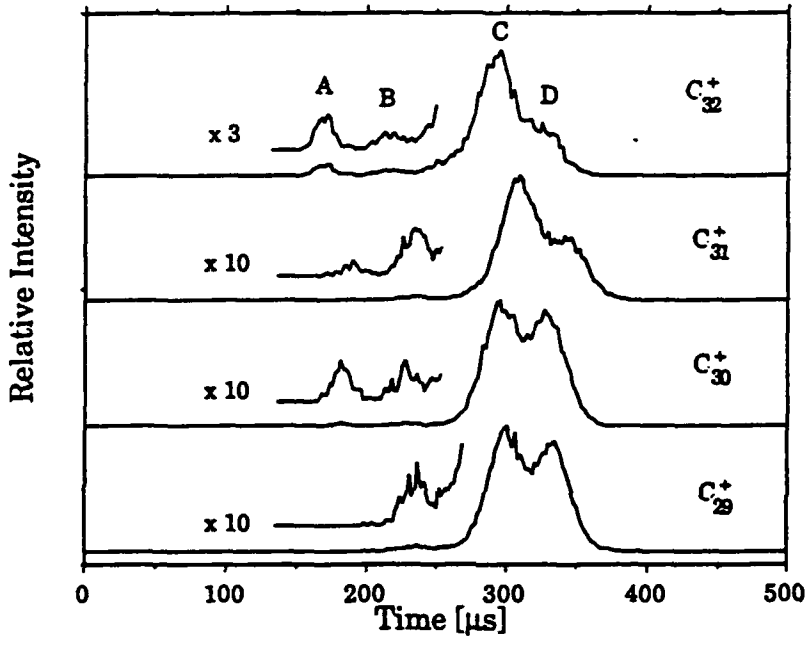

The peak at shortest time, labeled A, corresponds to the fullerene structure. Note that it is totally absent in the C_{29}^+ trace. Hence, the first fullerene appears at C_{30}^+. The peak labeled B is assigned as an "open" fullerene" and it's structure is somewhat unclear at that point. Peak C is assigned to bicyclic planar rings and peak D to a monocyclic ring.

For each peak, a mobility can be determined (units of $cm^2/v\text{-}s$). The inverse mobility is proportional the the cross-section of the cluster averaged over all orientations. A plot of the mobility^{-1} *vs* cluster size for the clusters examined so far is shown in Figure 2. The error bars are the relative errors in the measurements (± 3%). The lines are drawn only to guide the eye. Clearly, different "families" of carbon clusters can be identified. All clusters from n = 29 to 41 have at least three structural isomers with different mobilities. While C_3^+ and C_4^+ are grouped in the linear family, our resolution for these small clusters is such that we cannot distinguish linear from cyclic.

Fig.2 A plot of the mobility^{-1} versus cluster size for the positively charged cluster ions from n = 3 to n = 70.

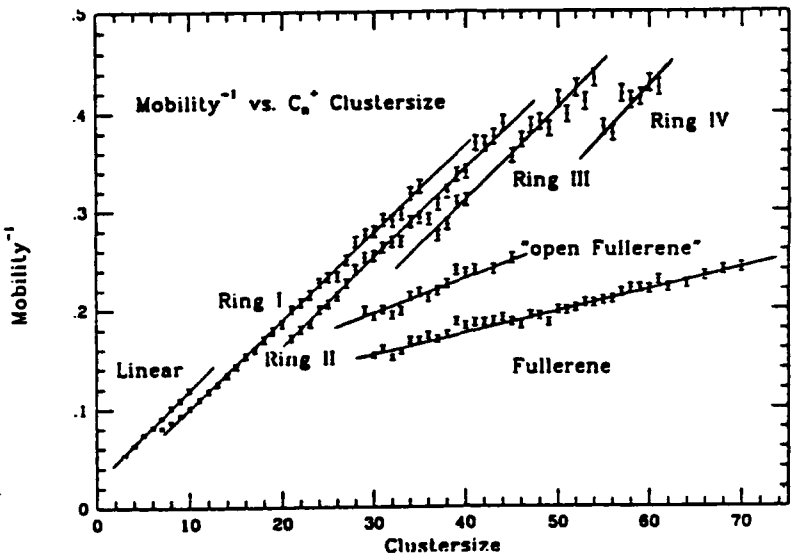

b)Calculated Structures and Simulated Mobilities

Structures and energies for some selected cluster with up to 32 atoms have been calculated using either semiempirical methods and/or Hartree-Fock ab-initio methods. Electron correlation is included for some clusters.

In order to compare the calculated structures with experimental mobilities, the mobility of the calculated structure has to be determined. The mobility is inversely proportional to the average cross-section. For an asymmetric body, the cross-section must be averaged over all possible orientations. Analytical solutions can be found only for a few, very simple structures. Instead, we calculate the average cross-section numerically by Monte-Carlo methods. The only two adjustable parameters in these simulations are the van der Waals radii of the carbon and helium atoms. These parameters are held constant for all clusters.

The mobilities for calculated structures of monocyclic rings with up to 32 atoms and linear clusters with up to 10 atoms have been simulated this way. The simulated mobilities agree with experimental results to within 2%.

Extensive geometry searches for a possible bicyclic structure of C_{21}^+ have been undertaken. Fig.3 shows the two lowest energy bicyclic structures we have been able to find. We have calculated the expected mobilities of these two structures aswell as a monocyclic structure not shown. The results are tabulated below, along with the experimental results for comparison.

Ring II	Mobility (cm2/v-s)
Experiment	5.84±0.1
Theory (Structure 3A)	5.83±0.1
Theory (Structure 3B)	5.97±0.1
Ring I	
Experiment	5.01±0.1
Theory	5.08±0.1

Fig.3 Possible bicyclic structures for C_{21}^+

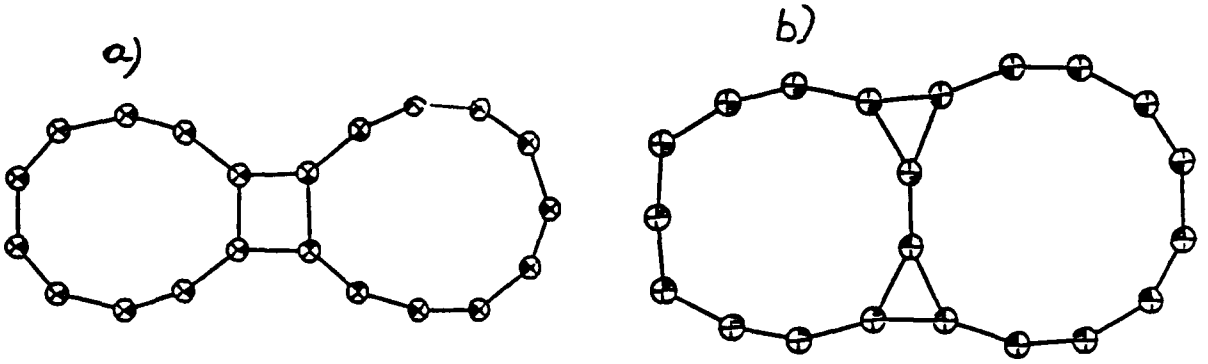

Clearly the agreement with experiment is very good for both structures in Fig.3 and on this basis we cannot decide between them. However, one or both of these structures is almost certainly the species giving rise to the "new" family of clusters we call Ring II originating at C_{21}^+.

Results on calculated structures and simulated mobilities for larger clusters will be presented.

ACKNOWLEDGEMENTS

This work was supported by the National Science Foundation under grant CHE88-17201 and the Air force Office of Scientific Research under grant AFOSR 89-0102. One of us, G.v.H., gratefully acknowledges the support of IBM Corporation for a graduate fellowship.

REFERENCES

(1) W. Kraetschmer, K. Fostropolos, D.R. Huffman, *Chem. Phys. Lett.* **170**, 167 (1990); G. Meijer, D.S. Bethune, *Chem. Phys. Lett.*, **175**, 1 (1990); R.E. Haufler, J. Conceicao, L.P.F. Chibante, Y. Chai, N.E. Byrne, S. Flanagan, M.M. Haley, S.C. O'Brien, C. Pan, Z. Xiao, W.E. Billups, M.A. Ciufolini, R.H. Hauge, J.L. Margrave, L.J.Wilson, R.F. Curl, R.E. Smalley, *J. Phys. Chem.*, **94**, 8634 (1990); F. Diederich, R. Ettl, Y. Rubin, R.L. Whetten, R. Beck, M. Alvarez, S. Anz, D. Sensharma, F. Wudl, K.C. Khemani and A. Koch, *Science,* **252**, 548 (1991); R. Taylor, J.P. Hare, A.K. Abdulsada and H.W. Kroto, *J. Chem. Soc. Chem. Comm.*, **N20**, 1423 (1990).

(2) H.W. Kroto, J.R. Health, S.C. O'Brien, R.F. Curl, R.E. Smalley, *Nature,* **318**, 162 (1985).

(3) See, for example, J.R. Heath, R.A. Sheeks, A.L. Cooksy, R.J. Saykally, *Science,* **249**, 895 (1990).

(4) K. Raghavachari, J.S. Binkley, *J. Chem. Phys.*, **87**, 2191 (1987);

Exciting Chemical Reactions

X.H. Wang, Y.F. Yen, R.J. Cross*, and M. Saunders

For the last few years we have used crossed, seeded nozzle beams to study the dynamics of several types of organic chemiionization reactions[1] where the reactants are neutral but the products are ions. We have recently found that at least one of these can be stimulated by the absorption of a photon *during* the reactive collision. The reaction is,

$$HI + Qn \rightarrow I^- + HQn^+, \quad (1)$$

where Qn is the bicyclic amine quinuclidine. This is the reaction of an acid and a base to give a salt.[2] The Qn beam is formed by passing the carrier gas (H_2, He, or a mixture of H_2 and He) through crystals of quinuclidine into a nozzle. The HI beam is made either by bubbling the carrier gas through t-butyl iodide and then pyrolizing the t-butyl iodide or by using a previously prepared mixture of HI and H_2. The first method gives a stable beam lasting for hours, but it contains impurities; the second method gives a pure beam that lasts for only an hour. The two beams are crossed at 90^o. Product ions are extracted with an electric field, mass analyzed by a quadrupole mass filter, and detected by an electron multiplier. Light is produced by a 350 W high-pressure mercury arc lamp and focused onto the reaction zone by a lens made of crown glass which excludes all light below 300 nm. The two beams are made with a low Mach number (6-10) so that vibrational relaxation is incomplete. By varying the temperature and type of carrier gas in the Qn nozzle, we can vary the translational energy of the beam and the vibrational temperature of the Qn. Raising the nozzle temperature increases both the translational and vibrational energies in the beam, changing carrier gases has little effect on the vibration.

Reaction (1) has a thermodynamic threshold of 3.53 eV.[3] In the absence of light the dark cross section rises rapidly above 4.0 eV in translational energy and shows a strong dependence on the vibrational energy in Qn, since the cross section depends strongly on the type of carrier gas. The photochemical data are shown in the figure. The large

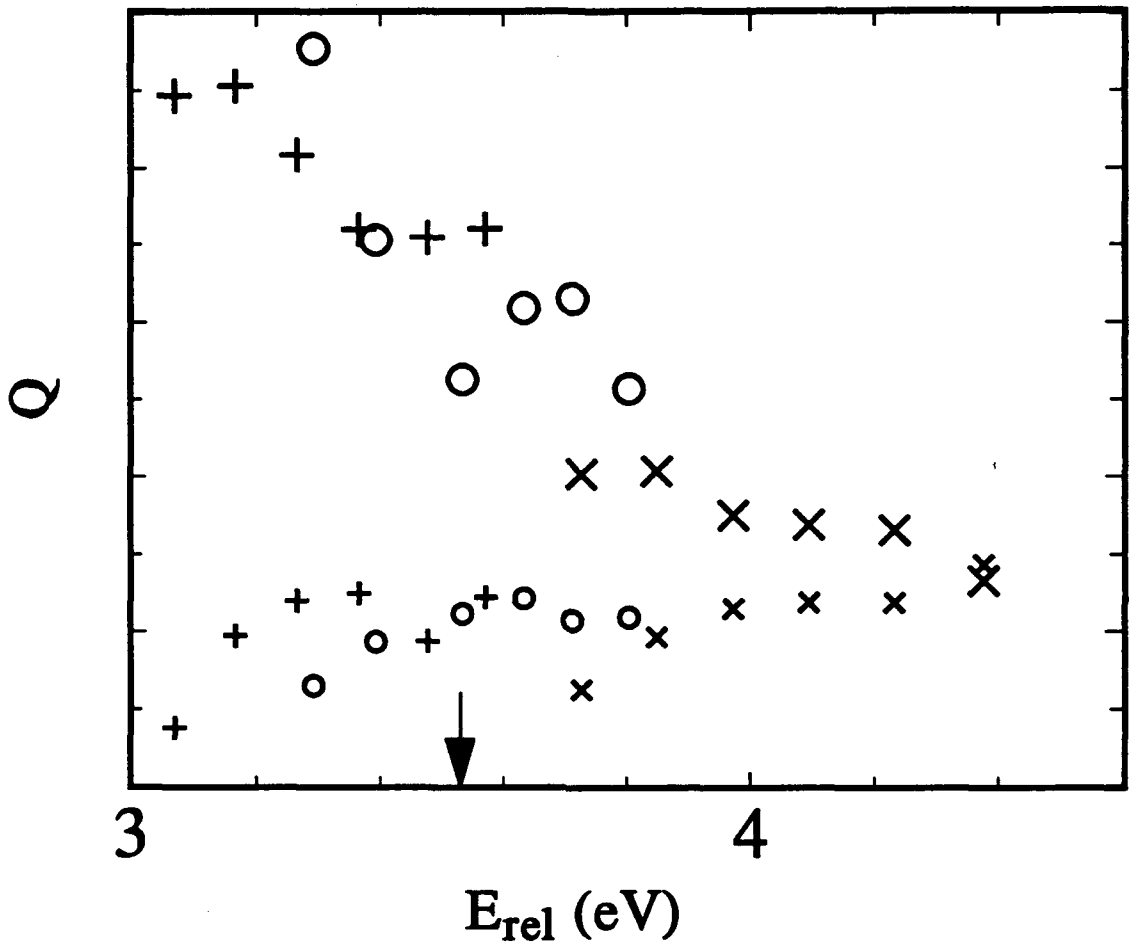

symbols show the photochemical cross section (light on minus light off). The symbols indicate data for the three carrier gases: × (H_2), + (He), and o (a mixture of 40% H_2 and 60% He). The small symbols show the signal from the the residual dark background. The arrow indicates the thermodynamic threshold. This dark background is more than an order of magnitude lower than the signal at higher energies and is due to reactions of molecules in the high-energy tails of the beam distribution and to the reaction of dimers in one beam with monomers in the other. The photochemical signal requires both beams and the light. Only the two product ions are seen in the positive and negative ion mass spectra.

Other sources of the photochemical signal are easily ruled out. Quinuclidine does not absorb light above 256 nm.[4] The HI absorption band does extend above 300 nm, but the absorption is entirely dissociative, and neither the H atom nor the I atom can react to

form the observed products. Charge exchange with I atoms or with HI has a higher threshold than that of reaction (1). Reaction on surfaces is possible, but the surface will remove all the incident energy, and the photon alone does not have enough energy to provide the necessary ΔH for the reaction.

Our model for the reaction is that the reactants start on a covalent potential-energy surface and then cross over to an ionic surface. The ionic surface has a deep bowl in it corresponding to a bound pair of ions. Below the threshold for the dark reaction, the system is trapped in the bowl. Because of the large number of vibrational degrees of freedom in Qn, we expect a long liftetime for the complex. Absorption of a photon then promotes the system to the dissociative covalent surface. A second surface crossing takes it to the ionic surface with enough energy to form the separated ion products.

Research from the National Science Foundation and the Petroleum Research Fund is gratefully acknowledged.

References

1) R.J. Cross and M. Saunders, *Accts. Chem. Res.* **24**, 104 (1991).

2) Y.F. Yen, R.J. Cross, *J. Phys. Chem.* **95**, 8753 (1991).

3) S.G. Lias, J.E. Bartmess, J.F. Liebman, J.L. Holmes, R.D. Levin, and W.G. Mallard, *J. Phys. Chem. Ref. Data* **17**, Suppl. 1, (1988).

4) A.M. Halpern, J.L. Roberts, K. Weiss, *J. Chem. Phys.* **49**, 1348 (1968).

Reactivity of Carbon Cluster Ions with Ar, O_2, and D_2

R. Weckwerth, E. Knoesel, and A. Ding

Optisches Institut, Technische Universität Berlin, Germany

There has been a considerable number of experiments investigating the reactivity of laser produced carbon clusters with various molecules. While most work has been done using neutral clusters/1/ we present here experiments investigating the reactivity of carbon cluster ions with different gases.

Carbon Cluster Ions have been generated using a laser evaporation technique: A Nd:YAG-laser is focussed onto a cylindrical target which leads to the evaporation of the target material. During and after the evaporation process a gas pulse is passed through the evaporation region and condenses the evaporated particles forming neutral clusters and a significant amount of ionic clusters. Using specially designed extraction techniques only ions are accelerated into a Wiley-McLaren type time-of-flight mass spectrometer as shown in Fig.1. The cluster ion beam is optimized by varying the pulse timing, the gas pressure, and the expansion geometry.

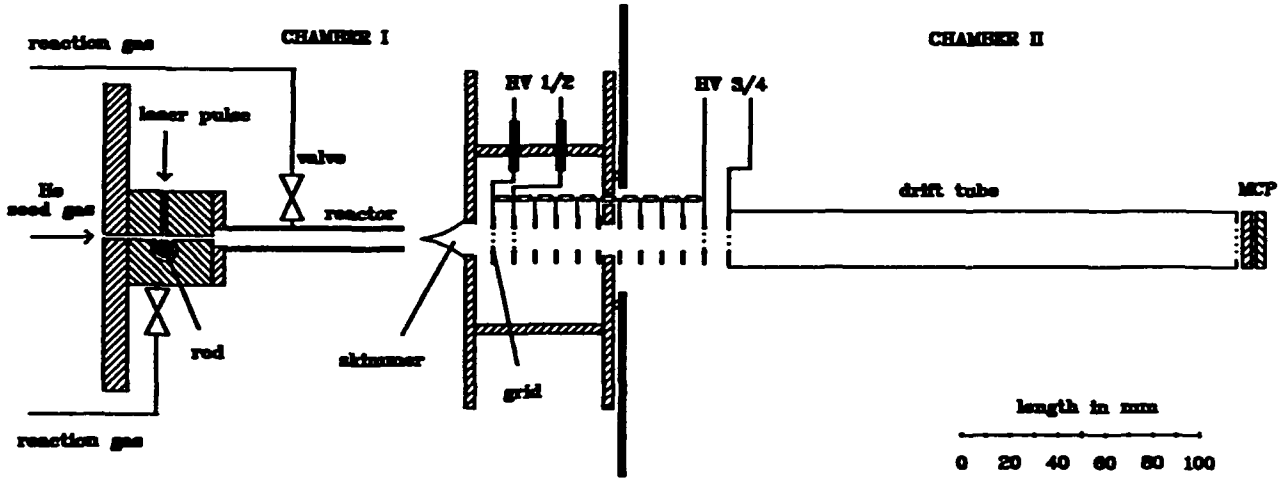

Fig1: Experimental set-up for the production of ionic clusters by laser evaporation

Particularly interesting is the fact that bimodal cluster ion distributions containing significant amounts of C_{60} and C_{70} can be obtained. Fig. 2 displays such distribution where odd numbered cluster ions are not found above C_{60}.

Several gas inlets at different locations have been added to the cluster source in order to investigate reactive processes of these cluster ions. Exploratory investigations have been performed using Ar, O_2, and D_2 as a reaction gas. They were either added to the expansion

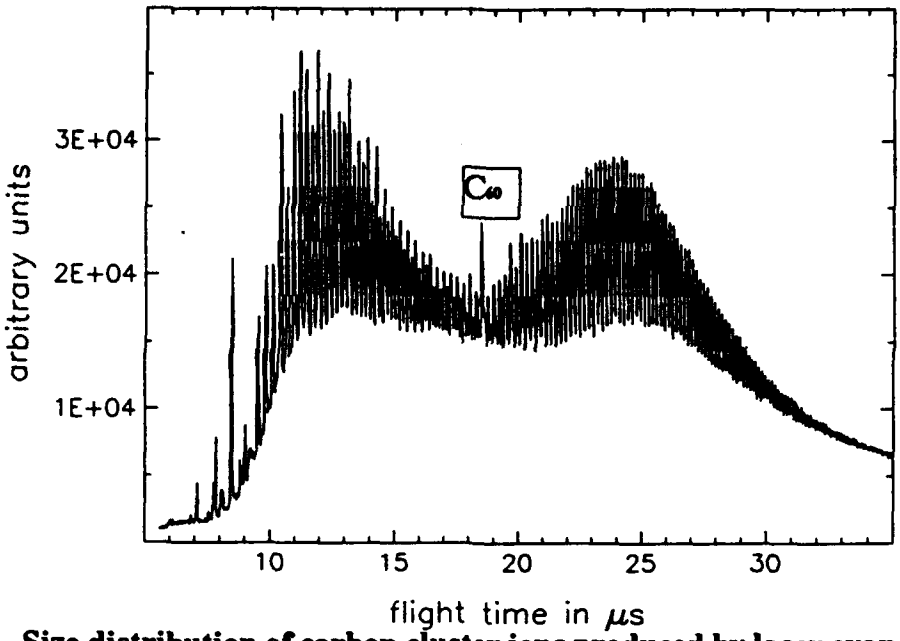

Fig. 2: Size distribution of carbon cluster ions produced by laser evaporation (Nd-YAG: $\lambda = 1064$ nm, 4 Hz)

gas (He) or led directly into the evaporation region. A severe effect has been observed leading either to reaction products or to a decomposition of different cluster sizes. Addition of D_2 increased the line width in the TOF-spectrum indicating the appearance of reaction products of the type C_mD_n /2/. Both O_2 and D_2 proved very effective in removing the odd numbered carbon cluster ions in the vicinity of C_{60}.

Application of O_2 produced a *significant effect: depending* on the gas pressure it reacted with small cluster ions forming products like C_nO^+ and $C_nO_2^+$. In particular, the reaction rate depended on the cluster size e.g. generating alternating size distribution of the sequence CO_2^+, $C_3O_2^+$, $C_5O_5^+$,..., $C_{11}O_2^+$. Reactivity forming such cluster ions containing oxygen are not found for n > 10, which is an indication for the intrinsic change in cluster ion geometry.

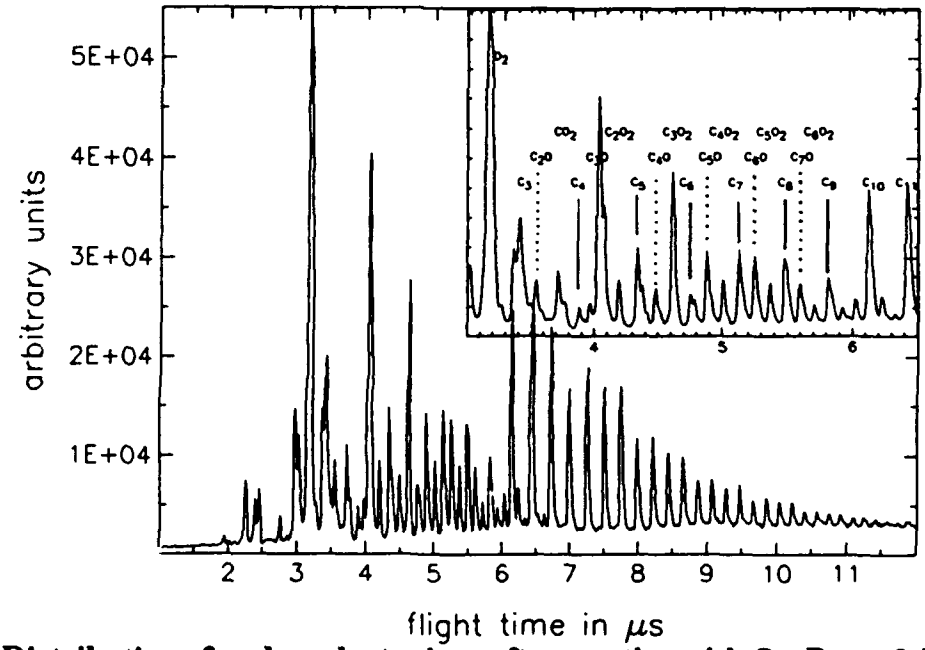

Fig. 3: Distribution of carbon cluster ions after reaction with O_2. Part of the spectrum containing the smaller cluster ions is displayed in the right upper corner

It is known that the geometric structure of carbon clusters may consist of chains, rings and sherical shapes (fullerenes). The observed reaction behaviour is a strong indication for a transition from a linear to a non-linear geometry: while linear molecules show a large reactivity, rings and fullerenes are more inert attack of O_2-molecules.

This is, however, not the only possible explanation: Such behaviour may also be explained by charge transfer processes, which would have the O_2 react differently with small and large carbon cluster ions:

$$C_n^+ + O_2 \rightarrow C_{n-1}O^+ + CO$$
$$\rightarrow C_{n-1}O_2^+ + C \qquad \text{for } n < n_o$$

$$C_n^+ + O_2 \rightarrow C_{n-1}^+ + CO_2$$
$$\rightarrow C_{n-2}^+ + 2\,CO \qquad \text{for } n >= n_o$$

Another sequence of experiments have been undertaken by adding Ar atoms with the carbon cluster ions:

$$C_n^+ + Ar \rightarrow C_kAr^+ + C_{(n-k)}$$

It is particularly interesting to note that some stable ionic reaction products like ArC^+, ArC_4^+, ArC_5^+,... can be detected. It is known from previous experimental and theoretical studies/3/ that the first member of this series is a stable molecular ion with a dissociation energy in excess of 1 eV. While -to the authors' knowledge - no other experiments with the large Ar compounds have been performed, it seems plausible that such stable molecular ions with bond energies exceeding those of van-der-Waals clusters exist. It is not known why only some cluster ions of this series are observed. This might be caused by different bond strength or different reactivities of the species under investigation.

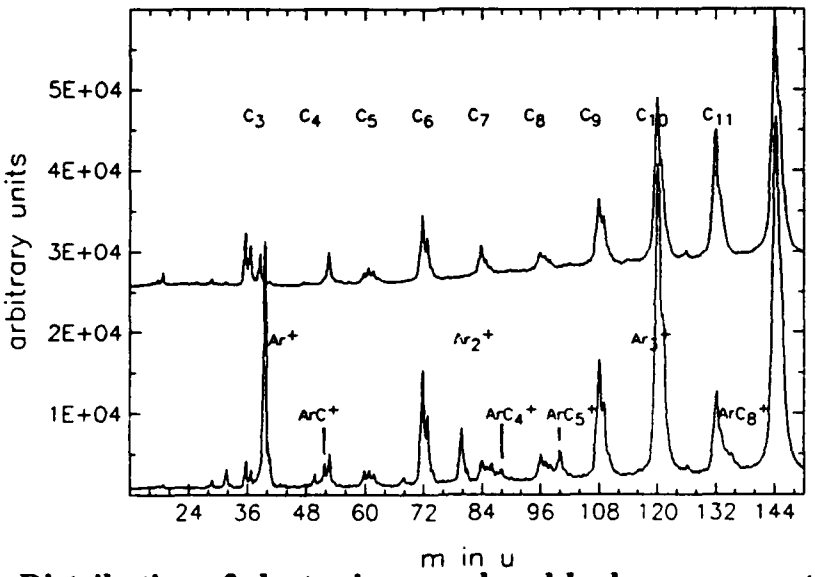

Fig. 4, bottom: Distribution of cluster ions produced by laser evaporation of graphite using a He-Ar mixture for expansion of the cluster beam.

top: Pure carbon cluster ions produced by expansion in pure He

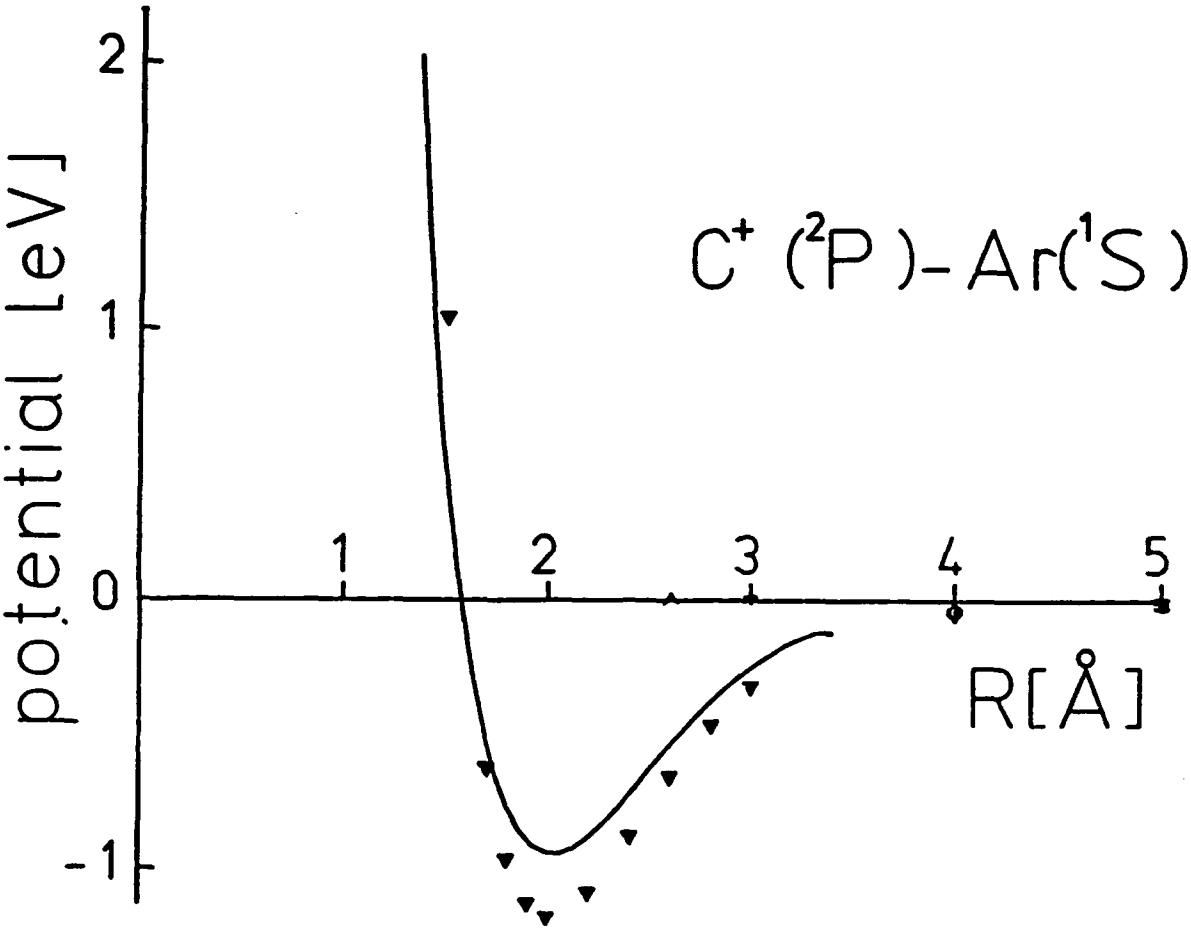

Fig. 5: **Potential of ArC^+ ($X^2\Pi$) /3/ (solid line: experiment, triangle: calculation)**

References:

/1/ **Q.L. Zhang, S. O'Brian, J.R. Heath, Y. Liu, C.F. Curl, H.W.Kroto, R.E.Smalley**
J.Phys.Chem. 90, 525 (1986)

/2/ **M. Doverstal, B. Lindgren, U. Sassenberg, H. Yu**
Z.Phys.D 19, 447 (1991), Physica Scripta 43, 572 (1991)

/3/ **I.H. Hillier, M.F.Guest, A. Ding, J. Karlau, and J. Weise**
J.Chem.Phys. 70, 864 (1979)

A Crossed Beam Study of the Reaction $C(^3P) + N_2O$: Energy Partitioning Between the $NO(X^2\Pi)$ and $CN(X^2\Sigma^+)$ Products*

F. Winterbottom, S. A. Reid, D. C. Scott, J. de Juan and H. Reisler

Department of Chemistry, University of Southern California, Los Angeles, CA 90089-0482

INTRODUCTION

The reactions of ground-state atomic carbon (^3P) are important in combustion environments, hydrocarbon synthesis, electric discharges and graphite ablation, in addition to their fundamental interest. In contrast to the corresponding reactions of ground-state $O(^3P)$, relatively few studies have examined reactions of $C(^3P)$, due mainly to difficulties in source preparation. At this meeting, we report preliminary results on the $C(^3P) + N_2O$ reaction at a collision energy of ~ 0.9 eV obtained with a crossed beam apparatus, employing free laser ablation for production of the atom beam. Full details of this work will be published shortly [1].

Assuming the validity of spin conservation and symmetry correlation rules and an intermediate of C_S symmetry, the reaction of ground state atomic carbon with nitrous oxide may proceed through the following allowed pathways:

$$C(^3P_J) + N_2O(X^1\Sigma^+) \rightarrow CO(a^3\Pi) + N_2(X^1\Sigma^+) \quad \Delta H = -3.41 \text{ eV} \quad (1)$$

$$\rightarrow CO(X^1\Sigma^+) + N_2(B^3\Pi) \quad \Delta H = -2.07 \text{ eV} \quad (2)$$

$$\rightarrow CN(X^2\Sigma^+) + NO(X^2\Pi) \quad \Delta H = -2.88 \text{ eV} \quad (3)$$

$$\rightarrow CN(A^2\Pi) + NO(X^2\Pi) \quad \Delta H = -1.47 \text{ eV} \quad (4)$$

Chemiluminescence from the electronically excited products of reactions (1) and (2) has not been observed, while $CN(A \rightarrow X)$ chemiluminescence from reaction (4) has been observed in one study [2] but not in another [3] and remains a source of controversy.

$CN(X^2\Sigma^+)$ product from channel (3) has been detected by laser induced fluorescence (LIF) under both rotationally relaxed [3] and single collision [4,5] conditions. The observed CN excitation limit, which corresponded to approximately half of the available energy, led to the suggestion that a large amount of energy must reside in the NO fragment [5]. Determination of the NO state distributions should therefore be valuable in clarifying the mechanism of the reaction and revealing added details of the PES associated with the reaction channel leading to $CN(X^2\Sigma^+)$ and $NO(X^2\Pi)$.

EXPERIMENTAL SECTION

The crossed molecular-beam apparatus employed in these studies consists of an octagonal stainless steel reaction chamber and an ablation chamber containing the carbon source maintained at $\leq 8 \times 10^{-5}$ Torr and $\leq 3 \times 10^{-5}$ Torr respectively during an experimental run. The atomic beam is generated by free laser ablation of a spectroscopic-grade graphite rod. A pulsed beam of short temporal duration (10-20 μs FWHM) is

*Research supported by the U.S. Department of Energy.

produced by focusing approximately 20 mJ of 355 nm radiation from a Nd:YAG laser.(14 ns FWHM) to a 1-mm spot at the graphite rod surface. The rod is placed 6.6 cm from the center of the chamber and maintained in constant helical motion to ensure good shot-to-shot stability. The resultant atomic beam is collimated to ~ 10° by a stainless steel skimmer (3 mm dia.). Removal of ionic species is accomplished by a pair of deflection plates located inside the skimmer mount; however, no differences were observed in spectra taken with the field on and off.

The neutral beam is generated by expansion of a 10% mixture of N_2O (MG Industries, 99.9%, used without further purification) in He (Spectra, 99.999%) through the 0.5-mm orifice of a pulsed nozzle (Lasertechnics LPV-1) at a typical stagnation pressure of 10 psig (0.7 atm). The nozzle is oriented perpendicular to the atomic beam centerline and typically set 20-mm (40 nozzle diameters) above the scattering center.

The pulsed nozzle and the ablation laser are triggered so that the carbon and N_2O beams overlap temporally at the center of the chamber. The probe laser pulse is delayed by 15 μs with respect to the ablation pulse. Product detection is achieved by excitation of the $\Delta v = 0, -1$, and -2 sequences of the $B^2\Sigma^+ \leftarrow X^2\Sigma^+$ transition of CN and the $\Delta v = 0$ sequence of the $A^2\Sigma^+ \leftarrow X^2\Pi$ transition of NO.

RESULTS

LIF signals were obtained for both $CN(X^2\Sigma^+)$ and $NO(X^2\Pi)$. The CN product was found to be rotationally and vibrationally 'hot' with bandheads of $v \leq 7$ identified and maximum population in $v = 3$. The high rotational excitation is clearly evident in Fig. 1, which shows part of the P branch of the (0,0) band. Rotational levels ≤ 60 are significantly populated and easily identified before the onset of the (1,1) bandhead.

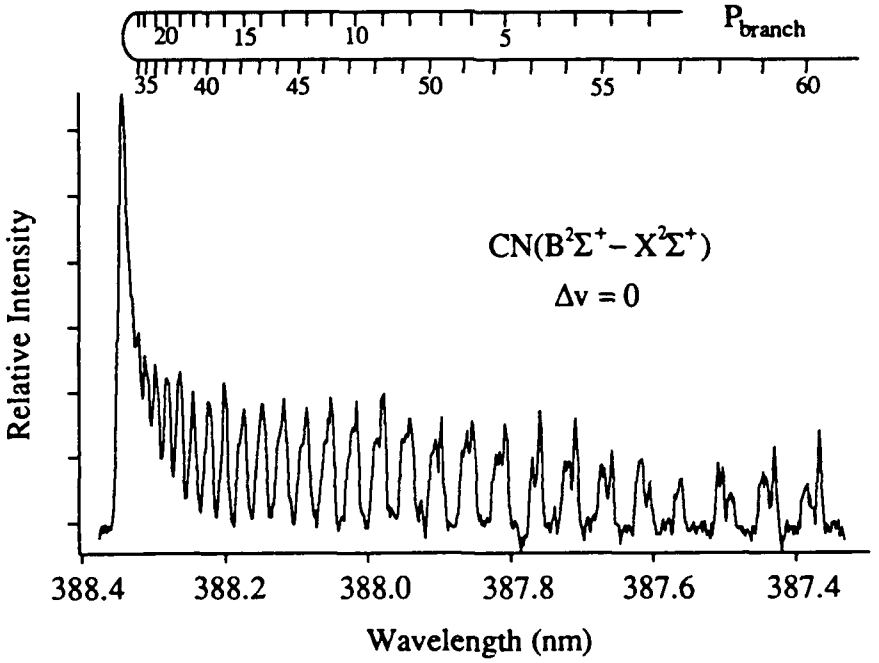

Figure 1 Nascent $CN(B^2\Sigma^+ - X^2\Sigma^+)$ LIF spectrum displaying the P branch of the (0,0) bandhead. The $\Delta v = 0$ sequence was excited and fluorescence was observed on the $\Delta v = 0$ sequence.

In analogy to CN, a high degree of rotational excitation is observed in the NO ($A^2\Sigma^+ - X^2\Pi$) spectrum with levels in excess of J = 60.5 being detected. The rotational distribution for the v = 0 level of NO($^2\Pi_{1/2}$) is displayed in Fig. 2, and a similar distribution is obtained for NO($^2\Pi_{3/2}$). The distribution is inverted with a maximum population in J = 49.5.

Vibrational population ratios were obtained by comparing intensities in the bandheads of each level under conditions of partial rotational but negligible vibrational relaxation [40 psig (2.7 atm) stagnation pressure]. The vibrational population in NO($X^2\Pi$) v = 0:1:2 was found to be 1:0.45:0.12.

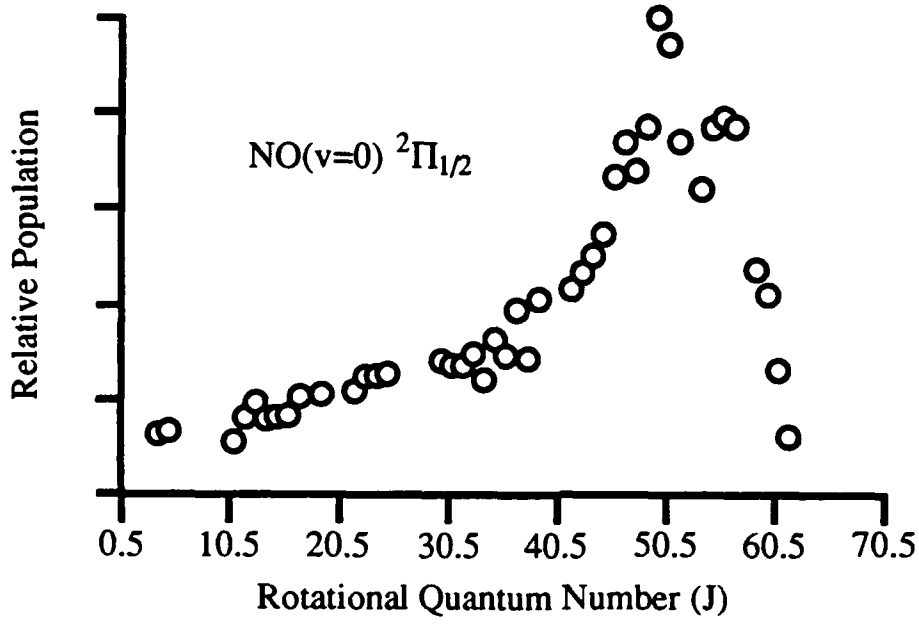

Figure 2 Nascent rotational distribution of the v = 0 level of NO($^2\Pi_{1/2}$) produced in the C(^{3}P) + N_2O reaction. Random measurement error is ≤ 7%.

DISCUSSION

The total energy available for partitioning between the internal degrees of freedom and recoil velocity of the reaction fragments is estimated to be 3.9 ± 0.4 eV.

The CN excitation limit observed by Costes *et al.* and ourselves suggests that nearly half of this energy appears as internal excitation of CN. Of the remaining ≥ 50%, significantly less is deposited as internal energy of the NO fragment, which is formed vibrationally cool; $\langle f_v \rangle \approx 5\%$ while $\langle f_R(NO) \rangle \approx \langle f_R(CN) \rangle$, where f_i is the fraction of energy deposited in the ith degree of freedom. Such non-statistical energy partitioning with one vibrationally 'hot' and one vibrationally 'cold' product is indicative of a reaction mechanism with substantial direct character.

Classical trajectory calculations of reaction (3), assuming a pseudo-triatomic CNN' intermediate, were run on a PES constructed using a MNDO semi-empirical CI SCF calculation [6,7]. The surface, presumably a triplet of A" symmetry, showed a deep well favoring the formation of a long-lived intermediate. High CN vibrational excitation was found, although overestimated; the calculated vibrational distribution was strongly inverted

with maximum population in v = 11 and 12 (cf. experimentally $v_{max} = 3$). Vibrational inversion despite the presence of a deep well was attributed to the high exoergicity of reaction, and it was concluded that the reaction, although indirect, possessed some direct character. At the large collision energies employed in this work we suggest that the $C(^3P)$ + N_2O reaction is predominantly direct and attractive in nature although exhibiting some indirect character. An interaction between CN and NO induced by the presence of the well corresponding with the CNNO complex intermediate allows some flow of energy into the NO bond before the fragments separate permanently.

In this reaction, the large reduced mass, high collision energy, and large range of reactive impact parameters (evidenced by the large reaction cross section) suggest that fragment rotational excitation is not restricted by reactant orbital angular momentum. In such a case, the fraction of angular momentum appearing as product rotation is determined by details of the PES, namely the anisotropy in the potential or the geometry of the reactive path. The 'hot' rotational distributions observed suggest a non-linear intermediate such that forces acting towards fragmentation impart a torque on the departing radicals. A shallow angular dependence of the potential for collinear C atom attack at NN' was determined theoretically [6], and the barriers to non-linear approach can be easily overcome by the translational energy of the reactants, suggesting that a broad distribution of CNN angles may lead to reaction.

The reaction of $C(^3P)$ with N_2O can yield $NO(X^2\Pi)$ via two pathways corresponding to CN in its ground ($X^2\Sigma^+$) and first excited ($A^2\Pi$) states. Chemiluminescence on the $CN(A^2\Pi \rightarrow X^2\Sigma^+)$ transition was detected in one study [2] but failed to be observed in another [3] and a theoretical study [6] has postulated that $CN(A^2\Pi)$ might be formed by a nonadiabatic transition from the 1A' to 2A" surface which correlates with N_2O in an excited triplet state and carbon ^3P or ^1D. The NO rotational excitations obtained in this work show no evidence for the involvement of two reaction channels. For example, no bimodality in the rotational distributions is observed, which might be expected if reaction (4), with 1.41 eV less available energy, was important.

Although we have gone some way in elucidating the dynamics of this reaction, it is apparent that many questions still remain. Investigation of the effect of translational energy on intermediate lifetime and thus relative energy deposition in the reaction fragments is at present in progress. Future work will involve analysis of fine-structure components and determination of vector correlations.

REFERENCES

[1] S.A. Reid, F. Winterbottom, D.C. Scott, J. de Juan and H. Reisler, *Chem. Phys . Lett.*, (Accepted).
[2] M. Costes, G. Dorthe and M. Destriau, *Chem. Phys. Lett.*, 61 (1979) 588.
[3] H. Sekiya, M. Tsuji and Y. Nishimura, *J. Chem. Phys.*, 84 (1986) 3739.
[4] C. Naulin, M. Costes and G. Dorthe, *Chem. Phys.*, 153 (1991) 519.
[5] M. Costes, C. Naulin, G. Dorthe and Z. Moudden, *Laser Chem.*, 10 (1990) 367.
[6] J.C. Rayez, M.T. Rayez and B. Duguay, *J. Chem. Phys.*, 78 (1983) 827.
[7] R. Bouachir, M.T. Rayez, B. Duguay and J.C. Rayez, *Chem. Phys.*, 90 (1984) 325.

Electron Photodetachment Cross Sections of Small Carbon Clusters. Evidences for Non Linear Isomers.

D. Zajfman, H. Feldman, O. Heber,
D. Kella, D. Majer, and Z . Vager
Department of Nuclear Physics

and

R. Naaman
Department of Chemical Physics
Weizmann Institute of Science, Rehovot 76100, Israel

ABSTRACT

A novel combination of laser and the Coulomb Explosion Imaging (CEI) technique is being applied for the study of the structure of cluster isomers correlated with their electronic affinity. In recent experiments the absolute cross-sections for the photodetachment of C_n (n=3,...,8) clusters were obtained. Previously unknown compact isomers were observed. Their abundance was found to depend on the methods of production.

AUTHOR INDEX

Alexander M.	387	Bassi D.	23, 415
Amar F.G.	267	Baumgartel H.	393
Anderson R.	375	Beck R.D.	223
Anex D.S.	195, 427	Beck S.M.	227
Aoiz F.J.	197	Bennett F.R.	19
Aono M.	357	Berden G.	123, 251
Aquilanti V.	201, 205	Beuhler R.J.	93
Arnold D.W.	209	Bewig L.	231
Atkinson D.B.	211	Bieske E. J.	19
Auerbach D.J.	189	Bishea G.A.	257
Bae Y.K.	93	Bishop G.G.	173
Balko B. A.	215	Blake T.A.	223
Banks, Jr. J.F.	339	Bloemink H.I.	447
Barker J. A.	217	Bondybey V.E.	275
Barnes M.D.	219	Bontuyan L.S.	141
Barnett R.N.	71	Bowers M.T.	451
Barrett J.J.	387	Box F.M.A.	383
Bartz J.A.	157	Bradforth S.E.	209

Bréchignac P. 267

Brenner V. 323

Bristow G.H. 235

Brooks P.R. 219

Brucker G.A. 149

Brutschy B. 239, 393

Buck U. 7, 231

Burose A.W. 243

Butler L.J. 137

Candori R. 201

Cappelletti D. 201, 205

Castano E. 335

Cavanaugh K. 211

Ceyer S.T. 167

Chapovsky P.L. 447

Chen Y. 149

Chern G. 173

Cheshnovsky O. 317

Chu P. 361

Chu S. 41

Chu Y.Y. 93

Cid-Aguero P. 247

Cline J.I. 445

Colonell J.I. 181

Consalvo D. 251

Continetti R. 107

Coreno M. 255

Crim F.F. 157

Cross, Jr. R.J. 455

Curl R.F. 219

Curtiss T.J. 181

Cyr D.M. 257

Cyr D.R. 107

Daley S.P. 167

Davis H. F. 153

de Juan J. 463

de Vivie R. 99

de Vries M.S. 371, 123

DeKieviet M.F.M. 259
Ding A.M.G. 161, 243, 459
Ding C. 263
Dmitrijev O. 23
Doak R.B. 185
Douin S. 267
Drabbles M. 251
Dresch T. 243
Drewello T. 161
Driessen J.P.J. 99
Duan J. 173
Dubois L.H. 185
Duncan M.A. 85
Eggers D. 223
Eno L. 99
Fantoni R. 271
Feldman H. 467
Fenn J.B. 339
Fieber-Erdmann M. 161
Field R. 57
Fischer I. 275
Fraser G.T. 115
Friedlander G. 93
Friedman L. 93
Fuerstenau S.D. 339
Fukawa T. 301
Gallogly E. 277
Gambogi J. 279
Garay M. 335
Giardini-Guidoni A. 255
Gilbert B. D. 61
Gillman E.S. 173
Giniger R. 317
Giorgi M. 271
Gittins C. 57
Glenewinkel-Meyer T. 157
Goerke A. 77
Govoni S.T. 91

Goyal S. 75

Greeley J.N. 319

Green D.S. 283

Grover J.R. 247

Gu Y. 419

Halberstadt N. 11

Hanisco T.F. 287

Hanning-Lee M. 91

Harland P.W. 219

Harris N. 57

Hatano Y. 47

Hawley M. 291, 309

Hayden B.E. 171

He G.Z. 295

Heaven M.C. 3

Heber O. 467

Hecht J.H. 227

Hekkert S. te L. 127

Helden G.V. 131, 379

Hepburn J.W. 53, 433

Hermans L.J.F. 447

Hermine P. 267

Herrero V.J. 197

Herschbach D.R. 37

Hertel I.V. 77, 413

Him E.H. 209

Hinch B.J. 185

Houston P.L. 141

Hsu M-T. 451

Hüglin C. 413

Hunziker H.E. 123

Ionov S.I. 149

Jackson W.M. 277

Jacobs D.C. 319

Janda K.C. 11, 49

Janssen M.H.H. 299

Jaques C. 149

Jego M.N. 433

Johnson A.D. 167

Johnson J.R. 49

Johnson M.A. 257

Jouvet C. 323, 327

Kalogerakis K.S. 441

Kasai T. 301

Keil M. 387

Kella D. 467

Kemper P.R. 451

Kerstel E.T. 15

Kim S.K. 145

King M.E. 91

Kleyn A.W. 383

Knickelbein M.B. 305

Knight A. 19

Knight W.D. 81, 409

Knoesel E. 459

Kong W. 53

Kowalski D.V. 91

Krätschmer W. 161

Krause J.L. 369

Kresin V. 81, 409

Kukolich S.G. 397

Kummel A.C. 287

Kuwata K. 301

Lahmann C. 239, 393

Lainé D.C. 365

Lardeux-Dedonder D. 323, 327

Latimer D.R. 309

Lavrich D.J. 257

Le Calvé J. 345

Leach C.A. 441

Leahy D.J. 391

Lee Y.T. 29, 153, 195, 215, 349, 361, 427

Lehmann K.K. 115, 279

Lengsfield III B.H. 369

Leonardi C. 415

Leone S.R. 99

Lewerentz M.	223	Martin J.S.	319
Li K.	419	Martin R.M.	103
Lin F.J.	313	Martrenchard-Barra S.	323, 327
Lineberger W.C.	1	Matsuriami T.	301
Linskens A.	127	Mayne H.R.	387
Lipinska-Kalita M.	271	Mazely T.L.	235
Liuti G.	205	McKay R.I.	19
Lorent V.	205	McMahon M.	71
Lou N.	295	McMaster M.C.	331
Lovas F.J.	223	Meerts W.L.	119, 123, 251
Lovejoy E.R.	145	Mehlmann C.	231
Ludviksson A.	103	Meijer G.	123
Luzzatti E.	201	Mele A.	255
Mack J.A.	131, 379	Melosh N.	309
Madix R.J.	331	Menegotti L.	415
Majer D.	467	Menendez M.	335
Mank A.	433	Menezes W.J.C.	305
Markovich G.	317	Meng C.K.	339
Marsden J.E.	313	Miau T.T.	29

Michelsen H.A. 189

Miller D. 95

Millié P. 323

Minton T.K. 91, 343

Mons M. 345

Moore C. B. 145

Moore T.A. 343

Muller-Dethlefs K. 275

Myers J.D. 349

Naaman R. 371, 405, 467

Nakamura M. 353, 357

Nathanson G.M. 91

Nelson C.M. 343

Nelson H.H. 291

Neumark D.M. 107, 209

Neusser H.J. 111

Niedner-Schatteburg G. 275

Nitsch C. 413

Nohmi T. 339

Nooney M. 103

North S.W. 361

O'Shaughnessy D. M. 365

Ohoyama H. 301

Okumura M. 343

Orel A.E. 369

Osborne D. 107

Park H. 391

Parker D.H. 251, 299

Parmenter C.S. 61

Parneix P. 267

Pate B.H. 115, 279

Paz Y. 371, 405

Pearson A. 375

Peterlinz K.A. 181

Piccirillo S. 255

Pirani F. 201, 205

Pollack S. 317

Pratt D.W. 49

Price J.M.	103, 131, 379	Saunders M.	455
Pursell C.J.	61	Scarton M.G.	257
Rábanos V.	197	Scheidemann A.A.	409
Rademann K.	73	Schmidt M.	345
Raukema A.	383	Schnieder L.	27
Rawluk L.J.	387	Schulz C.P.	77, 413
Reid K.L.	391	Schutt D.L.	75
Reid S. A.	463	Scoles G.	15, 75, 115, 259, 279
Reisler H.	463	Scotoni M.	415
Rettner C.T.	189, 217	Scott D.C.	463
Reuss J.	127, 251	Shao J.	419
Riehn C.	239, 393	Sharma R.D.	423
Rodgers D.	53	Sheb S.	339
Roehrig M.	397	Sibener S.J.	181
Rogaski C.A.	131, 401	Sindoni J.M.	423
Roncero Octavio	11	Skofronick J.G.	173
Rudich Y.	405	Slotterback T.J.	49
Saecker M.E.	91	Smalley R.E.	69
Safron S.	173	Smith C.J.	99

Smith M.A.	211, 235, 309	Tosi P.	23
Smoliar L.	427	Tramer A.	327
Snels M.	271	Tsekouras A.A.	441
Soldo Y.	23	Tseng S-H.	223
Solgadi D.	323, 327	Tsukada M.	357
Soulen S.A.	331	Unger G.	413
Stalder K.R.	429	Urena A. G.	335
Starrs C.	433	Utz A.L.	167
Stiller W.	437	Vager Z.	467
Stinnett J.A.	331	van der Avoird A.	299
Stolow A.	195	van der Meer G.J.	447
Stolte S.	299	Vecchiocattivi F.	33
Strobel A.	275	Verdasco E.	335
Strumia F.	43	von Helden G.	451
Suits A.	141	Wall M.C.	445
Tao Y.	419	Wallace S.C.	283
Tepper G.	95	Walters E.A.	247
Tomer J.L.	445	Wang K.	419
Tonner D.S.	445	Wang X.H.	455

Wassermann B. 239
Watts R.O. 223
Weckwerth R. 459
Weiss H. 177
Weige K. 27
Wendt H.R. 123
Western C.M. 49
Whaley K.B. 71
Whitaker B.J. 141
Winter M. 231
Winterbottom F. 463
Wittig C. 149
Wodtke A. M. 103, 131, 379, 401
Xu M. 103
Yan C. 287
Yang D. 263
Yang H. 419
Yang X. 15, 131, 279, 379
Yen Y.F. 455
Yuan L. 419
Zajfman D. 467
Zare R.N. 391, 441
Zhang J. 29, 215
Zhang J. 29, 215
Zhou Y. 263
Zhu Q-H. 263